Methods and tools for studying ecto-5’-nucleotidase (CD73)

Dissertation

zur

Erlangung des Doktorgrades (Dr. rer. nat.)

der

Mathematisch-Naturwissenschaftlichen Fakultät

der

Rheinischen Friedrich-Wilhelms-Universität Bonn

vorgelegt von

Riham Mohammed Omer Ali Idris

aus

Omdurman, Sudan

Bonn 2024

Angefertigt mit Genehmigung der Mathematisch-Naturwissenschaftlichen Fakultät
der Rheinischen Friedrich-Wilhelms-Universität Bonn

Gutachterin / Betreuerin: Prof. Dr. Christa E. Müller
Gutachterin: Prof. PD. Dr. Anke C. Schiedel

Tag der Promotion: 29.10.2024
Erscheinungsjahr: 2024

Die vorliegende Arbeit wurde in der Zeit von Novermber 2018 bis May 2024 am Pharmazeutischen Institut der Rheinischen Friedrich-Wilhelms-Universität Bonn unter Anleitung von Prof. Dr. Christa E. Müller durchgeführt.

DEDICATION

To

My parents

To

Mohamed, Leen, Yosr and Talia

Table of content

Abstract v
1. Introduction 1
1.1. Purinergic signaling 1
1.2. Purine receptors 1
1.3. Nucleobase, nucleoside and nucleotide transporters 2
1.4. Purinergic signaling molecules 3
1.5. Ectonucleoside triphosphate diphosphohydrolases (NTPDases) 5
1.6. Ectonucleotide pyrophosphatase/phosphodiesterase (NPPs) 6
1.7. Nicotinamide adenine dinucleotide glycohydrolase (CD38) 6
1.8. Alkaline phosphates (APs) 7
1.9. Acid phosphatases (AcP) 7
1.10. Ecto-5'-nucleotidase (CD73) 8
1.10.1. *NT5E*, the CD73 coding gene 8
1.10.2. Structure of CD73 9
1.10.3. Post-translational modifications of CD73 10
1.10.4. Substrates hydrolyzed by CD73 11
1.10.5. Cofactor preference 12
1.10.6. Substrate binding mode 12
1.10.7. Human CD73 expression 13
1.10.8. CD73 expression in human cancers 14
1.10.9. Immunosuppressive effects of CD73-generated adenosine 16
1.10.10. Role of CD73 in tumor growth and proliferation 17
1.10.11. Role of CD73 in tumor metastasis 18
1.10.12. Role of CD73 in tumor angiogenesis 18
1.10.13. CD73 as a potential immunotherapeutic target for cancer treatment 19
1.11. Biochemical methods to study CD73 20
1.11.1. Steady-state enzyme kinetics 25
1.11.2. The significance of K_M and V_{max} 27
1.11.3. Enzyme inhibitors 28
1.11.3.1. Competitive inhibition 28
1.11.3.2. Noncompetitive inhibition 29

1.11.3.3. Uncompetitive inhibition 29
1.12. Binding assays 30
1.12.1. Theoretical background of binding assays 31
1.12.2. Saturation binding 32
1.12.3. Time-course of binding and dissociation 33
1.12.4. Competition binding experiment 34
1.12.5. Radioligand binding assays 35
1.12.6. NanoBRET binding assays 38
1.13. CD73 inhibitors 41
1.13.1. Small molecule CD73 inhibitors 41
1.13.1.1. Nucleotide analogs 42
1.13.1.2. Non-nucleotidic inhibitors of CD73 49
1.13.1.3. Natural products and derivatives as CD73 inhibitors 55
1.13.2. Monoclonal antibodies 56
1.14. Anti-CD73 candidates in clinical trials 57
1.15. Pharmacological probes to study CD73 61
2. Published articles 64
2.1. 2-Substituted AMPCP derivatives 64
2.2. 3-Methylcytidine-5'-α,β-methylenediphosphonate as CD73 inhibitor 67
3. Manuscript prepared for publishing 71
3.1. Establishment of a radioligand binding assay for CD73 71
3.2. Nano-luciferase tagging of soluble and membrane-bound CD73 and establishment of NanoBRET assays 113
4. Preparations and samples of CD73 141
4.1. Recombinant soluble rat CD73 141
4.2. Recombinant soluble mouse CD73 141
4.3. Recombinant soluble human CD73 145
4.4. Recombinant soluble human CD73 with 6xHis-tag at the C-terminus 148
4.5. Phospholipase C-treated MDA-MB-231 cells 150
4.6. Ecto-5'-nucleotidase (CD73) in milk-derived extracellular vesicles (EVs) 152
4.7. Summary and outlook 153
4.8. Experimental 155
5. Identification of potential modulators for CD73 165
5.1. AMPCP-based CD73 competitive inhibitors 165

5.1.1. N^6- Substituted AMPCP derivatives 165
5.1.2. 2-Halo-N^6-mono- and N^6-disubstituted AMPCP derivatives 171
5.1.3. N^6-alkynyl-AMPCP derivatives 176
5.1.4. 7-Deaza-AMPCP derivatives 177
5.1.5. Conjugated AMPCP derivatives 179
5.1.6. Conclusions and outlook 183
5.2. Biological evaluation of a series of nucleotide mimetic at CD73 185
5.2.1. Pharmacological test results 185
5.2.2. Summary and outlook 190
5.3. Effects of adenine-derived fragments and nucleotide mimetics on the activity of soluble human CD73 190
5.3.1. Results 190
5.3.2. Summary and outlook 195
5.4. Identification of non-nucleotide-derived inhibitors of CD73 195
5.4.1. Pharmacological evaluation results 196
5.4.2. Summary and outlook 206
5.5. Xanthine derivatives as allosteric modulators of CD73 207
5.5.1. Results 207
5.5.2. Summary and outlook 211
5.6. Screening of potential CD73 modulators with a heterocyclic scaffold 212
5.6.1. Results 212
5.6.2. Summary 214
5.7. Screening of thiophosphate nucleotides derivatives at human CD73 214
5.7.1. Results 214
5.7.2. Summary and outlook 217
5.8. Summary of activities of allosteric CD73 modulators 217
5.9. Experimental methods 218
6. Functionalized CD73 inhibitor for nanogel preparation 222
6.1. Results 222
6.2. Summary and outlook 227
6.3. Experimental methods 227
7. Incomplete projects 228
7.1. AMP-based derivatives and analogs as inhibitors of human CD73 228
7.2. Sulfonamides as inhibitors of human CD73 231

References 236
List of abbreviations 276
Acknowledgements 278
Appendices i
Appendix I: 2-Substituted AMPCP published article ii
Appendix II: Cytidine-based CD73 inhibitor published article xlii
Appendix III: Screening of imipenem and related compounds at human CD73 lxvii
Appendix IV: DNA sequences of various CD73 constructs lxx

Abstract

Ecto-5'-nucleotidase (CD73), a glycosylphosphatidylinositol (GPI)-anchored glycoprotein expressed mainly in the membranes of immune and endothelial cells and released in exosomes or as a soluble protein, has emerged as a potential target in cancer immunotherapy. CD73 is the main extracellular protein that catalyzes the hydrolysis of AMP to adenosine. CD73 expression is upregulated in several types of cancer, resulting in a surge in extracellular adenosine concentration in the tumor milieu. Adenosine activates adenosine receptors, thereby exerting immunosuppressive effects and enhancing tumor proliferation and metastasis. Small molecule inhibitors of CD73 and monoclonal antibodies are currently being evaluated in clinical trials as monotherapy or in combination for cancer therapy.

Research on small molecule inhibitors of CD73 has already identified potent α,β-methylene-ADP analogs (AMPCP derivatives) with K_i values in the subnanomolar range. In this study, we aimed to explore the structure-activity relationships (SARs) of AMPCP derivatives and to identify new scaffolds with potentially more favorable pharmacokinetic profiles as inhibitors of CD73. We identified several highly potent inhibitors of CD73 based on N^6-substitued AMPCP showing picomolar potency (for example, PSB-19294 and PSB-19301). Additionally, potent derivatives with reduced molecular weight were obtained (e.g. N^6-alkynyl-AMPCP and 2-substituted AMPCP derivatives). An adenine-based α-carboxy-phosphononucleoside derivative (Cork82) was identified as a dual CD73/CD39 inhibitor with moderate potency. Several hit compounds that target allosteric sites on CD73 have been identified. For example, indole scaffolds have been thoroughly studied, leading to the identification of the hit compound PZB17718005A. An anthraquinone-based inhibitor, PZB17718022A, has been identified displaying submicromolar potency. Interestingly, these inhibitors selectively inhibited recombinant soluble human CD73, but not membrane-anchored CD73 natively expressed in MDA-MB-231 cells. Moreover, a xanthine derivative (GR178) was identified as a potent activator of human CD73. Such a compound has potential for the treatment of inflammatory and cardiovascular diseases.

Biological results obtained for several scaffolds showed discrepancies between rat and human CD73 or between soluble and membrane-bound CD73. This observed selectivity prompted us to express various soluble human and mouse CD73 proteins and to

additionally study a phospholipase C-cleaved soluble CD73 preparation. Modulators that were inactive at membrane-bound CD73 were also inactive at the cleaved soluble CD73, suggesting that variations in the glycosylation pattern of CD73 might affect the inhibitors' activity determined on MDA-MB-231 tumor cells. The obtained results indicated that a C-terminal His-tag did not interfere with the activity.

A further aim was to establish new binding assays for CD73 to enable studies of the binding kinetics and residence times of inhibitors. Radioligand binding assays and nano-luciferase bioluminescence resonance energy transfer (NanoBRET) assays were successfully developed and applied to characterize a series of CD73 inhibitors. Moreover, through nano-luciferase tagging of the soluble and membrane-bound forms of CD73, we provide structural insights, namely which sites and methods are tolerated for conjugation of CD73 without affecting enzyme functionality.

This study provides valuable insights into the biochemistry and pharmacology of the promising drug target CD73, a key player in purinergic signaling.

1. Introduction

1.1. Purinergic signaling

The concept of purinergic signaling (i.e., nucleotides acting as chemical transmitters and modulators) was proposed in early 1970 by Burnstock. However, it was not accepted until the 1990's when the involved receptors were cloned and characterized.[1] Purinergic receptor signaling is crucial in many biological processes in all organs and tissues, e.g. exocrine and endocrine secretion, platelet aggregation, endothelium-mediated vasodilatation, modulation of the immune system, and the control of cell proliferation, differentiation and apoptosis.[2,3]

1.2. Purine receptors

Purinergic receptors have been classified into three classes: P0 receptors, P1 receptors, and P2 receptors.

P2 receptors. Extracellular nucleotides, e.g., adenosine triphosphate (ATP), adenosine diphosphate (ADP), uridine triphosphate (UTP), and uridine diphosphate (UDP), act on P2 receptors. The P2 receptors are subclassified into two families: metabotropic P2Y receptors (P2YRs, eight subtypes) and ionotropic P2X receptors (P2XRs, seven subtypes). P2YRs are G protein-coupled receptors (GPCRs) with different preferences for ATP, UTP, ADP, UDP and other nucleotides, including nucleotides, sugars and dinucleotides such as UDP-glucose and Ap_4A.[4] On the other hand, ATP activates P2XRs which are ligand-gated, cation-selective channels permeable to Na^+, K^+ or Ca^{2+}.[5]

P1 receptors. Adenosine interacts with P1 receptors which are G protein-coupled comprising four subtypes, A_1, A_{2A}, A_{2B}, and A_3ARs. As members of the GPCR superfamily, P1 receptors possess a seven α-helix transmembrane structure, with an extracellular amino-terminus and an intracellular carboxy-terminus. *N*-glycosylation sites in the N-terminal domain can affect trafficking of the receptors to the plasma membrane. The C-terminus possesses serine and threonine residues which are targets for phosphorylation by protein kinases enabling receptor desensitization. Moreover, the C-terminus and the third intracellular loop enable coupling of the ARs to G proteins. A_1 and A_{2A}ARs display high affinity for adenosine (nanomolar range) while A_{2B} and A_3AR typically exhibit relatively

low affinity for adenosine (micromolar range). They show differential coupling to adenylate cyclase thereby modulating cyclic adenosine monophosphate (cAMP) levels. A_1 and A_3ARs are coupled to $G_{i/o}$ proteins and their activation inhibits cAMP production, while A_{2A} and A_{2B}ARs are coupled to $G_{s/olf}$ proteins leading to a stimulation of cAMP production.[6] Coupling to other G_α proteins has also been described.[7]

P0 receptors. In 2002, E. Bender et al. characterized an orphan GPCR in rat that interacts with adenine as an endogenous ligand (rAde1R).[8] Later on, Müller et al. designated adenine-activated GPCRs as purine P0 receptors.[9] The sequence of these receptors has been found to be closely related to the MAS-related G protein-coupled receptors (MRGPRs). The AdeR1s belongs to the MRGPRA subfamily expressed in rodents.[10] As indicated by mRNA expression, the Ade1R is highly abundant in the dorsal root ganglia of rats, specifically in the subset of small neurons, proposing a role in nociception. It was also found to be expressed in the lung, hypothalamus, peripheral blood leukocytes, and ovaries of rats.[8] In 2007, von Kügelgen was successful in cloning an additional adenine receptor from mouse brain (mAde2R, mouse MRGPRA9).[11] Further adenine receptors were cloned and characterized in mouse (mAde1R, mouse MRGPRA10) and hamster (cAdeR, hamster MRGPRA).[12] The mouse MRGPRA10 and the hamster MRGPRA were found to be coupled to G_i proteins resulting in inhibition of adenylate cyclase. Moreover, the hamster MRGPRA expressed in CHO cells was found to be additionally coupled to Gq proteins leading to an increase in intracellular calcium levels.[12] Several studies proposed the existence of human orthologs of adenine receptors. For instance, high plasma adenine levels were detected in patients with chronic renal failure [13] and proposed the existence of G_i protein-coupled adenine receptors in the basolateral membrane of the pig proximal tubule, which inhibited Na^+-ATPase activity.[14] However, so far, a human adenine receptor has not been cloned.

1.3. Nucleobase, nucleoside and nucleotide transporters

Two intrinsically distinct transporters families are responsible for cellular uptake and release of nucleobases and nucleobase analogs: sodium-dependent concentrative transporters (CNTs) and sodium-independent passive equilibrative transporters (ENTs) which facilitate diffusion depending on the substrate concentration gradient.[15]

Nucleosides and their analogs cross cellular membranes using the similar carriers, CNTs and ENTs.[16] In humans (h), the ENT family (current nomenclature is solute carrier organic

anion transporter (SLC43A3) consists of four isoforms (hENT1−4); they are in most cases facilitative uniporters (one molecule is transported independent of the other molecules).[16] hENT1 and hENT2 were additionally found to facilitate nucleobase transport.[15] CNTs (SLC23A4) are active symporters (two molecules are transported in the same direction) that transport nucleosides against theirs concentration gradient by thermodynamic coupling with an electrochemical gradient of cations. They comprise three isoforms (hCNT1−3).[16]

In general, nucleotides are proposed to be transported through facilitated diffusion by nucleotide-specific ATP-binding cassette (ABC) transporters such as the cystic fibrosis transmembrane conductance regulator (CFTR), the multidrug resistance proteins (P-glycoprotein (P-gp)), and the multiple organic anion transporters.[17]

Nucleotides, particularly ATP, are transported via the vesicular nucleotide transporter (VNUT) which belongs to the solute carrier organic anion transporter family (SLC17).[18] VNUT is energetically coupled to the vacuolar proton ATPase (V-ATPase) that hydrolyzes ATP and pumps protons into vesicles.[18]

1.4. Purinergic signaling molecules

ATP, ADP, UTP, UDP, UDP-glucose, dinucleotide polyphosphates (e.g., Ap_4A), and the nucleoside adenosine are the most important molecules that interact with purinergic receptors leading to a signal.[19]

ATP is present in high concentration inside the cell (5-10 mM) and typically only at nanomolar concentration in the extracellular space (10-100 nM).[5] Within the tumor milieu, in addition to hypoxia, a surge in ATP concentrations occurs (100–500 μM) which is attributed to plasma membrane damage caused by stressed or dying cells.[5] Independent of cellular damage, controlled ATP release may be mediated through vesicular release or channel-dependent mechanisms (e.g., through pannexins or connexins).[5] As ATP dephosphorylation is the main source of extracellular adenosine, the concentration of adenosine follows a similar manner of distribution as that of ATP. **Table 1** shows the concentration of ATP and its metabolite adenosine under physiological and pathological conditions.

Table 1.(Patho)physiological ATP and adenosine concentrations

Location	ATP	Adenosine
Intracellular	5-10 mM [5]	10-100 nM [20]
Extracellular (healthy state)	10-100 nM [5]	50-200 nM [21]
Extracellular (tumor milieu)	100–500 µM [5]	10–100µM [22]

In the extracellular space, the ATP concentration is controlled through its sequential dephosphorylation to adenosine caused by the action of enzymes, mainly ectonucleoside triphosphate diphosphohydrolase 1 (cluster of differentiation 39 (CD39)) and ecto-5'-nucleotidase (CD73).[17,23] Adenosine monophosphate (AMP) accumulation in the extracellular space is mainly achieved by the action of CD39 on ATP, however, alternative pathways can play a role e.g., direct hydrolysis of ATP by ectonucleotide pyrophosphatase/phosphodiesterase-1 (NPP1), and also by the sequential hydrolysis of NAD^+ by nicotinamide adenine dinucleotide glycohydrolase (CD38) and NPP1.[23,17] Interestingly, it was found that, the NPP1/CD73 alternative axis for adenosine production can compensate for the main CD39/CD37 pathway in CD39-deficient cells.[24] Although adenosine is mainly generated through the catalytic reaction of CD73, some CD73-independent pathways contribute to its extracellular concentration, such as prostatic acid phosphatase (PAcP),[25] and tissue nonspecific alkaline phosphatase (TNAP).[26,27]

Most of the pathways that contribute to AMP/adenosine concentrations in the extracellular space will be discussed very briefly in the following sections; the major contributors are shown in **Figure 1**. However, the main focus will be on the enzyme ecto-5'-nucleotidase (CD73).

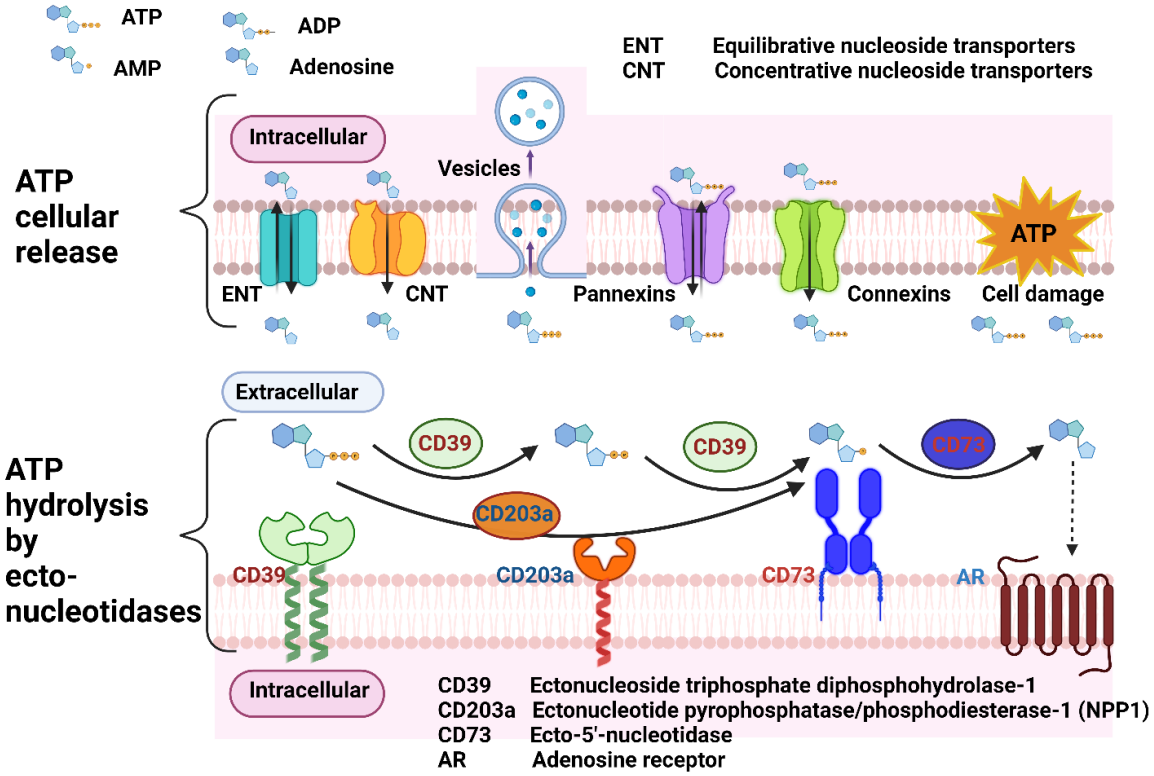


Figure 1. Regulation of nucleotide and nucleoside levels in the extracellular space. Created with BioRender.com

1.5. Ectonucleoside triphosphate diphosphohydrolases (NTPDases)

NTPDases are a family of enzymes that hydrolyze extracellular nucleoside triphosphates and diphosphates producing nucleoside monophosphates. The catalytic activity requires the presence of Ca^{2+} or Mg^{2+} ions and a pH value between 7–8. Up to now, eight members of this family have been identified. NTPDase1/CD39, NTPDase2, NTPDase3, and NTPDase8 are cell-surface located enzymes while NTPDases 4–7 are localized intracellularly. NTPDases 5 and 6 also exist as secreted forms. The plasma membrane-embedded members have a molecular mass of ~70–80 kDa and can exist as monomers or homooligomers (dimers or tetramers).[28,29] They contain two transmembrane domains with intracellular C- and N-terminus, and a large extracellular loop with 5 conserved hydrophobic domains known as apyrase-conserved regions (ACR). These ACRs determine the catalytic activity and substrate specificity of the enzymes.[30,31] The most important member of the family is NTPDase1/CD39 which is widely expressed on vascular endothelial, smooth muscle cells, exocrine pancreas, and on different immune cell types, e.g., monocytes, dendritic cells

(DCs), regulatory T (Treg) cells and natural killer (NK) cells. NTPDase2 is mainly expressed by pericytes and adventitia cells of the vascular system, and by astrocytes, non-myelinating Schwann cells and other glial cells of the peripheral and central nervous system.[32,33] Recent studies demonstrated its role in controlling purinergic signaling of embryonic, postnatal and adult neurogenesis [34] and the triggering of eye development.[35] The expression of NTPDase3 is mostly involved in the regulation of extracellular ATP in synaptic junctions; it thereby coordinates behaviors like sleep-wake cycle and feeding.[36] NTPDase8 is predominantly expressed in the bile canaliculi and large blood vessels of the liver.[37]

1.6. Ectonucleotide pyrophosphatase/phosphodiesterase (NPPs)

Seven isoforms of the NPP family exist (NPP1-7). NPP1 (known as CD203a) preferentially dephosphorylates ATP to AMP and diphosphate (pyrophosphate, PP_i) and thereby has a recognizable role in purinergic signaling.[38] NPP3 (CD203c) works on a broad range of substrates (for example, nucleoside triphosphates and diphosphates, NAD^+, UDP-sugars, and di-nucleoside polyphosphates), while NPP4 also has broad spectrum of substrates, but is so far mainly known for hydrolyzing the dinucleotides Ap_3A and Ap_4A.[38,39,40] NAD^+ was recently identified as a substrate for NPP5.[41] The catalytic activity of NPP2 (autotaxin), NPP6, and NPP7 is restricted to phospholipids.[23,17,38]

1.7. Nicotinamide adenine dinucleotide glycohydrolase (CD38)

CD38 is a cell surface glycoprotein that hydrolyzes NAD^+ to cyclic-ADP ribose (cADPR) and further to AMP. Alternatively, cADPR can be hydrolyzed by NPP1 producing AMP. CD38 is expressed on cell membranes of activated peripheral blood T and B lymphocytes, thymocytes, DCs, and plasma cells. It was also found to be released as soluble form.[23] Its effect is not limited to the generation of adenosine in the tumor microenvironment through the CD38/CD73 axis, but is also involved in regulation of the ribosylation by ADP-ribosyltransferase 1 and 2 (ART1, 2) which is reported to affect the activity of P2X7 receptors and more recently of CD73 as well (**Figure 2**).[23,42,43]

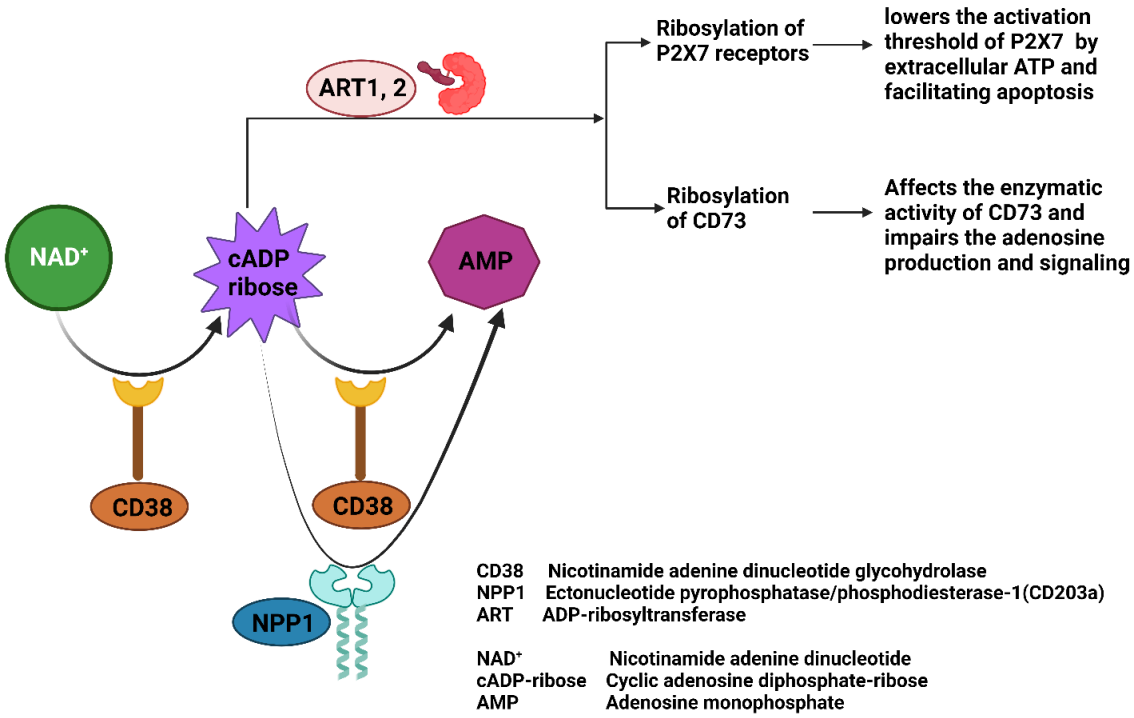


Figure 2. Regulation of cADP-ribose and AMP levels by CD38 and NPP1 and ART enzymes. Created with BioRender.com

1.8. Alkaline phosphates (APs)

APs are membrane-bound (GPI-anchored) isoenzymes that catalyze the dephosphorylation of a variety of phosphate-containing compounds such as nucleotides, diphosphates (pyrophosphates), inorganic polyphosphates, and glucose-phosphates thereby producing inorganic phosphate. Cofactors (two Zn^{2+}, one Mg^{2+} metal ions), and an alkaline pH (8 to 11) are required for optimum activity. APs are attached to the membrane through a glycosylphosphatidylinositol (GPI) anchor and are also released in soluble form.[44,45] APs are subdivided into tissue-specific AP (i.e. intestinal AP, placental AP and germinal APs), and tissue-nonspecific AP (TNAP) which is highly expressed in bone, liver, and kidney and is considered the major source of the circulating AP in serum.[46,47] Involvement of TNAP in bone mineralization, and metabolism of vitamin B6 in the liver has been described.[44,47]

1.9. Acid phosphatases (AcP)

AcPs catalyze the hydrolysis of phosphate ester bonds at an optimal pH below 7.[48] In human, acid phosphates comprise five isoenzymes: prostatic acid phosphatase (PAcP), lysosomal (LAcP), erythrocytic (soluble acid phosphatase, EAcP), osteoclastic (OAcP),

and macrophagic acid phosphatase (MAcP).[25,48] Acid phosphatases can also be grouped based on their resistance to inhibition by tartrate into tartrate-sensitive (PAcP) and tartrate-resistant AcP (OAcP and EAcP). AcPs are normally present at low concentrations in healthy individuals, however, significant changes occur in certain diseases (e.g., cancer) which suggests their usefulness as diagnostic biomarkers.[25,48] Human PAcP is one of the most studied AcP due to its clinical significance in prostate cancer. It is a glycoprotein comprised of two subunits each with a molecular weight of 50 kDa. PAcP can be localized intracellularly (cPAcP) or secreted into the seminal fluid (sPAcP). A third isoform containing a transmembrane domain was detected later on prostatic vesicles and membranes (TM-PAcP).[25]

1.10. Ecto-5'-nucleotidase (CD73)

Ecto-5'-nucleotidase (*e*N, CD73, EC 3.1.3.5) is a glycosylphosphatidylinositol (GPI)-anchored glycoprotein which belongs to the superfamily of metallo-phosphoesterases.[49] The cluster of differentiation 73 (CD73) was designated at the Fourth International Workshop on Human Leukocyte Differentiation Antigens (Vienna, February, 1989). Designation was based on results obtained from the full characterization of antibodies that inhibited enzymatic activity in both placental extracts and intact human T and B cells, and immunoprecipitated a 73 kDa protein from human placental extracts and the human myeloma cell line (U266), in addition to its immunofluorescent staining pattern on T and B cells.[50] CD73 is therefore utilized as a T and B lymphocyte differentiation marker.[51,52,53]

1.10.1. *NT5E*, the CD73 coding gene

In humans, the *NT5E* gene is located on chromosome 6. It encodes five transcripts (splice variants, shown in **Table 2**), however, only two transcripts are annotated by the Consensus Coding Sequence (CCDS). These transcripts encode for ecto-5'-nucleotidase isoform 1, and isoform 2. Isoform 1 is the canonical long CD73 protein that is catalytically active and is expressed as a homodimer on the cell surface. In contrast, isoform 2 is shorter, missing 50 amino acid residues (404–453), localized mainly in the cytoplasm; it is catalytically inactive.[54]

Table 2. *NT5E* gene transcripts (splice variants) [55]

Transcript ID	Name	bp	Protein	CCDS	UniProt Match
ENST00000257770.8	**NT5E-201**	**3562**	**574aa**	**CCDS5002**	**P21589-1**
ENST00000369651.7	**NT5E-203**	**3918**	**524aa**	**CCDS56439**	**P21589-2**
ENST00000369646.7	NT5E-202	974	264aa	-	Q96B60
ENST00000437581.1	NT5E-205	738	179aa	-	H0Y3X5
ENST00000416334.5	NT5E-204	689	230aa	-	H0Y7R7

In 2011, a group of scientists was able to identify several mutations (c.662C→A, p.S221X, c.1073G→A, p.C358Y, c.662C→A and c.1609dupA (V537fsX7)) in the *NT5E* gene that related to symptomatic arterial and joint calcification in three families.[56] All mutations resulted in low expression at the mRNA and protein levels as well as an enzymatically inactive CD73.[56] Hillaire and co-workers proposed that low and inactive CD73 led to decreased adenosine levels which in turn increases tissue non-specific alkaline phosphatase (TNAP) expression. High TNAP levels affect the concentration of diphosphate (pyrophosphate) and thereby increase calcification.[56] A couple of years later, the underlying mechanisms by which these mutations diminished the enzymatic activity of CD73 were investigated through the observation of subcellular trafficking of the wild-type (wt) and mutant fusion proteins using confocal microscopy and Western blot analysis.[57] All mutations resulted in a protein with impaired trafficking to the plasma membrane compared to the wt protein.[57]

A single nucleotide variation (ACG>GCG) was also reported creating the benign natural variant T376A of CD73 at a frequency of A=0.216517 (21.7%, 57310/264690, TOPMED).[58]

1.10.2. Structure of CD73

Based on the resolved crystal structures, human CD73 is a homodimeric protein. It has different apparent molecular weights (60-80 kDa) due to variations in glycosylation.[59,60] Each subunit of the homodimer has two structural domains, an N-terminal domain (residues 27–317) and a C-terminal domain (residues 337–549).[61] The enzyme dimerizes through the C-terminal domains which incorporate the substrate binding sites. The N-terminal domain accommodates two Zn^{2+} ions that are important for hydrolytic activity. C- and N-terminal domains are connected via a single α helix (residues 318–336) which provides the required elasticity during the shift between closed and open conformations. Upon substrate binding,

the N-terminal domains rotate (by 114°) into the closed conformation to form the active site with the substrate bound by the C-terminal domain. **Figure 3** depicts the main structural characteristics of CD73.[61]

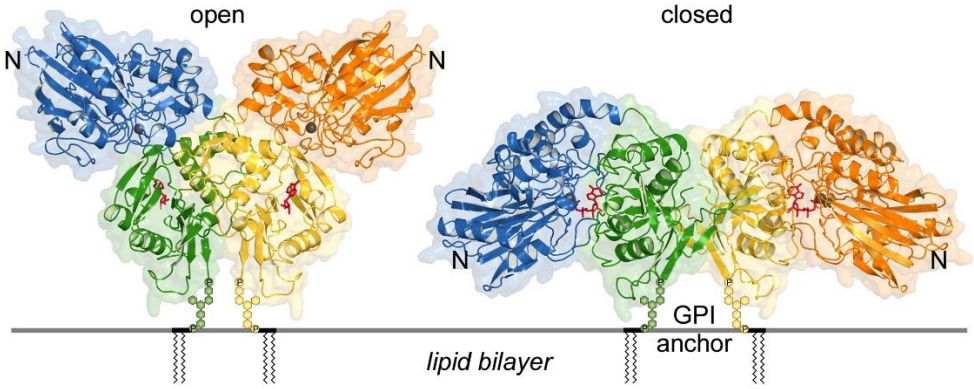


Figure 3. Structural features of open and closed conformation of human CD73.[61] Reprinted from Structure, 20, Knapp et al., Crystal Structure of the Human Ecto-5′-Nucleotidase (CD73): Insights into the Regulation of Purinergic Signaling, 2161–2173, Copyright (2012), with permission from Elsevier.

CD73 exists as membrane-bound and soluble forms. The soluble form is generated through cleavage of the GPI-anchor by the action of phosphatidylinositol-specific phospholipase C (PI-PLC) or by proteolytic cleavage through matrix metalloproteinase 9 (MMP-9).[62,63,64,65] Furthermore, CD73 can be released as CD73-containing extracellular vesicles (exosomes) present in many body fluids like synovial, pancreatic juice, milk and serum.[19,66]

1.10.3. Post-translational modifications of CD73

Several secondary modifications are known to regulate the activity of proteins, among them is ADP-ribosylation mediated by ADP-ribosyltransferase 1 (ART1) utilizing NAD^+ as a substrate. Recent studies on arginine-specific mono-ADP-ribosylation in human CD73 revealed six sites of which residues R328, R354, and R545 seem to have the potential to affect the enzymatic activity of CD73 after ribosylation, either due to direct involvement in substrate binding or by effects on the stability of the dimer.[43] ADP-ribosylation was reported to massively impair adenosine production and signaling. Consequently, high expression of CD73 might not be used as a predictor for an elevated level of the anti-inflammatory immunosuppressive signaling molecule adenosine.[43]

CD73 has four *N*-linked glycosylation sites (asparagine sites 53, 311, 333 and 403). Heterogenous glycosylation of these sites has led to isoforms with different molecular

weight and catalytic activity.[22,67] Changes in the *N*-linked glycoproteome are traits of many diseases especially cancers.[68] For example, in human hepatocellular carcinoma, CD73 expressed by tumor cells showed deficiency in hybrid and complex glycans on residues N311 and N333 as compared to the non-tumor CD73.[69] A site-directed mutagenesis study to block glycosylation on these sites produced CD73 with considerable loss of catalytic activity and perinuclear localization.[69] In contrast, a highly glycosylated, catalytically active isoform of the enzyme was identified in the plasma of patients with cervical cancer.[22] However, deglycosylation of mouse CD73 expressed in liver and muscle of dystrophic *Lama2dy* mice did not modify its hydrolytic activity.[70,71]

Furthermore, the human natural killer-1 (HNK-1) epitope, a sulfated glucuronic acid-containing carbohydrate, has been identified on the CD73 surface of Torpedo electric organs and in developing kitten visual cortex.[72,73] As many glycoproteins involved in cell adhesion and recognition possess the HNK-1 epitope, a nonenzymatic activity (i.e. participate in cell-cell or cell-extracellular matrix connections) was proposed for CD73.[72]

1.10.4. Substrates hydrolyzed by CD73

Ecto-5'-nucleotidase mainly hydrolyzes the phosphoric ester bond of ribonucleoside 5'-monophosphates (**Figure 4**) and less effectively that of deoxyribonucleoside monophosphates yielding the corresponding nucleoside and inorganic phosphate. The catalytic activity of the enzyme is fully dependent on Zn^{2+} as a cofactor and on homodimer formation. The pH optimum for catalysis is between 7 and 8.[67]

Its preference for ribonucleoside 5'-monophosphate substrates is in the following order: AMP > UMP > CMP > IMP > GMP, AMP being the most preferred substrate with a K_M value of 1-50 µM. Binding to AMP is stereoselective, only D-ribose derivatives being hydrolyzed.[3,19,74]

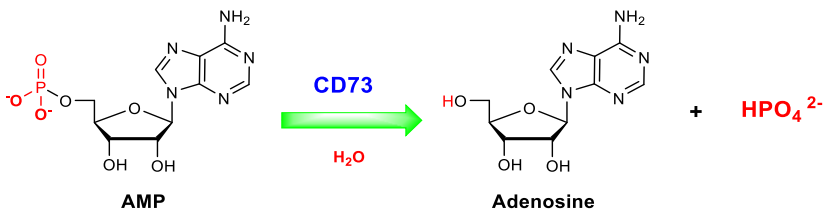


Figure 4. Hydrolytic reaction of AMP by CD73.

It was reported that human CD73 is able to hydrolyze nicotinamide mononucleotide and NAD^+, but with much lower turnover rates.[75]

Interestingly, some 2-substituted AMP derivatives, like 2-hexylthio-AMP, 2-cyclopentylthio-AMP, 2-cyclohexylmethylthio-AMP, and 2-cyclohexylethylthio-AMP were found to be hydrolyzed by CD73 to the corresponding 2-substituted adenosine derivatives which show a relatively high $A_{2A}AR$ agonistic activity. These prodrugs preferentially hydrolyzed at the targeted tissue sites with high CD73 expression due to inflammation.[76,19]

1.10.5. Cofactor preference

In 2012, Heuts et al. reported the preference of CD73 for different metal cations.[27] In that study, the enzyme was stripped off Zn^{2+} through dialysis against a 2 mM solution of ethylenediaminetetraacetic acid (EDTA). Activity of the produced apoenzyme was lost and could only be recovered when reconstituted with Co^{2+} (30%) or Zn^{2+} (60%). Fe^{2+} and Cu^{2+} were found to further reduce the residual activity while Mn^{2+} and Ni^{2+} enhanced the activity slightly. Mg^{2+} showed no considerable effect.[59] The obtained results confirmed earlier reports on CD73 catalytic activity being Zn^{2+}-dependent.[49,77] Moreover, interaction with Zn^{2+} has also been described to affect the inhibitory activity of AMPCP-derived CD73 inhibitors.[27]

1.10.6. Substrate binding mode

A high-resolution crystal structure of human CD73 bound to its preferred substrate AMP in an open conformation became recently available (PDB 7P9N, 1.55 Å resolution).[74] The obtained crystal structure showed positioning of the adenine base between phenylalanine residues 417 and 500 of the C-terminal domain through π-stacking of the aromatic rings. Possible H-bond interactions between N3 of the adenine ring and the NH_2 side chain of N390, and adenine N1 and two water molecules were illustrated. The ribose sugar is centered through interactions with sidechains of N390 and D506 and the backbone of residues G392 and G447. The α-phosphate group is coordinated by R354 and R395 (**Figure 5**). No major changes were observed when the structure of CD73 in complex with AMP is superimposed over the unligated CD73 structure (PDB ID 6TVE)[78] indicating that the binding site is preconfigured for AMP binding. Only, insignificant movement of R354, R395 and F417 sidechains was noticed. Furthermore, F500 was unable to attain a secondary

conformation seen on the unligated crystal structure due to steric hindrance by the adenine ring. An attractive feature for structure-based inhibitor design is the water-filled C2 pocket. It was found occupied by a glycerol molecule (from the cryo-buffer used) interacting with the polar sidechains of the pocket. Consequently, a glycerol-like substituent at the C2-position of the adenine base could be a successful inhibitor-designing strategy. Overlay of the AMP-ligated crystal structure in the CD73 open conformation with the AMPCP-ligated one in the closed state (PDB ID 2H2I)[61] showed no major differences regarding binding interactions. Thus, the open form crystal structure is considered applicable to study binding of other nucleotide-based inhibitors.[74]

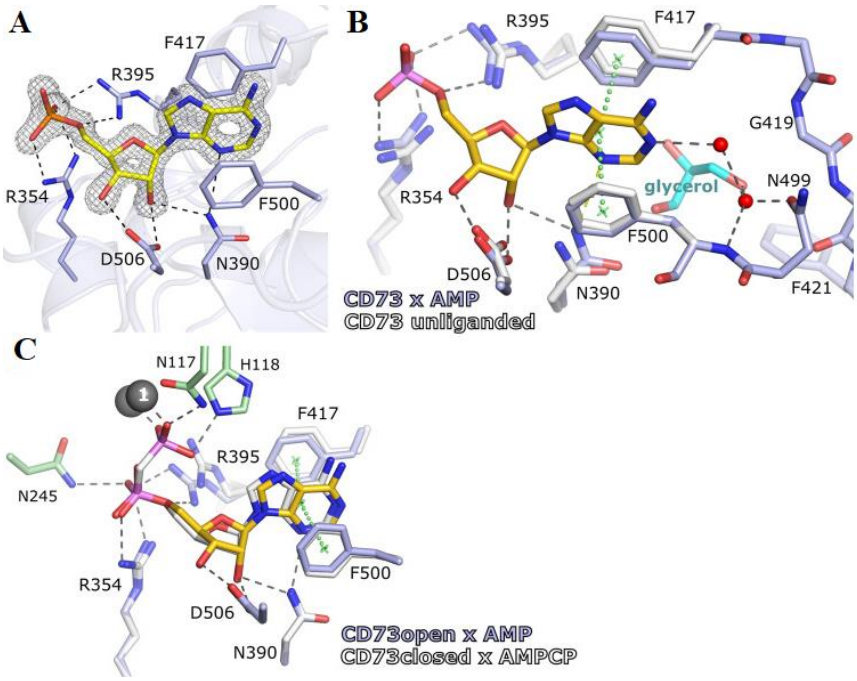


Figure 5. Binding of AMP to the catalytic site of human CD73.[74] **A**) Substrate binding mode of AMP (yellow) to CD73 in open state. **B**) $CD73^{open}$ x AMP superimposed with unliganded CD73 (PDB 6TVE) in open state. **C**) Superposition of $CD73^{open}$ x AMP with $CD73^{closed}$ x AMPCP (PDB 4H2I). Taken from Purinergic Signal. 2021 Dec; 17(4): 693–704. The article is under a Creative Commons License (http://creativecommons.org/licenses/by/4.0/.).

1.10.7. Human CD73 expression

Immune cells. In peripheral human blood, CD73 is expressed mainly by B cells (75%), 50% of $CD8^+$ T cells, and to a lesser extent by $CD4^+$ T cells (10%), and natural killer (NK) cells (2%- 5%).[79] Although the proportion of $CD73^+$ $CD4^+$ T cells is low under normal conditions, chronic inflammation as in inflammatory bowel disease (IBD) significantly

elevates its level.[80] In healthy individuals NK cells have undetectable CD73 expression in contrast to tumor-infiltrating NK cells which exhibit high levels of expression.[81,82] As a point to be mentioned, most of the immune cells co-express CD39 and CD73, indicating a role of adenosine generation in modulating the immune system.[81]

Central nervous system. CD73 was reported to be localized in the brain striatum[83,84] and also in the globus pallidus, choroid plexus, and meninges.[84]

Cardiovascular system. CD73 expression was identified on endothelial cells,[85,86] smooth muscle cells [87] and resident immune cells.[88]

Lung. Human pneumocytes showed high expression of CD73 in membranes and cytoplasm, epithelial and endothelial cells.[89,90,91]

Liver. CD73 is expressed on the apical membrane of hepatocytes of a normal liver and to lower levels in endothelial cells.[92] In the course of hepatic inflammation, $CD73^+$ regulatory B cells (B regs) are recruited to the liver.[93]

Kidney expression. Kidneys show high CD73 expression.[94] CD73 is abundantly expressed on the luminal membranes of proximal tubular cells, the peritubular interstitium, intercalated epithelial cells of the distal nephron, and cortical fibroblasts.[95,96]

Intestinal expression. CD73 is highly expressed in intestinal epithelial cells.[97] A reported study showed that CD73 is generally highly abundant in the colon with catalytic activity twice as high as that manifested in kidney.[94]

1.10.8. CD73 expression in human cancers

Studies and reports on different types of tumors have identified upregulation of CD73 expression as a prognostic marker for poor clinical outcomes in several cancers e.g., breast cancer, ovarian, melanoma, glioblastoma, head and neck cancer, colorectal, kidney, bladder and prostate cancers.[98,99] Hypoxia and activation of hypoxia-inducible transcription factors (HIF) are among the major driving factors for CD73 upregulation in the tumor microenvironment (TME).[100,101,102] However, further oncogenic pathways contribute to CD73 overexpression including but not limited to Wnt (wingless/integrated), epithelial-to-mesenchymal transition (EMT), Tumor protein 53 (TP53), Kirsten rat sarcoma viral oncogene homolog (KRAS), transforming growth factor-β (TGF- β), and inactivation of estrogen receptor signaling.[103,104,105,106,107,108]

In contrast, high CD73 expression was linked to good prognosis in a stage I-III breast cancer study and in endometrial tumors.[109,110] A molecular mechanism in endometrial carcinoma was found to be based on positive CD73-generated adenosine effects on endothelial cell integrity through activation of the A_1AR.[110] In the breast cancer study, immunohistochemistry was applied to quantify CD73 expression using an anti-CD73 antibody. It has, however, been proven that CD73 expression is not always linked to its catabolic activity; secondary modifications like alternative splicing, ribosylation and glycosylation which result in catalytically-modified isoforms, some of which are species- and tissue-specific, should be considered.[54,43,22,71] Moreover, co-expressed adenosine receptor subtypes could also affect the overall outcomes of high CD73 expression in the tumor milieu.[111,112]

Besides being a prognostic marker, CD73 overexpression was also related to chemotherapy resistance.[99] In triple negative breast cancer, chemoresistance to doxorubicin, and more recently to cisplatin was related to high CD73 expression which results in activation of A_{2A}ARs by adenosine.[108,113] CD73 was found to modulate the expression and activity of multidrug-resistance protein-1 (MRP-1) which is involved in vincristine-resistant glioblastoma multiforme cells.[114,115]

Interestingly, high plasma concentrations of soluble CD73 (sCD73) were detected in cancer patients as well as in patients with acute inflammatory pancreatitis.[116,117] It was shown that A_{2B}AR activation in erythrocytes by sCD73-produced adenosine enhances oxygen delivery and adaptation to hypoxia. However, it is still to be investigated whether the tumor makes use of this interaction to adapt to hypoxia.[118]

Recently, cancer-derived exosomes were identified to be positive for CD73 and other ectonucleotidases (e.g., CD39) which might also contribute to immune evasion and tumor metastasis.[119,120]

As a consequence of high CD73 abundance, adenosine accumulates in the TME and its immunosuppressive and tumorigenic effects through interaction with A_{2A} and A_{2B}ARs become predominant (summarized in **Figure 6**).[121]

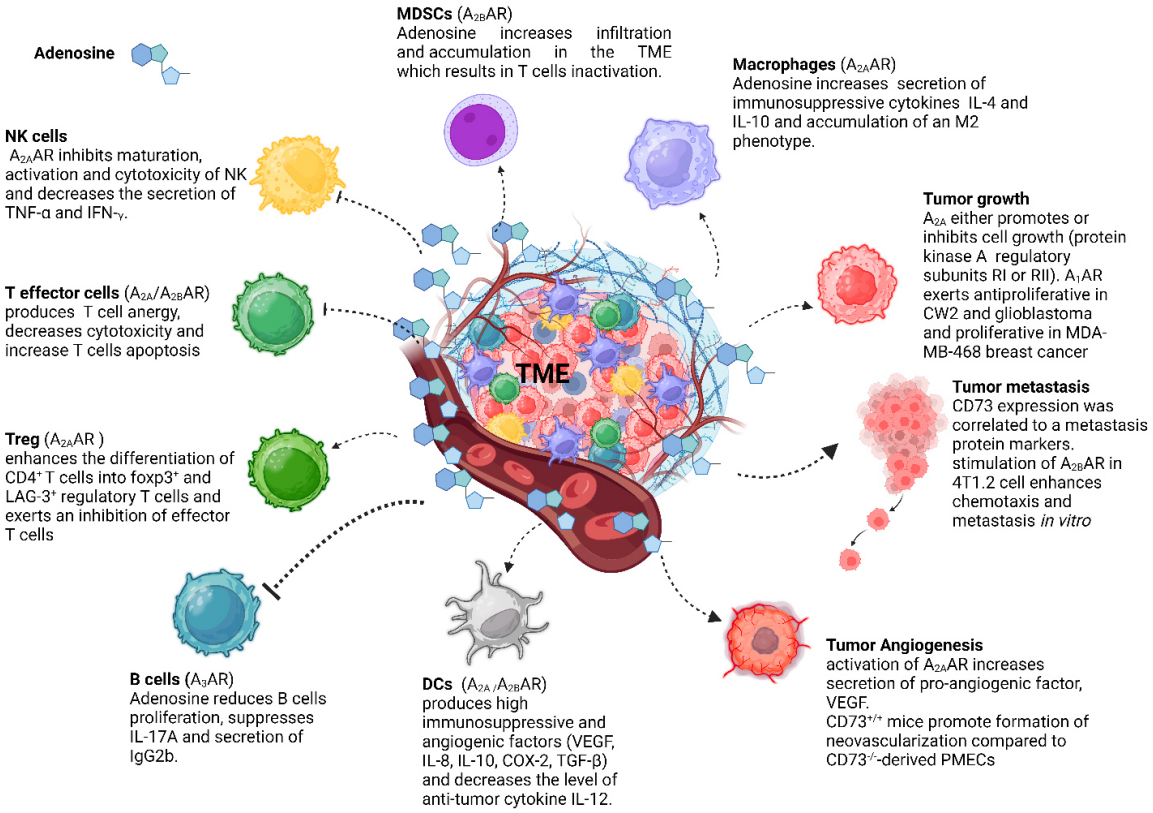


Figure 6. Adenosine effects promoting immune escape, tumor growth and metastasis. MDSCS: myeloid-derived suppressor cells; CW2: human colon cancer cell; PMECS: pulmonary microvascular endothelial cells; TME: tumor microenvironment. Created in BioRender.com.

1.10.9. Immunosuppressive effects of CD73-generated adenosine

Elevated levels of adenosine in the TME inhibit maturation, activation and cytotoxicity of NK cells mediated through A_{2A}ARs. Adenosine decreases the release of tumor necrosis factor-α (TNF-α) and interferon-γ (IFN-γ) by NK.[122,123] Adenosine, through A_{2B}ARs promotes differentiation of dendritic cells (DCs) into a distinguished population of cells called adenosine-differentiated DCs which produce highly immunosuppressive and angiogenic factors like vascular endothelial growth factor (VEGF), interleukin 8 (IL-8), IL-10, cyclooxygenase-2 (COX-2), and transforming growth factor β (TGF-β).[124] In addition, activation of A_{2A}ARs on DCs leads to diminished levels of the anti-tumor cytokine IL-12.[125]

It was also reported that myeloid-derived suppressor cells (MDSCs) showed increased infiltration and accumulation in the tumor-milieu mediated by A_{2B}ARs activation which results in T cells inactivation.[126] On the other hand, activation of A_{2A}ARs on macrophages

leads to an increase in secretion of tumor-growth promoters and immunosuppressive cytokines, IL-4 and IL-10.[127] Furthermore, adenosine increases the accumulation of the M2 phenotype of macrophages which is pro-tumorigenic.[123]

Adaptive immunity is also affected. Adenosine activates A_{2A}ARs on effector T cells inducing T cell anergy by decreasing antitumor activity and increasing T cell apoptosis.[123,128,129] Adenosine also enhances the differentiation of $CD4^+$ T cells into $foxp3^+$ and LAG-3^+ regulatory T cells (Treg) and interacts with A_{2A}ARs on Treg to exert a Treg-mediated inhibition of effector T cells.[123] High adenosine suppresses IL-17A and reduces B cell proliferation and secretion of IgG2b through A_3ARs.[123,130]

Taken together, it is obvious that CD73-generated adenosine modulates the immune response through divergent pathways leading to suppression of anti-tumor immune cells while activating immunosuppressive regulatory cells. Thus, inhibiting CD73 or antagonizing adenosine receptors (A_{2A}, A_{2B}) is considered as potential strategy in oncological immunotherapy.

1.10.10. Role of CD73 in tumor growth and proliferation

In addition to the immunomodulatory roles of CD73-generated adenosine, adenosine possesses also growth-modulating effects mediated through A_{2A}ARs, which either promote or inhibit cell growth depending on the abundance of a specific subtype of the cAMP-dependent protein kinase A (PKA) regulatory subunits RI or RII.[131,132]

Studies in renal cell carcinoma (769-P and Caki-1 cell lines) indicated that, pharmacological blockage with a selective A_{2B}AR antagonist (MRS1754), and A_{2B}AR knockdown reduced the proliferation and migration *in vitro* and tumor growth *in vivo* using nude mice.[133]

Furthermore, A_3AR agonists were found to strongly inhibit cancer cells growth in prostate, malignant mesothelioma, and glioblastoma cells. Moreover, A_3AR agonists, CF101 and CF102, showed antitumor effect when tested in *in vivo* animal models of various cancers such as, colorectal, prostate, melanoma and liver carcinomas.[134]

It was reported that A_1AR agonists exert antiproliferative effects on breast cancer cells T47D, HS578T and MCF-7, and on leukemia MOLT-4 cells.[135,136,111] In agreement with these findings, adenosine was found to inhibit glioblastoma growth through A_1ARs[137] and

more recently to induce apoptosis of the human colon cancer cell line (CW2) through activation of caspase-3, -8, and -9 via A_1AR stimulation.[138] In contrast, several studies demonstrated the proliferative effect induced by the A_1ARs, for example, resulting in apoptosis observed in the A_1AR-depleted-breast carcinoma cell line MDA-MB-468.[139]

1.10.11. Role of CD73 in tumor metastasis

CD73 expression was correlated to metastasis protein markers α_5-, β_1-, β_3-integrins, and CD44.[140] Stimulation of A_{2B}ARs in 4T1.2 breast tumor cells enhances chemotaxis and metastasis *in vitro*.[141] Inactivation of CD73 has been confirmed to inhibit adhesion to extracellular matrix (ECM) proteins and subsequent migration of human mammary cancer cells,[142,143] and also melanoma cells.[140]

According to Stagg et al. (2011), lung metastasis of B16F10 melanoma was reduced in $CD73^{-/-}$ mice, indicating the pivotal role of host-derived CD73 in cancer spread.[144] The pro-metastatic activity of CD73 was attributed to its expression on nonhematopoietic cells (mainly endothelial cells).[144] Later on, the same research group reported that metastasis of B16F10 melanoma cells was correlated with CD73 expression in wt mice and mediated through activation of A_{2A} and A_{2B}ARs. Activation of A_{2A}ARs inhibited perforin-dependent NK cell cytotoxicity, while an immune-independent pathway mediated through A_{2B}ARs was proposed to be involved in B16F10 melanoma cell metastasis.[145] Furthermore, CD73 expression was reported to promote epithelial plasticity and invasiveness through activation of epithelial-mesenchymal transition (EMT) in gallbladder carcinoma.[103]

In studies with monoclonal anti-CD73 antibodies (mAbs), therapy was successful in inhibiting breast cancer growth and metastasis through an adenosine-dependent mechanism in immune-competent mice.[141] Another study reported a non-enzymatic action mediated through clustering and internalization of CD73 resulting in alleviating metastasis of mammary carcinoma in a mouse model of human metastatic breast cancer.[146]

1.10.12. Role of CD73 in tumor angiogenesis

In a recent study, CD73-deficient C57BL/6 mice inoculated with B16F10 melanoma cells showed a decrease in vascular density compared to wild-type mice. CD73 inhibition with AMPCP further reduced the vascular beds.[147] Pulmonary microvascular endothelial cells (PMECs) derived from $CD73^{+/+}$ mice promoted neovascularization compared to $CD73^{-/-}$-derived PMECs. [148] This angiogenic effect was ascribed to the upregulation of the pro-

oncogenic cyclin D1 protein induced by CD73.[148] Moreover, adenosine mediated the production and secretion of the potent pro-angiogenic vascular endothelial growth factor (VEGF) via activation of A_{2A}ARs.[148] This adenosine-dependent angiogenic effect has also been confirmed using a 4T1.2 breast cancer mouse model in a study by Allard et al in 2014.[149] In an *in vitro* study using CD73-shRNA-expressing HUVECs (CD73 gene-silencing using CD73-short hairpin RNA-expressing human umbilical vein endothelial cell) co-expressing A_{2A} and A_{2B}ARs, CD73 expression was found to be linked to angiogenesis independent of its catabolic activity.[149]

Based on published results, both hydrolytic and non-hydrolytic functions of CD73 have been reported to promote tumor progression *in vitro* and in mouse model. Hydrolytic CD73 activity producing adenosine suppresses the immune system, induces angiogenic VEGF production, and enhances tumor growth and metastasis. Moreover, CD73 was proposed to promote the formation of capillary-like structures in endothelial cells[149] and to facilitate tumor cell adhesion to ECM proteins through pathways independent of its enzymatic activity.[150,151] Some authors suggested that the use of a more potent and selective CD73 inhibitor than the widely applied AMPCP would possibly exclude any residual hydrolytic activity and thus clearly distinguish between enzymatic and non-enzymatic functions of CD73.[99] However it should be noted that some of these studies did not employ AMPCP but rather CD73-deficient mice or tumor cells as a control to prove their hypothesis.

1.10.13. CD73 as a potential immunotherapeutic target for cancer treatment

CD73 is over-expressed in many types of tumors (extensively reviewed in[98,152]), and host-derived CD73 involvement in cancer progression was confirmed,[144] in addition to the immunosuppressive, proliferative, and pro-metastatic effects of CD73-generated adenosine (refer to sections 1.10.9-12). Taken together, it has become obvious that CD73 is a potential target in clinical oncology. Indeed, several anti-CD73 mAbs and small molecule CD73 inhibitors have been developed with proven anti-tumor effects in preclinical settings.[146,153,154,155,156,157] For instance, anti-CD73 mAb or AMPCP significantly reduced tumor growth and metastasis in breast cancer-bearing mice.[146,158] Quemliclustat (AB680), a small molecule inhibitor of CD73, inhibited CD73 in the TME and showed synergistic effects with anti-PD-1 therapy in a preclinical mouse model of melanoma.[157] Several anti-CD73 mAbs (MEDI9447, BMS986179, IPH5301, CPI-006/CPX-006, TJ004309) [27,123,159]

and small molecule inhibitors (AB680 (**Figure 19**), ORIC-533 (**Figure 20**), LY-3475070 (**Figure 30**)) are currently being evaluated in clinical trials.

Moreover, the correlation between CD73 expression and prognosis in several cancers in addition to personalized patient response to chemotherapy advocate for its use as potential biomarker in clinical diagnosis and translation.

1.11. Biochemical methods to study CD73

Several methods based on the quantification of the dephosphorylation products of CD73 were developed and applied for the screening and biological characterization of various CD73 activity modulators, and have played crucial roles in drug development campaigns (**Table 3**). These assays involve chromatographic,[160,161] spectroscopic (UV/Vis, NMR, MS),[162,163,164,165,166] electrophoretic,[167,168,169] radiometric,[170,171,172] and luminescence-based techniques.[173] Several colorimetric assays were developed to monitor CD73 activity, however, the malachite green assay is currently the most widely applied one. It is based on the quantification of inorganic phosphate through the generation of a colored complex between phosphomolybdate and the malachite green dye with a λ_{max} of 630 nm. This assay is considered one of the simplest formats and has been applied for screening of a large number of compound libraries. However, it shows low sensitivity, and a high substrate concentration has to be employed. Interference from colored, and phosphate-containing samples is another limitation.[166,174,175] To enhance the sensitivity of the assay, CMP was employed by researchers in Vitae Pharmaceuticals as a substrate instead of AMP. Since CMP has a higher K_M value for CD73 than that of AMP,[59,74] a higher concentration of CMP could be utilized in the assay that would still be beyond the K_M value for the enzyme. Accordingly, several types of inhibitors could be evaluated accurately.[176]

A capillary electrophoresis-based method with UV detection at 260 nm was developed.[167] The enzymatic reaction could be conducted either off-capillary or in-capillary.[167] In the case of the off-capillary method, the separation took 8 min with an eCAP fused-silica capillary and 40 mM borate running buffer (pH 9.1) using normal polarity. For the in-capillary method, the reaction is carried out inside a fused-silica capillary using a sandwich technique in which first the substrate, dissolved in Hepes buffer (10 mM, pH 7.4) is injected followed by enzyme, and then the substrate again, with an elution time of 4 min. This in-capillary method was applied to measure the enzymatic activity of CD73 natively expressed on

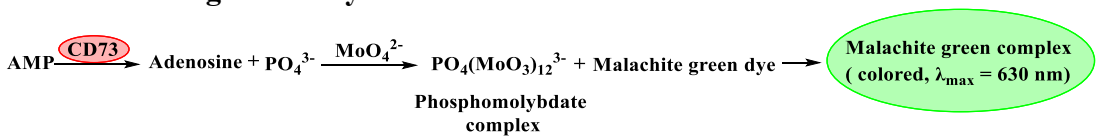
melanoma cell membranes offering a short determination time of around 6 min.[167] However, the method required high substrate concentrations (AMP of up to 500 μM) which restricts its ability to identify weakly competitive inhibitors; moreover, it is of limited applicability for high throughput screening (HTS). More recently, Raza et al. applied a reversed electroosmotic flow (EOF) to achieve a faster separation of nucleotide and nucleoside (< 2 min).[168] However, the same constraints of high substrate concentration (500 μM) and limited HTS applicability still exist.

One of the applied commercial screening methods developed by the research laboratory of MedImmune is based on the detection of luminescence emitted from ATP-dependent luciferin oxidation by luciferase.[177] AMP is a competitive inhibitor of luciferase. Addition of CD73 relieves the AMP-mediated inhibition of the luminescence signal and hence allows to indirectly quantify the reaction product adenosine. The simplicity of this method and its homogenous protocol facilitate its application when HTS is in demand. It also has low background interference. However, high substrate concentration is required (300 μM) coupled to the fact that ATP also exerts a (weak) competitive inhibition on CD73 activity which might affect the intensity of the produced light.

The drug discovery unit of Sanofi company published a RapidFire–tandem mass spectrometry (RF-MS/MS)-based multiplexing assay.[164] Four different CD73 reactions were conducted in parallel using four different isotope-labeled AMP substrates ($[^{15}N]_5$-AMP, $[^{13}C]_{10}[^{15}N]_5$-AMP, $[^{2}H]_2$-AMP, or $[^{13}C]_5$-AMP) in 384-well assay plates. The formed isotope-labeled adenosine in the different plates was pooled and reinjected for analysis using RF-tandem MS. The assay offered suitable conditions for the determination of all types of inhibitors by adopting low substrate concentration ([AMP], 5 μM) close to the K_M value of the enzyme. Furthermore, HTS was achieved by applying the RF high-throughput MS readout.[164] However, a pre-incubation period of enzyme and inhibitor for 1 h is needed. In addition, the highly sophisticated and expensive technique is not straight-forward and not simply available in most laboratories.

Table 3. Comparison of the main biochemical methods developed to study CD73 enzymatic activity and to screen for inhibitors

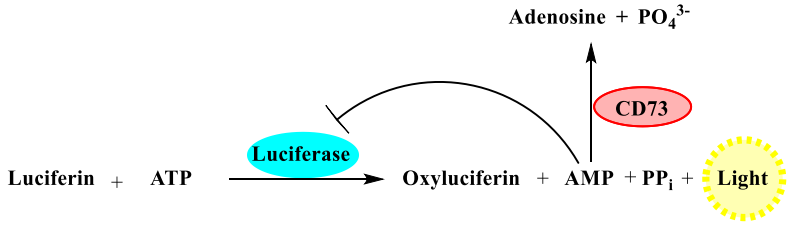
1. Malachite green assay[166,174,175]



Inorganic phosphate is detected by formation of a colored complex with the malachite green dye (λ_{max} = 630 nm).

Advantages:	Drawbacks:
• Simple and fast • HTS-applicable	• Interference by phosphate-containing samples and colored samples • Low sensitivity • High substrate concentration (above the enzyme K_M value) is required

2. Luciferase-based assay[177]



Luciferase utilize ATP to oxidize luciferin generating AMP and light. AMP is a competitive inhibitor of luciferase (K_i = 100 µM)[178]. Addition of CD73 blocks the AMP-mediated inhibition of the luminescence signal.

Advantages:	Drawbacks:
• Simple, and homogenous format • HTS-applicable • Low background interference	• High substrate concentration required (300 µM) • ATP exerts a weak competitive inhibition on CD73 activity which might affect the intensity of the produced light

3. Capillary electrophoresis assay[167,168]

In this assay, adenosine is separated from AMP based on the compounds' electrophoretic mobility in a fused-silica capillary under the influence of an applied voltage. The separated molecules are detected by UV.

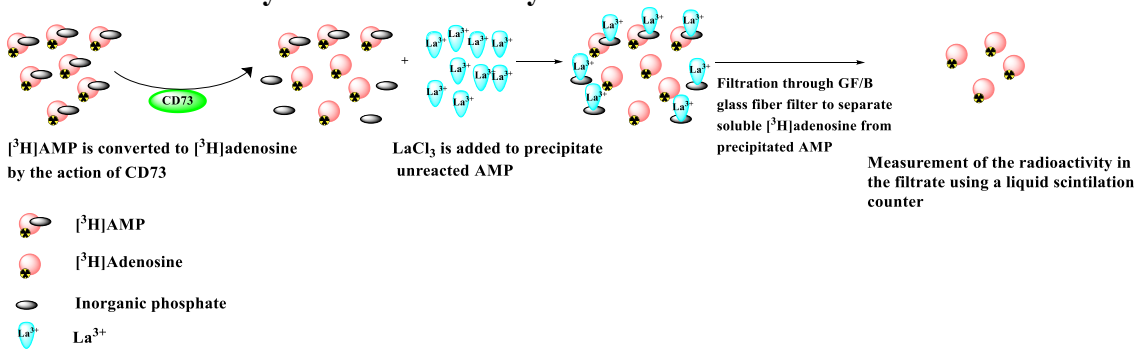
Advantages:	Drawbacks:
• Simple and fast • High separation efficiency • No chromophore or phosphate interference	• High substrate concentration required (AMP up to 500 µM), LOD (adenosine) = 1.06 µM[167], 1.76 µM[168] • Limited HTS-applicability

4. RapidFire-tandem MS/MS[164]

Four different isotope-labeled AMP substrates ($[^{15}N]_5$-AMP, $[^{13}C]_{10}[^{15}N]_5$-AMP, $[^{2}H]_2$-AMP, or $[^{13}C]_5$-AMP) are applied. Integrated peak areas of labeled adenosine were normalized to unlabeled adenosine used as internal standard for quantification.

Advantages:	Drawbacks:
• High sensitivity, low substrate concentration (~1·K_M) • High specificity of mass spectrometry • HTS-applicable	• Preincubation of test compound with CD73 for 1 h at room temperature (RT) • Highly sophisticated and expensive technique that is not straight-forward and not generally available

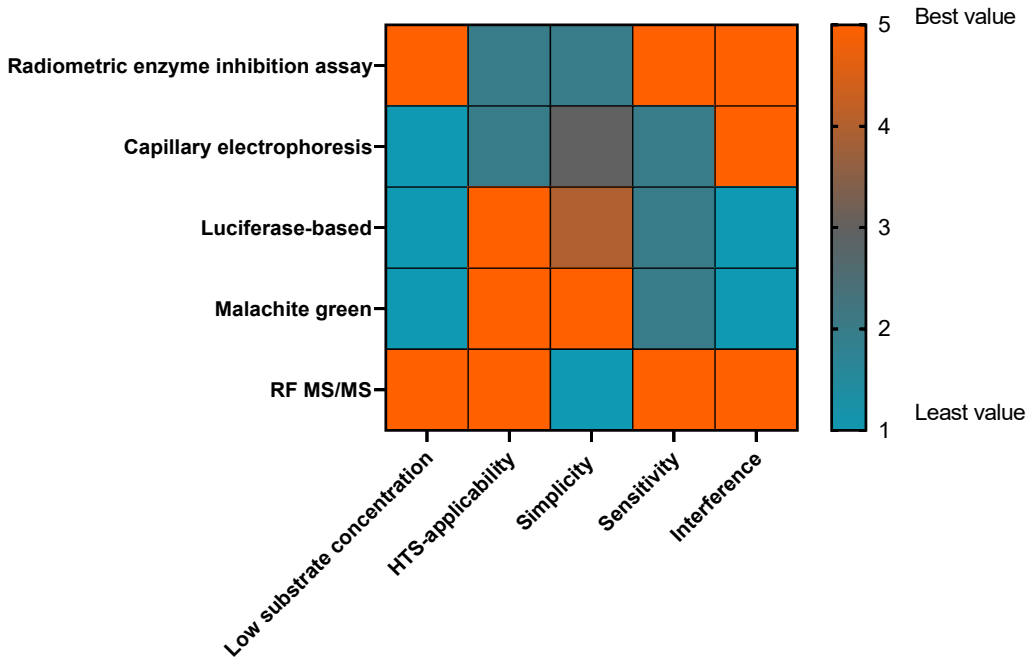
5. Radiometric enzyme inhibition assay[170]



The assay monitors the conversion of radiolabeled [^{3}H]AMP into [^{3}H]adenosine. Radioactive adenosine is collected in scintillation vials and radioactivity is measured in a liquid scintillation counter.

Advantages:	Drawbacks:
• High sensitivity (adenosine LOD = 0.028 µM) • Low substrate concentration (~1·K_M) • High accuracy, no interference from colored or phosphate-containing samples	• Not HTS-applicable • Radioactivity restrictions

6. Heatmap diagram to illustrate the general characteristics of CD73 biochemical assay



LOD: limit of detection; HTS: high-throughput screening

An enzyme inhibition assay developed in our research group, published in 2014,[170] is considered one of the most sensitive and accurate CD73 assay methods developed so far (LOD for adenosine = 0.028 µM). It is currently applied in our laboratory for the screening and characterization of CD73 modulators together with further orthogonal assays. The assay monitors the conversion of radiolabeled [^{3}H]AMP into [^{3}H]adenosine. The product adenosine is separated from AMP after precipitation of AMP with lanthanum chloride and subsequent filtration through GF/B glass fiber filters. Radioactive adenosine present in the filtrate is then collected in scintillation vials, and radioactivity is measured after addition of scintillation cocktail using a liquid scintillation counter. Employing a low substrate concentration of 5 µM enables high sensitivity in identifying a variety of inhibitor classes, yet the method is not HTS-compatible. The assay principle is shown in **Table 3** and the assay format is illustrated in **Figure 7**.

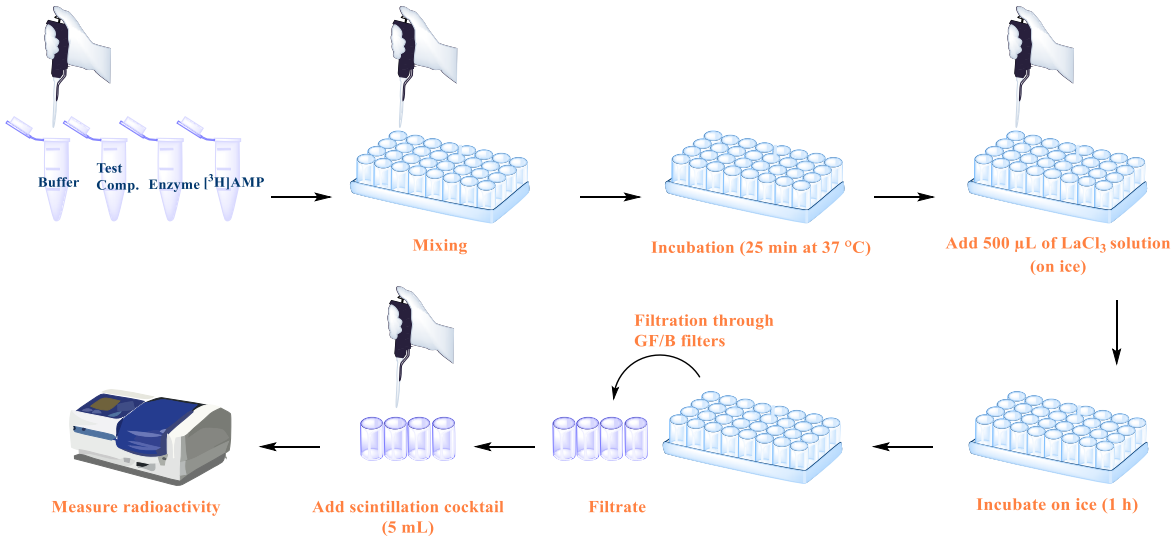


Figure 7. Graphical representation of the radiometric enzymatic CD73 assay.[170]

This assay format was employed in the current research project, to characterize the kinetics of CD73 enzyme constructs by estimation of Michael-Menten parameters, V_{max} and K_M values. Moreover, it was used to screen and measure the biological activity of synthesized test compounds and to determine the mode of inhibition of these molecules.

1.11.1. Steady-state enzyme kinetics

The substantial enhancement in reaction rates that occur in enzyme-catalyzed reactions is due to the formation of enzyme(E)-substrate(S) complexes (transition states) with a lower activation energy (Δ G). The following simple enzyme-catalyzed reaction is considered in which one substrate (S) is transformed into one product (P):[179]

$$E + S \underset{k_{-1}}{\overset{k_1}{\rightleftharpoons}} E\text{-}S \xrightarrow{k_2} P + E \qquad \text{eq. 1}$$

In enzyme kinetics, we measure the initial rate of product formation, V_0, which is given by:

$$V_0 = \left(\frac{d[P]}{dt}\right)_0 = k_2\,[E\text{-}S] \qquad \text{eq. 2}$$

When enzyme and substrate are mixed, the concentration of the enzyme–substrate complex will reach a constant value so that the steady-state approximation can be applied as follows:[179]

$$\frac{d[E\text{-}S]}{dt} = 0 = k_1[E][S] - k_{-1}[E\text{-}S] - k_2[E\text{-}S]$$

$$= k_1([E]_0\text{-}[E\text{-}S])[S] - (k_{-1} + k_2)[E\text{-}S] \qquad \textbf{eq. 3}$$

solving it for [E-S], we get:

$$[E\text{-}S] = \frac{k_1[E]_0\,[S]}{k_1[S] + k_{-1} + k_2} \qquad \textbf{eq. 4}$$

substituting the generated [E-S] value in eq.1 above, gives:

$$V_0 = \left(\frac{d[P]}{dt}\right)_0 = k_2\,[E\text{-}S] = \frac{k_1\,k_2\,[E]_0\,[S]}{k_1[S] + k_{-1} + k_2}$$

$$= \frac{k_2\,[E]_0\,[S]}{K_M + [S]} \qquad \textbf{eq. 5}$$

where K_M, the Michaelis constant is defined as

$$K_M = \frac{k_{-1} + k_2}{k_1} \qquad \textbf{eq. 6}$$

K_M is equal to the dissociation constant ($K_D = k_{-1}/k_1$) when $k_{-1} >> k_2$.

A plot of the initial reaction rate against the initial substrate concentration at a constant enzyme concentration will yield a saturation kinetics curve, where a plateau is observed at high [S] (**Figure 8**). This plot has two regions that are of great importance. First, when [S] is very low, the reaction rate is linearly related to [S] and obeys first-order kinetics; under these conditions, reaction rates can be used to quantitate the substrate. The second region of interest occurs at very high [S], where the reaction rate is independent of [S] (zero-order kinetics); under these conditions, all of the available enzyme exists as E-S, and the initial rate must be at its maximum value (V_{max}) and can be used to determine the total amount of enzyme present in the sample as follow;

$$V_{max} = k_2\,[E]_0 \qquad \textbf{eq. 7}$$

Substituting V_{max} in the initial reaction rate equation gives,

$$V_0 = \frac{V_{max}[S]}{K_M + [S]} \qquad \text{eq. 8}$$

When the initial rate is equal to half of the maximum rate ($V_0 = V_{max}/2$), [S] is equal to the K_M value. Both, V_{max} and K_M values can be determined from a plot of V_0 versus [S] (**Figure 8**).[179]

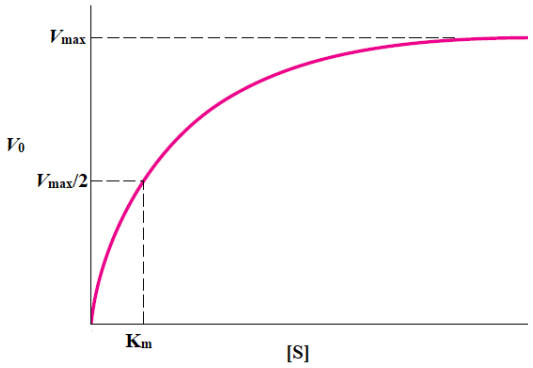


Figure 8. Michaelis-Menten kinetics (graphical determination of V_{max} and K_M values).

1.11.2. The significance of K_M and V_{max}

The Michaelis constant, the K_M value, is equal to the substrate concentration at half of the maximum reaction rate. This means it is equal to the substrate concentration at which half of the enzyme active sites are occupied by substrate molecules. Its value is sometimes equal to the dissociation constant of the E-S complex, when $k_{-1} >> k_2$, and the higher the K_M value, the weaker the binding.[179] Different substrates have varied K_M values at the same enzyme. Moreover, the K_M value depends on temperature, pH, and ionic strength of the buffer. Any variation in K_M (for the same enzyme and substrate under the same conditions) indicates the presence of a modulator.

The maximum velocity, V_{max}, is the rate at which the total enzyme is present as E-S complex. If E_0 is known, then the value of the first order rate constant k_2 can be calculated ($k_2 = V_{max}/[E]_0$). It is known as the turnover number (the number of substrate molecules (or moles) that are turned into product per unit of time, also k_{cat}, the catalytic constant) and has the unit of "per unit time" (s^{-1} or min^{-1}). At physiological conditions, most enzymes have

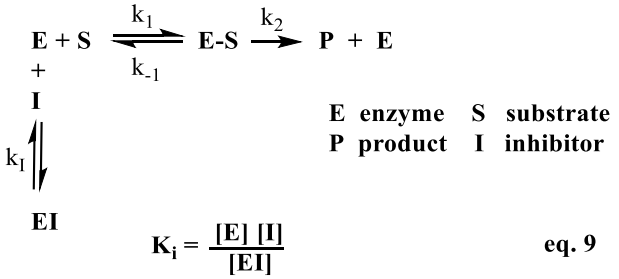
a turnover number (k_{cat}) between 1 and 10^5 s^{-1}. The catalytic efficiency of an enzyme is measured by the ratio k_{cat}/K_M (which has the unit M^{-1} s^{-1}). A high ratio favors the formation of product.[179]

1.11.3. Enzyme inhibitors

Enzyme inhibitors are molecules that decrease the activity of an enzyme. Inhibition is reversible when an equilibrium exists between the enzyme and the complex, and removal of the inhibitor restores the enzymatic activity. It affects the Michaelis–Menten parameters for the enzyme, K_M and V_{max}. Irreversible inhibition leads to permanent loss of activity due to reduction in the concentration of active enzyme present in the sample.
Reversible inhibition may be divided into three types that will be discussed in details below.

1.11.3.1. Competitive inhibition

Competitive inhibitors (I) compete with the substrate for the enzyme's active site (as illustrated below). They are not converted to products after they are bound, but block the active site preventing the binding of the substrate. The potency of competitive inhibitors is characterized by their inhibition constant, K_i, which is the dissociation constant of the enzyme–inhibitor complex.



$$K_i = \frac{[E]\,[I]}{[EI]} \qquad \text{eq. 9}$$

Lineweaver–Burk plots constructed at different inhibitor concentrations allow for elucidating the mode of inhibition. **Figure 9A** shows that, at increasing concentration of competitive inhibitor, identical y intercepts ($1/V_{max}$), and decreasing x intercepts ($1/K_M$) are obtained.[179]

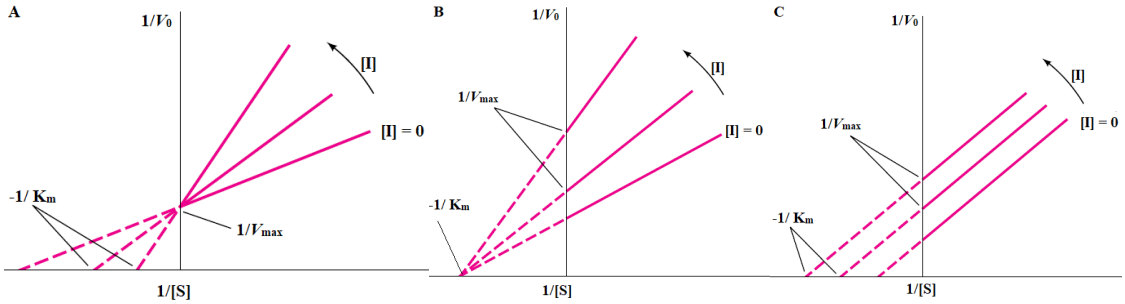
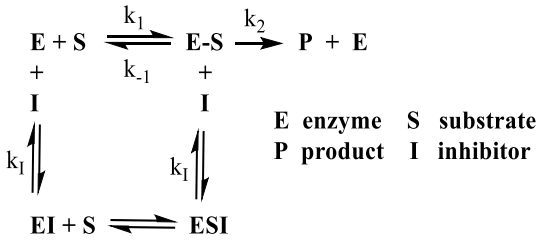


Figure 9. Lineweaver–Burk plots for different classes of enzyme inhibitors. **A**) Competitive inhibitor. **B**) Noncompetitive inhibitor. **C**) Uncompetitive inhibitor.

1.11.3.2. Noncompetitive inhibition

Noncompetitive inhibitors bind to the enzyme at a site distinct from the substrate binding pocket.

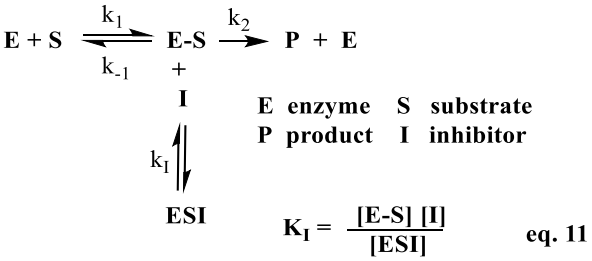


eq. 10

They interact reversibly with the free enzyme and the substrate-enzyme complex to form an inactive species, and lead to a decrease in the effective concentration of the active enzyme and accordingly slow down the rate of conversion into product (V_{max} decreases). The binding of the inhibitor has no effect on substrate binding, and vice versa, which is illustrated by the unchanged apparent affinity (K_M) of the enzyme for its substrate (**Figure 9B)**. Accordingly, the effect of a noncompetitive inhibitor cannot be reversed by increasing the substrate concentration. This type of inhibition is characterized by two equilibrium constants, one for E-I (K_i) and one for the ESI complex (αK_i), where α indicates the relative affinity of the inhibitor (I) for the free enzyme (E) and enzyme-substrate complex (E-S). When (I) has equal affinity for both, α = 1.[179]

1.11.3.3. Uncompetitive inhibition

Unlike the noncompetitive inhibitor, uncompetitive inhibitors bind only to the E-S complex, decreasing the effective concentration of the E-S complex so the V_{max} is decreased.



As the concentration of the E-S complex is decreased in the reaction, according to Le Chatelier's principle, the equilibrium will shift towards producing more E-S complex, increasing its concentration. This increment in E-S amount is manifested by the reduction in the K_M value which indicates an increase in substrate affinity. Since the inhibitor (I) does not interfere with the formation of E-S, uncompetitive inhibition cannot be reversed by increasing the substrate concentration. **Figure 9C** illustrates this mode of inhibition.[179]

1.12. Binding assays

Up to now, several biochemical methods have been implemented in CD73 drug development projects to estimate the inhibitory potency of corresponding ligands. However, none of the currently applied methods is suitable to measure ligand binding kinetics and to define binding affinities at equilibrium.

Recently, studies on the dissociation rate of drugs and their residence time have gained high attention in drug development programs.[180,181,182] Moreover, studies on the localization and expression of the target protein under different conditions is important in both basic and translational research. Binding studies could therefore be highly useful.

In binding assays, measurement is based on the ability of a test compound to modulate binding of a labeled ligand to the target protein. Usually, labeling is the first and critical step in the development of any binding assay. Although label-free methods (e.g., based on surface plasmon resonance (SPR) and bio-layer interferometry (BLI)) have recently emerged, they are not widely applicable and often not reliable.[183]

Thus, the development of orthogonal binding assays is important to allow for advanced and comprehensive studies on CD73 (i.e., investigating expression and trafficking) as well as for the development and characterization of CD73 inhibitors. Thus, two different methods and techniques were designed and developed, namely radioligand binding assays, and nano-luciferase bioluminescence resonance energy transfer (NanoBRET) binding assays. Both will be discussed in more detail in subsequent sections.

1.12.1. Theoretical background of binding assays

Binding assays involve bimolecular interaction between a target protein (in this case an enzyme, **E**) and a labeled ligand (**L**) to form an enzyme-ligand complex (**E-L**) according to the following law of mass action model:[184]

$$E + L \underset{k_{off}}{\overset{k_{on}}{\rightleftharpoons}} E\text{-}L \qquad \text{eq. 12}$$

The association rate constant, k_{on}, defines the rate of formation of the E-L complex which is given by $k_{on} \cdot [E] \cdot [L]$, where [E] and [L] are the molar concentrations of unbound enzyme and free labeled ligand, respectively. Likewise, the dissociation rate constant k_{off}, describes the rate of dissociation of the E-L complex and is given by $k_{off} \cdot [E\text{-}L]$, where [E-L] is the molar concentration of bound enzyme.[184]

The law of mass action is based on several assumptions:[185]

- All enzyme molecules are equally accessible to ligands.
- Enzyme molecules are either free or bound to ligand. The model ignores any states of partial binding.
- Binding alters neither ligand nor receptor.
- Binding is reversible.

At equilibrium, the rate of forward reaction (association) equals the rate of reversed reaction (dissociation):

$$k_{on} \cdot [E] \cdot [L] = k_{off} \cdot [E\text{-}L] \qquad \text{eq. 13}$$

After rearrangement,

$$k_{on} = \frac{[E\text{-}L]}{k_{off}\ [E] \cdot [L]} \qquad \text{eq. 14}$$

The equilibrium dissociation constant, K_D, is equal to k_{off}/k_{on};

$$K_D = [E] \cdot [L] \,/\, [E\text{-}L] \qquad \text{eq. 15}$$

The K_D is also the concentration of free ligand (expressed in molar) at which 50% of the target protein molecules are occupied by ligand.[186] A low K_D value implies high ligand affinity and low concentration needed to occupy 50% of the target protein molecules. A ligand at 0.1 K_D concentration only occupies around 10% of the protein molecules and at 10 K_D an occupancy of greater than 90% is achieved. Maximum occupancy of the target protein is defined as B_{max}, which is the measure of the total number of available binding

sites in a given protein amount. There are three main experiments that could be conducted in binding assays to measure the binding parameters of the ligand-enzyme complex: saturation experiments, competition binding experiments, and binding kinetics, all of will be discussed below.[186]

1.12.2. Saturation binding

In this set of experiments, different concentrations ($0.1\text{-}10 \cdot K_D$)[186] of the labeled ligand are incubated with the protein in the absence and in the presence of an unlabeled ligand to determine total binding and nonspecific binding, respectively. At high ligand concentration, the binding sites are all occupied and a plateau is observed in the specific binding curve. A hyperbolic curve results from plotting specific binding against labeled ligand concentrations with a maximum at B_{max} (**Figure 10**). K_D and B_{max} values are estimated based on the following one-site equation.

$$[E\text{-}L] = \frac{B_{max} \cdot [L]}{[L] + K_D} \qquad \textbf{eq. 16}$$

Practically, specific binding cannot be measured directly in binding assays, instead, nonspecific binding is measured and subtracted from the total binding of the radioligand.

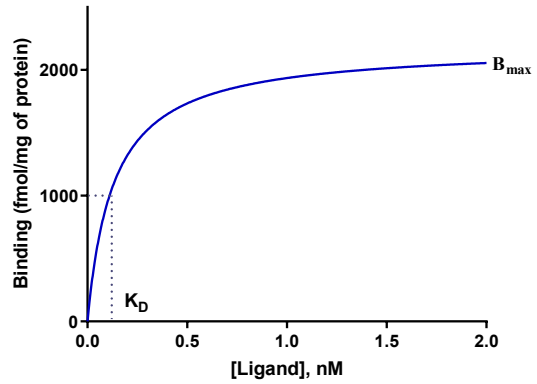


Figure 10. Saturation curve. Specific binding increases linearly with increasing ligand concentration until a plateau is reached where all enzyme binding sites are occupied. B_{max}, is an estimate of the total number of enzyme binding sites accessible to the ligand (corresponding to the target protein expression in a given sample). The dissociation constant K_D corresponds to the ligand concentration at which half of the binding sites are occupied.

The measured readout in binding assays is the specific binding of the labeled ligand to the

protein of interest plus off-target binding named nonspecific binding (NSB). Non-specific binding could arise from binding of the tracer to other proteins expressed in the sample, from the radioligand being adsorbed to the phospholipids in the membrane, and/or from simple attachment to the filters used to perform separation, or to the glassware. Nonspecific binding is weak and unsaturable, showing a linear increase with the concentration of the tracer. A high saturable concentration of a competing ligand (100-1000·K_D)[186,187] should be used to inhibit binding of the tracer to the target protein with no effect on nonspecific low-affinity interactions. It is recommended to use a structurally unrelated unlabeled ligand to measure nonspecific binding in order to avoid overestimation of specific binding. Reaction conditions could be optimized to reduce NSB, e.g., through supplementing the binding or washing buffers with protein (albumin or gelatine) or detergents. When NSB is attributed to the adsorption to filters, presoaking, e.g., with polyethyleneimine (PEI), might decrease the NSB of ligands.[186]

1.12.3. Time-course of binding and dissociation

Studying binding kinetics is an important prelude to equilibrium binding assays (saturation and competition) to estimate the incubation time required to reach equilibrium and to attest the binding reversibility. The rate of binding (association) of the labeled ligand-protein complex is studied during a time course using a fixed concentration of the ligand. Nonspecific binding may be determined at one time point unless it shows changes with time. A plot of specific binding versus time yields a single exponential curve, described by the equation:[184]

$$[E\text{-}L] = [E\text{-}L]_{eq} \cdot (1\text{-}e^{-k.t}) \qquad \textbf{eq. 17}$$

where $[E\text{-}L]_{eq}$ is the specific binding at equilibrium for the ligand concentration used, t is time, and k is the observed association rate constant (which reflects both the association and dissociation of the E-L complex during equilibrium). The association rate constant, k_{on}, may then be calculated using the following equation:[184]

$$K = k_{on} \cdot [L] + k_{off} \qquad \textbf{eq. 18}$$

To study dissociation of the labeled ligand from the target protein, a preincubation period of a fixed concentration of the ligand with a defined amount of the protein is performed until binding reaches equilibrium. Dissociation is initiated by either addition of a saturable

concentration of an unlabeled competing ligand, by removing the labeled ligand, or by diluting the binding buffer (20-100-fold).[184] If the E-L complexes dissociate, and the total binding reduces to the nonspecific binding, the binding is considered fully reversible. The dissociation rate constant, k_{off}, can be directly calculated from a single-phase exponential decay equation:

$$\textbf{Total binding} = [E\text{-}L]_0 \cdot e^{-k_{off} \cdot t} + NSB \qquad \textbf{eq. 19}$$

where, $[E\text{-}L]_0$ is the specific binding at time zero. The half-time of the equilibration reaction is given by $t_{1/2} = 0.693/k_{off}$. The use of an incubation time greater than 5x $t_{1/2}$ is recommended to ensure that equilibrium is attained. Association and dissociation rate constants (k_{on} and k_{off}) are the parameters obtained and used to calculate the kinetic K_D ($K_D = k_{off}/k_{on}$). Association and dissociation curves are illustrated in **Figure 1.**

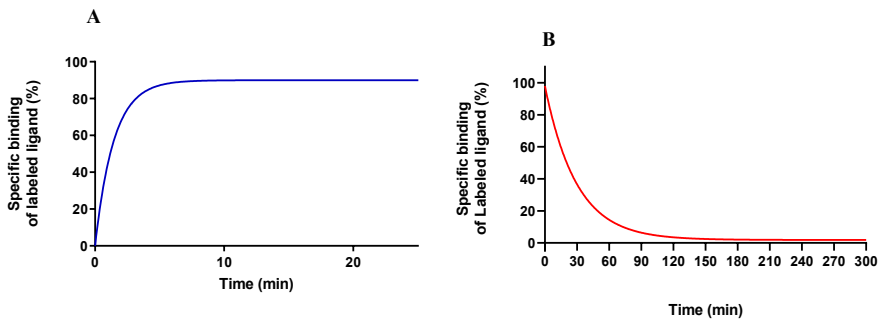


Figure 11. Binding kinetics of a labeled ligand. **A**) Association curve for a fixed concentration of radioligand. The curve plateau is reached after less than 10 min in this example (when reaching equilibrium). **B**) Time course of dissociation initiated by the addition of a high concentration of unlabeled ligand.

1.12.4. Competition binding experiment

Displacement experiments allow the estimation of affinities of unlabeled ligands. For a predefined time, a fixed concentration of the labeled ligand is incubated with varying concentrations of the unlabeled test compound until equilibrium is reached. It should be mentioned that the labeled ligand may require longer time to achieve equilibrium in the presence of an unlabeled ligand. An inverse sigmoidal curve is obtained by monitoring the reduction in the concentration of bound labeled ligand with increasing concentration of the competing ligand (competitor, allosteric, or irreversible). When the ligand under study (A)

competes for the same binding site, the following equation can be used to estimate the concentration of the bound ligand:[185]

$$\text{Total binding} = \frac{\text{NSB} + (\text{Total-NSB})}{1 + 10^{(\log A - \log IC50)}} \qquad \text{eq. 20}$$

Total binding is measured at different concentrations of a competing ligand, in the absence of competing ligand. The concentration of the unlabeled ligand that displaces 50% of the labeled ligand-protein complex is referred to as IC_{50} value and is used to calculate the equilibrium inhibition constant, the K_i value, using the Cheng-Prusoff equation:[188]

$$K_i = \frac{IC_{50}}{1 + [L]/K_D} \qquad \text{eq. 21}$$

Obviously, the mechanism of inhibition cannot be determined by indirect displacement experiments unless a series of sigmoidal curves are constructed using different fixed concentrations of the labeled ligand. An increase in the IC_{50} value of an unlabeled ligand is observed with higher concentrations of the labeled ligand if the two ligands compete for the same binding site (orthosteric site). However, no effect is seen in case of noncompetitive unlabeled ligands. An allosteric ternary complex (AEL) is formed when an allosteric modulator (A) binds to a target protein to which a labeled ligand (L) is already bound. Often, an incomplete inhibition is generated leading to a plateau at a level higher than the NSB depending on the cooperativity factor, α, which describes the effect of unlabeled ligand binding on the K_D value of the labeled ligand. In addition, an increase in the IC_{50} value may also be observed depending on the following equation:[186]

$$IC_{50} = \frac{K_i\,(1 + [L]/K_D)}{\alpha\,(1 + [L]/K_D)} \qquad \text{eq. 22}$$

Furthermore, the binding of an allosteric unlabeled ligand might not change the affinity (K_D) of the labeled ligand but modify its binding kinetics (association and/or dissociation rates).[189]

1.12.5. Radioligand binding assays

Traditionally, radiolabeled ligands have been successfully applied to determine the affinity and binding kinetics of a ligand. This is mainly due to the high sensitivity besides the applicability to native proteins. Availability of a potent and selective labeled ligand is fundamental. Usually, the introduction of radioisotopes such as tritium does not alter the activity or the selectivity of the ligand towards a specific target, and therefore it is often

preferred. Furthermore, radioligand binding assays integrated with autoradiography can be applied for visualization of proteins within a tissue.

Several isotopes are available for labeling, e.g, ^{125}I, ^{3}H (tritium), and the less commonly used ^{35}S, ^{32}P, and ^{33}P. Labeling with ^{125}I is preferred when dealing with low density proteins due to its high specific activity (~2,000 Ci/mmol of ^{125}I atom). It also decreases the exposure time needed to visualize the target protein distribution in autoradiography and phosphor imaging studies. Furthermore, samples can usually be counted directly without the addition of scintillation cocktail which in turn reduces the costs. However, ^{125}I has a relatively short half-life of 59.9 days compared to ^{3}H ($t_{1/2}$ of 12.4 years).[183] Thus tritium labeling (^{3}H) provides a radiolabeled ligand with very long half-life that can be used for a long time. It has a low specific activity (~30 Ci/mmol of ^{3}H atom) which necessitates long exposure times in imaging, and the use of a scintillation cocktail.[183]

The basic protocol for a radioligand binding assay is to incubate the radiotracer with a target protein-expressing sample (membrane preparation, intact cells or homogenates) at a specific temperature for a defined period of time to reach equilibrium binding. NSB is determined under the same conditions in the presence of a high concentration of an unlabeled ligand (100-1000·K_D).[186,187] To separate bound from free radioligand, filtration is carried out and radioactivity corresponding to the protein-bound radiotracer is measured. Specific binding is measured by subtracting nonspecific binding from total binding. **Figure 12** shows the general principle of radioligand binding assays.

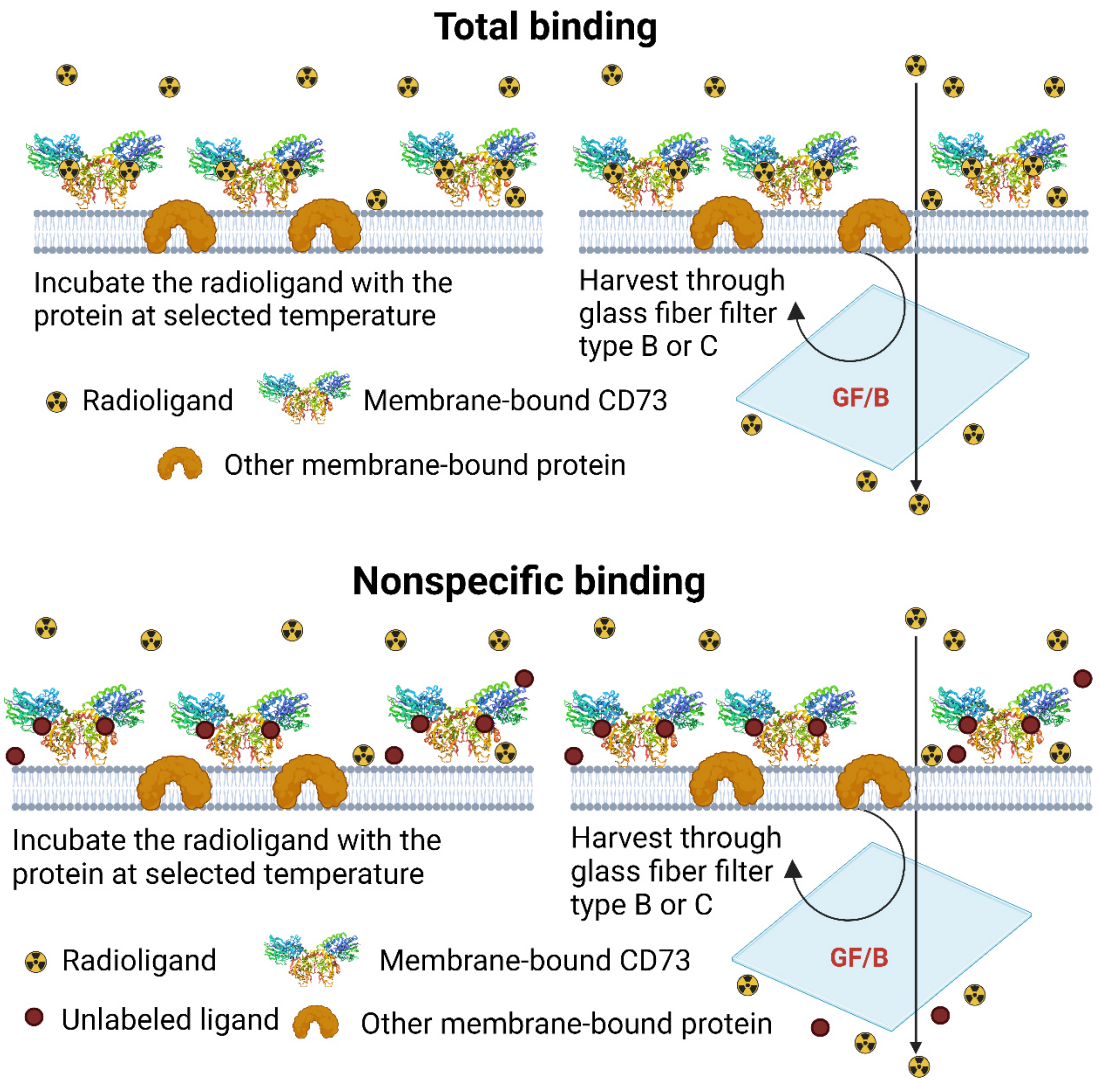


Figure 12. Radioligand binding assay principle. Created in BioRender.com.

The use of a radiotracer in binding assays encounters several drawbacks. Technically, it cannot be carried out in a homogeneous format and requires separation and washing steps which add to the complexity that hinders the determination of real-time single-point kinetics. Although the recent development of scintillation proximity assays (SPA) provides opportunities for a homogenous format, the high cost of the required beads limits its broad application. Ecologically and financially, the restriction of radioactive waste disposal and required medical checkups add high cost to the technique. As a result, non-radioactive methods have been introduced to overcome these limitations, e.g., fluorescence-based binding assays for example, NanoBRET binding assays.

1.12.6. NanoBRET binding assays

Binding assays based on fluorescent probes are promising alternatives to radioligand-based assays. Protocols are conducted in a homogeneous format which facilitates the applicability of HTS and enables single point real-time kinetic studies.[183] Furthermore, fluorescent ligands have received widespread applicability in confocal microscopy to localize and study protein trafficking in living cells and may be utilized in flow cytometry.[183] Nevertheless, the generation of potent fluorescent ligands is challenging, e.g., due to the steric demands of fluorophores, which can significantly change the ligand's interaction with the target protein.

The BRET technique is based on light energy transfer from a luciferase donor to a fluorescent acceptor subsequent to oxidation of a substrate by luciferase. It is a proximity-based assay, and the energy transfer is manifested only if donor and acceptor are within close proximity (<10 nm). Following energy transfer, the excited fluorophore itself emits light with a longer wavelength.[190,191] A spectral overlap is required between the donor emission and the acceptor excitation spectrum. The BRET technique emerged as a method to study protein-protein interactions (PPI) and has recently also been applied in protein-ligand binding studies. A graphical representation of the BRET assay principle is shown in **Figure 13**.

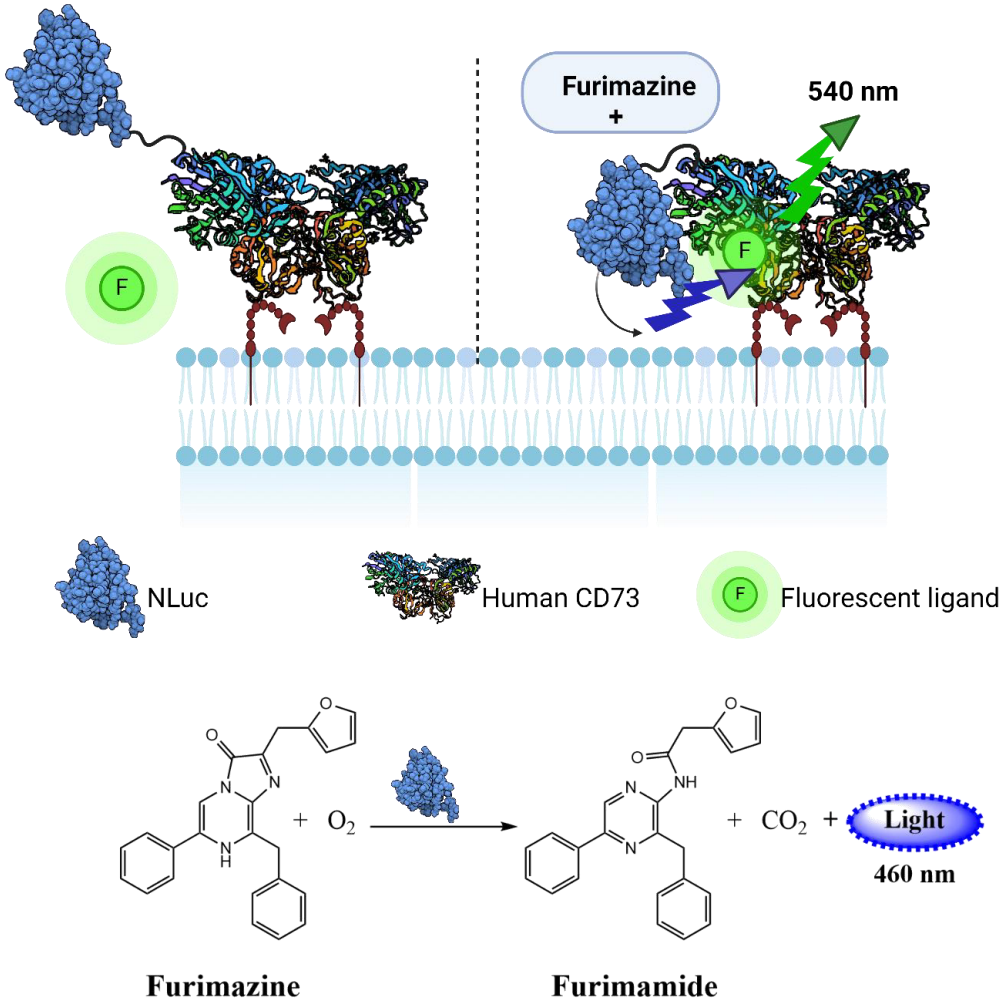


Figure 13. Graphical representation of the NanoBRET assay principle with CD73, developed in the present study, as an example. Created in BioRender.com.

The first step in developing a BRET-based assay to study ligand binding is to label the protein of interest with a luciferase mostly in the extracellular regions of the N- or C-terminus depending on the localization of the protein in the membrane.[192] A variety of luciferase enzymes has been used to tag proteins of interest. Some enzymes utilize D-luciferin in ATP-dependent reactions e.g., click beetle (*Pyrophorus plagiophthalamus*) and firefly luciferase (Fluc) (*Photinus pyralis*). Other enzymes are ATP-independent and employ coelenterazine as a substrate e.g., Renilla (Rluc), and Renilla mutant (Rluc8).[193] Most of these variants have large sizes (64-36 kDa) which may result in steric hindrance

affecting ligand binding or trafficking of the protein to the extracellular membrane and hence providing challenges to the labeling of membrane proteins. Size limitation has been overcome by the recently developed small size Gaussia from *Gaussia princeps* (Gluc) and deep-sea shrimp nano-luciferase (Nluc) variants. However, the light intensity of Gluc decays rapidly, and its coelenterazine substrate is chemically unstable and has a high autoluminescence background.[194] Nluc is derived from a naturally occurring heteromeric luciferase isolated from the deep-sea shrimp (*Oplophorus gracilirostris*) and is composed of two 35 kDa subunits and two 19 kDa subunits. The bioluminescence property of the enzyme was found to be linked to the smaller 19 kDa catalytic subunits.[195] Not only does the small size of Nluc contribute to its suitability in the labeling of the extracellular N-terminus, but having a natural secretory protein character facilitates the trafficking of the tagged protein to the extracellular space. Several mutations and optimizations have been performed in the 19 kDa subunit to generate a more stable (half-life >2 h), and brighter luciferase (~150x of Fluc or Rluc) with a sustainable bioluminescence signal.[191] Although Nluc can utilize coelenterazine as a substrate, it produces a 30-fold brighter bioluminescence signal when furimazine is used instead. Moreover, furimazine shows higher stability in cell culture medium.[192] This increased luminescence allows NanoBRET assays to monitor low prevalence PPIs which have been difficult to detect using classical BRET assays. Additionally, as seen in **Figure 14**, the Nluc emission spectrum shows a blue shift (λ_{max} 460 nm) relative to Rluc and substantial emission at longer wavelength which broadens its suitability for different fluorescent probes and allows for better spectral separation between donor and acceptor emission spectra.[191]

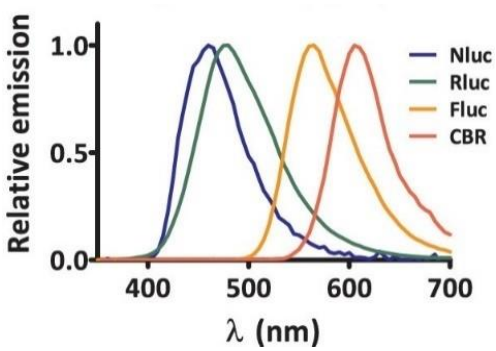


Figure 14. Spectral profiles for Nluc (furimazine) compared to other luciferases, Rluc (coelenterazine), Fluc (D-luciferin), and click beetle red luciferase (CBR) (D-luciferin). Emission peaks: Nluc (460 nm), Rluc (480 nm), Fluc (565 nm), and CBR (605 nm). RLU = relative luminescence units. Adapted from *ACS Chem. Biol.* 2012, 7, 11, 1848-1857. https://pubs.acs.org/doi/10.1021/cb3002478.

Initially, Nluc was tested as an alternative to other luciferases in gene and fusion reporters studies.[194] Recently, several studies have demonstrated Nluc's ability as an energy donor to be applied in conventional BRET experiments to monitor conformation and dimerization of proteins as well as ligand-protein binding.[196,197,198,199,200] In addition, Nluc was applied in *in vitro* imaging using a high-content microscope or a bioluminescence-dedicated inverted fluorescence microscope.[201,202] However, the blue light of Nluc limits it's *in vivo* applicability due to absorption and scattering of blue light by tissue.[191] Therefore, development of fusion reporters such as LumiFluors (Nluc fused to either green GFP or mOrange fluorescent protein) and Antares (orange-red fluorescent protein CyOFP1 fused to Nluc), which result in intramolecular BRET, have been applied in deep tissue analysis by bioluminescence imaging *in vivo*.[203,204]

Generally, NanoBRET assays are conducted in a homogenous format which requires plating of the cell line expressing the Nluc-tagged protein one day before the experiment in an opaque plate. On the next day, the medium is changed and incubation of the cell line with a specific concentration of the fluorescent ligand is performed for a predetermined time period at a specific temperature. Afterwards, the substrate (furimazine) is added followed by measurement of the bioluminescence using a 460 nm filter, and the fluorescence at a fixed wavelength depending on the emission spectra of the fluorescent acceptor ligand, using a plate reader. The BRET ratio is calculated by dividing the acceptor emission/donor emission at 460 nm. A normalized BRET ratio is obtained through subtraction of the BRET ratio generated from the Nluc-tagged protein, with no added fluorescent tracer, from the BRET ratio of the Nluc-tagged protein incubated with the fluorescent ligand.

1.13. CD73 inhibitors

Small molecules as well as macromolecules, in particular antibodies, have been developed as CD73 inhibitors, and optimized for high *in vivo* efficacy and selectivity.

1.13.1. Small molecule CD73 inhibitors

After the development of anti-CD73 antibodies, the focus of cancer drug development programs has recently been shifted back to small molecules targeting CD73 due to their favorable pharmacokinetic properties based on their small size (molecular weight < 500

g/mol). Small molecule inhibitors are either structurally related to the substrate and natural inhibitor (nucleotide-mimetics) or based on various other scaffolds.

1.13.1.1. Nucleotide analogs

ATP (shown on **Figure 15**) was the first nucleotide-based inhibitor to be identified and investigated against CD73 by Baer et al. in 1966. It was found to have a K_i value of 1.83 µM on CD73 isolated from rat heart.[205] Another reported K_i value is 48 µM at *Torpedo marmorata* CD73.[206] A couple of years later, ADP and its more stable α,β-methylenephosphonate analog (AMPCP, synthesized by Terrell C. Myers et al. in 1965, **3**, **Figure 15**)[207] were tested against CD73 prepared from smooth muscles of pig small intestine. Both ADP and AMPCP were able to inhibit the catalytic activity of the enzyme though to different extents. At a concentration of 3.3 µM, AMPCP fully blocked the activity, whereas ADP caused only a 10% inhibition.[208] Since then, many studies reported similar K_i values for each of these inhibitors, e.g., 22 µM and 0.85 µM for ADP and AMPCP, respectively.[206]

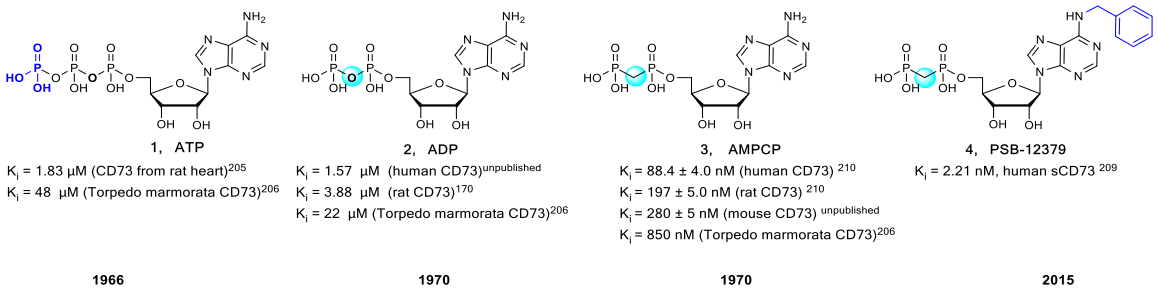


Figure 15. Early-discovered adenine nucleotides as ecto-5'-nucleotidase (CD73) inhibitors.

Extensive structure-activity-relationship studies (SARs) have been initiated in our research group employing AMPCP as a lead compound to develop more potent, selective and metabolically stable inhibitors. In these studies, we discovered that substitution of the N^6-position resulted in potent inhibitors, e.g., PSB-12379, N^6-benzyl-AMPCP, with a K_i value of 2.21 nM at recombinant human CD73 (**4**, **Figure 15**).[209] An unsubstituted ribose, an unmodified diphosphonate moiety, and an unsubstituted C8-position of the adenine ring were found to be optimal for inhibitory activity.[209]

Structure-based strategies in development of small molecules targeting CD73 became possible in 2012 when the first crystal structure of human CD73 in the close state was resolved by Knapp, Sträter et al.[61] Further work driven by our group, resulted in the co-crystal structure of PSB-12379 (PDB 6S7F) by Sträter and coworkers.[210] It revealed a pocket close to C2 of the adenine ring of PSB-12379. This pocket was addressed through several substitutions, but only halogen (chloro or iodo) substituents were able to enhance the potency significantly.[210] The crystal structure 6S7F was successfully employed in the design and synthesis of the improved CD73 inhibitor PSB-12489 (**Figure 16A**), showing subnanomolar potency (K_i = 0.318 nM soluble human CD73).[210] This increased potency was explained by hydrogen bonds formed between the chloro-substituent at position C2 and the sidechain of N390, and further by a water molecule coordinated to the carboxy group of N499 (**Figure 16B-C**).[210] Of note, a potential dephosphorylated metabolite of PSB-12489 as an N^6-disubstituted AMPCP derivative is expected to show limited potential to interact with adenosine receptors compared to mono-substituted N^6-benzyl AMPCP (PSB-12379).[210]

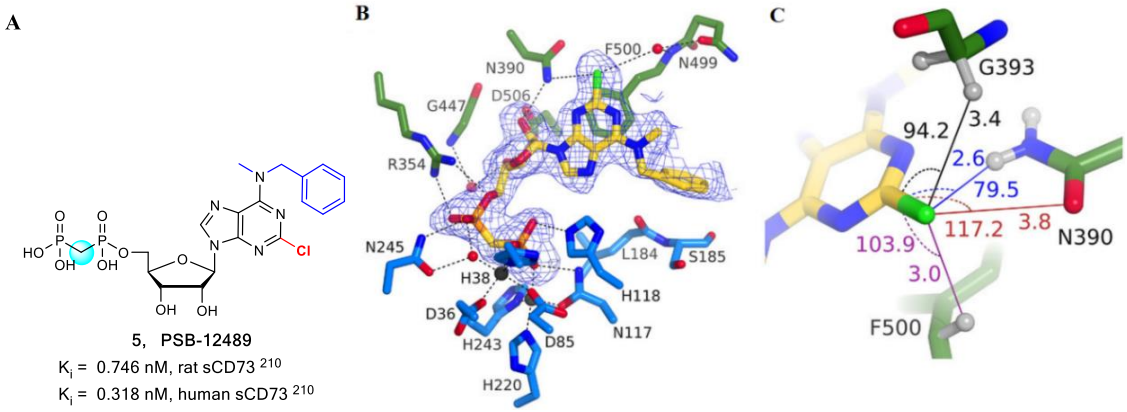


Figure 16. **A**) Structure of PSB-12489. **B**) PSB-12489 within the substrate binding site formed by the N-terminal (blue) and C-terminal (green) domains. **C**) The proposed interactions of the chloro substituent (green) at the C2-position of PSB-12489. The NH group of N390 is positioned for a favorable interaction with the chloro substituent. The carbonyl oxygen of N390 is too far away from a linear C—Cl···O halogen bonding interaction. (Taken from Advanced Therapeutics, Volume: 2, Issue: 10, First published: 31 July 2019. Open access https://creativecommons.org/licenses/by/4.0/).

SAR studies were continued in our group with the aim to generate more potent inhibitors through exploring single substitution at the C2-position of AMPCP without a bulky N^6-benzyl substituent.[78] A number of inhibitors with variable potency were generated having

C2-substituents of different polarity and size.[78] The low molecular weight 2-iodo and 2-chloro substitutions of AMPCP (**Figure 17**) showed the most beneficial effect on the inhibitory activity (K_i = 3.59 nM, and 5.93 nM, respectively, compared to unsubstituted AMPCP, 88.4 nM, determined at recombinant soluble human CD73).[78]

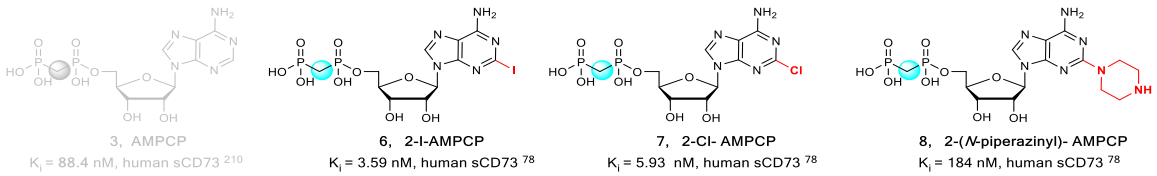


Figure 17. Effect of substituents in the C2-position of AMPCP.

This study revealed that certain substituents such as 2-hydrazinyl, and 2-(*N*-piperazinyl) residues led to high species differences of 7.5-fold, and 12.5-fold respectively, between rat and human. The compounds being more potent at the human enzyme. On the other hand, 2-allylthio-, and 2-cyclohexylthio-AMPCP were equipotent at the rat and human enzyme. Crystallization of selected 2-substituted AMPCP inhibitors with human CD73 showed alternative binding modes adopted due to the 2-substituent (e.g., 2-(*N*-piperazinyl)-AMPCP, **Figure 17**). A bulky, inflexible substituent at the C2-position resulted in a flipped binding mode to that observed in other AMPCP derivatives (shown in **Figure 18A**).[78] This aberrant binding was attributed to the unfavorable hydrophilic environment of the C2-pocket top rim which resulted in reorientation of 2-(*N*-piperazinyl)-AMPCP with a bulky rigid structure, to the more compatible interdomain rift. In this binding mode, the F500 residue showed a different sidechain orientation which led to proper interaction with L184. Since rat shows an F500Y mutation, the OH group of tyrosine in rat CD73 results in unfavorable interaction with L184 in the bound state compared to the unbound state (**Figure 18B-C**), thereby explaining the large species differences.[78]

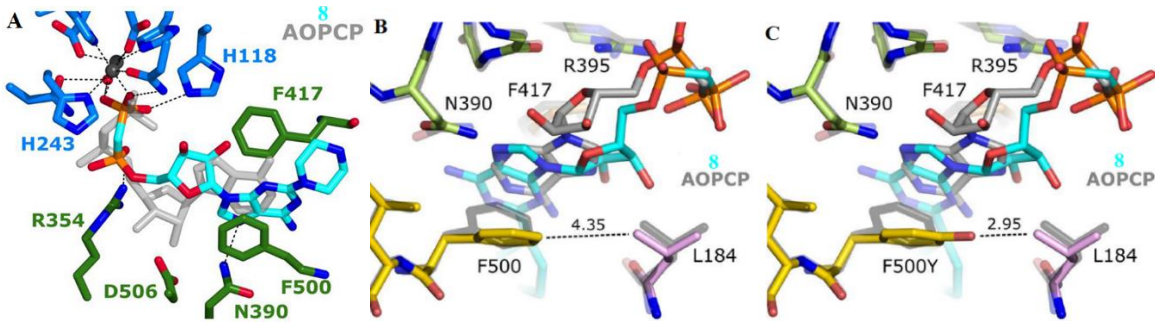


Figure 18. **A**) Superposition of the binding modes of 2-(*N*-piperazinyl)-AMPCP (cyan, 6TWF) and AMPCP (grey, 4H2I) in human CD73. In the CD73×**8** structure F500 adopts a different side chain conformation to accommodate the flipped binding mode of **8**. **B**) F500 forms a favourable hydrophobic contact to L184 (of the N-terminal domain). **C**) A model for a F500Y substitution, which is present in rat CD73, shows that the phenolic OH-group is in close contact for a C-H···O interaction with L184. While this is acceptable and not resulting in clash, it is unfavourable compared to a stronger OH···OH_2 hydrogen bonding interaction that the tyrosine can offer. The two different models are shown in a pseudo-stereo figure. Adapted with permission from {*J. Med. Chem*. 2020, 63, 6, 2941–2957}. Copyright {2020} American Chemical Society [78]

Based on the novel SAR studies conducted in our group,[209,211,210] and the published crystal structure of human CD73 in complex with AMPCP in the closed state (PDB 4H2I),[61] Arcus Biosciences Inc. developed its exceptionally potent AMPCP derivative Quemliclustat (AB680, compound **10,** K_i = 5 pM, **Figure 19**).[211,212,213] Quemliclustat exhibited slow, tight binding kinetics as indicated by changes in IC_{50} values relative to the incubation time and enzyme concentration.[212] N^6- and C2-substitutions were in complete agreement with our previous findings.[209,210] However, the adenine base was modified, namely N1 was replaced by CH and N7 was moved from the 7- to the 8-position.[213] Quemliclustat tested in our in-house assays showed a K_i value of 0.0294 nM in a radioligand binding assay and of 0.0197 nM using an enzyme inhibition assay utilizing radioactive AMP as a substrate.[170] These K_i values fall within the same range as some of our developed unpublished inhibitors (e.g., compound **9**, PSB-19294, **Figure 19**).[211]

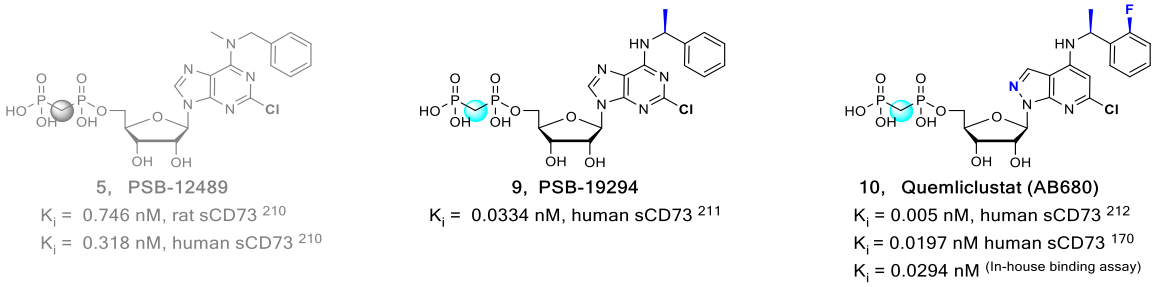
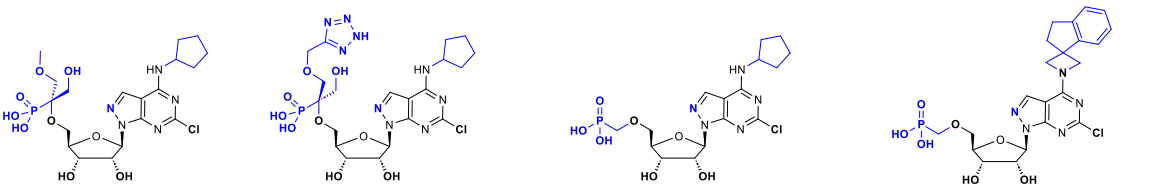


Figure 19. Structures of nucleotide-based CD73 inhibitors with subnanomolar potency.

Based on the binding mode of AMPCP to human CD73, ORIC Pharmaceuticals developed OP-5244 (**11**, **Figure 20**) and ORIC-533 (**12**, **Figure 20**) as orally available CD73 inhibitors with IC_{50} values of 0.25 nM and 0.1 nM, respectively.[214,215] One year later, Arcus Biosciences published a closely related methylenephosphonic acid derivative (**13**, **Figure**

20) with a K_i value of 2.5 nM.[216] Eternity Biosciences also published SHR170008 (**14**, **Figure 20**) with an IC_{50} value of 0.05 nM. SHR170008 enhanced the anti-tumor activity of PD-1 blockade in a breast cancer mouse model.[217] In all methylenephosphonic acid inhibitors shown in **Figure 20**, the adenine base was replaced by a pyrazolopyrimidine to maximize the π–π stacking between F500 and F417 residues.



11, OP-5244
IC_{50} = 0.25 nM (soluble human CD73)[214]
(ORIC PHARMACEUTICALS)

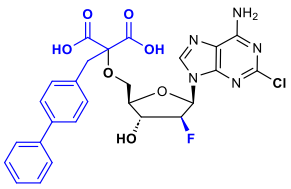
12, ORIC-533
IC_{50} = 0.1 nM (soluble human CD73)[215]
(ORIC PHARMACEUTICALS)

13
IC_{50} = 2.6 nM (soluble human CD73)[216]
(Arcus Biosciences Inc.)

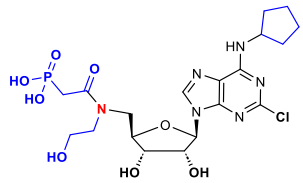
14
IC_{50} = 0.050 nM (soluble human CD73)[217]
(Eternity Biosciences)

Figure 20. Structures of monophosphonate as CD73 inhibitors.

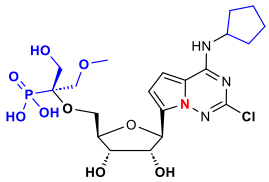
Several patents have been filed by various companies for CD73 inhibitors featuring slightly modified adenine or phosphate/phosphonate moieties. Examples for these compounds are presented in **Figure 21**.[218,219,220,221,222,223]



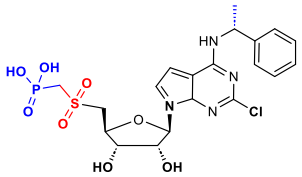
15
IC_{50} = **29** nM [218]
(patent WO 2018/049145) by CALITHERA BIOSCIENCES



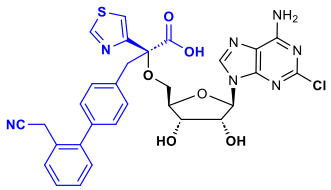
16
IC_{50} = < 100 nM [219]
(patent WO 2018/094148) by ARCUS BIOSCIENCE



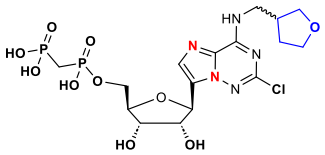
17
IC_{50} = < 0.5 nM [220]
(patent WO 2021/011689) by ORIC PHARMACEUTICALS



18
IC_{50} = < 10 nM [221]
(patent WO 2018/183635) by PELOTON THERAPEUTICS, INC



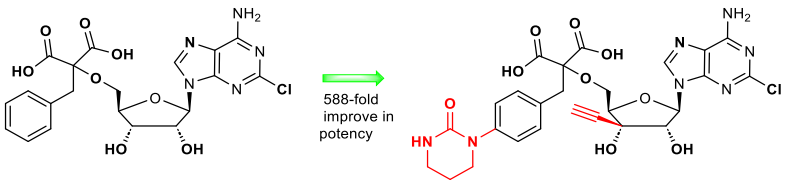
19
IC_{50} = 35 nM [222]
(patent WO 2020/257429) by CALITHERA BIOSCIENCES



20
IC_{50} = < 1 nM [223]
(patent WO 2020/211672) by BIOARDIS LLC [US]/[US]

Figure 21. Selection of recently patented nucleotide analogs as CD73 inhibitors.

More recently, Calithera Biosciences reported the discovery of a series of orally bioavailable potent nucleoside inhibitors of CD73 based on hit compound **21** (IC_{50} = 100 nM, **Figure 22**).[224] The most potent inhibitor (compound **22**, IC_{50} = 0.17 nM, **Figure 22**) showed nearly 590-fold improvement in potency compared to the hit **21**. Moreover, **22** inhibited CD73 in serum samples from cancer patients and reversed adenosine-mediated suppression of CD^{8+} T cells.[224]

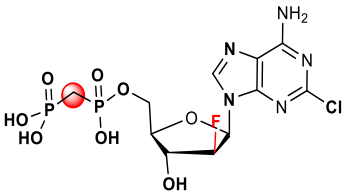


21
IC_{50} = 100 nM (biochemical CD73 assay)[224]
(Calithera Biosciences)

22
IC_{50} = 0.17 nM (biochemical CD73 assay)[224]
(Calithera Biosciences)

Figure 22. Nucleoside-derivatives developed by Calithera Biosciences as potent CD73 inhibitors.[224]

Dumontet et al. introduced α,β-methylenebisphosphonate for CD73 inhibition into the structure of three nucleoside analogs used as anti-cancer drugs.[225] 5'-(a,β-Methylene)diphosphate of clofarabine (**23**, **Figure 23**) was the most potent CD73 inhibitor of this series with an IC_{50} of 0.180 µM. However, the cytotoxicity of the molecule was reduced compared to the parent clofarabine.[225]



23, Clofarabine-Diphosphonate
IC_{50} = 0.180 µM [225]

Figure 23. clofarabine-5'-(a,β-methylene)diphosphate as CD73 inhibitor.

In a collaboration project with Prof. Kenneth A. Jacobson (National Institute of Diabetes, Digestive and Kidney Diseases, NIH, USA), further SAR studies of nucleotide analogs were initiated to investigate modifications of the ribose moiety, the adenine base, and to study pyrimidine nucleotides as alternatives to purine-based CD73 inhibitors.[226] In these studies, the 7-deaza analog of AMPCP was found to be 2-fold more potent than AMPCP (88.6 nM vs. 167 nM), whereas 1-deaza- and 3-deaza-AMPCP were inactive. Loss of inhibitory activity of uridine-based inhibitors was observed when replacing the methylene linker between the phosphonate groups with ethylene.[226] A small and highly electronegative fluorine atom at position 5 of uracil led to a large increase in inhibitory potency (**24**, UMPCP, 1830 nM vs. **25**, 5-fluoro-UMPCP, 4.51 nM (membrane-bound CD73), **Figure 24**). Various modifications on the cytidine scaffold were successful resulting in the most potent inhibitor among this series, N^4-[O-(4-benzyloxy)]-3-methyl-cytidine-5'-diphosphonate (**26**, K_i = 3.67 nM (rat CD73), 7.96 nM (membrane-bound CD73), **Figure 24**). Alterations of the ribose ring were not tolerated except for 2′-ara-fluoro-2′-deoxy-UMPCP which was as potent as UMPCP (K_i = 1750 nM and 1830 nM, respectively).[226]

Further exploration of N3-methyl-N^4-substituted cytidine through substitutions on the N^4-benzyl ring were attempted to improve potency and to investigate SARs.[227] Assessment of various substituents at different positions on the benzyl ring yielded derivatives with 10- to 20-fold enhanced potency relative to the lead structure N^4-[O-(4-benzyloxy)]-3-methyl-cytidine (**25**). The best tolerated substitution on the benzyl ring was a *para*-substitution providing a derivative with the highest inhibitory activity among this cluster, the 4-iodo-substituted N3-methyl-N^4-benzyloxyimino-cytidine diphosphonate with a K_i value of 0.436 nM (**27**, **Figure 24**).[227]

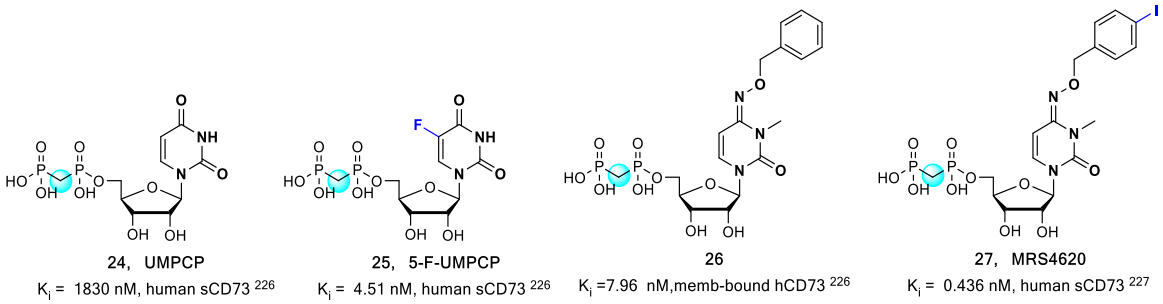


Figure 24. Structures of selected uridine- and cytidine-based CD73 inhibitors.

Multitarget ectonucleotidase inhibitors acting on CD73 and CD39 were identified by our group within a series of ATP derivatives that were primarily developed to target CD39.[228] The most potent inhibitor obtained (**28**, **Figure 25**) showed K_i values of 0.185 µM and 1.51 µM at CD73 and CD39, respectively. An acyclic analog of AMPCP (**29**, **Figure 25**) was identified as dual CD73/NPP1 inhibitor.[229]

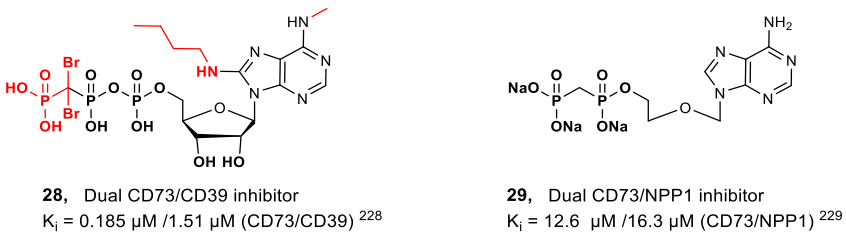


Figure 25. Multitarget CD73 inhibitors.

1.13.1.2. Non-nucleotidic inhibitors of CD73

Research on the development of non-nucleotidic inhibitors of CD73 had been started early, however, has been less successful than the development of nucleotide analogs. The

anthraquinone dye Reactive Blue 2 was previously identified to interact with several nucleotide-binding proteins such as P2X, P2Y receptors and NTPDases.[230,231,232,233,234] Accordingly, the anthraquinone scaffold was anticipated to potentially interact with CD73 as well. First, Reactive Blue 2 and Acid Blue 25 dyes (**Figure 26**) were screened for CD73 inhibition in our group and K_i values of 3.07 µM and 15.2 µM were , respectively, determined.[235] This was followed by extensive SAR studies which led to the discovery of the most potent non-nucleotide-based inhibitors know until recently, 1-amino-4-[4-fluoro-2-carboxyphenylamino]-9,10-dioxo-9,10-dihydroanthracene-2-sulfonate (**30**, PSB-0952, K_i = 260 nM) and 1-amino-4-[2-anthracenylamino]-9,10-dioxo-9,10-dihydroanthracene2-sulfonate (**31**, PSB-0963, K_i = 150 nM) shown in **Figure 26**.[235] This scaffold showed a competitive mode of inhibition.

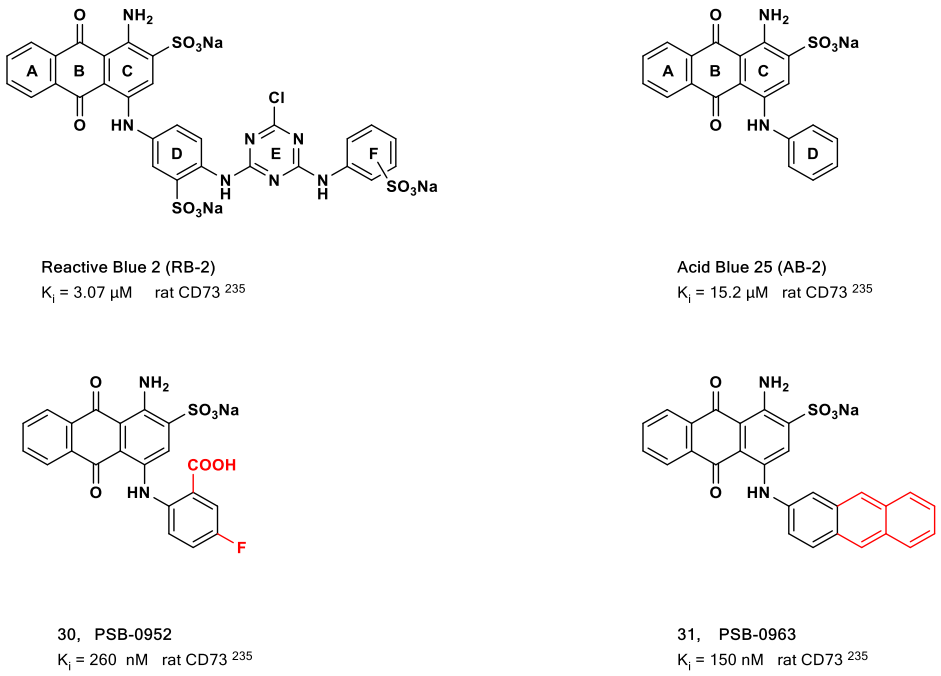


Figure 26. Anthraquinone-based CD73 inhibitors.

Prior to the disclosure of the human CD73 crystal structure in 2012, virtual screening of 70000 test compounds was performed using a model of ecto-5'-nucleotidase. The aim was to identify new scaffolds that might be orally bioavailable.[236] A diverse set of 51 compounds was selected and subjected to *in vitro* screening, in which 13 sulfonamide-containing compounds were identified as CD73 inhibitors. 6-Chloro-2-oxo-N-(4-sulfamoylphenyl)-2*H*-chromene-3-carboxylic acid amide (**32**, **Figure 27**) was the most potent compound in this series showing an IC_{50} value of 1.90 µM and a competitive mode of inhibition. Later

on, compound **32** was characterized in another study as a noncompetitive inhibitor of CD73.[164] Most of the identified hits were comprised of a heterocycle or benzene ring linked by either an amide, a urea or a hydrazone to a sulfonamide group.[236] The ring was proposed to mimic the π-π stacking of the adenine base, and the sulfonamide group was thought to bind to the zinc dimetal center. However, a co-crystal structure has so far not been obtained to unambiguously prove its binding site and interactions.

In vitro screening of 13 commercially available sulfonic acid-substituted compounds identified compound **33** (**Figure 27**) as the most potent CD73 inhibitor within the series.[237] The compound was reported to be about 8-fold more potent at human CD73 as compared to rat CD73 (IC_{50} = 1.32 µM and 10.4 µM at human and rat CD73, respectively).[237]

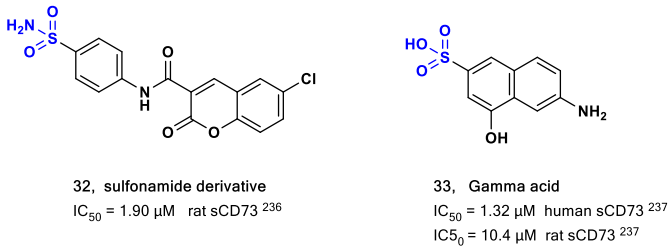


Figure 27. Non-nucleotide inhibitors identified in different virtual and *in vitro* screening programs.

A group of researchers from the University of Montpellier, France, adopted a different bioinformatic approach to identify allosteric modulators of CD73 that target the dimerization interface.[238] Several hit compounds were obtained as non-competitive inhibitors and others as mixed inhibitors. The most potent molecule (**34**, RR3, **Figure 28**) exhibited a K_i value 0.53 µM.[238] Based on these results further *in silico* approach was implemented by the same research group to design new allosteric inhibitors of CD73 based on hit compounds **35** and **36** (**Figure 28**).[239] Morpholino-substituted derivatives (**37** and **38**, **Figure 28**) were found to reverse the immune suppression of human T cells mediated by adenosine.[239]

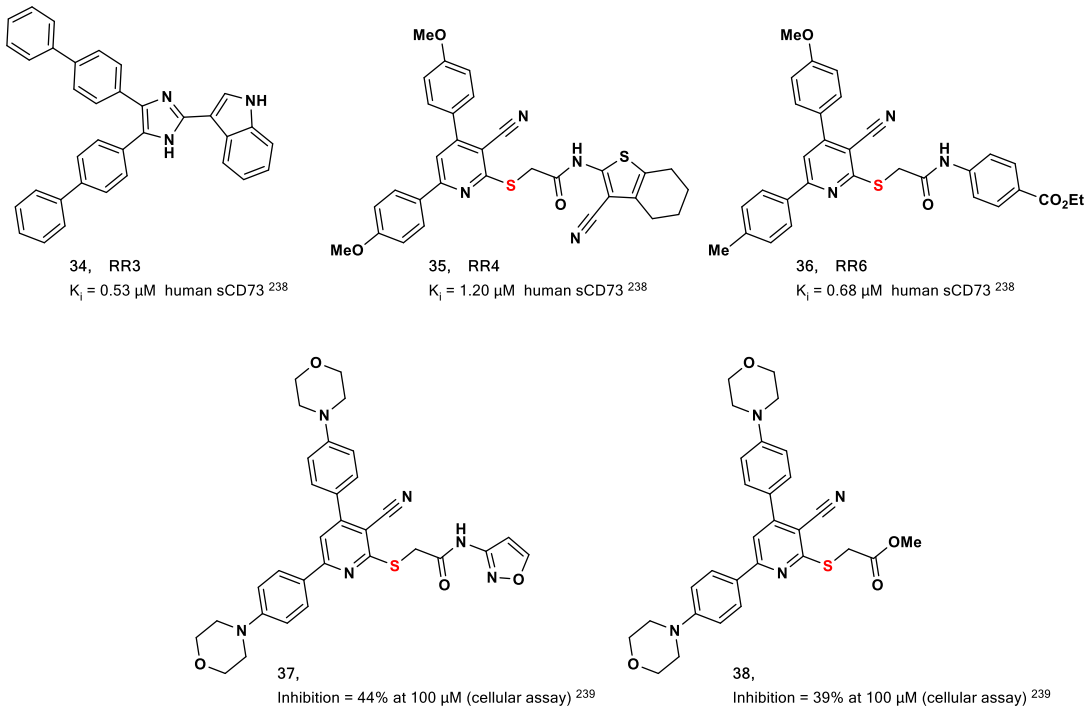


Figure 28. Allosteric modulators targeting the dimer interface of human CD73.[238,239]

In 2017, GlaxoSmithKline (GSK) patented a series of 187 benzothiadiazine derivatives as CD73 inhibitors, some of which are presented on **Figure 29** with their respective IC_{50} values.[240] The declared most potent compound within this cluster, compound **44**, showed an IC_{50} value of 15.9 nM determined by the RapidFire mass spectrometry assay.[240]

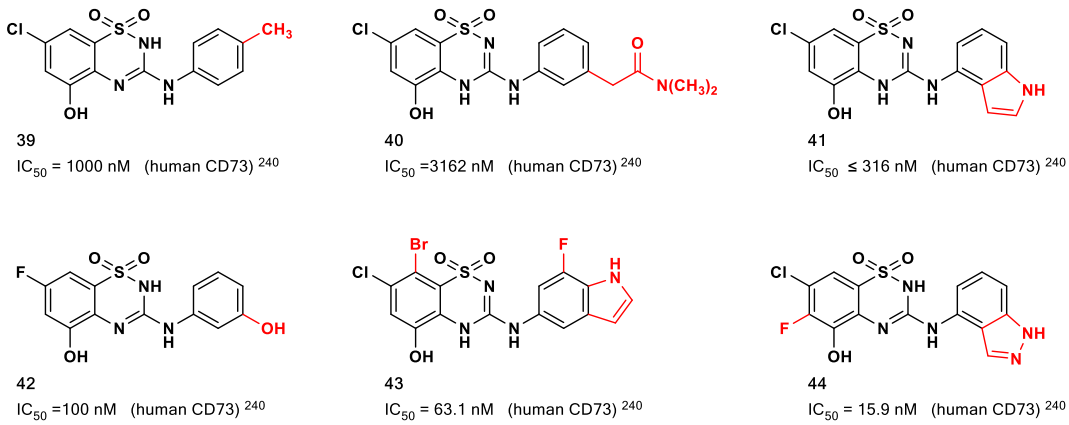
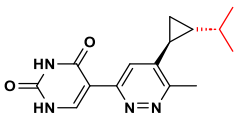
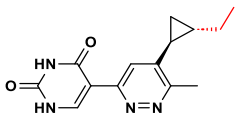


Figure 29. Benzothiadiazine-based CD73 inhibitors disclosed in a GSK patent (WO2017/098421).

Several nitrogen-containing heterocycles were investigated as new scaffolds to generate CD73 inhibitors. In 2019, Eli Lilly patented derivatives of 5-[5]-[2-cycloalkyl]-6-pyridazin-3-yl]-1*H*-pyrimidine-2,4-dione as CD73 inhibitors.[241] The most potent compound, LY-3475070 (5-[5-[(lS,2R)-2-isopropylcyclopropyl]-6-methyl-pyridazin-3-yl]-l*H*-pyrimidine-2,4-dione, **45**, **Figure 30**) exhibited an uncompetitive mode of inhibition with an IC_{50} value of 0.028 µM at soluble human CD73, and of 0.0073 µM in a cellular assay using the Calu-6 cell line (human lung adenocarcinoma cell line). This compound was about 6-fold more potent at human as compared to mouse CD73. A second derivative with a 2-ethylcyclopropyl substituent (**46**, **Figure 30**) showed a more than 3-fold drop in potency compared to the 2-isopropylcyclopropyl derivative LY-3475070 (**45**).[241]



45, LY-3475070
IC_{50} = 0.028 µM (soluble human CD73)
IC_{50} = 0.175 µM (soluble mouse CD73)
IC_{50} = 0.0073 µM (Calu-6 human cell assay) [241]



46, Eli Lilly compound
IC_{50} = 0.043 µM (soluble human CD73)
IC_{50} = 0.028 µM (Calu-6 human cell assay) [241]

Figure 30. Eli Lilly and Company patent inhibitors of CD73 (WO2019/168744).[241]

Arcus Biosciences patented (WO2020/046813) and published the SARs of the most potent non-nucleotidic CD73 inhibitors known to date.[242,243] In this study, nine inhibitors with diverse scaffolds were identified through HTS of a library of more than 200,000 compounds using the malachite green assay.[243] Compound **47,** depicted in **Figure 31** (IC_{50} = 15.6 µM), was selected as a lead structure for further optimization. Chemical and metabolic stability of the hit compound **47** were to be optimized as well as the potency. This resulted in two potent inhibitors, 4-({5-[4-fluoro-1-(2*H*-indazol-6-yl)-1*H*-1,2,3-benzotriazol-6-yl]-1*H*-pyrazol-1-yl}methyl)-benzonitrile (**48**, IC_{50} = 12 nM) and 4-({5-[4-chloro-1-(2*H*-indazol-6-yl)-1*H*-1,2,3-benzotriazol-6-yl]-1*H*-pyrazol-1-yl}methyl)-benzonitrile (compound **49**, IC_{50} = 19 nM) shown on **Figure 31**.[243] Compound **49** was co-crystallized with human CD73. The obtained crystal structure indicated binding to the active site with the benzotriazole ring sandwiched between F411 and F500. However, these potent inhibitors were found to have low metabolic stability and high inhibitory effects on cytochromes P450 (CYP) isoenzymes. Further optimization, in which the benzimidazolone scaffold was replaced with an indazole ring, yielded compound **50** (IC_{50} = 53.5 nM) with more favorable

pharmacokinetic properties. However, the potency dropped by 4-fold compared to compound **48**.[243]

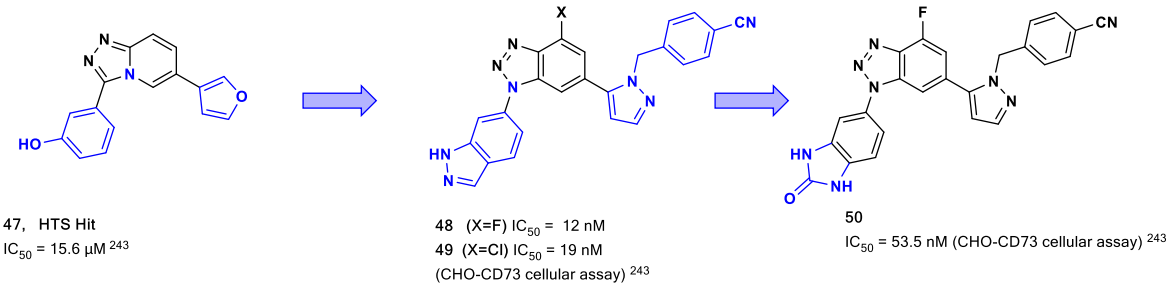


Figure 31. Arcus Bioscience patent: most potent competitive non-nucleotidic inhibitors of CD73.[243]

A very recently published patent (US2024/0116928A1, April 2024) by Gilead Sciences Inc. showed a series of 30 heterocyclic N-containing compounds as CD73 potent inhibitors. All patent molecules have IC_{50} values below 50 nM, with molecule **51** (**Figure 32**) been the most potent among this series with an IC_{50} value of 1.157 nM.[244] Hoffmann-La Roche also filed a patent of closely related structure with a much less potency against CD73. Compound **52** (**Figure 32**) showed an IC_{50} value of 254 nM.[245]

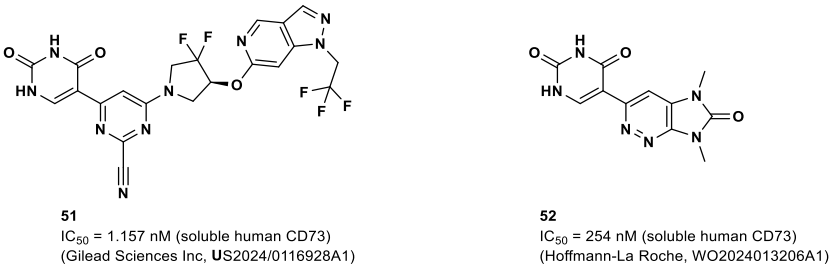


Figure 32. Recently patent non-nucleotidic inhibitors of CD73 by Gilead Sciences Inc and Hoffmann-La Roche.[244,245]

In another study, a molecular hybridization strategy was employed by F. Varano et al. to design dual CD73/A_{2A}AR blockers.[246] Pharmacophoric units obtained from two previously identified active scaffolds, namely thiazolo[5,4-*d*]pyrimidines and benzenesulfonamides (discovered in our lab) were linked to generate new bifunctional molecules (e.g. **53**, **Figure 33**). The reported compounds were highly selective and potent at the A_{2A}AR subtype, however they exhibited very weak CD73 inhibition at concentrations of up to 100 µM.[246]

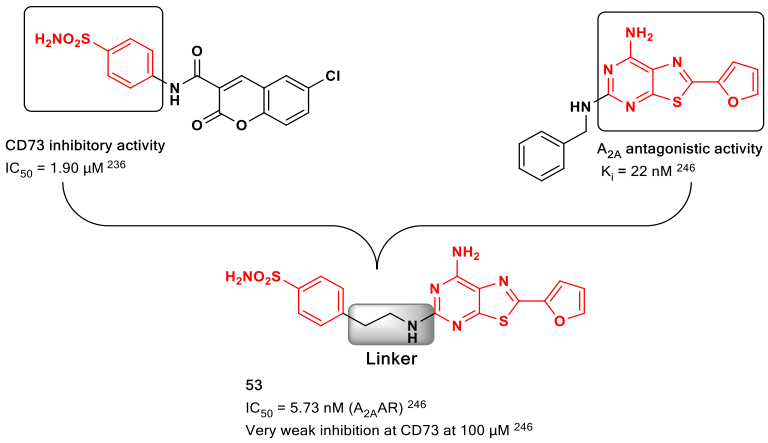


Figure 33. Molecular hybridization approach to develop dual CD73/A_{2A}AR blockers.[246]

1.13.1.3. Natural products and derivatives as CD73 inhibitors

Naturally occurring flavonoids were suggested as early as 2002 to play a beneficial role in inhibiting tumorigenesis.[247] Quercetin (**54**, **Figure 34**), which is abundant in a wide range of fruits and vegetables, was identified as an inhibitor of CD73 activity (IC_{50} = 45.3 µM) and a modulator of its expression in U138MG glioma cells.[248] Quercetin was found to exhibit a noncompetitive mode of inhibition.[248] Another flavonoid, Baicalin (**55**, **Figure 34**), was crystallized in complex with human CD73 in a binding mode similar to that of AMPCP derivatives with the planar chromene ring and the glucuronic acid moiety replacing the adenine base and the ribose sugar moiety interactions.[61]

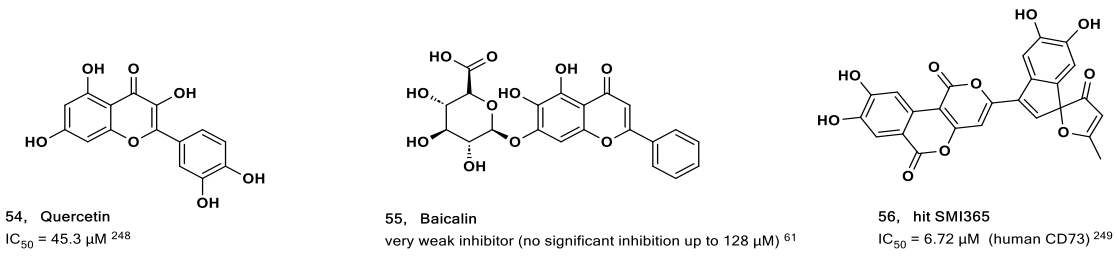


Figure 34. Natural flavonoids and Phelligridin-containing compounds as CD73 inhibitors.[61,248, 249]

Furthermore, phelligridin-containing compounds were identified as new CD73 inhibitors through structure-based virtual screening of the Chemdiv-Plus database, with hit compound **56** having an IC_{50} value of 6.72 µM (**Figure 34**).[249] Docking studies suggested that the

phelligridin ring showed a π-π stacking interaction between F417 and F500 residues similar to that exhibited by the adenine base.[249]

Iqbal et al. identified spirooxindole as a natural product-derived scaffold for CD73 inhibitors.[250] The most potent compounds, presented in **Figure 35**, were **57** (IC_{50} = 0.15 µM against human CD73 and **58** (IC_{50} value of 0.19 µM against rat CD73). Compound **57** showed a noncompetitive mode of inhibition at human CD73 and compound **58** inhibited rat CD73 uncompetitively.[250] Although the studied mode of inhibition indicated binding to an allosteric site, *in silico* studies were conducted by docking of the most potent derivative (**57**) into the human enzyme's orthosteric site and they were used to rationalize the obtained biological activities.

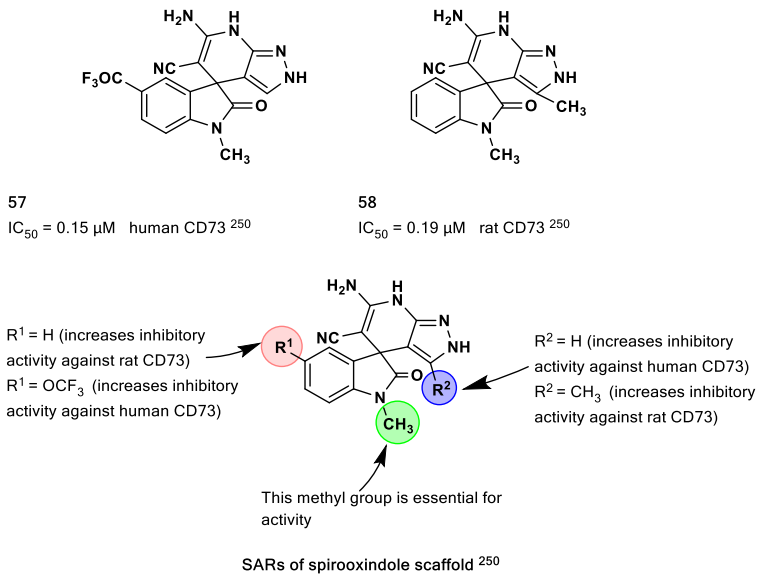


Figure 35. Spirooxindole scaffold as CD73 inhibitors.[250]

1.13.2. Monoclonal antibodies

Although monoclonal antibodies (mAbs) as macromolecules have penetration limitations and an unfavorable route of administration, a number of inhibitory mAbs was developed as CD73 inhibitors and tested in clinical settings. For example, MedImmune produced the most advanced monoclonal CD73 antibody, MEDI9447, which provides distinct noncompetitive dual inhibition through inter-CD73 dimer crosslinking and/or steric impedance that inhibits CD73 to attain the catalytically active closed conformation.[156] MEDI9447 (Oleclumab) is currently evaluated in phase 2 clinical trials, as a monotherapy

or in combination with other antitumor drugs (see **Table 4**), for the treatment of recurrent, refractory, or metastatic sarcoma, pancreatic adenocarcinoma, luminal breast cancer, prostate cancer, and non-small cell lung cancer.[251,252,253]

Another mAb, AGEN1423 (Dalutrafusp alfa), is a multitarget anti-CD73-TGFβ-Trap bifunctional antibody developed by Agenus, which is presently under assessment in a phase 2 interventional study for the treatment of advanced pancreatic cancer.[254] Besides these examples, several further mAbs were developed e.g., BMS986179, SRF373 (NZV930), CPI-006 (CPX-006), IPH5301, and TJ004309, which are currently being evaluated in clinical trials (refer to **Table 4**).[255]

1.14. Anti-CD73 candidates in clinical trials

In addition to the mAbs mentioned in the previous section, several small molecules are now being assessed in clinical studies as anti-CD73 drugs. Quemliclustat (AB680) is the first small molecule inhibitor of CD73 undergoing clinical trials. According to clinicaltrial.gov, it is currently evaluated for the treatment of metastatic castrate-resistant prostate cancer, locally advanced pancreatic ductal adenocarcinoma, metastatic colorectal cancer and other gastrointestinal (GIT) malignancies. In late 2022, ORIC Pharmaceutical announced its highly potent orally available clinical candidate ORIC-533 which is being evaluated in phase 1 studies.[215] Another small molecule inhibitor developed by Eli Lilly, LY-3475070, completed recruitment for a phase 1 clinical trial in mid-2022.[256]

A comprehensive list of ongoing clinical studies involving anti-CD73 treatment is presented in **Table 4**.

Table 4. Ongoing clinical studies involving anti-CD73 candidates (retrieved on 25.02.2024 from clinicaltrials.gov)

NCT number	Interventions	Sponsor	Phase
Small molecule CD73 inhibitors			
NCT05688215	Fluorouracil (anti-metabolite); Irinotecan (topoisomerase I inhibitor); Leucovorin (folic acid analog); Oxaliplatin (alkylating agent); **Quemliclustat (AB680, CD73 inhibitor)**; Zimberelimab (anti-PD-1 monoclonal antibody)	Jonsson comprehensive cancer center	Phase 1/Phase 2
NCT04104672	**AB680 (CD73 inhibitor)**; Zimberelimab (anti-PD-1 mAb); Nab-paclitaxel (taxane chemotherapeutic agent); Gemcitabine (nucleoside chemotherapeutic agent)	Arcus biosciences, inc.	Phase 1
NCT03677973	**AB680 (CD73 inhibitor)**, placebo	Arcus biosciences, inc.	Phase 1
NCT04575311	**AB680 (CD73 inhibitor)**, placebo	Arcus biosciences, inc.	Phase 1
NCT04660812	**AB680 (CD73 inhibitor)**; Etrumadenant (dual A_{2A}/A_{2B} antagonist); Zimberelimab (anti-PD-1 mAb); Bevacizumab (VEGF-A mAb); m-FOLFOX-6 regimen (5-Fluorouracil, leucovorin, and oxaliplatin) Regorafenib (multi kinase inhibitor)	Arcus biosciences, inc.	Phase 1/Phase 2
NCT04381832	Etrumadenant (dual A_{2A}/A_{2B} antagonist); Zimberelimab (anti-PD-1 mAb); **Quemliclustat (CD73 inhibitor AB680)**; Enzalutamide (androgen receptor (AR) inhibitor); Docetaxel (Taxane)	Arcus biosciences, inc.	Phase 1/Phase 2
NCT05329766	Domvanalimab (anti-TIGIT mAbs); **Quemliclustat (AB680, CD73 inhibitor)**; Zimberelimab (anti-PD-1 mAb); Fluorouracil; Leucovorin; Oxaliplatin	Arcus biosciences, inc.	Phase 2
NCT04148937	**LY3475070 (CD73 inhibitor)**; Pembrolizumab (anti-PD-1 mAb)	Eli Lilly and company	Phase 1

NCT05227144	**ORIC-533 (CD73 inhibitor)**	Oric pharmaceuticals	Phase 1
Anti-CD73 monoclonal antibodies			
NCT05632328	**AGEN1423 (Anti-CD73-TGFβ-Trap bifunctional antibody)**; Balstilimab (anti-PD-1 antibody); Gemcitabine; Nab-paclitaxel	Bruno Bockorny	Phase 2
NCT05173792	**AK119 (Anti-CD73 mAb)**	Akeso	Phase 1
NCT05559541	**AK119 (anti-CD73 mAb)**; AK104 (bi-specific PD-1/ CTLA-4 antibody)	Akeso	Phase 1/Phase 2
NCT04516564	**AK119 (anti-CD73 mAb)**, placebo	Akesobio Australia	Phase 1
NCT05689853	**AK119 (Anti-CD73 mAb)**; AK112 (PD-1/VEGF bi-specific antibody)	Akeso	Phase 1/Phase 2
NCT04572152	**AK119 (Anti-CD73 mAb)**; AK104 (bi-specific PD-1/ CTLA-4 antibody)	Akeso	Phase 1
NCT06166888	**AK131 (anti-PD-1 and CD73 bispecific antibody)**	Akeso	Phase 1
NCT03454451	**CPI-006 (anti-CD73 mAb)**; CPI-006 + Ciforadenant (adenosine A_{2A} receptor antagonist) CPI-006 + Pembrolizumab (anti-PD-1 mAb)	Corvus pharmaceuticals	Phase 1
NCT03954704	**Dalutrafusp alfa (specific bifunctional antibody against CD73 and TGF-β)**; mFOLFOX6 Regimen (5-Fluorouracil, leucovorin, and oxaliplatin)	Gilead sciences	Phase 1
NCT04797468	**HLX23 (anti-CD73 mAb)**	Shanghai Henlius biotech	Phase 1
NCT06056323	**HB0045 (anti-CD73 mAb)**	Shanghai Huaota	Phase 1/Phase 2
NCT05246995	**IBI325 (anti-CD73 mAb)**; Sintilimab (anti PD-1 mAb)	Shandong cancer hospital and institute	Phase 1
NCT05119998	**IBI325 (anti-CD73 mAb)**; Sintilimab (anti PD-1 mAb)	Innovent biologics (suzhou) co. Ltd.	Phase 1

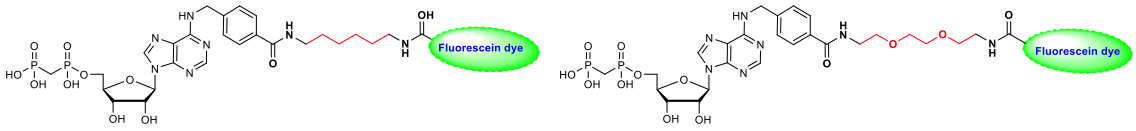
NCT05143970	**IPH5301 (anti-CD73 mAb)** alone or in combination with chemotherapy and trastuzumab (anti-HER2 mAb)	Institut Paoli-calmettes	Phase 1
NCT05174585	**JAB-BX102 (anti-CD73 mAb)**; Pembrolizumab (anti-PD-1 mAb)	Jacobio pharmaceuticals	Phase 1/Phase 2
NCT03549000	**NZV930 (anti-CD73 mAb)**; PDR001 (anti-PD-1 mAb); NIR178 (A_{2A}AR antagonist)	Novartis pharmaceuticals	Phase 1
NCT04262375	Durvalumab (anti-PD-L1 mAb); **Oleclumab (anti-CD73 mAb, MEDI9447)**	University health network, Toronto	Phase 2
NCT04668300	Durvalumab (anti-PD-L1 mAb); **Oleclumab (anti-CD73 mAb, MEDI9447)**	M.d. anderson cancer center	Phase 2
NCT04940286	Durvalumab; Gemcitabine; Nab-paclitaxel; **Oleclumab (anti-CD73 mAb, MEDI9447)**	M.d. anderson cancer center	Phase 2
NCT06060405	Durvalumab (anti-PD-L1 mAb); **Oleclumab (anti-CD73 mAb, MEDI9447)**	University health network, Toronto	Phase 2
NCT03267589	Durvalumab (anti-PD-L1 mAb); Tremelimumab (anti- CTLA-4 mAb); **MEDI9447 (anti-CD73 mAB)**; MEDI 0562 (anti- OX40 mAb)	Nordic society of gynecological oncology	Phase 2
NCT04262388	Durvalumab; **Oleclumab (anti-CD73 mAb, MEDI9447)**	University health network, Toronto	Phase 2
NCT02503774	**Oleclumab (anti-CD73 mAb, MEDI9447)**; Durvalumab (anti-PD-L1 mAb)	Medimmune	Phase 1
NCT03801902	Durvalumab (anti-PD-L1 mAb); Monalizumab (anti-NKG2A blocking mAb); **Oleclumab (anti-CD73 mAb, MEDI9447)**	National cancer institute (NCI)	Phase 1
NCT03381274	**Oleclumab (anti-CD73 mAb, MEDI9447)**; Osimertinib (epidermal growth factor receptor tyrosine kinase inhibitor); AZD4635 (inhibitor of A_{2A}AR)	Medimmune	Phase 1/Phase 2
NCT05431270	**PT199 (anti-CD73 mAb)**; Tislelizumab (anti-PD-1 monoclonal antibody	Phanes therapeutics	Phase 1
NCT04672434	Sym021(anti-PD1 mAb); **Sym024 (anti-CD73 mAb)**	Symphogen A/S	Phase 1

NCT06162572	S095018 (anti-TIM3 antibody); **S095024 (anti-CD73 mAb)**; S095029 (anti-NKG2A mAb); Cemiplimab (anti-PD1 mAb)	Servier Bio-innovation	Phase 1/Phase 2
NCT05001347	**TJ004309 (anti-CD73 mAb)**	I-mab biopharma limited	Phase 2
NCT03835949	**TJ004309 (anti-CD73 mAb)**; Atezolizumab (anti-PD-L1 mAb)	Tracon pharmaceuticals	Phase 1
NCT04322006	**TJ004309 (anti-CD73 mAb)**; Toripalimab (anti-PD-1 mAb)	I-mab biopharma co. Ltd.	Phase 1/Phase 2

*In **Bold** are anti-CD73 interventions

1.15. Pharmacological probes to study CD73

Until recently, AMPCP and anti-CD73 antibodies were the only commercially available pharmacological tools that were used for the characterization of CD73 for target validation studies *in vitro* and *in vivo*. AMPCP (**3**, K_i = 197 nM (soluble rat), 88 nM (soluble human), 207 nM (human MDA-MB-231 membrane-bound), 280 nM (mouse 4T1.2 membrane-bound), **Figure 15**) exerts moderate ancillary inhibition on NPP1 (K_i = 16500 nM). It was also found to have low metabolic stability as it is completely metabolized within 15 min of incubation in rat liver microsomes.[209] Several nucleotide derivatives were developed by our group that show higher potency and stability compared to AMPCP with low off-target effects. Examples include, PSB-12379 (**4**, **Figure 15**), an N^6-benzyl derivative of AMPCP that is commercially available,[209] PSB-12651, and PSB-12489 (**5**, **Figure 16**) with sub-nanomolar potency at soluble human CD73.[210] AB680 (Quemliclustat), a highly potent (**10**, K_i = 5 pM, **Figure 19**) showing selective (>10000-fold selective over other ectonucleotidases) small molecule inhibitor of CD73 developed by Arcus Biosciences and is also commercially available.[213] Compound **48**, the most potent non-nucleotide inhibitor of CD73 (K_i = 12 nM, **Figure 31**) provides another alternative for CD73 studies. However, compound **48** suffers from metabolic instability and inhibition of CYP enzymes which renders it only applicable in *in vitro* or *ex vivo* studies, and it is not commercially available.[243]



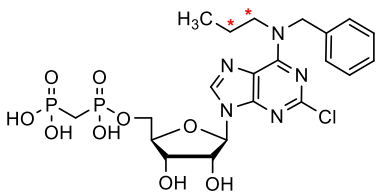
59, PSB-18332
K_i = 2.98 nM, human sCD73 [257]

60, PSB- 19416
K_i = 12.6 nM, human sCD73 [257]

Figure 36. Fluorescein-labeled CD73 inhibitors.[257]

Several labeled ligands are available for studying CD73; they were mostly designed and synthesized by our group. Examples are the fluorescent probes PSB-19416 and PSB-18332 (shown in **Figure 36**). In these tracers, fluorescein was attached to the benzyl residue of PSB-12379 via two different linkers, an ethylene glycol or an alkyl linker, resulting in PSB-19416 (K_i = 12.6 nM) and PSB-18332 (K_i = 2.98 nM), respectively.[257] These fluorescent probes were employed in fluorescence microscopy studies to localize CD73 in different cell lines and tissue specimens.[257] Moreover, they were applied in a recently developed NanoBRET assay that will be discussed further in the Results section of this thesis.

Pioneering research in our group also yielded compound PSB-17230 (K_i = 0.0733 nM, **Figure 37**), whose precursor has been tritium-labeled, representing the first available radiolabeled ligand of CD73 ([^{3}H]PSB-17230, 108 Ci/mmol specific activity). This potent radioligand was applied in a newly established radioligand binding assay using triple negative breast cancer cells (MDA-MB-231) (see Results section). Furthermore, [^{3}H]PSB-17230 was successfully used as a diagnostic tool in autoradiography studies.

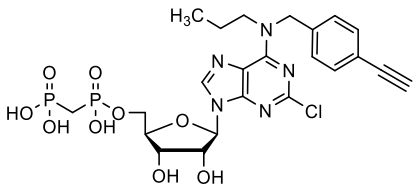


61, [^{3}H]PSB-17230
The unlabeled tracer has a K_i = 0.0733 nM (soluble human CD73)

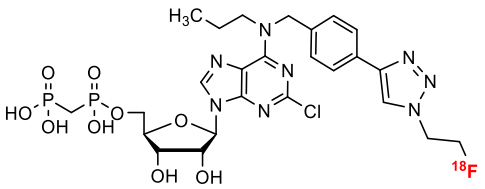
Figure 37. Tritium-labeled CD73 inhibitor.

Moreover, a novel positron emission tomography (PET) tracer (**63**, [^{18}F]PSB-19427, **Figure 38**) was designed and synthesized in our research group and further radiolabeled in collaboration with Anna Junker (European Institute for Molecular Imaging (EIMI),

University of Münster, Germany). Extensive studies are ongoing and results will be published soon.



62, PSB-19425 (PET precursor)
K_i = 0.372 nM (soluble human CD73)



63, [^{18}F]PSB-19427 (PET tracer)
Unlabeled-tracer K_i = 1.02 nM (soluble human CD73)

Figure 38. Development of novel PET tracer by the laboratories of Christa Müller (University of Bonn) and Anna Junker (University of Münster, currently university of Tübingen).

2. Published articles

2.1. 2-Substituted AMPCP derivatives

2-Substituted α,β-Methylene-ADP Derivatives: Potent Competitive Ecto-5′-nucleotidase (CD73) Inhibitors with Variable Binding Modes

Sanjay Bhattarai, Jan Pippel, Emma Scaletti, ***Riham Idris****, Marianne Freundlieb, Georg Rolshoven, Christian Renn, Sang-Yong Lee, Aliaa Abdelrahman, Herbert Zimmermann, Ali El-Tayeb, Christa E. Müller, and Norbert Sträter*

J. Med. Chem. **2020**, 63, 2941−2957. doi.org/10.1021/acs.jmedchem.9b01611

Introduction

CD73 is a glycosylphosphatidylinositol (GPI)-anchored homodimeric glycoprotein. It hydrolyzes nucleotide monophosphates to their corresponding nucleosides, mainly AMP to adenosine.[61,67] Adenosine interacts with four subtypes of G-protein-coupled receptors, A_1, A_{2A}, A_{2B} and A_3, and exerts anti-inflammatory and immunosuppressive effects in the tumor microenvironment.[258,259,143] Coupled with the fact that CD73 expression is upregulated in many types of tumors,[152] development of potent inhibitors of CD73 enzymes is considered to have a significant impact in the area of immuno-oncology.

After the discovery of N^6-benzyl- (PSB-12379, K_i = 2.21 nM)[209] and 2-chloro-N^6-benzyl-AMPCP (PSB-12651, K_i = 0.134 nM)[210] by our research group, the question of whether a single substitution at the C2 position of AMPCP would provide measurable improvement in the potency of AMPCP, was raised. Such modifications – (in the absence of a bulky N^6-benzyl substituent)- were anticipated to enhance the drug-like properties of the molecule. Accordingly, a series of 2-substituted AMPCP derivatives was synthesized and tested against soluble human and membrane-bound human CD73 obtained from membrane preparation of the triple negative breast cancer cell line MDA-MB-231 employing our published enzyme inhibition assay.[260] Moreover, species differences were evaluated by studying the compounds' inhibitory potency at rat CD73 as well.

Summary and outlook

Generally, bulky and/or rigid substituents at the C2-position were not favored. Nevertheless, most of the tested C2-substituents provided improved potency over unsubstituted AMPCP, except for PSB-12604 (compound **21**, Table 1, attached article in Appendix I) with a 2-(*N*-piperazinyl) group, which was 2-fold less potent than AMPCP (PSB-12604, K_i = 184 nM vs. AMPCP, K_i = 88.4 nM). Substitution of the C2-position with an iodo (**15**, K_i = 3.59 nM), a chloro (**16**, K_i = 5.93 nM), a hydrazinyl (PSB-12646, K_i = 15.5 nM), an amino (PSB12676, K_i = 38.8 nM), a cyclohexyl-ethylthio (**29**, K_i = 46.9 nM) or an allylthio (**28**, K_i = 61.9 nM) group resulted in more potent derivatives of AMPCP (for structures see Table 1, attached article in appendix 1). The 2-iodo- and 2-chloro-AMPCP were the most potent inhibitors among this series providing 25-fold and 15-fold increase in affinity, respectively. These 2-substituted derivatives were equipotent at soluble and membrane-bound CD73 with a slight preference for membrane-bound CD73 expressed on MDA-MB-231 cells (especially for compounds **15**, **16** and PSB-12646 with small iodo, chloro and hydrazinyl substituents). On the other hand, bulky substituents exhibited a slight reduction or similar potency at membrane-bound CD73 compared to soluble CD73 e.g., *N*-piperazinyl (PSB-12604, K_i = 184 nM (soluble CD73), 238 nM (membrane-bound CD73)), cyclohexyl-ethylthio (**29**, K_i = 46.9 nM (soluble CD73), 49.1 nM (membrane-bound CD73)) and allylthio (**28**, K_i = 61.9 nM (soluble CD73), 65.4 nM (membrane-bound CD73)).

All tested compounds were less potent at rat CD73 compared to human CD73, as shown previously also for AMPCP. Some substituents induced large species differences such as hydrazinyl (PSB-12646, K_i = 15.5 nM (human), 116 nM (rat), 7-fold difference) and *N*-piperazinyl (SB-627a, K_i = 184 nM (human), 2290 nM (rat), 12-fold difference). Co-crystallization of inhibitors PSB-12646 (PDB 6TWA) and PSB-12604 (PDB 6TWF) with human CD73 provided an explanation for this variation.[78] For hydrazinyl as a substituent at the C2-position, N499S exchange in rat affects the position of water molecules in the C2-pocket which was proposed as a leading cause for the decrease in potency at the rat enzyme.[78]

For the piperazinyl group, an alternative flipped binding mode (ribose and adenine base were flipped by 180°) was adopted in the binding pocket compared to the canonical AMPCP binding. In this new binding mode, the C2-pocket accommodates the N^6-amino group whereas the C2-substituent (piperazinyl) is oriented towards the interdomain cleft

which is normally occupied by the N^6-substitution. Two consequences resulted from this flipped mode: (i) loss of the canonical H-bonding interactions of the ribose moiety, which is translated into a 2-fold drop in potency compared to AMPCP, (ii) residue F500 adopts a different orientation than that previously shown for AMPCP, leading to a favorable interaction with L184. However, this phenylalanine residue is changed to a tyrosine in rat CD73 (F500Y). The consequent new interaction between the OH group of tyrosine and L184 in the rat enzyme is unfavorable and this explains the massive loss in potency at rat as compared to human CD73 (12-fold).[78]

Based on the obtained results, it is suggested that designing substituents with a more favorable contact to the residues in the C2 pocket might result in a further enhancement in potency. Moreover, it is clearly seen that none of the tested 2-substituted AMPCP compounds superseded the potency of N^6-benzyl-AMPCP (PSB-12379, K_i = 2.21 nM) which points out the importance of N^6-substitution for high CD73 inhibitory activity. In addition, taking into consideration the further improvement in potency imposed upon 2-chloro substitution of N^6-benzyl-AMPCP (PSB-12651, K_i = 0.134 nM), it was thought that additional exploration of combined C2- and N^6-substitution could possibly result in remarkably potent inhibitors. Furthermore, bulky and rigid substituents at the C2-position, such as piperazinyl, exhibited alternative flipped binding mode with a moderate loss of potency compared to AMPCP. Further investigation of such substituents with alternative binding mode is warranted.

Author contribution

The author performed concentration-inhibition curves for all test compounds (18) at two different enzyme preparations soluble and membrane-bound human CD73, additionally tested compound GR305 at rat CD73, analyzed data, and generated K_i values.

2.2. 3-Methylcytidine-5'-α,β-methylenediphosphonate as CD73 inhibitor

Structure−Activity Relationship of 3-Methylcytidine-5′-α,β- methylenediphosphates as CD73 Inhibitors

Mirko Scortichini, ***Riham Mohammed Idris****, Susanne Moschütz, Antje Keim, Veronica Salmaso, Clemens Dobelmann, Paola Oliva, Karolina Losenkova, Heikki Irjala, Samuli Vaittinen, Jouko Sandholm, Gennady G. Yegutkin, Norbert Sträter, Anna Junker, Christa E. Müller, and Kenneth A. Jacobson**

J. Med. Chem. 2022, 65, 2409−2433.doi.org/10.1021/acs.jmedchem.1c01852

Introduction

Several reports confirmed the ani-inflammatory, immunosuppressive, and metastatic activities of adenosine.[261,111,258] These adenosine effects in the tumor microenvironment can be prevented through a blockade of extracellular adenosine formation. A key enzyme in this context is ecto-5'-nucleotidase (CD73), which catalyzes the hydrolysis of AMP to adenosine. Direct blocking of adenosine receptors (ARs) activation is an alternative approach.[262,263] Small molecule inhibitors of CD73 as well as inhibitory monoclonal antibodies are currently being evaluated in clinical trials as monotherapies or in combination with other immune checkpoint inhibitors or anti-cancer drugs.[157,214,154]

Both nucleotides and non-nucleotides have been developed and identified as potent inhibitors of CD73.[157,214,209,210,78,235,243,255] Exploration of nucleobases pyrimidine rather than purine resulted in the discovery of potent CD73 inhibitors with a 3-methylcytidine-5′-α,β-methylenediphosphonate scaffold.[264] This compound was previously showed high selectivity towards CD73 compared to P2Y6 receptor.[264] This scaffold, if metabolized, will not produce adenosine derivatives, and would hence less likely activate ARs. In this study, broad modifications were performed to improve the compounds' potency and to study their structure-activity-relationships (SARs).

Summary and outlook

In this collaboration project, various cytosine- and uridine-based nucleotides were synthesized by the research group of Dr. Kenneth A. Jacobson (National Institute of Diabetes and Digestive and Kidney Diseases, NIH, USA), which were tested at Bonn University for inhibition of human soluble CD73. The lead structure, N^4-benzyloxy-3-methylcytidine-5′-α,β-methylene- diphosphonate showed high potency (**9**, K_i = 10.6 ± 0.4 nM, Table 1, attached article in Appendix II) at soluble human CD73 as previously described.[264] The first approach was to study the effects of chloro substitution at different positions of the phenyl ring of **9**. This generally resulted in a 6- to 7-fold improvement in potency observed for *ortho*- (**10**) and *meta*- (**11**) substitution (K_i = 1.63 nM, and 1.58 nM, respectively). In fact, *para*-chloro substitution resulted in the highest activity with around 20-fold increase in inhibitory activity (**16**, K_i = 0.673 nM). A trifluoromethyl group was introduced at the *meta*- (**12**, K_i =1.27 nM) and *para*-positions (**19**, K_i =1.08 nM) of the aromatic ring of compound **9**. The obtained results confirmed that substitution with a chloro or trifluoromethyl residue was best tolerated at the *para*-position.

To probe the effect of the halogen atom size at the *para*-position, chlorine was replaced with fluorine (**15**, K_i =1.14 nM), bromine (**17**, K_i = 0.441 nM) or iodine (**18**, K_i = 0.436 nM) in the lead structure. The halogen atom with the largest atomic radius was preferred: I > Br > Cl > F. The *para*-iodo-substituted derivative (**18**, K_i = 0.436 nM) was the most active one among all compounds in this cluster. Exchanging halogen at the *para*-position for a bioisosteric pentafluorosulfanyl group (compound **10**, **20**, K_i = 0.511 nM) yielded equipotent inhibitors.

Replacement of the substituents in the *para*-position with different carbonyl-containing groups, such as a carboxylate (**22**, K_i = 14.1 nM), a methyl ester (**21**, K_i = 0.848 nM) or a carbamoyl group (**23**, K_i = 1.76 nM), indicated that a neutral substituent is preferred. The free carboxylic acid group (**22**, K_i = 14.1 nM) was less potent than the lead structure (compound **1**, K_i = 10.6 nM). The methyl ester was 2-fold more potent than the amide. Applying a carboxylate group as a linker to couple different amine congeners to the *para*-position was highly tolerated providing compounds (**24**, K_i = 0.627 nM) and (**25**, K_i = 1.78 nM). This indicated that an ethyl linker between the two amino groups is favored over a longer spacer.

Furthermore, *β*-alanine (**26**, K_i = 2.61 nM) or *β*-alanine-ethyl ester moieties (**27**, K_i = 2.51 nM) were coupled to the carboxylic acid of **22** (K_i = 14.1 nM), resulting in a 5-fold improvement in potency compared to the unsubstituted carboxylic acid **22**.
Substitution at the *para*-position with various short chain hydrocarbons was assessed, and methyl (**13**, K_i = 0.894 nM) was found to be superior to ethyl (**14**, K_i = 3.50 nM).

Introduction of a functionizable ethynyl group in the *para*-position of the aromatic ring was successfully achieved (MRS4632, K_i = 0.664 nM, unpublished data). Compound MRS4632 was utilized as a precursor to develop a PET tracer (unlabeled ligand) and a fluorescent ligand. For this purpose, a 2-fluoroethyl)1-*H*-1,2,3-triazole (MRS4648, K_i = 0.627 nM, unpublished data) or a 2-fluoroethyl)-5-iodo-1-*H*-1,2,3-triazole (MRS4700, K_i = 0.788 nM, unpublished data) was introduced at the *para*-position of the phenyl ring of compound **1** yielding equipotent compounds. A fluorescent ligand was synthesized by coupling of the Alexa Flour 488 dye to a *para*-1-*H*-1,2,3-triazole moiety through an amide linker (MRS4647). The obtained fluorescent compound (MRS4647) exhibited a high inhibitory activity against human CD73 (K_i = 2.22 nM, unpublished data).
To investigate the influence of the 4-oxoimino linker on the activity of the scaffold under study, compound MRS4603 (**30**, K_i = 71.5 nM) was synthesized using a urea linker connecting the benzyl group. The activity of the new compound was 7-fold lower than the lead structure (compound **1**, K_i = 10.6 nM).
The ribose moiety in compound MRS4598 (**(**K_i = 0.673 nM) was replaced by a bicyclo[3.1.0]hexyl ring to obtain an (*N*)-methanocarba analog of the nucleotide, **29** (K_i = 59.2 nM). The calculated K_i value showed an 88-fold decrease in activity which emphasized the significance of the ribose ring for high potency at CD73. The inhibitory activity was completely lost in an (*N*)-methanocarba analog of UMPCP (**28**, K_i > 50000 nM). 5-F-UDP (compound **31**), a nucleoside 5'-diphosphate, exhibited weak inhibitory potency (K_i = 2540 nM) similar to that of ADP. However, the diphosphates may have been partly cleaved during incubation and the potency might therefore be underestimated. The metabolically- and chemically-stable 5-F-UMPCP (**20**, K_i = 5.33 nM) was a very potent CD73 inhibitor.

Crystal structures of **16** (*p*-chloro) and **21** (*p*-methyl ester) in complex with human CD73 were obtained in open and closed states. Both compounds exhibited very similar binding interactions. The benzyloxyimino group of **16** and **21** possesses an *E*-configuration. Like

in AMPCP derivatives, polar contacts of the bisphosphonate and the ribose moieties with the amino group of N390 and π-π stacking of the nucleobase with F417 and F500 residues are observed. The cleft between the two domains accommodates the N^4-substituents in a similar binding orientation to that of the N^6-substituents of AMPCP derivatives. The β-phosphonate group fully overlapped in both compound classes, while shifts of up to 1 Å were observed for the α-phosphonate, the ribose, and the nucleobase substructures.

To test for inhibitory activity of selected synthesized compounds against CD73 in a more biological relevant context, an *in situ* assay was conducted using specimens of human head and neck squamous cell carcinoma (HNSCC) and palatine tonsils as enzyme sources.[264] Both, AMPase activity and CD73 expression levels, were determined. Incubation of tissue cryosections with increasing concentrations of **18** and **20** (50−250 nM) led to a concentration-dependent decrease in the catalytic activity of tumor- and tonsil- associated CD73.

In this research study, SARs of cytidine-based CD73 inhibitors were explored leading to compounds with greater than 20-fold improvement in potency compared to the lead structure, compound **1**. Effects of the most potent inhibitors were investigated in tumor tissues. A thorough evaluation of a variety of N^4-substituents is planned, since in the present study, only substituted N^4-benzyloxy groups had been probed. Structural characterization of the developed inhibitors based on X-ray crystallography in addition to molecular dynamics studies was performed. The most potent identified inhibitor among this series is the *p*-iodo derivative with a K_i value of 0.436 nM. Identification of potent inhibitors of CD73 based on a pyrimidine scaffold may provide new opportunities for the development of future immuno-oncology drugs.

Author contribution

The author performed the *in vitro* characterization experiments to test for the biological activity at CD73 for the all 27 compounds in this series. The author constructed the concentration-inhibition curves, analyzed data, calculated the K_i values and presented concentration-inhibition curves using GraphPad Prism software. The author also provided a complete SAR analysis report based on the obtained K_i value

3. Manuscript prepared for publishing

3.1. Establishment of a radioligand binding assay for CD73

Design, development and evaluation of a radiotracer for CD73 – a versatile research tool and diagnostic agent for personalized medicine

***Riham M. Idris*[1*], *Haneen Al-Hroub*[1*], *Constanze C. Schmies*[1*], *Patrick Riziki*[1], *Christian Renn*[1], *Tobias Claff*[1], *Katharina Sylvester*[1], *Susanne Moschütz*[2], *Julia Reinhardt*[4], *Winnie Deuter-Conrad*[3], *Jennifer Dietrich*[5, 6], *Marieta Toma*[7], *Bernd K. Fleischmann*[6], *Daniela Wenzel*[5, 6], *Herbert Zimmermann*[8], *Michael Hölzel*[4], *Norbert Sträter*[2], *Christa E. Müller*[1]

[1] PharmaCenter Bonn, Pharmaceutical Institute, Department of Pharmaceutical & Medicinal Chemistry, University of Bonn, An der Immenburg 4, D-53121 Bonn, Germany
[2] Center for Biotechnology and Biomedicine, Institute of Bioanalytical Chemistry, University of Leipzig, Deutscher Platz 5, 04103 Leipzig, Germany
[3] Helmholtz-Zentrum Dresden-Rossendorf, Institute of Radiopharmaceutical Cancer Research, Department of Neuroradiopharmaceuticals, 04318 Leipzig, Germany
[4] Institute of Experimental Oncology (IEO), University Hospital Bonn, Venusberg-Campus 1, 53127 Bonn, Germany
[5] Department of Systems Physiology, Institute of Physiology, Medical Faculty, Ruhr University of Bochum, Germany
[6] Institute of Physiology I, Life & Brain Center, Medical Faculty, University of Bonn, Bonn Germany
[7] Institute of Pathology, University Hospital Bonn (UKB), Medical Faculty, University of Bonn, Bonn, Germany
[8] Institute of Cell Biology and Neuroscience, Goethe-University, Frankfurt am Main, Germany

* These authors participated equally

Corresponding Author
Prof. Dr. Christa E. Müller
Pharmazeutisches Institut
Pharmazeutische & Medizinische Chemie
An der Immenburg 4, D-53121 Bonn, Germany
Phone: +49-228-73-2301
Fax: +49-228-73-2567
E-mail: christa.mueller@uni-bonn.de

Abstract

Tumor cells over-express ectonucleotidases that metabolize pro-inflammatory ATP to immunosuppressive, tumor growth-stimulating, pro-metastatic and angiogenic adenosine. Ecto-5'-nucleotidase (CD73) is the main enzyme that catalyzes the hydrolysis of extracellular AMP producing adenosine; it therefore possesses potential as a novel drug target for the (immuno)therapy of cancer. **Methods**: The potent and selective CD73 inhibitor PSB-12651 (K_i = 0.134 nM, human CD73), was selected for the development of a tritium-labeled radioligand. The substitution pattern of N^6-disubstituted AMPCP derivatives was further explored through combining the beneficial N^6-benzyl or N^6-α-methylbenzyl substituent with methyl or propyl as a second N^6-substituent. An alkynyl residue for hydrogenation was introduced in the last reaction step. The resulting tracer was characterized and utilized for radioligand binding assays and autoradiography studies. **Results**: Extensive exploration of the lead structures yielding new highly potent N^6-disubstituted AMPCP derivatives **6**-**8**. A metabolically stable radiotracer, [^{3}H]PSB-17230, with high affinity (human soluble CD73, K_i = 0.0891 nM) was developed. Selectivity of [^{3}H]PSB-17230 was confirmed using melanoma MaMel65-CD73 knockout cells. The radiotracer displays low nonspecific binding when tested in MDA-MB-231 and MaMel65-CD73^{wt} cell lines. Co-crystal structure with human CD73 confirmed the characteristics of binding of previous AMPCP derivatives. The radioligand binding assay was employed to characterize CD73 inhibitors and to study expression levels of the enzyme in different rodent tissues and tumor cell lines with advantage over immunodetection-based methods as the radiotracer specifically binds to the catalytically active isoform of the enzyme. Moreover, [^{3}H]PSB-17230 was successfully employed in autoradiography studies to determine CD73 expression in healthy and diseased tissues. **Conclusions**: [^{3}H]PSB-17230 represents the first high-affinity tracer for CD73 which is anticipated to find broad application in biological studies, drug screening, and for diagnostic purposes.

Keywords

Autoradiography; CD73, ecto-5'-nucleotidase, immuno-oncology, radioligand binding

Introduction

Human ecto-5'-nucleotidase (cluster of differentiation 73 (CD73), EC 3.1.3.5) is a glycosylphosphatidylinositol (GPI)-anchored glycoprotein.[19,61] Two transcript variants are encoded by the *NT5E* gene, isoform 1 and 2. Isoform 1 is the canonical CD73 protein that is catalytically active and expressed at the cell surface as a homodimer. Isoform 2 is a shorter, catalytically inactive form, missing 50 amino acids residues (404–453); it is mainly localized in the cytoplasm.[54] Each monomer of the mature isoform 1 consists of 549 amino acids and possesses four *N*-glycosylation sites (asparagine 53, 311, 333 and 403) with a calculated molecular mass of 61 kDa, different molecular weights attributed to heterogenous glycosylation have been reported.[67,22] A large domain movement of about 114° is required to switch between open and closed (active) state conformations (see **Figure 39**).[61] Beside the membrane-bound isoform, a soluble form can be released through cleavage of the GPI anchor e.g. by phosphatidylinositol-specific phospholipase C (PI-PLC) or by proteolytic cleavage. CD73 has also been detected in exosomes derived from cancer and immune cells. [67,65,66]

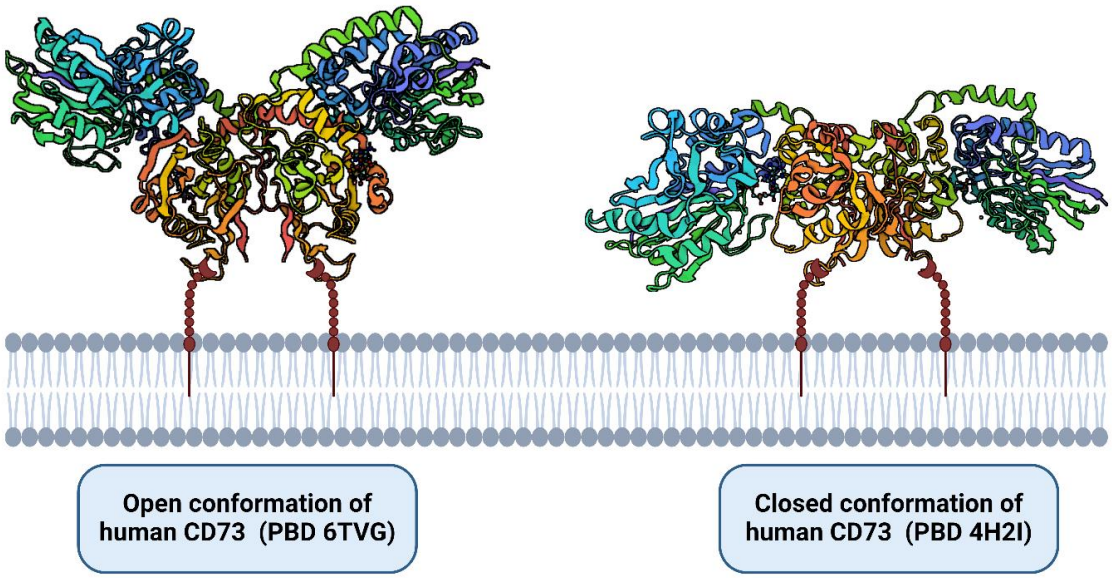


Figure 39. Open and closed conformation of human ecto-5'-nucleotidase in complex with AMPCP (I) (PDB 6TVG and 4H2I). Created in Biorender.com.

CD73 belongs to the super-family of ectonucleotidases that cleave extracellular nucleotides. The two main ectonucleotidases are ectonucleoside triphosphate

diphosphohydrolase (NTPDase1/CD39) and CD73. CD39 catalyzes the sequential hydrolysis of ATP via ADP to AMP. Alternatively, AMP can be generated through direct hydrolysis of ATP by ectonucleotide pyrophosphatase/phosphodiesterase 1 (NPP1, CD203a), and by sequential action of nicotinamide adenine dinucleotide glycohydrolase (CD38) and NPP1 on NAD^+. Then, CD73 takes over cleaving AMP to produce adenosine (**Figure 40**).[19,265,23,17] Subsequent activation of A_{2A} and A_{2B} adenosine receptors (ARs) on immune cells can lead to profound immunosuppressive effects.[266,263,267] The A_{2A}AR is widely expressed on immune cells including macrophages, dendritic cells, natural killer cells, T cells and monocytes, while A_{2B}AR is mainly found on macrophages and dendritic cells. Activation of A_{2A} and A_{2B}AR inhibits immune responses through diverse pathways, e.g., inhibition of effector T cell proliferation and differentiation, activation of Treg-mediated inhibition of effector T cells, and suppression of natural killer cell maturation.[261,258] The net result of adenosine-mediated effects is the attenuation of protective immune cells while augmenting regulatory immune cell pathways thereby leading to a strong immunosuppressive effect.[258] High adenosine levels in the tumor microenvironment (TME) constitute an important mechanism of immune evasion. Thus, the development of CD73 inhibitors to prevent adenosine formation is a novel strategy in the immunotherapy of cancer.[261,157] In addition, ARs particularly A_{2A} and A_{2B}ARs, can be overexpressed on tumor cells, [268,269,270] and their stimulation by adenosine enhances tumor cell proliferation, angiogenesis and metastasis.[98,148,145,144]

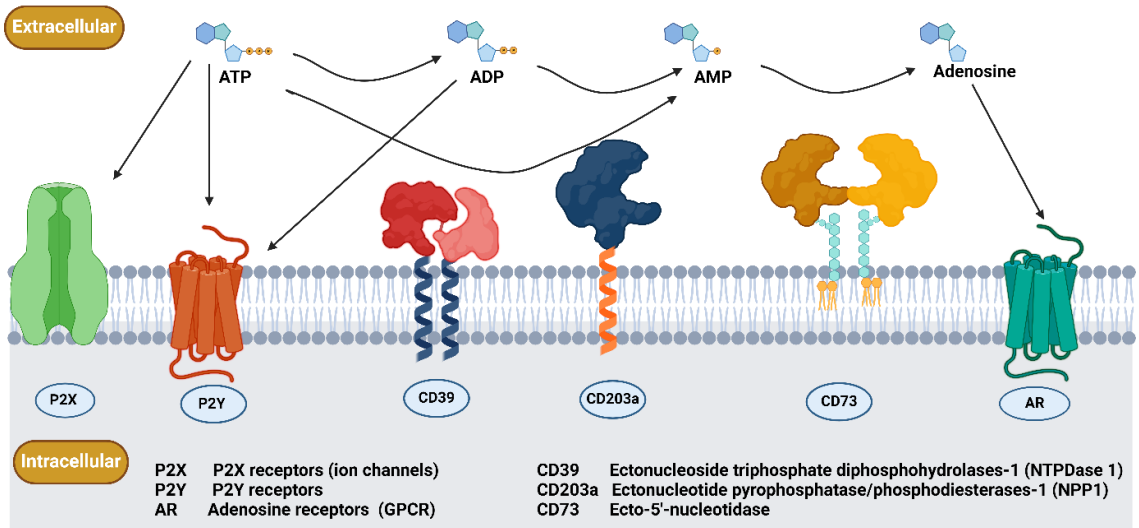


Figure 40. Purinergic signaling. ATP activates P2X and P2Y receptor subtypes. ADP activates P2Y receptor subtypes. Concerted action of ectonucleoside triphosphate diphosphohydrolases-1 (CD39) and ecto-5'-nucleotidase (CD73) produces adenosine from ATP. Alternatively, ectonucleotide pyrophosphatase/ phosphodiesterases-1 (NPP1, CD203a) hydrolyzes ATP to AMP. Created in Biorender.com.

Both nucleotidic and non-nucleotidic inhibitors of CD73 have been developed (for examples see **Figure 41**). ATP and ADP act as weak physiological CD73 inhibitors with micromolar potency.[208] The ADP analog AMPCP (I, **Figure 41**) was the first inhibitor showing submicromolar potency. Based on AMPCP as a lead structure, extensive structure-activity relationship (SARs) studies have been performed leading to highly potent inhibitors, e.g. PSB-12379 (**II**), PSB-12489 (**IV**), PSB-22826 (**V**), Quemliclustat (**VI**), OP-5244 (**VII**) and ORIC-533 (**VIII**), with K_i values in the picomolar to low nanomolar range.[209,210,211,213,214,215] The most potent non-nucleotide-derived inhibitors reported to date are **IX** and LY-3475070 (**X**).[243,271] Further early inhibitors were based on anthraquinone and sulfonamide scaffolds showing moderate CD73 inhibitory activity.[235,236] Three small molecule inhibitors of CD73 are currently evaluated in clinical trials: LY-3475070 (**X**) completed recruitment for a phase I clinical trial, while Quemliclustat (AB680, **VI**) is currently in phase I/II clinical trials for the treatment of advanced solid malignancies, and ORIC-533 (**VIII**) is in phase I for relapsed or refractory multiple myeloma.[215,272,273]
Besides small molecules, monoclonal antibodies have been developed several of which are currently investigated in clinical trials.[274,153]

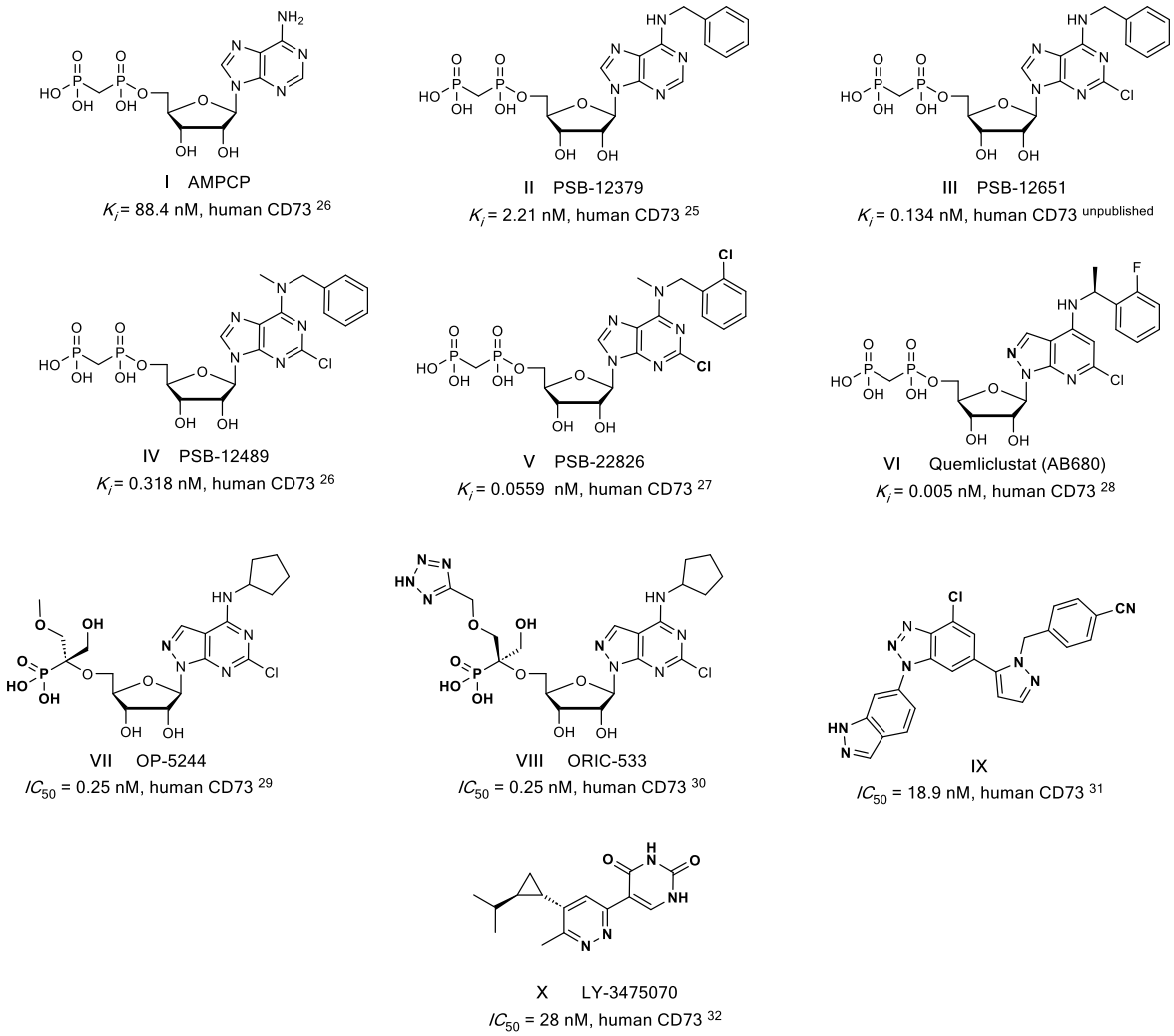


Figure 41. Structures of potent CD73 inhibitors.

Upregulation of CD73 expression has been described in pathological conditions. [98,99] In several studies on gastric, colorectal, gallbladder, triple negative breast cancer, prostate cancer, and melanoma, overexpression of CD73 has been associated with poor prognosis.[99] It has been reported that CD73 expression is not always linked to its hydrolytic activity since secondary modifications (e.g., glycosylation, ribosylation and alternative splicing) may result in catalytically-modified isoforms.[54,22,43,71]

Moreover, CD73 upregulation has been studied in certain acute and chronic inflammations.[17,65,275,276,277] For instance, CD73 was proposed as a biomarker for acute inflammatory pancreatitis.[117] In that study, the activity and concentration of soluble CD73 were higher in patients with acute pancreatitis compared to healthy individuals.[117] However, both the activity and protein concentration decreased relative to the severity of

the disease, indicating and an inverse association of the CD73 biomarker with acute pancreatitis severity. [117]

Up to date several methods to monitor nucleoside monophosphate hydrolysis by CD73 have been described.[162,167,170,164,173,163] All of them are useful for determining the enzymatic activity and the potency of inhibitors, but none of these methods is able to study direct binding and hence to determine affinities, or binding kinetics. The measurement of protein expression levels (B_{max}) e.g., in cancer tissues, requires binding rather than functional assays.

In the present study, we present the design and synthesis of a high-affinity radiotracer, [^{3}H]PSB-17230, and its in-depth characterization and application for basic research, drug development, and as a diagnostic tool allowing personalized medicine.

Methods

Chemistry

General methods

All reagents were commercially obtained from various producers (Acros, Fluorochem, Merck, Carbosynth, Santa Cruz, Sigma Aldrich, and TCI) and used without further purification. Commercial solvents of specific reagent grade were used without additional purification or drying. The reactions were monitored by thin layer chromatography (TLC) using Merck silica gel 60 F254 aluminum sheets with dichloromethane (DCM)/methanol (9:1 or 3:1) as mobile phase. The TLC plates were analyzed by ultraviolet (UV) light irradiation at a wavelength (λ) of 254 nm. Column chromatography was carried out on silica gel (0.040-0.060 mm, pore diameter ca. 6 nm). Mass spectra were recorded on an API 2000 mass spectrometer (Applied Biosystems, Darmstadt, Germany) with a turbo ion spray ion source coupled to an Agilent 1100 HPLC system (Agiland, Böblingen, Germany) using an EC50/2 Nucleodur C18 Gravity 3 µm (Macherey-Nagel, Düren, Germany), or on a micrOTOF-Q mass spectrometer (Bruker, Köln, Germany) with an ESI-source coupled with an HPLC Dionex Ultimate 3000 (Thermo Scientific, Braunschweig, Germany) using an EC50/2 Nucleodur C18 Gravity 3 µm column (Macherey-Nagel, Düren, Germany). The LC-MS samples were prepared by dissolving 1 mg/ ml of compound in H_2O/CH_3OH (1:1) containing 2 mM ammonium acetate. A sample of 10 µl, or 1 µl respectively, was injected into an HPLC instrument, and elution was performed with a gradient of water/methanol (containing 2 mM ammonium acetate) from 90:10 to 0:100 for 20 min at a flow rate of 250 µL/min, or with a gradient of water/acetonitrile (containing 2 mM ammonium acetate) from 90:10 to 0:100 for 9 min at a flow rate of 0.3 ml/min. UV absorption was detected from 220 to 400 nm using a diode array detector (DAD). NMR spectra were recorded on a Bruker Avance 500 or 600 MHz spectrometer. DMSO-d_6 or D_2O was used as a solvent. ^{31}P-NMR spectra were recorded at 25 °C; phosphoric acid was used as external standard. For spectra recorded in D_2O, sodium 3-(trimethylsilyl)propionate-d_4 was used as external standard. When DMSO-d_6 was employed, spectra were recorded at 30 °C. Shifts are given in ppm relative to the external standard (in ^{31}P-NMR spectra) or relative to the remaining protons of the deuterated solvents used as internal standard (^{1}H, ^{13}C-NMR). Coupling constants are given in Hertz (Hz). The designation used to assign the peaks in the spectra is as follows: singlet (s), doublet (d), triplet (t), quartet (q), multiplet (m), broad (br).

Melting points were determined on a Büchi 530 melting point apparatus and are uncorrected.

Purification of nucleotides

Semi-preparative HPLC was performed on a Knauer Smartline 1050 HPLC system equipped with a Eurospher-100 C18 column, 250 mm x 20 mm, particle size 10 µm. UV absorption was detected at 254 nm. Fractions were collected, and appropriate fractions were pooled, diluted with water, and lyophilized several times, using a CHRIST ALPHA 1-4 LSC freeze dryer, to remove the NH_4HCO_3 buffer, yielding the nucleotides as white powders. The structures of the synthesized nucleosides and nucleotides were confirmed by ^{1}H- and ^{13}C-NMR spectroscopy, in addition to LC/ESI-MS performed in both positive and negative mode. The nucleotides were additionally characterized by ^{31}P-NMR spectroscopy.

2',3',5'-Tri-O-acetyl-2,6-dichloropurine riboside (2)

Tetraacetylribose (5.0 g, 16.0 mmol, 1.0 eq) was melted at 85 °C, and 2,6-dichloropurine (3.0 g, 16.0 mmol, 1.0 eq) was added upon stirring. To the reaction mixture trifluoromethane sulfonic acid (70 µL, 0.8 mmol, 0.05 eq) was added to catalyze the reaction. The reaction mixture was stirred at 85 °C under reduced pressure for 1 h. TLC analysis indicated that the reaction was completed, and the mixture was allowed to cool down to room temperature. The product was recrystallized from absolute ethanol yielding the desired product as a white solid (4.84 g, 69% yield). ^{1}H-NMR (600 MHz, DMSO-d_6) δ 8.89 (s, 1H, N=C<u>H</u>N) 6.31 (d, 1H, J =5.0 Hz, C<u>H</u>N) 5.90 (q, 1H, J = 5.2 Hz, C<u>H</u>O) 5.61 (t, 1H, J =5.5 Hz, C<u>H</u>O) 4.43 (m, 1H, C<u>H</u>CH$_2$) 4.39 (dd, 1H, J =3.6, 12.1 Hz, CHC<u>H$_2$</u>O) 4.29 (m, 1H, CHC<u>H$_2$</u>O) 2.11 (s, 3H, COC<u>H$_3$</u>) 2.05 (s, 3H, COC<u>H$_3$</u>) 2.01 (s, 3H, COC<u>H$_3$</u>). ^{13}C-NMR (151 MHz, DMSO-d_6) δ 170.12, 169.47, 169.33, 152.92, 151.46, 150.41, 146.98, 131.38, 86.38, 80.01, 72.51, 69.92, 62.76, 20.61, 20.48, 20.34. LC/ESI-MS (m/z): positive mode 447.1 $[M+H]^+$. Purity determined by HPLC-UV (254 nm)-ESI-MS: 93.4%. mp: 160 °C.

2-Chloro-N^6-benzyl-N^6-propyladenosine (3)

A mixture of 2',3',5'-tri-O-acetyl-2,6-dichloropurine riboside (0.2 g, 0.6 mmol, 1.0 eq), *N*-benzylpropylamine (0.6 ml, 4.4 mmol, 2.0 eq), and Et_3N (2.0 ml, 1.3 mmol, 2.0 eq) in absolute ethanol (10 ml) was refluxed at 60 °C for 36 h. After completion of the reaction,

the solution was evaporated in vacuum. Purification using silica gel chromatography (CH_3OH/dichloromethane (DCM), 1:49) yielded the protected intermediate (0.7 g). To this intermediate product dissolved in methanol (5 ml), 0.5% NaOMe in methanol (10 ml) was added. After 36 h at room temperature, the solution was evaporated and the crude product was purified by column chromatography (CH_3OH/DCM, 1:49). Recrystallization from diethyl ether yielded the desired product as a white solid (0.64 g, 66%). ^{1}H-NMR (600 MHz, CD_3OD) δ 8.21 (s, 1H, N=C<u>H</u>N) 7.37 - 7.27 (m, 5H, aryl) 5.96 (d, 1H, *J* =6.1 Hz, C<u>H</u>N) 5.61 (br s, 1H, 1x NC<u>H</u>$_2$) 5.04 (br s, 1H, 1x NC<u>H</u>$_2$) 4.73 (m, 1H, C<u>H</u>CH$_2$) 4.36 (dd, 1H, *J* =5.0, 3.0 Hz, C<u>H</u>OH) 4.19 (q, 1H, *J* =2.7 Hz, C<u>H</u>OH) 4.13 (br s, 1H, 1x NC<u>H</u>$_2$) 3.93-3.79 (d m, 2H, CHC<u>H</u>$_2$) 3.64 (br s, 1H, 1x NC<u>H</u>$_2$) 1.72 (br s, 2H, C<u>H</u>$_2$CH$_3$) 0.95 (t, 3H, *J* =7.4 Hz, CH$_2$C<u>H</u>$_3$). ^{13}C-NMR (151 MHz, CD_3OD) δ 156.45, 154.86, 152.80, 140.85, 139.38, 129.90, 129.17, 128.74, 120.79, 91.23, 88.12, 75.57, 72.70, 63.67, 22.83, 21.58, 15.73, 11.48. LC/ESI-MS (m/z): positive mode 434.2 $[M+H]^+$. Purity determined by HPLC-UV (254 nm)-ESI-MS: 96%. mp: 92 °C.

2-Chloro-N^6-(1-benzylethyl)-N^6-methyladenosine (4)

This compound was synthesized in analogy to compound (**3**) above using *N*,*N*-methyl-(1-phenyl)ethanamine (0.7 ml, 4.5 mmol, 2.0 eq) yielding a white solid (0.54 g, 58%). ^{1}H-NMR (600 MHz, DMSO-d$_6$) δ 8.44 (s, 1H, N=C<u>H</u>N) 7.36-7.27 (m, 5H, aryl) 5.87 (d, *J* =5.7 Hz, 1H, <u>CH</u>N) 5.48 (d, 1H, *J* =6.0 Hz, CHO<u>H</u>) 5.19 (d, 1H, *J* =5.1 Hz, CHO<u>H</u>) 5.03 (m, 1H, CH$_2$O<u>H</u>) 4.52 (m, 1H, C<u>H</u>OH) 4.14 (m, 1H, C<u>H</u>OH) 3.95 (q, *J* =3.8 Hz, 1H, C<u>H</u>CH$_2$), 3.68-3.53 (d m, 2 H, CHC<u>H</u>$_2$) 3.37 (q, *J* =7.0 Hz, 1H, NC<u>H</u>), 2.84 (br s, 2H, NC<u>H</u>$_3$), 1.62 (s, 3H, CHC<u>H</u>$_3$) 1.08 (t, 1H, *J* =7.0 Hz, NC<u>H</u>$_3$). ^{13}C-NMR (151 MHz, DMSO-d$_6$) δ 154.52, 152.77, 151.22, 140.44, 139.00, 128.70, 127.49, 127.02, 118.65, 87.47, 85.80, 73.89, 70.42, 65.04, 54.33, 29.60, 16.50. LC/ESI-MS (m/z): positive mode 420.2 $[M+H]^+$. Purity determined by HPLC-UV (254 nm)-ESI-MS: 91%. mp: 120 °C

2-Chloro-N^6-(1-benzylethyl)-N^6-propyladenosine (5)

This compound was synthesized in analogy to compound (**3**) using *N*,*N*-(1-phenylethyl)-1-propanamine HCl (0.9 g, 4.4 mmol, 2.0 eq) yielding a white solid (0.13 g, 13%). ^{1}H-NMR (500 MHz, DMSOd$_6$) δ 8.43 (s, 1H, N=C<u>H</u>N) 7.38-7.26 (m, 5H, aryl) 5.87 (d, *J* =5.6 Hz, 1H, C<u>H</u>N) 5.45 (br s, 1 H, CH$_2$O<u>H</u>) 5.20 (br s, 1 H, CHO<u>H</u>) 5.02 (br s, 1 H, CHO<u>H</u>) 4.52 (dd, 1H, *J* =5.3, 6.2 Hz, C<u>H</u>OH) 4.13 (m, 1H, C<u>H</u>OH) 3.95 (q, *J* =3.5 Hz, 1H, C<u>H</u>CH$_2$),

3.66-3.53 (d m, 1H, CHC<u>H</u>$_2$), 3.13 (br s, 1H, NC<u>H</u>), 1.64 (d, 3H, *J* =6.5 Hz, CHC<u>H</u>$_3$), 1.39 (br d, *J* =90.3 Hz, 2H, C<u>H</u>$_2$CH$_3$) 0.74 (br s, 3H, CH$_2$C<u>H</u>$_3$). ^{13}C-NMR (126 MHz, DMSO-d$_6$) δ 154.16, 152.71, 151.80, 140.88, 139.39, 128.60, 127.55, 127.32, 118.61, 87.42, 85.81, 73.88, 70.50, 61.46, 54.87, 23.27, 21.12, 17.06, 11.22. LC/ESI-MS (m/z): positive mode 448.1 $[M+H]^+$. Purity was determined by HPLC-UV (254 nm)-ESI-MS: 98%. mp: 105 °C.

Preparation of triethylammonium hydrogen carbonate buffer (TEAC)

A 1 M solution of TEAC was prepared by slowly adding dry ice to a 1 M triethylamine solution in water over several hours until a pH value of approximately 7.4−7.6 was measured using a pH meter.

2-Chloro-N^6-benzyl, N^6-propyladenosine-5'-O-[(phosphonomethyl)phosphonic acid] (6)

A solution of methylenebis(phosphonic dichloride) (0.3 g, 1.2 mmol, 5.0 eq) in trimethyl phosphate (5 ml), cooled to 0 °C was added to a suspension of 2-chloro-N^6-benzyl, N^6-propyladenosine (0.1 g, 0.23 mmol, 1.0 eq) in trimethyl phosphate (3 ml) at 0 °C. The reaction mixture was stirred at 0 °C and samples were taken at intervals of 15 min for TLC analysis. After 40 min, when no nucleoside was present anymore, 10 ml of cold 0.5 M aqueous TEAC solution (pH 7.4-7.6) was added. The solution was stirred at 0 °C for 15 min followed by stirring at room temperature for 1 h. Trimethyl phosphate was extracted using 2 x 100 ml of *tert.*-butylmethylether, and the aqueous phase was lyophilized. The crude product was then purified by semi-preparative HPLC (0-50% MeCN/50 mM NH_4HCO_3 buffer within 20 min, 20 ml/min) followed by lyophilization to obtain the final product as a white powder (0.12 g, 91%). ^{1}H-NMR (600 MHz, D$_2$O) δ 8.37 (s, 1H, N=C<u>H</u>N) 7.30-7.23 (m, 5 H, aryl) 6.01 (d, 1H, *J* = 5.3 Hz, C<u>H</u>N) 5.27 (br s, 2H, NC<u>H</u>$_2$) 4.69 (t, 1H, *J* = 5.0 Hz, C<u>H</u>OH) 4.52 (m, 1H, C<u>H</u>OH) 4.35 (br s, 1H, C<u>H</u>CH$_2$) 4.16 (br s, 2H, CHC<u>H</u>$_2$) 3.93 (br s, 2H, NC<u>H</u>$_2$) 2.16 (t, 2H, *J* = 19.0 Hz, PC<u>H</u>$_2$P) 1.61 (br s, 2 H, C<u>H</u>$_2$CH$_3$) 0.84 (t, 3H, *J* =7.1 Hz, CH$_2$C<u>H</u>$_3$). ^{13}C-NMR (151 MHz, D$_2$O) δ 157.65, 156.45, 153.99, 140.97, 140.02, 131.50, 130.26, 130.12, 120.78, 89.71, 86.64, 77.09, 72.97, 66.36, 55.64, 55.60, 30.37, 27.95, 13.10. ^{31}P-NMR (243 MHz, D$_2$O) δ19.15 (s, 1P, P$_\beta$) 14.63 (s, 1P, P$_\alpha$). LC/ESI-MS (m/z): positive mode 592.1115 $[M+H]^+$ and negative mode 590.0978 $[M-H]^-$ (calcd. 591.88). Purity determined by HPLC-UV (254 nm)-ESI-MS: 97.6%. mp: 220 °C.

2-Chloro-N^6-(1-methylbenzyl), N^6-methyladenosine-5'-*O*-[(phosphonomethyl) phosphonic acid] (7)

The synthesis was performed in analogy to compound (**6**) using 2-chloro-N^6-(*1*-methylbenzyl), N^6-methyladenosine. A white powder (0.07 g, 51%) was obtained. ^{1}H-NMR (600 MHz, D_2O) δ 8.43 (s, 1H, N=C<u>H</u>N) 7.39-7.31 (m, 5 H, aryl) 6.06 (d, J =5.5 Hz, 1H, C<u>H</u>N) 4.75 (t, 1H, J =5.3 Hz, C<u>H</u>OH) 4.54 (t, 1H, J =4.5 Hz, C<u>H</u>OH) 4.38 (m, 1H, C<u>H</u>CH_2) 4.18 (br s, 2H, CHC<u>H_2</u>) 3.19 (q, 1H, J =7.3 Hz, NC<u>H</u>) 3.02 (br s, 3 H, NC<u>H_3</u>) 2.21 (m, 2 H, PC<u>H_2</u>P) 1.67 (br s, 3H, CHC<u>H_3</u>). ^{13}C-NMR (151 MHz, D_2O) δ 157.83, 156.55, 153.94, 142.90, 140.87, 131.48, 130.44, 129.91, 121.08, 89.67, 86.80, 77.05, 73.06, 66.39, 57.83, 30.19, 18.70, 11.07. ^{31}P-NMR (243 MHz, D_2O) δ 17.14 (d, 1P, J =8.0 Hz, Pβ) 14.07 (d, 1P, J =8.4 Hz, Pα). LC/ESI-MS (m/z): positive mode 578.0940 $[M+H]^+$ and negative mode 576.0858 $[M-H]^-$ (calcd. 577.85). Purity determined by HPLC-UV (254 nm)-ESI-MS: 95.4%. mp: 202 °C.

2-Chloro-N^6-(1-methylbenzyl), N^6-propyladenosine-5'-*O*-[(phosphonomethyl) phosphonic acid] (8)

The synthesis was performed in analogy to compound (**6**) using 2-chloro-N^6-(1-methylbenzyl), N^6-propyladenosine. A white powder (0.03 g, 20%) was produced. ^{1}H-NMR (600 MHz, D_2O) δ 8.36 (s, 1H, N=C<u>H</u>N) 7.21 (m, 5 H, aryl) 6.01 (s, 1H, C<u>H</u>N) 4.66 (m, 1H, C<u>H</u>OH) 4.49 (br s, 1H, C<u>H</u>OH) 4.33 (br s, 1H, C<u>H</u>CH_2) 4.15 (br s, 2H, CHC<u>H_2</u>) 3.81-3.02 (br s, 1H, N(C<u>H</u>)CH_2) 2.26 (t, 2H, J =9.7 Hz, PC<u>H_2</u>P) 1.57 (br s, 3H, CHC<u>H_3</u>) 1.28 (br s, 2 H, CH_2C<u>H_2</u>CH_3) 0.63 (br s, 3H, CH_2C<u>H_3</u>). ^{13}C-NMR (151 MHz, D_2O) δ 157.27, 156.41, 154.04, 143.17, 140.75, 131.25, 130.35, 130.18, 120.95, 89.77, 86.47, 77.13, 73.00, 66.57, 49.10, 29.85, 22.16, 19.13, 13.34, 11.04. ^{31}P-NMR (243 MHz, D_2O) δ 17.92 (s, 1P, Pβ) 16.84 (s, 1P, Pα). LC/ESI-MS (m/z): positive mode 606.1279 $[M+H]^+$ and negative mode 604.1183 $[M-H]^-$ (calcd. 605.91). Purity determined by HPLC-UV (254 nm)-ESI-MS: 96%. mp: 149 °C.

***N*-Benzylprop-2-yn-1-amine (10)**

Propargyl bromide (1-bromo-2-propyne, 80% in toluene, 3 ml, 0.035 mmol, 1.0 eq) was added to benzylamine (21 ml, 0.21 mmol, 6.0 eq), and the mixture was stirred at rt overnight. After completion of the reaction, the mixture was evaporated and purified by column chromatography in petroleum ether/ethyl acetate (1:9 →1:3) yielding the desired

product as a colorless oil (4.2 g, 85%). ^{1}H-NMR (500 MHz, DMSO-d_6) δ 7.32-7.19 (m, 5H, aryl) 3.73 (s, 2H, NHC$\underline{H}_2$) 3.26 (d, 2H, J =2.4 Hz, NHC$\underline{H}_2$) 2.40 (s, 1H, C≡C$\underline{H}$). ^{13}C-NMR (125 MHz, DMSO-d_6) δ 140.19, 128.19, 128.11, 126.71, 82.91, 73.73, 51.38, 36.74, 24.20. LC/ESI-MS (m/z): positive mode 146.0 $[M+H]^+$. Purity determined by HPLC-UV (254 nm)-ESI-MS: 95.7%.

2-Chloro-N^6-benzyl-N^6-propargyladenosine (11)

2',3',5'-Tri-O-acetyl-2,6-dichloropurine riboside (1.0 g, 2.2 mmol, 1.0 eq) was suspended in absolute ethanol. To the suspension, Et_3N (0.6 ml, 4.4 mmol, 2.0 eq) and *N*-benzylprop-2-yn-1-amine (0.65 g, 4.4 mmol, 2 eq) were added and the reaction mixture was refluxed overnight. The crude product was purified by silica gel column chromatography (CH_3OH/DCM, 1:19) yielding the protected intermediate (1.2 g). To the intermediate product in methanol (5 ml), 0.5% NaOMe in methanol (2 ml) was added. After 18 h at room temperature, the solution was evaporated and the crude product was extracted with diethyl ether yielding the desired product as a waxy yellow substance (0.9 g, 97%). ^{1}H-NMR (600 MHz, DMSO-d_6) δ 8.50 (s, 1H, N=C$\underline{H}$N) 7.3 (m, 5H, aryl) 5.88 (d, 1H, J = 5.7 Hz, C$\underline{H}$N) 5.6 (br s, 1H, 1x N(C$\underline{H}_2$)$_2$) 5.49 (d, 1H, J = 6.0 Hz, CHO$\underline{H}$) 5.19 (d, 1H, J = 5.1 Hz, CHO$\underline{H}$) 5.02 (t, 1H, J = 5.5 Hz, $CH_2O\underline{H}$) 4.51 (q, 1H, J = 5.6 Hz, C$\underline{H}$OH) 4.39 (br s, 1H, 1x N(C$\underline{H}_2$)$_2$), 4.13 (q, 1H, J = 4.8 Hz, C$\underline{H}$OH) 3.95 (q, 1H, J = 3.8 Hz, C$\underline{H}CH_2$), 3.72 (s, 1H, C≡C$\underline{H}$) 3.67-3.52 (d m, 2H, CHC$\underline{H}_2$) 3.26 (d, 1H, J = 2.3 Hz, 1x N(C$\underline{H}_2$)$_2$) 3.22 (br s, 1H, 1x N(C$\underline{H}_2$)$_2$). ^{13}C-NMR (151 MHz, DMSO-d_6) δ 153.94, 152.62, 151.96, 140.23, 139.88, 128.72, 128.25, 128.16, 127.60, 126.77, 118.65, 87.53, 85.84, 82.96, 73.89, 73.85, 70.40, 61.36, 51.41, 40.79, 36.77. LC/ESI-MS (m/z): positive mode 430.0 $[M+H]^+$. Purity determined by HPLC-UV (254 nm)-ESI-MS: 95.3%.

2-Chloro-N^6-benzyl, N^6-(prop-2-ynyl)adenosine-5'-O-[(phosphonomethyl) phosphonic acid (12)

A solution of methylenebis(phosphonic dichloride) (0.27 g, 1.1 mmol, 5.0 eq) in trimethyl phosphate (5 ml), cooled to 0 °C was added to a suspension of 2-chloro -N^6-benzyl, N^6-(prop-2-ynyl)adenosine (0.1 g, 0.22 mmol, 1.0 eq) in trimethyl phosphate (3 ml) at 0 °C. The reaction mixture was stirred at 0 °C and samples were withdrawn at 15 min intervals for checking the reaction progress by TLC. After 40 min, on disappearance of the nucleoside, 10 ml of cold 0.5 M aqueous TEAC solution (pH 7.4-7.6) was added. The

solution was stirred at 0 °C for 15 min followed by stirring at room temperature for 1 h. Trimethyl phosphate was extracted twice using 100 ml of *tert.*-butylmethylether each, and the aqueous layer was lyophilized. The crude product was then purified by semi-preparative HPLC (0-50% MeCN/50 mM NH_4HCO_3 buffer within 20 min, 20 ml/min) followed by lyophilization to obtain the final product as a white powder (0.05 g, 37%). ^{1}H-NMR (600 MHz, D_2O) δ 8.46 (s, 1H, N=C<u>H</u>N) 7.36 (m, 5 H, aryl) 6.08 (d, 1H, J = 5.5 Hz, C<u>H</u>N) 5.30 (br s, 2H, NC<u>H</u>$_2$) 4.75 (t, 1H, J = 5.3 Hz, C<u>H</u>OH) 4.65 (br s, 2H, NC<u>H</u>$_2$) 4.54 (m, 1H, C<u>H</u>OH) 4.38 (m, 1H, C<u>H</u>CH$_2$) 4.17 (m, 2H, CHC<u>H</u>$_2$) 2.64 (s, 1H, C≡CH) 2.19 (t, 2H, J =19.7 Hz, PC<u>H</u>$_2$P). ^{13}C-NMR (151 MHz, D_2O) δ 157.42, 156.44, 154.50, 141.88, 139.25, 131.66, 130.68, 130.57, 121.88, 89.81, 86.88, 86.84, 82.06, 77.13, 76.18, 73.09, 66.41, 54.39, 49.54, 30.32, 11.11. ^{31}P-NMR (243 MHz, D_2O) δ 18.7 (d, 1P, J = 9.9 Hz, P_β) 15.02 (d, 1P, J =9.9 Hz, P_α). LC/ESI-MS (m/z): positive mode 588.0787 $[M+H]^+$ and negative mode 586.0669 $[M-H]^-$ (calcd. 587.07). Purity determined by HPLC-UV (254 nm)-ESI-MS: 97.7%. mp: >260 °C (dec.).

Tritium labeling: preparation of [^{3}H]PSB-17230

The synthesized and characterized precursor **12** and the unlabeled ligand PSB-17230 were sent to RC TRITEC (Teufen, Switzerland) Company for custom-labeling by catalytic hydrogenation with tritium gas. The produced radiotracer was analyzed by HPLC using the following chromatographic conditions: HPLC column: Waters Sunfire C18, 5 mm, 4.6 mm I.D. x 250 mm L; mobile phase A: water 10 mM NH_4OAc, adjusted to pH 10; mobile phase B: MeCN. Run conditions: 0 min 5% B; 10-14.5 min 95% B; 15 min 5% B. Flow rate: 1.0 ml/min. Sample: 5.5 mCi/ml (203.5 MBq/ml) in EtOH. Injection: 2.0 ml (11.0 mCi, 407 KBq). UV-detection: 254 nm. Temperature: 30 °C. Radiodetector: Berthold LB 513. Cocktail: Zinsser Quickszint Flow 302. Flow rate: 2.0 ml/min. Retention time: 6.49 min (UV); 6.52 min (radiodetector); the delay between UV and radiosignal is due to the serial detection system.

X-ray crystallography

For co-crystallization of PSB-17230 with human CD73, construct 8.01His was chosen. Details about this construct, protein expression in HEK293 cells and enzyme purification have been published previously.[227] Crystals were grown by vapor diffusion at 19 °C. One microliter of CD73 solution containing PSB-17230 (10 mM) and $ZnCl_2$ (10 μM) was mixed

with an equal amount of a reservoir buffer consisting of 20 % polyethylene glycol (PEG 3350) and 0.1 M Tris-HCl pH 7.0. The crystal was transferred in a stepwise manner to a cryo-buffer composed of 5 % PEG 200, 10 mM PSB-17230, 20 % PEG 3350, 10 µM $ZnCl_2$ and 0.1 M Tris pH 7.0 and it was flash-cooled in liquid nitrogen.

X-ray data were collected at 100 K at EMBL beamline P14 at the DESY synchrotron (Hamburg). For data reduction, the programs XDS,[278] and aimless were applied.[279] The pipedream software was used for automatic refinement and ligand placement.[280] COOT[281] was used for manual model building, and phenix for the final refinement steps. Restraint dictionaries for inhibitors were generated using the GRADE web server (http://grade.globalphasing.org). Crystallographic parameters are listed in Table S2. Figures were prepared using PYMOL (http://pymol.org). Difference density maps were generated using the phenix polder algorithms.[282]

Biology

Preparation of soluble recombinant CD73

Spodoptera frudiperga (Sf9) insect cells were used for recombinant expression of soluble rat and human CD73 as previously described.[283,226] A 6xHis-tag was fused to the C-terminus of the cDNA encoding for the soluble human CD73, residues 27 to 549 (based on Genbank accession no. NM_002526 corresponding to the natural variant T376A P21589/VAR_022091/UniProtKB/Swiss-Prot). The generated construct was then ligated into the pACGP67B vector. For transfection, Sf9 cells grown in Insect-XPRESS™ medium (#: BE12-730Q, Lonza, Switzerland) at 60-70% confluence, supplemented with 10 mg/L gentamicin were infected with 1 µL of the recombinant vector (1000 ng/µL) premixed with 2.5 µL of baculovirus genomic DNA ProEasy™ (AB vector, CA, USA). The produced soluble enzyme was concentrated using Amicon® Ultra-15, 10 kDa cut-off (Merck Millipore, MA, USA), then subjected to high-capacity nickel-IMAC purification using HisPur™ Ni-NTA Spin Columns (#: 88226, Thermo Fisher Scientific, MA, USA). The purified soluble enzyme was subsequently aliquoted and stored at -80 °C until further use.

Enzyme inhibition assays

A previously developed sensitive method based on monitoring of the conversion of [2,8-^{3}H]AMP to [2,8-^{3}H]adenosine was applied.[170] To 80 µL of the reaction buffer (Tris-HCl 25 mM, NaCl 140 mM, sodium dihydrogen phosphate 25 mM, pH 7.4), 10 µL of the

test compound was added, followed by 10 µL of CD73 enzyme preparation (soluble human or rat CD73, or membrane-bound enzyme natively expressed in MDA-MB-231 cells, of predetermined activity). The reaction was initiated by the addition of 10 µL of diluted substrate [2,8-^{3}H]AMP (specific activity 7.4 x 108 Bq/mmol (20 mCi/mmol), American Radio-labeled Chemicals, MO, USA, distributed by Hartmann Analytic, Germany). After 25 min of incubation at 37 °C, the reaction was quenched by adding 500 µL of ice-cold precipitation buffer (lanthanum chloride 100 mM, sodium acetate 100 mM, pH 4), and the mixture was incubated on ice for 1 h to allow for AMP precipitation. The soluble [2,8-^{3}H]adenosine was then separated from its precipitated precursor [2,8-^{3}H]AMP by filtration through GF/B glass fiber filters using a Brandel cell harvester (M-48, Brandel, MD, USA), and washed three times with 400 µL each of ice-cold water. The filtrate was collected in scintillation vials. The samples were measured after mixing with 5 ml of scintillation cocktail (ULTIMA Gold XR, PerkinElmer, MA, USA) using a Tri-Carb 2900TR (Packard/PerkinElmer) scintillation counter (54% counting efficiency). Three independent experiments were conducted, each in duplicate. The results were analyzed with GraphPad Prism software version 8.0 (GraphPad Software Inc., San Diego, CA, USA), by applying baseline correction, normalization against the positive control (without test compound) and fitting to the nonlinear regression equation, sigmoidal dose-response curve.

Generation of melanoma MaMel65 knockout cell lines

Human melanoma CD73^{KO} cell lines was generated using the CRISPR-Cas9 technology as described previously.[284] For retroviral reconstitution, plasmids were constructed as follows: CD73 wildtype (wt) transcript was amplified from MaMel.54a cDNA and gel-purified PCR product was digested using BamHI and XhoI and ligated into pRP233. In a next step an enzymatically inactive variant of CD73 harboring a H118A mutation (CAT → GCT) was cloned using site- directed mutagenesis and overlap-2-step-PCR on the pRP233-CD73 vector. First, a reverse primer spanning and introducing the region to be mutated was chosen and combined with a forward primer at the transcript's 5'-end. In parallel, a forward primer spanning and introducing the region to be mutated was chosen and combined with a reverse primer at the transcript's 3'-end. PCR products were purified and used as a template for a second PCR using only the forward and reverse primers of the transcript's 5'- and 3'-end, respectively. Gel-purified PCR product was digested using BamHI and XhoI and ligated into pRP233. Retroviral particles of pRP233, pRP233-CD73-wt and pRP233-CD73-

H118A were produced in HEK293T cells by calcium phosphate-based transfection using vesicular stomatitis virus glycoprotein (VSV-G) envelope for pseudotyping and puromycin as selection marker for successfully infected MaMel.65 CD73 knockout cell lines.

NT5E sequencing in MDA-MB-231, 4T1.2, and melanoma MaMel65 ($CD73^{wt}$ and $CD73^{KO}$) cell lines

Human triple negative breast cancer cells (MDA-MB-231), mouse breast cancer cells (4T1.2) and human melanoma cells (MaMel65) natively expressing CD73 ($CD73^{wt}$), and human melanoma CD73 knockout cell lines ($CD73^{KO}$) were characterized with respect to CD73 expression. For cDNA sequencing, RNA was extracted from $5x10^6$ cells using the Direct-zol RNA miniprep kit (Zymo Research) and eluted with 50 µL of nuclease-free water (PCR H_2O). Reverse transcription was started by heating a mixture of 1 µL Oligo dT 500 µg/ml, 2 µL RNA 1 µg, 4 µL dNTP mix (10 mM) and 12 µl of PCR H_2O at 65 °C for 5 min, the reaction mixture was cooled on ice followed by the addition of 4 µl of 5x first-standard buffer, 2 µl dithiothreitol (DTT, 0.1M), heated at 42 °C for 2 min, then 1 µl of SuperScript II Reverse Transcriptase 200 units and 20 µL of H_2O were added, and the mixture was heated again at 42 °C for 50 min, then inactivated at 70 °C for 15 min. A standard polymerase chain reaction was conducted with the obtained cDNA using CD73-specific primers. An agarose gel (1%) was run with β-actin as a positive control. The obtained cDNA was ligated into a pJET1.2 vector, and transformed into a DH5α *E. coli* strain. The plasmid was isolated with a Zymo Research miniprep kit, then subjected to Sanger sequencing by Eurofins Genomics (Ebersberg, Germany). The obtained sequence results were aligned using SnapGene 3.2.1 software.

Membrane preparations of triple negative breast cancer (MDA-MB-231) and melanoma MaMel65 cells ($CD73^{WT}$, $CD73^{KO}$, and $CD73^{H118A}$ mutant)

Cell culture

MDA-MB-231 breast cancer and MaMel65 melanoma human cell lines were grown in Dulbecco's Modified Eagle Medium (DMEM, #: 41966, Thermo Fisher Scientific, MA, USA) and Gibco Roswell Park Memorial Institute (RPMI Medium 1640), respectively. The medium was supplemented with 10% fetal bovine serum (FBS, #: P30-1502, PAN Biotech, Germany), 100 U/ml penicillin + 100 µg/ml streptomycin (#: P06-07100, PAN Biotech, Germany), and 2 mM L-glutamine. Cells were incubated for 72 h at 37 °C and 5% CO_2 to reach 70-80% confluence. Then, they were washed with 10 ml phosphate-buffered saline

(PBS) and detached by 2 ml of trypsin/ethylenediaminetetraacetic acid (EDTA) (0.05%/0.6 mM), split 1:10, and seeded into culture plates.

Membrane preparation

Cells grown to confluence on the culture plates were washed with 10 ml of PBS and frozen overnight. Membrane preparation buffer (Tris 25 mM, Na_2EDTA 1 mM, sucrose 0.32 M, pH 7.4, supplemented with protease inhibitor cocktail (Cat-No: P8340, Sigma Aldrich, 1 ml dissolved in 100 ml buffer directly before use) was used to scratch the cells off the plates. The cell lysate was homogenized for 30 s, and subsequently subjected to centrifugation at 1000 *g* for 10 min to remove cell debris. The supernatant was collected and centrifuged for 40 min at 48000 *g* and 4 °C. Pellets were then resuspended in 25 ml Tris buffer 50 mM, pH 7.4, and washed for 30 min at 48000 *g* and 4 °C. The washing step was repeated two more times under the same conditions. The obtained pellets were resuspended in 10 ml of Tris buffer 50 mM, pH 7.4, rapidly frozen in liquid nitrogen, and stored at -80 °C until further use.

Membrane preparation of various tissues and tumor cells

Membrane preparations of rodent and human cancer cell lines were obtained according to the same procedure described for MDA-MB-231 and MaMel65 cells. Rat brains (Pel-Freez®, Rogers, Arkansas, USA) were thawed in a 0.32 M sucrose solution and dissected to obtain cortex and striatum. Membrane preparations were prepared according to the published procedure.[285] A healthy Female CD1 mice (Janvier Labs, Le Genest-Saint-Isle, France) were sacrificed by cervical dislocation at the age of 10–12 weeks. The respective organs (kidney, liver, lung, heart and brain) were dissected, snap-frozen in liquid nitrogen, and stored at −80 °C until use. The tissue samples were prepared according to the published procedure.[285]

Protein determination

The Lowry method was applied for protein determination using bovine serum albumin (BSA) as a reference standard.[286] The absorbance was measured at 750 and 500 nm.

Establishment and optimization of a radioligand binding assay

Different incubation buffers (Tris-HCl 25 mM and 50 mM, *N*-2-hydroxyethylpiperazine-*N*-2-ethane sulfonic acid (HEPES), 25 mM), addition of various ions (NaCl, $MgCl_2$, sodium pyrophosphate, sodium dihydrogen phosphate) at acidic (6.5) or physiological blood pH value (7.4) were tried to optimize the conditions for high specific binding of [^{3}H]PSB-17230. Optimal conditions were identified that resulted in low nonspecific binding and avoided depletion of the radioligand. A variety of competitive inhibitors were evaluated for determination of nonspecific binding including ADP, AMPCP, and PSB-12379 at different concentrations. The following optimized conditions were employed for all experiments (unless otherwise stated): incubation at 25 °C for 100 min in a buffer consisting of Tris-HCl, 25 mM and sodium dihydrogen phosphate 25 mM, pH 7.4 (final volume 400 µL). A protein amount of 5 µg/vial and a final concentration of 1 nM of the radioligand [^{3}H]PSB-17230 were employed. Nonspecific binding was determined in the presence of 2 µM of PSB-12379. Binding experiments were performed in polypropylene test tubes (≠: 55.535, SARSTEDT, Nümbrecht, Germany). Separation of bound from unbound radioligand was performed by filtration through GF/B glass fiber filters using a Brandel cell harvester (M-48, Brandel, MD, USA). Samples were washed three times with ice-cold Tris-HCl buffer 25 mM, pH 7.4, 3 ml each. The filters were punched out and transferred into scintillation vials, where they were incubated with 2.5 ml of scintillation cocktail (ProSafe FC$^+$, Triskem) for 9 h. Radioactivity was then measured using a Tri-Carb 2900TR, Packard/PerkinElmer scintillation counter (54% counting efficiency).

Binding to melanoma MaMel65 cells (CD73^{wt}, CD73^{KO} and CD73^{H118A} mutant)

MaMel65 melanoma cells (membrane preparations) and CD73-knockout cells and CD73^{H118A} mutant cells obtained through knockout/knockin using the CRISPR-Cas9 technology were investigated.

Saturation binding experiments

Membrane protein derived from MDA-MB-231 cells (2 µg of protein/vial) was incubated with an increasing concentration of [^{3}H]PSB-17230 (0.1-3 nM, final concentration) at 25 °C for 120 min, or at 37 °C for 60 min, respectively. Nonspecific binding was determined at each radioligand concentration using 2 µM of PSB-12379. The one site-fit total and

nonspecific binding equation was applied to calculate B_{max} and K_D values using GraphPad Prism software version 8.0.1 (GraphPad Software Inc., San Diego, CA, USA).

Kinetic studies

Association of 1 nM of [^{3}H]PSB-17230 to 5 µg of protein of a MDA-MB-231 cell membrane preparation was too fast to monitor. Therefore, the concentration of the radiotracer was reduced to a final concentration of 0.2 nM, and the amount of protein/vial to 2 µg to avoid depletion. Association was closely monitored at 25 °C, or at 37 °C for up to 90 min until binding equilibrium had been reached. Dissociation was initiated by the addition of 4 µL of PSB-12379 solution (final concentration 2 µM) to an assay mixture preincubated for 90 min at room temperature. Association half-time and $K_{on(obs)}$ were calculated based on the pseudo-first order association kinetics equation $Y=Y_0 + (Plateau-Y_0)*(1-exp(-K*x))$ using normalized specific binding values. Dissociation $t_{½}$ and K_{off} were obtained through data analysis using the dissociation - one phase exponential decay equation $Y=(Y_0-NS)*exp(-K*X)+NS$. The half-life ($t_{½}$) equals the ln(2) divided by K (0.693/K). Analysis and curve presentation were performed using GraphPad Prism software version 8.0 (GraphPad Software Inc., San Diego, CA, USA).

Competition binding experiments

Competition binding experiments were carried out using serial dilutions of the test compound. After addition of a membrane suspension (5 µg of protein per vial), the mixture was incubated for 100 min at 25 °C with gentle shaking using the optimized conditions described above. Three independent experiments were performed each in duplicate. Results were analyzed by the GraphPad Prism software version 8.0 (GraphPad Software Inc., San Diego, CA, USA) using one site-homologous or one site-fit K_i models.

Radioligand binding to intact triple-negative breast cancer cells (MDA-MB-231)

Binding to intact MDA-MB-231 cells was studied using 50,000 cell/vial. Full characterization was conducted using the optimized conditions (see above).

Screening of tissues and tumor cell lines

Membrane preparations of cell lines of human and rodent origin, were screened for CD73 using the developed method. Binding of 1 nM of [^{3}H]PSB-17230 to 5 µg of protein preparation was investigated.

Autoradiography

Tissue sections were thawed, air-dried and pre-equilibrated in (Tris-HCl buffer 50 mM, pH 7.4) to remove endogenous ligand. The slides were then mounted and incubated with 2.6 nM (for mouse tissues) or 1 nM (for human tissues) of [^{3}H]PSB-17230 in Tris-HCl buffer 25 mM, NaCl 120 mM, KCl 5 mM, $CaCl_2$ 2 mM, $MgCl_2$ 1 mM, pH 7.4 for 120 min at room temperature. Nonspecific binding was determined in the presence of 2 µM of PSB-12379 for mouse tissues and 1 µM of PSB-12489 for human tissues. Subsequently, all sections were flushed twice for 2 min with ice-cold Tris-HCl buffer, 50 mM, and dipped for 10 s into ice-cold distilled water. Sections were dried rapidly in a stream of cold air, mounted onto a photoplate (BAS TR2025, FUJIFILM, Minato, Japan), and incubated for 3 weeks. The scanned autoradiographic images were analyzed with the AIDA software (version 4.27) by defining regions of interest in tissue sections and densitometric analysis. Calibrated standards (ART0123B/C; American Radiolabeled Chemicals, St. Louis, USA) were used to calculate the radioligand concentration per mg of tissue.

Histological staining

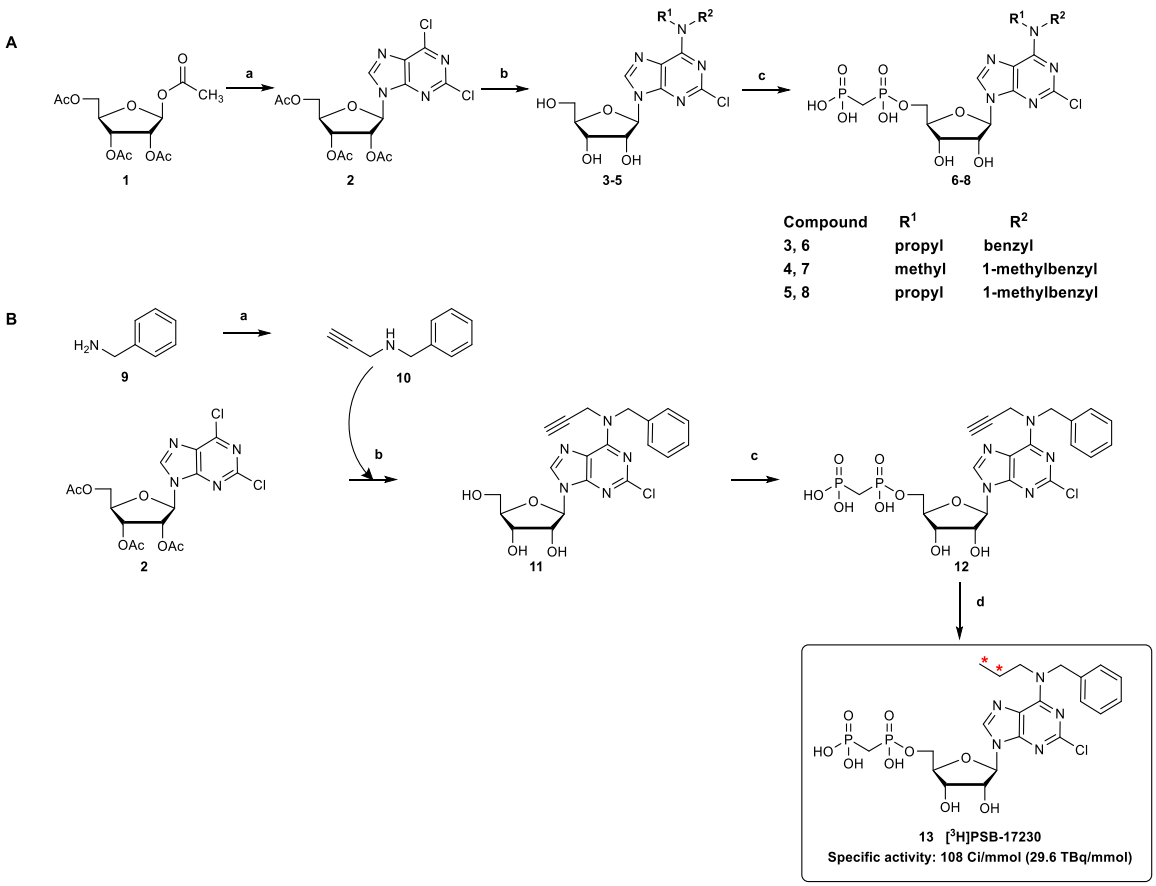
Brain slices were thawed, dried, and covered with Nissl staining solution (1.5% cresyl violet in aqueous ammonium acetate buffer, pH 4.6). After 5 min of incubation, sections were washed with distilled water, then with increasing concentrations (70% and 100%) of ethanol, and dried. For lung tissue, hematoxylin-eosin (HE)-staining was performed. Dried tissue slices were covered with hematoxylin staining solution. After 5 min, slides were quickly washed with deionized water, and rinsed in running warm tap water for 3-5 min. Subsequently, slides were dipped into 100% ethanol for 10 s and incubated with eosin Y solution for 3 min. Then a dehydration step was performed with 100% ethanol for 3 min and slides were allowed to dry. Each stained slide was mounted with NeoMount (Merck Millipore, Burlington, MA, USA) medium and covered with a coverslip. Microscopic images of stained tissues were obtained by an EVOS microscope.

Results and Discussion

Design and development of a radioligand for CD73

In previous studies, we have developed potent and selective competitive CD73 inhibitors based on the ADP analog AMPCP (**I**), leading to the observation that large residues are tolerated at the exocyclic amino group of the adenine partial structure.[209,210,211] X-ray co-crystal structures indicated a second, small lipophilic pocket allowing the introduction of a methyl group as a second substituent on the N^6 nitrogen atom, and a small, more polar pocket at C2 of the adenine ring, ideally harboring a chloro substituent as for example, in PSB-12489 (**IV**) (see Figure 3).[210,211]

In the present study, we further explored the substitution pattern of N^6-disubstituted AMPCP derivatives. In particular, we combined the beneficial larger N^6-benzyl or N^6-α-methylbenzyl substituent with methyl or propyl as a second N^6-substituent yielding the new N^6-disubstituted AMPCP derivatives **6-8**, in addition to the previously described derivative **IV** (see Scheme 1 and **Table 5**). The aim was to introduce a residue that would be suitable for tritium-labeling, preferably in the last reaction step. Moreover, the resulting CD73 inhibitor was supposed to display high potency at human, rat and mouse CD73 for use in clinical and preclinical research and applications. The new target compounds were synthesized as depicted in Scheme 1A. Acetyl-protected 2,6-dichloropurine ribofuranoside (**2**) was used as a starting compound.[210] Tetraacetyl-β-D-ribose (**1**) was reacted with 2,6-dichloropurine in the presence of trifluoromethane sulfonic acid as a catalyst under reduced pressure to give the desired acetylated nucleoside (**2)** (Scheme 1A).[287] The C6-position was substituted with the appropriate *N*,*N*-disubstituted amine in the presence of triethylamine in absolute ethanol. The obtained nucleosides were purified by silica gel column chromatography.[209] After deprotection using sodium methoxide in methanol, the 2-chloro-N^6-disubstituted nucleosides **3-5** were phosphorylated using methylenebis(phosphonic dichloride) in trimethylphosphate followed by hydrolysis with aqueous triethylammonium hydrogen carbonate (TEAC) buffer (Scheme 1A).[209,288] The crude reaction mixtures were extracted with *tert.*-butylmethylether to remove the trimethylphosphate. Purification by high pressure liquid chromatography (HPLC) on reverse-phase C18 material to remove inorganic phosphates yielded the desired pure derivatives **6-8**. The target compounds were obtained in yields of 20-90%, with high purity (>95%). Their structures were confirmed by ^{1}H-, ^{13}C, and ^{31}P-NMR spectroscopy, and LC/ESI-MS.



Scheme 1. **A**. Synthesis of AMPCP derivatives. Reagents and conditions: a) CF_3SO_3H, 0.9 bar, 1 h, 85 °C to room temperature. b) two steps: (i) appropriate disubstituted amine, Et_3N, absolute EtOH, reflux, 5 h. (ii) 0.5% $NaOCH_3$, methanol, room temperature, 10 min. c) two steps: (i) methylenebis(phosphonic dichloride), $PO(OCH_3)_3$, 0 °C, 30 min. (ii) 0.5M TEAC buffer pH 7.4-7.6, room temperature, 1 h. **B**. Synthesis of the radioligand. Reagents and conditions: a) propargyl bromide, room temperature, overnight. b) two steps: (i) **10**, Et_3N, absolute EtOH, reflux, 18 h. (ii) 0.5% $NaOCH_3$, methanol, room temperature, overnight. c) two steps: (i) methylenebis(phosphonic dichloride), $PO(OCH_3)_3$, 0 °C, 30 min. (ii) 0.5M TEAC buffer pH 7.4-7.6, room temperature, 1 h. d) catalytic hydrogenation with tritium gas.

CD73 preparations

Soluble recombinant human and rat CD73 were expressed in *Sf9* insect cells. CD73 sequencing was performed to characterize the cell lines used to develop binding assays, namely MDA-MB-231, 4T1.2 and MaMel65 ($CD73^{wt}$ and $CD73^{KO}$) cell lines. Agarose gel electrophoresis showed cDNA bands for CD73 in all test cell lines except for $CD73^{KO}$ cells (data not shown). Mouse 4T1.2 cells were observed to express a lower CD73 level compared to the human MDA-MB-231 cell line. DNA sequencing confirmed the

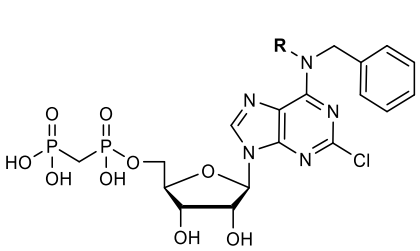
expression of a natural CD73 variant (T376A) in MDA-MB-231 and melanoma MaMel65 (Figure S2C), while the mouse 4T1.2 cell line expressed wild-type CD73. T376A is caused by a single nucleotide variation (ACG>GCG) at a frequency of A=0.216517 (21.6%, 57310/264690, TOPMED).[58] T376 has no ligand contact, and the variant does not affect the catalytic activity of CD73 as confirmed in enzyme inhibition assays.

Pharmacological evaluation of new CD73 inhibitors

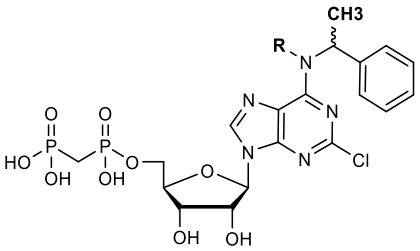
The CD73 inhibitory potency of the new AMPCP derivatives was determined by an enzymatic inhibition assay using [^{3}H]AMP as a substrate.[170] Compounds **7** and **8** possessing a chiral center in one of the N^6-substituents, were tested as a mixture of two diastereomers. All designed and synthesized compounds showed high inhibitory potency at rat and human CD73 with submicromolar K_i values being even more potent than the lead structure PSB-12489 (**IV**) (see **Table 5**). Compound **6**, the propyl analog of **IV**, showed K_i values of 0.0733 nM and 0.0891 nM at recombinant soluble human and human native membrane-bound CD73, respectively. This indicated that a propyl residue was well tolerated as a second N^6-substituent. In combination with an (*R*/*S*)-α-methylbenzyl substituent at N^6 (compound **8**), an N^6-propyl substituent was similarly potent compared to a methyl residue (see compounds **6**, **7** and **8** in **Table 5**). All of the AMPCP derivatives investigated in this study were somewhat less potent at rat CD73 than at human CD73 (2- to 8-fold), but still showed subnanomolar potency at the rat enzyme. We selected inhibitor **6** for further characterization, (i) since a propyl group would be ideal for introducing tritium atoms by catalytic hydrogenation of a propargyl precursor, and (ii) because a benzyl residue would be less complex than a chiral 1-methylbenzyl group. Next, **6** was additionally investigated as inhibitor of mouse CD73 natively expressed in the mouse breast cancer cell line 4T1.2.[155] At mouse CD73, it was less potent than at human and rat CD73, but still displayed low nanomolar potency (K_i = 5.31 nM) which is considered to be sufficient for a radiotracer (see **Figure 42A**).

Table 5. CD73 inhibitory potencies of N^6-disubstituted AMPCP derivatives

N^6-Disubstituted AMPCP derivatives



IV, 6



7, 8

Compound	R	$\mathbf{K_i}$ ± SEM (nM)		
		Soluble rat CD73 [a]	Soluble human CD73 [b]	Human membrane-bound CD73 [c]
IV PSB-12489	methyl	**0.746** ± 0.246 [210]	**0.318** ± 0.020 [210]	ND
6 PSB-17230	propyl	**0.567** ± 0.086	**0.0733** ± 0.0013	**0.0891** ± 0.0111
7	methyl	**0.388** ± 0.095	**0.0705** ± 0.0056	**0.0657** ± 0.0257
8	propyl	**0.582** ± 0.161	**0.159** ± 0.034	**0.113** ± 0.015

[a] Soluble recombinant soluble rat CD73 enzyme, [b] Soluble recombinant soluble human CD73 enzyme, [c] Membrane preparation of triple negative breast cancer (MDA-MB-231 cell). ND; not determined

Compound **6** was further tested for its metabolic stability, and human plasma protein binding. It was observed to be metabolically highly stable in both human and mouse liver microsomal preparations (**Figure 42B**). Within 60 min no degradation was observed in human microsomes, and only very minor degradation (ca. 10%) was seen in mouse microsomes. Such an extraordinarily metabolic stability has previously been exhibited by N^6-substitueted AMPCP analogs[209,213] although AMPCP itself is quickly metabolized.[209] The compound displayed relatively high plasma protein binding of 99.6%, which can still be regarded as suitable for *in vivo* applications.

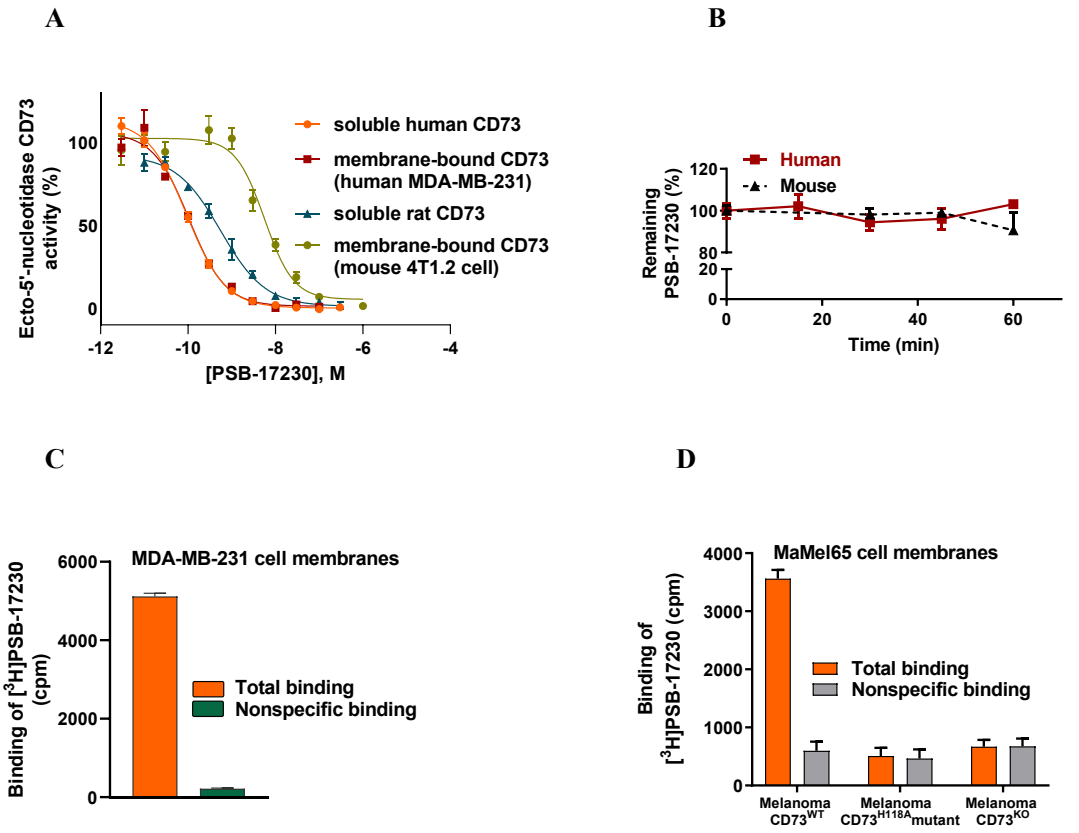


Figure 42. **A**) Concentration-inhibition curves for PSB-17230 at different CD73 preparations using 5 µM of [2^{3}H]AMP as a substrate. Data points are means of three independent experiments. Error bars represent the standard error of the mean (SEM). K_i values: 0.567 ± 0.086 nM (soluble rat CD73), 0.0733 ± 0.0013 nM (soluble human CD73), 0.0891 ± 0.0111 nM (membrane preparation from MDA-MB-231 human triple negative breast cancer cells), and 5.31 ± 0.91 nM (membrane preparation from 4T1.2 mouse breast cancer cells). **B**) Metabolic stability of PSB-17230 (**6**). Microsomal stability was tested at a final concentration of 1 µM. Error bars represent standard errors of the mean (SEM). Half-life was >> 60 min. **C**) Total binding and nonspecific binding of 1 nM of [^{3}H]PSB-17230 using 5 µg of protein/vial of MDA-MB-231 membrane preparation, incubated in Tris-HCl buffer (25 mM) containing sodium dihydrogen phosphate (25 mM), pH 7.4, at room temperature. GF/B filters were used, and washed with ice-cold Tris-HCl buffer 25 mM, pH 7.4. Nonspecific binding was determined in the presence of 2 µM of PSB-12379. **D**) Binding of [^{3}H]PSB-17230 at 25 °C to 5 µg of membrane preparations of human MaMel65 melanoma cell lines (wild-type, CD73-knockout, and CD73-H118A mutant) under the same conditions as in **C**.

Synthesis of a radioligand precursor for tritiation

Due to its excellent pharmacological and pharmacokinetic properties compound **6** was selected for radiolabeling. Its propargyl analog **12** was designed as a radioligand precursor since the triple bond allows for the introduction of up to four tritium atoms by catalytic

hydrogenation and is expected to lead to high specific activity. *N*-Benzyl, *N*-propargylamine **10** was obtained by alkylation of benzylamine **9** with propargyl bromide (**Scheme 1B**). Amine **10** was subsequently reacted with acetyl-protected 2,6-dichloropurine-ribofuranoside **2** in the presence of triethylamine in absolute ethanol, and the product was purified by silica gel column chromatography. After deprotection using sodium methoxide, compound **11** was phosphorylated with methylenebis(phosphonic dichloride) in trimethylphosphate followed by hydrolysis with aqueous TEAC buffer (Scheme 1B) in analogy to described procedures.[209,288] The crude reaction mixture was extracted with *tert.*-butylmethylether to remove trimethylphosphate, followed by HPLC purification on reverse-phase C18 material yielding the desired product **12** (yield, 37%; purity, 97.7%).

Radiolabeling

The radiotracer [^{3}H]PSB-17230 was subsequently obtained by catalytic hydrogenation of the propargyl precursor **12** using tritium gas (see Scheme 1B, for details see Experimental section). A radiochemical purity of 99% was achieved. The specific activity was determined to be 108 Ci/mmol (29.6 TBq/mmol) indicating the incorporation of almost four ^{3}H atoms per molecule, the maximal number achievable upon hydrogenation of a triple bond (Scheme 1B).

Co-crystallization of PSB-17230 with human CD73

PSB-17230 binds at the interface of the two protein domains in the catalytic site (Figure 5). The binding mode is in agreement with previously observed complexes of CD73 with AMPCP derivatives and analogs including the partial flexibility of the N^6-alkyl and -aryl groups.[61,209,210,213,78,216,74] This is indicated by the weak density of these moieties (**Figure 43A-B**). Even for substituents conferring substantial affinity increase compared to AMPCP or 2-chloro-AMPCP, alternative binding modes are characteristic of this compound class. Thus, favorable hydrophobic interactions exist for almost isoenergetic conformations. The phenyl ring of the N^6-benzyl substituent is stacked against the main chain region of residues 184 to 186 while the propyl group has contacts to G419 and N499, but is mostly solvent-exposed (**Figure 43B**).

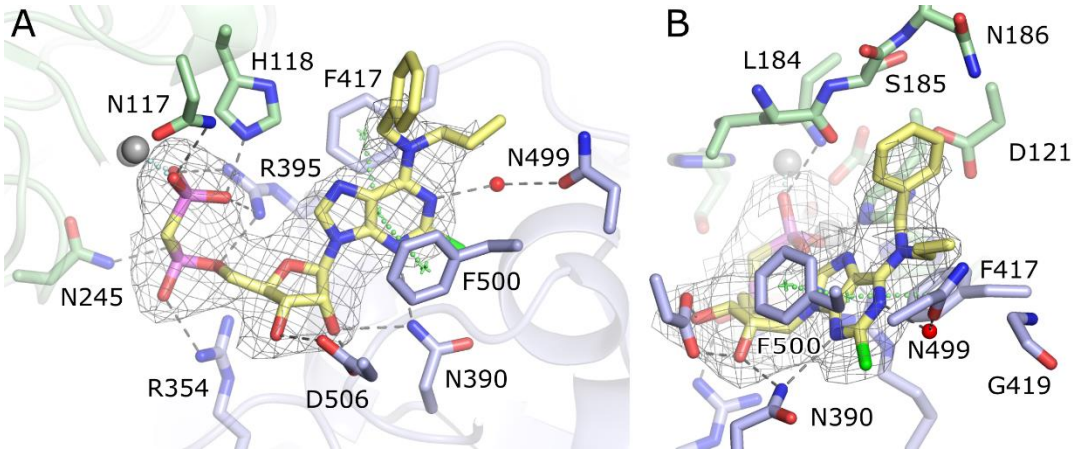


Figure 43. Binding mode of PSB-17230 to CD73 in the closed state. Residues of the N-terminal domain are depicted in green and those of the C-terminal domain in blue. **A**) The terminal β-phosphonate group is coordinated in a bidentate bridging mode to the di-zinc center while the adenine is stacked between F417 and F500. The difference density polder omit map of the ligand is contoured at 3.0 σ_{rms}. **B**) View onto the N^6-substituents. At lower contour levels (shown is 2.0 σ_{rms}) the partially flexible benzyl and propyl groups are defined by the difference density polder map.

Establishment of a radioligand binding assay

With the ^{3}H-labeled CD73 inhibitor PSB-17230 in hand, we established a radioligand binding assay using membrane preparations derived from the human triple negative breast cancer cell line, MDA-MB-231, that natively expresses CD73 on the cell surface. [226,155] Several conditions (different filter types, incubation buffers, protein amounts and radioligand concentrations) were investigated with the aim to obtain high specific binding and to avoid depletion. High specific binding and very low nonspecific binding of less than 10% of total binding were observed when using 1 nM of the radioligand, and membrane preparations of MDA-MB-231 (5 µg of protein) in Tris-HCl buffer 25 mM containing 25 mM of sodium dihydrogen phosphate, pH 7.4. Addition of sodium dihydrogen phosphate was beneficial to decrease filter binding of the radiotracer. These results indicated that [^{3}H]PSB-17230 is an excellent radioligand for the labeling of CD73, showing extraordinarily low nonspecific binding to cell membranes and glass fiber filters. Moreover, the results showed that MDA-MB-231 cells have a very high expression level of CD73 (**Figure 42C**). The radiotracer [^{3}H]PSB-17230 showed higher specific binding to membrane preparations of MDA-MB-231 than to MaMel65 cells (**Figure 42D**).

Binding studies using melanoma MaMel65 cell membranes

The H118 residue is conserved in this family of metallophosphatases.[61] The X-ray crystal structure of human CD73 in complex with PSB-17230 (**Figure 43**) showed its direct interaction with the β-phosphonate group. The specificity of the radioligand [^{3}H]PSB-17230 binding was further investigated using the human melanoma cell line MaMel65 natively expressing the wild-type CD73. In addition, the same cell line with CD73 knockout, or the CD73-KO cells with enzymatically inactive $CD73^{H118A}$ mutant knockin, were studied. [^{3}H]PSB-17230 was found to bind specifically to the $CD73^{WT}$, while it exhibited no high-affinity binding to the $CD73^{KO}$, or the $CD73^{H118A}$ mutant (see **Figure 42D**).

Saturation binding experiments

Binding of [^{3}H]PSB-17230 to MDA-MB-231 membrane preparations was saturable with an apparent K_D value of 0.131 ± 0.016 (at 25 °C) and 0.139 ± 0.009 nM (at 37 °C), and a high expression level of 2.0-2.2 pmol/mg of protein (**Figure 44**). Biphasic evaluation of saturation data did not provide a better fit than the depicted monophasic curves. The saturation K_D value (0.131 ± 0.016 nM) is nearly identical to the K_i value calculated in an enzyme inhibition assay (0.0891 ± 0.0111 nM).

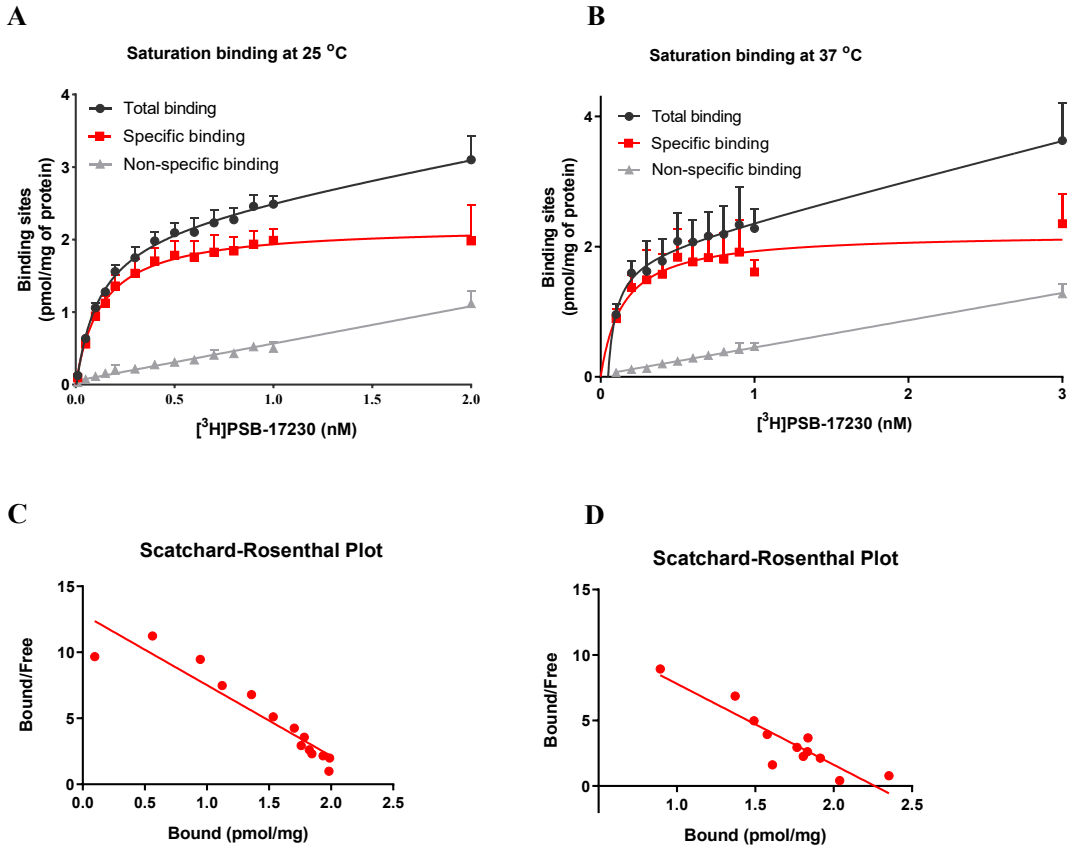


Figure 44. **A**), **B**). Saturation binding experiments of [^{3}H]PSB-17230 to MDA-MB-231 cell membranes at 25 °C and at 37 °C, with corresponding Scatchard-Rosenthal plots (**C**, **D**). [^{3}H]PSB-17230 (0.01-3 nM) was incubated with 2 µg of protein for 120 min at 25 °C, or for 60 min at 37 °C, respectively. Nonspecific binding was determined in the presence of 2 µM of PSB-12379. Data are means ± SEM from at least three independent experiments, each performed in duplicates.

Association and dissociation kinetics

As a next step, radioligand binding kinetics were investigated at 25 °C using 0.2 nM of [^{3}H]PSB-17230. Association was fast with a t½ of 3.2 ± 0.1 min, and a K_{obs} of 0.18 ± 0.04 min^{-1} was calculated. The apparent steady-state was achieved within 25 min and lasted for at least 90 min. Addition of 2 µM of PSB-12379 subsequent to the attainment of the apparent steady-state induced displacement from the binding site with a t½ of 21.5 ± 0.9 min at 25 °C. As shown in Figure 3, binding was completely reversed within 150 min with an exponential decay constant (K_{off}) of 0.03 ± 0.00 min^{-1}. Binding kinetics were further evaluated at 37 °C, the radiotracer showing faster kinetics at this temperature, as expected, with an association $t_{1/2}$ of 1.0 ± 0.4 min, a K_{obs} of 0.94 ± 0.35 min^{-1}, a dissociation $t_{1/2}$ of

11.3 ± 0.8 min, and a K_{off} rate of 0.07 ± 0.01 min^{-1} (**Figure 45** and **Table 6)**. The kinetically derived K_D values, calculated from the obtained off and on rates (K_{off}/K_{on}), were found to be 0.0896 ± 0.0189 nM (at 25 °C), and 0.0389 ± 0.0150 nM (at 37 °C). The radiotracer has a calculated residence time of around 30 min at 25 °C and of 15 min at 37 °C. The kinetically derived K_D value (0.0896 ± 0.0189 nM) and the saturation K_D value (0.131 ± 0.016 nM) and were nearly identical and well in agreement with the K_i value calculated by the enzyme inhibition assay (0.0891 ± 0.0111 nM).

Fitting of the dissociation data into a logarithmic plot (**Figure 45E-H**) gave a line with two slopes. As CD73 is a homodimeric protein, this might be interpreted as two different dissociation rates from each of the two binding sites of the homodimer. At 25 °C, around 80% of the bound tracer dissociated with a $t_{1/2}$ of 23 min and a K_{off} value of 0.031 min^{-1}. After one hour, the remaining bound radioligand dissociated at a different rate with a K_{off} value of 0.013 min^{-1} and a $t_{1/2}$ of 53 min. However biphasic evaluation of saturation data did not give a better fit indicating the same affinity of both sites without cooperativity.

Table 6. Kinetic and saturation binding parameters of [^{3}H]PSB-17230 to membrane preparations and intact MDA-MB-231 cells

	Membrane preparation at **37** °C	Membrane preparation at **25** °C	Intact cells at **25** °C
Association			
Half-life (min)	**1.0** ± 0.4	**3.2** ± 0.1	**4.3** ± 0.1
K_{on} ($nM^{-1} \cdot min^{-1}$)	**1.80** ± 0.39	**0.43** ± 0.09	**0.23** ± 0.05
K_{obs} (min^{-1})	**0.94** ± 0.35	**0.18** ± 0.04	**0.17** ± 0.02
Dissociation			
Half-life (min)	**11.3** ± 0.8	**21.5** ± 0.9	**19.3** ± 1.9
K_{off} (min^{-1})	**0.07** ± 0.01	**0.03** ± 0.00	**0.04** ± 0.00
RT (min)	**15.4**	**31.3**	**27.4**
K_D [K_{off}/K_{on}] (nM)	**0.0389** ± 0.0150	**0.0896** ± 0.0189	**0.168** ± 0.026
Saturation binding			
K_D (nM)	**0.139** ± 0.009	**0.131** ± 0.016	**0.644** ± 0.019
B_{max}	**2.02** ± 0.07 (pmol/mg)	**2.20** ± 0.32 (pmol/mg)	**302,000** ± 26,000 (binding sites/cell)

K_{on}: association rate constant; K_{obs}: apparent association rate constant; K_{off}: dissociation rate constant; RT: residence time; K_D: equilibrium dissociation constant: B_{max}: maximum number of binding sites

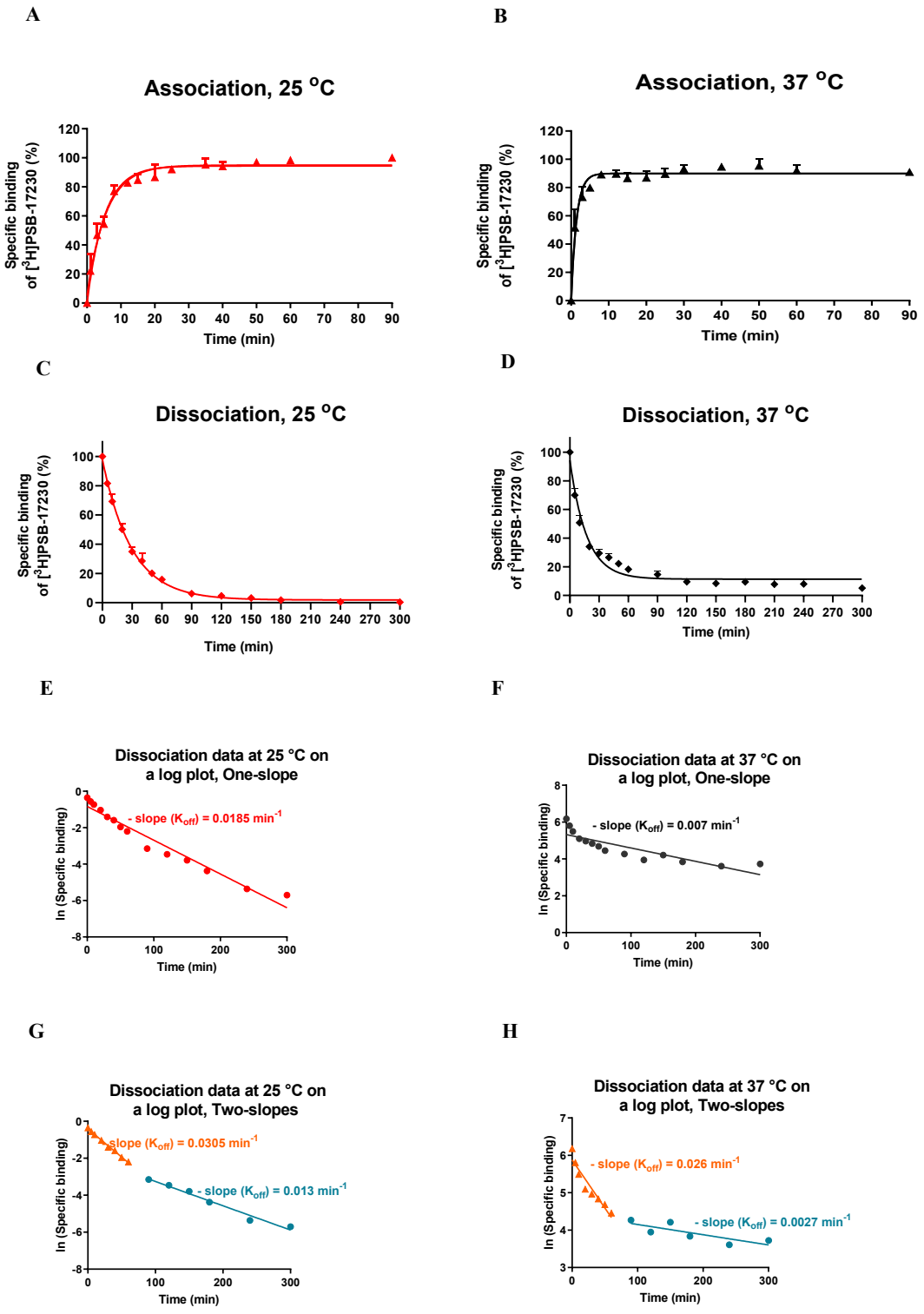


Figure 45. Association and dissociation kinetics of [^{3}H]PSB-17230 (0.2 nM) to membrane preparations of MDA-MB-231 cell line (2 µg protein/ vial) performed at 25 °C (**A** and **C**) and at 37 °C (**B** and **D**) with corresponding log plots for dissociation data (E, F, G and H). The calculated $t_{1/2}$, kinetics rates and K_D values are showed in **Table 6**. Data points represent means ± SEM from at least three independent experiments, each performed in duplicates.

Competition binding assays

Next, homologous competition binding assays were performed at membrane preparations derived from the two cell lines, MDA-MB-231 and MaMel65 (**Figure 46A-B**). The determined K_D values of 0.149 ± 0.001 nM (25 °C, MDA-MB-231 cells), 0.312 ± 0.195 nM (37 °C, MDA-MB-231 cells) and 0.225 ± 0.046 nM (25 °C, MaMel65 cells) were consistent with those obtained in saturation binding and kinetic assays.

Structurally diverse competitive inhibitors (see **Figure 41**) were subsequently investigated in competition binding assays (for concentration-inhibition curves see **Figure 46C**). The determined K_i values compared well with values derived from enzyme inhibition assays at soluble human CD73, and the same order of potency was observed in both assays (see **Figure 46D**).

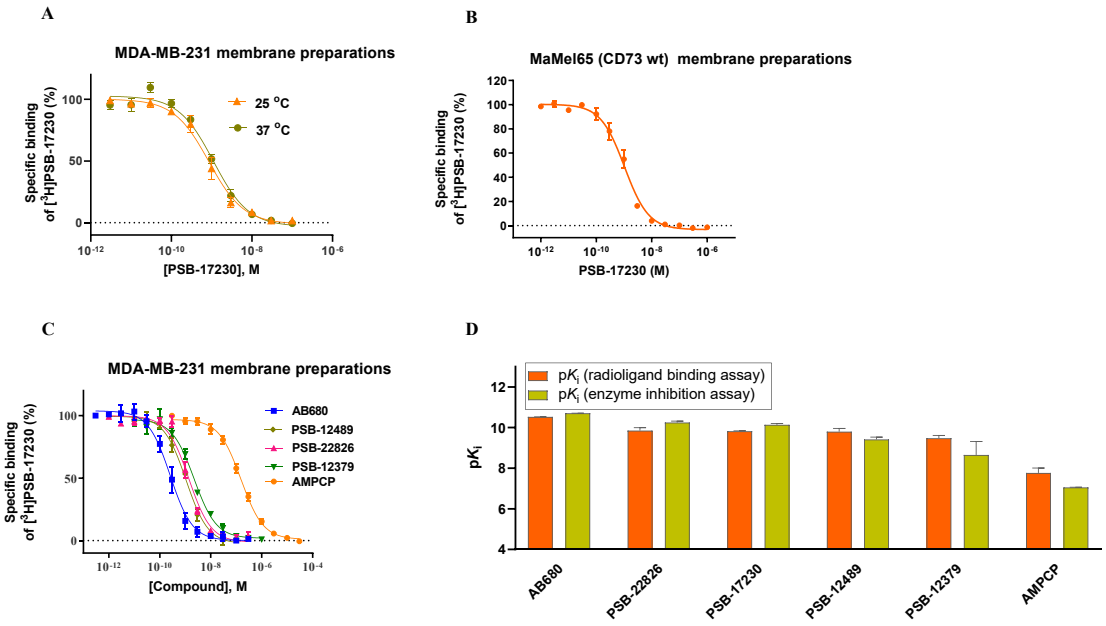


Figure 46. **A)** Homologous competition performed at 25 °C and 37 °C using 1 nM [^{3}H]PSB-17230 and 5 µg of protein from MDA-MB-231 membrane preparations. **B**) Homologous competition performed at 25 °C using 1 nM [^{3}H]PSB-17230 and 5 µg from MaMel65 (CD73 wt) membrane preparations. **C**) Heterologous competition binding experiments. Serial dilutions of each competitor were incubated with 1 nM [^{3}H]PSB-17230 and 5 µg of protein (membrane preparation of MDA-MB-231) for 100 min at 25 °C. **D**) pK_i values of selected inhibitors determined in enzyme inhibition assays (using soluble human CD73) compared to pK_i values obtained by the radioligand binding assay. Data are means ± SEM from at least three independent experiments, each performed in duplicates.

Binding studies at intact cells

To check the validity of the developed method in a more physiologically relevant context, binding assays at intact MDA-MB-231 cells were performed.

Saturation binding studies at intact cells

Binding of various concentrations of [^{3}H]PSB-17230 to intact MDA-MB-231 cells (50,000 cells/vial) was studied at 25 °C. The apparent K_D value was found to be 0.644 ± 0.019 nM, and a B_{max} value of 302,000 ± 26,000 binding sites/cell was calculated confirming a very high expression level (**Figure 47A**). For comparison, human platelets were found to express as 10.600 ± 2.100 binding sites/cell of G_q protein,[285] and $P2Y_{12}$ receptors displayed an expression of 62,000 ± 10,000 binding sites/cell in recombinant 1321N1 astrocytoma cell.[289]

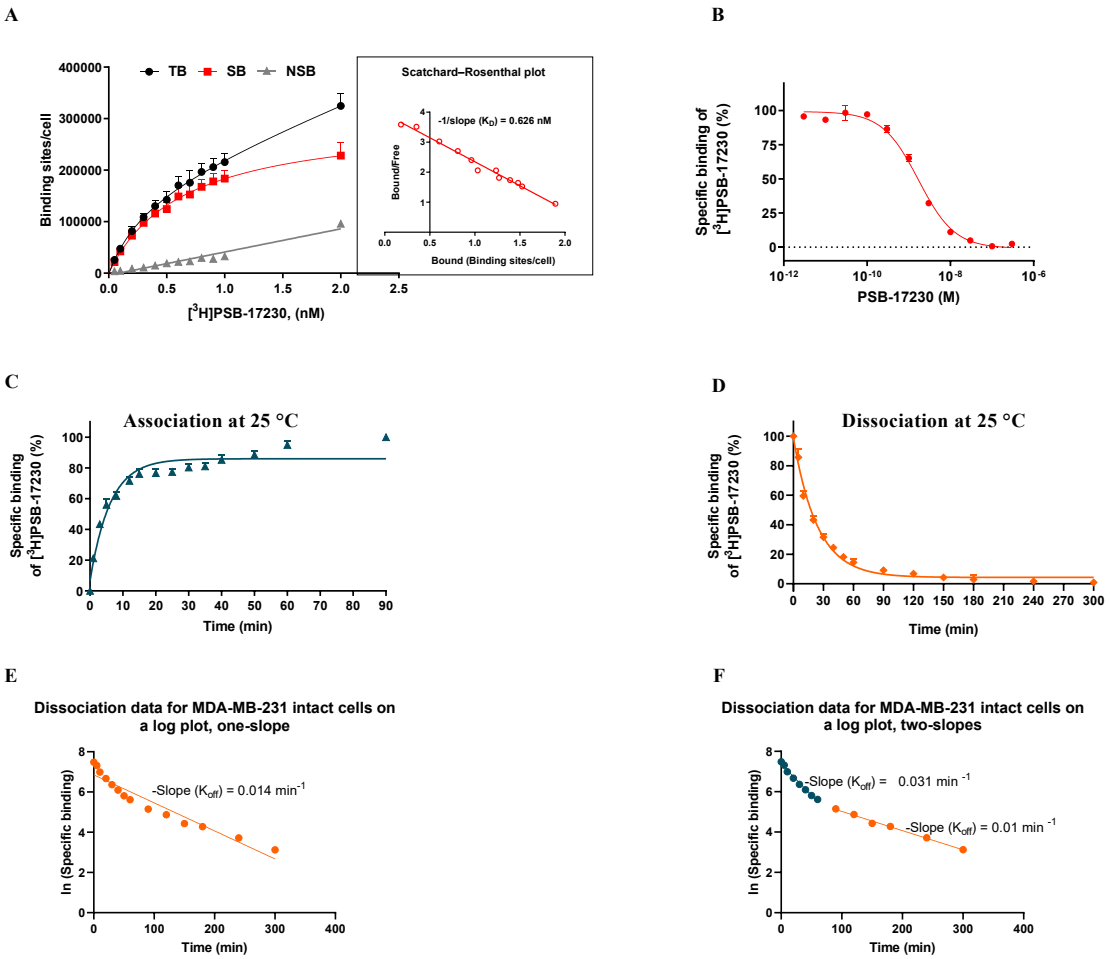


Figure 47. Characterization of radioligand binding to intact MDA-MB-231 cells. **A**) Saturation binding experiments of [^{3}H]PSB-17230 using intact MDA-MB-231 cell at 25 °C with corresponding Scatchard-Rosenthal plot. [^{3}H]PSB-17230 (0.01 - 2 nM) was

incubated with 50,000 cells/vial for 120 min at 25 °C. TB: total binding, SB: specific binding. NSB: nonspecific binding. **B**) Homologous competition binding curve at 25 °C using 1 nM of [^{3}H]PSB-17230, and 50,000 MDA-MB-231 cells/vial. The calculated K_i and B_{max} values were 0.557 ± 0.021 nM and 249,988 ± 9,559 binding sites/cell. **C**, **D**) Association and dissociation kinetics of [^{3}H]PSB-17230 (0.2 nM) to intact MDA-MB-231 cell (50,000 cells / vial) performed at 25 °C. The calculated $t_{1/2}$, kinetic rates and K_D values are shown in Table 2. Nonspecific binding was determined in the presence of 2 µM PSB-12379. Data points represent means ± SEM from at least three independent experiments, each performed in duplicates.

Binding kinetics at intact MDA-MB-231 cells

The association and dissociation parameters of [^{3}H]PSB-17230 binding to intact MDA-MB-231 cells were similar to those observed at membrane preparations. Intact cells showed fast association with a $t_{1/2}$ value of 4.3 min and a K_{obs} value of 0.17 min^{-1} compared to 3.2 min and 0.18 min^{-1} for membrane preparations. Dissociation of the radiotracer was also similar in both studies with $t_{1/2}$ of 19.3 min and 21.5 min, and K_{off} values of 0.04 min^{-1} and 0.03 min^{-1} for intact cells, and membrane preparations, respectively (**Figure 47C-D**, **Table 6**). The kinetically derived K_D value, was found to be 0.168 ± 0.026 nM (at 25 °C), which is highly comparable to that obtained with membrane preparation at the same temperature (0.0896 ± 0.0189 nM). The radiotracer has a calculated residence time of ca. 27 min at 25 °C. Presenting the dissociation data on a logarithmic scale indicated two different slopes (**Figure 47E-F**). Around 75% of the bound radiotracer dissociated within the first 60 min with a $t_{1/2}$ of 22 min and a K_{off} value of 0.031 min^{-1}. The remaining 15% showed very low unbinding kinetics with a $t_{1/2}$ of 69 min and a K_{off} value of 0.01 min^{-1}. Interestingly, this had also been observed for the binding kinetics determined at membrane preparations which might indicate that the majority (up to 75%) of the bound tracer dissociated within 60 min with very similar rate from membrane preparations and intact MDA-MB-231 cells, while 15 % of it dissociated much more slowly. Fitting the saturation and competition data to a two-sites model did not give better fit indicating no cooperativity in the binding to the dimeric enzyme.

Homologous competition binding at intact MDA-MB-231 cells

Homologous competition binding of the unlabeled PSB-17230 versus [^{3}H]PSB-17230 (**Figure 47B**) revealed a K_D value of 0.557 ± 0.021 nM. All K_D values obtained from

equilibrium and kinetics experiments were in agreement to that obtained using an established enzymatic assay (0.0891 ± 0.0111 nM).

Quantification of CD73 expression in different tissues and cell lines

Next, the developed method was applied to the determination of CD73 expression levels in different human and rodent cell lines and tissues (**Figure 48**). Native healthy tissues showed much lower specific binding than most of the investigated cancer cell lines. Mouse breast cancer cell 4T1.2 and Chinese hamster ovary cells CHO express negligible amount of CD73. Expression of CD73 was very low in human cervix carcinoma cell Hela and embryonic kidney cell HEK-293. CD73 was undetected in human T lymphoblast Jurkat T cell which was also shown in the human protein atlas. Glioma and astrocytoma cells (C6, LN-229, U-87 and 1321N1) exhibited high expression levels which confirms the previously reported expression of CD73 in brain cancers.[290] Among human glioblastoma cells, U-87 cells expressed about 4-fold as much CD73 as LN-229 cells. Published results showed a difference in migration and proliferation between these two cell lines. Genetic differences were studied and suggested to affect their mechanisms toward tumor progression [291,292], however, *NT5E* was not among the studied genes. Since its role in cancer cell proliferation and migration is well known [259,293], the difference in its expression might contribute to the different properties of the studied cells. Comparable low specific binding was detected in the hepatocellular carcinoma cell lines (Hep G2 (human) and McA-RH7777(rat)) indicating low expression of CD73. Hep G2 cells were reported to overexpress the inactive CD73 (isoform 2) [54] which is not detected by the radiotracer. The radioligand recognizes only the active form of CD73, unlike immunodetection methods based on antibody recognition, since CD73 antibodies typically cannot differentiate between isoforms. The melanoma cell line MaMel65 showed high levels of CD73 expression as earlier reported [284] while no specific binding was observed for the corresponding $CD73^{KO}$ cells.

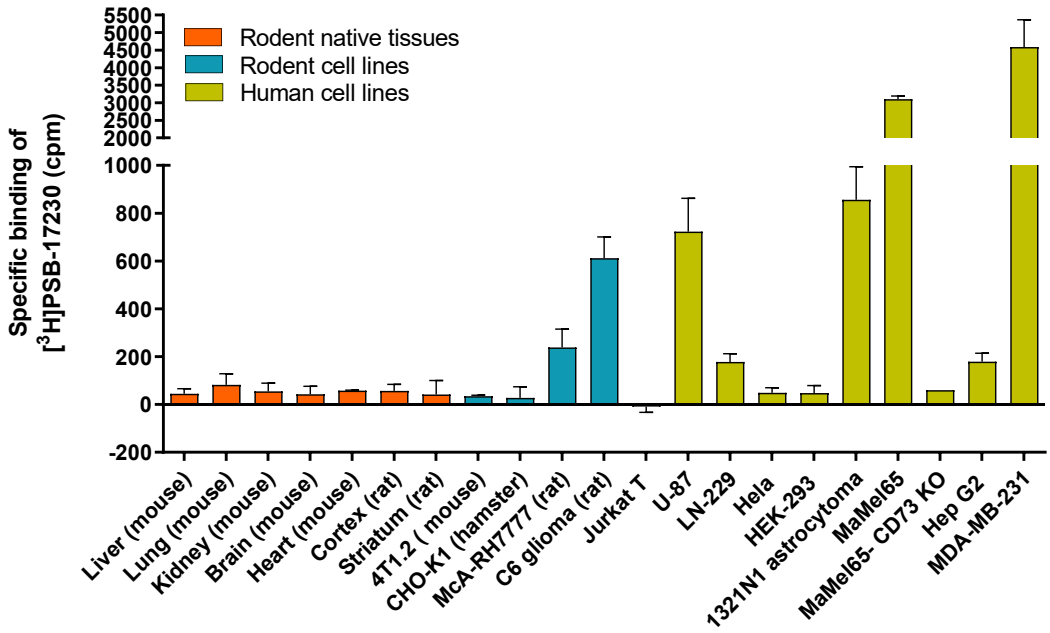


Figure 48. Specific binding of [^{3}H]PSB-17230 (1 nM) to membrane preparations of various cells and tissues (5 µg of protein). Nonspecific binding was determined in the presence of PSB-12379 (2 µM). Values represent means ± SEM of at least three independent experiments. Cell lines: 4T1.2: mouse breast cancer; CHO-K1: subclone of Chinese hamster ovary cells; McA- RH7777: rat liver hepatoma cells; C6 glioma: rat glioma cells; Jurkat T: human Jurkat T-lymphocytes; U87: human glioblastoma cells; LN-229: human glioblastoma cells; Hela: human cervix carcinoma cells; HEK-293: human embryonic kidney cells;1321N1 astrocytoma: human astrocytoma cell line; MaMel 65: human melanoma cells; MaMel65 CD73-KO: human melanoma cells in which CD73 had been knocked out by CRISPR-Cas9; Hep G2: human hepatocellular carcinoma cell; MDA-MB-231: human triple negative breast cancer cells.

Autoradiography studies

Finally, we investigated whether the new CD73 radiotracer would be suitable for CD73 imaging of organ slices. To this end we studied the expression of CD73 in different brain regions and in spleen of healthy mice. Brain sections were additionally stained with cresyl violet (Nissl staining; blue staining of basophilic molecules, e.g., RNA and DNA), while spleen sections were stained with hematoxylin-eosin (blue staining of basophilic structures and red staining of eosinophilic structures) (**Figure 50A-B**). The expression of CD73 was calculated by densitometric analysis (**Figure 49A**), indicating an average expression level in the brain of 207 fmol per mg of tissue. Slightly higher radioligand binding was found in the cerebellum (CB, 269 fmol/mg). Cortex (CO, 176 fmol/mg) displayed intermediate CD73 enzyme expression levels, while striatum (ST) expressed somehow less CD73 (134

fmol/mg). The spleen, an organ associated with the immune system, showed a substantially higher B_{max} value of 1599 fmol/mg. This data reflects that CD73 is differentially expressed across various healthy organs, likely resulting in significant implications for immune regulation and other biological processes. Understanding alterations in CD73 expression, especially in disease, could be important for developing targeted therapies for diseases, such as cancer and autoimmune disorders.

Mouse asthma model

In a recent study, CD73 expression and activity was reported to be increased in mouse asthma models induced by ovalbumin sensitization.[90,294] We utilized autoradiography to examine the distribution of the CD73 protein in mouse lung sections, comparing healthy with asthmatic mice using the same model (**Figures 49B** and **50C**). In fact, there was a noticeable difference in the lungs of asthmatic mice as compared to healthy mice. While the asthmatic lungs showed a CD73 expression of 326 fmol/mg of tissue, the healthy lungs had an 8-fold lower expression of only 38.4 fmol/mg of tissue.

Human tissues

Subsequently, we examined the expression and distribution of CD73 in human tumor samples and their surrounding healthy tissues (**Figure 49C**). In mammary glands, both healthy and cancerous tissue exhibited low levels of CD73 expression (85.4 and 50.1 fmol of CD73/mg of tissue). In rectum samples (**Figure 50E**), CD73 expression was high and found to be uniformly distributed. Although the healthy rectal tissue seemed to express slightly more CD73 enzyme than the tumor tissue, the difference was statistically insignificant. Colon samples exhibited similar levels of CD73 of rectum tissues with areas of lower radioligand binding that could not be clearly associated with any defined structure when compared to hematoxylin-eosin-stained samples (**Figure 50F**; 165 and 125 fmol of CD73/mg of tissue for control and tumor samples, respectively). In human kidney biopsies, a relatively high specific binding equal to 216 fmol of CD73/mg of tissue was evenly distributed in the cancer tissues, and there was a significant difference compared to the healthy control sections (6.67 fmol of CD73/mg) as illustrated in **Figures 49C**, **50G**.

In summary, this study offers a thorough examination of CD73 protein expression and distribution across various crucial organ systems in healthy mice, disease models, and human cancer samples alongside adjacent healthy tissues. Our investigation revealed that

[^{3}H]PSB-17230, the first radiotracer for CD73, exhibits high affinity and selectivity combined with a relatively low residence time, enabling precise quantitative measurements of CD73 protein expression. The findings align with extant literature suggesting that CD73, known for its ecto-5'-nucleotidase activity, exhibits tissue-specific expression patterns.

In the BALB/c asthmatic model mouse, a significant upregulation of CD73 protein observed within lungs and airways. An investigated kidney tumor sample demonstrated a 32-fold higher expression of CD73 compared to control human healthy sections, whereas other samples, namely breast, rectum, and colon tumor, displayed negligible differences. In breast tissue, the absence of marked upregulation of CD73 in tumorous tissue contradicts what is known about the high CD73 expression and its correlation with breast cancer diagnosis. This discrepancy could be attributed to the heterogeneity of breast cancer subtypes. Further investigation into the breast cancer samples in our study could provide deeper insights into these findings. As for rectum and colon tissues, the lack of significant differential expression of CD73 in our study aligns with a subset of colorectal cancer studies that suggest that the role of CD73 is complex and may not always be associated with the immunosuppressive adenosinergic pathway.[295] The intricate nature of the tumor microenvironment in colorectal cancer involves a multitude of immune cells and signaling molecules, wherein CD73 might play roles beyond its enzymatic function, such as in cell adhesion and migration.

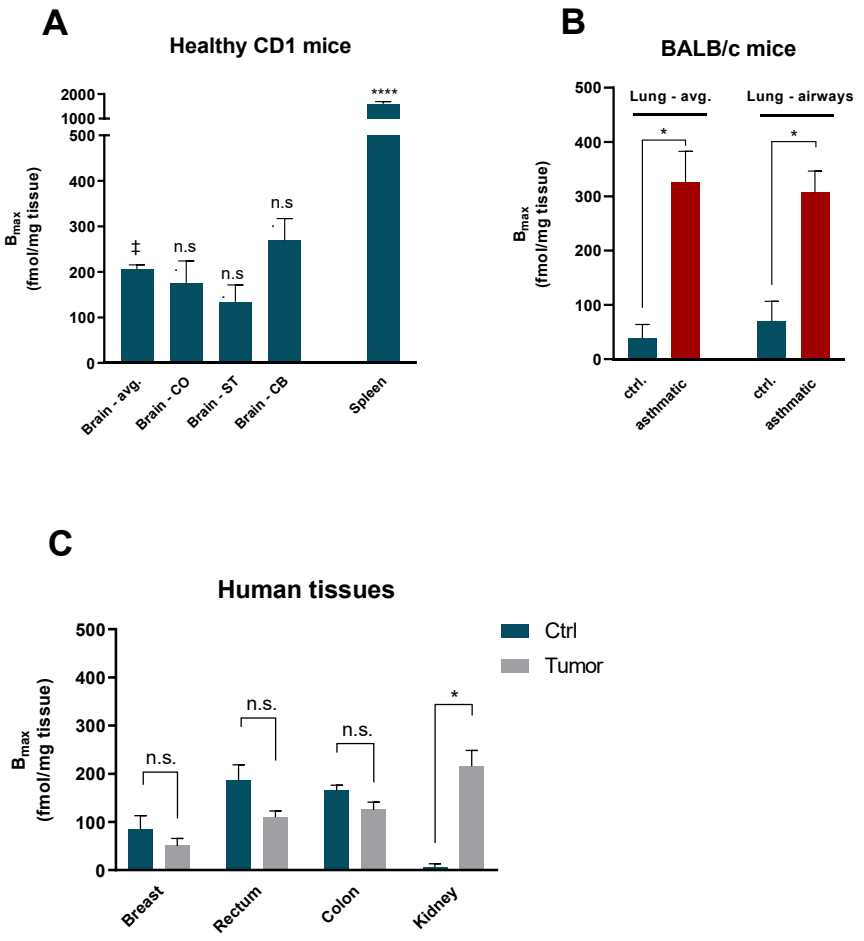


Figure 49. CD73 protein expression (B_{max}, given in fmol CD73 per mg tissue) **A**) tissues obtained from healthy female CD1 mice. **B**) BALB/c mice treated with ovalbumin to induce symptoms of acute asthma (asthmatic) or untreated BALB/c mice (ctrl.). **C**) Samples from human cancers and surrounding healthy tissue. Values are presented as mean ± SEM from three (**A**) or two (**B**) individual animals, each measured at least in triplicates. avg., average; CO, cortex; ST, striatum; CB, cerebellum. Comparisons between two mean values were performed by an unpaired, two-sided t-test, if necessary, corrected for multiple comparisons; if more than two mean values were compared, a one-way ANOVA with Dunnett's post-hoc test was employed, in which all means were compared to the tissue average (mouse brain). Significance levels are defined as follow: n.s., $p > 0.05$; *, $p < 0.05$; **, $p < 0.01$, ***, $p < 0.001$, the reference value is indicated with ‡ in case of multiple comparisons.

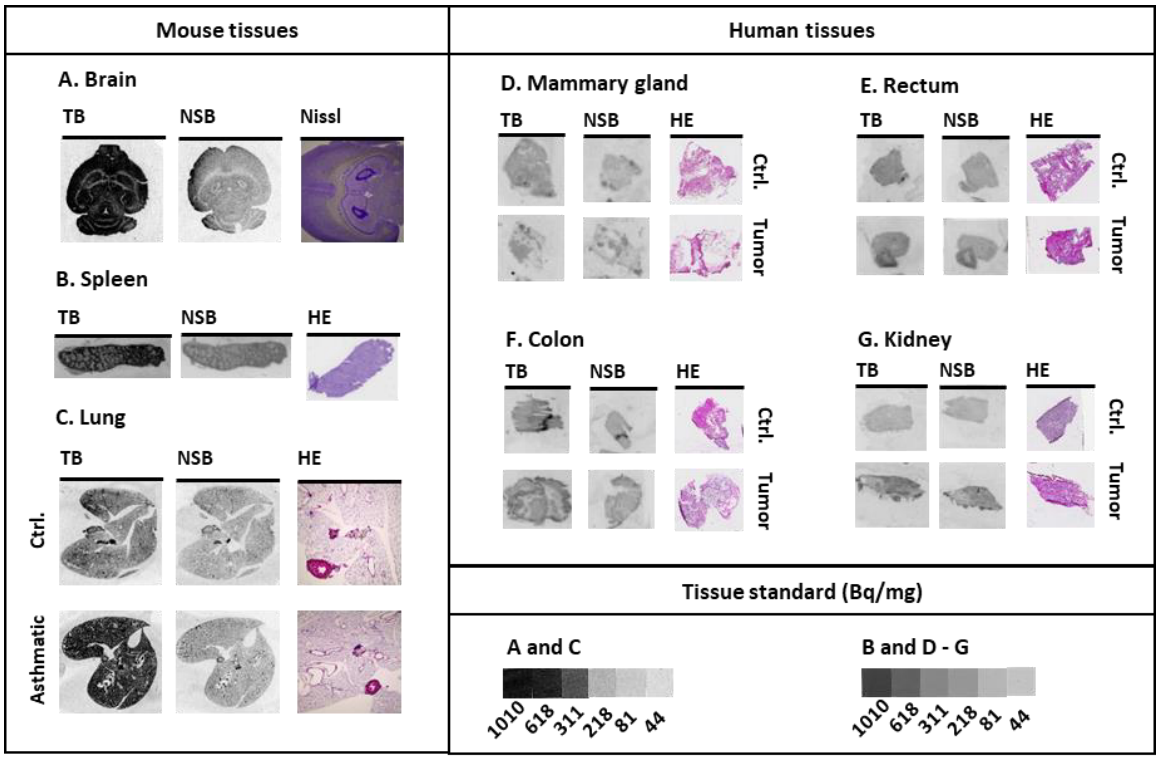


Figure 50. Representative images of mouse and human sections. **A**) Brain, **B**) Spleen, **C**) Lung, **D**) Mammary gland, **E**) Rectum, **F**) Colon, **G**) Kidney. TB, total radioligand binding; NSB, nonspecific binding (determined in the presence of 2 μM of PSB-12379 for mouse tissues and 1 μM of PSB-12489 for human tissues), HE, hematoxylin-eosin staining. For autoradiography, organ slices were incubated with 2.6 nM of [^{3}H]PSB-17230 (mouse) or with 1 nM of [^{3}H]PSB-17230 (human) for 120 min at room temperature. Tissue equivalent standards are shown at the bottom left.

Conclusions

In the present study, we designed and synthesized the first radioligand [^{3}H]PSB-17230 for the labeling of the cell surface protein, CD73. The unlabeled competitive inhibitor of CD73, PSB-17230, exhibited very high inhibitory potency tested in different species combined with high metabolic stability. [^{3}H]PSB-17230 in the radioligand binding assay showed very low nonspecific binding. Furthermore, the expression levels of CD73 were evaluated in different tumor cell lines and tissues and correlated well with the catalytically active isoform 1. Unlike immunodetection-based methods, this will allow for better identification of patients who would benefit most from CD73 blockage.

Obtained X-ray co-crystal structure showed the residues involve in the interaction with the radiotracer. Moreover, the clinical applicability of the new radiotracer[^{3}H]PSB-17230 was assessed in autoradiography studies.

Author contribution

The author developed and optimized the radioligand binding assays, performed saturation experiments and characterized the kinetics at 37 °C. In addition, the author characterized binding interactions at 25 °C, screened various tissues and tumor cell lines and study binding to intact cells in collaboration with Haneen Al-Hroub. Moreover, she collaborated with Tobias Claff to perform the sequencing experiments, and with Patrick Riziki to characterize the inhibitors using an enzyme inhibition assay. The manuscript was written by the author with contribution from all co-authors.

3.2. Nano-luciferase tagging of soluble and membrane-bound CD73 and establishment of NanoBRET assays

Nluc-tagged ecto-5'-nucleotidase (CD73): effects on binding kinetics and interactions in soluble and membrane-bound isoforms

Riham M. Idris [1], *Haneen Al-Hroub* [1], *Nobert Sträter* [2], *Christa E. Müller* [1]

[1] PharmaCenter Bonn, Pharmaceutical Institute, Department of Pharmaceutical & Medicinal Chemistry, University of Bonn, An der Immenburg 4, D-53121 Bonn, Germany

[2] Center for Biotechnology and Biomedicine, Institute of Bioanalytical Chemistry, University of Leipzig, Deutscher Platz 5, 04103 Leipzig, Germany

Corresponding Author

Prof. Dr. Christa E. Müller

Pharmazeutisches Institut

Pharmazeutische & Medizinische Chemie

An der Immenburg 4, D-53121 Bonn, Germany

Phone: +49-228-73-2301

Fax: +49-228-73-2567

E-mail: christa.mueller@uni-bonn.de

Abstract

Ecto-5'-nucleotidase (CD73) catalyzes the hydrolysis of extracellular AMP to adenosine, which exerts immunosuppressive and cancer-promoting effects. Therefore, it is currently investigated as a potential target for the immunotherapy of cancer. In present study we designed and expressed Nano-luciferase (Nluc)-labeled CD73 to establish a bioluminescence resonance energy transfer (BRET) binding assay. To this end, Nluc tag was introduced into the N- or C-terminus of soluble or membrane-bound isoforms of human CD73. Nluc tag at the N-terminus of soluble human CD73 was found to significantly affect the substrate binding pocket. The IC_{50} value of the competitive inhibitor AMPCP was around 18-fold higher compared to the native enzyme. In contrast, the C-terminally tagged enzyme showed the same IC_{50} value as the untagged CD73. However, the fluorescent tracer PSB-18332 exhibited very slow unbinding kinetics with a residence time of 63 min at 37 °C at soluble CD73. In contrast, both N- and C-terminally tagged membrane-bound human CD73 exhibited significantly faster kinetics than soluble tagged protein. A binding assay was developed for testing of inhibitors. K_i values determined in the developed NanoBRET assay using N- and C-terminally tagged membrane-bound CD73 showed high correlation with data obtained in radioligand binding assays and enzyme inhibition assays for a series of diverse competitive inhibitors. The newly established homogenous assay allows the determination of residence times and is suitable for high-throughput screening.

Keywords

Ecto-5'-nucleotidase; CD73; Nluc tag; NanoBRET assay; PSB-18332

Introduction

Ecto-5'-nucleotidase (CD73) is a homodimeric glycoprotein that plays a key role in nucleotides homeostasis. Each subunit of the dimer consists of 574 amino acid residues subdivided into an N-terminal domain (amino acid residue 27-317) that incorporates a Zn^{2+} cation, and a C-terminal domain (residue 337-549) harboring the substrate binding site. Two signal peptides exist: a secretory signal peptide at the N-terminus comprises the first twenty-six amino acids, and a second signal peptide at the C-terminus attaches the protein to the membrane via a glycosylphosphatidylinositol (GPI) anchor. An α-helix (residues 318-336) connects the two domains and act as a hinge allowing the protein to switch between an open and a hydrolytically active closed conformation (see **Figure 51**).[61,78,296,243,74,214,216] The enzyme is active in its membrane-anchored form as well as soluble protein. The soluble form is shedded through cleavage of the GPI anchor by phospholipase C or proteases.[67] CD73-positive exosomes have been detected in many body fluids.[66,19,65]

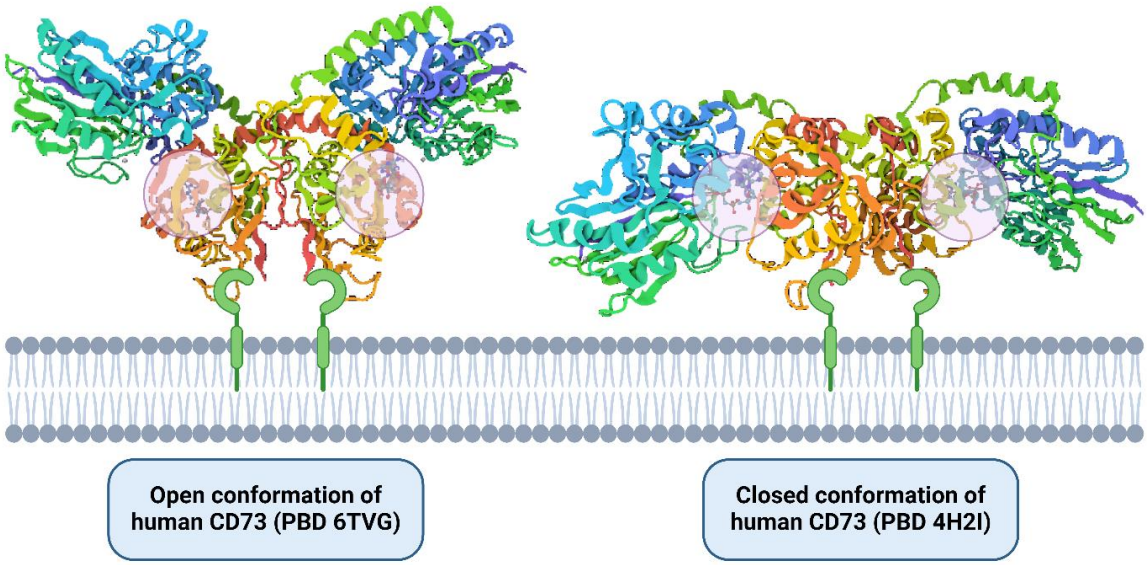


Figure 51. Human CD73 in open and closed conformations in complex with AMPCP (PDB 6TVG and 4H2I). Substrate binding pocket is circled. Created with BioRender.com.

Extracellular adenosine triphosphate (ATP) is hydrolyzed to adenosine monophosphate (AMP) mainly by the action of ectonucleoside triphosphate diphosphohydrolase-1 (CD39), which is subsequently cleaved by CD73 to produce adenosine.[19,265] Adenosine induces the activation of adenosine receptors resulting in immunosuppressive effects, tumor cell

proliferation, and metastasis.[261,258] Over-expression of CD73 has been linked to a bad prognosis in several types of cancer.[152,297,293] Thus CD73 inhibitors are currently developed as novel therapeutics for the immunotherapy of cancer.[274]

Small molecule inhibitors as well as monoclonal antibodies have been developed as CD73 inhibitors, some of which are being evaluated in clinical studies.[78,243,214,210,264,211,213,273,155,154,215] Structures of selected potent inhibitors are depicted in **Figure 52**.

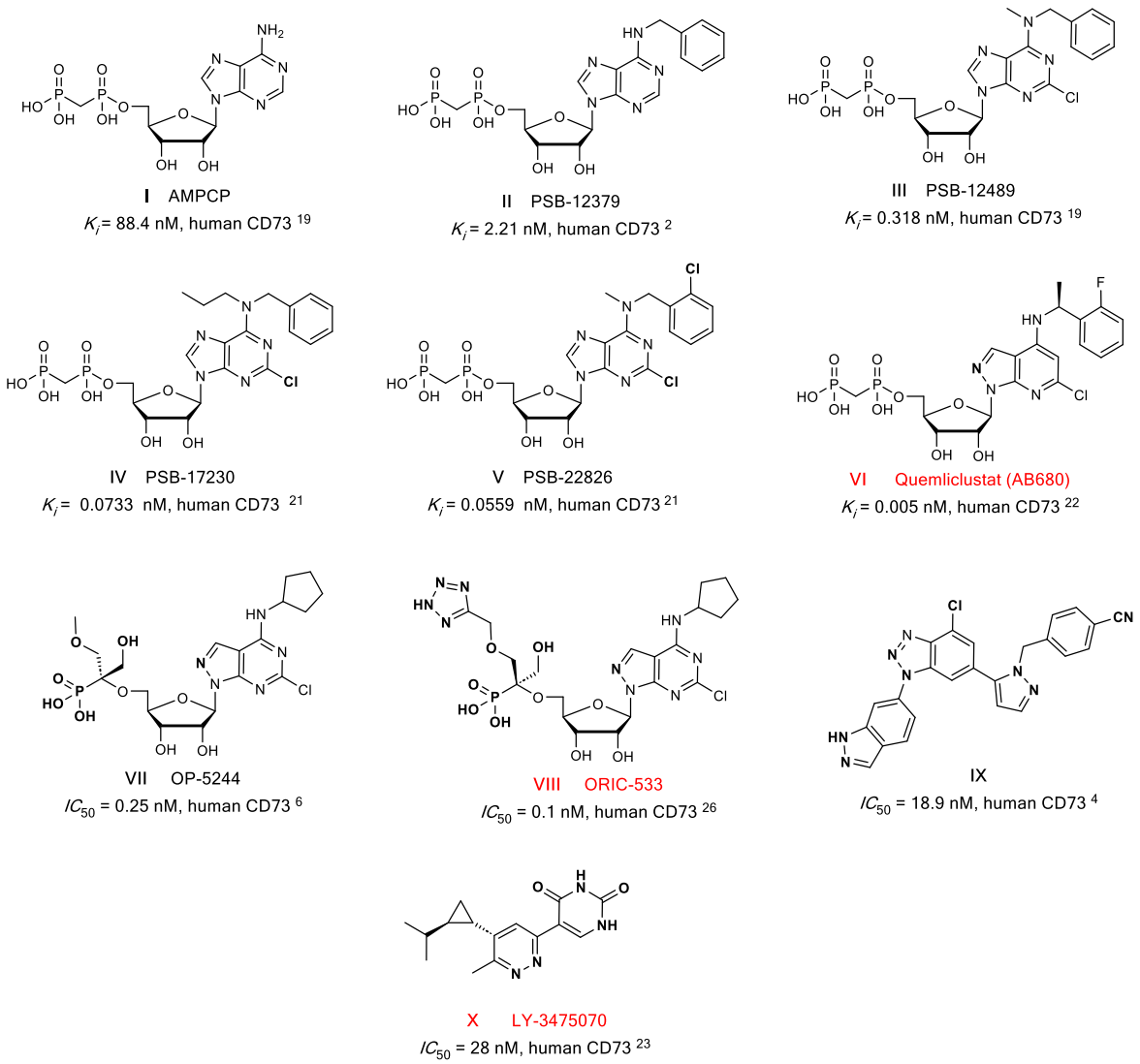


Figure 52. Structures of selected inhibitors of CD73 (in red are drug candidates in clinical development).

In the present study, we aimed at developing a labeled version of the functional enzyme by introducing nano-luciferase (Nluc). This would allow a range of applications.

We herein report for the first time tagging of CD73 as soluble and membrane-bound forms with the nano-luciferase tag (Nluc) which is optimized mostly for secretory proteins. Establishment of a nano-luciferase bioluminescence resonance energy transfer (NanoBRET) assay for CD73 provides many advantages over biochemical methods currently in use or the conventional radioligand binding assays. Biochemical methods lack the ability to study the kinetics of binding interaction and radioligand binding assay has the drawbacks of dealing with radioactivity besides the need to separate the bound from free ligand. On the other hand, NanoBRET assay allows for a homogeneous, fast "mix-and-measure" format with a real-time detection of binding kinetics to living cells. Moreover, this method provides a suitable tool to study residence time which has been emerged as a critical factor to be optimized during drug development campaigns.[181,182] Both, structure-activity-relationship and structure-kinetics-relationship studies are feasible.

We employ in this method a recently published fluorescent ligand of CD73, PSB-18332, that was designed, synthesized and fully characterized in our research group.[257]

Methods

Nluc-tagged to soluble CD73

DNA manipulation

cDNA coding for the secretory Nluc was amplified between EcoRI and BamHI in a standard polymerase chain reaction (PCR) using a predesigned forward and reverse primers together with the pNLF1-secN vector as a template. The insert was then ligated at the N-terminus of the soluble human CD73 (w^{27}-S^{549}-6xHis) previously cloned in pFastBac1 vector to produced N-terminally tagged CD73 (pFB1-secNluc-GGGSGS-sCD73-6xHis).

Site-directed mutagenesis was first applied to insert XhoI site at the C-terminus (after Serine residue 549) of the soluble human CD73 cloned in pFastBac1 vector. Afterwards, cDNA encoding for the Nluc was amplified between XhoI and HindIII. The generated vector pFB1-10xHis-sCD73-XhoI and the insert Nluc were double digested with XhoI and HindIII then ligated in-frame to produce pFB1-10xHis-sCD73-GGGS-Nluc construct.

Transformation into DH10Bac *E. coli*

To 50 µl of DH10Bac *E. coli* competent cell, 1.5 µl of pFB1-secNluc-GGGSGS-sCD73-6xHis or pFB1-10xHis-sCD73-GGGS-Nluc was added and mixed gently then incubated on ice for 30 min. Heat shock was applied for 45 seconds at 42 °C, chilled on ice for 2 min, then 600 µl of room temperature Luria-Bertani broth (LB media) was added and incubated at 37 °C, 350 rpm for 3 h. The products were diluted 1:10 with LB medium then 100 µl was inoculated into (3+2) agar plate (10 µg/ml Tetracycline, 7 µg/ml Gentamicin, 50 µg/ml Kanamycin, 40 µg/ml isopropyl ß-D-1-thiogalactopyranoside (IPTG), 100 µg/ml X-Gal) and incubated wrapped in thin foil at 37 °C for at least 48 h.

Picking of selected colonies

Inoculated plates contain white (successful) and blue colonies. White colonies were selected and picked with a pipette tip, transferred into culture falcon tube containing 5 ml of LB medium (supplemented with Tetracycline (10 mg/ml), Gentamicin (7 mg/ml) and Kanamycin (50 mg/ml)) and incubated overnight (at least 16 h) at 37 °C, 220 rpm in a bacterial shaker.

Bacmid preparation

QIAGEN buffers were used for miniprep of recombinant bacmid DNA coupled to alcohol precipitation. The culture falcon tubes were centrifuged at 2500 *g*, 4 °C for 10 min and the supernatant was discarded. P1 buffer (400 µl) was added to resuspend the pellets by pipetting up and down then transferred into 2 ml sterile Eppendorf tube. P2 buffer (400 µl) was added and the tubes were inverted gently, then 400 µl from neutralizing buffer P3 was transferred. Tubes were inverted gently then centrifuged at 1400 *g*, 4 °C for 15 min. The supernatants from last centrifugation process were transferred into empty sterile 2 ml Eppendorf tubes each contain 800 µl isopropanol at room temperature then incubated at -20 °C freezer for 30 min. Samples were centrifuged at 12000 *g*, 4 °C for 15 min (pellets contain the bacmid), and the supernatant was drained by vacuum pump. Bacmid pellets were washed with pre-chilled ethanol 70% (500 µl) followed by centrifugation at 12000 *g*, 4 °C for 5 min and draining of the supernatant. Washing steps were repeated 2 to 3 times then pellets were dried in the sterile hood for 20 min. Finally, a 30 µl of nuclease-free water was added under the sterile hood and the concentration was measured using Colibri Microvolume Spectrometer (Titertek Berthold, Pforzheim, Germany). Bacmid samples (5 µl) were transferred into a fresh set of sterile 1.5 ml Eppendorf tubes and kept in the fridge for transfection. The remaining volume was used to run the bacmid PCR verification test.

Bacmid verification PCR test

PCR with M13 primers was run in a total volume of 25 µl.

- Primers
    - pUC/M13 forward 5′-CCCAGTCACGACGTTGTAAAACG-3′
    - pUC/M13 reverse 5′-AGCGGATAACAATTTCACACAGG-3′

The PCR product was then analyzed with 1% agarose gel electrophoresis using the following criteria: band at **300** bp (bacmid alone no transposition), band at **4000-5000** bp (successful transposition (pFB1 (**2300** bp) + size of the insert (**2238** bp for secNluc-CD73 and **2226** bp for CD73-Nluc).

Maintaining of *Spodoptera frugiperda* (*Sf*9) insect cells culture

Cryovial stocks of *Sf*9 cells at a 1 x 10^7 cells/ml density in 1 ml volume was thawed in a water bath at 37 °C then transferred into 20 ml of prewarmed growth medium (ESF 921 Insect Cell Culture Medium, serum-free, cat. # 96-001-01, Expression Systems, USA)

contained in T-25 flask and incubated at 27 °C. When cells adhered to the flask (in about 1 h), medium was changed to remove dimethyl sulfoxide (DMSO) used in freezing medium. Growth medium was changed after three days and cells continued incubated until 90% confluence was reached which might take up to two weeks. Cells were detached gently and transferred into a shake flask (Optimum Growth® Flasks, Thomson, USA) at $1x10^6$ cells/ml density in a 40 ml total volume, kept at 27 °C and 160 rpm with a 10 mm amplitude. At least three passages were needed until cells attained maximum growth rate and can be used for transfection. *Sf*9 cells were subcultured on Mondays and Thursdays at a density of $0.8x10^6$ cells/ml.

Bacmid transfection into *Sf*9 insect cells

A 24-well culture plate along with sterile 1.5 ml Eppendorf tubes were placed inside a sterile hood under UV light for 15 min. Transfection media was warmed up to room temperature and used to prepare the transfection master mix as follow: 3 µl X-tremeGENE HP was added to 100 µl transfection media. The transfection mix (103 µl) was then mixed with 5 µl of bacmid DNA by gentle tapping of the tubes followed by 15 min incubation at room temperature. *Sf*9 cells (2.5 ml at $1x10^6$ cells/ml) was transferred into each well of the 24-well culture block. The bacmid-DNA mix was transferred into each well and the plate was shaken in a Thermoshaker for 96 h at 27 °C and 400 rpm. Samples (~50 µl) to perform GP64 assay were withdrawn from each transfection before the plate was centrifuged at 2000 rpm for 15 min to harvest the baculovirus stock (P0). Supernatant (P0) was filter-sterilized through 0.45 µm filter in a fresh falcon tube. The falcon tube was then stored wrapped with thin foil at 4 °C.

GP64 flow cytometry assay

Five µl of transfected cells sample was mixed with equal volume of anti-GP64 (Phycoerythrin-conjugated anti-GP64, Expression Systems, Cat. # 97-201, used 1:100 dissolved 1xTris-buffered saline (TBS) + 4% Bovine serum albumin (BSA)) and incubated at 4 °C for 20 min. At the end of the incubation period, 90 µl of TBS buffer was added and samples were measured using flow cytometer (Guava easyCyte HT, Merck).

Amplification of baculoviral stock (P0)

400 µl from P0 was used to infect 40 ml of a freshly-grown *Sf*9 cells at $2\text{-}3x10^6$ cells/ml density in a 125 ml shake flask (Optimum Growth® Flasks, Thomson, USA). Cells were

incubated at 27 °C and 150 rpm for 48 h then centrifuged (Allegra X-30R Centrifuge, Beckman Coulter) at 2000 rpm for 15 min in a 50 ml falcon tube. The supernatant, P1 amplified baculoviral stock, was collected and stored at 4 °C until further use.

Nluc-tagged to membrane-bound human CD73

DNA manipulation

The cDNA encoding for the full length CD73 isoform-1 was obtained from reverse transcription of RNA extracted from MDA-MB-231 cells that natively express CD73 and cloned in pJET1.2. In this PCR, the CD73 insert was amplified between XhoI and XbaI without the signaling peptide starting from tryptophan residue 27. The amplified gene was then ligated in-frame at the C-terminus of secNluc in pNLF1-secN generating pNLF1-secN-CD73 plasmid.

As CD73 is bound to the cell membrane through GPI anchor to its C-terminus, we were unable to tag Nluc at the C-terminus of the membrane-bound enzyme. However, we tried to find a suitable region on the C-terminal domain without affecting the binding site, the dimer interface, or the glycosylation sites. To achieve this, human CD73 was tagged with Nluc between serine residue 520 and isoleucine residue 525 as follow. The full length CD73 was amplified between BmtI and XbaI using pJET1.2-CD73 isoform-1 as a template. The digested full length CD73 isoform-1 was then ligated into pNLF1 vector lacking secNluc (digested with BmtI and XbaI to eliminate secNluc). Afterwards, Nluc cDNA was amplified between BstEII and EcoRV using pNLF1-secN as a template and predesigned primers. The amplified insert was then double digested and ligated into a pretreated pNLF1-CD73 vector between serine 520 and isoleucine 525 residues of human CD73. We have previously found that, MDA-MB-231 cells express T376A natural variant of CD73, accordingly both constructs were subjected to site-directed mutagenesis to obtain the wildtype CD73. Both membrane-bound CD73 constructs were transfected into HEK293 cells as follow.

Transfection of HEK293 cell

Cell Culture

HEK293 cells were maintained in DMEM (Dulbecco's Modified Eagle Medium, cat. # 11995-065) supplemented with 10% fetal bovine serum (FBS, cat. # P30-1502, PAN Biotech, Germany) plus 100 mg/ml penicillin/streptomycin (cat. # P06-07100, PAN Biotech, Germany) at 37 °C and 5% CO_2 for 72 h. At 80-90% confluence, cells were washed

with 10 ml of phosphate-buffered saline (PBS) and detached by adding 2 ml of trypsin/ethylenediaminetetraacetic acid (EDTA) (0.05%/0.6 mM), incubated for 2-3 min. Trypsin was deactivated by addition of 8 ml of growth medium and cell suspension was centrifuged at 1200 rpm for 5 min, resuspended in fresh growth and split 1:10.

Transfection

One day before transfection, $1x10^6$ HEK293 cells were seeded into four T25 flasks each contain 5 ml of complete growth medium and incubated at 37 °C, 5% CO_2. Three hours before transfection, the medium was exchanged for all flasks with 5 ml antibiotic-free Opti-MEM™ medium (Gibco™, cat # 31985070). The Lipofectamine 2000 transfection reagent (Invitrogen, cat. # 11668019) and the DNA were brought to room temperature then prediluted with Optimum and incubated for 5 min at room temperature. The prediluted DNA was added to the prediluted Lipofectamine reagent and incubated for further 20 min. Afterwards, the transfection mix was transferred into respective cell flask (pNLF1-secN-CD73, pNLF1-CD73-Nluc (S^{520}-I^{525}). All flasks contain transfected cells, a control flask contains all reagent except the target genes DNA, and a fourth flask with un-transfected cells were incubated at 37 °C, 5% CO_2 for 24 h. Later, the medium was changed with complete growth medium and the incubation was continued for one more day. Cells were then detached and seeded into new T75 flasks with the selection medium (DMEM supplemented with 10% FBS, 100 mg/ml pencillin/streptomycin, and 200 µg/ml Hygromycin B). The selection medium was renewed every 3 days for three weeks. The transfected cells were maintained in complete DMEM with 100 µg/ml Hygromycin B.

Evaluation of the expression of Nluc-tagged constructs

One day before conducting the experiment, 20,000 cells/well were seeded into white-bottomed 96-well plate (Thermo Scientific™, cat. # 136101). On the next day, the medium was changed with 90 µl of Opti-MEM™ (Gibco™, cat # 31985070), and 25 µl of diluted furimazine was added (Nano-Glo® substrate, cat. # N1571, Promega, diluted 1:10000 in assay buffer). For soluble constructs, 10 µl of cell culture supernatant was diluted in 80 µl of Opti-MEM™ then mixed with 25 µl of diluted furimazine (Nano-Glo® Substrate, cat. # N1571). The Bioluminescence was measured with 460 filter using Mithras LB 940 instrument (Berthold Technologies GmbH & Co.KG, Bad Wildbad, Germany).

Evaluation of binding affinity of transfected HEK293 cells (N-terminally- and C-terminally-tagged CD73) in radioligand binding assays using [^{3}H]PSB-17230

The generated Nluc-tagged membrane-bound CD73 were assessed in a newly developed radioligand binding assay. The radiotracer [^{3}H]PSB-17230 was used at 1 nM concentration with 200,000 cells/vial. The mixture was incubated for 100 min at 25 °C in a binding buffer consists of Tris-HCl, 25 mM and sodium dihydrogen phosphate 25 mM, pH 7.4. Nonspecific binding was determined in the presence of 2 µM of PSB-12379. Homologous curves were conducted using the cold ligand PSB-17230 to generate and compare the K_D values. Data were analyzed by the Prism software version 9.0 (GraphPad Software Inc., San Diego, CA, USA) using one site-homologous or one site-fit K_i models.

Evaluation of the catalytic activity of the soluble constructs (N-terminally- and C-terminally-tagged CD73) in enzyme inhibition assays

A previously published enzyme inhibition assay employing diluted [^{3}H]AMP as a substrate was used to evaluate the catalytic activity of the obtained soluble constructs.[170] In brief, 10 µl from the cell culture supernatant was used as the source of protein and incubated in assay buffer with the substrate (5 µM) at 37 °C for 25 min. Reaction was stopped by addition of ice-cold lanthanum chloride with further incubation on ice to facilitate precipitation of unreacted AMP. Filtration through glass fiber filters (GF/B) was applied and soluble [^{3}H]adenosine was collected in scintillation vials. Radioactivity was measured in Tri-Carb 2900TR (Packard/PerkinElmer) after addition of 5 ml of scintillation cocktail (ULTIMA Gold XR, PerkinElmer, MA, USA). Data were analyzed using the GraphPad Prism software version 9.0 (GraphPad Software Inc., San Diego, CA, USA).

NanoBRET assay using fluorescent ligand PSB-18332

Saturation experiment

One day before the experiment, a white-bottomed 96-well plate (Thermo Scientific™, cat. # 136101) was seeded with 5000 cells/well. On the next day, the medium was exchanged carefully for the control and total binding wells with 95 µl of Opti-MEM™ (Gibco™, cat # 31985070) supplemented with 2% FBS (cat. # P30-1502, PAN Biotech, Germany). For the soluble CD73-Nluc protein, 10 µl from cell culture supernatant of infected *Sf*9 (diluted 1:100 in assay buffer) was mixed with 85 µl of Opti-MEM™ (Gibco™, cat # 31985070). Nonspecific binding was determined in the presence of 2 µM PSB-12379 using 10 µl from a 25 µM stock solution. Five µl of different concentrations of the fluorescent ligand PSB-

18332 (0.5-600 nM) were added and incubated at 37 °C and 5% CO_2 for 1 h, 2 or 4 h for the CD73-Nluc(S^{520}-I^{525}), Nluc-CD73 and sCD73-Nluc, respectively. At the end of the incubation period, 25 µl of Nano-Glo substrate (cat. # N157, Promega GmbH, Germany) diluted 1:10000 in the assay buffer was added and the bioluminescence was measured with 460 nm filter for the donor emission and 540/40 nm for the acceptor emission using Mithras LB 940 instrument (Berthold Technologies GmbH & Co.KG, Bad Wildbad, Germany). BRET ratio was obtained by dividing the acceptor emission at 540/40 nm by the donor emission at 460 nm, then the ratio was corrected using buffer control. GraphPad Prism version 9.0 was used to fit total binding into one site-total and specific binding to one site-specific binding equation Y = Bmax*X/ (Kd + X). Linear regression was used to fit the nonspecific data.

Binding kinetics

A fixed concentration (5 µl, 20 nM) of the fluorescent ligand PSB-18332 was added to a previously seeded cells (5000 cells/well) or to soluble CD73-Nluc protein contained in a white-bottomed 96-well plate (Thermo Scientific™, cat. # 136101) at a respective time point. The association was monitored for 30 min at 37 °C. Dissociation was initiated by adding 10 µl of the competing ligand PSB-12379 (final concentration = 2 µM) to each well and continued to be measured up to 4 h. Real-time kinetics was evaluated at room temperature as follow, the Nano-Glo substrate (diluted 1:10000 in assay buffer, 25 µl) was added to 5000 cells/well contained in an 85 µl assay buffer. The buffer control was measured first then the fluorescent ligand PSB-18332 (20 nM final concentration) was added and the emission was measured up to 60 min and continued after addition of the competing ligand PSB-12379 at 2 µM final concentration to detect the unbinding kinetics. Corrected association BRET ratios were fitted to one phase association model and dissociation ratios into one phase decay equation in GraphPad prism version 9.0 K_D value was calculated by dividing K_{off}/K_{on} values.

Competition experiments

To 5000 cells/well in 85 µl assay buffer (or 10 µl from soluble CD73-Nluc protein dissolved in 75 µl of Opti-MEM™), 10 µl from serial dilutions of the test compounds were added followed by 5 µl of the fluorescent ligand PSB-18332 (20 nM) and incubated at 37 °C and 5% CO_2. Nano-Glo substrate (25 µl) was added and the emission was measured using the same filters combination of 460 nm for donor and 540/40 nm for acceptor. Nonspecific

binding was determined using 2 µM of PSB-12379. BRET ratios corresponding to the specific binding were fitted into one site-fit K_i model using GraphPad Prism version 9.0 and K_i values for test compounds were calculated based on $K_{D(kin)}$.

The Nluc-tagged soluble human CD73 applied in all experiments using 10 µl of the sCD73-Nluc protein (cell culture supernatant of infected *Sf*9, diluted 1:100 in Opti-MEM™).

Results

Design of the Nluc tagged CD73

To the best of our knowledge, CD73 has never been tagged before except for purification purposes (i.e., His-tag), therefore it was unknown which terminus of the enzyme would tolerate an Nluc tag. For this, soluble human CD73 was labeled with Nluc at either the N- or C-terminus as shown in **Figure 53A-B** below.

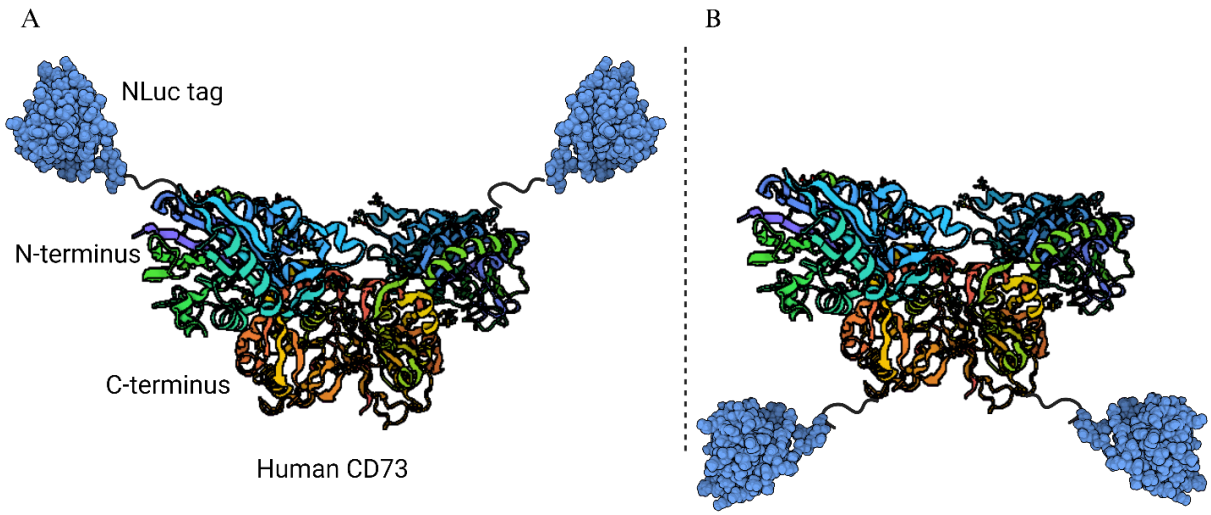


Figure 53. Tagging of Nluc at: **A**) N- terminus of soluble human CD73. **B**) C-terminus of soluble human CD73. Created with bioRender.com.

For the membrane-bound CD73, tagging of Nluc at the N-terminus was straightforward, while tagging at the C-terminus was complicated due to the presence of the GPI-anchor signal peptide. Accordingly, an alternative site for tagging at the C-terminal domain was investigated. After extensive study of the structure and function of the amino acid residues, a specific site between serine residue 520 and isoleucine 525 was selected. This site has no interactions with the binding pocket, is not involved in glycosylation, and is not a part of the dimerization interface.

Evaluation of the Nluc constructs expression

The expression of newly generated Nluc-tagged CD73 constructs was evaluated. Values of the bioluminescence measured at 460 nm for the four constructs indicated successful expression of the Nluc-tagged CD73 compared to the non-transfected HEK293 and *Sf*9

cells (**Figure 54A-B**). Furthermore, BRET ratio was evaluated at different assay buffers using the recently published fluorescent ligand PSB-18332 as an acceptor (**Figure 54C-D**).

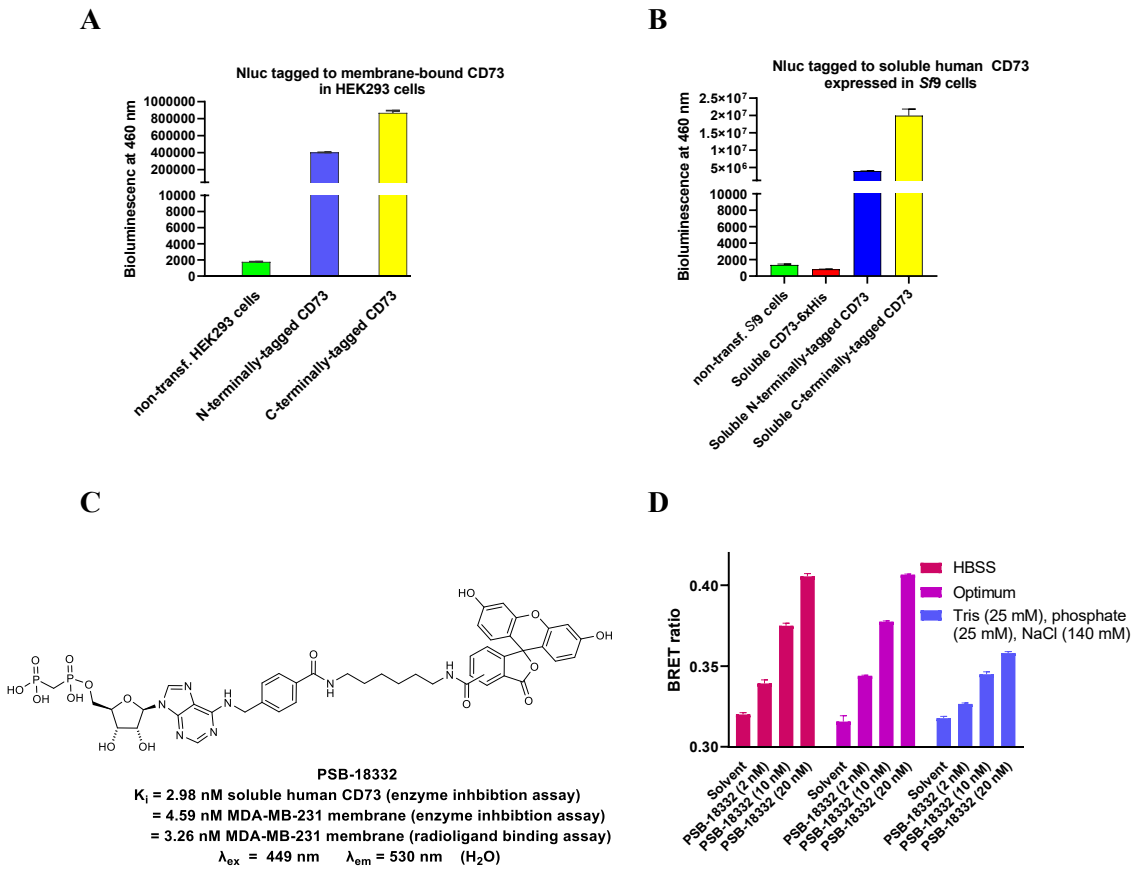


Figure 54. **A**) Bioluminescence obtained from HEK293 cell transfected with C-terminally-tagged CD73, N-terminally-tagged CD73 or wild-type (wt) HEK293 cells (20,000 cells/well) using Nano-Glo substrate. **B**) Bioluminescence obtained with 90 µl of *Sf*9 culture supernatant of soluble C-terminally-tagged CD73, N-terminally-tagged CD73, or non-transfected *Sf*9 cells using Nano-Glo substrate. **C**) Structure of the fluorescent ligand PSB-18332. **D**) BRET ratio using different assay buffers for soluble C-terminally-tagged CD73.

Based on the obtained results (**Figure 54D**), Hank's Balanced Salt Solution (HBSS) and Optimum medium provided higher BRET ratios than Tris-HCl, 25 mM for the same concentrations of the fluorescent tracer. Optimum was selected to perform further BRET experiments.

Evaluation of the catalytic activity of the soluble construct using enzyme inhibition assays

The soluble Nluc-tagged CD73 proteins were evaluated for their catalytic activity in a previously published enzyme inhibition assay using 5 µM of diluted [^{3}H]AMP as a substrate.[170] Both constructs retained the catalytic activity and could be inhibited by the competitive CD73 inhibitor, AMPCP (I) (**Figure 55A**). However, tagging Nluc at the N-terminus of CD73 led to an 18-fold drop in AMPCP affinity as seen in **Figure 55B**. Interestingly, AMPCP showed similar inhibition IC_{50} value to that of the native soluble human CD73 (IC_{50} = 57.6 nM) when tested using soluble C-terminally tagged CD73 (IC_{50} = 82.7 nM) which indicates no effect on the binding pockets by the tag attached to the C-terminus. Based on the obtained result, further BRET experiments were conducted using soluble C-terminally-tagged CD73.

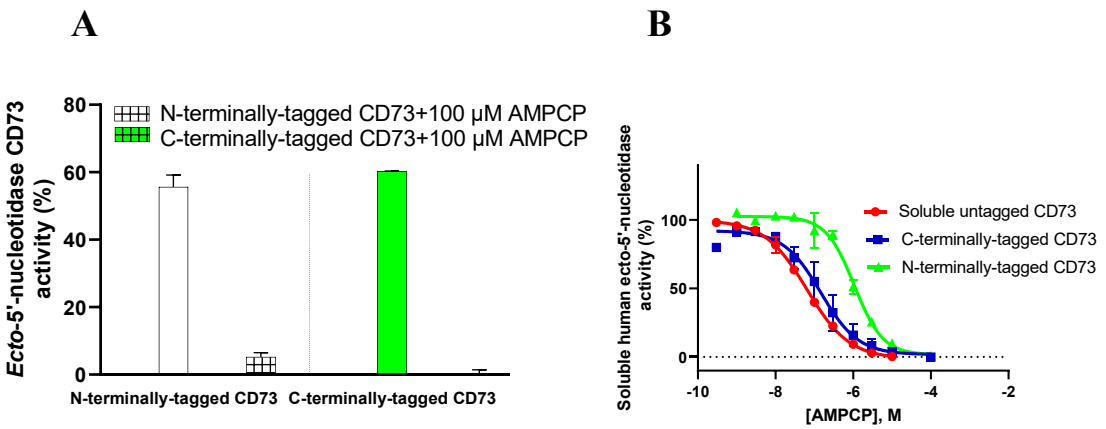


Figure 55. Characterization of the soluble constructs in enzyme inhibition assay.[170] **A**) Inhibition of the AMPase activity by 100 µM AMPCP. **B**) Concentration-inhibition curves for AMPCP using the Nluc-tagged enzymes compared to the untagged CD73. AMPCP IC_{50} values: using untagged soluble CD73 (57.6 nM), C-terminally-tagged soluble CD73 (82.7 nM), and N-terminally-tagged soluble CD73 (1043 nM).

Evaluation of the binding affinity of the Nluc-tagged CD73 transfected HEK293 cells in radioligand binding assays using [^{3}H]PSB-17230

When testing the transfected cell lines (intact cells) in a recently developed radioligand binding assay, the specific binding of the radiotracer [^{3}H]PSB-17230 was higher for both constructs compared to the non-transfected HEK293 cells (**Figure 56A**). However, C-terminally tagged-expressing cells showed low specific binding compared to the N-terminally tagged-expressing cells. This low specific binding might be attributed to low

expression. However, it might indicate that the binding site was affected by tagging, though, mistrafficking of the protein to intracellular organelles can also not be excluded.

A homologous competition curve (**Figure 56B**) was constructed for the N-terminally tagged HEK293 cells, the obtained K_D value (5.27 ± 3.87 nM) was comparable to the K_D value of untagged CD73 in MDA-MB-231 cell (0.644 nM), yet the radioligand [^{3}H]PSB-17230 showed around 8-fold drop in potency in Nluc-tagged CD73.

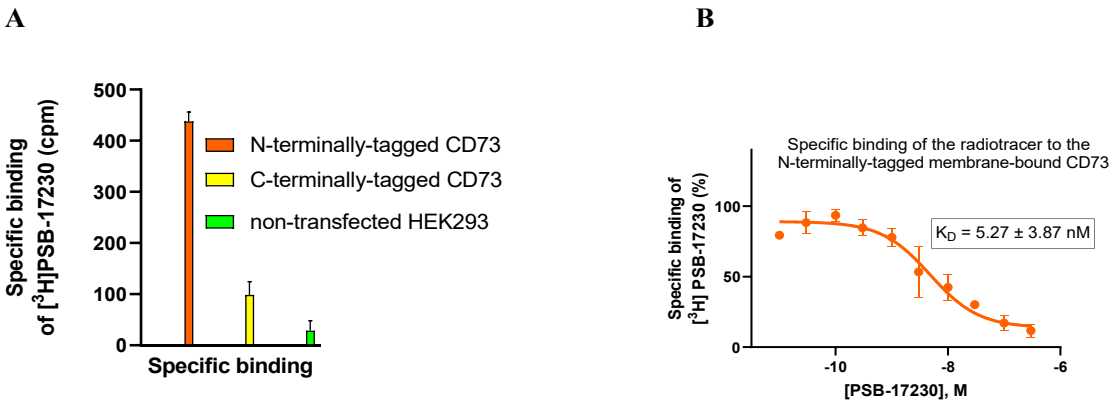


Figure 56. Testing of the transfected HEK293 cells in a radioligand binding assay. **A**) Binding of 1 nM of the radiotracer [^{3}H]PSB-17230 to transfected and non-transfected HEK293 cells (200,000 cells/vial). **B**) Homologous competition curve at 25 ºC using 1 nM [^{3}H]PSB-17230, 400,000 of N-terminally-tagged CD73 transfected cells/vial. [PSB-17230, 0.000003-0.3 µM]. Nonspecific binding was determined in the presence of 2 µM PSB-12379. Data points represent means ± SEM of two independent experiments, each performed in duplicates.

NanoBRET assay using the soluble construct (C-terminally-tagged CD73)

Saturation experiment

We investigated binding of different concentration of the fluorescent ligand PSB-18332 (500-fold) to the soluble C-terminally-tagged protein (**Figure 57A**). Binding was saturable within 2 h incubation in a plate shaker at 37 °C with a K_D value of 63.3 ± 0.6 nM. Very low non-specific binding was detected.

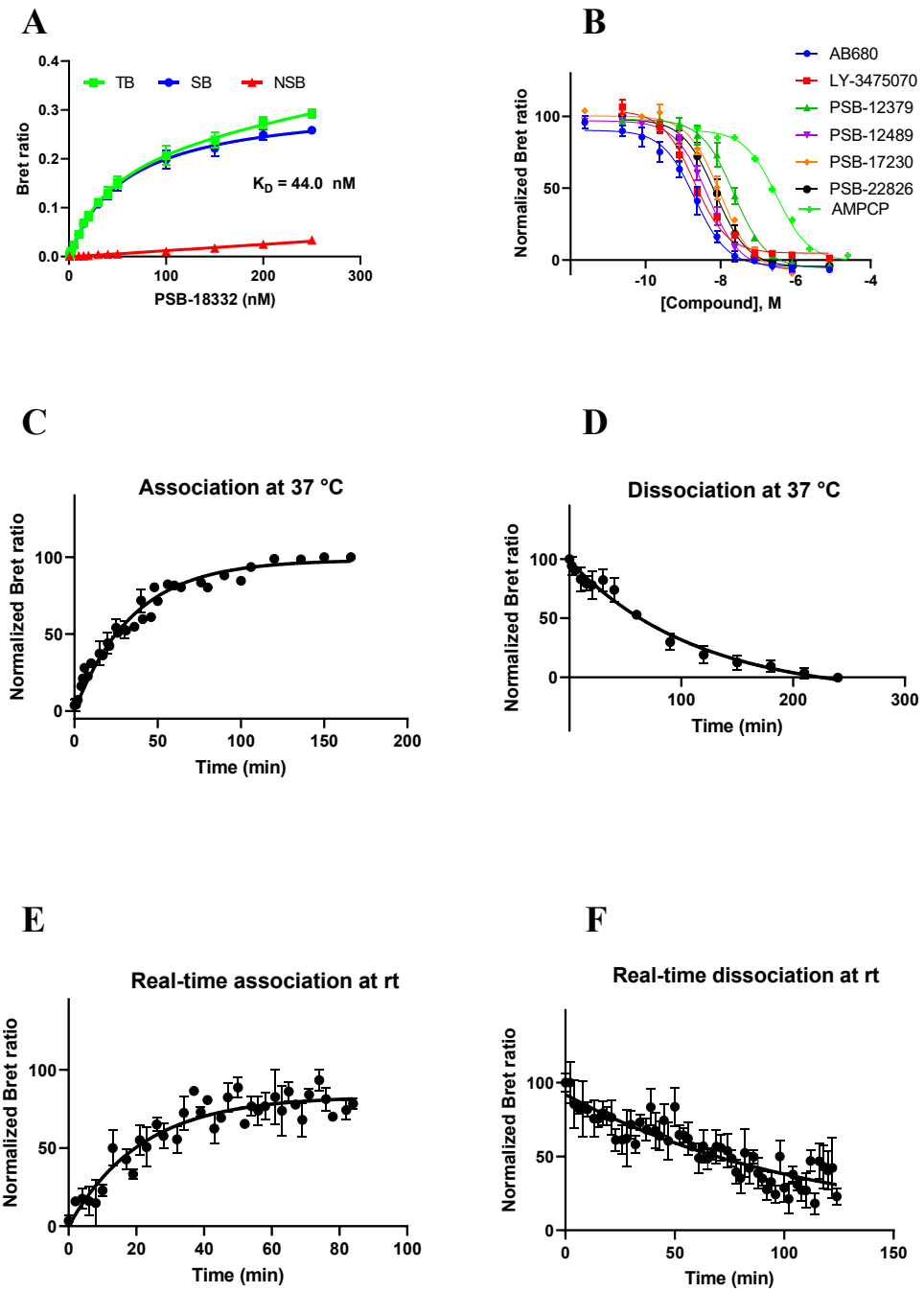


Figure 57. Characterization of **soluble C-terminally-tagged CD73**. **A**) Saturation curve conducted at 37 °C. PSB-18332 (0.5-250 nM) was incubated with the enzyme for 4 h. Nonspecific binding was determined in the presence of 2 µM PSB-12379. The calculated K_D were means ± SEM from at least three independent experiments. **B**) Competition binding experiments. Serial dilutions of each competitor were incubated with 20 nM of PSB-18332 for 120 min at 37 °C. **C&D**) Association and dissociation kinetics of PSB-18332 (20 nM) performed at 37 °C. **E&F**) Real-time association and dissociation kinetics of PSB-18332 (20 nM) performed at rt. The calculated $t_{1/2}$, Kinetics rates and K_D values showed in **Table 9**. Data points represent means ± SEM from at least three independent experiments, each performed in duplicates.

Binding Kinetic

Association and dissociation studies were conducted at 37 °C using 20 nM of the fluorescent ligand (**Figure 57C-D**). The obtained K_{off} and K_{on} values were 0.016 ± 0.003 min^{-1} and 0.001 ± 0.00014 nM^{-1} min^{-1}, respectively. The fluorescent ligand PSB-18332 showed very slow unbinding kinetics with a $t_{1/2}$ value of 47 min. While the calculated K_D value (23.6 ± 5.8 nM) is more comparable to the values obtained from ligand binding and enzyme inhibition assays (**Table 7**) with slight drop in affinity, the saturation K_D value (63.3 nM) is much higher (≈ 15-fold). Referring to the very slow dissociation, we assumed that the equilibrium may have not been attained within 2 h incubation especially for the lowest concentrations. Accordingly, the saturation experiment was repeated with 4 h incubation at 37 °C and the obtained K_D value was dropped to 44.0 ± 3.8 nM. It was clear that, binding of the very low concentrations of the fluorescent ligand required much more time to equilibrate due to the very low dissociation rate. Based on these results we considered the K_D value obtained from kinetics and employed it to calculate the K_i values of other competing ligands tested with this method. Furthermore, real-time kinetics were assessed at rt by monitoring the BRET ratio prior and subsequent to the addition of the fluorescent ligand PSB-18332 followed by the initiation of the dissociation with 2 µM PSB-12379 after 85 min (**Figure 57E-F**). Interestingly, the K_D values derived from K_{off} and K_{on} rates of real-time kinetics at room temperature was in complete agreement to published reference values (**Table 7**). The calculated kinetically-derived K_D value at 37 °C was ca.4-fold higher than that determined at rt.

Table 7. K_i value of the fluorescent ligand **PSB-18332** in different assay systems compared to the K_D values obtained in NanoBRET assay using soluble C-terminally-tagged CD73

	K_i value (nM)					
	Enzyme inhibition assay	Radioligand binding assay	NanoBRET assay at rt		NanoBRET assay at 37 °C	
			$K_{D\ (kin)}$	$K_{D\ (sat)}$	$K_{D\ (kin)}$	$K_{D\ (sat)}$
PSB-18332	2.98*, 4.59**	3.26***	**5.02**	ND	**23.6**	**44.0**

* Value determined using soluble human CD73, ** value determined using membrane of MDA-MB-231, *** value determined using membrane preparation of MDA-MB-231 in radioligand binding assay. ND: not determined.

Competition experiments

Additionally, BRET competition experiments were run to determine the K_i values for a selected set of test compounds with a wide range of potency (**Figure 57B**). Most of the test

compounds showed K_i values comparable to the published ones (**Table 8**). Exceptionally, the most potent inhibitors AB680, PSB-22826, and PSB-17230 showed up to 67-fold loss in potency which might be attributed to an unattained equilibrium due to the very long residence time of the fluorescent ligand PSB-18332 bound to the soluble C-terminally-tagged CD73.

Table 8. Comparison of K_i values for a set of inhibitors in NanoBRET assay using soluble CD73-Nluc construct compared to reference values

	K_i (nM ± SEM)	
	NanoBRET assay using soluble **CD73-Nluc** protein	Reference values *
AB680	**1.24** ± 0.32	**0.019** ± 0.010
PSB-22826	**4.28** ± 1.35	**0.0641** ± 0.0055
PSB-17230	**5.15** ± 0.68	**0.0891** ± 0.0011
PSB-12489	**1.99** ± 0.28	**1.28** ± 0.016
PSB-12379	**12.3** ± 3.1	**9.72** ± 3.33
AMPCP	**144** ± 35	**207** ± 6.0

* Enzyme inhibition assay using membrane preparations from MDA-MB-231 cells and 5 μM [^{3}H]AMP as substrate; ** tested using soluble human CD73 in the enzyme inhibition assay.

NanoBRET assay using membrane-bound constructs

Saturation experiment

Binding of the fluorescent ligand PSB-18332 to the N- and C-terminally-tagged CD73 expressed on membranes of HEK293 cells was saturable with a K_D value of 122 nM and 58.4 nM, respectively. Non-specific binding was minimal up to 600 nM of PSB-18332 (**Figure 58A** and **59A**). The saturation K_D value for the N-terminally tagged CD73 was about 40-fold higher than the reference value (**Table 7**), whereas the value for the C-terminal domain tagged was closer (~14-fold) to the reference value using enzyme inhibition assay. Since NanoBRET is a proximity-based assay, binding of the fluorescent ligand to nonspecific sites outside the detection range (>10 nm) are likely not detected.

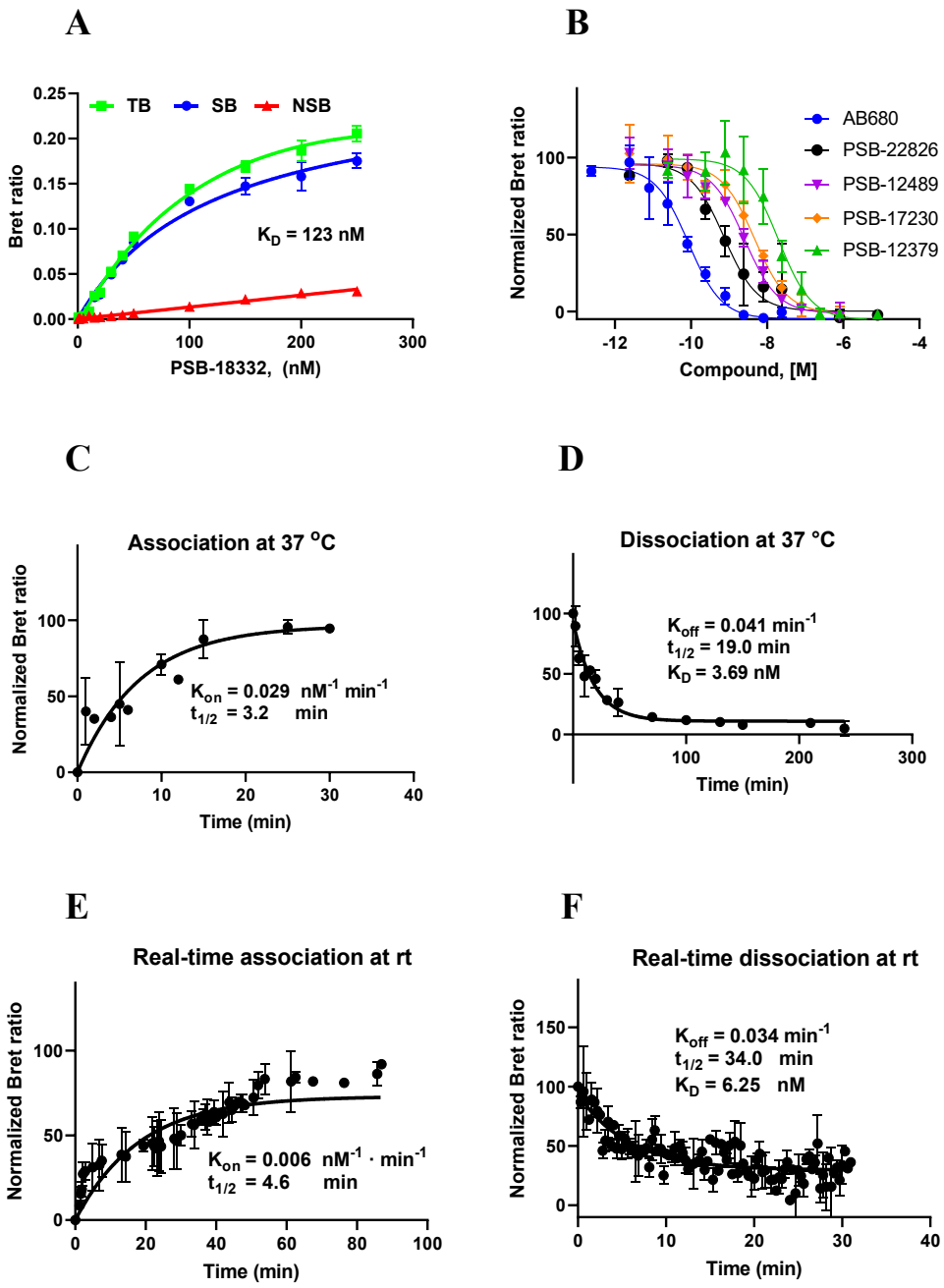


Figure 58. Characterization of **membrane-bound N-terminally-tagged CD73**. **A**) Saturation curve conducted at 37 °C. PSB-18332 (0.5-250 nM) was incubated with the enzyme for 2 h. Nonspecific binding was determined in the presence of 2 µM PSB-12379. The calculated K_D were means ± SEM from at least three independent experiments. **B**) Competition binding experiments. Serial dilutions of each competitor were incubated with 20 nM of PSB-18332 for 120 min at 37 °C. **C&D**) Association and dissociation kinetics of PSB-18332 (20 nM) performed at 37 °C. **E&F**) Real-time association and dissociation kinetics of PSB-18332 (20 nM) performed at rt. The calculated $t_{1/2}$, Kinetics rates and K_D values showed in **Table 9**. Data points represent means ± SEM from at least three independent experiments, each performed in duplicates.

Binding Kinetics

Binding of the fluorescent ligand PSB-18332 over a wide range of time was studied at 37 °C. Association was very fast with a $t_{1/2}$ value of 3.2 min and a K_{on} value of 0.029 ± 0.023 nM^{-1} min^{-1} for the N-terminally tagged CD73 and a $t_{1/2}$ value of 2.8 min and a K_{on} value of 0.05 ± 0.015 nM^{-1} min^{-1} for the C-terminal domain-tagged CD73 (**Figure 58C** and **59C**). Dissociation was initiated by the addition of PSB-12379 at a 2 µM concentration following a preincubation period of 60 min. The half-life was attained within 19 min with a K_{off} value of 0.041 ± 0.010 min^{-1} (N-terminally-tagged) or within 8.3 min with a K_{off} value of 0.091 ± 0.015 min^{-1} (C-terminally-tagged) (**Figure 58D** and **59D**). Moreover, real-time kinetics (**Figure 58** and **59E-F**) were evaluated at rt and the obtained values are presented in **Table 9**. The obtained K_D value from kinetic studies at 37 °C (3.69 nM and 2.32 nM) for both constructs were in complete agreement with the value derived from enzyme inhibition assay and radioligand binding assay (2.59 nM, 3.26 nM, **Table 7**).

Table 9. Saturation and kinetics values derived from BRET-based assay at rt and at 37 °C

Protein	**NanoBRET assay (37 °C)**					**NanoBRET assay (rt)**			
	$K_{D(sat)}$, nM	$K_{D(Kin)}$, nM	K_{off}	K_{on}	$t_{1/2}$, min	$K_{D(Kin)}$, nM	K_{off}	K_{on}	$t_{1/2}$, min
Soluble C-terminally-tagged CD73	44.0 ± 3.8	23.6 ± 5.8	0.016 ± 0.003	0.001 ± 0.00014	47 ± 12	5.02 ± 1.05	0.008 ± 0.001	0.002 ± 0.0003	87 ± 5
HEK293-N-terminally-tagged CD73	123 ± 12	3.69 ± 1.43	0.041 ± 0.010	0.029 ± 0.023	19 ± 4	6.25 ± 4.36	0.034 ± 0.021	0.006 ± 0.001	34 ± 21
HEK293-C-terminally-tagged CD73	58.4 ± 3.3	2.32 ± 0.81	0.091 ± 0.015	0.05 ± 0.015	8 ± 2	5.58 ± 3.34	0.045 ± 0.002	0.012 ± 0.007	16 ± 1

K_{off} in min^{-1}, K_{on} in $nM^{-1}.min^{-1}$.

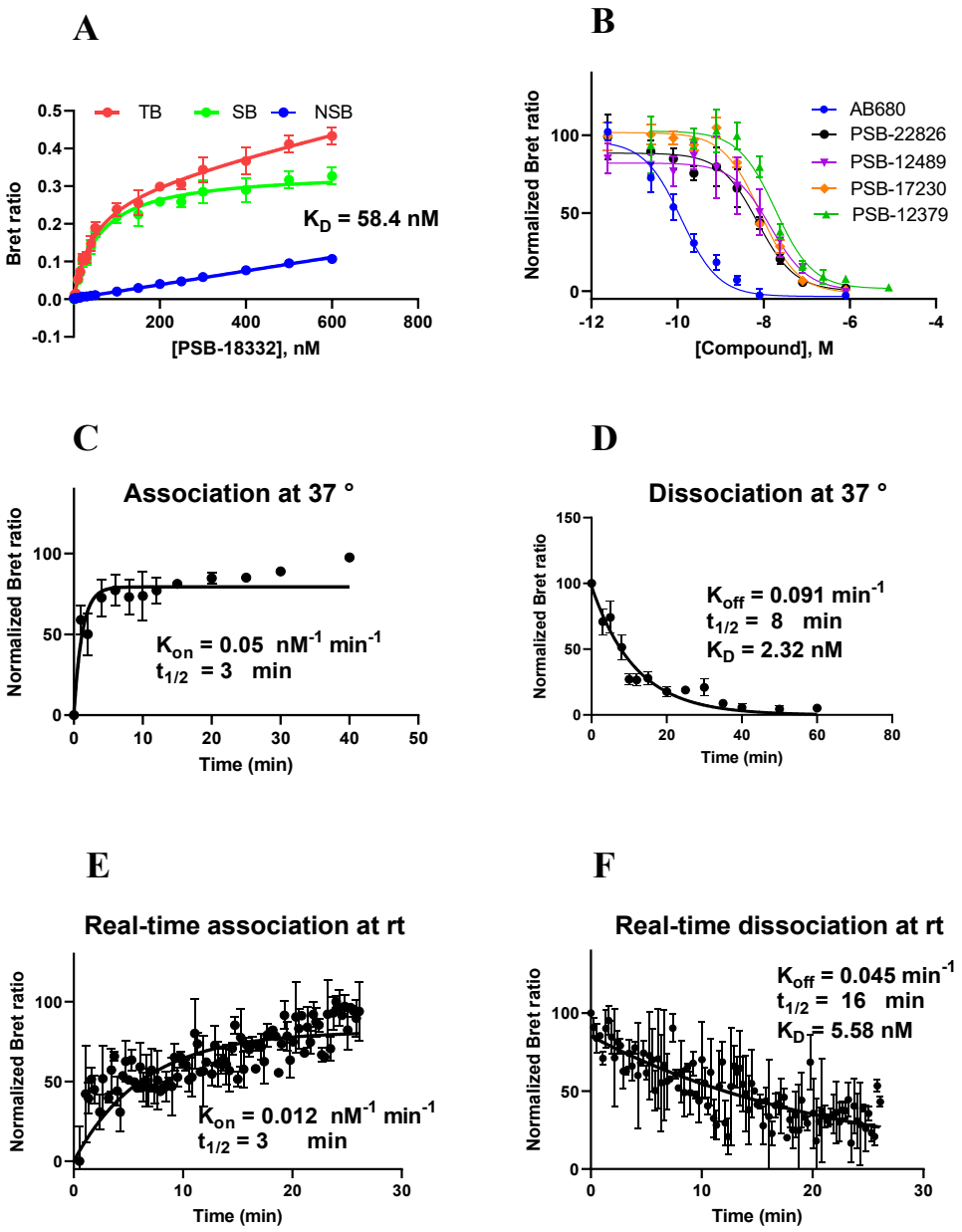


Figure 59. Characterization of membrane-bound C-terminally-tagged CD73. **A**) Saturation curve conducted at 37 °C. PSB-18332 (0.5-600 nM) was incubated with the enzyme for 1 h. Nonspecific binding was determined in the presence of 2 µM PSB-12379. The calculated K_D were means ± SEM from at least three independent experiments. **B**) Competition binding experiments. Serial dilutions of each competitor were incubated with 20 nM of PSB-18332 for 60 min at 37 °C. **C** & **D**) Association and dissociation kinetics of PSB-18332 (20 nM) performed at 37 °C. **E** & **F**) Real-time association and dissociation kinetics of PSB-18332 (20 nM) performed at rt. The calculated $t_{1/2}$, Kinetics rates and K_D values showed in **Table 9**. Data points represent means ± SEM from at least three independent experiments, each performed in duplicates.

Competition experiments

Various concentrations of inhibitors were incubated at 37 °C with fixed concentration of the fluorescent ligand PSB-18332 (20 nM). The established inhibition-concentration curves are illustrated in **Figure 58B** and **59B** and the obtained K_i values are compared in **Table 10** and **Figure 60**. The developed method using membrane-bound tagged CD73 showed high accuracy in determining the K_i values compared to the reference values and hence the fluorescent ligand PSB-18332 could be considered as a potential molecular tool to investigate and characterize CD73 inhibitors. The determined K_i values were slightly higher (~5-fold) than these determined using an in-house radioligand binding assay method. However, the order of potency of test compounds was retained.

Table 10. Comparison of K_i values derived using the Nluc tagged membrane-bound constructs of human CD73 to the reference values

	K_i ± SEM		
	NanoBRET assay using **Nluc-CD73**	NanoBRET assay using **CD73-Nluc(S^{520}-I^{525})**	Reference values*
AB680	**0.0163** ± 0.004	**0.0195** ± 0.0076	**0.0294** ± 0.0081
PSB-22826	**0.229** ± 0.132	**0.515** ± 0.291	**0.139** ± 0.009
PSB-17230	**0.857** ± 0.154	**0.859** ± 0.0825	**0.149** ± 0.001
PSB-12489	**0.494** ± 0.02	**0.698** ± 0.292	**0.158** ± 0.011
PSB-12379	**3.6** ± 0.44	**2.06** ± 0.30	**0.332** ± 0.021

* Tested in radioligand binding assay using membrane preparations of MDA-MB-231 cells and 1 nM of the [^{3}H]PSB-17230 radiotracer

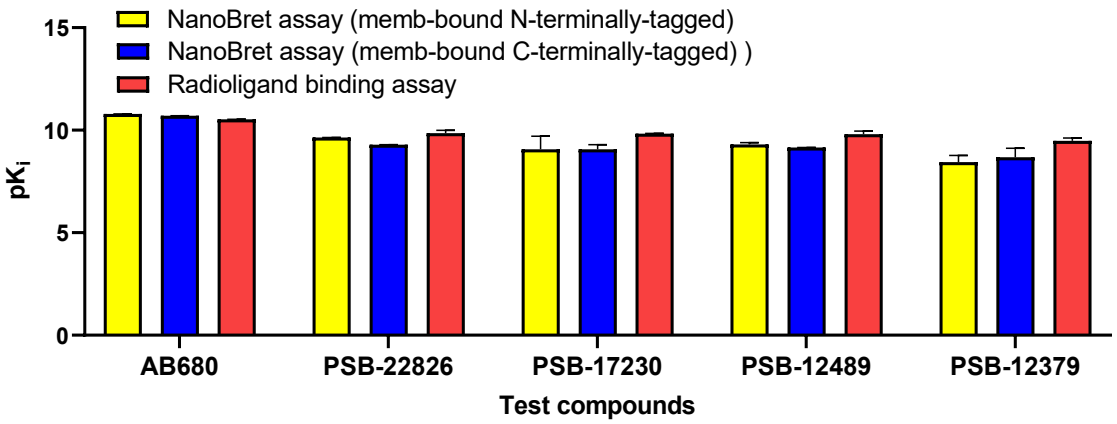


Figure 60. pK_i values of test compounds using the two membrane-bound constructs compared to reference values. pK_i values were mean of at least three independent

experiments each performed in duplicates. Data were subjected to one-way ANOVA test and there was no significant difference in all obtained values.

Residence time studies

Furthermore, the developed method was found to be successful in determining the binding kinetics of unlabeled ligands (**Figure 61A-D**). A selected set of compounds with wide range of affinity were evaluated in competitive association experiments. The generated K_{off} values were used to calculate the residence time (τ) for the unlabeled ligands. The most potent inhibitor AB680 showed the highest residence time value of 20 min compared to 5 min for the least potent compound PSB-12379 among the test set. Applying this method, the residence time was found to be correlated to the affinity of the test compounds with an R^2 value of 0.96 (**Figure 61E**). Furthermore, the obtained residence time values correlate well with values determined in radioligand binding assays (**Figure 61F**).

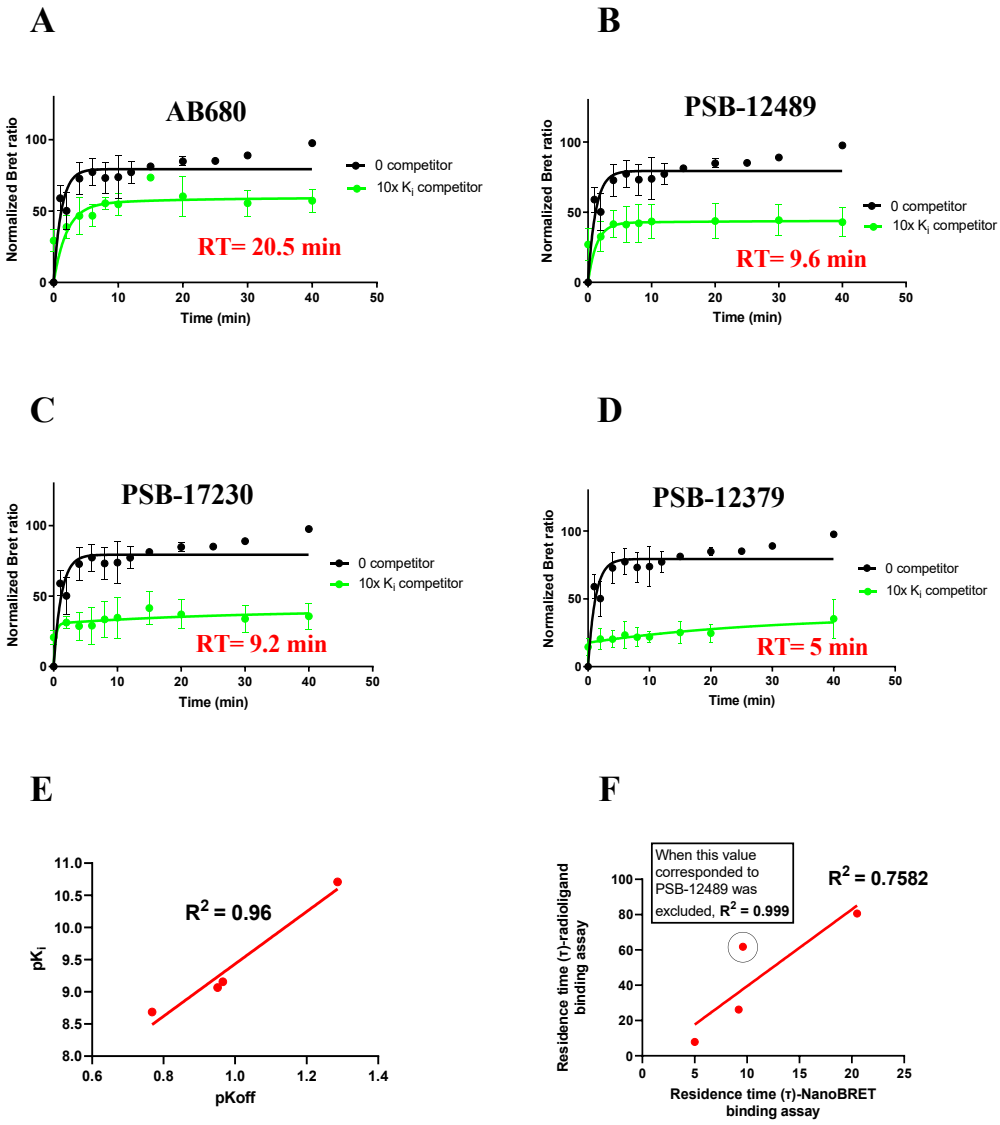


Figure 61. Competition-association binding assays of PSB-18332 against test competitor. **A**) AB680, **B**) PSB-12379, **C**) PSB-12489 and **D**) PSB-17230) at 10-fold their K_i value. **E**) Correlation between pK_i values derived from competition experiments and pK_{off} values derived from competition-association experiments. **F**) Correlation between residence time values derived from NanoBRET and radioligand binding assays. Data shown as mean ± SEM from at least two independent experiments, each performed in duplicates.

Conclusions

Nluc tag was introduced into the two isoforms of human CD73, soluble and membrane-bound to study ligand-protein interaction through applying NanoBRET assay. Tagging was attempted on both terminals for soluble human CD73, however, at the N-terminal it affected the binding pocket of the enzyme which was evident by the IC_{50} value of the standard inhibitor AMPCP (IC_{50} = 1043 nM vs. 57.6 nM for untagged). On the other hand, C-terminal Nluc-tag seemed to affect the kinetics of the enzyme rather than the binding pocket. The IC_{50} value obtained from untagged soluble CD73 in an enzyme inhibition assay was in complete agreement with that obtained with C-terminally tagged CD73 (IC_{50} = 82.7 nM vs. 57.6 nM for untagged). However, C-terminally-tagged soluble enzyme showed very slow unbinding kinetics with a t½ value of 47 min and a kinetic K_D value of 23.6 nM. We though this very long residence time of the fluorescent tracer might affect the equilibrium attained by a competing ligand tested with this method. Test compounds showed comparable K_i values to reference values when tested using the C-terminally-tagged soluble protein, however, the most potent inhibitors were less estimated using this construct. Furthermore, Nluc was tag at the N-terminus and between S^{520}-I^{525} residues of the C-terminal domain of the membrane-bound CD73. Both membrane-bound-tagged CD73 provided faster dissociation kinetics (t½ = 19 min and 8 min for N and C-terminally tagged CD73, respectively) compared to the soluble tagged protein (t½ = 47 min). The kinetic derived K_D values for N- (K_D = 3.69 nM) and C-terminally (K_D = 2.32 nM) tagged membrane bound-enzyme were in complete agreement to the reference values which might indicate unchanged kinetics of the tagged membrane-bound enzyme. Moreover, determination of the inhibition constants for a selected set of CD73 inhibitors was accurately achieved (**Table 10**). In addition, the developed NanoBRET method was applied to estimate the residence time for a selected inhibitors using membrane-bound C-terminally tagged protein. Obtained values of residence time was found to be correlated to the affinity of the test compounds. Moreover, residence time values were in agreement with that obtained using radioligand binding assay.

The results obtained here might provide hints for introducing other tags (e.g., GFP) without losing the functionality of the enzyme.

Author contribution

The author designed, cloned and expressed all recombinant gene constructs in *Sf*9 and HEK293 cells. She developed and optimized the NanoBRET assays, characterized the binding interactions, and performed all experiments shown on this manuscript. The author collaborated with Haneen Al-Hroub to conduct the radioligand binding assay experiments for the transfected HEK293 cells. The manuscript was written by the author and edited based on comments she received from the corresponding author, Christa Müller.

4. Preparations and samples of CD73

4.1. Recombinant soluble rat CD73

Recombinant soluble rat CD73 was kindly provided by Prof. Dr. Herbert Zimmermann (University of Frankfurt, Germany). Rat CD73 cDNA was heterologously expressed in *Sf*9 insect cells as glutathione-S-transferase fusion protein using the baculovirus expression system as described.[283] Crude protein was purified with affinity chromatography using agarose-coupled reduced glutathione (GSH) and AMP-Sepharose columns. Stocks provided in 20 mM Hepes pH 7.4, were diluted 1:1 in Tris 25 mM buffer pH 7.4 supplemented with 4 mM iodoacetamide, and 50% glycerol. Aliquots were kept stored at -80 °C.

4.2. Recombinant soluble mouse CD73

Aim of the project

Several studies on ecto-5'-nucleotidase (CD73) confirmed its potential role in tumor proliferation, metastasis, and immunosuppression.[67,129,81,123] CD73 inhibitors were found to restore the immune functions and to exhibit antitumor activities.[274,153,157]

Our previous co-workers expressed soluble human CD73 in *Sf*9 insect cells to screen and characterize test compounds as inhibitors of ecto-5'-nucleotidase.[283,226] To broaden studies on species differences, the mouse enzyme was to be expressed as an important model for preclinical studies.

cDNA mouse CD73 construct

The codon-optimized cDNA of mouse (*Mus musculus*) CD73 based on Genbank accession no. NM_011851 was synthesized by BioCat company (Heidelberg, Germany) and provided ligated into the pFastBac1 vector. A truncated soluble form was designed in which the secretory signal peptide (amino acids 1-28 on the N-terminus) and the GPI signal peptide (amino acids 552-576 on the C-terminus) were omitted. For purification with immobilized metal ion affinity chromatography (IMAC), a 10xHis-tag was fused upstream to the mouse cDNA followed by a protease cleavage site. The obtained construct was reproduced through DHα5 transformation and confirmed by sequencing (Eurofins Genomics Germany GmbH, Ebersberg, Germany).

Results

Transformation into DH10Bac *E. coli* and generation of recombinant bacmid

The generated construct was transformed into DH10Bac *E. coli* competent cell, followed by bacmid preparation using QIAGEN buffers and alcohol precipitation. Recombinant bacmid was successfully obtained as indicated by the result of the bacmid verification test shown in **Figure 62**. The following criteria were applied: unsuccessful (no transposition, bacmid alone): band at 300 bp; successful: band at around 4007 bp (pFastbac1+ insert size: 2300 bp + 1707 bp). All picked white colonies showed successful transposition of bacmid DNA with a band between 5000 and 3500 bp. The blue colony showed a negative band at around 300 bp (**Figure 62**).

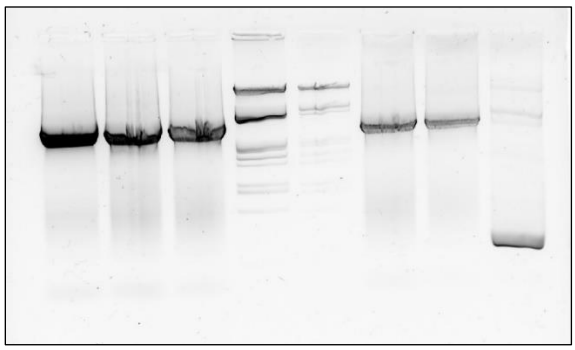


Figure 62. Bacmid verification test on 1% agarose gel. From left, Lane 1-3: white colonies; Lane 4, 5: λ DNA marker; Lane 6,7: white colonies; Lane 8: Control (blue colony).

Bacmid transfection into *Sf*9 insect cells

The obtained recombinant bacmid was transfected into *Sf*9 insect cells using X-tremeGENE HP reagent (Roche). Successful transfection was confirmed by GP64 flow cytometry assay using conjugated anti-GP64 antibodies (Phycoerythrin-conjugated anti-GP64, Expression Systems, Cat. #97-201) (**Figure 63A**). In this assay, anti-GP64 antibodies bind exclusively to GP64 envelope glycoprotein on transfected cells which enable them to emit yellow fluorescence in contrast to un-transfected cells. In addition, the transfected cell sample showed a lower number of cells indicated effective transfection. CD73 activity was detected in the supernatant of the infected *Sf*9 cells using enzyme inhibition assays. Results shown in **Figure 63B** indicated the successful expression of mouse CD73. Moreover, the detected activity was inhibited by a standard CD73 inhibitor, AMPCP.

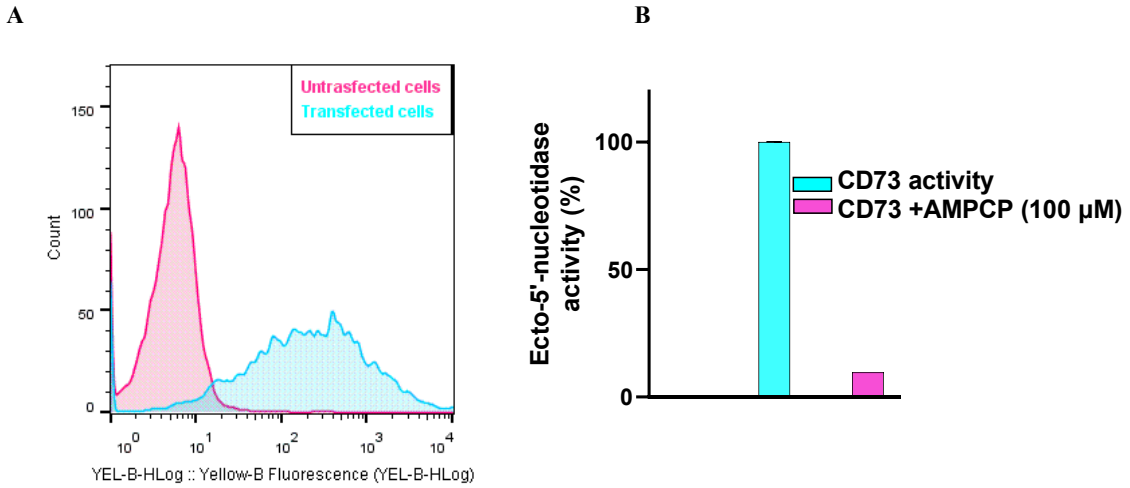


Figure 63. **A**) Detection of GP64 baculoviral protein expressed on the surface of transfected cells in flow cytometry using fluorescence-labeled antibody. Un-transfected *Sf*9 cell compared to cells transfected with target gene (mouse CD73). **B**) Ecto-5'-nucleotidase activity detected on infected cell culture supernatant of P_1 viral stock using enzyme inhibition assay (AMP = 5 µM). The activity of the enzyme is inhibited by addition of 100 µM AMPCP (n=1).

Protein expression and purification

The amplified P1 baculoviral stock was applied for large scale expression of soluble mouse CD73 (1000 ml). The crude protein mixture was first concentrated using Amicon® centrifugal filters (Merck) then subjected to purification with Talon superflow resin (Cobalt resin). Next, sodium dodecyl-sulfate polyacrylamide gel electrophoresis (SDS-PAGE) was run for crude and purified samples, and Coomassie blue dye was applied for protein staining. **Figure 64A** showed that soluble mouse CD73 was successfully obtained and purified as His-tagged protein indicated by appearance of a band with a molecular weight just below 65 kDa. The calculated molecular weight for the soluble mouse CD73 is 60.3 kDa without possible glycosylation which would increase the weight. However, the His-tag-free protein (native) was not obtained (unsuccessful protease cleavage reaction). Moreover, the purified His-tagged mouse CD73 was confirmed in Western blot (**Figure 64B**) using Horseradish peroxidase (HRP)-conjugated anti-His antibodies.

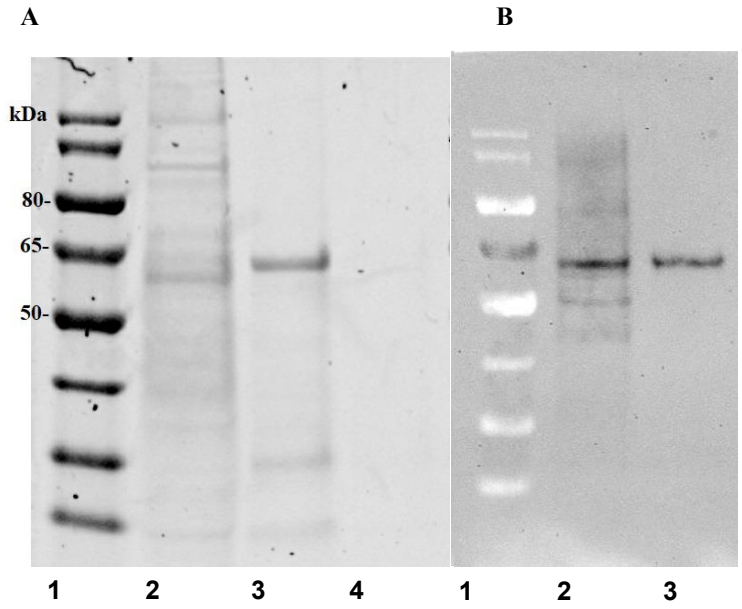


Figure 64. **A**) SDS-PAGE of crude and purified samples. **B**) Western Blot for crude and purified samples of soluble mouse CD73. From left, 1: PageRuler protein marker; 2: crude mixture sample; 3: purified His-tagged sample; 4: purified sample subjected to protease cleavage. Mouse CD73 MW= 60.3 kDa.

Characterization of recombinantly expressed soluble mouse CD73

The kinetics of the newly expressed soluble mouse CD73 was studied using our standard enzyme inhibition assay.[170] Initial velocities of the dephosphorylation reaction were measured for different substrate (AMP) concentrations (**Figure 65A**). Soluble mouse CD73 enzyme was found to exhibit K_M and V_{max} values of 282 μM and 1.4 μmol/min/mg protein, respectively. Based on the obtained K_M value, the produced soluble mouse CD73 has a lower affinity for AMP substrate than soluble rat (K_M = 53 μM, 5-fold) and various human CD73 preparations (K_M = 17 μM, 65.2 μM, 4-17-folds) recombinantly expressed in our lab. Lower inhibitory activity of competitive and uncompetitive inhibitors of CD73 in mouse compared to human has been described previously.[213,271] Moreover, the catalytic activity was also lower than that of the rat and the human enzymes as manifested by the low V_{max} value which was also described elsewhere (AcroBiosystems, USA).

In addition, the inhibitory activity of a competitive inhibitor of CD73, PSB-12489, was studied using the newly expressed soluble mouse CD73. A concentration-inhibition curve (**Figure 65B**) was constructed and the calculated K_i value was 4.79 ± 1.09 nM. Compared to other species, PSB-12489 was 15-fold less potent at mouse compared to human (K_i =

0.318 nM) and 6-fold less potent compared to the rat enzyme (K_i = 0.746 nM). The decrease in potency of this competitive inhibitor at mouse CD73 reflects its high K_M value for AMP compared to other species, i.e. rat and human.

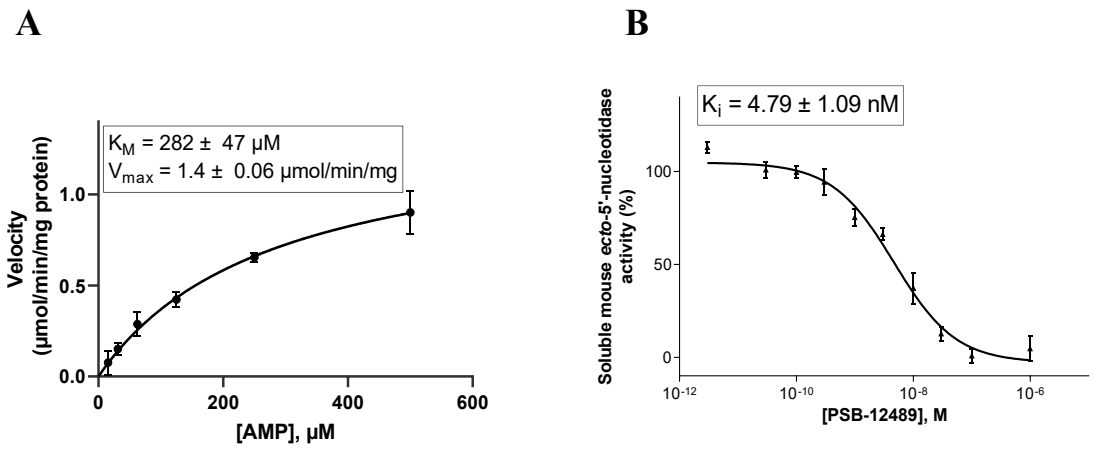


Figure 65. **A**) Michaelis-Menten kinetics for soluble mouse CD73. Initial substrate turnover rates were plotted against different substrate concentrations. **B**) Concentration-inhibition curve for PSB-12489 at recombinant soluble mouse CD73 (K_M = 282 µM). Data points are means ± SEM of three independent experiments, each performed in duplicates.

4.3. Recombinant soluble human CD73

Aim of the project

Soluble human CD73 was previously expressed by our former co-worker, Dr. Christian Renn. However, the applied expression system was complicated and time- and material-consuming as at least seven rounds of viral stock amplification were needed before protein expression. To further improve the production process, soluble human CD73 was ligated into the pFastBac1 vector and expressed using the Bac-to-Bac Baculovirus expression system in collaboration with Dr. Tobias Claff.

cDNA CD73 construct (template)

The cDNA of human CD73 was generously provided by Prof. Dr. Norbert Sträter (University of Leipzig, Germany) based on the Genbank accession no. NM_002526 and the identified natural variant of human CD73 T376A (P21589/VAR_022091, UniProtKB/Swiss-Prot). The secretory signal peptide (amino acids 1-26 on the N-terminus) and GPI-anchor signal peptide (amino acids 550-574 on the C-terminus) were omitted, and

a 6xHis-tag was fused to the cDNA at the C-terminus. The obtained construct was then ligated into the pACGP67B vector by Prof. Dr. med. Michael Hölzel (Institute of Clinical Chemistry and Clinical Pharmacology, University of Bonn).

Results

Molecular cloning

The GP64 signal peptide was ligated upstream and in-frame with the cDNA corresponding to the soluble human CD73^{T376A} into the pFastBac1 (pFB1) vector. Next, the DNA sequence of the HRV 3C protease cleavage site followed by a 10xHis-tag were inserted at the N-terminus of CD73^{T376A} ligated in pFB1. Sequence results confirmed the successful insertion of the protease cleavage site and the 10xHis-tag at the N-terminus. However, the generated construct contained a silent mutation for the amino acid 101(GCC →GCT = alanine). In the last step, the natural variant CD73^{T376A} was corrected into CD73^{wt}. All cloning steps conducted to generate the recombinant pFB1-CD73^{wt} vector are summarized in **Figure 66**.

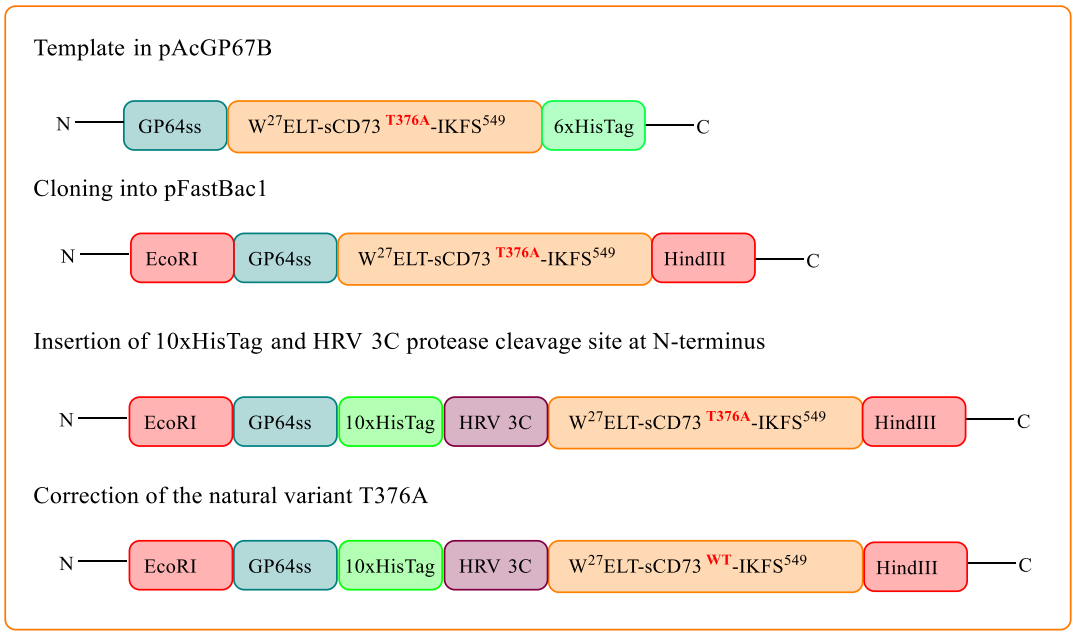


Figure 66. Molecular cloning steps to generate the recombinant pFB1-CD73^{wt} vector.

Generation of the recombinant bacmid and transfection of *Sf*9 insect cells

The obtained pFB1-CD73^{wt} was transformed into DH10Bac *E. coli* competent cells and recombinant bacmid was generated and verified by polymerase chain reaction (PCR) followed by 1% gel electrophoresis. The verified bacmid was then transfected into *Sf*9 insect cells to generate a P_0 baculoviral stock. Successful transfection was confirmed by

flow cytometry using the GP64 assay (**Figure 67A**). Moreover, the hydrolytic activity of the baculovirus stocks was tested using an enzyme inhibition assay[170] (**Figure 67B**). The obtained results indicate that, CD73 is expressed detected in supernatant of transfected and infected *Sf*9 cells.

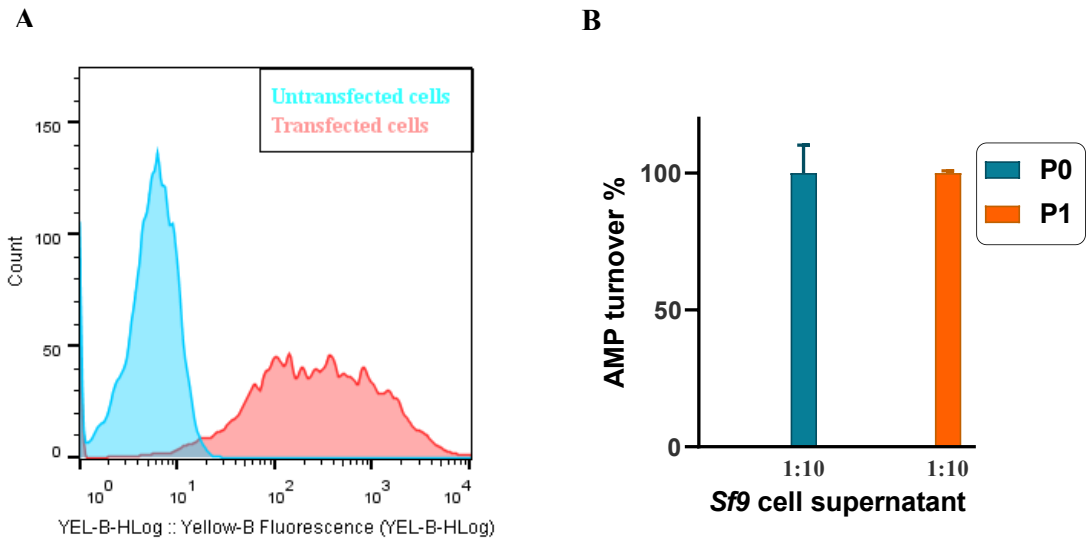


Figure 67. **A**) Detection of GP64 baculoviral protein expressed on the surface of transfected cells in flow cytometry using fluorescence-labeled antibody. Un-transfected *Sf*9 cell compared to cells transfected with target gene (human CD73). **B**) Hydrolytic activity of the produced viral stocks (P_0 and P1) confirming successful infection.

Protein expression and purification

The amplified baculoviral stock (P1) was used to infect 1000 ml of *Sf*9 cell culture for protein expression. The produced crude protein mixture was subjected to double purification using a Ni-column and a cobalt resin after concentration with Amicon filters. Samples withdrawn during the purification steps were analyzed using SDS-PAGE. Coomassie blue-stained gel (**Figure 68A**) and Western blot using mouse anti-His antibodies (**Figure 68B**) indicated successful production of purified soluble human CD73, however, protease cleavage was unsuccessful and thus the enzyme was obtained as His-tagged protein.

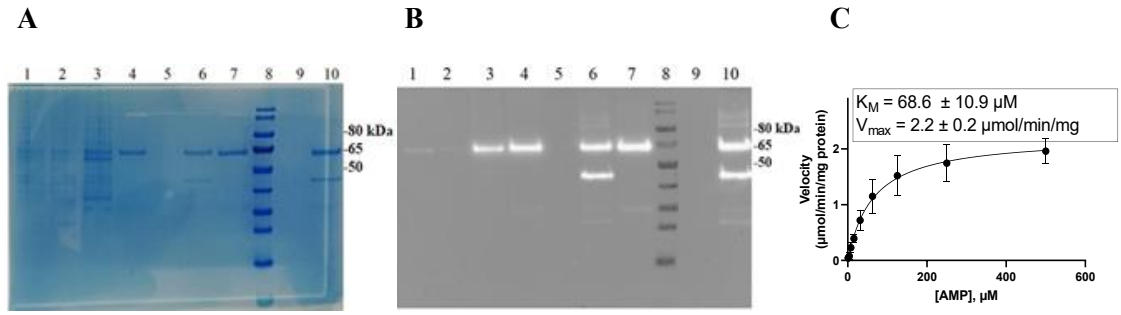


Figure 68. **A**) Coomassie blue-stained SDS-PAGE. **B**) Western blot analysis of purification steps. Lanes; 1: *Sf9* cell culture; 2: Ni-column flow through; 3: Ni-column 1st wash; 4: Ni-column elute; 5:1st Co-column flow through; 6: protease cleavage reaction; 7: 1st Co-column elute (pure His-tagged CD73); 8: PageRuler Ladder; 9: final protein after desalting; 10: 2nd Co-column elute (should contain only protease). (CD73 MW = 60.7 kDa, Protease MW = 47.8 kDa). **C**) Michaelis-Menten kinetics of recombinant soluble human CD73. The initial velocity of AMP hydrolysis was monitored against different substrate concentrations. Data points are means ± SEM of three independent experiments each performed in duplicates.

The purified His-tagged soluble human CD73 enzyme (0.5 ml, 0.8 mg/ml) was obtained in low yield. However, Bac-to-Bac Baculovirus expression was very fast, protein expression was conducted using P1 viral stock while P7 was applied in case of the expression using the pACGP67B vector. Nevertheless, further optimization of the purification steps was needed to enhance the amount of the enzyme produced.

Michaelis-Menten Kinetics of soluble human CD73

The produced soluble human CD73 was subjected to further characterization using enzyme inhibition assays.[170] The rate of substrate turnover was monitored at different initial concentrations (**Figure 68C**). V_{max} and K_M values were found to be 2.2 µmol/min/mg protein and 68.6 µM, respectively. The obtained K_M value was comparable to the values stated in literature for soluble human CD73.[3,19]

4.4. Recombinant soluble human CD73 with 6xHis-tag at the C-terminus

Aim of the project

To study whether a polyHis-tag at the C-terminus of soluble human CD73 affect its substrate binding site, experiments to clone the His-tag downstream in the cDNA of CD73

were performed. As the protease cleavage reaction was previously unsuccessful, and a considerable amount of protein was lost during purification of the pFB1-10xhis-humanCD73 protein, further optimization was attempted. A small GGGS linker was introduced upstream of the protease cleavage site and the 6xHis-tag at the C-terminus to expose the protease cleavage site to proteolysis and to render the 6xHis-tag more accessible to the Ni^{2+} or Co^{2+} resins used for purification.

Results

pFB1-10xHis-humanCD73 was used as a template to amplify the human CD73 flanked between BamHI and HindIII. A GGGS linker was introduced upstream to the protease cleavage site and the 6xHis-tag at the C-terminus. Similar transfection, protein expression and purification procedures were applied to produce soluble human CD73 using the new construct. The enzyme was purified and recovered as His-tagged (0.6 mg/ml, 2 ml) and native protein (**Figure 69A**). The protease reaction was successful; however, a very low yield was obtained (0.05 mg/ml, 1 ml). Both, His-tagged and native enzymes were characterized in the enzyme inhibition assays (**Figure 69B -C**). The obtained V_{max} and K_M values were 2.1 µmol/min/mg protein, 65.2 µM, (His-tagged) and 1.9 µmol/min/mg protein and 56.0 µM (native enzyme), respectively. The similar calculated K_M values obtained from N- (68 µM) and C-terminally (65 µM) His-tagged CD73, together with the native CD73 (His-tag-cleaved CD73, K_M = 56 µM) indicated that, the presence of a His-tag upstream or downstream of the soluble human CD73 did not affect the enzyme's affinity for its substrate (K_M), and consequently we expected that the potency of competitive inhibitors follows the same rule.

Moreover, the C-terminally tagged soluble human CD73 was characterized using the competitive inhibitor PSB-12489, and the obtained K_i value (0.486 ± 0.011 nM) was comparable to the published value using soluble human CD73 (0.318 ± 0.020 nM).[210]

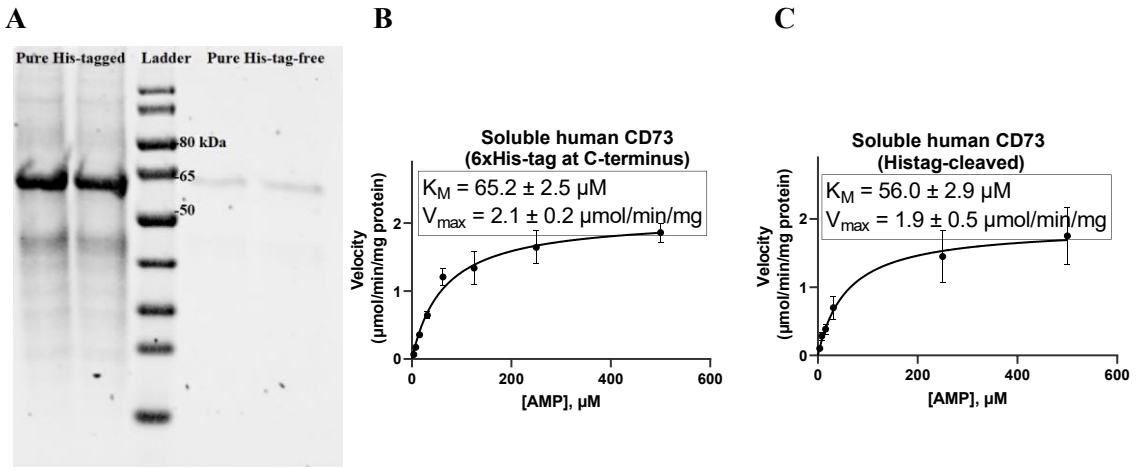


Figure 69. **A**) Coomassie blue staining of SDS-PAGE analysis of recombinant soluble human CD73. From left, lane 1&2 are purified His-tagged soluble human CD73 (MW= 58.9 kDa), lane 3 is the protein marker, lane 4&5 are purified His-tag-cleaved soluble human CD73 (MW= 57.9 kDa). **B**) Michaelis-Menten kinetics of His-tagged recombinant soluble human CD73. **C**) Michaelis-Menten kinetics of Histag-cleaved recombinant soluble human CD73. The initial velocities of AMP hydrolysis were monitored against different substrate concentrations. Data points are means ± SEM of at least two independent experiments each performed in duplicates.

4.5. Phospholipase C-treated MDA-MB-231 cells

Aim of the project

Several inhibitors of CD73 that were identified in our group showed selective inhibition of soluble human CD73 but were inactive at the membrane-bound enzyme expressed in MDA-MB-231 cells, a triple negative breast cancer cell line. To find an explanation, phosphatidylinositol-specific phospholipase C (PI-PLC, Invitrogen, cat. # P6466) was used to cleave off CD73 which is GPI-anchored to the membrane of MDA-MB-231 cells.[298,299]

Results

The supernatant of MDA-MB-231 cells subjected to PI-PLC hydrolysis exhibited an AMPase activity that was not detected in the supernatant of untreated MDA-MB-231 cells (**Figure 70A**). Moreover, the catalytic activity of the supernatant (PLC-cleaved CD73) was inhibited by the selective, potent, and competitive CD73 inhibitor PSB-12489 with a K_i value of 0.167 nM (**Figure 70B**). The calculated K_i value was comparable to the published value (K_i = 0.318 nM) using recombinant soluble human CD73[210] and to a K_i value (0.158 nM) obtained using radioligand binding assays conducted with membrane preparations of

MDA-MB-231 cells. Furthermore, the Michaelis-Menten kinetics were investigated, and K_M and V_{max} values for the PLC-cleaved CD73 were found to be 83.0 µM and 0.8 µmol/min/mg protein, respectively (**Figure 70C**). The calculated K_M value was slightly higher than the K_M value determined for the native soluble CD73 obtained through cleavage of the purification His-tag (K_M = 56.0 µM) which might be attributed to different post-translational modifications (i.e. glycosylation). Furthermore, the determined K_M value for CD73 anchored to the membrane of the MDA-MB-231cells (K_M = 14 µM, determined by a previous co-worker) was found to be lower than that of its PLC-cleaved form (K_M = 83 µM). PLC treatment may influence the interaction with the active site. It is well described that the GPI anchor might affect both the conformation and thus the structure of its attached protein.[300] An example, is the loss of affinity of an antibody that binds the GPI-anchored protein procyclin when treated with PLC.[301] Moreover, OX7 antibody directed towards the GPI-anchored protein Thy-1 also failed to bind the same protein subjected to PLC hydrolysis.[302] Accordingly, the higher obtained K_M values for soluble and PLC-cleaved CD73 might indicate that, conformational changes occur when GPI-anchored human CD73 lost its attachment to the plasma membrane, and these changes might affect its substrate affinity, which is, however, moderate (6-fold).

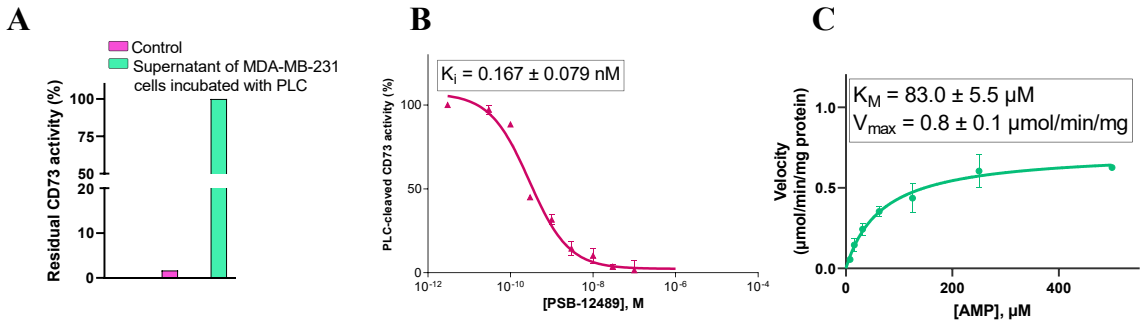


Figure 70. **A**) Hydrolytic activity of PLC-cleaved CD73 compared to a control (supernatant of PLC-untreated cells) tested in enzyme inhibition assays using 5 µM of AMP. **B**) Concentration-inhibition curve for PSB-12489 using PLC-cleaved CD73 (n=1) performed in duplicates. **C**) Michaelis-Menten kinetics of recombinant soluble human CD73 (n=2). The initial velocity of AMP hydrolysis was monitored against different substrate concentrations. Data points are means ± SEM of two independent experiments each performed in duplicates.

4.6. Ecto-5'-nucleotidase (CD73) in milk-derived extracellular vesicles (EVs)

Aim of the project

Several samples of bovine and goat milk-derived exosomes purified by tangential flow filtration (TFF) or by ultracentrifugation (UC) were provided by our collaboration partner Prof. Dr. Nicole Meisner-Kober (University of Salzburg, Austria). Proteomics data obtained for these samples indicated high expression of ecto-5'-nucleotidase protein. Enzyme inhibition assays were performed to detect and confirm the hydrolytic activity of CD73 by these exosomes, in comparison to heat-inactivated samples used as a negative control.

Results

Activity of CD73 in all samples of EVs was tested using a previously published enzyme inhibition assay, in which [^{3}H]AMP at a concentration of 5 µM was employed as a substrate.[170] CD73 activity was detected in all samples, except for the heat-inactivated exosome preparation (**Figure 71**) . The sample of EVs from goat showed the lowest ecto-5'-nucleotidase activity which might indicate low CD73 protein expression in the goat milk. The detected CD73 activity was inhibited by a potent selective inhibitor of CD73, PSB-12489.[210]

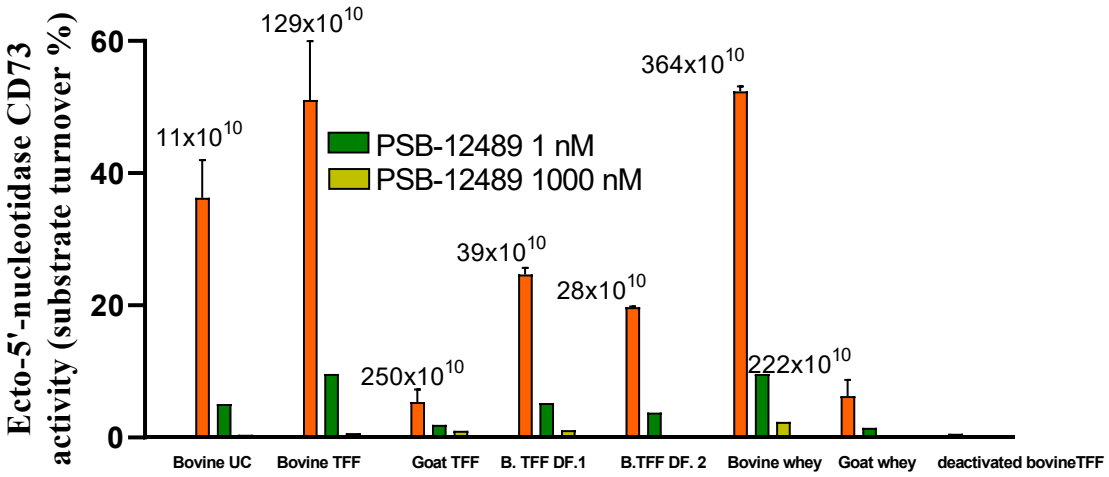


Figure 71. Activity testing of CD73 in EVs and its inhibition by PSB-12489. In an enzyme inhibition assay using 5 µM of AMP as a substrate. Bovine UC: bovine milk exosome purified by ultracentrifugation ($11x10^{10}$ particles/ml); Bovine TFF: bovine milk exosome purified by tangential flow filtration ($129x10^{10}$ particles/ml); Goat TFF: goat milk exosome purified by tangential flow filtration ($250x10^{10}$ particles/ml); B.TFF D.F.1: dry form 1 of

bovine milk exosome purified by tangential flow filtration ($39x10^{10}$ particles/ml); B.TFF D.F.2: dry form 2 of bovine milk exosome purified by tangential flow filtration ($28x10^{10}$ particles/ml); Bovine whey: starting material for bovine EVs ($364x10^{10}$ particles/ml); Goat whey: starting material for goat EVs ($222x10^{10}$ particles/ml). Tested using 5 µM of [^{3}H]AMP as a substrate.

Concentration-inhibition curves were determined using goat (**Figure 72A**) and bovine (**Figure 72B**) TFF samples. The estimated IC_{50} values (0.0935 ± 0.0089 nM, goat) and (0.214 ± 0.026 nM, bovine) were comparable to the published K_i value (0.318 nM) using soluble human CD73.[210] Another calculated K_i value for PSB-1248 tested using in-house radioligand binding assay was 0.158 nM for human CD73. These similar K_i values indicated a highly conserved CD73 binding pocket among human, goat, and bovine species. However, direct comparison of IC_{50} and K_i values is not highly valid.

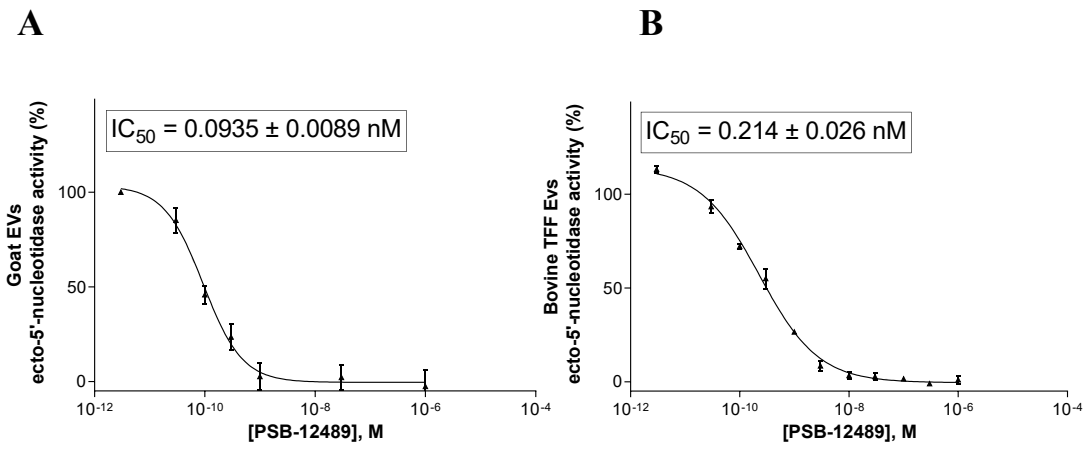


Figure 72. **A**) Concentration-inhibition curve for PSB-12489 using goat TFF EVs- CD73 (n=2). **B**) Concentration-inhibition curve for PSB-12489 using bovine TFF EVs- CD73 (n=3). Data points are means ± SEM of at least two independent experiments, each performed in duplicates.

4.7. Summary and outlook

Constructs of soluble human CD73 ligated into pFastBac1 vector were generated either N- or C-terminally tagged with a poly-histidine purification tag. Soluble human CD73 with 10xhis-tag at the N-terminus was successfully obtained as purified His-tagged protein with a K_M value of 68.6 µM. The applied Bac-to-Bac baculovirus expression system was very

fast and simple. However, a low protein yield was obtained, and the protease cleavage reaction was unsuccessful.

With a 6xHis-tag downstream of the soluble human CD73, and a GGGS linker upstream the cleavage site, both His-tag and native protein (His-tag-free, proteolysis reaction was successful) were recovered. The obtained K_M values were 65.2 μM (His-tagged) and 56.0 μM (native enzyme), respectively. Obviously, the presence of the His-tag at the C-terminus of soluble human CD73 did not affect its affinity to the substrate (K_M value).

In general, the K_M values of all obtained recombinant soluble human CD73 samples were comparable to those reported in literature.[3,19] However, they are slightly higher than that of soluble human CD73 (K_M = 17 μM) produced by our previous co-workers.

Soluble mouse CD73 recombinantly expressed in *Sf*9 insect cells was successfully obtained and purified as His-tagged protein. A protease cleavage site was inserted into the cDNA construct to obtain a native protein after purification. However, proteolysis was unsuccessful even though a linker was introduced to create an exposed protease cleavage site. The generated enzyme has a K_M value of 282 μM. This high K_M value obtained for mouse CD73 compared to human CD73 was expected since a lower inhibitory activity of some published competitive inhibitors tested at the mouse species had been reported compared to human.[213,271] Further experiments with selected inhibitors of CD73 were planned to study species difference and to further characterize the soluble mouse CD73 enzyme with regard to stereoselectivity.

Native soluble human CD73 was obtained through PI-PLC solubilization of CD73 anchored to the membrane of MDA-MB-231 cells. The K_M value for the PLC-cleaved CD73 was 83 μM which was higher than that of the membrane-bound isoform (14 μM) and similar to that of recombinant soluble enzyme (56.0 μM) produced in our group.

CD73 activity was detected in bovine and goat milk-derived exosomes. Bovine milk EVs exhibited higher CD73 activity than goat milk exosomes. Moreover, the detected CD73 activity was inhibited by a selective and potent CD73 inhibitor, PSB-12489. The calculated IC_{50} values for PSB-12489 using bovine and goat EVs were 0.214 nM, and 0.0935 nM, respectively.

4.8. Experimental

Material and reagents

Bac-to-Bac™ Baculovirus Expression System kit was purchased from Invitrogen (cat. # 10359016, Darmstadt, Germany). All enzymes and competent cells were obtained from New England Biolabs (Frankfurt, Germany). All primers were designed using Agilent QUCKCHANCE II primer designing tool or SnapGene software and synthesized by Invitrogen (Darmstadt, Germany). The insect cell culture medium ESF921 was supplied by Expression systems (California, USA). Supplements and antibiotics were purchased from Invitrogen (Darmstadt, Germany). Reagents and chemicals were supplied by Roth (Karlsruhe, Germany), Sigma-Aldrich (Taufkirchen, Germany) or AppliChem (Darmstadt, Germany).

Primers

All primers applied in polymerase chain reactions in this section are listed in **Table 11**.

Table 11. Primers used for molecular cloning of soluble human CD73 in pFastBac1 vector

No.		Primer sequence
1-1	Forward	5′…gatccgaattcatgctactagtaaatcagtcacaccaaggc…3′
1-2	Reversed	5′…gatccaagcttttagctaaacttgatccgaccttcaactgc…3′
2-1	Forward	5′…cctttgcggcggatcttggatcccaccatcatcaccatcatcaccaccaccacctgg aggtgctcttccagggtccctgggagcttacgattttgcacac…3′
2-2	Reversed	5′…gtgtgcaaaatcgtaagctcccagggaccctggaagagcacctccaggtggtggt ggtgatgatggtgatgatggtgggatccaagatccgccgcaaagg…3′
3-1	Forward	5′…taacaacaacctgagacacaccgatgaaatgttctggaacc…3′
3-2	Reversed	5′…ggttccagaacatttcatcggtgtgtctcaggttgttgtta…3′
4-1	Forward	5′…gatccggatcctgggagcttacgattttgcac…3′
4-2	Reversed	5′…gatccaagcttttagtggtgatggtgatgatggggcccctggaacagaacttccag gcttcctccaccgctaaacttgatccgaccttcaactgctgg…3′

Molecular cloning

General procedures

Polymerase chain reaction (PCR)

The following reaction mixture and thermocycler program (**Table 12)** was applied in all PCR steps. Stock solutions (100 µM) of the forward and the reversed primers (**Table 11**) were diluted 1:20 with nuclease-free water. All PCR ingredients were mixed on an ice block.

Table 12. Applied PCR reaction mixture and thermocycler program

PCR ingredients		Thermocycler program (2.5 h)	
5xGC buffer	5 µl	98°	3 min
PCR H_2O	18.25 µl	98°	0.3 min
dNTP (10mM mixture)	0.6 µl	58°	0.45 min
DMSO	0.25 µl	72°	5 min] 20x
Phusion-polymerase	0.3 µl	72°	10 min
Template DNA	0.3 µ	12°	finish
Forward primer (x-1)	0.6 µl		
Reversed primer (x-2)	0.6 µl		

Agarose gel (1%) DNA electrophoresis

Agarose (0.5 g) was transferred into a flask contains 50 ml of 1x TAE buffer (40 mM Tris-acetate, 1 mM EDTA) and heated at low energy in the microwave with regular check until complete dissolution. After cooling down, 2.5 µl of GelRed nucleic acid dye was added and the mix was poured into the gel mold. PCR products were pipetted into gel cavities after dilution with the gel loading dye (Purple (6X), cat. # B7024S, New England Biolabs). Diluted DNA ladder (Lambda DNA/EcoRI plus HindIII Marker, cat. # SM0191, Thermo Scientific ™) were also pipetted into different gel cavities. The electrophoresis was run at 80-90 volt for 60 min.

DNA gel recovery

DNA was recovered from gel using Zymoclean gel DNA recovery kit (cat. # D4007/D4008, Zymo Research Corporation) following the manufacturer protocol. Gel slice with the required DNA band was weighted and melted in 3x its weight volume from ADB buffer at 55°C for 5-10 min. Melted solution was then transferred into Zymo-spin column in a collection tube, and centrifuged at 14.000 for 30 seconds. The flow-through was discarded and column was washed with 200 µl of DNA wash buffer (ethanol should be added to the wash buffer) followed by further centrifugation at 14.000 for 30 seconds. Finally, the flow-through was discarded and 6 µl of nuclease-free water was added into the column matrix, the column was then placed inside a fresh 1.5 ml PCR Eppendorf tube and centrifuged for 30 second at 14.000 g to elute the DNA. DNA concentration was measured using Colibri Microvolume Spectrometer (Titertek Berthold, Pforzheim, Germany).

Restriction enzyme digest

The protocol for double digest was generated from New England Biolabs based on the restriction enzymes set.

Ligation reaction with N4 DNA ligase

The manufacturer protocol was applied for ligation with N4 DNA ligase (cat. # M0202S, New England Biolabs).

Digestion with DpnI

0.5 µl of DpnI (cat. # R0176S, New England Biolabs) was added to the PCR product to digest the parent DNA template and incubated at 37°C for at least 2.5 h.

Transformation into DH5α *E. coli*

50 µl of DH5α *E. coli* competent cell was added to 5 µl ligation product or DpnI digestion product, mixed by tapping the tube gently then incubated on ice for 30 min. Heat shock was applied for 45 seconds at 42 °C, followed by a second incubation period on ice for 2 min, then 100 µl of room temperature Luria-Bertani (LB) broth was added and incubated at 37 °C, 300 rpm for 1 h. Afterward, the product was pipetted and spread out in ampicillin agar plate (pFB1 vector has Ampicillin resistance gene) and incubated overnight at 37 °C.

Picking of selected colonies

Successful transformation was achieved when ampicillin agar plate contains white colonies. Pipette tip was used to pick separate colony and place it into culture falcon tube containing 5 ml of LB medium + 5 µl ampicillin (100 mg/ml). The culture was then incubated overnight on a bacterial shaker at 37 °C and 220 rpm.

Plasmid miniprep

ZymoPURE Plasmid Miniprep Kit (cat. # D4210, Zymo Research Corporation) was used to isolated the recombinant plasmids from the *E. coli* cell lysates according to the manufacturer protocol.

Specific procedures

Subcloning steps of soluble human CD73 in pFastBac1 vector

1. Polymerase chain reaction (PCR) using pACGP67B-sCD73^{T376A} as template and primers 1-1 and 1-2 (**Table 11**)
2. Agarose gel (1%) DNA electrophoresis
3. Zymoclean Gel DNA recovery kit
4. Restriction enzyme digest using protocol for double digest (EcoRI & HindIII)

5. Agarose gel (1%) DNA electrophoresis
6. Zymoclean Gel DNA recovery kit
7. Ligation of $CD73^{T376A}$ insert and pFB1 vector using N4 DNA ligase
8. Transformation of ligation product into DH5α *E. coli* competent cells
9. Selection of colony
10. Plasmid miniprep using ZymoPURE Plasmid Miniprep Kit
11. Sequence confirmation (Eurofins Genomics Germany GmbH)

Insertion of HRV 3C protease cleavage site and 10xHistag at the N-terminus

1. Polymerase chain reaction (PCR) using the cloned pFB1-$CD73^{T376A}$ as template and primers 2-1 and 2-2 mentioned in **Table 11**
2. Digestion with DpnI
3. Transformation into DH5α *E. coli* competent cells
4. Selection of colony
5. Plasmid miniprep using ZymoPURE Plasmid Miniprep Kit
6. Sequence confirmation (Eurofins Genomics Germany GmbH)

Correction of the natural variant T376A

1. Polymerase chain reaction (PCR) using pFB1-10xHis-protease site-$CD73^{T376A}$ as a template and primers 3-1 and 3-2 (**Table 11**)
2. Digestion with DpnI
3. Transformation into DH5α *E. coli* competent cells
4. Selection of colony
5. Plasmid miniprep using ZymoPURE Plasmid Miniprep Kit
6. Sequence confirmation (Eurofins Genomics Germany GmbH)

Cloning of soluble human CD73 C-terminally tagged with 6xHis

1. Polymerase chain reaction (PCR) using pFB1-10xHis-protease site-$CD73^{wt}$ as a template and primers 4-1 and 4-2 (**Table 11**) to amplify soluble human with 6xhis-tag at C-terminal flanked between BamHI and HindIII
2. Agarose gel (1%) DNA electrophoresis
3. Zymoclean Gel DNA recovery kit
4. Restriction enzyme digest using protocol for double digest (BamHI & HindIII, New England Biolabs) for the amplified insert and the template

5. Agarose gel (1%) DNA electrophoresis
6. Zymoclean Gel DNA recovery kit
7. Ligation using N4 DNA ligase
8. Transformation of ligation product into DH5α *E. coli* competent cells
9. Selection of colony
10. Plasmid miniprep using ZymoPURE Plasmid Miniprep Kit
11. Sequence confirmation (Eurofins Genomics Germany GmbH)

Generation of recombinant bacmid and transfection of *Sf*9 insect cells

Transformation, preparation of recombinant bacmid, transfection of *Sf*9 insect cells, GP64 assay, and amplification of baculoviral stock were performed as previously mentioned under Section 3.2, pages 118-121.

Large scale protein expression

The amplified viral stock P1 was used (6 ml) to infect 1000 ml of freshly-grown *Sf*9 at a 2-3x10^6 cells/ml density in 1.6 L shake flask (Optimum Growth® Flasks, Thomson, USA). Cells were incubated for 48 h at 27 °C and 250 rpm, afterwards precipitated by centrifugation (Allegra X-30R Centrifuge, Beckman Coulter) in 500 ml centrifuge tubes at 2000 rpm for 20 min. The supernatant which contains the soluble protein was collected and stored at 4 °C for purification.

Protein purification

Purification of Histag protein using cobalt or nickel resin

The infected *Sf*9 cell culture (1000 ml) was first filtered through 0.45 µm pore size filter using vacuum pump then concentrated with Amicon® Ultra 15 ml Centrifugal Filters (MWCO 30,000, Merk) to 5 ml. Concentrated protein mixture was exchanged against Tris 25 mM and incubated with either a prewashed 50% slurry of Co^{2+} resin (Talon Superflow resin, cat. # 635506, Takara Bio Company) or transferred into a prewashed nickel column (HisPur™ Ni-NTA Spin Columns, 3 ml, Thermo Scientific) and kept overnight in an orbital shaker (Multi Bio RS-24 Programmable rotator, Biosan) at 4 °C. On the next day, the column was centrifuged at 700 *g* for 2 min and the supernatant was collected. Co^{2+} resin was transferred into a collecting column (Poly-Prep Columns #7311550EDU, Bio-Rad) and was washed 3x5 ml washing buffer (Tris 25 mM pH 7.4, NaCl 500 mM, imidazole 20 mM), the Ni^{2+} column was washed directly. His-tagged protein was then eluted with five fractions

of 500 µl elution buffer (Tris 25 mM pH 7.5, NaCl 500 mM, imidazole 220 mM) and stored until further use at 4 °C.

To minimize time needed for protein concentration using Amicon® Ultra 15 ml Centrifugal Filters, direct loading of the cell culture supernatant supplemented with 5 mM imidazole into the HisPur™ Ni-NTA Spin Columns, 3 ml (Thermo Scientific™) was tried. An infusion set was used at a 150 ml/ h rate to deliver the cell culture dropwise into the Ni-column. The column was washed three times and an elution buffer 3x3ml (Tris 25 mM + 250 mM imidazole) was applied to elute the protein.

Exchange the imidazole-rich buffer

The imidazole-rich buffer was exchanged as high imidazole concentration interferes with removal of the protease enzyme after proteolysis. Exchange was done against Tris 50 mM, NaCl 150 mM, pH 8 by using either a desalting column (PD-10 Desalting column, GE Healthcare) or Amicon® Ultra 15 ml Centrifugal Filters (MWCO 30,000, Merk).

Histag cleavage by Pierce™ HRV 3C Protease

His-tag cleavage was conducted using protease enzyme (Pierce™ HRV 3C Protease, cat. # 88946, Thermo Scientific) according to the manufacturer protocol. Defined volume of protease enzyme -depending on the amount of the His-tagged protein in a sample- was added to the concentrated and purified His-tagged protein and incubated overnight at 4 °C.

Removal of protease enzyme with Cobalt resin

To get rid of His-tagged protease, 1 ml of prewashed 50% slurry of cobalt resin (TALON Superflow Resin, cat. # 635506, Takara Bio Company) was added and incubated for 1 h on an orbital shaker (Multi Bio RS-24 Programmable rotator, Biosan) at 4 °C. Sample was then transferred into a collecting column (Poly-Prep Columns #7311550EDU, Bio-Rad) and the flow-through was collected (contains the Histag-free protein). Protease enzyme was eluted with 5 ml of elution buffer. Purified protein was kept in Tris buffer 25 mM and 20% glycerol, at -80 °C until further use.

Sodium Dodecyl Sulfate Polyacrylamide Gel Electrophoresis (SDS-PAGE)

10% SDS-PAGE gels molded using *bis*-2-amino-2-(hydroxymethyl)propane-1,3-diol (*bis*-Tris) buffer was applied as they provide high band resolution and long shelf life. Samples withdrawn during all purification steps were evaluated by SDS-PAGE. Protein samples were mixed in a loading dye (NuPAGE 4x, Invitrogen) contains 200 mM dithiothreitol

(DTT) which was added to denature the protein, then incubated at 65 °C for 10 min. Samples were centrifuged to remove any precipitate before loaded into gel cavities. Protein ladder (5 µl, PageRuler ™ prestained protein ladder, Thermo Scientific™) was loaded into separate gel cavity to determine the molecular mass of the separated proteins. Electrophoresis was run in MOPS buffer (50 mM MOPS, 50 mM Tris, 1 mM EDTA, 0.1% SDS) at 50 V using (PowerPac Universal™, Bio-Rad Laboratories, USA) until the protein marker started to fractionate (left the stacking gel), then increased to 120 V. Staking gel was removed and gels were subjected to Coomassie staining or antibodies detection using Western blot.

Coomassie blue staining

Gels were cooked in a microwave with suitable volume of Coomassie blue dye solution for a couple of minutes then washed several times with water to destain the gel. For better visualization, gels were kept overnight incubated in water on a plate shaker. Stained gels were visualized in a white tray of ChemiDoc™ MP Imaging System, Bio Rad.

Western blot

The polyacrylamide-separated gel and a nitrocellulose blotting membrane (Amershan™ Protan™ 0.45 µm, GE HealthCare, USA) were incubated on a transfer buffer (48 mM Tris+39 mM glycine+10% ethanol+0.1% sodium dodecyl-sulfate (SDS)) for 5-10 minutes before assembling the transfer sandwich into a gel transfer device (Trans-Blot Turbo, Bio-Rad, blotting conditions: 1.3 A (const.), 25 V, 15 min). After successful transfer, membrane was incubated in the blocking buffer (5% milk powder dissolved in phosphate buffered saline + 0.1% Tween 20 (PBS-T)) for 1 h at room temperature, then the buffer was removed and 8 ml of the primary antibody (mouse anti-His (HIS.H8), Invitrogen) diluted 1:1000 in the blocking buffer) was added. At the end of an overnight incubation period at 4 °C with gentle rotation, the primary antibody was re-pipetted and the membrane was washed with 4x5ml of blocking buffer. Around 10 ml of the secondary antibody (horseradish peroxidase-conjugated anti-mouse antibodies, diluted 1:4000 in the blocking buffer) was added and incubated for 90 min at room temperature. The secondary antibody was removed and the membrane was washed with PBS-T 5 times with a 30 min incubation on the last step. Finally, the membrane was transferred into a visualizing black tray (ChemiDoc™ MP Imaging System, Bio Rad) and 800 µl of the enhanced chemiluminescence (ECL)-

substrates (Pierce™ ECL Western Blotting Substrate, cat. # 32106, Thermo Scientific™) was added dropwise to cover all the membrane.

Determination of protein concentration

Protein concentration of crude and purified samples was determined directly by measuring the absorbance at 280 using Colibri Microvolume Spectrometer (1 A_{280} equals 1 mg/ml protein, Titertek Berthold, Pforzheim, Germany) or through coupling with Folin phenol reagent (Lowry method).[286] In this method, a volume of 1000 µl of Biuret reagent (2% Na_2CO_3, 0.1 N NaOH, 0.5% Cu_2SO_4, 1% Na- Tartrat) was added to a 200 µl of diluted protein sample and incubated for 20 min at room temperature. Folin- Ciocalteu's phenol reagent (100 µl) was then added followed by a second incubation period for 30 min at room temperature. Absorbance was measured at 750 nm or at 550 nm using DU530 spectrophotometer (Beckman Coulter, Brea, CA, USA). Serial dilutions of 0.1% BSA was applied to generate a standard calibration curve.

Testing for CD73 activity and Michaelis-Menten kinetics studies using radiometric enzyme inhibition assay

A previously published enzyme inhibition assay [170] was applied to test the hydrolytic activity of all produced crude and purified proteins. This method was developed in our research group by Dr. Marianne Freundlieb.[170] It was applied in this thesis with some modifications. The reaction buffer used here composed of 25 mM Tris, 140 mM NaCl, 25 mM NaH_2PO_4, adjusted to pH 7.4 at 37 °C. Moreover, the final washing steps were performed with 400 µl each of ice-cold Mili-Q water and not 1 ml of precipitation buffer. In this assay, a tritium-labeled AMP substrate (specific activity 7.4 x 108 Bq/mmol (20 mCi/mmol), American Radio-labeled Chemicals, USA, distributed by Hartmann Analytic, Germany) was used diluted at a concentration of 5 µM. Protein samples to be tested for AMPase activity (10 µl) was added to 80 µl of the assay buffer (Tris-HCl 25 mM supplemented with NaCl 140 mM, sodium dihydrogen phosphate 25 mM, pH 7.4) contained in polypropylene test tube (cat. # 55.535, SARSTEDT, Nümbrecht, Germany). Reaction was initiated by addition of a 10 µl of diluted [^{3}H]AMP and continued with a 25 min incubation period in a water bath at 37 °C. Quenching of the reaction was achieved by addition of 500 µl of ice-cold precipitation buffer (lanthanum chloride 100 mM, sodium acetate 100 mM, pH 4) and a further incubation on ice for at least 1 h. Samples were filtered through GF/B glass fiber filters (Whatman™ GE Healthcare, USA) using a Brandel cell harvester (M-48, Brandel, MD, USA) followed by 3x400 µl washing steps with ice-cold

Milli-Q ultrapure water. The filtrate ([^{3}H]adenosine) was collected in a scintillation vial (8 ml Midi-Vial, PerkinElmer Inc) and the radioactivity was measured after addition of a 5 ml of a scintillation cocktail (ULTIMA Gold XR, PerkinElmer, USA) using a Tri-Carb 2900TR (Packard/PerkinElmer) scintillation counter (50%-54% counting efficiency). Negative and positive controls in which a 10 µl assay buffer was used instead of the 10 µl protein sample were applied for baseline correction and normalization, respectively. Positive control samples were not subjected to filtration to provide 100% turnover. Results were analyzed using GraphPad Prism software version 8.0 (GraphPad Software Inc., San Diego, CA, USA).

For Michaelis-Menten kinetic studies, the same procedure mentioned above was applied, however, diluted enzyme preparation and substrate solution were preincubated for 5 min at 37 °C. In this experiment, K_M and V_{max} values were determined by studying reaction rates at different substrate concentrations (0.97 µM-500 µM). Reaction rates were initiated by the addition of 10 µl of prewarmed enzyme preparation to 10 µl of diluted [^{3}H]AMP substrate premixed with 80 µl reaction buffer. Negative and positive controls were prepared by adding 10 µl of [^{3}H]AMP substrate to 90 µl of reaction buffer. Negative control and test samples were subjected to harvesting, positive control to calculate 100% turnover were measured without filtration. Negative control values were applied for baseline correction and positive control value to calculate the product adenosine turnover in µmol. Obtained values were fitted to Michaelis-Menten with X intercept model using GraphPad Prism software version 9.0 (GraphPad Software Inc., San Diego, CA, USA

Phosphatidylinositol-specific phospholipase C (PI-PLC) cleavage process

MDA-MB-231 cells grown to 90% confluence in Dulbecco's Modified Eagle Medium (DMEM, cat. # 41966, Thermo Fisher Scientific, USA) supplemented with 10% fetal bovine serum and 100 U/ml penicillin + 100 µg/ml streptomycin. Cells were washed with 10 ml phosphate-buffered saline (PBS) and detached by 2 ml of trypsin/ ethylenediaminetetraacetic acid (EDTA) (0.05%/0.6 mM) solution. Growth medium (8 ml) was added to deactivate the trypsin/EDTA solution then cells were centrifuged at 12000 rpm for 5 min and resuspended in a fresh 10 ml growth medium. 1 ml of MDA-MB-231 cells was added to each of two tubes (1.5 ml Eppendorf tube). One served as a control to which 10 µl of purified water was added and to the second one 10 µl of PI-PLC (Phospholipase C Protein, Phosphatidylinositol-Specific (from Bacillus cereus), cat. #

P6466, Invitrogen ™) was transferred. Both tubes were incubated at 37 °C for 1 h at 200 rpm followed by a centrifugation at 15.000 *g* and 4 °C for 1 h. The supernatants of both tubes were collected and kept, separately.

Heat-inactivated exosome sample

Diluted sample of bovine TFF EVs (MH11TEK1, $129x10^{10}$ particles/ml) was heated in a water bath at 90 °C for 10 min then ice-cooled.

5. Identification of potential modulators for CD73

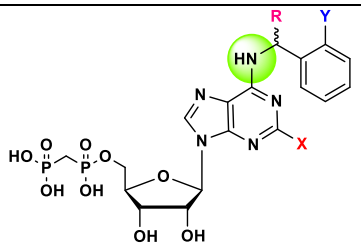
5.1. AMPCP-based CD73 competitive inhibitors

5.1.1. N^6- Substituted AMPCP derivatives

Aim of the project

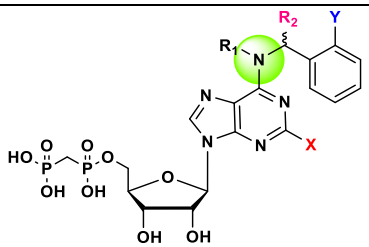
As previously mentioned, extensive studies to improve the potency and stability of AMPCP resulted in N^6-benzyl AMPCP (PSB-12379, K_i = 2.21 nM) which provided an around 40-fold increase in potency compared to AMPCP (K_i = 88.4 nM) at soluble human CD73.[209,210] The crystal structure of human CD73 in complex with PSB-12379 (PDB 6S7F) revealed a pocket close to the C2 of the adenine ring.[210] The polar rim of this pocket is formed by residues N390, D524, NH group of F417 and F500, and G393. The side chains of F412, P498, L415, L389, and I364 provide a hydrophobic base. Accordingly, a series of 2-substituted-N^6-benzyl-AMPCP was synthesized in which the 2-chloro substitution was the most potent one at rat CD73 (PSB-12651, K_i = 1.23 nM, **Table 13**).[210] Furthermore, N^6,N^6-di-substituted AMPCP were explored with introduction of a methyl group at the N^6-position (PSB-12437, K_i = 4.64 nM).[210] This modification has an additional advantage of eliminating any possible interaction of potential metabolites with adenosine receptors. Combination of these two modifications, i.e. 2-chloro and N^6,N^6-di-substitution in one molecule yielded one of the most potent inhibitors of CD73, compound PSB-12489 with a K_i value of 0.318 nM.[210] Following this great discovery of PSB-12489 by our group, extensive structure-activity relationships studies (SARs) were continued to explore the effect of combined substitutions at the C2, the α-carbon and the *ortho*-positions of the N^6-benzyl group. A number of AMPCP derivatives were synthesized by medicinal chemists of our research group (Dr. Sanjay Bhattarai, Dr. Constanze Schmies, Dr. Georg Rolshoven and Eugen Potaptschuk). The obtained compounds were tested mainly against soluble human CD73 recombinantly expressed in *Sf9* insect cells. Selected inhibitors were further characterized in different species using a previously developed enzyme inhibition assay utilizing 5 µM of [^{3}H]AMP as a substrate.[170] Concentration-inhibition curves are presented in **Figure 73** and **74**, and inhibitory constants (K_i) of the competitive inhibitors were calculated by the Cheng-Prusoff equation (**Table 13**).[188]

Table 13. Inhibitory potency of N^6-substituted AMPCP derivatives



N^6-Mono-substituted AMPCP derivatives

Test compound	X	Y	R	K_i value (nM ± SEM)		
				Soluble rat CD73[a]	Soluble human CD73[b]	Human membrane CD73[c]
PSB-12651 (GR378)	Cl	H	H	**1.23** ± 0.04 [210]	**0.134** ± 0.019	ND
EP-051	Br	Cl	H	ND	**0.0723** ± 0.0110	ND
PSB-14650 (SB-650b)	Cl	H	CH_3(*R*/*S*)	**1.20** ± 0.04	**0.0692** ± 0.0055	**0.0633** ± 0.0074
PSB-19294	Cl	H	CH_3(*S*)	**0.594** ± 0.076	**0.0334** ± 0.0073	ND
PSB-19296	Cl	H	CH_3(*R*)	**0.857** ± 0.182	**0.169** ± 0.093	ND
EP-056B	Br	F	CH_3(*S*)	ND	**0.128** ± 0.019	ND



N^6-Di-substituted AMPCP derivatives

Test compound	X	Y	R_1	R_2	Soluble rat CD73[a]	Soluble human CD73[b]	Human membrane CD73[c]
PSB-12489* [210]	Cl	H	CH_3	H	**0.746** ± 0.246	**0.318** ± 0.020	ND
SB-466a	NH_2	H	CH_3	H	**7.37** ± 1.36	**5.48** ± 0.51	**8.20** ± 0.73
SB-826d	Cl	Cl	CH_3	H	**2.96** ± 2.27	**0.0559** ± 0.0018	**0.0641** ± 0.0055
CS-231	Cl	H	CH_3	CH_3 (*R*/*S*)	**0.388** ± 0.095	**0.0705** ± 0.0056	**0.0657** ± 0.0257
GR373	Cl	H	CH_3	CH3 (*S*)	**0.879** ± 0.095	**0.0522** ± 0.0126	ND
GR397**	Cl	H	CH_3	CH_3 (*R*)	**0.388** ± 0.016	**3.60** ± 1.32	ND

GR316	Cl	Cl	CH_3	CH_3 (*R*/*S*)	**0.815** ± 0.212		**0.0746** ± 0.0239	ND
CS-232	Cl	H	C_3H_7	CH_3 (*R*/*S*)	0.582 ± 0.161		**0.159** ± 0.034	**0.113** ± 0.015

[a] Soluble recombinant rat ecto-5'-nucleotidase enzyme (K_M value 59 µM).
[b] Soluble recombinant human ecto-5'-nucleotidase enzyme (K_M value 17 µM or 65 µM)
[c] Membrane preparation of triple negative breast cancer (MDA-MB-231 cell) (K_M value 14.8 µM)
* Published result using different assay system
** Tested by Katharina Sylvester. Rat data in light grey color were obtained by previous co-workers

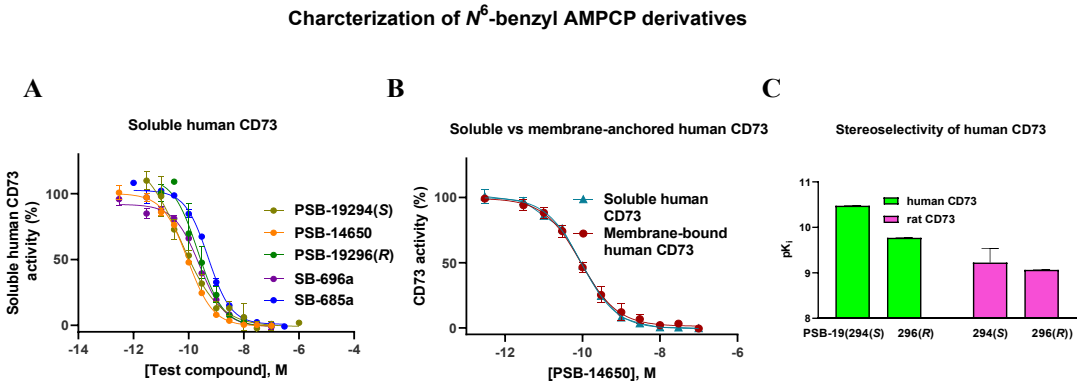


Figure 73. Concentration–inhibition curves of N^6-benzyl-AMPCP derivatives. **A**) Recombinant soluble human ecto-5'-nucleotidase (K_M = 17 µM). **B**) Equipotent activity of PSB-14650 at soluble and membrane-bound (preparation from triple negative breast cancer cells MDA-MB-231 (K_M = 14.8 µM). **C**) Stereoselectivity of human CD73 vs. rat CD73. Substrate (AMP) concentration = 5 µM. Data points are mean of three independent experiments performed in duplicates. Error bars represent the standard error of the mean (SEM).

Structure-activity relationships (SARs)

Test compounds could be classified into mono- and di-substituted AMPCP derivatives with respect to the exocyclic amino group of the adenine base.

N^6-Mono-substituted AMPCP derivatives (N^6-benzyl-AMPCP derivatives)

Regarding N^6-benzyl-AMPCP derivatives, addition of a chloro substituent at the C2-position of the adenine base (PSB-12651) resulted in ca. 16-fold improvement in inhibitory activity against human CD73, compared to N^6-benzyl-AMPCP (PSB-12379, K_i = 2.21 nM vs. PSB-12651, K_i = 0.134 nM, **Table 13**).[209] Further substitution with a chlorine at the *ortho*-position of the N^6-benzyl ring was tolerated and resulted in an inhibitor (EP-051, K_i = 0.0723 nM) that was twice as potent as the lead structure PSB-12651 (K_i = 0.134 nM). Two-fold improvement was also seen with the addition of a methyl group at the α-position of the N^6-benzyl ring (PSB-14650, K_i = 0.0692 nM vs. PSB-12651, K_i = 0.134 nM). This

α-methyl group creates a chiral center, and compound PSB-14650 was tested as a racemic mixture of two diastereomers. To further evaluate the stereoselectivity of the interaction, the *R*- and *S*-isomers were synthesized and tested at rat and human CD73. Both isomers showed comparable K_i values at soluble rat CD73 (PSB-19294(*S*), K_i = 0.594 nM vs. PSB-19296(*R*), K_i = 0.857 nM). Interestingly, human CD73 seemed to display stereoselectivity, the *S*-isomer showing around 5-fold higher affinity than the *R*-isomer (PSB-19294(*S*), K_i = 0.0334 nM vs. PSB-19296(*R*), K_i = 0.169 nM). Thus, an α-methyl group is better tolerated if *S*-configurated. The potency of the *R*-isomer is similar to that of the unsubstituted analog (PSB-12651, K_i = 0.134 nM). The stereochemistry at the α-carbon was described by Lawson et al., 2020, to affect both affinity and metabolic stability of the compounds, depending on the nucleoside core.[213]

However, combining the advantageous features regarding substitutions of compounds EP-051 (K_i = 0.0723 nM) and PSB-19294 (K_i = 0.0334 nM), i.e., an (*S*)-α-methyl group, and an *ortho*-halo group on the phenyl ring, in one molecule was not tolerated, yielding a compound with a potency similar to that of the unsubstituted lead structure (EP-056B, K_i = 0.128 nM vs. PSB-12651, K_i = 0.134 nM). An explanation could be that, the high potency achieved by an (*S*)-α-methyl benzyl group was due to adoption of a new binding mode. In this case, a halo-substitution at the *ortho*-position of the benzyl ring might have hindered attaining this favorable binding mode and hence no increase in potency was observed.

Generally, this series of inhibitors exhibited equipotency at soluble and membrane-bound isoforms of human CD73 as indicated by the K_i values of PSB-14650 (K_i = 0.0692 nM vs. 0.0633 nM at soluble, and membrane-bound CD73, respectively). On the other hand, these N^6-benzyl-AMPCP derivatives showed higher activity at human than at rat CD73 (up to 9-fold). Rat and human CD73 show around 89% sequence identity, with three amino acid exchanges inside the binding pocket of rat compared to human: S244T, F500Y and N499S (human vs. rat).[78] Based on that, the lower binding affinity at rat CD73 could be explained mainly by the F500Y and the N499S substitutions.[78] Residue F500 is involved in π-π stacking of the adenine ring and N499 has polar interaction with the C2-halo group and coordinates binding to water molecules inside the C2 pocket.[213,78] An exceptionally huge species difference is observed with the introduction of the α-methyl(*R*/*S*) group (PSB-14650, K_i = 1.20 nM (rat) vs. 0.0692 nM (human), 17-fold). The difference is profound for the *S*-isomer (PSB-19294(*S*), K_i = 0.594 nM (rat) vs. 0.0334 nM (human), 18-fold), but less in case of the weaker *R*-isomer (PSB-19296(*R*), K_i = 0.857 nM (rat) vs. 0.169 nM (human), 5-fold) (**Figure 73C**). The obtained results might propose that, the *R*-isomer binds in the

same canonical AMPCP binding mode while the *S*-configuration induces a different binding conformation which is favored in the case of the human species. Nevertheless, a clear explanation of these results will become soon available upon co-crystallization of the *R*- and *S*-isomers in complex with the human CD73 (Prof. Norbert Sträter, University of Leipzig).

N^6, N^6-Di-substituted AMPCP derivatives (N^6-alkyl, N^6-benzyl-AMPCP derivatives)

It was previously discovered by our group that further substitution at the N^6-position with a methyl group enhances the inhibitory potency towards rat CD73 (PSB-12651, K_i = 1.23 nM vs. PSB-12489, K_i = 0.746 nM).[210]

To investigate if a small polar group at C2 position is tolerated, the 2-chloro substituent of PSB-12489 was replaced by a 2-amino group. This modification was not favorable and led to a large reduction in inhibitory activity (17-fold, SB-466a**,** K_i = 5.48 nM vs. PSB-12489, K_i = 0.318 nM, human CD73). This drop in potency is corresponding to that observed in the case of the 2-amino AMPCP derivative (PSB-12676, K_i =38.8 nM) which was attributed to the loss of hydrogen-bonding interactions with the N390 side chain (distance limitation).[78]

Introduction of chlorine at the *ortho*-position of the N^6-benzyl ring of PSB-12489 was well tolerated resulting in a 6-fold increase in potency (SB-826d, K_i = 0.0559 nM vs. PSB-12489, K_i = 0.318 nM). A 5-fold increase in the inhibitory potency was also observed when an α-methyl group was introduced to PSB-12489 (CS-321 (racemic mixture), K_i = 0.0705 nM vs. PSB-12489, K_i = 0.318) which indicates an unrestricted space around the exocyclic amino group. The previously obtained results from N^6-mono-substituted derivatives, the N^6-benzyl analogs (PSB-19294(*S*) and PSB-19296(*R*)), encouraged us to investigate the stereoselectivity of human and rat CD73 with respect to the N^6,N^6-disubstituted derivatives. The *S*- (GR373) and *R*- (GR397) isomers of CS-321 were accordingly synthesized. Interestingly, the rat enzyme showed around 2-fold insignificant preference for the *R*-isomer over the *S*-isomer (GR397(*R*), K_i = 0.388 nM vs. GR373(*S*), K_i = 0.879 nM, at rat), while the human enzyme exhibited preference for the *S* isomer, as was seen in the case of the corresponding N^6-monosubstituted derivative, though to a much greater extent (69-fold preference for *S* isomer, GR373(*S*), K_i = 0.0522 nM vs. GR397(*R*), K_i = 3.60 nM).

Unlike mono-substituted derivatives, combining the favorable effects of an *ortho*-chloro (SB-826d, K_i = 0.0559 nM) and an α-methyl group (CS-231, K_i = 0.0705 nM) in a single

molecule (GR316, K_i = 0.0746 nM) was tolerated but provided no added value to the potency over having only an *ortho*-chloro substitution (SB-826d, K_i = 0.0559 nM). This result might indicate that both *ortho*-chloro and α-methyl groups interact with the same residues inside the binding pocket. Hence, a molecule with either an *ortho*-halo or an (*S*)-α-methyl group would provide similar potency. Finally, extending the N^6-methyl substituent in CS-231 to an N^6-propyl residue was well tolerated with an only 2-fold loss in potency (CS-232, K_i = 0.159 nM vs. CS-231, K_i = 0.0705 nM).

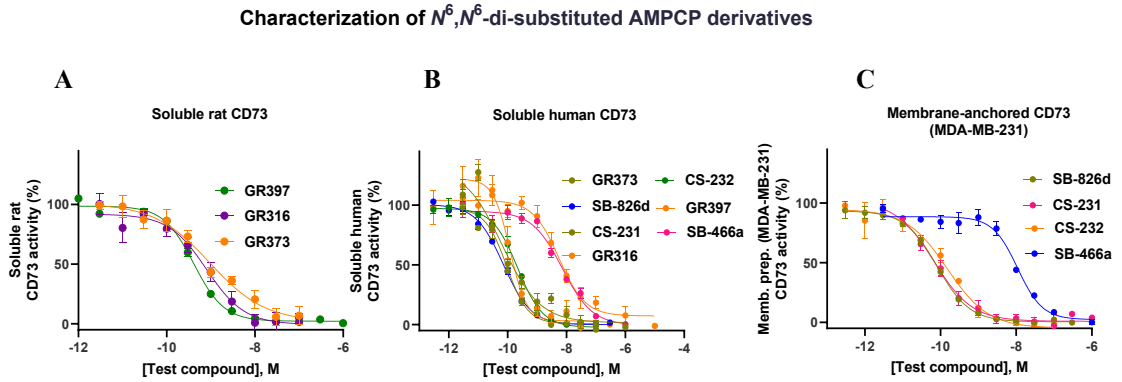


Figure 74. Concentration−inhibition curves of N^6,N^6-disubstituted AMPCP derivatives. **A**) Recombinant soluble rat ecto-5'-nucleotidase (K_M = 59 µM). **B**) At recombinant soluble human ecto-5'-nucleotidase (K_M = 17 µM). **C**) Membrane preparation of triple negative breast cancer cell line MDA-MB-231 (K_M = 14.8 µM). Substrate (AMP) concentration = 5 µM. Each data point is the mean of three independent experiments performed in duplicates. Error bars represent the standard error of the mean (SEM).

N^6,N^6-Di-substituted AMPCP derivatives were equipotent at soluble and membrane-bound isoforms of human CD73 (e.g., SB-826d, K_i = 0.0559 nM (soluble human), 0.0641 nM (membrane-bound)). Regarding rat and human enzymes, these N^6-disubstituted derivatives showed less than 3-fold difference slightly favoring human CD73 which could be attributed to the S244T, F500Y, N499S and L389V substitutions in rat CD73.[78] These substitutions affect the π-π stacking of the adenine base, and the C2-substituent interactions.[78] However, greater than 50-fold selectivity for human CD73 is created by introduction of an *ortho*-chloro substituent into compound PSB-12489 (SB-826d, K_i = 2.96 nM (rat) vs. 0.0559 (human)). We might explain this species difference by comparing the crystal structure of a closely-related compound AB680 (N^6-monosubstiuted pyrazolopyridine base, PDB 6Z9D, **Figure 75**), which is the only *ortho*-phenyl substituted derivative crystalized so far, compared to the crystal structure of PSB-12489 (PDB 6S7H). Unlike the unsubstituted

phenyl ring (in PSB-12489), orientation of residue F417 in the presence of an *ortho*-halo-phenyl ring is not favorable for parallel face-to-face stacking which is then only provided by F500. F500Y substitution in rat led to complete loss of π- π interaction together with a less profound interaction with F417 which could explain this difference between rat and human for *ortho*-chloro-N^6-benzyl substituted AMPCP derivatives and analogs. However, the presence of an α-methyl group on the benzyl substituent in compound AB680 may contribute to the orientation adopted by residue F417.

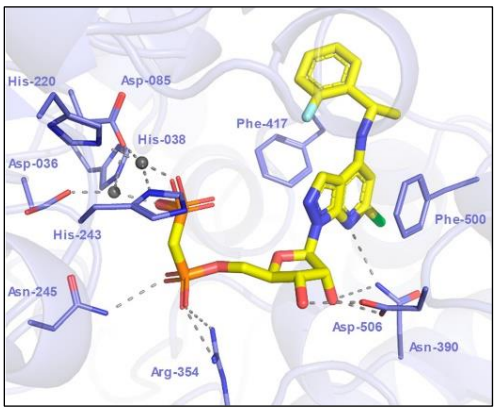


Figure 75. X-ray crystal structure of AB680 bound to human CD73 (closed form), PDB code 6Z9D.[213]

Moreover, (*S*)-α-methylbenzylamine substitution of AMPCP resulted in an around 17-fold preference for human (GR373(*S*), K_i = 0.0522 nM (human) vs. 0.879 nM (rat)), while the rat enzyme showed a 9-fold preference for the corresponding *R*-isomer (GR397(*R*), K_i = 3.60 nM (human) vs. 0.388 nM (rat)). Such relatively huge species difference was also observed for the N^6-mono-substituted benzyl derivatives and might indicate alternative binding modes adopted by *S*-isomers at human CD73. However, this observed selectivity of human over rat CD73 can only be conclusively explained by co-crystallization studies that are currently ongoing (Prof. Norbert Sträter, University of Leipzig).

5.1.2. 2-Halo-N^6-mono- and N^6-disubstituted AMPCP derivatives

Aim of the project

As discussed before, the obtained crystal structure of human CD73 in complex with N^6-benzyl-AMPCP, PSB-12379 (PDB 6S7F) identified a pocket with a volume of about 210

Å that could be targeted through suitable C2-substituents.[210] Moreover, when C2 was substituted with chlorine (e.g. PSB-12489), an improvement of 16-fold was observed, attributed to the favorable interactions of chlorine with neighboring amino acids as seen in the obtained crystal structure of human CD73 in complex with PSB-12489 (PDB 6S7H, **Figure 76**).[210]

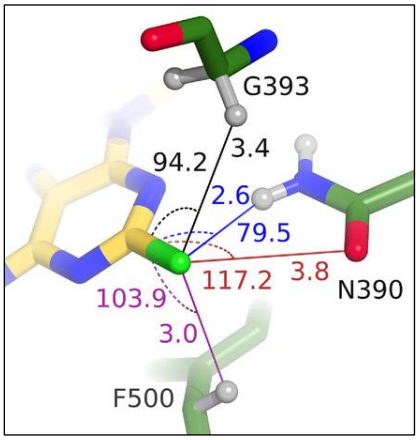


Figure 76. Interactions of chlorine in the C2-pocket of the active site of human CD73. PSB-12489 in complex with human CD73 (PDB 6S7H).[210]

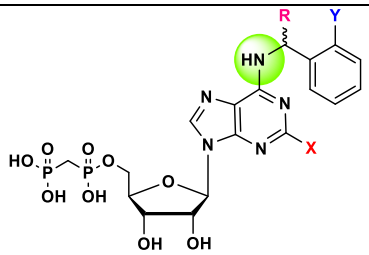
To explore the size of this pocket and to investigate whether halogens with a larger atomic radius will be able to form a halogen bond with the carbonyl group of N390, the chlorine atom at C2 in N^6-mono- and di-substituted-benzyl-AMPCP derivatives was replaced with halogens of different molecular size (bromine and iodine). The pharmacological results at soluble human CD73 are compared in **Table 14**, and the concentration-inhibition curves are presented in **Figure 77**.

Structure-activity relationships (SARs)

Comparing compounds PSB-12651 (K_i = 0.134 nM) with its bromo- (EP-017, K_i = 0.182 nM) and iodo- (SB-696a, K_i = 0.195 nM) analogs indicates that the C2-pocket can easily accommodate atoms of sizes up to 2.10 Å (iodine atomic radius),[303] and that substitution of chlorine with bromine or iodine was generally tolerated with very insignificant reduction in potency in the order of their atomic radius Cl>Br>I. Next, we aimed to investigate the effect of the size of the halogen atom at the C2-position on potency when combined with further substituents at the *ortho*-position of the N^6-benzyl group, namely *ortho*-fluoro group. EP-068 (K_i = 0.0840) and EP-064 (K_i = 0.0919 nM) in which a fluorine atom is present in the *ortho*-position while C2 was substituted either with chlorine (EP-068) or

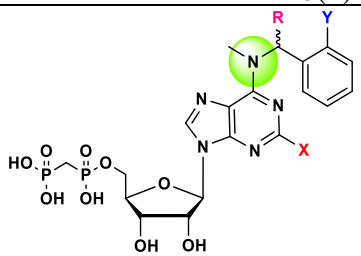
bromine (EP-064) showed comparable results. However, C2-chloro-substitution was preferred over bromo-substitution (Cl>Br) with 2-fold increase in affinity when having an α-methyl substitution (PSB-14650 (*R*/*S*), K_i = 0.0692 nM vs. (EP-049 (*R*/*S*), K_i = 0.149 nM), respectively). Although it is statistically insignificant, this preference was also maintained when their *S*-diastereomers were tested (Cl, PSB-19294, K_i = 0.0334 nM vs. Br, EP-043, K_i = 0.0711 nM**)**. Interestingly, co-introduction of an *ortho*-fluoro together with (*S*)-α-methyl substitution resulted in equipotent activity for a C2-chloro vs. C2-bromo substitution (EP-069 (*S*), K_i = 0.127 nM vs. EP-056B (*S*) (K_i = 0.128 nM, respectively), i.e., no influence of the size of the halogen atom at the C2 position on activity was observed.

Table 14. Effect of halogen atom size at the C2-position on the inhibitory activity of selected N^6-substituted AMPCP derivatives



Mono-substituted-N^6- benzyl AMPCP derivatives

Test compound	X	Y	R	K_i (nM ± SEM) Human CD73[a]
PSB-12651(GR378)	Cl	H	H	**0.134** ± 0.019
EP-017	Br	H	H	**0.182** ± 0.017
SB-696a	I	H	H	**0.195** ± 0.019
EP-068	Cl	F	H	**0.0840** ± 0.0089
EP-064	Br	F	H	**0.0919** ± 0.0109
PSB-14650 (SB-650b)	Cl	H	CH_3(*R*/*S*)	**0.0692** ± 0.0055
EP-049	Br	H	CH_3(*R*/*S*)	**0.149** ± 0.022
PSB-19294	Cl	H	CH_3(*S*)	**0.0334** ± 0.0073
EP-043	Br	H	CH_3(*S*)	**0.0711** ± 0.0051
EP-056B	Br	F	CH_3(*S*)	**0.128** ± 0.019
EP-069	Cl	F	CH_3(*S*)	**0.127** ± 0.031



Di-substituted-N^6- methyl, N^6-benzyl AMPCP derivatives

PSB-12489	Cl	H	H	**0.318** ± 0.020*
EP-018	Br	H	H	**0.0978** ± 0.0301
SB-699b	I	H	H	**0.151** ± 0.018

SB-826d	Cl	Cl	H	**0.0559** ± 0.0018
EP-022	Br	Cl	H	**0.0674** ± 0.0191
PSB-19301	I	Cl	H	**0.0502** ± 0.0161
CS-231	Cl	H	CH_3(*R*/*S*)	**0.0705** ± 0.0056
GR362	Br	H	CH_3(*R*/*S*)	**0.0859** ± 0.0365
GR300	I	H	CH_3(*R*/*S*)	**0.165** ± 0.019
GR316	Cl	Cl	CH_3(*R*/*S*)	**0.0746** ± 0.0239
GR310	I	Cl	CH_3(*R*/*S*)	**1.77** ± 0.36

[a] Soluble recombinant human ecto-5'-nucleotidase (K_M value 17 μM)
* Published result using different assay system

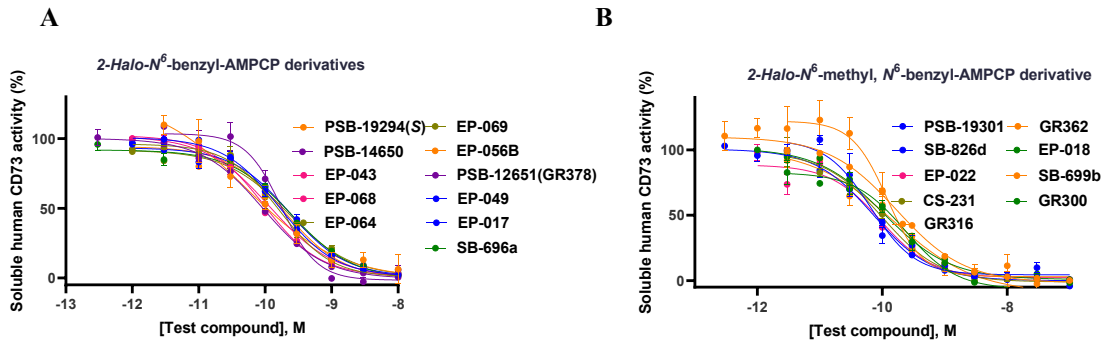


Figure 77. Concentration−inhibition curves at recombinant soluble human ecto-5'-nucleotidase (K_M = 17 μM). **A**) 2-Halo-N^6-benzyl-AMPCP derivatives. **B**) 2-Halo-N^6-methyl,N^6-benzyl-AMPCP derivatives. Substrate (AMP) concentration = 5 μM. Data points are mean of three independent experiments performed in duplicates. Error bars represent the standard error of the mean (SEM).

The effect of halogen atom size at C2 followed the same manner in N^6-mono- and di-substituted derivatives. Bromine (EP-018, K_i = 0.0978 nM) and iodine (SB-699b, K_i = 0.151 nM, 1.5-fold) provided similar potency in N^6-di-substituted compounds. Only the chloro-substituent (PSB-12489, K_i = 0.318 nM**)** showed an aberrant result which could be attributed to the different assay system used to test for that compound.[210] With a chlorine atom at the *ortho*-position of the phenyl ring in compound PSB-12489, compounds with either a chloro (SB-826d, K_i = 0.0559 nM), a bromo (EP-022, K_i = 0.0674 nM) or an iodo (PSB-19301, K_i = 0.0502 nM) group at the C2-position interact similarly. In α-methyl-benzyl substituted compounds, chlorine (CS-231, K_i = 0.0705 nM) and bromine (GR362, K_i = 0.0859 nM) at the C2-position of the adenine ring were equipotent while iodine, which has the highest atomic radius (GR300, K_i = 0.165 nM) showed an around 2-fold drop in potency. When α-methyl substitution was combined with chloro at the *ortho*-position, there was a large difference, the 2-chloro derivative (GR316, K_i = 0.0746 nM) being 20-fold more potent than the 2-iodo substituted compound (GR310, K_i = 1.77 nM).

In general, we can conclude that halogens at the C2-position of the N^6-benzyl-AMPCP interact similarly with very slight preference of chlorine over other halogens (bromine and iodine). Introduction of an α-methyl group created more than 2-fold preference for chlorine over iodine. An exception was seen for compound GR310 (K_i = 1.77 nM) in which iodine was not well tolerated (20-fold drop) compared to chlorine GR316 (K_i = 0.0746 nM). This result might indicate that due to the introduction of an α-methyl group combined with an *ortho* halogenation, the compound adopted a new orientation in which the size of the halogen substituent at the C2-position was critical. A clear answer would only be possible if crystal structures of these two compounds are obtained and analyzed.

Selected inhibitors were further characterized at soluble rat CD73 (**Table 15**). Similar halogen preference was observed compared to human CD73. The α-methyl-benzyl derivatives showed comparable tolerance for small size atom, however, iodine is somehow better tolerated at rat compared to human CD73 (changing the C2 substituent from chlorine (GR316**)** to iodine (GR310**)** led to 20-fold drop in potency in human while around 7-fold loss was observed for rat CD73).

Table 15. Effect of halogen substitution at the C2-position relative to species (rat vs. human CD73)

Test compound	C2-position	*Ortho*-position	α-methyl group substitution	Human CD73[a]	Rat CD73[b]
Mono-substituted N^6-benzyl-AMPCP derivatives					
PSB-12651 (GR378)	Cl	H	H	**0.134** ± 0.019	**1.23** ± 0.04 [210]
SB-696a	I	H	H	**0.195** ± 0.019	**1.53** ± 0.24**
Di-substituted N^6-methyl,N^6-benzyl-AMPCP derivatives					
SB-826d	Cl	Cl	H	**0.0559** ± 0.0018	**2.96** ± 2.27**
PSB-19301	I	Cl	H	**0.0502** ± 0.0161	**0.432** ± 0.262
CS-231	Cl	H	CH_3(*R*/*S*)	**0.0705** ± 0.0056	**0.388** ± 0.095**
GR362	Br	H	CH_3(*R*/*S*)	**0.0859** ± 0.0365	**0.508** ± 0.214
GR300	I	H	CH_3(*R*/*S*)	**0.165** ± 0.019	**1.02** ± 0.27
GR316	Cl	Cl	CH_3(*R*/*S*)	**0.0746** ± 0.0239	**0.815** ± 0.212
GR310	I	Cl	CH_3(*R*/*S*)	**1.77** ± 0.36	**5.35** ± 1.71

[a] Soluble recombinant human ecto-5'-nucleotidase enzyme (K_M value 17 μM)
[b] Soluble recombinant rat ecto-5'-nucleotidase enzyme (K_M value 59 μM)
** Tested by previous co-workers

5.1.3. N^6-alkynyl-AMPCP derivatives

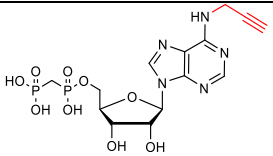
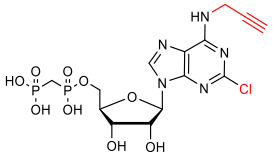
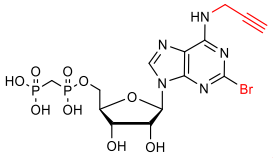
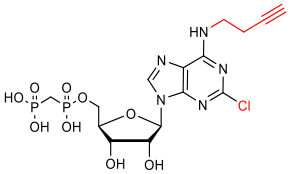
Aim of the project

Since N^6-benzyl-AMPCP has been extensively studied, further exploration was initiated in our group aimed at identifying a new substituent, other than benzyl, for the N^6-position, which is smaller in size and offers functionalization. Therefore, an alkyne group was selected.

Structure-activity relationships (SARs)

N^6-Propargyl-AMPCP (GR293, K_i = 3.64 nM) was found to be equipotent to N^6-benzyl-AMPCP (PSB-12379, K_i = 2.21 nM).[209] Further substitution at the C2-position with chlorine (GR383, K_i = 0.573 nM) or bromine (EP-060, K_i = 0.894 nM) enhanced the potency by 6- and 4-fold, respectively. Similar to the N^6-benzyl-AMPCP derivatives, chlorine is favored over bromine at the C2-position. Exchanging the propargyl with a butynyl group (EP-092, K_i = 0.193 nM) in the presence of a C2-chloro group resulted in about 3-fold improvement in inhibitory activity towards soluble human CD73 (GR383, K_i = 0.573 nM vs EP-092, K_i = 0.193 nM). The obtained results are shown in **Table 16** and **Figure 78**.

Table 16. Potency of selected N^6-alkynyl-AMPCP at soluble human CD73

Test compound	Structure	Human CD73[a] K_i ± SEM (nM)
GR293		**3.64** ± 1.16 nM
GR383*		**0.573** ± 0.319
EP-060		**0.894** ± 0.141
EP-092		**0.193** ± 0.030

[a] Soluble recombinant human ecto-5'-nucleotidase enzyme (K_M value 17 µM)

* Tested by Katharina Sylvester

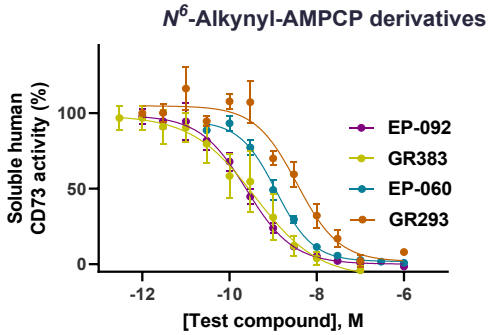


Figure 78. Concentration−inhibition curves of N^6-alkynyl-AMPCP derivatives tested at recombinant soluble human ecto-5'-nucleotidase (K_M = 17 µM). Substrate (AMP) concentration = 5 µM. Data points are mean of three independent experiments performed in duplicates. Error bars represent the standard error of the mean (SEM).

5.1.4. 7-Deaza-AMPCP derivatives

Aim of the project

We have previously reported that 7-deaza-AMPCP is twice as potent as AMPCP at recombinant soluble rat CD73 (88.6 nM vs. 167 nM, respectively).[264] Furthermore, analyzing the binding interactions of AMPCP inside the binding pocket in open and closed conformations reflected that N7 is not involved in any possible interaction with the amino acid residues of the binding cavity (**Figure 79A-B**). Similar results were also obtained by Lawson et al., in which 7-deaza derivatives were more potent than pyrazolopyrimidine and pyrazolopyridine derivatives investigated in the study (shown in **Figure 80**).[213] Based on these preliminary results, further exploration was planned and implemented (**Table 17** and **Figure 79C**).

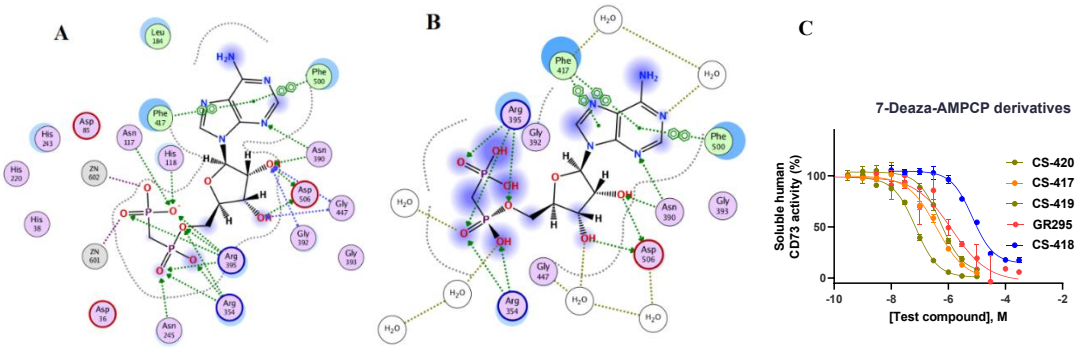


Figure 79. 2D interaction diagram of AMPCP in the binding pocket of human CD73. **A**) Generated from AMPCPxCD73^{closed} (PDB 4H2I). **B**) AMPCPxCD73^{open} (PDB 6TVG). **C**) Concentration−inhibition curves of 7-deaza-AMPCP derivatives tested at recombinant soluble human ecto-5'-nucleotidase (K_M = 17 µM). Substrate (AMP) concentration = 5 µM.

Data points are mean of three independent experiments performed in duplicates. Error bars represent the standard error of the mean (SEM).

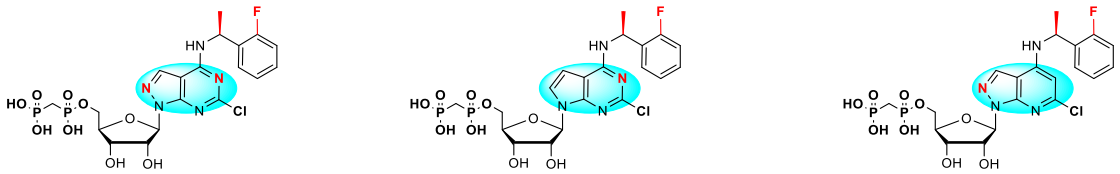
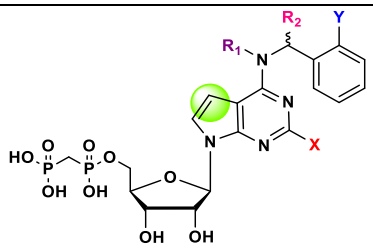


Figure 80. Potency of 7-deaza-AMPCP compared to pyrazolopyrimidines and pyrazolopyridines [213]

Table 17. Potency of 7-deaza-AMPCP derivatives at soluble human CD73



Test compound	R_1	R_2	X	Y	K_i ± SEM (nM) human CD73[a]	**AMPCP analogs**, human CD73[a]
7-Deaza-AMPCP	H	H	H	H	**88.6** ± 4.0 [264] (rat sCD73)	AMPCP, **197** ± 5 [210] (rat sCD73)
CS-417	H	H	Cl	H	**305** ± 59	**PSB-12651**, **0.134** ± 0.019
CS-420	H	H	Cl	Cl	**55.4** ± 7.1	**SB-685a**, **0.387** ± 0.034
GR295	H	CH_3(*R*)	Cl	H	**307** ± 152	**PSB-19296**(*R*), **0.169** ± 0.093
CS-418	C_3H_7	H	Cl	H	**5990** ± 620 (**7640** ± 360 rat sCD73)	**PSB-17230**, **0.0733** ± 0.0013
CS-419	CH_3	H	Cl	H	**413** ± 29	**PSB-12489**, **0.318** ±0.020 [210]

[a] Soluble (s) recombinant human ecto-5'-nucleotidase (K_M value 17 µM)

Structure-activity relationships (SARs)

Based on the obtained results, no further improvement was seen on any of the 7-deaza-AMPCP derivatives investigated so far at soluble human CD73. Interestingly, the 7-deaza-AMPCP derivatives seemed to follow a different pattern of substitution preference compared to their AMPCP analogs. An example is 2-chloro-N^6-propyl-N^6-benzyl-AMPCP

(PSB-17230, K_i = 0.0733 ± 0.0013 nM) which was about 4-fold more potent than 2-chloro-N^6-methyl-N^6-benzyl-AMPCP (PSB-12489, K_i = 0.318 nM). In contrast, their 7-deaza-AMPCP analogs showed around 14-fold preference for the methyl substituent over propyl (CS-419, K_i = 413 nM vs. CS-418, K_i = 5990 nM, respectively). Generally, alkyl substitution at the N^6-amino- or the α-position of N^6-benzyl or chloro-substitution at the C2-position were not tolerated. An exception is the 2-chloro-N^6-(*ortho*-chloro-benzyl) derivative (CS-420) which showed a K_i value of 55.4 nM, which might indicate an alternative binding mode. Moreover, the 7-deaza scaffold exhibits equipotency at human and rat CD73 attested by the K_i values of compound CS-418 (K_i = 5990 nM, human CD73, 7640 nM, rat CD73).

5.1.5. Conjugated AMPCP derivatives

Several probes were developed in our group and in collaboration projects based on the discovery of the potent AMPCP derivatives, PSB-12379**,** PSB-12651 and PSB-17230. Both adenine-based and cytidine-based labeled compounds were designed, synthesized, and evaluated for the biological activity against soluble human CD73 recombinantly expressed in *Sf*9 insect cell (**Table 18** and **Figure 81A**).

First, precursors suitable for the intended labeling technique were synthesized and characterized in radiometric enzyme inhibition assay.[170] An example is EP-103, that was assessed and evaluated as a precursor for further coupling to different fluorescent dyes. Despite the10-fold drop in potency compared to the lead structure, PSB-12651 (EP-103, K_i = 1.38 nM vs. PSB-12651, K_i = 0.134 nM), the obtained result (K_i = 1.38 nM) was highly promising considering the bulky substitution on EP-103. Because of the long linker created between the pharmacophore and the fluorescent tag, no further drop in activity was anticipated.

The recently published fluorescent probes PSB-18332 (λ_{ex} = 450 nm, λ_{em} = 530 nm) and PSB-19416 (λ_{ex} = 451 nm, λ_{em} = 524 nm) were 5(6)-carboxyfluorescein-labeled, in which the alkyl linker (PSB-18332, K_i = 2.98 nM) was favored over the ethylene glycol linker (PSB-19416, K_i = 12.6 nM).[257] PSB-18332 is currently utilized for NanoBRET assays that is discussed in more details in Section 3.2, page 113.

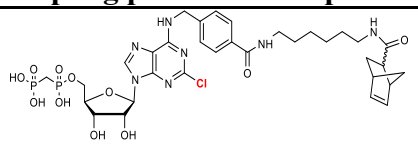
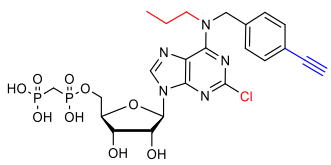
Coupling of the Alexa Fluor 488 dye to a cytidine-based CD73 inhibitor (MRS4647, K_i = 2.22 nM, λ_{ex} = 490 nm, λ_{em} = 525 nm, Prof. Kenneth Jacobson, NIH, USA) was successful

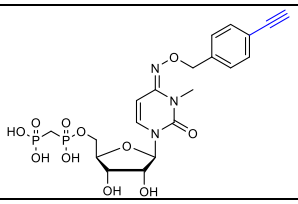
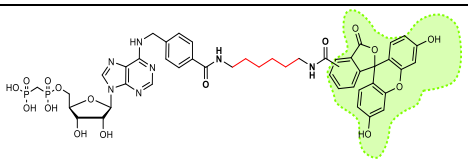
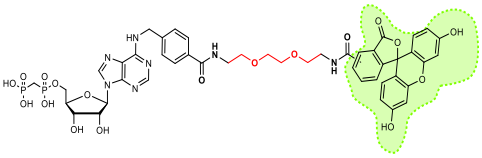
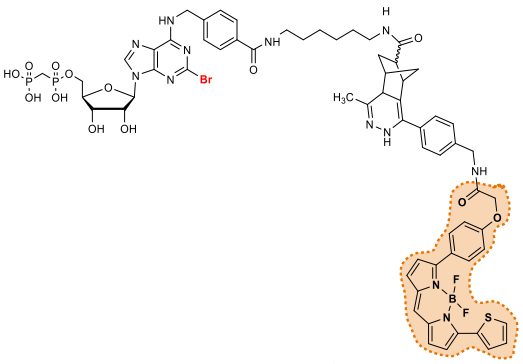
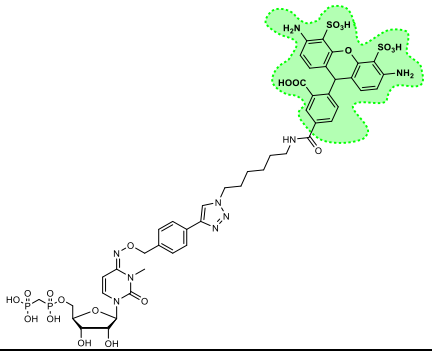
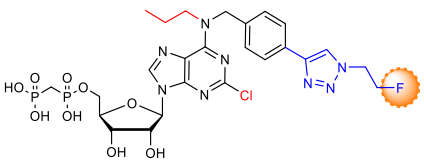
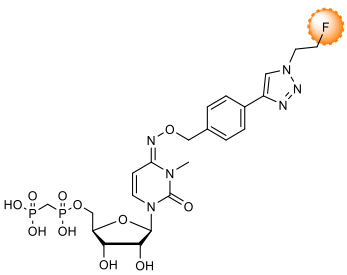
and provided a more photostable alternative to fluorescein-labeled probes. EP-119, our recently developed bright and photostable BODIPY TR-labeled probe (λ_{ex} = 595 nm, λ_{em} = 650 nm) exhibited the highest potency among all fluorescent probes developed so far (K_i = 1.66 nM (human sCD73), 2.32 nM (membrane-bound CD73)). Due to its spectral characteristics and photostability, BODIPY TR is considered superior to fluorescein and rhodamine dyes and provides opportunities for application in live cell imaging and trafficking studies as well as in flow cytometry.

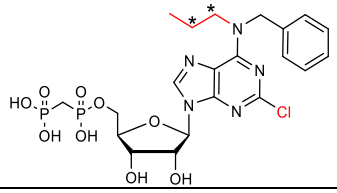
Prior to developing positron emission tomography (PET) tracers, biological activities of the precursors (CS-425, K_i = 0.372 nM, MRS4632, K_i = 0.664 nM) and the unlabeled ligands (PSB-19427, K_i = 1.02 nM, MRS4648, K_i = 0.627 nM) were evaluated using soluble human CD73. Substitution with a (2-fluoroethyl)-*1H*-1,2,3-triazole group in a cytidine-based PET tracer was well tolerated (MRS4632, K_i = 0.664 nM vs. MRS4648, K_i = 0.627 nM) compared to adenine derivative (CS-425, K_i = 0.372 nM vs. PSB-19427, K_i = 1.02 nM). This could be attributed to a different orientation adopted by the (2-fluoroethyl)*1H*-1,2,3-triazol group in cytidine and adenine scaffolds. The obtained results were satisfactory, and PSB-19427 and MRS4648 were ^{18}F-labeled (Dr. Anna Junker, European Institute for Molecular Imaging (EIMI), University of Münster, Germany).

A tritium-labeled version of compound PSB-17230 (K_i = 0.0733 ± 0.0013 nM, shown in **Table 18**) was designed and synthesized and a radioligand binding assay was developed that will be discussed later in Section **4.1** of the thesis.

Table 18. Biological evaluation of labeled-probes for CD73 and their precursors

Tool compound	Structure	Soluble human CD73 K_i ± SEM (nM)
Coupling precursor compounds		
EP-103		**1.38** ± 0.212
CS-425		**0.372** ± 0.030

MRS4632		**0.664** ± 0.089
Fluorescent probes		
PSB-18332		**2.98** ± 0.77
PSB-19416 (CS-416)		**12.6** ± 0.7
EP-119		**1.66** ± 0.18 (**2.32** ± 0.27 membrane-bound, MDA-MB-231)
MRS4647		**2.22** ± 0.35
F-substituted CD73 inhibitors for development of PET tracers		
PSB-19427 (CS-427)		**1.02** ± 0.11
MRS4648		**0.627** ± 0.099

Tritium-labeled CD73 inhibitor		
PSB-17230		**0.0733** ± 0.0013

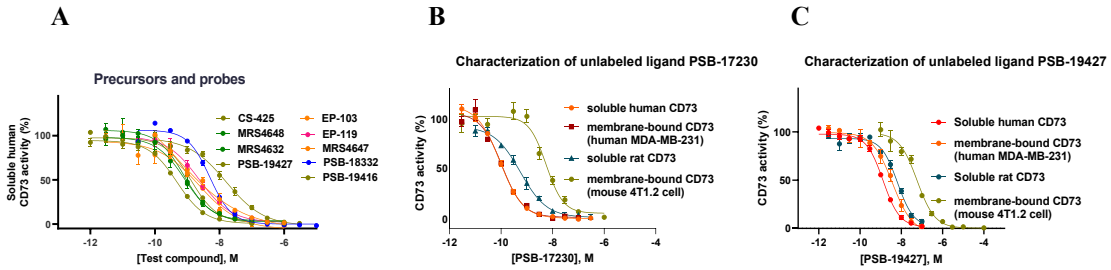


Figure 81. Concentration−inhibition curves. **A**) Labeled probes and precursors at recombinant soluble human ecto-5'-nucleotidase (K_M = 17 µM). **B**) Characterization of PSB-17230 in different species of CD73. **C**) Characterization of PSB-19427 in different species of CD73. Substrate (AMP) concentration = 5 µM. Data points are mean of three independent experiments performed in duplicates. Error bars represent the standard error of the mean (SEM).

Next, full characterization of PSB-17230 and PSB-19427 and the fluorescent probe EP-119 were carried out at different preparations of CD73 (**Table 19**, **Figure 81B-C**).

Table 19. Characterization of PSB-17230 and PSB-19427 at CD73 of different species

Test compound	K_i ± SEM (nM)			
	Human soluble CD73[a]	Human membrane-bound CD73[b]	Rat soluble CD73[c]	Mouse membrane-bound CD73[d]
PSB-19427	**1.02** ± 0.11	**2.78** ± 0.47	**6.09** ± 0.74	**47.8** ± 10.5
PSB-17230	**0.0733** ± 0.0013*	**0.0891** ± 0.0111*	**0.567** ± 0.086	**5.31** ± 0.91
EP-119	**1.66** ± 0.18	**2.32** ± 0.27	ND	ND

[a] Soluble recombinant human ecto-5'-nucleotidase enzyme (K_M17 µM, substrate [AMP] 5 µM)
[b] Membrane preparation of human TNBC (MDA-MB-231 cell) (K_M 14.8 µM, substrate [AMP] 5 µM)
[c] Soluble recombinant rat ecto-5'-nucleotidase enzyme (K_M 59 µM, substrate [AMP] 5 µM)
[d] Membrane preparation of mouse 4T1.2 breast cancer cell (K_M 67.6 µM, substrate [AMP] 5 µM)
ND: not determined. * Data obtained in collaboration with Dr. Christian Renn. Performed by Dr. Christian Renn

5.1.6. Conclusions and outlook

Several modifications on the lead structures (PSB-12651, K_i = 0.134 nM) and PSB-12489 (K_i = 0.318 nM) were designed, synthesized and evaluated leading to comprehensive SAR studies (**Figure 82A**). Compounds with increased potency were obtained (PSB-19294, K_i = 0.0334 nM, 4-fold improvement, and PSB-19301, K_i = 0.0502 nM, 6-fold improvement compared to lead structures PSB-12651and PSB-12489, respectively).

An interesting result was obtained when testing the *R*- and *S*-isomers of AMPCP derivatives with an N^6-α-methylbenzyl substituent (e.g. PSB-19294, PSB-19296, GR373 and GR397). The human but not the rat enzyme was found to be stereoselective for the *S*-isomer in both N^6-mono- and N^6,N^6-di-substituted derivatives. We suggest that this species difference could be attributed to a new binding mode adopted by the *S*-isomer which is favored only in the human species. The crystal structures of the human CD73 in complex with the *R*- and *S*-diastereomers will be resolved soon and should explain the difference (Prof. Norbert Sträter, University of Leipzig). It will also be interesting to check if mouse CD73 will show the same unselectivity exhibited by rat CD73. Future studies using soluble mouse CD73 recombinantly expressed in *Sf*9 insect cell are planned.

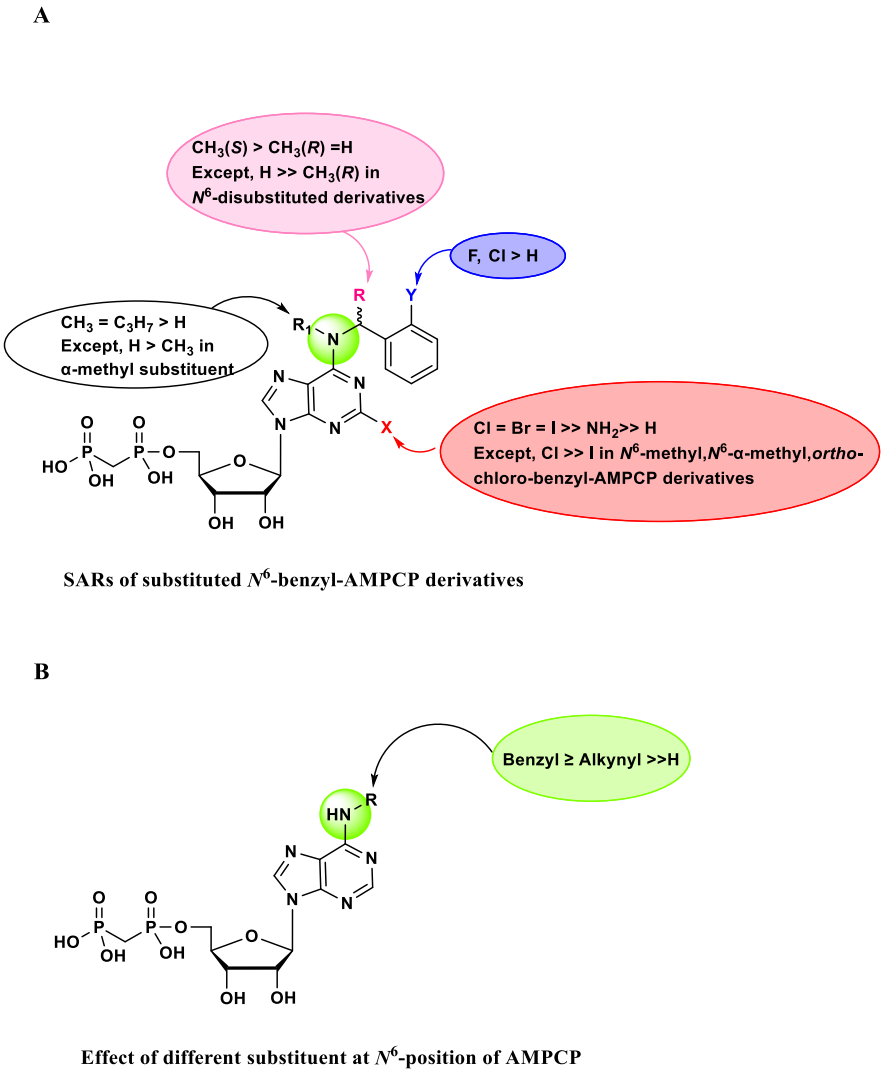


Figure 82. **A**) Summary of structure-activity relationships of N^6-substitued AMPCP derivatives. **B**) Effect of different substituent at the exocyclic amino group of the adenine ring.

When exploring the C2 pocket with halogen of different atomic sizes, no significant preference was observed, and all tested halogens (chlorine, bromine and iodine) were similarly active. With introduction of an α-methyl group, a 2-fold preference for chlorine (PSB-14650, PSB-19294) over bromine (EP-049, EP-043**)** was created, further study with iodine is proposed for more investigation. In another example, huge preference was observed for chlorine over iodine (Cl, GR316, K_i = 0.0746 nM, 20-fold higher vs. I, GR310, K_i = 1.77 nM) which necessitate further exploration.

Furthermore, N^6-alkynyl-AMPCP and 2-substituted AMPCP derivatives were obtained and studied representing molecules with comparable potency to N^6-benzyl-AMPCP (**Figure 82B**) but with reduced molecular weight.

No improvement was seen in 7-deaza-AMPCP derivatives that have been synthesized and tested so far. However, resynthesis of the published most potent 7-deaza-AMPCP derivative and its co-crystallization with human CD73 is proposed to study the significance of N7 in the interactions inside the binding pocket.

Several fluorescent probes covering green and red spectra and radiolabeled ligands were obtained and their biological activity were fully characterized in different species. Successful development of assays and imaging procedures using these tracers was also achieved.

5.2. Biological evaluation of a series of nucleotide mimetic at CD73

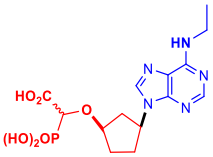
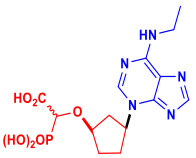
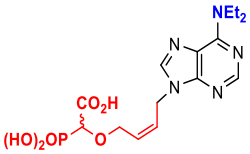
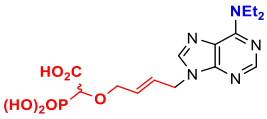
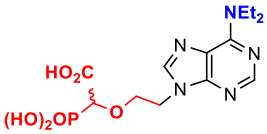
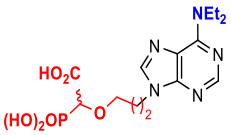
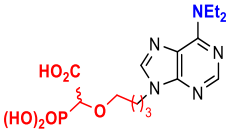
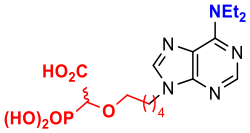
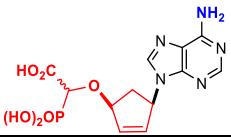
Aim of the project

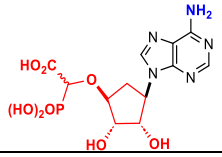
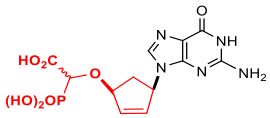
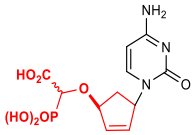
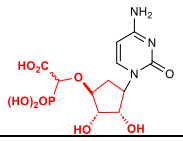
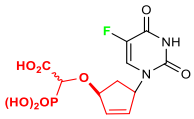
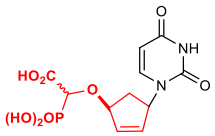
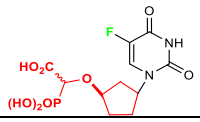
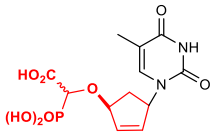
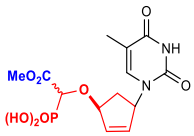
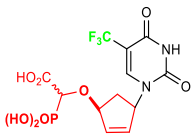
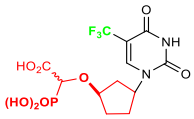
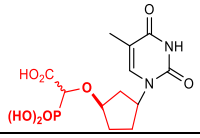
A library of nucleotide mimetics (α-carboxy-phosphononucleosides) was designed and synthesized by a collaboration partner (Prof. Anita R. Maguire, School of Chemistry, University College Cork, Ireland) for activity testing at human ectonucleotidases, CD73 and CD39.

5.2.1. Pharmacological test results

A previously published enzyme inhibition assay employing [2,8-^{3}H]AMP (5 μM) as a substrate was used for the screening of the provided compounds at 100 μM concentration against soluble human CD73 (**Table 20**).[260] Screening results are shown on **Figure 83A** and concentration-inhibition curve for the hit compound Cork82 is depicted in **Figure 83B**.

Table 20. Screening test results of Cork-compounds on **CD73** and **CD39**.

Test compound	Structure	Inhibition of soluble **CD73** at 100 µM (%) ± SEM (IC_{50} ± SEM, µM) [a]	Inhibition of **CD39** at 100 µM (%) ± SEM (IC_{50} ± SEM, µM)[b]
Phosphonoacetic acid		**0**	ND
Adenine-based compounds			
Cork72		**-33** ± 17	ND
Cork73		**-49** ± 3	ND
Cork76 (batch AJF-9-58)		**24** ± 7	**15** ± 2
Cork77 (batch AJF-9-61)		**30** ± 14	**10** ± 1
Cork78 (batch AJF-9-57)		**8** ± 7	**14** ± 5
Cork79 (batch AJF-9-59)		**24** ± 9	**11** ± 2
Cork80 (batch AJF-9-54)		**17** ± 5	**15** ± 2
Cork81 (batch AJF-9-60)		**26** ± 10	**20** ± 3
Cork82		**45** ± 5 (**16.8** ± 3.1)	**55** ± 4 (**153** ± 23)

Cork84		**36** ± 4	**59** ± 2 (**101** ± 26)
Guanine-based compounds			
Cork83		**34** ± 4	**30** ± 3
Cytosine-based compounds			
Cork74		**22** ± 6	**64** ± 3 (**296** ± 35)
Cork85		**0** ± 3	**28** ± 4
Uracil-based compounds			
Cork42 (batch OL-1-43)		**21** ± 8	**34** ± 8 (**391** ± 65)
Cork75 (batch OL-1-46)		**16** ± 5	**48** ± 7 (**159** ± 21)
Cork88		**14** ± 4	**65** ± 1 (**111** ± 23)
Thymine-based compounds			
Cork37 (batch AF-22/04B)		**23** ± 4	**9** ± 5
Cork36 (batch AF-22/04A)		**18** ± 9	**7** ± 1
Cork86		**-11** ± 6	**9** ± 2
Cork87		**19** ± 2	**75** ± 2 (**86.3** ± 4.4)
Cork89		**25** ± 3	**-1** ± 2

[a] Soluble recombinant human ecto-5'-nucleotidase enzyme (K_M value 17 µM), substrate (AMP) concentration 5 µM. [b] experiments were conducted by Dr. Laura Schäkel. ND: not determined

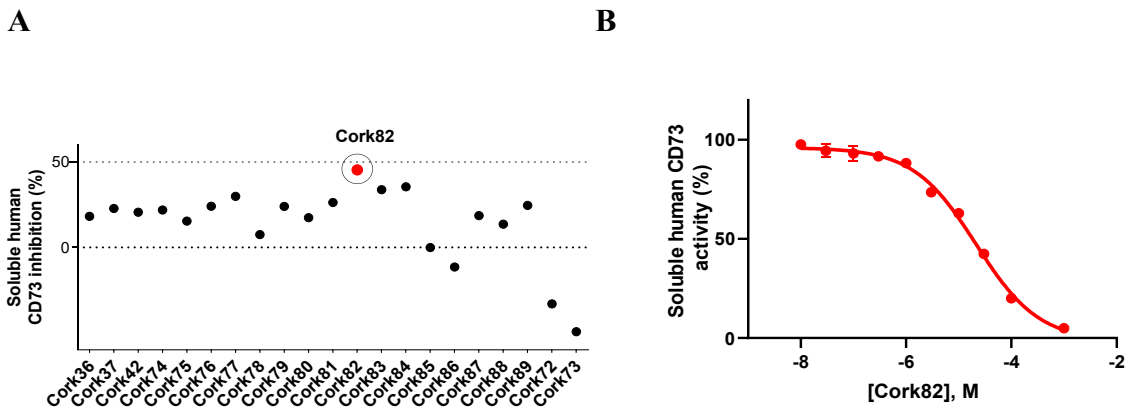


Figure 83. **A**) Screening results of Cork compounds at soluble human ecto-5'-nucleotidase (CD73) at 100 µM. **B**) Concentration-inhibition curve for Cork82 at soluble human ecto-5'-nucleotidase (K_M = 17 µM). Data points represent means ± SEM of at least three independent experiments, each performed in duplicates.

Structure-activity relationships

Phosphonoacetic acid was tested as a control and found to exhibit no inhibitory activity against CD73. Among the adenine-based derivatives, activity towards both CD39 and CD73 was increased in cyclic as compared to acyclic ribose analogs. At CD73, unsaturated cyclopentenyl substitution was better tolerated than 2,3-dihydroxycyclopentyl substitution and provided the most potent CD37 inhibitor in this series (Cork82, IC_{50} = 16.8 ± 3.1µM vs. Cork84, percent inhibition = 36%), while at CD39 they were equipotent (Cork82, IC_{50} = 153 ± 23 µM; Cork84, IC_{50} = 101 ± 26 µM). Structures containing an N^6-ethyl residue were slightly activating CD73 regardless of whether their cyclopentane ring was attached to N3 (Cork73, percent inhibition = -46%) or N9 (Cork72, percent inhibition = -33%) of the adenine base. The guanine derivative Cork83 (percent inhibition = 34%) was less potent compared to the corresponding adenine derivative (Cork82, percent inhibition = 46%).

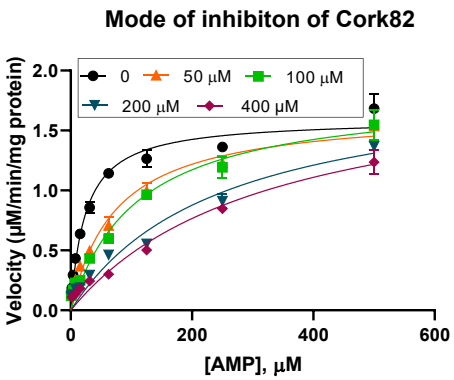
The cytosine derivative Cork83 (percent inhibition = 34% (CD37), 30% (CD39)) was less potent than the corresponding adenine derivative Cork82 (percent inhibition = 46% (CD73), 55% (CD39)) at both targets. Similar to adenine derivatives, the unsaturated cyclopentenyl residue (Cork74, 22% (CD73), 296 µM (CD39)) was superior to the di-hydroxycyclopentyl moiety (Cork85, 0% (CD73), 28% (CD39)).

Uracil derivatives showed higher inhibitory potency at CD39 than at CD73 (e.g., Cork88, 14% at CD73, 65% at CD39). In contrast to CD73, 5-F-substitution resulted in an around 2.5-fold drop in potency at CD39 (5-F, Cork42, IC_{50} = 391 µM vs. Cork75, IC_{50} = 159 µM). The saturated cyclopentane (Cork88, IC_{50} = 111 µM) was favored over the unsaturated cyclopentenyl (Cork42, IC_{50} = 391 µM).

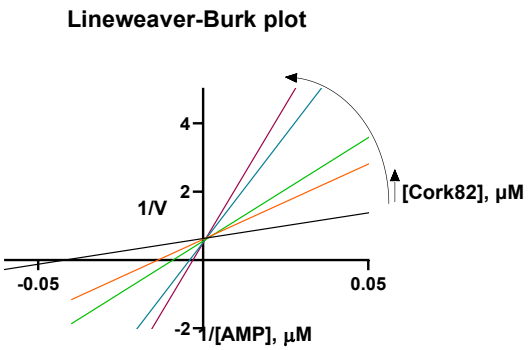
Thymine derivatives showed the lowest potency at CD39. However, CF_3 substitution at position 5 instead of CH_3 yielded the most potent CD39 inhibitor in this series with an IC_{50} of 86.3 µM (Cork87).

The mode of inhibition of Cork82 at soluble human CD73 was investigated. The obtained results (**Figure 84**) indicated a competitive mode of inhibition. With increasing concentrations of Cork82, the K_M value increased, while V_{max} remained unchanged.

A



B



C

Best-fit value for K_M and V_{max}

Cork82 concentration (µM)	0	50	100	200	400
K_M (µM)	24	73.4	110	246	325
V_{max} (µmol/min/mg protein)	1.60	1.67	1.82	1.96	2.01

Figure 84. Determination of mode of inhibition of CD73 by Cork82. **A**) Michaelis-Menten kinetics at different inhibitor concentrations. **B**) Lineweaver-Burk plot, all lines intersected at the same point on the y-axis indicating unchanged V_{max} value, while intersecting at different points on the x-axis indicating changed K_M values (increased), which indicated a competitive type of inhibition. **C**) Best-fit values for K_M and V_{max} at different concentrations of Cork82.

5.2.2. Summary and outlook

Adenine-based α-carboxy-phosphononucleoside derivatives were more potent inhibitors of CD73 than derivatives of other nucleobases (Cork82, IC_{50} = 16.8 μM) and showed a competitive mode of inhibition. The adenine base was previously reported to exhibit the highest activity towards CD73 among other nucleobases.[74] Cork82 is a dual CD73/CD39 inhibitor. However, it is around 9-fold more potent at CD73 compared to CD39 (IC_{50} (CD39) = 153 μM). Its dihydroxy derivative, Cork84, was more potent at CD39 (IC_{50} (CD39) = 101 μM). Thymine derivative Cork87 (5-CF_3) was the most potent CD39 inhibitor in this series with an IC_{50} of 86.3 μM. Its uracil analog, Cork88, with 5-F substitution exhibited similar potency (IC_{50} = 111 μM).

Based on the obtained results we suggested that, dihydroxy analogs of Cork87 and Cork88 should be synthesized and tested. In addition, an analog of Cork88 without 5-F substitution would be of interest as it seemed to decrease the activity against CD39.

5.3. Effects of adenine-derived fragments and nucleotide mimetics on the activity of soluble human CD73

Aim of the project

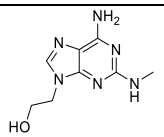
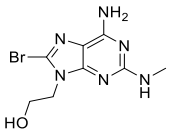
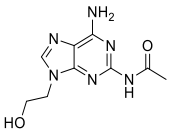
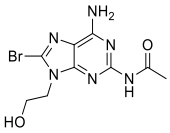
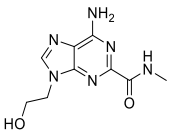
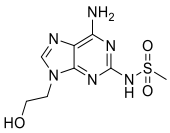
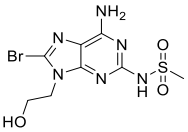
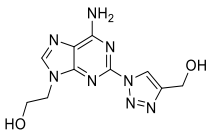
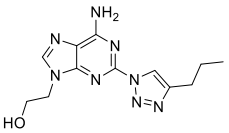
In this subproject, a series of adenine-derived fragments were synthesized as dual A_{2A}/CD73 inhibitors in the research group of Prof. Jens Carlsson (Uppsala University, Uppsala, Sweden). These fragments were designed based on the crystal structure of soluble human CD73 in complex with adenosine in an open conformation (PDB 4H2F). Furthermore, a series of 16 nucleotide analogs were designed based on the closed conformation of soluble human CD73 in complex with AMPCP (PDB 4H2I). Activity testing was conducted at recombinant soluble human CD73. ^{3}H-labeled AMP was used as a substrate at a concentration of 5 μM, and the formation of ^{3}H-labeled adenosine was determined according to Freundlieb et al., 2014.[170]

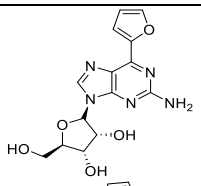
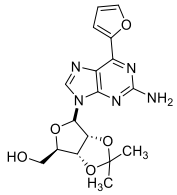
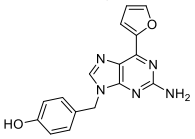
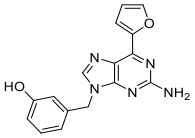
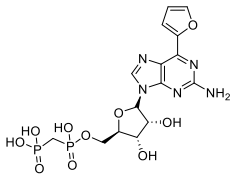
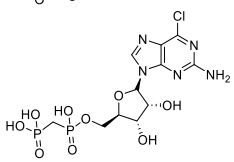
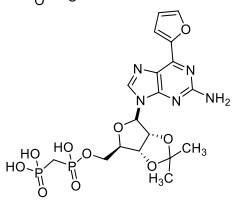
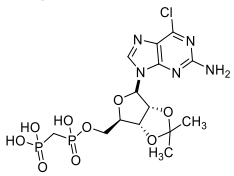
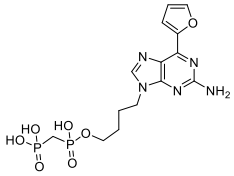
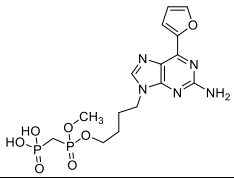
5.3.1. Results

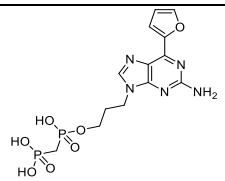
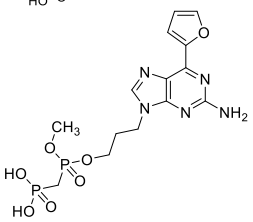
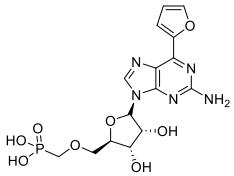
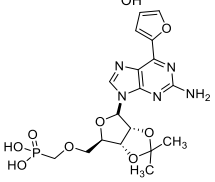
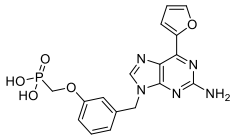
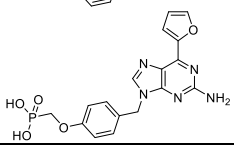
Adenine-based fragments were screened at a high concentration (100 μM) using recombinant soluble human CD73. The obtained results (**Table 21** and **Figure 85A)**

indicated that, none of the tested adenine derivatives showed inhibition of CD73. In contrast, they appeared to activate the enzymatic activity of CD73 to different extents. This activation was further confirmed in membrane-bound human CD73 using membrane preparations of MDA-MB-231 cell line (**Figure 85B**). A concentration-activation curve for the most potent activator, DV496, showed an EC_{50} value of 19.7 μM (**Figure 85C**).

Table 21. Activity of adenine-derived fragments and nucleotide mimetics (provided by Prof. Carlsson) at soluble human ecto-5'-nucleotidase enzyme

Test compound	Structure	Inhibition results at 100 μM or 10 μM (% ± SEM) [a]	K_i (μM ± SEM)
Adenine-based fragments			
DV462		-40 ± 8 (100 μM)	ND [b]
DV494		-54 ± 6 (100 μM)	ND
DV460		-25 ± 9 (100 μM)	ND
DV464		-46 ± 7 (100 μM)	ND
DV497		-38 ± 7 (100 μM)	ND
DV489		-82 ± 19 (100 μM)	ND
DV493		-36 ± 7 (100 μM)	ND
DV495		-73 ± 23 (100 μM)	ND
DV496		-103 ± 1 (100 μM)	19.7 μM (EC_{50}) [maximum activation, 157%]

Nucleotide-based mimetics			
DV 833		27 ± 2 (10 µM)	ND
DV 841		6 ± 8 (10 µM)	ND
DV 845		10 ± 7 (10 µM)	ND
DV 846		25 ± 13 (10 µM)	ND
DV 837		100 ± 2 (10 µM)	0.000748 ± 0.000126
DV 835		95 ± 5 (10 µM)	0.0425 ± 0.0143 (published inhibitor, K_i = 23.6 nM [78])
DV 843		77 ± 2 (10 µM)	0.788 ± 0.529
DV 842		76 ± 5 (10 µM)	1.56 ± 0.38
DV 838F1		61 ± 8 (10 µM)	6.61 ± 1.65
DV 838F2		16 ± 8 (10 µM)	ND

DV 844F1		43 ± 5 (10 µM)	ND
DV 844F2		17 ± 2 (10 µM)	ND
DV 860		95 ± 8 (10 µM)	0.692 ± 0.001
DV 854		38 ± 4 (10 µM)	ND
DV 855		74 ± 2 (10 µM)	1.44 ± 0.53
DV 856		28 ± 10 (10 µM)	ND

[a] Testing of nucleotide-mimetics was conducted by Katharina Sylvester. All experiments were performed using soluble recombinant human ecto-5'-nucleotidase enzyme (K_M = 17 µM). [b] not determined

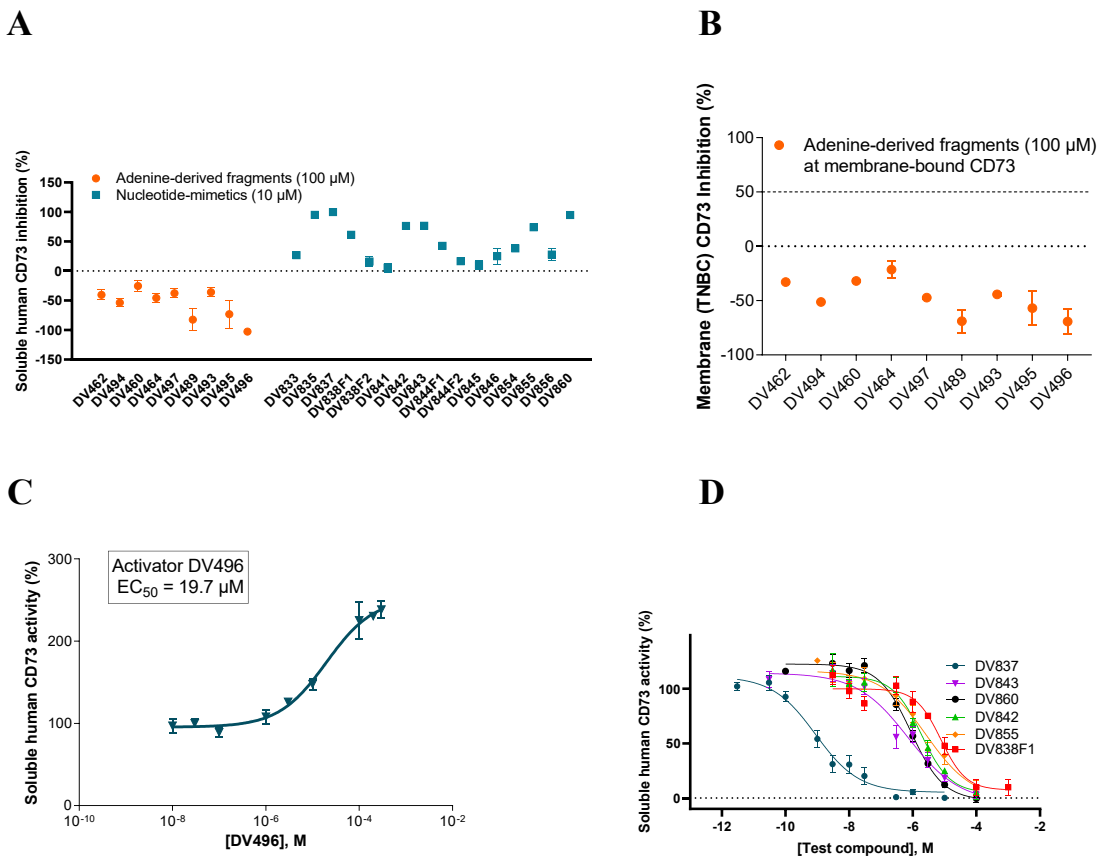


Figure 85. **A**) Screening results of adenine fragments and nucleotide-mimetics at soluble human CD73 (K_M = 17 µM). **B**) Screening results of adenine fragments at membrane-bound CD73 (K_M = 14 µM, n=2). **C**) Concentration-activation curve for DV496 using soluble human CD73. **D**) Concentration-inhibition curves for potent nucleotide analogs at soluble human CD73 (K_M = 17 µM). Data points are means ± SEM of three independent experiments, performed in duplicates.

Results for nucleotide analogs are summarized in **Table 21** and concentration-inhibition curves are depicted in **Figure 85D**. Generally, this scaffold showed weak to moderate inhibitory activity towards soluble human CD73. DV837, an AMPCP derivative in which the amino group at position 6 of adenine base was substituted with furan ring and an amino group was introduced at C2 position, was the most active molecule identified among this series (K_i = 0.000748 µM (0.748 nM)). This high inhibitory activity of DV837 highlighted the key role of Zn^{2+}-coordinating group in the potency of competitive inhibitors. Moreover, DV837 showed nearly 120-fold higher activity at soluble human CD73 compared to AMPCP (K_i = 88.4 nM),[210] and around 50-fold compared to 2-amino-AMPCP (PSB12676, K_i = 38.8 nM).[78] This finding indicated that, a five-membered heterocyclic aromatic ring at C6 of adenine ring was better tolerated than an amino group. Chlorine at C6 was less tolerated than furan, yielded compound DV 835 (K_i = 0.0425 µM) with greater than 50-

fold drop in potency compared to DV837 (K_i = 0.000748 µM). This compound, DV835, was previously designed and synthesized in our group, it showed a K_i value of 23.6 nM.[78] Protection of the 2,3-hydroxyl groups of the ribose sugar of DV837 provided DV843 (K_i = 0.788 µM) with greater than 1000-fold drop in inhibitory activity against human CD73 compared to DV837 (K_i = 0.000748 µM). Replacing the ribose ring of DV837 with carbon atoms linker was generally unfavorable. For example, with four carbon atoms linker, DV838F1 (K_i = 6.61 µM) showed 9000-fold drop compared to DV837.
Coupling of the inactive nucleoside structure in molecule DV833 to a monophosphonate group at the 5' of the ribose moiety gave an inhibitor (DV860) with a K_i value of 0.692 µM.

5.3.2. Summary and outlook

Adenine-based fragments were found to act as activators of soluble human CD73. The most potent activator identified was DV496 with an EC_{50} value of 19.7 µM (maximum activation = 157%). Activation of CD73 is interesting with regard to inflammatory and cardiovascular diseases. DV496 should be more thoroughly studied at membrane-bound CD73. Moreover, nucleotide mimetics were evaluated for CD73 inhibition. The most potent inhibitor of CD73 identified in this series was the AMPCP-based compound DV837 with a K_i value of 0.748 nM. The potency of the 2-amino,6-furanyl-substituted AMPCP derivative indicated that an aromatic ring, directly attached to C8 of the purine core, is well tolerated by CD73.

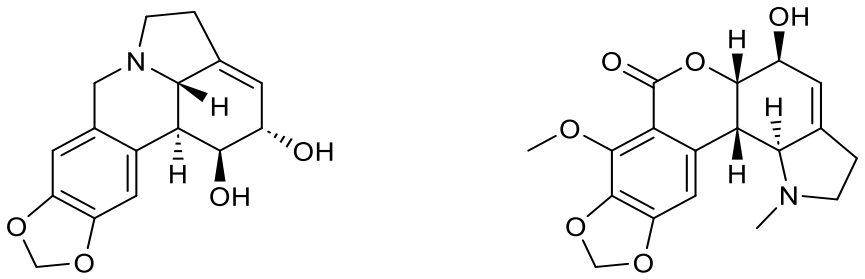
5.4. Identification of non-nucleotide-derived inhibitors of CD73

Aim of the project

Alkaloids as naturally occurring secondary metabolites have shown a wide range of biological activities including cytotoxic, antibacterial, antifungal, antimalarial, antiviral and analgesic effects. In a recent study, lycorine and candimine alkaloids (**Figure 86**) from plants of the family *Amaryllidaceae* have been tested against *Trichomonas vaginalis* parasite ecto-5'-nucleotidase which is suggested to be involved in mechanisms related to host–parasite interactions. Both alkaloids inhibited ecto-5'-nucleotidase activity without affecting its expression level relative to control.[304]

A collaboration project with Prof. Edgar Haak (Institute of Chemistry, University of Magdeburg) was subsequently initiated who provided a compound library based on

terpenoid- or alkaloid-like structures for activity testing and further characterization at human ecto-5'- nucleotidase (CD73) with the aim of identifying new scaffolds that possess drug-like properties.



Lycorine Candimine

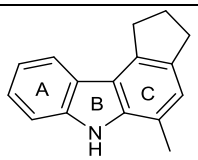
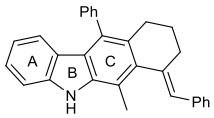
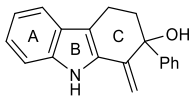
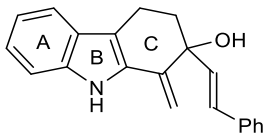
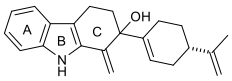
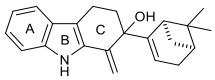
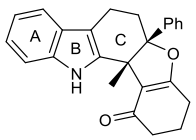
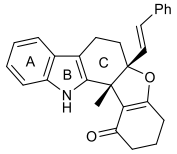
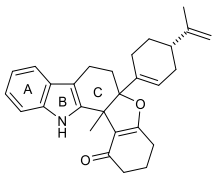
Figure 86. Alkaloids active against *Trichomonas vaginalis* parasite ecto-5'-nucleotidase.[304]

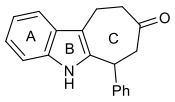
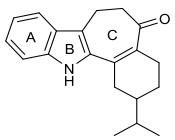
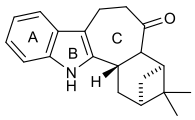
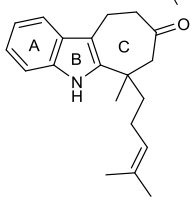
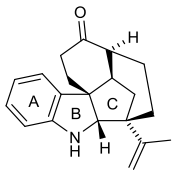
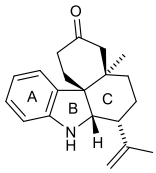
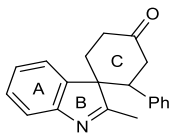
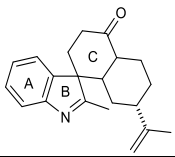
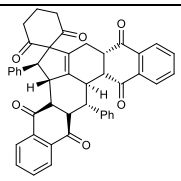
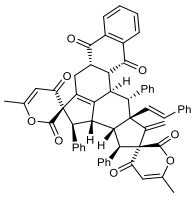
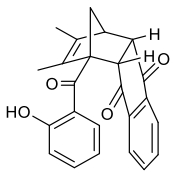
5.4.1. Pharmacological evaluation results

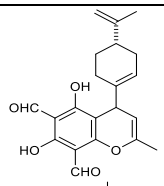
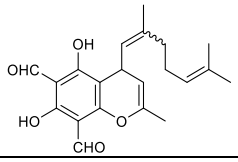
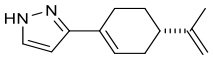
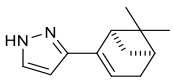
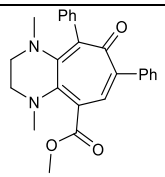
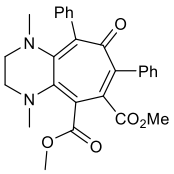
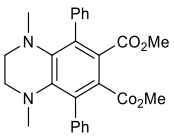
Test compounds were evaluated at recombinant soluble human CD73 expressed in *Sf*9 insect cell using our published enzyme inhibition assay method.[170] The test compounds were further evaluated for selectivity against human ectonucleoside triphosphate diphosphohydrolase-1 (CD39) enzyme. Results of screening and IC_{50} value determination are listed in **Table 22**. Concentration-inhibition curves for compounds that showed greater than 50% inhibition at 10 µM concentration are depicted in **Figure 87**.

For a better presentation of data and for ease of understanding, this compound library is divided into two groups: indole-based and non-indole-based compounds. The first group contains series one to six, in which the nitrogen-containing base is indole (ring A & B, **Table 22**, compounds PZB17718001A- PZB17718020A). In the second group, the indole is replaced by different scaffolds, namely anthraquinone (series 7, compounds PZB17718021A- PZB17718023A), chromene (series 8, compounds PZB17718024A, PZB17718025A), pyrazole (series 9, compounds PZB17718026A, PZB17718027A), or piperazine (series 10 & 11, compounds PZB17718028A- PZB17718030A).

Table 22. Test results for **non-nucleotide derivatives** at soluble human ecto-5'-nucleotidase (CD73) and selectivity versus human ectonucleoside triphosphate diphosphohydrolase-1 (CD39)

Test compound	Structure	**Soluble human CD73** [a] **IC_{50} ± SEM (µM) [maximal inhibition]** (or % inhibition at indicated concentration)	**Human CD39** inhibition at 20 µM (%) *
	Indole-based inhibitors		
PZB17718001A (1a)		>10 (39%)	3%
PZB17718002A (1b)		**0.409** ± 0.011 [100%]	12%
PZB17718004A (2a)		**0.826** ± 0.027 [100%]	-5%
PZB17718005A (2b)		**0.350** ± 0.056 [100%]	-29%
PZB17718006A (2c)		**0.609** ± 0.039 [93%]	2%
PZB17718007A (2d)		**0.512** ± 0.046 [97%]	11%
PZB17718009A (3a)		**1.01**± 0.040 [100%]	12%
PZB17718010A (3b)		**1.81** ± 0.11 [79%]	3%
PZB17718011A (3c)		**1.22** ± 0.09 [100%]	-19%

PZB17718013A (4a)		**2.39** ± 0.47 [100%]	-5%
PZB17718014A (4b)		**1.42** ± 0.27 [100%]	-2%
PZB17718015A (4c)		**5.00** (n=1) [100%]	-4%
PZB17718016A (4d)		**3.36** ± 0.64 [100%]	12%
PZB17718017A (5a)		**0.844** ± 0.079 [82%]	-1%
PZB17718018A (5b)		**0.979** ± 0.033 [100%]	11%
PZB17718019A (6a)		**0.423** ± 0.076 [100%]	-5%
PZB17718020A (6b)		**0.691** ± 0.070 [90%]	0%
Anthraquinone-based compounds			
PZB17718021A (7a)		**0.964** ± 0.016 [80%]	-14%
PZB17718022A (7b)		**0.241** ± 0.028 [65%]	-22%
PZB17718023A (7c)		**1.88** ± 0.24 [90%]	-8%

Chromene-based compounds			
PZB17718024A (8a)		>10 (38%)	50% **33.5** ± 53.1 (IC_{50} ± SD, µM, n=4)
PZB17718025A (8b)		>10 (43%)	32%
Pyrazole -based compounds			
PZB17718026A (9a)		>10 (49%)	-1%
PZB17718027A (9b)		>10 (33%)	-10%
Piperazine-based compounds			
PZB17718028A (10a)		>10 (13%)	-12%
PZB17718029A (10b)		>10 (23%)	-3%
PZB17718030A (11a)		>10 (12%)	-14%

[a] Soluble recombinant human ecto-5'-nucleotidase enzyme (K_M value 17 µM); Ph: phenyl ring; Me: methyl
*CD39 experiments were conducted by Dr. Laura Schäkel

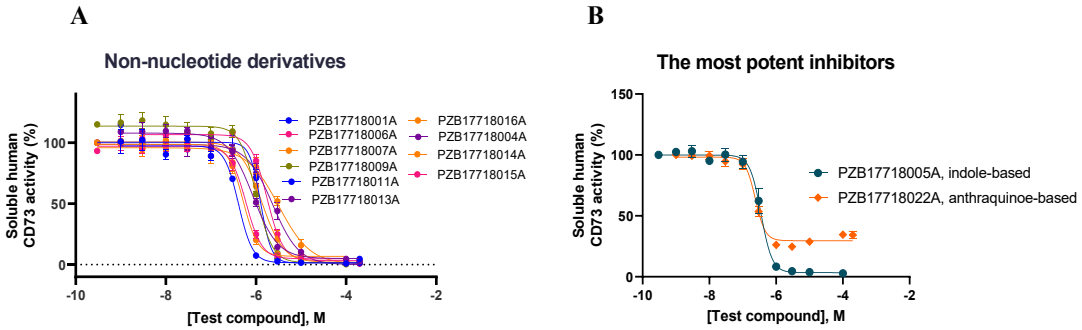


Figure 87. **A**) Concentration−inhibition curves of selected non-nucleotide derivatives at recombinant soluble human ecto-5'-nucleotidase (K_M = 17 µM). **B**) Concentration−inhibition curves of the most potent alkaloid mimetics inhibitors among the series (PZB17718005A and PZB17718022A) at recombinant soluble human ecto-5'-

nucleotidase (K_M = 17 μM). Substrate (AMP) concentration = 5 μM. Data points are mean of three independent experiments performed in duplicates. Error bars represent the standard error of the mean (SEM).

Structure-activity relationships (SARs)

Indole-based compounds

Series 1

The carbazole is obtained through fusion of an aromatic 6-membered ring (ring C) to the indole moiety. A cyclopentane fused at position 3 and 4 of ring C provided compound PZB17718001A (**Table 22**) with a weak inhibitory activity against human CD73. Replacing the cyclopentane ring with an α-(cyclohexylidenemethyl)-benzene (or a (phenylmethylene)cyclohexane) fused at position 2, and 3 of ring C, in addition to a phenyl group at position 4 of ring C increased the inhibitory potency (PZB17718002A, IC_{50} = 0.409 μM, **Table 22**).

Series 2

Replacing aromatic ring C with the 1- methylenecyclohexanyl ring was tolerated, resulting in an IC_{50} value of 0.826 μM in the presence of a 2-hydroxy-2-phenyl substitution (PZB17718004A, IC_{50} = 0.826 μM). Employing a propene linker between the 2-phenyl group and the saturated hexyl ring C of PZB17718004A provided the most potent indole-based inhibitor (PZB17718005A) with an IC_{50} value of 0.350 μM.

Exchanging the phenyl ring at position 2 of ring C of PZB17718004A with a monoterpene limonene (PZB17718006A, IC_{50} = 0.609 μM) or pinene (PZB17718007A, IC_{50} = 0.512 μM) resulted in less potent compounds than PZB17718005A (IC_{50} = 0.350 μM).

Series 3

Different compounds were obtained through a modification involving the hydroxyl group to benzofuran-4-one in series 2 compounds PZB17718004A, PZB17718005A, and PZB17718006A. The obtained compounds (PZB17718009A, PZB17718010A and PZB17718011A) were still active with IC_{50} values in the range of 1 to 2 μM. However, the hydroxyl group is superior to the benzofuran-4-one (e.g. PZB17718005A, IC_{50} = 0.350 μM vs PZB17718010A, IC_{50} = 1.81 μM).

Series 4

Replacement of the 6-membered ring C of series 1 with a 7-member ring (cycloheptan-1-one) as in compounds PZB17718013A, PZB17718014A, PZB17718015A, and PZB17718016A was not tolerated and led to a drop in potency particularly in the presence of a fused terpene (pinene) at position 1 and 2 of the cycloheptan-1-one ring (PZB17718015A, IC_{50} = 5 µM).

Series 5

Ring C was changed either to a 5-membered ring fused to modified nootkatone terpene (PZB17718017A, IC_{50} = 0.844 µM) or nootkatone was directly fused to the indole ring (PZB17718018A, IC_{50} = 0.979 µM). No significant difference was observed when modified nootkatone terpene was fused directly to the indole or bridged through a 5-membered ring.

Series 6

Spiro compounds either with substituted cyclohexanone (PZB17718019A, IC_{50} = 0.423 µM) or modified terpene (PZB17718020A, IC_{50} = 0.691 µM) at position 3 of the indole base were investigated. Both compounds inhibited soluble human CD73, however, the 3-phenyl cyclohexanone was around 2-fold preferred over the terpene.

A summary of the SARs of the indole-based test compounds is shown in **Figure 88**.

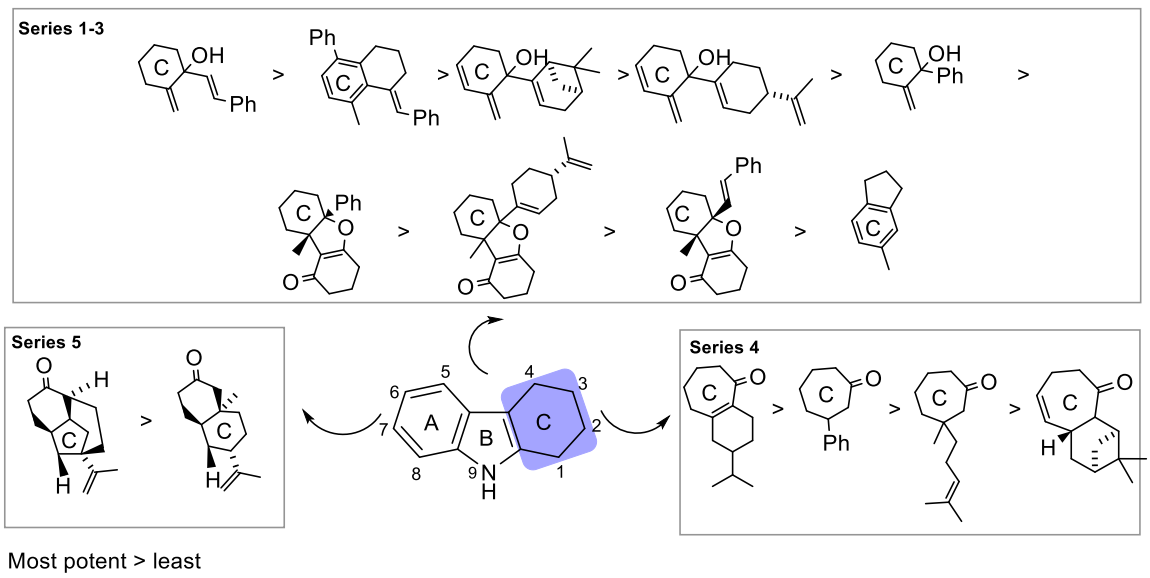


Figure 88. Structure-activity relationships of **indole-based** inhibitors (compounds PZB17718001A- PZB17718020A).

Non-indole-based compounds

Series 7

A variously substituted anthraquinone nucleus was evaluated. All tested derivatives (PZB17718021A (IC_{50} = 0.964 μM), PZB17718022A (IC_{50} = 0.241 μM) and PZB17718023A (IC_{50} = 1.88 μM)) inhibited human CD73 enzyme. Compound PZB17718022A was the most potent inhibitor identified among all series. However, the compound exhibited partial inhibition of 65% (IC_{50} = 0.241 μM) which might indicate an allosteric binding mode.

Series 8 & 9

Weak or no inhibitory activity (>10 μM) was found for chromene (PZB17718024A, PZB17718025A) and pyrazole (PZB17718026A, PZB17718027A) derivatives substituted with terpenoids.

Series 10 & 11

Piperazine fused to a 6-membered (PZB17718030A) or 7-membered (PZB17718028A, PZB17718029A) aromatic ring was assessed. No activity was detected.

The identified most potent indole-based CD73 inhibitor (PZB17718005A, IC_{50} = 0.350 μM) and anthraquinone-derived CD73 inhibitor (PZB17718022A, IC_{50} = 0.241 μM) were subjected to further characterization at membrane-bound CD73 natively expressed in triple negative human breast cancer cells MDA-MB-231 (membrane preparation from MDA-MB-231 cells were employed). Interestingly, these compounds lost their potency at the membrane-anchored enzyme (**Figure 89**). Testing of the two most potent inhibitors on membrane preparations derived from a mouse breast cancer cell line (4T1.2) provided similar results (no inhibition at concentrations up to 200 μM).

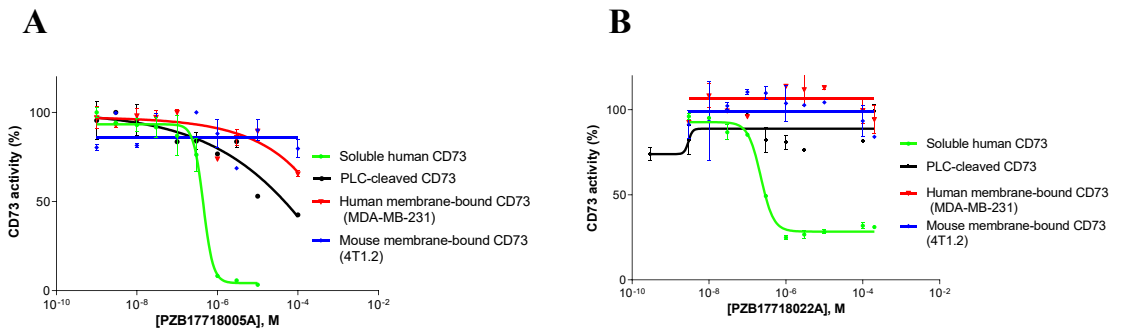


Figure 89. Characterization of the most potent inhibitors at soluble and membrane-anchored isoforms of CD73 enzyme. **A**) Concentration-inhibition curves for PZB17718005A. **B**) Concentration-inhibition curves for PZB17718022A. Recombinant soluble human ecto-5'-nucleotidase, K_M = 17 µM. PLC-cleaved CD73, K_M = 83 µM. Membrane preparation from triple negative breast cancer cell (MDA-MB-231), K_M = 14.8 µM. Membrane preparation of mouse 4T1.2 breast cancer cell, K_M = 67.6 µM. Substrate (AMP) concentration = 5 µM. Data points are mean of at least two independent experiments performed in duplicates. Error bars represent the standard error of the mean (SEM).

The observed discrepancy in the results between soluble and membrane-bound isoforms of CD73 could rely on the compounds being selective inhibitors of the soluble over the membrane-bound form of the enzyme. To investigate this possibility, membrane-bound CD73 from MDA-MB-231 cells was cleaved using phosphatidylinositol-specific phospholipase C (PLC). The same MDA-MB-231 cell line had been employed as a source for the membrane-bound enzyme. The activity of the most potent inhibitors, PZB17718005A and PZB17718022A, was then investigated using PLC-cleaved CD73. The compounds were however not active, as was it the case on the membrane-bound form.

Next, we investigated whether the His-tag at the recombinant soluble human enzyme had an effect on binding of the compounds. To this end, a new construct for expressing soluble human CD73 was generated in which a protease cleavage site was introduced before to the 6xHis-tag. This newly expressed CD73 was Histag-free (native) and was used to assess the activity of the identified most potent inhibitors. Similar results to those obtained with the His-tagged CD73 were obtained, indicating no significant impact exerted by the His-tag on the inhibitory activity of the newly identified scaffolds (**Figure 90**).

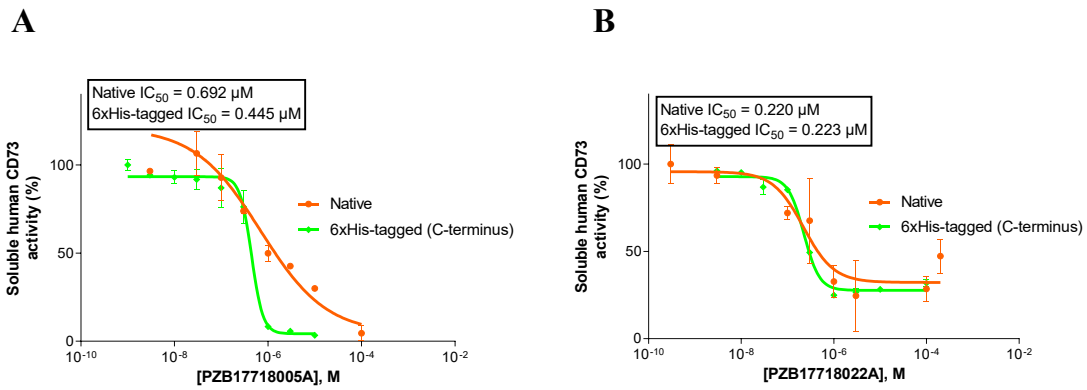


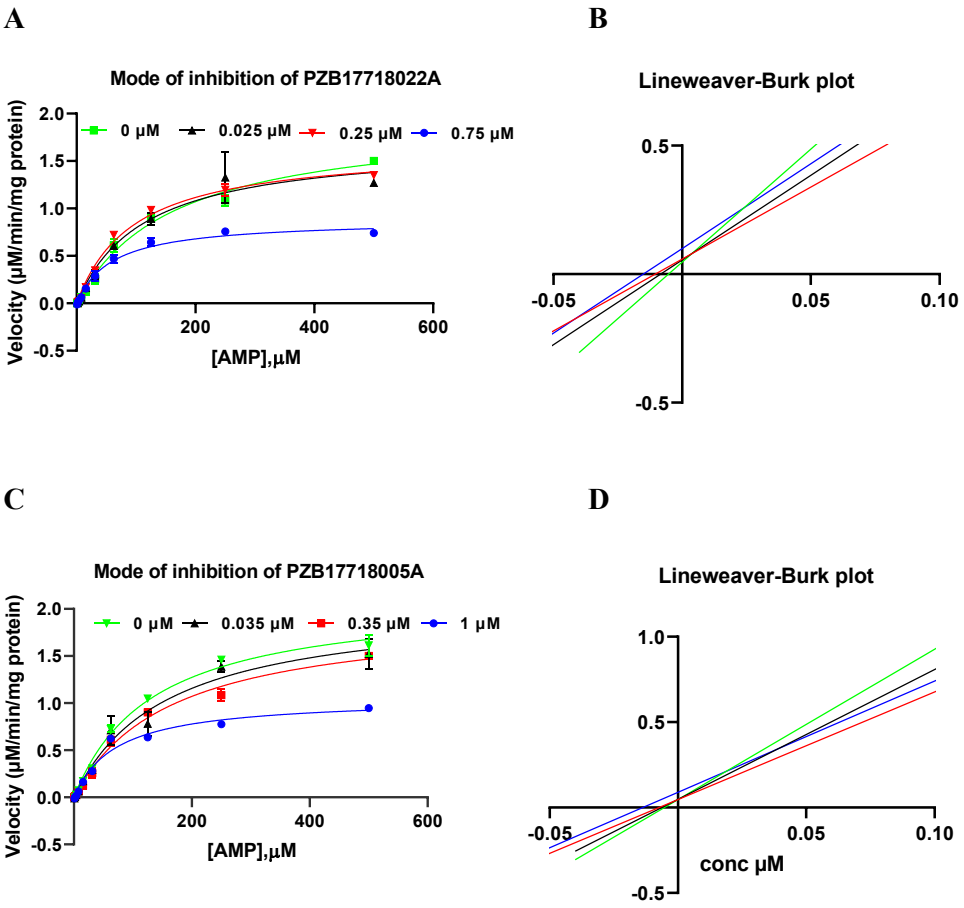
Figure 90. Characterization of the most potent inhibitors at native and His-tagged soluble human CD73. **A**) Concentration-inhibition curves for PZB17718005A. **B**) Concentration-inhibition curves for PZB17718022A. Recombinant soluble 6xHis-tagged ecto-5'-nucleotidase, K_M = 17 µM. Recombinant soluble native (His-tag-cleaved) ecto-5'-nucleotidase, K_M = 56 µM. Substrate (AMP) concentration = 5 µM. Data points are mean of one experiment performed in duplicates. Error bars represent the standard error of the mean (SEM).

Inactivity on the membrane-bound or PLC-cleaved CD73 derived from triple negative breast cancer cell line (MDA-MB-231) requires further evaluation. We propose this inactivity might arise from possible secondary modifications (mainly glycosylation) which is a disease trait in cancer. Glycosylation was previously reported to affect the catalytic function of the enzyme [22,69] however, further impact on allosteric binding sites might not be excluded. A thorough investigation using deglycosylated form of the membrane-bound CD73 is proposed.

Apoint to mention, similar discrepancy has been recently reported by Ghoteimi et al, 2023, in selected allosteric inhibitors based on 4,6-biaryl-2-thiopyridine scaffold investigated at soluble and membrane-bound CD73 (MDA-MB-231).[239] Dissimilarity was attributed to genetic variation of CD73 in MDA-MB-231 cells. They observed two transcripts, short and canonical CD73 as that earlier reported in hepatocellular carcinoma cells.[239]

Lastly, the mode of inhibition of the newly identified scaffolds using soluble human CD73 was investigated. The kinetics was monitored and the Michaels-Menten parameters were determined at different concentrations of the test compounds. The obtained values of K_M and V_{max} for both inhibitors (PZB17718022A and PZB17718005A) showed reduction with increasing inhibitor concentration (**Figure 91**) which indicates uncompetitive mode of

inhibition. In this type of inhibition, the inhibitor binds only to the E-S complex and not to the free enzyme, which leads to a decrease in E-S complex manifested by a lower V_{max} and K_M values. However, the obtained K_M value at inhibitor-free condition (K_M = 160 µM) was ca. 2-fold higher than that determined previously for the same soluble human enzyme (K_M = 65.2 µM). Moreover, no significant changes were observed in K_M and V_{max} values except with the highest concentration of the inhibitors.



Best-fit values for K_M and V_{max}

	K_M (µM)				V_{max} (µmol/min/mg)			
Test compound	0	0.035 µM	0.35 µM	1 µM	0	0.035 µM	0.35 µM	1 µM
PZB17718005A	160 ± 1	153 ± 18	125 ± 8	72 ± 20	1.9 ± 0.0	2.1 ± 0.2	2.1 ± 0.1	1.0 ± 0.1
	0	0.025 µM	0.25 µM	0.75 µM	0	0.025 µM	0.25 µM	0.75 µM
PZB17718022A	160 ± 1	120 ± 8	101 ± 11	67 ± 20	1.9 ± 0.0	1.7 ± 0.1	1.7 ± 0.0	0.9 ± 0.1

Figure 91. Studies on inhibition type at soluble human CD73 for the identified most potent inhibitors. **A&B**) Michaelis-Menten Kinetics and Lineweaver-Burk plot at different concentration of PZB17718022A. **C&D**) Michaelis-Menten Kinetics and Lineweaver-Burk plot at different concentrations of PZB17718005A. Data points are means ± SEM of at least two independent experiments, each performed in duplicates.

Selectivity Studies

Some alkaloids were previously reported to exhibit equipotent activity at *Trichomonas vaginalis* parasite CD73 and CD39.[304] Selectivity studies were thus initiated against human ectonucleoside triphosphate diphosphohydrolase-1 (CD39**)** enzyme at 20 μM (**Table 22**). All investigated compounds were inactive at CD39 except chromene derivatives which showed weak activity, (PZB17718024A, IC_{50} = 33.5 μM).

5.4.2. Summary and outlook

Biological results at recombinant soluble human CD73 identified several compounds with submicromolar inhibitory activity. The most potent indole derivative among the test compounds is PZB17718005A with an IC_{50} value of 0.350 μM. The anthraquinone-based PZB17718022A was the most potent inhibitor identified in this screening campaign (IC_{50} = 0.241 μM). However, only partial inhibition (65%) was observed suggesting that PZB17718022A acts as an allosteric inhibitor of CD73. Some other molecules were found active with IC_{50} values between 1-5 μM and 80-100 % maximal inhibition.

These compounds showed high selectivity for CD73 versus ectonucleoside triphosphate diphosphohydrolase-1 (CD39).

Both indole- and anthraquinone-based inhibitors exhibited an uncompetitive mode of inhibition (allosteric binding), the V_{max} and K_M values of the enzyme showing considerable decrease with increased inhibitor concentration.

Interestingly, these inhibitors were selectively inhibiting the recombinant soluble human CD73, but not the membrane-bound enzyme in MDA-MB-231 cell line. Further investigation using deglycosylated membrane-bound CD73 should be investigated next. It might be that these inhibitors bind to an allosteric site sensitive to changes in glycosylation of the enzyme. Recombinant expression of membrane-bound CD73 in *Sf*9 insect cells could be helpful for investigating this hypothesis.

In this study, the indole-based compounds constitute a newly identified scaffold for ecto-5'-nucleotidase inhibition. Further modification based on this initial structure-activity relationship would be recommended to improve the potency.

5.5. Xanthine derivatives as allosteric modulators of CD73

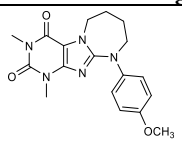
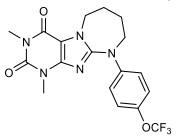
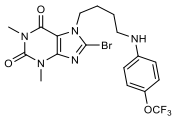
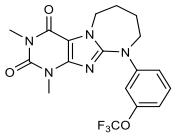
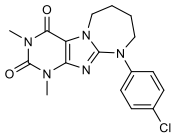
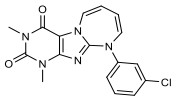
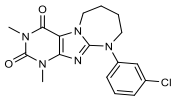
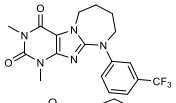
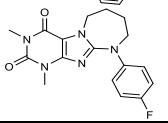
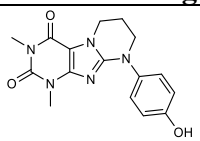
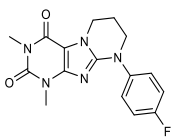
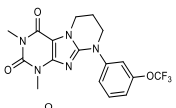
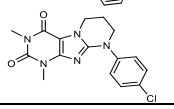
Aim of the project

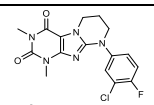
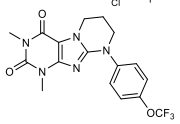
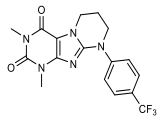
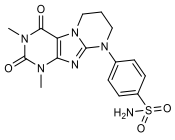
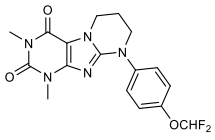
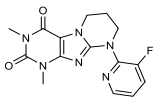
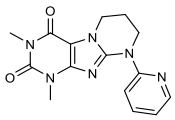
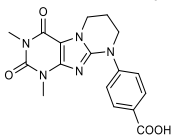
Xanthine derivatives were identified by our previous co-worker Dr. Christian Renn in a high throughput screening (HTS) campaign of an in-house compound library consisting of 5641 derivatives. These xanthine-based compounds were either synthesized by medicinal chemists in our group or by collaboration partners and had originally been designed to antagonize A_{2A} adenosine receptors. The obtained results were not surprising since caffeine was previously shown to weakly inhibit CD73.[305] Development of dual CD73/A_{2A} blockers would be advantageous, and for this purpose, xanthine derivatives might be superior to other scaffolds. The biological activity of the xanthine-based hits was determined using soluble rat CD73 at 10 μM concentration in an optimized malachite green assay.[306] The most potent identified inhibitors (e.g., PZB01808057, IC_{50} = 3.30 ± 0.34 μM and PZB01808014, IC_{50} = 23.1 ± 8.3 μM, shown in **Table 23**) were further characterized at soluble human CD73. Surprisingly, these inhibitors of rat CD73 interacted differently with human soluble and membrane-bound (membrane preparation of MDA-MB-231 cell line) isoforms. For example, PZB01808057 activated both CD73 human isoforms weakly, while PZB01808014 exerted more potent inhibition (IC_{50} = 6.57 ± 1.0 μM) at the soluble form but no activity at membrane-bound human CD73 was detected. By employing compounds PZB01808057 and PZB01808014 as lead structures, a series of xanthine-based molecules were synthesized by the medicinal chemist Dr. Georg Rolshoven aiming to explore the SARs and to improve the potency of the compounds at human CD73.

5.5.1. Results

An enzyme inhibition assay utilizing 5 μM of [^{3}H]AMP as a substrate was applied for biological screening studies.[170] The synthesized compounds were screened at two different concentrations, 10 μM and 20 μM, using soluble rat and human CD73. Screening results are presented in **Table 23** and **Figure 92A-B**.

Table 23. Biological activity of xanthine-derived compounds at recombinant soluble human and rat CD73 [a]

No.	Test compound	Structure	Inhibition of human CD73 (% ± SEM)		Inhibition of rat CD73 (% ± SEM)	
			at 20 µM	**at 10 µM**	**at 10 µM**	**at 20 µM**
7-membered ring-substituted xanthine derivatives						
1	PZB01808057		ND	-42 [306]	(IC_{50} = 3.30 ± 0.34 µM) [306]	
2	GR161a		-31 ± 3	-9 ± 13	13 ± 5	-14 ± 4
3	GR161b		16 ± 6	18 ± 5	33 ± 7	24 ± 0
4	GR171		-26 ± 3	13 ± 1	-17 ± 1	16 ± 6
5	GR173		24 ± 5	24 ± 2	-16 ± 7	0 ± 5
6	GR178		(EC_{50} = 0.672 ± 0.327 µM, [73%])		-16 ± 7	39 ± 2
7	GR182		16 ± 2	17 ± 4	22 ± 6	32 ± 2
8	GR187		-8 ± 4	6 ± 5	-2 ±1	15 ± 1
9	GR201		16 ± 5	16 ± 8	-9 ± 7	30 ± 4
6-membered ring-substituted xanthine derivatives						
10	PZB01808014		(IC_{50} = 6.57 ± 1.0 µM) [306]		(IC_{50} = 23.1 ± 8.3 µM) [306]	
11	GR204		-1 ± 1	13 ± 3	-4 ± 7	14 ± 13
12	GR205		-19 ± 4	-17 ± 7	-7 ± 6	13 ± 4
13	GR206		11 ± 6	12 ± 6	-28 ± 12	18 ± 8

14	GR207		30 ± 4	25 ± 2	7 ± 5	23 ± 4
15	GR208		12 ± 3	5 ± 3	13 ± 3	31 ± 9
16	GR210		9 ± 6	12 ± 4	19 ± 16	29 ± 6
17	GR211		20 ± 3 (no inhibitory activity up to 500 µM)	31 ± 8	14 ± 12	18 ± 13
18	GR212		22 ± 3 (no inhibitory activity up to 300 µM)	17 ± 2	15 ± 2	1 ± 5
19	GR218		ND	4 ± 4	-20 ± 9	11 ± 6
20	GR223		ND	-5 ± 1	15 ± 9	28 ± 10
21	GR227		ND	7 ± 4	16 ± 3	34 ± 7

[a] [^{3}H]AMP (5 µM) was used as a substrate; K_M value = 17 µM for recombinant soluble human and 59 µM for recombinant soluble rat CD73. ND: Not determined

The biological activity of the synthesized compounds was tested at soluble human CD73 (**Figure 92A**, **Table 23**). None of the test compounds showed inhibition closed to 50% against soluble human CD73, rather, an activator of human CD73 was identified. Compound GR178, was the most potent xanthine-based activator of human CD73 identified so far, with an EC_{50} value of 0.672 ± 0.327 µM and a maximum activation of 73% (**Figure 92C**). Furthermore, the lacking inhibitory activities of compounds GR211 and GR212 were confirmed by measuring concentration-inhibition curves (**Figure 92D**). GR211 was only able to inhibit soluble human CD73 activity by 36% at a concentration of 500 µM, whereas GR212 inhibited human CD73 activity at 300 µM by 28%. Comparing the biological screening results at the two concentrations revealed a non-concentration-dependent activity at soluble human CD73 for most of the test compounds which indicated

inactivity at human CD73. To test if these compounds maintained their inhibitory activity towards soluble rat CD73 relative to the lead structures, screening was conducted using recombinant soluble rat CD73 (**Figure 92B**). All of the newly synthesized xanthine derivatives were less potent than the lead structures at rat CD73. Although none of them inhibited the activity of rat CD73 by more than 50% at 20 μM, they showed a concentration-dependent activity. Interestingly, the identified activator of human CD73 (GR178, EC_{50} = 0.672 ± 0.327 μM) was found to inhibit rat CD73 (39%, at 20 μM).

PZB01808057 was previously reported to exhibit a mixed type of inhibition at rat CD73 (i.e. the inhibitor binds to free enzyme and to enzyme-substrate complex as well).[306] Since binding to an allosteric site was proposed, the obtained weak activation and inhibition results exhibited by this scaffold are not unexpected. Allosteric modulators could inhibit the attainment of the active conformation of the enzyme (negative allosteric modulator, NAM) or stabilize it (positive allosteric modulator, PAM). The obtained human and rat CD73 results were in complete agreement with these reported by Dr. Christian Renn in his PhD thesis for the lead structures.[306] An example is PZB01808057 that was found to exhibit CD73-inhibitory activity with an IC_{50} value of 3.30 ± 0.34 μM at soluble rat CD73, while slightly activating the human enzyme.[306] An exception is hit compound PZB01808014 which inhibited both, rat and human CD73 with IC_{50} values of 23.1 ± 8.3 μM and 6.57 ± 1.0 μM, respectively.[306] However, all newly modified compounds based on the PZB01808014 structure exhibited no inhibitory activity at human CD73.

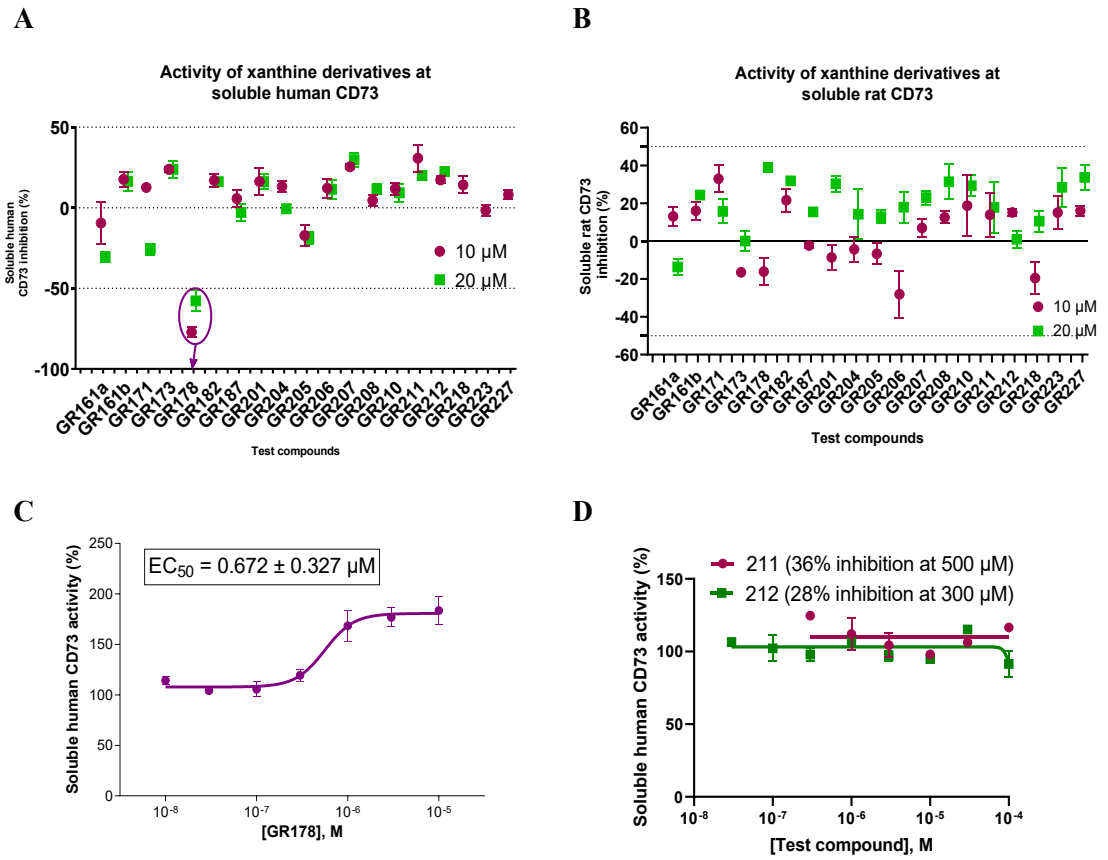


Figure 92. **A**) Biological activity of xanthine derivatives at soluble rat CD73, K_M value = 59 µM. **B**) Biological activity of xanthine derivatives at soluble human CD73, K_M value = 17 µM. **C**) Concentration-activation curve for the most potent activator, GR178, at soluble human CD73. **D**) Concentration-inhibition curves for GR211 and GR212 at soluble human CD73. Data points are means ± SEM form at least two independent experiments, performed in duplicates.

5.5.2. Summary and outlook

Xanthine derivatives were identified as potential inhibitors of soluble rat CD73 in a HTS campaign.[306] However, testing of selected hits at soluble human CD73 indicated either inactivity or activating effects.[306] Results of the newly synthesized xanthine-based derivatives compared well with the previous findings. No inhibitory activity was detected at human CD73, while weak inhibition was observed for the rat enzyme. In contrast, a potent activator of human CD73 (GR178) was identified with an EC_{50} value of 0.672 µM (maximum activation = 73%). GR178 will be subjected to further characterization in synovial fluid, and selectivity versus adenosine receptors will be studied. Moreover, drug metabolism and pharmacokinetic studies are planned. This potent activator of human CD73 was found to inhibit rat CD73 by 39% at a concentration of 20 µM, however, a complete

concentration-inhibition curve will be obtained soon. Human and rat CD73 show around 89% sequence identity.[78] The binding site is highly conserved showing only three amino acid residues substitutions, F500Y, N499S, and L389V. However, differences may be higher for allosteric sites. Consequently, the selectivity of xanthine scaffold towards rat CD73 is not excluded however further validation of the lead structures results in rat and human CD73 is planned.

Soluble human CD73 was recombinantely expressed in Sf9 insect cells as a His-tagged protein. Since all results - except for PZB01808014 - were similar for both human isoforms of CD73, soluble and membrane-bound in triple negative breast cancer cells (MDA-MB-231)[306], we would expect the His-tag not to interfere with the inhibitory activity of xanthine derivatives in the human enzyme.

5.6. Screening of potential CD73 modulators with a heterocyclic scaffold

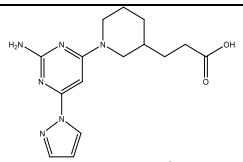
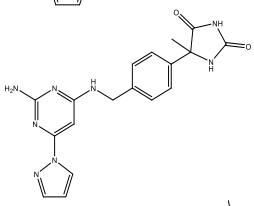
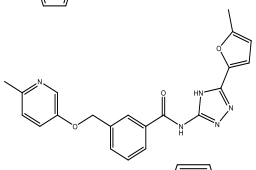
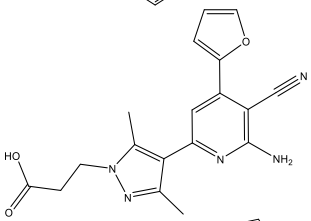
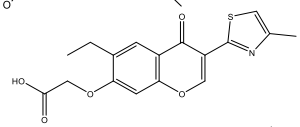
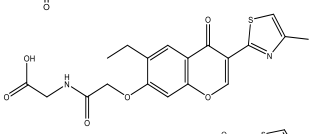
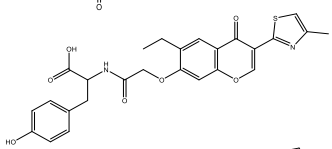
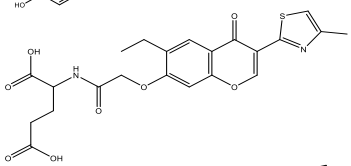
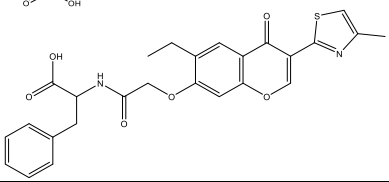
Aim of the project

Nine compounds were obtained from Prof. A.P. IJzerman (University of Leiden, Netherland) for screening at the human ecto-5'-nucleotidase (CD73) enzyme. The compounds were initially screened at 20 µM concentration using a formerly described enzyme inhibition assay.[170]

5.6.1. Results

Table 24 summarizes the screening, EC_{50} values and purity results. **Figure 93A** displays the screening results of the nine compounds. No compound showed inhibition of CD73. Some compounds increased the enzymatic activity of soluble human CD73. Concentration-activation curves for Gift996, Gift993 and Gift990 were subsequently determined as illustrated in **Figure 93B**. The obtained EC_{50} values were 5.48 µM, 46.4 µM, and 13.6 µM for Gift996, Gift993 and Gift990, respectively. EC_{50} value obtained for compound Gift990 should not be considered reliable since the compound had only a 26% purity.

Table 24. Screening, EC_{50} values and purity results for the tested compounds at soluble human CD73[a]

Test compound	Structure	Increase in CD73 activity at 20 µM (% ± SEM)	EC_{50} ±SEM (µM)	Purity (%)
Gift986		1 ± 10	ND	100.0
Gift987		10 ± 1	ND	98.0
Gift988		7 ± 5	ND	93.0
Gift990		53 ± 20	**13.6** ± 6.6 (unreliable)	26.0!
Gift992		38 ± 4	ND	95.0
Gift993		45 ± 10	**46.4** ± 13.4	96.0
Gift994		10 ± 2	ND	92.0
Gift995		2 ± 6	ND	90.0
Gift996		105 ± 5	**5.48** ± 0.65	82.0!

[a] Tested using soluble recombinant human ecto-5'-nucleotidase enzyme (K_M value 17 µM), substrate (AMP) = 5 µM. ND: Not determined

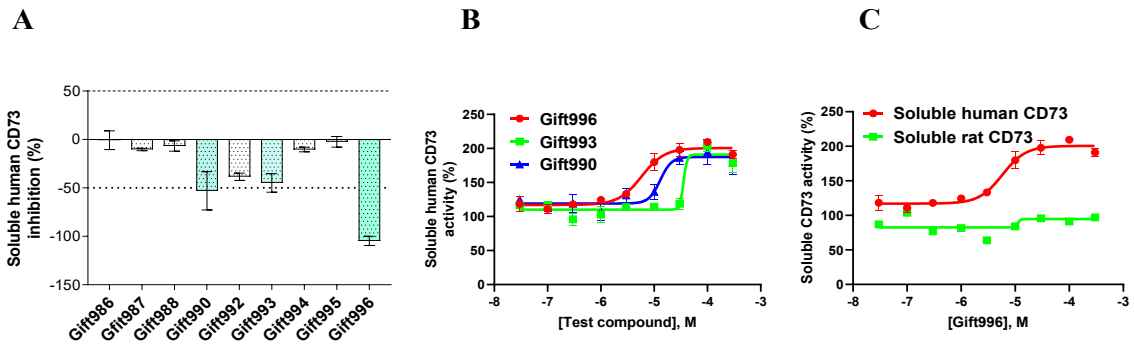


Figure 93. **A**) Screening result of Gift compounds (20 µM) at soluble human CD73. **B**) Concentration-activation curves for Gift996, 993 and 990 at soluble human CD73 (K_M = 17 µM). **C**) Concentration-activation curves for Gift996 at soluble human (K_M = 17 µM) and soluble rat (K_M= 59 µM) CD73. Data points are means ± SEM for at least three independent experiments, each performed in duplicates.

The most potent activator, compound Gift996, was tested at soluble rat CD73. The result shown in **Figure 93C** indicated that, Gift996 is a selective activator of human CD73 and inactive at rat CD73. Human and rat CD73 share around 89% sequence identity.[78] The binding pocket is highly conserved, however, allosteric sites are likely more diverse.

5.6.2. Summary

Some of the proposed CD73 inhibitors activated the enzyme by up to 100%. They were positive allosteric modulators (PAMs).

5.7. Screening of thiophosphate nucleotides derivatives at human CD73

Aim of the project

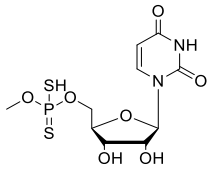
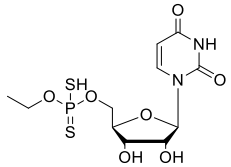
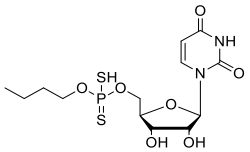
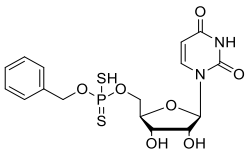
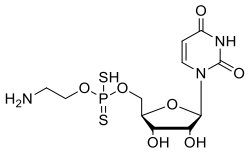
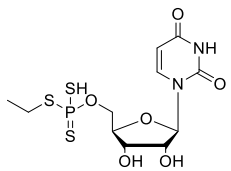
A series of uracil- and adenine-derived thiophosphate nucleotides were designed and synthesized in the research laboratory of Prof. Bilha Fischer (Department of Chemistry, Bar-Ilan University, Israel). The aim was to determine whether these thiophosphate/phosphonates would exhibit inhibitory activity against human CD73.

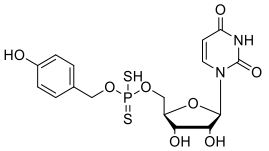
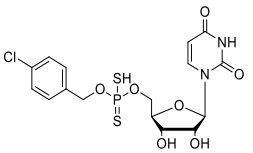
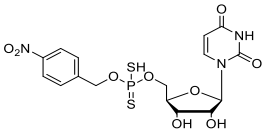
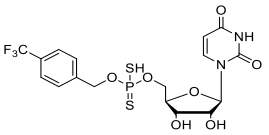
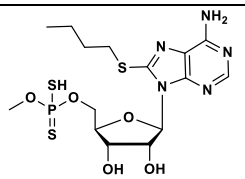
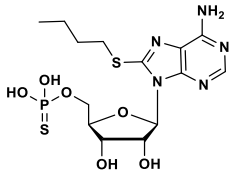
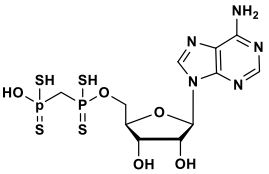
5.7.1. Results

Test compounds were evaluated for their ability to inhibit recombinant soluble human CD73 in a previously published enzyme inhibition assay.[170] No inhibitory activity was

detected for uracil-based nucleotides at concentrations of up to 200 µM. Instead, they were mostly activators of the soluble human CD73 (**Table 25** and **Figure 94A**). This activation was also manifested at CD73 anchored to the membranes of MDA-MB-231 cell lines (**Figure 94B**). Concentration-activation curve was determined for the most active one, Mn-181 (**Figure 94C**). However, an incomplete activation curve was obtained which might be due to precipitation at high concentration. In contrast, both thiophosphate analogues of 8-BuS-AMP (8-SBuAd-03 & 8-SBuAd-05) investigated at low concentration of 10 µM were inactive, while the thiophosphate derivative of AMPCP (AI-51) showed around 29% inhibition of soluble human CD73 at 10 µM concentration.

Table 25. Biological activity results for thiophosphate nucleotides at soluble and membrane-anchored human CD73 [a]

No.	Test compound	Structure	**Human CD73** inhibition result at 200 µM (% ± SEM)	**MDA-MB-231 CD73** inhibition result at 200 µM (% ± SEM)
		Uracil-based		
1	**Mn-180**		-31 ± 11	-60 ± 12
2	**Mn-181**		-66 ± 19	-89 ± 14
3	**Mn-182**		-37 ± 10	-43 ± 20
4	**Mn-183**		8 ± 3	-41 ± 30
5	**Mn-184**		-11 ± 5	-22 ± 21
6	**Mn-186**		15 ± 5	-35 ± 14

7	**Mn-187**		-39 ± 4	-60 ± 13
8	**Mn-189**		-42 ± 15	-28 ± 5
9	**Mn-191**		-37 ± 7	-28 ± 14
10	**Mn-190**		-48 ± 7	-76 ± 22
		Adenine-based		
11	**8-SBuAd-03**		-2 ± 2 (at 10 µM)	ND
12	**8-SBuAd-05**		-2 ± 1 (at 10 µM)	ND
13	**Al-51**		29% (at 10 µM)	ND

[a] Experiments were conducted using soluble recombinant human ecto-5'-nucleotidase (K_M value 17 µM) and MDA-MB-231 membrane-bound CD73 (K_M value 14.8 µM); ND: not determined

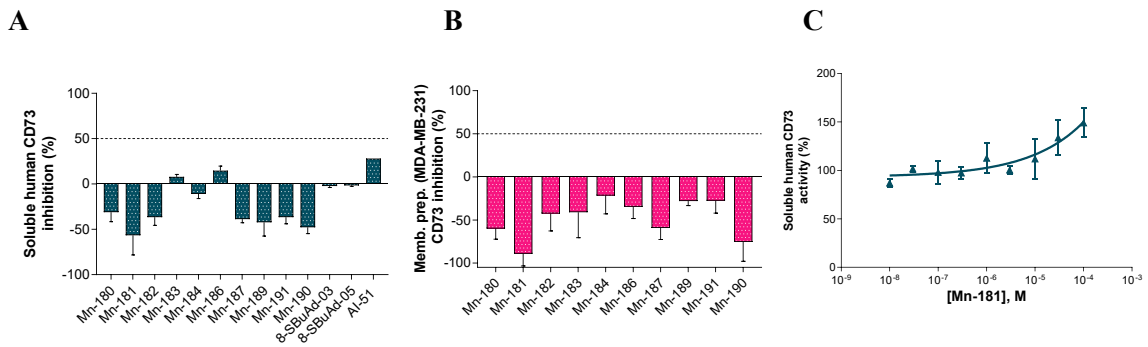


Figure 94. Screening results of thio-nucleotides at 200 µM concentration using: **A**) Soluble human CD73 (K_M = 17 µM). **B**) Membrane-bound CD73 (MDA-MB-231, K_M = 14 µM). **C**) Concentration-activation curve for Mn-181 at soluble human CD73. Data points are means ± SEM for three independent experiments, each performed in duplicates.

5.7.2. Summary and outlook

None of the thio-monophosphate derivatives among this series was active as an inhibitor of human CD73 at a concentration of up to 200 µM. Most of them showed low activation of CD73. Only the thio-phosphonate analog of AMPCP (**Al-51**) showed ca. 30% inhibition of soluble human CD73 tested at 10 µM concentration. Although further optimization of **Al-51** could improve potency, it is clear that the phosphate (oxygen) in AMPCP was better tolerated than thiophosphate. Although we expected the sulfur to complex with the Zn^{2+} dimetal center.

5.8. Summary of activities of allosteric CD73 modulators

As discussed before, the activity of selected identified allosteric modulators of CD73 showed some discrepancies when tested at CD73 of different species and/or different preparations of CD73 (summarized in **Table 26**). For example, the most potent indole-based derivative (PZB17718005A) was only active at soluble but not at membrane-bound human CD73. We cleaved off the membrane-bound CD73 in MDA-MB-231 cells by phospholipase C to investigate whether the compound is a selective inhibitor of the soluble form of CD73. However, this was not the case, since it was inactive at the soluble enzyme derived from the MDA-MB-231 cells. Next, a potential effect of the His-tag on activity at the recombinant soluble human CD73 was studied. However, after the His-tag was cleaved off, the inhibitor was still active indicating that the His-tag had not interfered.

Table 26. Summary of activities of various allosteric modulators of CD73

Scaffold		Activity at **human** CD73			Activity at soluble **rat** CD73 (GST-tagged)	Activity at **mouse** CD73 (membrane-bound, 4T1.2)
		Soluble (His-tagged)	Membrane-bound (MDA-MB-231)	PLC-cleaved		
Indole-based (PZB17718005A)		Inhibition	Not active	Not active	ND	Not active
Xanthine	PZB01808057	Activation	Not active	ND	Inhibition	ND
	PZB01808014	Inhibition	Not active	ND	Inhibition	ND
	GR178	Activation	ND	ND	Inhibition	ND

ND: not determined. Tested in enzyme inhibition assay using 5 µM of [^{3}H]AMP as a substrate

Further testing of this compound on CD73-expressing non-tumor cells is planned to investigate whether the inactivity in CD73 expressed by MDA-MB-231 cells can be attributed to a variation in posttranslational modification (e.g. glycosylation). In addition, experiments with deglycosylated membrane-bound CD73 are planned. Moreover, recombinant expression and investigation of membrane-bound CD73 in *Sf*9 insect cells will be performed.

5.9. Experimental methods

Biology

Membrane preparations of triple negative breast cancer (MDA-MB-231) and melanoma MaMel65 cells ($CD73^{WT}$, $CD73^{KO}$)

Maintaining of cell culture

Cell lines under study were grown in their respective supplemented growth medium shown on **Table 27**. Frozen cells were defrosted either at 37 °C water bath or by rubbing between hands. Defrosted cells were directly cultured in Corning T-175 cm^2 flask containing 20 ml of growth medium and incubated at recommended conditions to reach 80-90% confluence (ca. for 72 h). To get rid of dimethyl sulfoxide (DMSO) used in freezing medium, the growth medium was changed after two hours of incubation when cells were attached. Alternatively, defrosted cells were diluted in 10 ml of growth medium, centrifuged at 1000 *g* for 5 min, then pellets were resuspended in fresh growth medium and cultured as usual. Confluent cells were washed with 10 ml of phosphate-buffered saline (PBS) and detached by incubation with 2 ml of trypsin/ ethylenediaminetetraacetic acid (EDTA) (0.05%/0.6 mM) at 37 °C for 2-5 min. Excess trypsin was then deactivated by addition of 10 ml of growth medium and cells were split 1:10 and seeded into Corning flasks or cell culture dishes (152 cm^2, Roth, Germany).

Table 27. Growth medium and incubation conditions for the studied tumor cells

Cell line	Growth medium	Supplements	Incubation conditions
MDA-MB-231 (human triple negative breast cancer cells)	DMEM (cat. # 41966, Thermo Fisher Scientific, MA, USA)	- 10% fetal bovine serum (FBS, cat. # P30-1502, PAN Biotech, Germany) - 100 U/mL penicillin + 100 µg/mL streptomycin (cat # P06-07100, PAN Biotech, Germany)	37 °C and 5% CO_2
MaMel65, $CD73^{wt}$ and $CD73^{KO}$ (human melanoma cells)	Gibco Roswell Park Memorial Institute (RPMI Medium 1640)	- 10% fetal bovine serum (FBS, cat. # P30-1502, PAN Biotech, Germany) - 100 U/mL penicillin + 100 µg/mL streptomycin (cat # P06-07100, PAN Biotech, Germany) - 2 mM L-glutamine (GlutaMAX™ , cat. # 61870036, Thermo Fisher Scientific, Waltham, MA, USA)	37 °C and 5% CO_2
4T1.2 (mouse breast cancer cells)	Gibco Roswell Park Memorial Institute (RPMI Medium 1640)	- 10% fetal bovine serum (FBS, cat. # P30-1502, PAN Biotech, Germany) - 100 U/mL penicillin + 100 µg/mL streptomycin (cat # P06-07100, PAN Biotech, Germany) - 2 mM L-glutamine (GlutaMAX™ , cat. # 61870036, Thermo Fisher Scientific, Waltham, MA, USA)	37 °C and 5% CO_2

Cryopreservation of cell lines

Cells grown to confluence (80%-90%) in a Corning T-175 cm^2 flasks were washed with 10 ml of PBS and detached by addition of 2 ml of trypsin/ EDTA. Detached cells were diluted in 10 ml growth medium, transferred into flacon tube and centrifuged at 1000 g for 5 min. Cells pellet was collected and resuspended in a cryopreservation medium contains 90% FBS + 10% DMSO and aliquoted at 1 ml per cryovial. Cells in cryovials were subjected to gradual freezing using Mr. Frosty™ freezing container (Thermo Fischer Scientific,

Waltham, MA, USA) at -80 °C freezer overnight. Cryovials then kept at -80 °C or -150 °C until further use.

Preparation of plasma membrane fractions from cultured tumor cells

Cells grown to confluence (~70%) on culture dishes were washed with 10 ml of PBS and frozen overnight. Frozen cells were scratched from dishes using membrane preparation buffer (Tris 25 mM, Na_2EDTA 1 mM, sucrose 0.32 M, pH 7.4) supplemented with protease inhibitor cocktail (cat. # P8340, Sigma Aldrich, 1 ml dissolved in 100 ml buffer directly before use). The cell lysate collected in a beaker was homogenized 2x30 s, divided in centrifuge tubes and subjected to centrifugation at 1000 *g* and 4 °C for 10 min to remove cell debris. To obtain membrane fraction, the supernatant was collected and centrifuged for 40 min at 48000 *g* and 4 °C. Pellets were washed in 25 ml Tris buffer 50 mM, pH 7.4, for 30 min at 48000 *g* and 4 °C. Washing step was repeated twice under the same conditions. The obtained pellets were resuspended in 5-10 ml (0.1 ml /dish) of Tris buffer 50 mM, pH 7.4, rapidly frozen in liquid nitrogen, and stored aliquoted at -80 °C until further use.

Protein determination

Concentration of proteins was determined as previously mentioned in Section 4.8, page 162.

Enzyme inhibition assay used to test for biological activities of the test compounds

The applied method[170] was fully described under Section 4.8, page 162. Test compounds were either water- or dimethyl sulfoxide (DMSO)-soluble. DMSO was previously tolerated up to 2% in this assay,[170] therefore all DMSO-soluble compounds were added as 1 µl or maximally 2 µl volume. For concentration-inhibition or -activation curves, serial dilutions of test compound were transferred as 10 µl or 1µl to 70 µl or 79 µl of the reaction buffer contained in polypropylene test tubes (cat. # 55.535, SARSTEDT, Nümbrecht, Germany). To this test compound solution, 10 µl of enzyme preparation (recombinant soluble CD73 (human, rat, or mouse), cleaved CD73, membrane-anchored CD73) was added followed by a second 10 µl of the diluted tritium-labeled AMP substrate solution (5 µM). Tubes with positive and negative controls were prepared parallel to samples. Positive controls contain no test compound, 10 µl of enzyme preparation was added to 80 µl reaction buffer (for DMSO-soluble sample, control was prepared by adding 10 µl of enzyme preparation to 79 µl reaction buffer plus 1 µl of DMSO), followed by another 10 µl of [^{3}H]AMP substrate

solution. Negative controls constructed with 10 µl of [^{3}H]AMP substrate solution mixed with 90 µl reaction buffer, and contain no enzyme preparation. Samples and controls were measured in duplicates. Data were analyzed and presented with GraphPad Prism software version 9.0 (GraphPad Software Inc., San Diego, CA, USA). Values of radioactivity measured in counts per minute (cpm) for negative control was used for baseline correction of test compound value. The obtained corrected value was then normalized against positive control cpm value. Normalized values were fitted into sigmoidal dose-response (variable slope) to obtain IC_{50} values. K_i values were estimated using Cheng-Prusoff equation.[188]

Determination of the binding mode of small molecule inhibitors

To study the inhibition type of test compound, the same procedure stated in Section 4.8, page 162 was utilized. K_M and V_{max} values were determined by studying reaction rates at different substrate concentrations (0.97 µM-500 µM) with or without an inhibitor under investigation. K_M and V_{max} values were determined for at least three different concentrations of the inhibitor, concentration at ½ xIC_{50}, at 1xIC_{50}, and at 2xIC_{50} value of the test compound.). Obtained K_M and V_{max} values were compared and illustrated in the double reciprocal Lineweaver-Burk plot using GraphPad Prism software version 9.0 (GraphPad Software Inc., San Diego, CA, USA).

6. Functionalized CD73 inhibitor for nanogel preparation

Aim of the project

Although diverse immunotherapeutic approaches such as immune checkpoint inhibitors have revolutionized cancer treatment. Nevertheless, a considerable fraction of patients has remained unresponsive which necessitates alternative treatment strategies. To counteract an immuno-suppressive tumor microenvironment (TME), administration of modulators that activate immune cells have been widely reported.[307] However, systemic side-effects can limit their application. Site-specific drug delivery would improve their toxicity profile.[307] In this context, nanomedicine approaches to modulate the pharmacokinetic profile of the attached drug molecules are highly attractive.[307] Moreover, accumulation at the site of action, will result in improved therapeutic responses.[308]

In this project, a collaboration with Prof. Dr. Lutz Nuhn (Max-Planck-Institute, Mainz, currently at Julius Maximilian University Würzburg, Germany) was initiated. Prof. Nuhn was previously successful in conjugating an imidazoquinoline-based toll-like receptors (TLR7/8) agonist to 50-nm-sized degradable nanogels. The potency of the agonist-bound nanogels were retained both *in vitro* and *in vivo*, while no systemic toxicity was observed.[307,309] Nuhn's research group was also able to prove that the use of TLR7/8-conjugated nanoparticles (NP) as adjuvants for vaccination against the respiratory syncytial virus (RSV) improved the immunogenicity of the vaccine and performed better than TLR7/8-conjugated soluble chain polymers.[310]

The idea was to synthesize a functionalized CD73 inhibitor that was to be conjugated to different pH-degradable nanogels and polymers as targeted delivery systems. The CD73 inhibitor should only be released from pH-dependent, degradable nanoparticles in an acidic environment, i.e., in the TME. We aimed to investigate whether the produced CD73 inhibitor-conjugated nanogels still maintain the inhibitory activity against CD73 relative to the non-conjugated small molecule CD73 inhibitor.

6.1. Results

An ecto-5'-nucleotidase (CD73) inhibitor (PSB-20289, **Figure 95A**) bearing a functional group (primary amine) was synthesized by our previous co-worker, Dr. Georg Rolshoven. Pharmacological evaluation of the synthesized inhibitor was conducted at recombinant

soluble human CD73 using an enzyme inhibition assay in which [^{3}H]AMP was employed as a substrate at a concentration of 5 µM.[170] A concentration-inhibition curve (**Figure 95B**) was constructed and the K_i value was calculated as 0.349 ± 0.181 nM using the Cheng Prusoff equation.[188] The obtained K_i value indicated that substitution with an amino-methyl at the *para*-position of the N^6-benzyl ring was well tolerated compared to the unsubstituted derivative (PSB-17230, K_i = 0.0733 nM).[170] PSB-20289 was sent to Prof. Dr. Lutz Nuhn for conjugation to different types of pH-degradable nanoparticles (shown in **Figure 95C**).

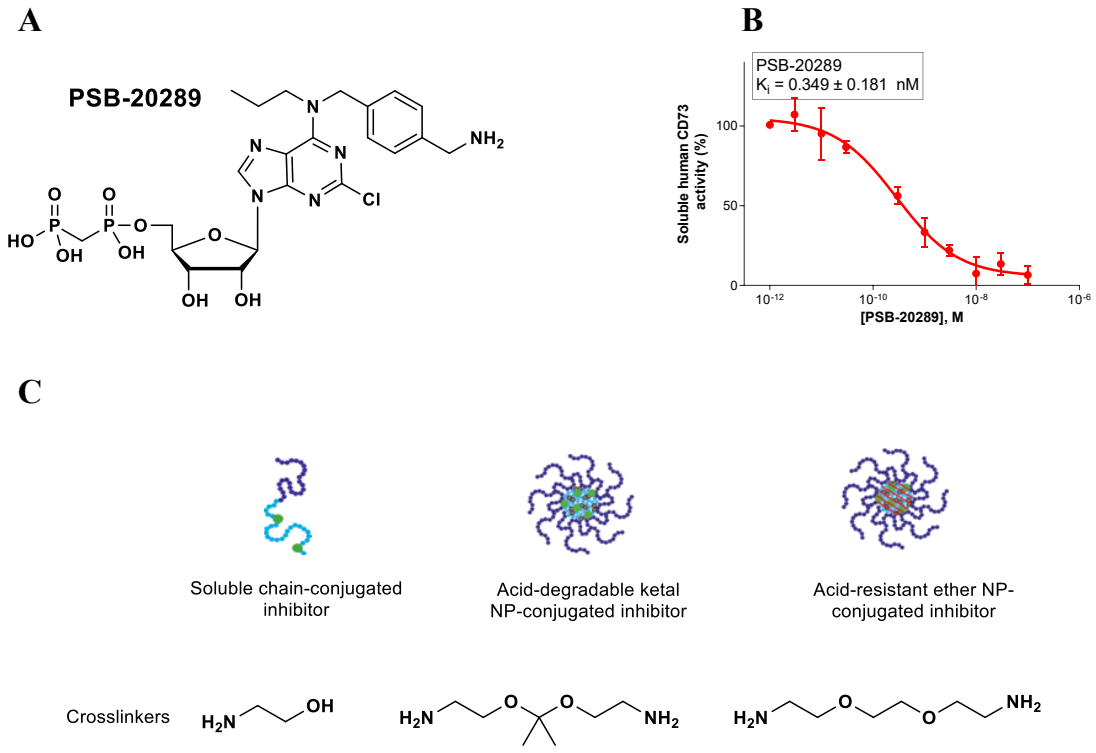


Figure 95. **A**) Chemical structure of the synthesized CD73 inhibitor, PSB-20289. **B**) Concentration-inhibition curve for PSB-20289 at soluble human CD73 (K_M = 65 µM). Substrate (AMP) concentration = 5 µM. Data points are mean ± SEM of three independent experiments performed in duplicates. **C**) PSB-20289-conjugated soluble chain polymers and nanoparticles (NP).

PSB-20289-conjugated polymers and nanogels were prepared as described previously by Nuhn et al, 2016.[309] Briefly, the amphiphilic copolymers that consist of a hydrophilic PEG-like polymer and a hydrophobic pentafluorophenyl (PFP) methacrylate polymer were self-assembled into nanoparticles in an aprotic polar solvent (DMSO). Next, the targeted CD73 inhibitor was covalently bound to the nanoparticle through amidation of PFP esters. Then,

the inhibitor-loaded nanoparticles were cross-linked either with a non-degradable, ether-based diamine or a pH-degradable ketal-based diamine polymer. Finally, the unreacted PFP esters were transformed into hydrophilic components through reaction with ethanolamine to produce fully-hydrated nanogels. Crosslinking was omitted for obtaining soluble chain polymers, and the remaining PFP esters were only reacted with ethanolamine. The produced nanogels were dialyzed against NH_3/H_2O (0.1%) to remove unbound inhibitor.[309]

The small molecule inhibitor, PSB-20289, was successfully incorporated into soluble polymers and nanogels (at ≥ 10% wt.) as indicated by the characterization methods applied in Prof. Nuhn's laboratory. PSB-20289-conjugated nanogels were obtained together with empty controls (polymers and nanogels uncoupled to PSB-20289) for activity testing at soluble human CD73.

The same sensitive method utilizing [^{3}H]AMP at 5 µM as a substrate was employed for activity testing of all samples.[170] Concentration-inhibition curves for all nanoparticle samples are presented in **Figure 96** and their calculated K_i values or percent inhibition values are summarized in **Table 28**.

Table 28. Biological evaluation of PSB-20289-bound polymers and nanogels compared to the free inhibitor at different pH values

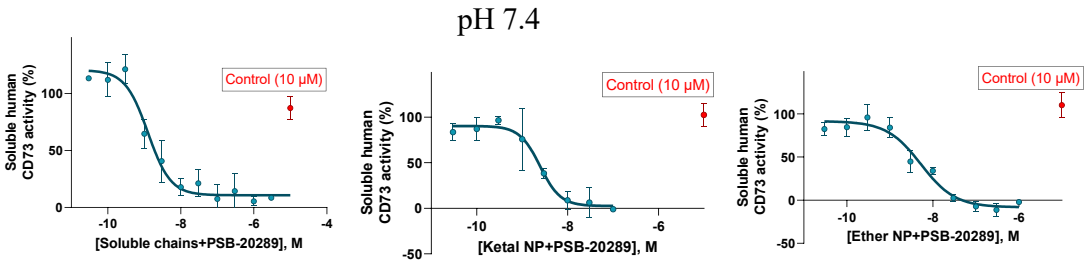
		K_i ± SEM, nM or (percent inhibition at 10 µM) [a]						
		PSB-20289	Soluble chain + PSB-20289	Soluble chain control	Ketal-NP + PSB-20289	Ketal-NP control	Ether-NP + PSB-20289	Ether-NP control
pH 7.4, n=3		0.349 ± 0.181	0.927 ± 0.504	> 10000 (-34 ± 6)	1.96 ± 0.06	> 10000 (26 ± 10)	3.46 ± 1.25	> 10000 (-23 ±17)
pH 5.0 n = 2	2 h	ND	0.898	ND	3.62	ND	3.42	ND
	4 h	ND	2.05 ± 0.46	ND	1.85 ± 0.25	ND	1.52 ± 0.28	ND
	72 h	ND	1.19	ND	7.62	ND	10.3	ND

[a] Tested using soluble recombinant human ecto-5'-nucleotidase (K_M value 65 µM), substrate (AMP) = 5 µM; ND: not determined, NP: nanoparticle

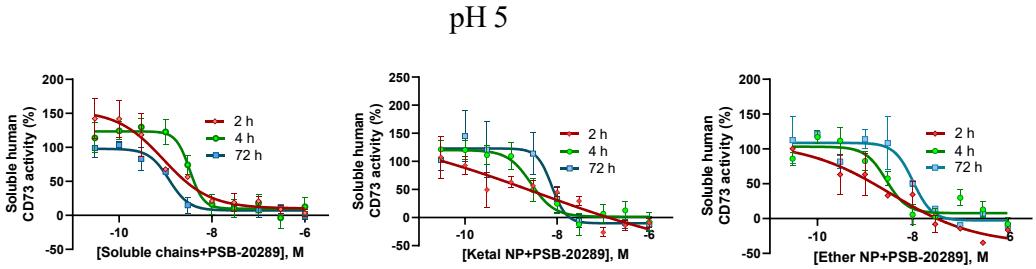
At physiological pH of 7.4, the activity was maintained against CD73 in all produced polymers and nanogels while negative controls (PSB-20289-free nanogels) were completely inactive. The inhibitory activity of the PSB-20289-conjugated soluble chain (K_i = 0.927 nM) was comparable to that of the unbound inhibitor (K_i = 0.349 nM) which might indicate either free access to the active site of the enzyme, or the inhibitor was readily released. Both, ketal- and ether-crosslinked nanogels were also active at pH 7.4 with K_i values of 1.96 nM and 3.46 nM, respectively. The pH-degradable ketal nanoparticles showed an around 6-fold loss in potency while ether nanogel was 10-fold less potent compared to the free inhibitor PSB-20289.

After incubation at acidic pH of 5.0 (acetate buffer, 100 mM) for 2 h at 37 °C, the soluble chain (K_i = 0.898 nM), non-degradable ether NP (K_i = 3.42 nM), and acid-degradable ketal NP (K_i = 3.62 nM) maintained their activity towards CD73. With incubation continued for 4 h, soluble chain (K_i = 2.05 nM), acid-degradable (K_i = 1.85 nM) and non-degradable (K_i = 1.52 nM) nanogels exhibited similar K_i values. Stability in acidic pH of 5.0 was assessed at day 3. Soluble chain polymer retained the same activity (K_i = 1.19 nM) compared to neutral pH (K_i = 0.927 nM), while ketal and non-degradable ether NP showed slightly lower potency. It is obvious that the obtained results were inconsistent with the concept of the study, namely release of the inhibitor PSB-20289 from the nanogels only in an acidic environment (i.e. in the TME), whereas at physiological pH, the CD73 inhibitor should be contained within the micelle core, covalently bound to the polymer and showing very slow degradation. Thus, no inhibition was expected by the degradable and non-degradable NP at neutral pH value.

A



B



C

K_i values of polymer and nanogels subjected to acid degradation

Nanoparticles	K_i value (nM)		
	pH 5, 37 °C, **2** h	pH 5, 37 °C, **4** h	pH 5, rt, **72** h
PSB-20289-conjugated soluble chain	0.898	2.05 ± 0.46	1.19
PSB-20289-conjugated ketal NP	3.62	1.85 ± 0.25	7.62
PSB-20289-conjugated ether NP	3.42	1.52 ± 0.28	10.3

(n=2, in duplicates)

Figure 96. Concentration-inhibition curve for PSB-20289 conjugated to soluble chain, acid-degradable ketal and non-degradable ether nanoparticles. **A**) at pH 7.4. **B**) at pH 5.0. **C**) K_i values of different PSB-20289-attached polymer and nanogels subjected to acid degradation. Controls were PSB-20289-nonconjugated NP. Experiments were conducted at pH 7.4 (n=3) and pH 5.0 for 4 h (n=2) using soluble human CD73 (K_M = 65 µM) and substrate concentration of 5 µM.

It remains unclear if the obtained results at pH 7.4 were due to the assay conditions (incubation in a shaking bath at 37 °C for 25 min leading to degradation) or whether the enzyme's active site is accessible to PSB-20289 attached to a 50 nm nanoparticle surface. However, we cannot exclude that the inhibitor PSB-20289 was unproperly coupled to the nanoparticle and hence it was superficially attached and became readily available in

aqueous medium. The latter was supported by the result of non-degradable NP. If PSB-20289 was covalently bound to the undegradable ether-crosslinked core, no activity should be detected neither in neutral nor in acidic environment.

6.2. Summary and outlook

An AMPCP-based CD73 inhibitor (PSB-20289) possessing an amino-methyl group in the *para*-position of the N^6-benzyl ring was successfully synthesized and evaluated with respect to its inhibitory activity against soluble human CD73. PSB-20289 was able to inhibit CD73 activity in an enzyme inhibition assay with a subnanomolar K_i value (K_i = 0.349 nM). This CD73 inhibitor, PSB-20289, was conjugated to a soluble chain polymer and to pH-degradable nanogels by Prof. Nuhn's research group (Max-Planck-Institute, Mainz). Biological evaluations at CD73 revealed that all polymers and nanogels were active against CD73 at physiological and acidic pH values, indicating that PSB-20289 was readily available for CD73 inhibition. This clearly indicates that CD73 inhibitor conjugates with polymers still possess high CD73-inhibitory potency.

6.3. Experimental methods

Preparation of nanogel samples for testing in an enzyme inhibition assay

1 mM stock solutions of nanoparticles and soluble chain polymers were prepared by dissolution in Tris HCl buffer (25 mM, pH 7.4) using an ultrasonic water: ice bath (50%) (Bandelin, Germany) for 20 min. Suitable working solutions were prepared and subjected to serial dilution to generate concentration-inhibition curves using enzyme inhibition assays [170] (also see Section 5.4, page 162).

pH stability study of PSB-20289-conjugated soluble chain and nanogels

Experiments in acidic medium were conducted using 100 mM acetate buffer, pH 5.0. Aliquots (10 µl) of nanoparticle stock solutions were incubated with 90 µl of acetate buffer at 37 °C for 4 h and continued at rt for 3 days. Samples were withdrawn after 2 h and directly diluted in assay buffer. Samples (10 µl) were pipetted into 90 µl of assay buffer (Tris HCl 25 mM, NaCl 140 mM, $NaHPO_4$ 25 mM, pH 7.4) and concentration-inhibition curves were determined.

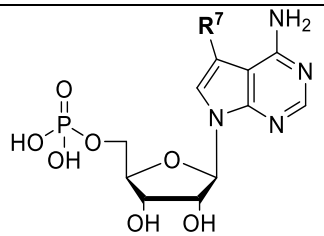
7. Incomplete projects

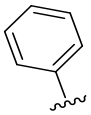
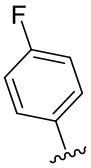
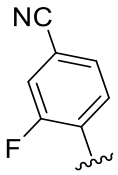
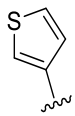
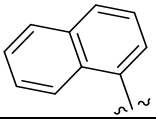
7.1. AMP-based derivatives and analogs as inhibitors of human CD73

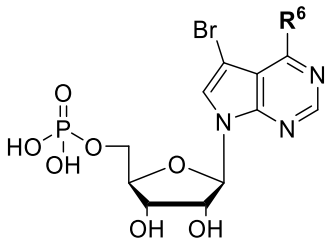
Project overview

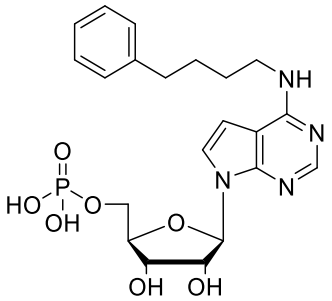
A series of AMP derivatives were primarily synthesized to target CD39. However, selectivity studies conducted on lead structures indicated human CD73 as an additional potential target of these compounds. Thus, further characterization of this scaffold was initiated. Biological screening of all synthesized AMP derivatives against soluble human CD73 was performed. Moreover, stability studies to determine whether these nucleotides are hydrolyzable by CD73 are ongoing (under investigation by co-worker Patrick Riziki). Screening results at CD73 are presented in **Table 29** and **Figure 97A**.

Table 29. Screening results and K_i values of AMP derivatives and analogs tested at soluble human CD73

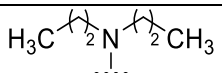
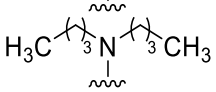
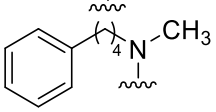
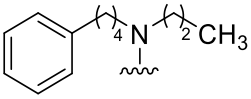
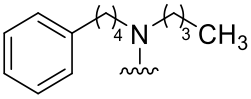


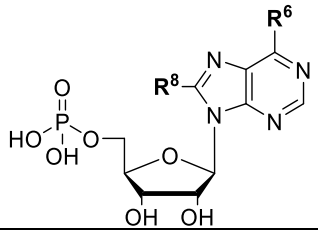
Test compound	R^7	Percent inhibition of soluble human CD73[a] at 50 µM or (K_i, µM, n=1)
Bcy-136	H	ND
Bcy-128	Br	91 ± 1 (2.59 µM)
Bcy-243		88 ± 0 (2.43 µM)
Bcy-323		82 ± 1 (8.42 µM)
Bcy-393		83 ± 0 (4.08 µM)
Bcy-356		79 ± 1 (6.67 µM)
Bcy-401		ND

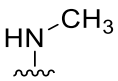
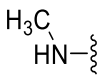
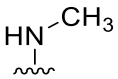
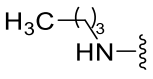
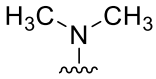
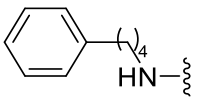
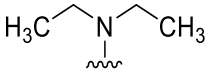
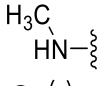
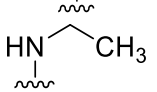
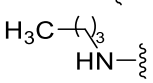
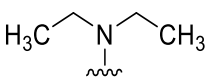
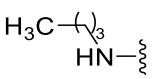
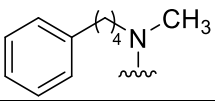
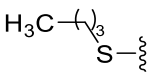


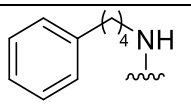
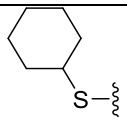
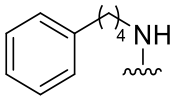
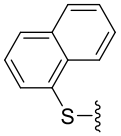
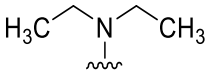
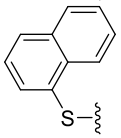
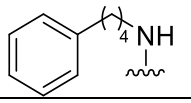
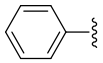


Bcy-153

Test compound	R^6	Percent inhibition of soluble human CD73 at 50 μM or (K_i, μM, n=1)
Bcy-336		ND
Bcy-343		48 ± 3
Bcy-349		ND
Bcy-344		ND
Bcy-338		ND
Bcy-153	*for structure see above*	79 ± 3 (9.97 μM)



Test compound	R^6	R^8	Percent inhibition of soluble human CD73 at 50 μM or (K_i, μM, n=1)
Bcy-389			ND
CS-210-1			60 ± 3
CS-287			64 ± 0 (31.0 μM)
CS-326-1			84 ± 0 (2.76 μM)
CS-401			59 ± 5 (6.92 μM)
CS-344 (CS-382A)			62 ± 3 (12.9 μM)
Bcy-348			96 ± 1 (0.500 μM)

Bcy-378			96 ± 0 (0.444 µM)
Bcy-379			ND
Bcy-375			90 ± 1 (1.80 µM)
Bcy-355			69 ± 0 (15.3 µM)

[a] All experiments were conducted using soluble recombinant human ecto-5'-nucleotidase (K_M = 17 µM). ND: not determined.

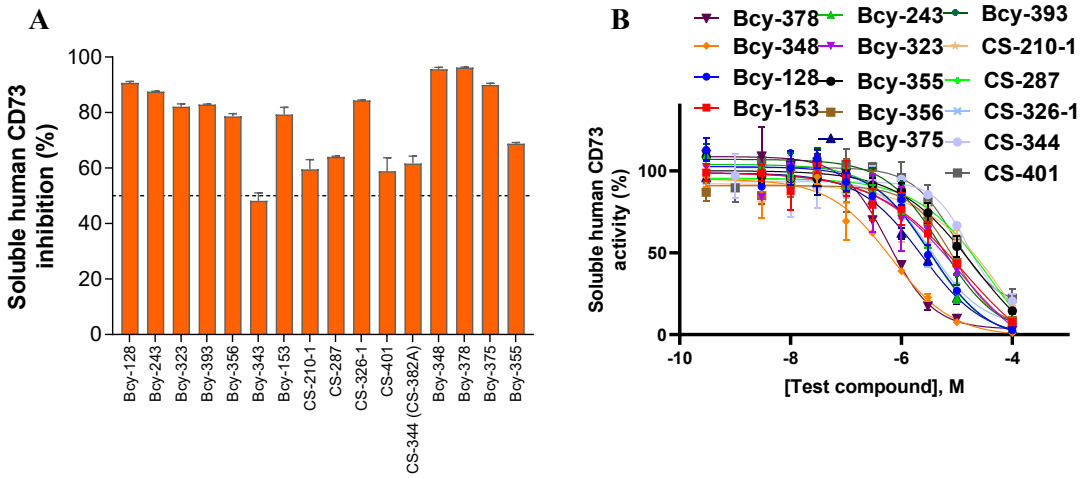


Figure 97. Biological evaluation of AMP derivatives. **A**) Screening results at 50 µM using recombinant soluble human ecto-5'-nucleotidase (K_M = 17 µM). **B**) Concentration-inhibition curves for selected inhibitors at soluble human CD73 (K_M = 17 µM). Substrate (AMP) concentration = 5 µM. Data points are mean of three independent experiments performed in duplicates. Error bars represent the standard error of the mean (SEM).

Several molecules showed almost 100% inhibition of CD73 at 50 µM concentration. Concentration-inhibition curves are displayed in **Figure 97B** and K_i values were calculated using the Cheng- Prusoff equation.[188] The structure-activity relationships will be studied after evaluation of the stability results.

7.2. Sulfonamides as inhibitors of human CD73

Aim of the project

Sulfonamides were previously identified as inhibitors of rat CD73 in a virtual screening campaign conducted in our research group (for more details see Introduction, page 50).[236] Further optimization of a lead structure (**27**, K_i value = 1.75 µM, **Figure 98**) resulted in the most potent sulfonamide-based inhibitors of CD73 known so far, Yazh-937 (K_i = 293 ± 50 nM, human CD73) and Yazh-842 (K_i = 194 ± 46 nM, rat CD73) (for structures see **Figure 98**).[306] It is obvious that successful strategies were implemented to obtain 8-fold more potent derivatives compared to the lead structure. However, there is still room for further substitutions to improve the potency. Thus, a series of sulfonamides based on naphthalene and coumarin scaffolds were synthesized by the medicinal chemist Dr. Thanigaimalai Pillaiyar and subjected to screening at soluble human CD73 using our published enzyme inhibition assay.[170]

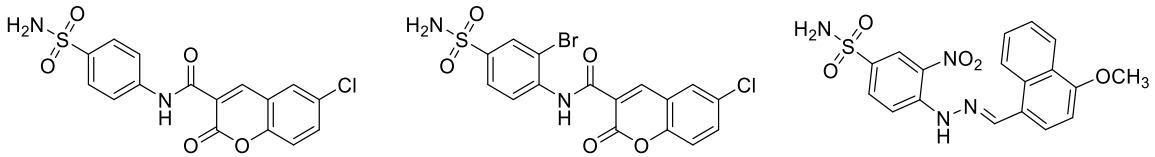
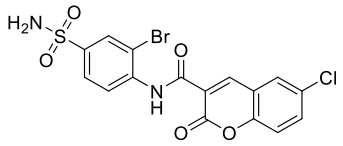
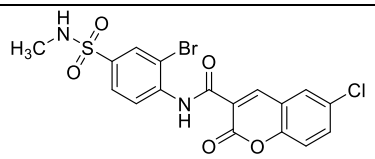
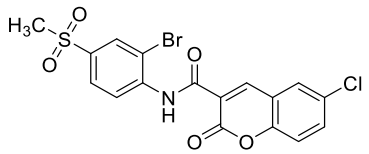
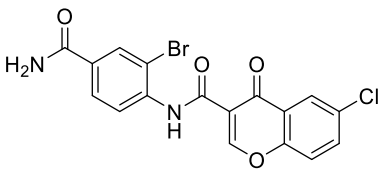
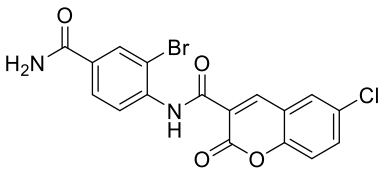
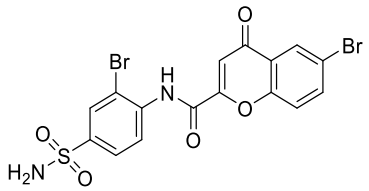
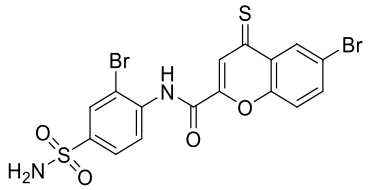
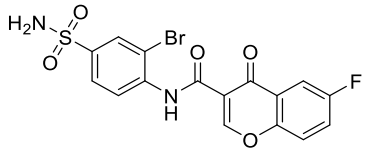
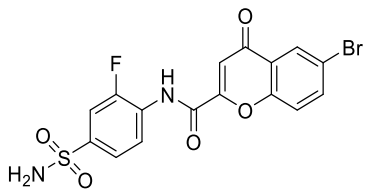


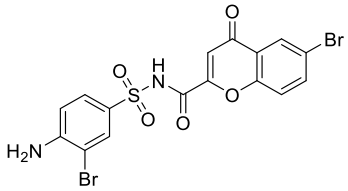
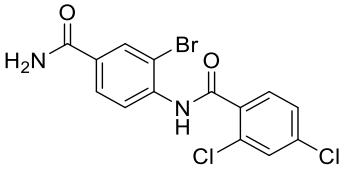
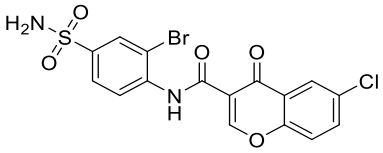
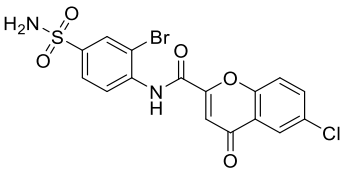
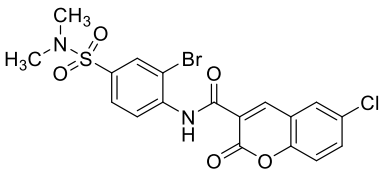
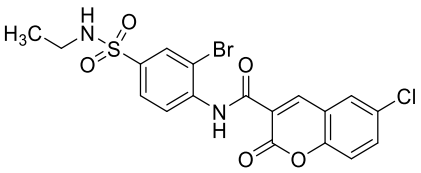
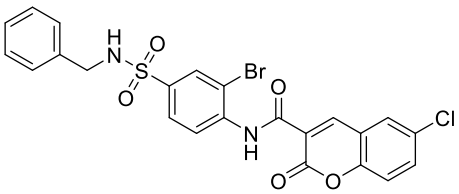
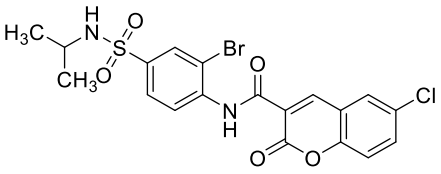
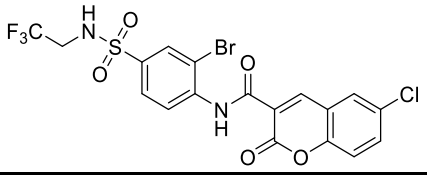
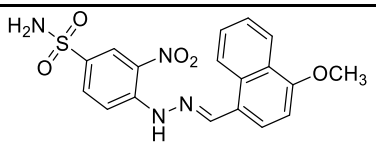
Figure 98. Structures of sulfonamide-based inhibitors

Results

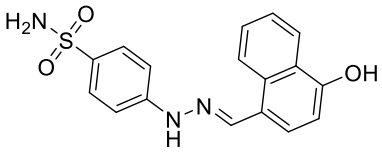
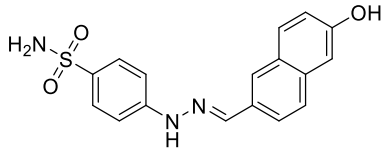
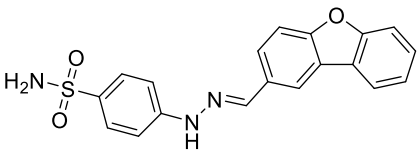
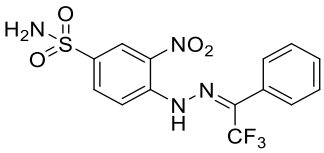
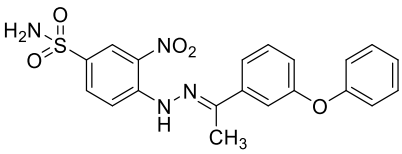
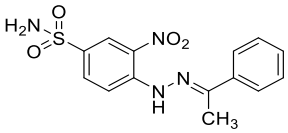
The biological screening results (**Table 30**, and **Figure 99A**) showed mostly low CD73 inhibition. None of the synthesized compounds exhibited more than 50% inhibition at 1 µM. Selected test compounds (Yazh-K911, 924, 934 and 936) were further assessed in concentration-inhibition curves. No inhibitory activity was detected for any of the coumarin-based sulfonamides (**Figure 99B**). Yazh-K924, which is a hydrazone-linked naphthalene sulfonamide, showed moderate inhibition with a K_i value equal to 3.02 µM (**Figure 99C**, n=1) which was higher than that of the lead structures.

Table 30. Test results of sulfonamide derivatives at soluble human ecto-5'-nucleotidase

No.	Test Compound	Structure	Inhibition % of soluble human CD73 at **1 µM** (% ± SEM, or K_i ± SEM, nM) [a]
1	**Yazh-937**	 Lead structure, coumarin derivative	198 ± 37 nM, rat CD73, 293 ± 50 nM, human CD73
2	**Yazh-K860**		22 ± 13
3	**Yazh-K862**		28 ± 4
4	**Yazh-K876**		27 ± 7
5	**Yazh-K908**		29 ± 12
6	**SBB-23**		19 ± 6
7	**SBB-25**		23 ± 4
8	**SBB-26**		24 ± 5
9	**SBB-27 exp b48**		29 ± 9

10	**SBB-18**		22 ± 13
11	**Yazh-K909**		17 ± 12
12	**Yazh-K911**		19 ± 16
13	**Yazh-K938**		21 ± 3
14	**Yazh-K928**		19 ± 5
15	**Yazh-K933**		20 ± 6
16	**Yazh-K936**		37 ± 11
17	**Yazh-K934**		32 ± 13
18	**Yazh-K935**		38 ± 5
19	**Yazh-842**		194 ± 46 nM, rat CD73

Lead structure, hydrazone-linked naphthalene

20	**Yazh-K923**		27 ± 9
21	**Yazh-K924**		30 ± 13 (K_i = 3.02 µM, n=1)
22	**Yazh-K925**		24 ± 6 (n= 2)
23	**Yazh-K968**		20 ± 4 (n= 2)
24	**Yazh-K969**		24 ± 4 (n= 2)
25	**Yazh-K970**		10 ± 6 (n= 2)

[a] Experiments were conducted using recombinant soluble human ecto-5'-nucleotidase (K_M = 17 µM)

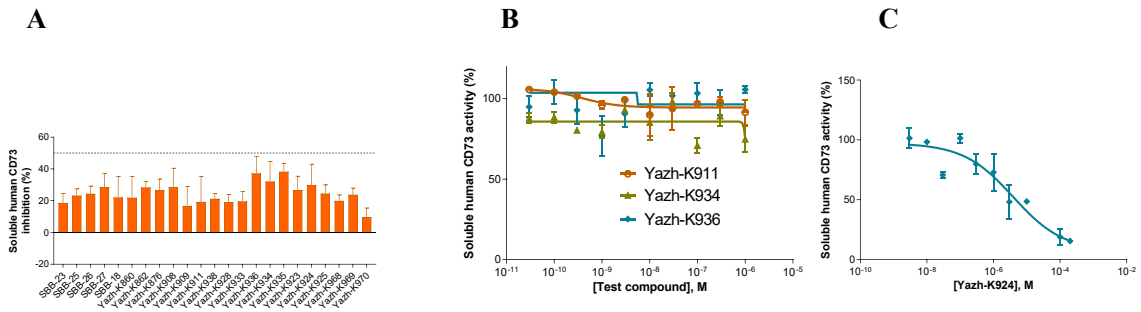


Figure 99. **A**) Screening results for hydrazone-linked naphthalene and coumarin-based sulfonamides at soluble human CD73 (K_M = 17 µM) at 1 µM concentration. **B**) Concentration-inhibition curves for Yazh-K911, 934, and 936 at soluble human CD73 (K_M = 17 µM). **C**) Concentration-inhibition curve for Yazh-K924 at soluble human CD73, n= 1 (K_M = 17 µM). Data points are means ± SEM of at least two independent experiments each performed in duplicates.

Conclusion and outlook

All of the synthesized compounds in this series are less potent than the lead structures. Only the hydrazone-linked naphthalene sulfonamide Yazh-K924 showed a concentration-dependent inhibition of human CD73 with a K_i value equal to 3.02 µM. Further confirmation of the lead structure results is planned in addition to a purity check.

References

(1) Burnstock, G. Purinergic Signalling: Therapeutic Developments. *Front. Pharmacol.* **2017**, *8* (September), 1–55. https://doi.org/10.3389/fphar.2017.00661.

(2) Goding, J. W.; Grobben, B.; Slegers, H. Physiological and Pathophysiological Functions of the Ecto-Nucleotide Pyrophosphatase/Phosphodiesterase Family. *Biochim. Biophys. Acta - Mol. Basis Dis.* **2003**, *1638* (1), 1–19. https://doi.org/10.1016/S0925-4439(03)00058-9.

(3) Zimmermann, H. 5'-Nucleotidase: Molecular Structure and Functional Aspects. *Biochem. J.* **1992**, *285 (Pt 2*, 345–365. https://doi.org/10.1042/BJ2850345.

(4) Rafehi, M.; Müller, C. E. Tools and Drugs for Uracil Nucleotide-Activated P2Y Receptors. *Pharmacol. Ther.* **2018**, *190*, 24–80. https://doi.org/10.1016/j.pharmthera.2018.04.002.

(5) Virgilio, F. Di. Extracellular ATP and P2 Purinergic Signalling in the Tumour Microenvironment. *Nat. Rev. Cancer* **2018**, *18* (October). https://doi.org/10.1038/s41568-018-0037-0.

(6) Sheth, S.; Brito, R.; Mukherjea, D.; Rybak, L. P.; Ramkumar, V. Adenosine Receptors: Expression, Function and Regulation. *Int. J. Mol. Sci.* **2014**, *15* (2), 2024–2052. https://doi.org/10.3390/ijms15022024.

(7) Voss, J. H.; Mahardhika, A. B.; Inoue, A.; Müller, C. E. Agonist-Dependent Coupling of the Promiscuous Adenosine A2BReceptor to Gα Protein Subunits. *ACS Pharmacol. Transl. Sci.* **2022**. https://doi.org/10.1021/acsptsci.2c00020.

(8) Bender, E.; Buist, A.; Jurzak, M.; Langlois, X.; Baggerman, G.; Verhasselt, P.; Ercken, M.; Guo, H. Q.; Wintmolders, C.; Van Den Wyngaert, I.; Van Oers, I.; Schoofs, L.; Luyten, W. Characterization of an Orphan G Protein-Coupled Receptor Localized in the Dorsal Root Ganglia Reveals Adenine as a Signaling Molecule. *Proc. Natl. Acad. Sci. U. S. A.* **2002**, *99* (13), 8573–8578. https://doi.org/10.1073/pnas.122016499.

(9) Knospe, M.; Müller, C. E.; Rosa, P.; Abdelrahman, A.; Kügelgen, I. Von. The Rat

Adenine Receptor : Pharmacological Characterization and Mutagenesis Studies to Investigate Its Putative Ligand Binding Site. **2013**, 367–381. https://doi.org/10.1007/s11302-013-9355-6.

(10) Al Hamwi, G.; Riedel, Y. K.; Clemens, S.; Namasivayam, V.; Thimm, D.; Müller, C. E. MAS-Related G Protein-Coupled Receptors X (MRGPRX): Orphan GPCRs with Potential as Targets for Future Drugs. *Pharmacol. Ther.* **2022**, *238*. https://doi.org/10.1016/j.pharmthera.2022.108259.

(11) Von Kügelgen, I.; Schiedel, A. C.; Hoffmann, K.; Alsdorf, B. B. A.; Abdelrahman, A.; Müller, C. E. Cloning and Functional Expression of a Novel Gi Protein-Coupled Receptor for Adenine from Mouse Brain. *Mol. Pharmacol.* **2008**, *73* (2), 469–477. https://doi.org/10.1124/mol.107.037069.

(12) Thimm, D.; Knospe, M.; Abdelrahman, A.; Moutinho, M.; Alsdorf, B. B. A.; von Kügelgen, I.; Schiedel, A. C.; Müller, C. E. Characterization of New G Protein-Coupled Adenine Receptors in Mouse and Hamster. *Purinergic Signal.* **2013**, *9* (3), 415–426. https://doi.org/10.1007/s11302-013-9360-9.

(13) Smolenski, E. M. S. M. S. R. T.; Swierczynski, B. R. J. High Plasma Adenine Concentration in Chronic Renal Failure and Its Relation to Erythrocyte ATP. *Nephron* **2002**, *91*, 286–291.

(14) Wengert, M.; Adão-Novaes, J.; Assaife-Lopes, N.; Leão-Ferreira, L. R.; Caruso-Neves, C. Adenine-Induced Inhibition of Na+-ATPase Activity: Evidence for Involvement of the Gi Protein-Coupled Receptor in the CAMP Signaling Pathway. *Arch. Biochem. Biophys.* **2007**, *467* (2), 261–267. https://doi.org/10.1016/j.abb.2007.08.018.

(15) Inoue, K. Membrane Transporters as Targets for the Development of Drugs and Therapeutic Strategies Molecular Basis of Nucleobase Transport Systems in Mammals. **2017**, *40* (8), 1130–1138.

(16) Wright, N. J.; Lee, S. Y. Toward a Molecular Basis of Cellular Nucleoside Transport in Humans. *Chem. Rev.* **2021**, *121* (9), 5336–5358. https://doi.org/10.1021/acs.chemrev.0c00644.

(17) Yegutkin, G. G. Nucleotide- and Nucleoside-Converting Ectoenzymes: Important

Modulators of Purinergic Signalling Cascade. *Biochim. Biophys. Acta - Mol. Cell Res.* **2008**, *1783* (5), 673–694. https://doi.org/10.1016/j.bbamcr.2008.01.024.

(18) Hasuzawa, N.; Moriyama, S.; Moriyama, Y.; Nomura, M. BBA - Biomembranes Physiopathological Roles of Vesicular Nucleotide Transporter (VNUT), an Essential Component for Vesicular ATP Release. *BBA - Biomembr.* **2020**, *1862* (12), 183408. https://doi.org/10.1016/j.bbamem.2020.183408.

(19) Zimmermann, Herbert. Zebisch, Matthias . Sträter, N. Cellular Function and Molecular Structure of Ecto-Nucleotidases. *Purinergic Signal.* **2012**, *8*, 437–502. https://doi.org/DOI 10.1007/s11302-012-9309-4.

(20) Fredholm, B. B. Adenosine, an Endogenous Distress Signal, Modulates Tissue Damage and Repair. *Cell Death Differ.* **2007**, *14* (7), 1315–1323. https://doi.org/10.1038/sj.cdd.4402132.

(21) Pedata, F.; Corsi, C.; Melani, A.; Bordoni, F.; Latini, S. Adenosine Extracellular Brain Concentrations and Role of AA2 Receptors in Ischemia. *Nature* 74–84.

(22) Muñóz-Godínez, R.; De Lourdes Mora-García, M.; Weiss-Steider, B.; Montesinos-Montesinos, J. J.; Del Carmen Aguilar-Lemarroy, A.; García-Rocha, R.; Hernández-Montes, J.; Azucena Don-López, C.; Ávila-Ibarra, L. R.; Torres-Pineda, D. B.; Molina-Castillo, G.; Chacón-Salinas, R.; Vallejo-Castillo, L.; Pérez-Tapia, S. M.; Monroy-García, A. Detection of CD39 and a Highly Glycosylated Isoform of Soluble CD73 in the Plasma of Patients with Cervical Cancer: Correlation with Disease Progression. *Mediators Inflamm.* **2020**, *2020* (Article ID 1678780), 14. https://doi.org/10.1155/2020/1678780.

(23) Giuliani, A. L.; Sarti, A. C.; Di Virgilio, F. Ectonucleotidases in Acute and Chronic Inflammation. *Front. Pharmacol.* **2021**, *11* (February), 1–20. https://doi.org/10.3389/fphar.2020.619458.

(24) Lee, S. Y.; Müller, C. E. Nucleotide Pyrophosphatase/Phosphodiesterase 1 (NPP1) and Its Inhibitors. *Medchemcomm* **2017**, *8* (5), 823–840. https://doi.org/10.1039/c7md00015d.

(25) Muniyan, S.; Chaturvedi, N. K.; Dwyer, J. G.; LaGrange, C. A.; Chaney, W. G.; Lin, M. F. Human Prostatic Acid Phosphatase: Structure, Function and Regulation. *Int.*

J. Mol. Sci. **2013**, *14* (5), 10438–10464. https://doi.org/10.3390/ijms140510438.

(26) Rader, B. A. Alkaline Phosphatase, an Unconventional Immune Protein. *Front. Immunol.* **2017**, *8* (AUG), 1–6. https://doi.org/10.3389/fimmu.2017.00897.

(27) Jeffrey, J. L.; Lawson, K. V.; Powers, J. P. Targeting Metabolism of Extracellular Nucleotides via Inhibition of Ectonucleotidases CD73 and CD39. *J. Med. Chem.* **2020**, *63* (22), 13444–13465. https://doi.org/10.1021/acs.jmedchem.0c01044.

(28) Zimmermann, H. Extracellular Metabolism of ATP and Other Nucleotides. *Naunyn. Schmiedebergs. Arch. Pharmacol.* **2000**, *362* (4–5), 299–309. https://doi.org/10.1007/s002100000309.

(29) Stout, J. G.; Kirley, T. L. Control of Cell Membrane Ecto-ATPase by Oligomerization State: Intermolecular Cross-Linking Modulates ATPase Activity. *Biochemistry* **1996**, *35* (25), 8289–8298. https://doi.org/10.1021/bi960563g.

(30) Robson, S. C.; Sévigny, J.; Zimmermann, H. The E-NTPDase Family of Ectonucleotidases: Structure Function Relationships and Pathophysiological Significance. *Purinergic Signal.* **2006**, *2* (2), 409–430. https://doi.org/10.1007/s11302-006-9003-5.

(31) Smith, T. M.; Kirley, T. L. Site-Directed Mutagenesis of a Human Brain Ecto-Apyrase: Evidence That the E-Type ATPases Are Related to the Actin/Heat Shock 70/Sugar Kinase Superfamily. *Biochemistry* **1999**, *38* (1), 321–328. https://doi.org/10.1021/bi9820457.

(32) Robson, S. C.; Wu, Y.; Sun, X.; Knosalla, C.; Dwyer, K.; Enjyoji, K. Ectonucleotidases of CD39 Family Modulate Vascular Inflammation and Thrombosis in Transplantation. *Semin. Thromb. Hemost.* **2005**, *31* (2), 217–233. https://doi.org/10.1055/s-2005-869527.

(33) Sévigny, J.; Sundberg, C.; Braun, N.; Guckelberger, O.; Csizmadia, E.; Qawi, I.; Imai, M.; Zimmermann, H.; Robson, S. C. Differential Catalytic Properties and Vascular Topography of Murine Nucleoside Triphosphate Diphosphohydrolase 1 (NTPDase1) and NTPDase2 Have Implications for Thromboregulation. *Blood* **2002**, *99* (8), 2801–2809. https://doi.org/10.1182/blood.V99.8.2801.

(34) Langer, D.; Ikehara, Y.; Takebayashi, H.; Hawkes, R.; Zimmermann, H. The Ectonucleotidases Alkaline Phosphatase and Nucleoside Triphosphate Diphosphohydrolase 2 Are Associated with Subsets of Progenitor Cell Populations in the Mouse Embryonic, Postnatal and Adult Neurogenic Zones. *Neuroscience* **2007**, *150* (4), 863–879. https://doi.org/10.1016/j.neuroscience.2007.07.064.

(35) Massé, K.; Bhamra, S.; Eason, R.; Dale, N.; Jones, E. A. Purine-Mediated Signalling Triggers Eye Development. *Nature* **2007**, *449* (7165), 1058–1062. https://doi.org/10.1038/nature06189.

(36) Belcher, S. M.; Zsarnovszky, A.; Crawford, P. A.; Hemani, H.; Spurling, L.; Kirley, T. L. Immunolocalization of Ecto-Nucleoside Triphosphate Diphosphohydrolase 3 in Rat Brain: Implications for Modulation of Multiple Homeostatic Systems Including Feeding and Sleep-Wake Behaviors. *Neuroscience* **2006**, *137* (4), 1331–1346. https://doi.org/10.1016/j.neuroscience.2005.08.086.

(37) Bigonnesse, F.; Lévesque, S. A.; Kukulski, F.; Lecka, J.; Robson, S. C.; Fernandes, M. J. G.; Sévigny, J. Cloning and Characterization of Mouse Nucleoside Triphosphate Diphosphohydrolase-8. *Biochemistry* **2004**, *43* (18), 5511–5519. https://doi.org/10.1021/bi0362222.

(38) Lopez, V.; Schäkel, L.; Maximilian Schuh, H. J.; Schmidt, M. S.; Mirza, S.; Renn, C.; Pelletier, J.; Lee, S. Y.; Sévigny, J.; Alban, S.; Bendas, G.; Müller, C. E. Sulfated Polysaccharides from Macroalgae Are Potent Dual Inhibitors of Human ATP-Hydrolyzing Ectonucleotidases NPP1 and CD39. *Mar. Drugs* **2021**, *19* (2). https://doi.org/10.3390/MD19020051.

(39) Albright, R. A.; Ornstein, D. L.; Cao, W.; Chang, W. C.; Robert, D.; Tehan, M.; Hoyer, D.; Liu, L.; Stabach, P.; Yang, G.; De La Cruz, E. M.; Braddock, D. T. Molecular Basis of Purinergic Signal Metabolism by Ectonucleotide Pyrophosphatase/Phosphodiesterases 4 and 1 and Implications in Stroke. *J. Biol. Chem.* **2014**, *289* (6), 3294–3306. https://doi.org/10.1074/jbc.M113.505867.

(40) Lopez, V. Identification and Pharmacological Characterization of Nucleotide Vittoria Lopez, University of Bonn, Germany, 2022.

(41) Gorelik, A.; Randriamihaja, A.; Illes, K.; Nagar, B. A Key Tyrosine Substitution

Restricts Nucleotide Hydrolysis by the Ectoenzyme NPP5. *FEBS J.* **2017**, *284* (21), 3718–3726. https://doi.org/10.1111/febs.14266.

(42) Adriouch, S.; Bannas, P.; Schwarz, N.; Fliegert, R.; Guse, A. H.; Seman, M.; Haag, F.; Koch-Noke, F. ADP-ribosylation at R125 Gates the P2X7 Ion Channel by Presenting a Covalent Ligand to Its Nucleotide Binding Site. *FASEB J.* **2008**, *22* (3), 861–869. https://doi.org/10.1096/fj.07-9294com.

(43) Hesse, J.; Rosse, M. K.; Steckel, B.; Blank-Landeshammer, B.; Idel, S.; Reinders, Y.; Sickmann, A.; Sträter, N.; Schrader, J. Mono-ADP-Ribosylation Sites of Human CD73 Inhibit Its Adenosine-Generating Enzymatic Activity. *Purinergic Signal.* **2022**, *18* (1), 115–121. https://doi.org/10.1007/s11302-021-09832-4.

(44) Millán, J. L. Alkaline Phosphatases. *Purinergic Signal.* **2006**, *2* (2), 335–341. https://doi.org/10.1007/s11302-005-5435-6.

(45) Say, J. C.; Ciuffi, K.; Furriel, R. P. M.; Ciancaglini, P.; Leone, F. A. Alkaline Phosphatase from Rat Osseous Plates: Purification and Biochemical Characterization of a Soluble Form. *BBA - Gen. Subj.* **1991**, *1074* (2), 256–262. https://doi.org/10.1016/0304-4165(91)90161-9.

(46) Zaher, D. M.; El-Gamal, M. I.; Omar, H. A.; Aljareh, S. N.; Al-Shamma, S. A.; Ali, A. J.; Zaib, S.; Iqbal, J. Recent Advances with Alkaline Phosphatase Isoenzymes and Their Inhibitors. *Arch. Pharm. (Weinheim).* **2020**, *353* (5). https://doi.org/10.1002/ardp.202000011.

(47) Millµn, J. L. *Mammalian Alkaline Phosphatases*; 2006.

(48) Kaija, H.; Patrikainen, L. O. T.; Alatalo, S. L.; Väänänen, H. K.; Vihko, P. T. Acid Phosphatases. *Dyn. Bone Cartil. Metab. Princ. Clin. Appl.* **2006**, 165–180. https://doi.org/10.1016/B978-012088562-6/50011-X.

(49) Knapp, K. M.; Zebisch, M.; Sträter, N. Crystallization and Preliminary X-Ray Analysis of the Open Form of Human Ecto-5′-Nucleotidase (CD73). *Acta Crystallogr. Sect. F Struct. Biol. Cryst. Commun.* **2012**, *68* (12), 1545–1549. https://doi.org/10.1107/S1744309112045447.

(50) Thompson, L. F.; Ruedi, J. M.; Glass, A.; Low, M. G.; Lucas, A. H. Antibodies to

5’-Nucleotidase (CD73), a Glycosyl-Phosphatidylinositol-Anchored Protein, Cause Human Peripheral Blood T Cells to Proliferate. *J. Immunol.* **1989**, *143* (6), 1815–1821. https://doi.org/10.4049/jimmunol.143.6.1815.

(51) Thompson, L. F.; Ruedi, J. M.; O’Connor, R. D.; Bastian, J. F. Ecto-5’-Nucleotidase Expression during Human B Cell Development. An Explanation for the Heterogeneity in B Lymphocyte Ecto-5’-Nucleotidase Activity in Patients with Hypogammaglobulinemia. *J. Immunol.* **1986**, *137* (8), 2496–2500. https://doi.org/10.4049/jimmunol.137.8.2496.

(52) Bono, M. R.; Fernández, D.; Flores-Santibáñez, F.; Rosemblatt, M.; Sauma, D. CD73 and CD39 Ectonucleotidases in T Cell Differentiation: Beyond Immunosuppression. *FEBS Lett.* **2015**, *589* (22), 3454–3460. https://doi.org/10.1016/j.febslet.2015.07.027.

(53) Fang, F.; Cao, W.; Zhu, W.; Lam, N.; Li, L.; Gaddam, S.; Wang, Y.; Kim, C.; Lambert, S.; Zhang, H.; Hu, B.; Farber, D. L.; Weyand, C. M.; Goronzy, J. J. The Cell-Surface 5′-Nucleotidase CD73 Defines a Functional T Memory Cell Subset That Declines with Age. *Cell Rep.* **2021**, *37* (6). https://doi.org/10.1016/j.celrep.2021.109981.

(54) Snider, N. T.; Altshuler, P. J.; Wan, S.; Welling, T. H.; Cavalcoli, J.; Omarya, M. B. Alternative Splicing of Human NT5E in Cirrhosis and Hepatocellular Carcinoma Produces a Negative Regulator of Ecto-52-Nucleotidase (CD73). *Mol. Biol. Cell* **2014**, *25* (25), 4024–4033. https://doi.org/10.1091/mbc.E14-06-1167.

(55) NT5E gene transcripts (splice variants) https://www.ensembl.org/Homo_sapiens/Gene/Summary?g=ENSG00000135318;r=6:85449584-85495791.

(56) Brusco, A.; Ph, D.; Groden, C.; Gill, F.; Carlson-donohoe, H.; Lederman, R. J.; Chen, M. Y.; Yang, D.; Ph, D.; Siegenthaler, M. P.; Arduino, C.; Mancini, C.; Sc, M.; Freudenthal, B.; Stanescu, H. C.; Zdebik, A. A.; Ph, D.; Gahl, W. A.; Ph, D.; Boehm, M. Mutations and Arterial Calcifications. **2011**.

(57) Fausther, M.; Lavoie, E. G.; Goree, J. R.; Baldini, G.; Dranoff, J. A. NT5E Mutations That Cause Human Disease Are Associated with Intracellular Mistrafficking of

NT5E Protein. **2014**, *9* (6), 1–11. https://doi.org/10.1371/journal.pone.0098568.

(58) NIH dbSNP Short Genetic Variations. rs222952 https://www.ncbi.nlm.nih.gov/snp/rs2229523.

(59) Heuts, D. P. H. M.; Weissenborn, M. J.; Olkhov, R. V.; Shaw, A. M.; Gummadova, J.; Levy, C.; Scrutton, N. S. Crystal Structure of a Soluble Form of Human CD73 with Ecto-5'-Nucleotidase Activity. *ChemBioChem* **2012**, *13* (16), 2384–2391. https://doi.org/10.1002/cbic.201200426.

(60) Adzic, M.; Nedeljkovic, N. Unveiling the Role of Ecto-5'-Nucleotidase/CD73 in Astrocyte Migration by Using Pharmacological Tools. *Frontiers in Pharmacology*. 2018. https://doi.org/10.3389/fphar.2018.00153.

(61) Knapp, K.; Zebisch, M.; Pippel, J.; El-Tayeb, A.; Müller, C. E.; Sträter, N. Crystal Structure of the Human Ecto-5′-Nucleotidase (CD73): Insights into the Regulation of Purinergic Signaling. *Structure* **2012**, *20* (12), 2161–2173. https://doi.org/10.1016/j.str.2012.10.001.

(62) MISUMI, Y.; OGATA, S.; OHKUBO, K.; HIROSE, S.; IKEHARA, Y. Primary Structure of Human Placental 5′-nucleotidase and Identification of the Glycolipid Anchor in the Mature Form. *Eur. J. Biochem.* **1990**, *191* (3), 563–569. https://doi.org/10.1111/j.1432-1033.1990.tb19158.x.

(63) R., M.; Klemens, W.; R. Sherman, Nels J. Holmberg, Julie M. Ruedi, Martin G. Low, and L. F. T. Characterization Of Soluble Vs Membrane-Bound Human Placental 5'-Nucleotidase. **1990**, *172* (3), 1371–1377.

(64) Vogel, M.; Kowalewski, H.; Zimmermann, H.; Hooper, N. M.; Turner, A. J. Soluble Low-K(m) 5'-Nucleotidase from Electric-Ray (Torpedo Marmorata) Electric Organ and Bovine Cerebral Cortex Is Derived from the Glycosyl-Phosphatidylinositol-Anchored Ectoenzyme by Phospholipase C Cleavage. *Biochem. J.* **1992**, *284* (3), 621–624. https://doi.org/10.1042/bj2840621.

(65) Schneider, E.; Rissiek, A.; Winzer, R.; Puig, B.; Rissiek, B.; Haag, F.; Mittrücker, H. W.; Magnus, T.; Tolosa, E. Generation and Function of Non-Cell-Bound CD73 in Inflammation. *Front. Immunol.* **2019**, *10*, 1729. https://doi.org/10.3389/fimmu.2019.01729.

(66) Schneider, E.; Winzer, R.; Rissiek, A.; Ricklefs, I.; Meyer-Schwesinger, C.; Ricklefs, F. L.; Bauche, A.; Behrends, J.; Reimer, R.; Brenna, S.; Wasielewski, H.; Lauten, M.; Rissiek, B.; Puig, B.; Cortesi, F.; Magnus, T.; Fliegert, R.; Müller, C. E.; Gagliani, N.; Tolosa, E. CD73-Mediated Adenosine Production by CD8 T Cell-Derived Extracellular Vesicles Constitutes an Intrinsic Mechanism of Immune Suppression. *Nat. Commun.* **2021**, *12* (1), 1–14. https://doi.org/10.1038/s41467-021-26134-w.

(67) Sträter, N. Ecto-5′-Nucleotidase: Structure Function Relationships. *Purinergic Signal.* **2006**, *2* (2), 343–350. https://doi.org/10.1007/s11302-006-9000-8.

(68) Sean R. Stowell, Tongzhong Ju, R. D. C. Protein Glycosylation in Cancer. *Annu Rev Pathol* **2015**, *2* (2), 473–510. https://doi.org/10.1146/annurev-pathol-012414-040438.Protein.

(69) Alcedo, K. P.; Guerrero, A.; Basrur, V.; Fu, D.; Richardson, M. L.; McLane, J. S.; Tsou, C. C.; Nesvizhskii, A. I.; Welling, T. H.; Lebrilla, C. B.; Otey, C. A.; Kim, H. J.; Omary, M. B.; Snider, N. T. Tumor-Selective Altered Glycosylation and Functional Attenuation of CD73 in Human Hepatocellular Carcinoma. *Hepatol. Commun.* **2019**, *3* (10), 1400–1414. https://doi.org/10.1002/hep4.1410.

(70) Morote-García, J. C.; García-Ayllón, M. S.; Campoy, F. J.; Vidal, C. J.; Muñoz-Delgado, E. Active and Inactive Ecto-5′-Nucleotidase Variants in Liver of Control and Dystrophic Lama2dy Mice. *Int. J. Biochem. Cell Biol.* **2004**, *36* (3), 422–433. https://doi.org/10.1016/S1357-2725(03)00266-8.

(71) Salud García-Ayllón, M.; Javier Campoy, F.; Vidal, C. J.; Muñoz-Delgado, E. Identification of Inactive Ecto-5′-Nucleotidase in Normal Mouse Muscle and Its Increased Activity in Dystrophic Lama2dy Mice. *J. Neurosci. Res.* **2001**, *66* (4), 656–665. https://doi.org/10.1002/jnr.10014.

(72) Vogel, M.; Kowalewski, H. J.; Zimmermann, H.; Janetzko, A.; Margolis, R. U.; Wollny, H. E. Association of the NHK-1 Epitope with 5'-Nucleotidase from Torpedo Marmorata (Electric Ray) Electric Organ. *Biochem. J.* **1991**, *278* (1), 199–202. https://doi.org/10.1042/bj2780199.

(73) Vogel, M.; Zimmermann, H.; Singer, W. Transient Association of the HNK-1

Epitope with 5′-Nucleotidase during Development of the Cat Visual Cortex. *Eur. J. Neurosci.* **1993**, *5* (11), 1423–1425. https://doi.org/10.1111/j.1460-9568.1993.tb00209.x.

(74) Scaletti, E.; Huschmann, F. U.; Mueller, U.; Weiss, M. S.; Sträter, N. Substrate Binding Modes of Purine and Pyrimidine Nucleotides to Human Ecto-5′-Nucleotidase (CD73) and Inhibition by Their Bisphosphonic Acid Derivatives. *Purinergic Signal.* **2021**, *17* (4), 693–704. https://doi.org/10.1007/s11302-021-09802-w.

(75) Garavaglia, S.; Bruzzone, S.; Cassani, C.; Canella, L.; Allegrone, G.; Sturla, L.; Mannino, E.; Millo, E.; De Flora, A.; Rizzi, M. The High-Resolution Crystal Structure of Periplasmic Haemophilus Influenzae NAD Nucleotidase Reveals a Novel Enzymatic Function of Human CD73 Related to NAD Metabolism. *Biochem. J.* **2012**, *441* (1), 131–141. https://doi.org/10.1042/BJ20111263.

(76) El-Tayeb, A.; Iqbal, J.; Behrenswerth, A.; Romio, M.; Schneider, M.; Zimmermann, H.; Schrader, J.; Müller, C. E. Nucleoside-5′-Monophosphates as Prodrugs of Adenosine A2A Receptor Agonists Activated by Ecto-5′-Nucleotidase. *J. Med. Chem.* **2009**, *52* (23), 7669–7677. https://doi.org/10.1021/jm900538v.

(77) Fini, C.; Palmerini, C. A.; Damiani, P.; Stochaj, U.; Mannherz, H. G.; Floridi, A. 5′-Nucleotidase from Bull Seminal Plasma, Chicken Gizzard and Snake Venom Is a Zinc Metalloprotein. *Biochim. Biophys. Acta (BBA)/Protein Struct. Mol.* **1990**, *1038* (1), 18–22. https://doi.org/10.1016/0167-4838(90)90004-Y.

(78) Bhattarai, S.; Pippel, J.; Scaletti, E.; Idris, R.; Freundlieb, M.; Rolshoven, G.; Renn, C.; Lee, S. Y.; Abdelrahman, A.; Zimmermann, H.; El-Tayeb, A.; Müller, C. E.; Sträter, N. 2-Substituted α,β-Methylene-ADP Derivatives: Potent Competitive Ecto-5′-Nucleotidase (CD73) Inhibitors with Variable Binding Modes. *J. Med. Chem.* **2020**, *63* (6), 2941–2957. https://doi.org/10.1021/acs.jmedchem.9b01611.

(79) Resta, R.; Yamashita, Y.; Thompson, L. F. Ecto-Enzyme and Signaling Functions of Lymphocyte CD73. *Immunol. Rev.* **1998**, *161*, 95–109. https://doi.org/10.1111/j.1600-065X.1998.tb01574.x.

(80) Mahfuz, M. Inflammatory Bowel Disease: Foiling Inflammatory Bowel Disease.

Sci. Transl. Med. **2013**, *5* (209), 3062–3072. https://doi.org/10.1126/scitranslmed.3007773.

(81) Allard, B.; Longhi, S.; John, C. R. The Ectonucleotidases CD39 and CD73 : Novel Checkpoint Inhibitor Targets. *Immunol. Rev.* **2017**, *276*, 121–144. https://doi.org/10.1111/imr.12528.

(82) Solinas, C.; Carbognin, L.; De Silva, P.; Criscitiello, C.; Lambertini, M. Tumor-Infiltrating Lymphocytes in Breast Cancer According to Tumor Subtype: Current State of the Art. *Breast* **2017**, *35*, 142–150. https://doi.org/10.1016/j.breast.2017.07.005.

(83) Elisabete Augusto, Marco Matos, Jean Se´vigny, Ali El-Tayeb, Margaret S. Bynoe, C. E. M.; Rodrigo A. Cunha, and J.-F. C. Ecto-5_-Nucleotidase (CD73)-Mediated Formation of Adenosine Is Critical for the Striatal Adenosine A2A Receptor Functions. *J. Neurosci.* **2013**, *33* (28), 11390 –11399.

(84) Kulesskaya, N.; Võikar, V.; Peltola, M.; Yegutkin, G. G.; Salmi, M.; Jalkanen, S.; Rauvala, H. CD73 Is a Major Regulator of Adenosinergic Signalling in Mouse Brain. *PLoS One* **2013**, *8* (6). https://doi.org/10.1371/journal.pone.0066896.

(85) Ohta, M.; Toyama, K.; Gutterman, D. D.; Campbell, W. B.; Lemaître, V.; Teraoka, R.; Miura, H. Ecto-5′-Nucleotidase, CD73, Is an Endothelium-Derived Hyperpolarizing Factor Synthase. *Arterioscler. Thromb. Vasc. Biol.* **2013**, *33* (3), 629–636. https://doi.org/10.1161/ATVBAHA.112.300600.

(86) Pluskota, E.; Ma, Y.; Bledzka, K. M.; Bialkowska, K.; Soloviev, D. A.; Szpak, D.; Podrez, E. A.; Fox, P. L.; Hazen, S. L.; Dowling, J. J.; Ma, Y. Q.; Plow, E. F. Kindlin-2 Regulates Hemostasis by Controlling Endothelial Cell-Surface Expression of ADP/AMP Catabolic Enzymes via a Clathrin-Dependent Mechanism. *Blood* **2013**, *122* (14), 2491–2499. https://doi.org/10.1182/blood-2013-04-497669.

(87) Yang, J.; Jian, R.; Yu, J.; Zhi, X.; Liao, X.; Yu, J.; Zhou, P. CD73 Regulates Vascular Smooth Muscle Cell Functions and Facilitates Atherosclerotic Plaque Formation. *IUBMB Life* **2015**, *67* (11), 853–860. https://doi.org/10.1002/iub.1448.

(88) Bönner, F.; Borg, N.; Burghoff, S.; Schrader, J. Resident Cardiac Immune Cells and Expression of the Ectonucleotidase Enzymes CD39 and CD73 after Ischemic Injury.

PLoS One **2012**, *7* (4). https://doi.org/10.1371/journal.pone.0034730.

(89) Hu, X.-M.; Shi, N.-R.; Zhang, J.-Z.; Zuo, Y.-Q.; Wang, X.; Zhao, Y.-F.; Wu, J.-S. CD73: Friend or Foe in Lung Injury. *Int. J. Mol. Sci.* **2023**, *24* (6), 5545. https://doi.org/10.3390/ijms24065545.

(90) Minor, M.; Alcedo, K. P.; Battaglia, R. A.; Snider, N. T. Cell Type- and Tissue-Specific Functions of Ecto-5'-Nucleotidase (CD73). *Am. J. Physiol. - Cell Physiol.* **2019**, *317* (6), C1079–C1092. https://doi.org/10.1152/ajpcell.00285.2019.

(91) Picher, M.; Burch, L. H.; Hirsh, A. J.; Spychala, J.; Boucher, R. C. Ecto 5′-Nucleotidase and Nonspecific Alkaline Phosphatase: Two AMP-Hydrolyzing Ectoenzymes with Distinct Roles in Human Airways. *J. Biol. Chem.* **2003**, *278* (15), 13468–13479. https://doi.org/10.1074/jbc.M300569200.

(92) Matsuura, S.; Eto, S.; Kato, K.; Tashiro, Y. Ferritin Immunoelectron Microscopic Localization of 5'-Nucleotidase on Rat Liver Cell Surface. *J. Cell Biol.* **1984**, *99* (1 I), 166–173. https://doi.org/10.1083/jcb.99.1.166.

(93) Almishri, W.; Deans, J.; Swain, M. G. Rapid Activation and Hepatic Recruitment of Innate-like Regulatory B Cells after Invariant NKT Cell Stimulation in Mice. *J. Hepatol.* **2015**, *63* (4), 943–951. https://doi.org/10.1016/j.jhep.2015.06.007.

(94) Colgan, S. P.; Eltzschig, H. K.; Eckle, T.; Thompson, L. F. Physiological Roles for Ecto-5′-Nucleotidase (CD73). *Purinergic Signal.* **2006**, *2* (2), 351–360. https://doi.org/10.1007/s11302-005-5302-5.

(95) Shirley, D. G.; Vekaria, R. M.; Sévigny, J. Ectonucleotidases in the Kidney. *Purinergic Signal.* **2009**, *5* (4), 501–511. https://doi.org/10.1007/s11302-009-9152-4.

(96) Vekaria, R. M.; Shirley, D. G.; Sévigny, J.; Unwin, R. J. Immunolocalization of Ectonucleotidases along the Rat Nephron. *Am. J. Physiol. - Ren. Physiol.* **2006**, *290* (2), 550–560. https://doi.org/10.1152/ajprenal.00151.2005.

(97) Synnestvedt, K.; Furuta, G. T.; Comerford, K. M.; Louis, N.; Karhausen, J.; Eltzschig, H. K.; Hansen, K. R.; Thompson, L. F.; Colgan, S. P. Ecto-5′-Nucleotidase (CD73) Regulation by Hypoxia-Inducible Factor-1 Mediates

Permeability Changes in Intestinal Epithelia. *J. Clin. Invest.* **2002**, *110* (7), 993–1002. https://doi.org/10.1172/jci200215337.

(98) Allard, D.; Chrobak, P.; Stagg, J. CD73 – Adenosine : A next-Generation Target in Immuno-Oncology. *Immunotherapy* **2016**, *8* (2).

(99) Luca Antonioli, Gennady G. Yegutkin, Pál Pacher, Corrado Blandizzi, G. H. Anti-CD73 in Cancer Immunotherapy: Awakening New Opportunities. *Trends Cancer* **2016**, *2* (2), 95–109. https://doi.org/10.1053/j.gastro.2016.08.014.CagY.

(100) Mhatre V. Ho, Ji-Ann Lee, and K. C. M.; Dien et al., 2013. Hostile, Hypoxia-A2-Adenosinergic Tumor Biology as the Next Barrier to the Tumor Immunologists. *Cancer Immunol Res* **2014**, *2* (7), 598–605. https://doi.org/10.1158/2326-6066.CIR-14-0075.Hostile.

(101) Kleiser, S.; Pastewski, M.; Hapuarachchi, T.; Hagmann, C.; Fauchère, J. C.; Tachtsidis, I.; Wolf, M.; Scholkmann, F. *Characterizing Fluctuations of Arterial and Cerebral Tissue Oxygenation in Preterm Neonates by Means of Data Analysis Techniques for Nonlinear Dynamical Systems*; 2016; Vol. 876. https://doi.org/10.1007/978-1-4939-3023-4_64.

(102) Mhatre V. Ho, Ji-Ann Lee, and K. C. M.; Dien et al., 2013. Systemic Oxygenation Weakens the Hypoxia and Hypoxia Inducible Factor 1α-Dependent and Extracellular Adenosine- Mediated Tumor Protection. *J Mol Med* **2014**, *92* (12), 1283–1292. https://doi.org/10.1007/s00109-014-1189-3.Systemic.

(103) Xiong, L.; Wen, Y.; Miao, X.; Yang, Z. NT5E and FcGBP as Key Regulators of TGF-1-Induced Epithelial-Mesenchymal Transition (EMT) Are Associated with Tumor Progression and Survival of Patients with Gallbladder Cancer. *Cell Tissue Res.* **2014**, *355* (2), 365–374. https://doi.org/10.1007/s00441-013-1752-1.

(104) Turcotte, M.; Spring, K.; Pommey, S.; Chouinard, G.; Cousineau, I.; George, J.; Chen, G. M.; Gendoo, D. M. A.; Haibe-Kains, B.; Karn, T.; Rahimi, K.; Le Page, C.; Provencher, D.; Mes-Masson, A. M.; Stagg, J. CD73 Is Associated with Poor Prognosis in High-Grade Serous Ovarian Cancer. *Cancer Res.* **2015**, *75* (21), 4494–4503. https://doi.org/10.1158/0008-5472.CAN-14-3569.

(105) Leclerc, B. G.; Charlebois, R.; Chouinard, G.; Allard, B.; Pommey, S.; Saad, F.;

Stagg, J. CD73 Expression Is an Independent Prognostic Factor in Prostate Cancer. *Clin. Cancer Res.* **2016**, *22* (1), 158–166. https://doi.org/10.1158/1078-0432.CCR-15-1181.

(106) Lawrence, R. T.; Perez, E. M.; Hernández, D.; Miller, C. P.; Haas, K. M.; Irie, H. Y.; Lee, S. I.; Blau, A. C.; Villén, J. The Proteomic Landscape of Triple-Negative Breast Cancer. *Cell Rep.* **2015**, *11* (4), 630–644. https://doi.org/10.1016/j.celrep.2015.03.050.

(107) Sunaga, N.; Shames, D. S.; Girard, L.; Peyton, M.; Larsen, J. E.; Imai, H.; Soh, J.; Sato, M.; Yanagitani, N.; Kaira, K.; Xie, Y.; Gazdar, A. F.; Mori, M.; Minna, J. D. Knockdown of Oncogenic KRAS in Non-Small Cell Lung Cancers Suppresses Tumor Growth and Sensitizes Tumor Cells to Targeted Therapy. **2012**, *10* (2), 336–346. https://doi.org/10.1158/1535-7163.MCT-10-0750.Knockdown.

(108) Loi, S.; Pommey, S.; Haibe-Kains, B.; Beavis, P. A.; Darcy, P. K.; Smyth, M. J.; Stagg, J. CD73 Promotes Anthracycline Resistance and Poor Prognosis in Triple Negative Breast Cancer. *Proc. Natl. Acad. Sci. U. S. A.* **2013**, *110* (27), 11091–11096. https://doi.org/10.1073/pnas.1222251110.

(109) Supernat, A.; Markiewicz, A.; Wełnicka-Jaśkiewicz, M.; Seroczyńska, B.; Skokowski, J.; Sejda, A.; Szade, J.; Czapiewski, P.; Biernat, W.; Zaczek, A. CD73 Expression as a Potential Marker of Good Prognosis in Breast Carcinoma. *Appl. Immunohistochem. Mol. Morphol.* **2012**, *20* (2), 103–107. https://doi.org/10.1097/PAI.0b013e3182311d82.

(110) Bowser, J. L.; Blackburn, M. R.; Shipley, G. L.; Molina, J. G.; Dunner, K.; Broaddus, R. R. Loss of CD73-Mediated Actin Polymerization Promotes Endometrial Tumor Progression. *J. Clin. Invest.* **2016**, *126* (1), 220–238. https://doi.org/10.1172/JCI79380.

(111) Gessi, S.; Merighi, S.; Sacchetto, V.; Simioni, C.; Borea, P. A. Adenosine Receptors and Cancer. *Biochim. Biophys. Acta - Biomembr.* **2011**, *1808* (5), 1400–1412. https://doi.org/10.1016/j.bbamem.2010.09.020.

(112) Di Virgilio, F.; Adinolfi, E. Extracellular Purines, Purinergic Receptors and Tumor Growth. *Oncogene* **2017**, *36* (3), 293–303. https://doi.org/10.1038/onc.2016.206.

(113) Qi, Y.; Li, M.; Li, S.; Zeng, D.; Xiao, Y.; Li, J.; Ye, Q.; Bremer, E.; Zhang, G. Notch1 Promotes Resistance to Cisplatin by Up-Regulating Ecto-5′-Nucleotidase (CD73) in Triple-Negative Breast Cancer Cells. *Cell Death Discov.* **2023**, *9* (1), 1–9. https://doi.org/10.1038/s41420-023-01487-x.

(114) Quezada, C.; Garrido, W.; Oyarzún, C.; Fernández, K.; Segura, R.; Melo, R.; Casanello, P.; Sobrevia, L.; San Martín, R. 5′-Ectonucleotidase Mediates Multiple-Drug Resistance in Glioblastoma Multiforme Cells. *J. Cell. Physiol.* **2013**, *228* (3), 602–608. https://doi.org/10.1002/jcp.24168.

(115) Torres, Á.; Arriagada, V.; Erices, J. I.; De Los Ángeles Toro, M.; Rocha, J. D.; Niechi, I.; Carrasco, C.; Oyarzún, C.; Quezada, C. FK506 Attenuates the MRP1-Mediated Chemoresistant Phenotype in Glioblastoma Stem-like Cells. *Int. J. Mol. Sci.* **2018**, *19* (9), 1–13. https://doi.org/10.3390/ijms19092697.

(116) Huang, Q.; Durham, N. M.; Sult, E.; Wu, Y.; Liu, J.; Holoweckyj, N.; Iciek, L.; Hollingsworth, R.; Hall, B.; Herbst, R.; Leow, C. C.; Sachsenmeier, K. Levels and Enzyme Activity of CD73 in Primary Samples from Cancer Patients. *Cancer Res.* **2015**, *75* (15_Supplement), 1538–1538. https://doi.org/10.1158/1538-7445.am2015-1538.

(117) Maksimow, M.; Kyhälä, L.; Nieminen, A.; Kylänpää, L.; Aalto, K.; Elima, K.; Mentula, P.; Lehti, M.; Puolakkainen, P.; Yegutkin, G. G.; Jalkanen, S.; Repo, H.; Salmi, M. Early Prediction of Persistent Organ Failure by Soluble CD73 in Patients with Acute Pancreatitis. *Crit. Care Med.* **2014**, *42* (12), 2556–2564. https://doi.org/10.1097/CCM.0000000000000550.

(118) Dayanand, K.; Olivia E. Atherton1, Jennifer L. Tackett2, Emilio Ferrer1, and R. W. R. Beneficial Role of Erythrocyte Adenosine A2B ReceptorMediated AMPK Activation in High Altitude Hypoxia. *Circulation* **2016**, *134* (5), 405–421. https://doi.org/10.1161/CIRCULATIONAHA.116.021311.Beneficial.

(119) Yang, C.; Robbins, P. D. The Roles of Tumor-Derived Exosomes in Cancer Pathogenesis. *Clin. Dev. Immunol.* **2011**, *2011*. https://doi.org/10.1155/2011/842849.

(120) Clayton, A.; Al-Taei, S.; Webber, J.; Mason, M. D.; Tabi, Z. Cancer Exosomes

Express CD39 and CD73, Which Suppress T Cells through Adenosine Production. *J. Immunol.* **2011**, *187* (2), 676–683. https://doi.org/10.4049/jimmunol.1003884.

(121) Allard, B.; Beavis, P. A.; Darcy, P. K.; Stagg, J. Immunosuppressive Activities of Adenosine in Cancer. *Curr. Opin. Pharmacol.* **2016**, *29*, 7–16. https://doi.org/10.1016/j.coph.2016.04.001.

(122) Raskovalova, T.; Huang, X.; Sitkovsky, M.; Zacharia, L. C.; Jackson, E. K.; Gorelik, E. Gs Protein-Coupled Adenosine Receptor Signaling and Lytic Function of Activated NK Cells. *J. Immunol.* **2005**, *175*, 4383–4391.

(123) Roh, M.; Wainwright, D. A.; Wu, J. D.; Wan, Y.; Zhang, B. Targeting CD73 to Augment Cancer Immunotherapy. *Curr. Opin. Pharmacol.* **2020**, *53*, 66–76. https://doi.org/10.1016/j.coph.2020.07.001.

(124) Novitskiy, S. V.; Ryzhov, S.; Zaynagetdinov, R.; Goldstein, A. E.; Huang, Y.; Tikhomirov, O. Y.; Blackburn, M. R.; Biaggioni, I.; Carbone, D. P.; Feoktistov, I.; Dikov, M. M. Adenosine Receptors in Regulation of Dendritic Cell Differentiation and Function. *Blood* **2008**, *112* (5), 1822–1831. https://doi.org/10.1182/blood-2008-02-136325.

(125) Schnurr, M.; Toy, T.; Shin, A.; Hartmann, G.; Rothenfusser, S.; Soellner, J.; Davis, I. D.; Cebon, J.; Maraskovsky, E. Role of Adenosine Receptors in Regulating Chemotaxis and Cytokine Production of Plasmacytoid Dendritic Cells. *Blood* **2004**, *103* (4), 1391–1397. https://doi.org/10.1182/blood-2003-06-1959.

(126) Ryzhov, S.; Novitskiy, S. V.; Goldstein, A. E.; Biktasova, A.; Blackburn, M. R.; Biaggioni, I.; Dikov, M. M.; Feoktistov, I. Adenosinergic Regulation of the Expansion and Immunosuppressive Activity of CD11b+Gr1+ Cells. *J. Immunol.* **2011**, *187* (11), 6120–6129. https://doi.org/10.4049/jimmunol.1101225.

(127) Kumar, V. Adenosine as an Endogenous Immunoregulator in Cancer Pathogenesis: Where to Go? *Purinergic Signal.* **2013**, *9* (2), 145–165. https://doi.org/10.1007/s11302-012-9349-9.

(128) L. Whiteside, T.; Mandapathil, M.; Schuler, P. The Role of the Adenosinergic Pathway in Immunosuppression Mediated by Human Regulatory T Cells (Treg). *Curr. Med. Chem.* **2011**, *18* (34), 5217–5223.

https://doi.org/10.2174/092986711798184334.

(129) Jin, D.; Fan, J.; Wang, L.; Thompson, L. F.; Liu, A.; Daniel, B. J.; Shin, T.; Curiel, T. J.; Zhang, B. CD73 on Tumor Cells Impairs Antitumor T-Cell Responses: A Novel Mechanism of Tumor-Induced Immune Suppression. *Cancer Res.* **2010**, *70* (6), 2245–2255. https://doi.org/10.1158/0008-5472.CAN-09-3109.

(130) Saze, Z.; Schuler, P. J.; Hong, C. S.; Cheng, D.; Jackson, E. K.; Whiteside, T. L. Adenosine Production by Human B Cells and B Cell-Mediated Suppression of Activated T Cells. *Blood* **2013**, *122* (1), 9–18. https://doi.org/10.1182/blood-2013-02-482406.

(131) Cho-Chung, Y. S.; Clair, T.; Tortora, G.; Yokozaki, H. Role of Site-Selective CAMP Analogs in the Control and Reversal of Malignancy. *Pharmacol. Ther.* **1991**, *50* (1), 1–33. https://doi.org/10.1016/0163-7258(91)90071-S.

(132) Marfella-Scivittaro, C.; Quiñones, A.; Orellana, S. A. CAMP-Dependent Protein Kinase and Proliferation Differ in Normal and Polycystic Kidney Epithelia. *Am. J. Physiol. - Cell Physiol.* **2002**, *282* (4 51-4), 693–707. https://doi.org/10.1152/ajpcell.00122.2001.

(133) Yi, Y.; Zhou, Y.; Chu, X.; Zheng, X.; Fei, D.; Lei, J.; Qi, H.; Dai, Y. Blockade of Adenosine A2B Receptor Reduces Tumor Growth and Migration in Renal Cell Carcinoma. *J. Cancer* **2020**, *11* (2), 421–431. https://doi.org/10.7150/jca.31245.

(134) Merighi, S.; Battistello, E.; Giacomelli, L.; Varani, K.; Vincenzi, F.; Borea, P. A.; Gessi, S. Targeting A3 and A2A Adenosine Receptors in the Fight against Cancer. *Expert Opin. Ther. Targets* **2019**, *23* (8), 669–678. https://doi.org/10.1080/14728222.2019.1630380.

(135) Dastjerdi, M. N.; Rarani, M. Z.; Valiani, A.; Mahmoudieh, M. The Effect of Adenosine A1 Receptor Agonist and Antagonist on P53 and Caspase 3, 8, and 9 Expression and Apoptosis Rate in MCF-7 Breast Cancer Cell Line. *Res. Pharm. Sci.* **2016**, *11* (4), 303–310. https://doi.org/10.4103/1735-5362.189301.

(136) Zamani Rarani, M.; Zamani Rarani, F.; Valiani, A.; Shrifian Dastjerdi, Z.; Kargar Abargouei, E.; Eftekhar, E.; Taheri Kafran, A.; Pourentezari, M.; Saghebray, M.; Razavi, F.; Hadizadeh, S.; Nikbakht Dastjerdi, M. Adenosine A1 Receptor

Antagonist Up-Regulates Casp3 and Stimulates Apoptosis Rate in Breast Cancer Cell Line T47D. *Int. Electron. J. Med.* **2020**, *9* (1), 14–20. https://doi.org/10.34172/iejm.2020.03.

(137) Synowitz, M.; Glass, R.; Färber, K.; Markovic, D.; Kronenberg, G.; Herrmann, K.; Schnermann, J.; Nolte, C.; Van Rooijen, N.; Kiwit, J.; Kettenmann, H. A1 Adenosine Receptors in Microglia Control Glioblastoma-Host Interaction. *Cancer Res.* **2006**, *66* (17), 8550–8557. https://doi.org/10.1158/0008-5472.CAN-06-0365.

(138) Saito, M.; Yaguchi, T.; Yasuda, Y.; Nakano, T.; Nishizaki, T. Adenosine Suppresses CW2 Human Colonic Cancer Growth by Inducing Apoptosis via A1 Adenosine Receptors. *Cancer Lett.* **2010**, *290* (2), 211–215. https://doi.org/10.1016/j.canlet.2009.09.011.

(139) Mirza, A.; Basso, A.; Black, S.; Malkowski, M.; Kwee, L.; Pachter, J. A.; Lachowicz, J. E.; Wang, Y.; Liu, S. RNA Interference Targeting of A1 Receptor-Overexpressing Breast Carcinoma Cells Leads to Diminished Rates of Cell Proliferation and Induction of Apoptosis. *Cancer Biol. Ther.* **2005**, *4* (12), 1355–1360. https://doi.org/10.4161/cbt.4.12.2196.

(140) Sadej, R.; Spychala, J.; Skladanowski, A. C. Ecto-5′-Nucleotidase (EN, CD73) Is Coexpressed with Metastasis Promoting Antigens in Human Melanoma Cells. *Nucleosides, Nucleotides and Nucleic Acids* **2006**, *25* (9–11), 1119–1123. https://doi.org/10.1080/15257770600894188.

(141) Stagg, J.; Divisekera, U.; McLaughlin, N.; Sharkey, J.; Pommey, S.; Denoyer, D.; Dwyer, K. M.; Smyth, M. J. Anti-CD73 Antibody Therapy Inhibits Breast Tumor Growth and Metastasis. *Proc. Natl. Acad. Sci. U. S. A.* **2010**, *107* (4), 1547–1552. https://doi.org/10.1073/pnas.0908801107.

(142) Zhi, X.; Chen, S.; Zhou, P.; Shao, Z.; Wang, L.; Ou, Z.; Yin, L. RNA Interference of Ecto-5′-Nucleotidase (CD73) Inhibits Human Breast Cancer Cell Growth and Invasion. *Clin. Exp. Metastasis* **2007**, *24* (6), 439–448. https://doi.org/10.1007/s10585-007-9081-y.

(143) Wang, L.; Zhou, X.; Zhou, T.; Ma, D.; Chen, S.; Zhi, X.; Yin, L.; Shao, Z.; Ou, Z.; Zhou, P. Ecto-5′-Nucleotidase Promotes Invasion, Migration and Adhesion of

Human Breast Cancer Cells. *J. Cancer Res. Clin. Oncol.* **2008**, *134* (3), 365–372. https://doi.org/10.1007/s00432-007-0292-z.

(144) Stagg, J.; Divisekera, U.; Duret, H.; Sparwasser, T.; Teng, M. W. L.; Darcy, P. K.; Smyth, M. J. CD73-Deficient Mice Have Increased Antitumor Immunity and Are Resistant to Experimental Metastasis. *Cancer Res.* **2011**, *71* (8), 2892–2900. https://doi.org/10.1158/0008-5472.CAN-10-4246.

(145) Beavis, P. A.; Divisekera, U.; Paget, C.; Chow, M. T.; John, L. B.; Devaud, C.; Dwyer, K.; Stagg, J.; Smyth, M. J.; Darcy, P. K. Blockade of A2A Receptors Potently Suppresses the Metastasis of CD73+ Tumors. *Proc. Natl. Acad. Sci. U. S. A.* **2013**, *110* (36), 14711–14716. https://doi.org/10.1073/pnas.1308209110.

(146) Terp, M. G.; Olesen, K. A.; Arnspang, E. C.; Lund, R. R.; Lagerholm, B. C.; Ditzel, H. J.; Leth-Larsen, R. Anti-Human CD73 Monoclonal Antibody Inhibits Metastasis Formation in Human Breast Cancer by Inducing Clustering and Internalization of CD73 Expressed on the Surface of Cancer Cells. *J. Immunol.* **2013**, *191* (8), 4165–4173. https://doi.org/10.4049/jimmunol.1301274.

(147) Koszałka, P.; Pryszlak, A.; Gołuńska, M.; Kolasa, J.; Stasiłojć, G.; Składanowski, A. C.; Bigda, J. J. Inhibition of CD73 Stimulates the Migration and Invasion of B16F10 Melanoma Cells in Vitro, but Results in Impaired Angiogenesis and Reduced Melanoma Growth in Vivo. *Oncol. Rep.* **2014**, *31* (2), 819–827. https://doi.org/10.3892/or.2013.2883.

(148) Wang, L.; Tang, S.; Wang, Y.; Xu, S.; Yu, J.; Zhi, X.; Ou, Z.; Yang, J.; Zhou, P.; Shao, Z. Ecto-5′-Nucleotidase (CD73) Promotes Tumor Angiogenesis. *Clin. Exp. Metastasis* **2013**, *30* (5), 671–680. https://doi.org/10.1007/s10585-013-9571-z.

(149) Allard, B.; Turcotte, M.; Spring, K.; Pommey, S.; Royal, I.; Stagg, J. Anti-CD73 Therapy Impairs Tumor Angiogenesis. *Int. J. Cancer* **2014**, *134* (6), 1466–1473. https://doi.org/10.1002/ijc.28456.

(150) Sadej, R.; Inai, K.; Rajfur, Z.; Ostapkowicz, A.; Kohler, J.; Skladanowski, A. C.; Mitchell, B. S.; Spychala, J. Tenascin C Interacts with Ecto-5′-Nucleotidase (EN) and Regulates Adenosine Generation in Cancer Cells. *Biochim. Biophys. Acta - Mol. Basis Dis.* **2008**, *1782* (1), 35–40. https://doi.org/10.1016/j.bbadis.2007.11.001.

(151) Sadej, R.; Skladanowski, A. C. Dual, Enzymatic and Non-Enzymatic, Function of Ecto-5'-Nucleotidase (En, CD73) in Migration and Invasion of A375 Melanoma Cells. *Acta Biochim. Pol.* **2012**, *59* (4), 647–652. https://doi.org/10.18388/abp.2012_2105.

(152) Gao, Z. W.; Dong, K.; Zhang, H. Z. The Roles of CD73 in Cancer. *Biomed Res. Int.* **2014**, *2014*. https://doi.org/10.1155/2014/460654.

(153) Gammelgaard, O. L.; Terp, M. G.; Renn, C.; Labrijn, A. F.; Hamaker, O.; Nielsen, A. Y.; Vever, H.; Hansen, S. W. K.; Gjerstorff, M. F.; Müller, C. E.; Parren, P. W. H. I.; Ditzel, H. J. Targeting Two Distinct Epitopes on Human CD73 with a Bispecific Antibody Improves Anticancer Activity. *J. Immunother. Cancer* **2022**, *10* (9), 1–12. https://doi.org/10.1136/jitc-2022-004554.

(154) Perrot, I.; Michaud, H. A.; Giraudon-Paoli, M.; Augier, S.; Docquier, A.; Gros, L.; Courtois, R.; Déjou, C.; Jecko, D.; Becquart, O.; Rispaud-Blanc, H.; Gauthier, L.; Rossi, B.; Chanteux, S.; Gourdin, N.; Amigues, B.; Roussel, A.; Bensussan, A.; Eliaou, J. F.; Bastid, J.; Romagné, F.; Morel, Y.; Narni-Mancinelli, E.; Vivier, E.; Paturel, C.; Bonnefoy, N. Blocking Antibodies Targeting the CD39/CD73 Immunosuppressive Pathway Unleash Immune Responses in Combination Cancer Therapies. *Cell Rep.* **2019**, *27* (8), 2411-2425.e9. https://doi.org/10.1016/j.celrep.2019.04.091.

(155) Qiao, Z.; Li, X.; Kang, N.; Yang, Y.; Chen, C.; Wu, T.; Zhao, M.; Liu, Y.; Ji, X. A Novel Specific Anti-CD73 Antibody Inhibits Triple-Negative Breast Cancer Cell Motility by Regulating Autophagy. *Int. J. Mol. Sci.* **2019**, *20* (5), 1057. https://doi.org/10.3390/ijms20051057.

(156) Geoghegan, J. C.; Diedrich, G.; Lu, X.; Rosenthal, K.; Sachsenmeier, K. F.; Wu, H.; Dall'Acqua, W. F.; Damschroder, M. M. Inhibition of CD73 AMP Hydrolysis by a Therapeutic Antibody with a Dual, Non-Competitive Mechanism of Action. *MAbs* **2016**, *8* (3), 454–467. https://doi.org/10.1080/19420862.2016.1143182.

(157) Piovesan, D.; Tan, J. B. L.; Becker, A.; Banuelos, J.; Narasapp, N.; DiRenzo, D.; Zhang, K.; Chen, A.; Ginn, E.; Udyavar, A. R.; Yin, F.; Paprcka, S. L.; Purandare, B.; Park, T. W.; Kimura, N.; Kalisiak, J.; Young, S. W.; Powers, J. P.; Schindler, U.; Sivick, K. E.; Walters, M. J. Targeting CD73 with AB680 (Quemliclustat), a Novel

and Potent Small-Molecule CD73 Inhibitor, Restores Immune Functionality and Facilitates Antitumor Immunity. *Mol. Cancer Ther.* **2022**, *21* (6), 948–959. https://doi.org/10.1158/1535-7163.MCT-21-0802.

(158) Zhou, X.; Zhi, X.; Zhou, P.; Chen, S.; Zhao, F.; Shao, Z.; Ou, Z.; Yin, L. Effects of Ecto-5′-Nucleotidase on Human Breast Cancer Cell Growth in Vitro and in Vivo. *Oncol. Rep.* **2007**, *17* (6), 1341–1346. https://doi.org/10.3892/or.17.6.1341.

(159) Overman, M. J.; LoRusso, P.; Strickler, J. H.; Patel, S. P.; Clarke, S. J.; Noonan, A. M.; Prasanna, T.; Amin, M. A.; Nemunaitis, J. J.; Desai, J.; O'Byrne, K. J.; George, T. J.; Englert, J.; She, D.; Cooper, Z. A.; Wu, Y.; Khan, A.; Kumar, R.; Bendell, J. C. Safety, Efficacy and Pharmacodynamics (PD) of MEDI9447 (Oleclumab) Alone or in Combination with Durvalumab in Advanced Colorectal Cancer (CRC) or Pancreatic Cancer (Panc). *J. Clin. Oncol.* **2018**, *36* (15_suppl), 4123. https://doi.org/10.1200/JCO.2018.36.15_suppl.4123.

(160) A Amici , M Emanuelli, N Raffaelli, S Ruggieri, G. M. One-Minute High-Performance Liquid Chromatography Assay for 5'-Nucleotidase Using a 20-Mm Reverse-Phase Column. *Anal. Biochem.* **1994**, *216*, 171–175.

(161) Janero, D. R.; Yarwood, C.; Thakkar, J. K. Application of Solid-Phase Extraction on Anion-Exchange Cartridges to Quantify 5'-Nucleotidase Activity. *J. Chromatogr. B Biomed. Sci. Appl.* **1992**, *573* (2), 207–218. https://doi.org/10.1016/0378-4347(92)80121-6.

(162) Kokkinopoulos, D.; Tsiapalis, C. M.; Perez, S.; Papamichail, M.; Courtis, N.; Trangas, T. A Colorimetric Assay for the Determination of 5′-Nucleotidase Activity. *J. Immunol. Methods* **1987**, *101* (1), 73–78. https://doi.org/10.1016/0022-1759(87)90218-3.

(163) He, Y.; Zhao, Y.; Nelson, D. M.; Klippel, A.; Reily, M. D. NMR-Based Assay for the Ex Vivo Determination of Soluble CD73 Activity in Serum. *Anal. Chem.* **2020**, *92* (21), 14501–14508. https://doi.org/10.1021/acs.analchem.0c02630.

(164) McManus, J.; He, T.; Gavigan, J. A.; Marchand, G.; Vougier, S.; Bedel, O.; Ferrari, P.; Arrebola, R.; Gillespy, T.; Gregory, R. C.; Licht, S.; Cheng, H.; Zhang, B.; Deng, G. A Robust Multiplex Mass Spectrometric Assay for Screening Small-Molecule

Inhibitors of CD73 with Diverse Inhibition Modalities. *SLAS Discov.* **2018**, *23* (3), 264–273. https://doi.org/10.1177/2472555217750386.

(165) Heinz, F.; Pilz, R.; Reckel, S.; Kalden, J. R. A New Spectrophotometric Method for the Determination of 5'-Nucleotidase. *J. Clin. Chem. Clin. Biochem* **1980**, *18*, 781–788.

(166) Baykov, A. A.; Evtushenko, A.; AVAEVA A N Belozersky, S. M. A Malachite Green Procedure for Orthophosphate Determination and Its Use in Alkaline Phosphatase-Based Enzyme Immunoassay. *Anal. Biochem.* **1988**, *171*, 266–270. https://doi.org/10.1016/0003-2697(88)90484-8.

(167) Iqbal, J.; Jirovsky, D.; Lee, S. Y.; Zimmermann, H.; Müller, C. E. Capillary Electrophoresis-Based Nanoscale Assays for Monitoring Ecto-5′-Nucleotidase Activity and Inhibition in Preparations of Recombinant Enzyme and Melanoma Cell Membranes. *Anal. Biochem.* **2008**, *373* (1), 129–140. https://doi.org/10.1016/j.ab.2007.09.028.

(168) Raza, R.; Bai, Y.; Liu, H. Development of a Fast CE Method for High Throughput Screening of Ecto-5′-Nucleotidase Inhibitors. *Electrophoresis* **2018**, *39* (20), 2612–2618. https://doi.org/10.1002/elps.201800105.

(169) Wu, F.; Li, P. L.; Zou, A. P. Microassay of 5'-Nucleotidase and Adenosine Deaminase Activity in Microdissected Nephron Segments. *Anal. Biochem.* **1999**, *266* (1), 133–139. https://doi.org/10.1006/abio.1998.2951.

(170) Freundlieb, M.; Zimmermann, H.; Müller, C. E. A New, Sensitive Ecto-5′-Nucleotidase Assay for Compound Screening. *Anal. Biochem.* **2014**, *446* (1), 53–58. https://doi.org/10.1016/j.ab.2013.10.012.

(171) Tucker-pian, C.; Bakay, B.; I, W. L. N. 5'-Nucleotidase: Solubilization, Radiochemical Analysis, and Electrophoresis. **1979**, *17*, 995–1005.

(172) Mary Kay Gentry, R. A. O. A Simple, Specific, Radioisotopic Assay for 5'-Nucleotidase. *Anal. Biochem.* **1975**, *64*, 624–627.

(173) Allard, B.; Cousineau, I.; Spring, K.; Stagg, J. *Measurement of CD73 Enzymatic Activity Using Luminescence-Based and Colorimetric Assays*, 1st ed.; Elsevier Inc.,

2019; Vol. 629. https://doi.org/10.1016/bs.mie.2019.10.007.

(174) Lanzetta, P. A.; Alvarez, L. J.; Reinach, P. S.; Candia, O. A. An Improved Assay for Nanomole Amounts of Inorganic Phosphate. *Anal. Biochem.* **1979**, *100* (1), 95–97. https://doi.org/10.1016/0003-2697(79)90115-5.

(175) Cogan, E. B.; Birrell, G. B.; Griffith, O. H. A Robotics-Based Automated Assay for Inorganic and Organic Phosphates. *Anal. Biochem.* **1999**, *271* (1), 29–35. https://doi.org/10.1006/abio.1999.4100.

(176) Cacatian, S.; Claremon, D. A.; Jia, L.; Morales-Ramos, A.; Singh, S. B. . V.-; Raman, S.; Xu, Z.; Zheng, Y. Purine Derivatives as CD73 Inhibitors for the Treatment of Cancer.

(177) Sachsenmeier, K. F.; Hay, C.; Brand, E.; Clarke, L.; Rosenthal, K.; Guillard, S.; Rust, S.; Minter, R.; Hollingsworth, R. Development of a Novel Ectonucleotidase Assay Suitable for High-Throughput Screening. *J. Biomol. Screen.* **2012**, *17* (7), 993–998. https://doi.org/10.1177/1087057112443987.

(178) Leitão, J. M. M.; Esteves da Silva, J. C. G. Firefly Luciferase Inhibition. *J. Photochem. Photobiol. B Biol.* **2010**, *101* (1), 1–8. https://doi.org/10.1016/j.jphotobiol.2010.06.015.

(179) Susan R. Mikkelsen, E. C. *Bioanalytical Chemistry*; Wiley, 2004.

(180) Copeland, R. A.; Pompliano, D. L.; Meek, T. D. Drug–Target Residence Time and Its Implications for Lead Optimization. *Nature* **2006**, *5*, 730–740.

(181) Tummino, P. J.; Copeland, R. A. Residence Time of Receptor-Ligand Complexes and Its Effect on Biological Function (Biochemistry (2008) 47, 20, (5481-5492)). *Biochemistry* **2008**, *47* (32), 8465. https://doi.org/10.1021/bi801226m.

(182) Bernetti, M.; Masetti, M.; Rocchia, W.; Cavalli, A. Kinetics of Drug Binding and Residence Time. **2019**.

(183) Dougall, I. G.; Unitt, J. *Evaluation of the Biological Activity of Compounds: Techniques and Mechanism of Action Studies*; Elsevier Ltd, 2015. https://doi.org/10.1016/B978-0-12-417205-0.00002-X.

(184) Hulme, E. C.; Trevethick, M. A. Ligand Binding Assays at Equilibrium: Validation and Interpretation. *Br. J. Pharmacol.* **2010**, *161* (6), 1219–1237. https://doi.org/10.1111/j.1476-5381.2009.00604.x.

(185) Motulsky, H. J.; Neubig, R. R. *Analyzing Binding Data*; 2010; Vol. 52. https://doi.org/10.1002/0471142301.ns0705s52.

(186) Flanagan, C. A. GPCR-Radioligand Binding Assays. In *Methods in Cell Biology*; Elsevier Ltd, 2016; Vol. 132, pp 191–215. https://doi.org/10.1016/bs.mcb.2015.11.004.

(187) Maguire, J. J.; Kuc, R. E.; Davenport, A. P. *Chapter 3 Radioligand Binding Assays and Their Analysis*; Vol. 897. https://doi.org/10.1007/978-1-61779-909-9.

(188) Yung-Chi, C.; Prusoff, W. H. Relationship between the Inhibition Constant (KI) and the Concentration of Inhibitor Which Causes 50 per Cent Inhibition (IC50) of an Enzymatic Reaction. *Biochem. Pharmacol.* **1973**, *22* (23), 3099–3108. https://doi.org/10.1016/0006-2952(73)90196-2.

(189) Langmead, C. J.; Christopoulos, A. Functional and Structural Perspectives on Allosteric Modulation of GPCRs. *Curr. Opin. Cell Biol.* **2014**, *27* (1), 94–101. https://doi.org/10.1016/j.ceb.2013.11.007.

(190) Dacres, H.; Michie, M.; Wang, J.; Pfleger, K. D. G.; Trowell, S. C. Effect of Enhanced Renilla Luciferase and Fluorescent Protein Variants on the Förster Distance of Bioluminescence Resonance Energy Transfer (BRET). *Biochem. Biophys. Res. Commun.* **2012**, *425* (3), 625–629. https://doi.org/10.1016/j.bbrc.2012.07.133.

(191) Dale, N. C.; Johnstone, E. K. M.; White, C. W.; Pfleger, K. D. G. NanoBRET: The Bright Future of Proximity-Based Assays. *Front. Bioeng. Biotechnol.* **2019**, *7* (MAR), 1–13. https://doi.org/10.3389/fbioe.2019.00056.

(192) Stoddart, L. A.; Kilpatrick, L. E.; Hill, S. J. NanoBRET Approaches to Study Ligand Binding to GPCRs and RTKs. *Trends Pharmacol. Sci.* **2018**, *39* (2), 136–147. https://doi.org/10.1016/j.tips.2017.10.006.

(193) Azad, T.; Janse Van Rensburg, H. J.; Morgan, J.; Rezaei, R.; Crupi, M. J. F.; Chen,

R.; Ghahremani, M.; Jamalkhah, M.; Forbes, N.; Ilkow, C.; Bell, J. C. Luciferase-Based Biosensors in the Era of the COVID-19 Pandemic. *ACS Nanosci. Au* **2021**, *1* (1), 15–37. https://doi.org/10.1021/acsnanoscienceau.1c00009.

(194) Hall, M. P.; Unch, J.; Binkowski, B. F.; Valley, M. P.; Butler, B. L.; Wood, M. G.; Otto, P.; Zimmerman, K.; Vidugiris, G.; MacHleidt, T.; Robers, M. B.; Benink, H. A.; Eggers, C. T.; Slater, M. R.; Meisenheimer, P. L.; Klaubert, D. H.; Fan, F.; Encell, L. P.; Wood, K. V. Engineered Luciferase Reporter from a Deep Sea Shrimp Utilizing a Novel Imidazopyrazinone Substrate. *ACS Chem. Biol.* **2012**, *7* (11), 1848–1857. https://doi.org/10.1021/cb3002478.

(195) Inouye, S.; Watanabe, K.; Nakamura, H.; Shimomura, O. Secretional Luciferase of the Luminous Shrimp Oplophorus Gracilirostris: CDNA Cloning of a Novel Imidazopyrazinone Luciferase. *FEBS Lett.* **2000**, *481* (1), 19–25. https://doi.org/10.1016/S0014-5793(00)01963-3.

(196) Machleidt, T.; Woodroofe, C. C.; Schwinn, M. K.; Méndez, J.; Robers, M. B.; Zimmerman, K.; Otto, P.; Daniels, D. L.; Kirkland, T. A.; Wood, K. V. NanoBRET-A Novel BRET Platform for the Analysis of Protein-Protein Interactions. *ACS Chem. Biol.* **2015**, *10* (8), 1797–1804. https://doi.org/10.1021/acschembio.5b00143.

(197) Shigeto, H.; Ikeda, T.; Kuroda, A.; Funabashi, H. A BRET-Based Homogeneous Insulin Assay Using Interacting Domains in the Primary Binding Site of the Insulin Receptor. *Anal. Chem.* **2015**, *87* (5), 2764–2770. https://doi.org/10.1021/ac504063x.

(198) Christiansen, E.; Hudson, B. D.; Hansen, A. H.; Milligan, G.; Ulven, T. Development and Characterization of a Potent Free Fatty Acid Receptor 1 (FFA1) Fluorescent Tracer. *J. Med. Chem.* **2016**, *59* (10), 4849–4858. https://doi.org/10.1021/acs.jmedchem.6b00202.

(199) Bartole, E.; Grätz, L.; Littmann, T.; Wifling, D.; Seibel, U.; Buschauer, A.; Bernhardt, G. UR-DEBa242: A Py-5-Labeled Fluorescent Multipurpose Probe for Investigations on the Histamine H3 and H4 Receptors. *J. Med. Chem.* **2020**, *63* (10), 5297–5311. https://doi.org/10.1021/acs.jmedchem.0c00160.

(200) Conroy, S.; Kindon, N. D.; Glenn, J.; Stoddart, L. A.; Lewis, R. J.; Hill, S. J.; Kellam, B.; Stocks, M. J. Synthesis and Evaluation of the First Fluorescent Antagonists of

the Human P2Y 2 Receptor Based on AR-C118925. *J. Med. Chem.* **2018**, *61* (7), 3089–3113. https://doi.org/10.1021/acs.jmedchem.8b00139.

(201) Kim, J.; Grailhe, R. Nanoluciferase Signal Brightness Using Furimazine Substrates Opens Bioluminescence Resonance Energy Transfer to Widefield Microscopy. *Cytom. Part A* **2016**, *89* (8), 742–746. https://doi.org/10.1002/cyto.a.22870.

(202) Goyet, E.; Bouquier, N.; Ollendorff, V.; Perroy, J. Fast and High Resolution Single-Cell BRET Imaging. *Sci. Rep.* **2016**, *6* (June), 1–12. https://doi.org/10.1038/srep28231.

(203) Schaub, F. X.; Reza, M. S.; Flaveny, C. A.; Li, W.; Musicant, A. M.; Hoxha, S.; Guo, M.; Cleveland, J. L.; Amelio, A. L. Fluorophore-NanoLuc BRET Reporters Enable Sensitive In Vivo Optical Imaging and Flow Cytometry for Monitoring Tumorigenesis. *Cancer Res.* **2015**, *75* (23), 5023–5033. https://doi.org/10.1158/0008-5472.CAN-14-3538.

(204) Chu, J.; Oh, Y.; Sens, A.; Ataie, N.; Dana, H.; Macklin, J. J.; Laviv, T.; Welf, E. S.; Dean, K. M.; Zhang, F.; Kim, B. B.; Tang, C. T.; Hu, M.; Baird, M. A.; Davidson, M. W.; Kay, M. A.; Fiolka, R.; Yasuda, R.; Kim, D. S.; Ng, H. L.; Lin, M. Z. A Bright Cyan-Excitable Orange Fluorescent Protein Facilitates Dual-Emission Microscopy and Enhances Bioluminescence Imaging in Vivo. *Nat. Biotechnol.* **2016**, *34* (7), 760–767. https://doi.org/10.1038/nbt.3550.

(205) Hans-Peter; Baer, G. I.; Drummond; and E. Loverne Duncan. Formation and Deamination of Adenosine by Cardiac Muscle Enzymes. **1966**, *2*, 67–76.

(206) Grondal, E. J.; Zimmermann, H. Purification, Characterization and Cellular Localization of 5'-Nucleotidase from Torpedo Electric Organ. *Biochem. J.* **1987**, *245* (3), 805–810. https://doi.org/10.1042/bj2450805.

(207) Terrell C. Myers, Kaname Nakamura, and A. B. D. Phosphonic Acid Analogs of Nucleoside Phosphates. III. The Synthesis of Adenosine-5'-Methylenediphosphonate, a Phosphonic Acid Analog of Adenosine-5'-Diphosphate. **1965**, *30* (May), 1517–1520.

(208) Burger, R. M.; Lowenstein, J. M. Preparation and Properties of 5'-Nucleotidase from Smooth Muscle of Small Intestine. *J. Biol. Chem.* **1970**, *245* (23), 6274–6280.

https://doi.org/10.1016/s0021-9258(18)62605-5.

(209) Bhattarai, S.; Freundlieb, M.; Pippel, J.; Meyer, A.; Abdelrahman, A.; Fiene, A.; Lee, S. Y.; Zimmermann, H.; Yegutkin, G. G.; Sträter, N.; El-Tayeb, A.; Müller, C. E. α,β-Methylene-ADP (AOPCP) Derivatives and Analogues: Development of Potent and Selective Ecto-5′-Nucleotidase (CD73) Inhibitors. *J. Med. Chem.* **2015**, *58* (15), 6248–6263. https://doi.org/10.1021/acs.jmedchem.5b00802.

(210) Bhattarai, S.; Pippel, J.; Meyer, A.; Freundlieb, M.; Schmies, C.; Abdelrahman, A.; Fiene, A.; Lee, S.; Zimmermann, H.; El-Tayeb, A.; Yegutkin, G. G.; Sträter, N.; Müller, C. E. X-ray Co-crystal Structure Guides the Way to Subnanomolar Competitive Ecto-5′-nucleotidase (CD73) Inhibitors for Cancer Immunotherapy. *Adv. Ther.* **2019**, *2* (10), 1900075. https://doi.org/10.1002/adtp.201900075.

(211) Bhattarai, S. Synthesis and Structure-Activity Relationships of α, β-Methylene-ADP Derivatives : Potent and Selective Ecto-5 ’-Nucleotidase Inhibitors, University of Bonn, Germany, 2015.

(212) Bowman, C. E.; Silva, R. G.; Pham, A.; Young, S. W. An Exceptionally Potent Inhibitor of Human CD73. *Biochemistry* **2019**, *58*, 3331–3334. https://doi.org/10.1021/acs.biochem.9b00448.

(213) Lawson, K. V.; Kalisiak, J.; Lindsey, E. A.; Newcomb, E. T.; Leleti, M. R.; Debien, L.; Rosen, B. R.; Miles, D. H.; Sharif, E. U.; Jeffrey, J. L.; Tan, J. B. L.; Chen, A.; Zhao, S.; Xu, G.; Fu, L.; Jin, L.; Park, T. W.; Berry, W.; Moschütz, S.; Scaletti, E.; Sträter, N.; Walker, N. P.; Young, S. W.; Walters, M. J.; Schindler, U.; Powers, J. P. Discovery of AB680: A Potent and Selective Inhibitor of CD73. *J. Med. Chem.* **2020**, *63* (20), 11448–11468. https://doi.org/10.1021/acs.jmedchem.0c00525.

(214) Du, X.; Moore, J.; Blank, B. R.; Eksterowicz, J.; Sutimantanapi, D.; Yuen, N.; Metzger, T.; Chan, B.; Huang, T.; Chen, X.; Chen, Y.; Duong, F.; Kong, W.; Chang, J. H.; Sun, J.; Zavorotinskaya, T.; Ye, Q.; Junttila, M. R.; Ndubaku, C.; Friedman, L. S.; Fantin, V. R.; Sun, D. Orally Bioavailable Small-Molecule CD73 Inhibitor (OP-5244) Reverses Immunosuppression through Blockade of Adenosine Production. *J. Med. Chem.* **2020**, *63* (18), 10433–10459. https://doi.org/10.1021/acs.jmedchem.0c01086.

(215) Junttila, M. R.; Ray, A.; Warne, R.; Chen, X.; Du, T.; Sutimantanapi, D.; Chang, J. H.; Blank, B.; Moore, J.; Ndubaku, C. O.; Zavorotinskaya, T.; Multani, P.; Nadeem, O.; Chauhan, D.; Anderson, K. C.; Friedman, L. S. Abstract 2074: ORIC-533, a Small Molecule CD73 Inhibitor with Best-in-Class Properties, Reversesimmunosuppression and Has Potential as an Immunomodulatory Therapy in Patients with Multiple Myeloma. In *Cancer Research*; 2022; Vol. 82, pp 2074–2074. https://doi.org/10.1158/1538-7445.am2022-2074.

(216) Sharif, E. U.; Kalisiak, J.; Lawson, K. V; Miles, D. H.; Newcomb, E.; Lindsey, E. A.; Rosen, B. R.; Debien, L. P. P.; Chen, A.; Zhao, X.; Scaletti, E. R.; Jin, L.; Xu, G.; Young, S. W.; Walker, N. P.; Stra, N.; Leleti, M. R.; Powers, J. P. Discovery of Potent and Selective Methylenephosphonic Acid CD73 Inhibitors. **2021**, *64*, 845–860. https://doi.org/10.1021/acs.jmedchem.0c01835.

(217) Liu, S.; Li, D.; Liu, J.; Wang, H.; Horecny, I.; Shen, R.; Zhang, R.; Wu, H.; Hu, Q.; Zhao, P.; Zhang, F.; Yan, Y.; Feng, J.; Zhuang, L.; Li, J.; Zhang, L.; Tao, W. A Novel Cd73 Inhibitor Shr170008 Suppresses Adenosine in Tumor and Enhances Anti-Tumor Activity with Pd-1 Blockade in a Mouse Model of Breast Cancer. *Onco. Targets. Ther.* **2021**, *14* (August), 4561–4574. https://doi.org/10.2147/OTT.S326178.

(218) Chen, L.; Li, J.; Sjogren, Eric, B.; Billedeau, Roland, J. Ectonucleotidase Inhibitors and Methods of Use Thereof. WO/2018/049145.

(219) Kalisiak, J.; Lawson, Kenneth, V.; Leleti, Manmohan, R.; Lindsey, Erick, A.; Miles, Dillon, H.; Newcomb, E.; Powers, Jay, P.; SHarif, Ehesan, U. Inhibitors of CD73-Mediated Immunosuppression. WO/2018/094148.

(220) Du, X.; Eksterowicz, J.; Fantin, V. R.; Sun, D.; Ye, Q.; Moore, J.; Zavorotinskaya, T.; Blank, B. R.; Kawai, H.; Yeh, C.-H.; Rew, Y.; Wu, K.; Pham, J. CD73 Inhibitors. WO/2021/011689.

(221) Wang, B.; Yang, H.; Bedke, K.; Wehn, P.; Rizzi, J. P. CD73 Inhibitors and Uses Thereof. WO/2018/183635.

(222) Chen, L.; Billedeau, Roland, J.; Li, J.; Stanton, Timothy, F. Ectonucleotidase Inhibitors and Methods of Use Thereof. WO/2020/257429.

(223) Chen, D.; Bailey, S.; Feng, J.; Kayser, F.; Liu, C.; Yuan, H. CD73 Inhibitors. WO/2020/211672.

(224) Li, J.; Chen, L.; Billedeau, R. J.; Stanton, T. F.; Chiang, J. T. P.; Lee, C. C.; Li, W.; Steggerda, S.; Emberley, E.; Gross, M.; Bhupathi, D.; Che, X.; Chen, J.; Dang, R.; Huang, T.; Ma, Y.; Mackinnon, A.; Makkouk, A.; Marguier, G.; Neou, S.; Sotirovska, N.; Spurlock, S.; Zhang, J.; Zhang, W.; Van Zandt, M.; Yuan, L.; Savoy, J.; Parlati, F.; Sjogren, E. B. Discovery of a Series of Potent, Selective, and Orally Bioavailable Nucleoside Inhibitors of CD73 That Demonstrates in Vivo Antitumor Activity. *J. Med. Chem.* **2023**, *66* (1), 345–370. https://doi.org/10.1021/acs.jmedchem.2c01287.

(225) Dumontet, C.; Peyrottes, S.; Rabeson, C.; Cros-Perrial, E.; Géant, P. Y.; Chaloin, L.; Jordheim, L. P. CD73 Inhibition by Purine Cytotoxic Nucleoside Analogue-Based Diphosphonates. *Eur. J. Med. Chem.* **2018**, *157*, 1051–1055. https://doi.org/10.1016/j.ejmech.2018.08.035.

(226) Junker, A.; Renn, C.; Dobelmann, C.; Namasivayam, V.; Jain, S.; Losenkova, K.; Irjala, H.; Duca, S.; Balasubramanian, R.; Chakraborty, S.; Börgel, F.; Zimmermann, H.; Yegutkin, G. G.; Müller, C. E.; Jacobson, K. A. Structure-Activity Relationship of Purine and Pyrimidine Nucleotides as Ecto-5'- Nucleotidase (CD73) Inhibitors. *J Med Chem* **2019**, *62*, 3677–3695.

(227) Scortichini, M.; Idris, R. M.; Moschütz, S.; Keim, A.; Salmaso, V.; Dobelmann, C.; Oliva, P.; Losenkova, K.; Irjala, H.; Vaittinen, S.; Sandholm, J.; Yegutkin, G. G.; Sträter, N.; Junker, A.; Müller, C. E.; Jacobson, K. A. Structure-Activity Relationship of 3-Methylcytidine-5′-α,β-Methylenediphosphates as CD73 Inhibitors. *J. Med. Chem.* **2022**, *65* (3), 2409–2433. https://doi.org/10.1021/acs.jmedchem.1c01852.

(228) Schäkel, L.; Schmies, C. C.; Idris, R. M.; Luo, X.; Lee, S. Y.; Lopez, V.; Mirza, S.; Vu, T. H.; Pelletier, J.; Sévigny, J.; Namasivayam, V.; Müller, C. E. Nucleotide Analog ARL67156 as a Lead Structure for the Development of CD39 and Dual CD39/CD73 Ectonucleotidase Inhibitors. *Front. Pharmacol.* **2020**, *11* (September), 1–23. https://doi.org/10.3389/fphar.2020.01294.

(229) Nassir, M.; Arad, U.; Lee, S. Y.; Journo, S.; Mirza, S.; Renn, C.; Zimmermann, H.;

Pelletier, J.; Sévigny, J.; Müller, C. E.; Fischer, B. Identification of Adenine-N9-(Methoxy)Ethyl-β-Bisphosphonate as NPP1 Inhibitor Attenuates NPPase Activity in Human Osteoarthritic Chondrocytes. *Purinergic Signal.* **2019**, *15* (2), 247–263. https://doi.org/10.1007/s11302-019-09649-2.

(230) Baqi, Y.; Hausmann, R.; Rosefort, C.; Rettinger, J.; Schmalzing, G.; Müller, C. E. Discovery of Potent Competitive Antagonists and Positive Modulators of the P2X2 Receptor. *J. Med. Chem.* **2011**, *54* (3), 817–830. https://doi.org/10.1021/jm1012193.

(231) Weyler, S.; Baqi, Y.; Hillmann, P.; Kaulich, M.; Hunder, A. M.; Müller, I. A.; Müller, C. E. Combinatorial Synthesis of Anilinoanthraquinone Derivatives and Evaluation as Non-Nucleotide-Derived P2Y2 Receptor Antagonists. *Bioorganic Med. Chem. Lett.* **2008**, *18* (1), 223–227. https://doi.org/10.1016/j.bmcl.2007.10.082.

(232) Glänzel, M.; Bültmann, R.; Starke, K.; Frahm, A. W. Constitutional Isomers of Reactive Blue 2 - Selective P2Y-Receptor Antagonists? *Eur. J. Med. Chem.* **2003**, *38* (3), 303–312. https://doi.org/10.1016/S0223-5234(02)01449-6.

(233) Baqi, Y.; Weyler, S.; Iqbal, J.; Zimmermann, H.; Müller, C. E. Structure-Activity Relationships of Anthraquinone Derivatives Derived from Bromaminic Acid as Inhibitors of Ectonucleoside Triphosphate Diphosphohydrolases (E-NTPDases). *Purinergic Signal.* **2009**, *5* (1), 91–106. https://doi.org/10.1007/s11302-008-9103-5.

(234) Baqi, Y.; Rashed, M.; Schäkel, L.; Malik, E. M.; Pelletier, J.; Sévigny, J.; Fiene, A.; Müller, C. E. Development of Anthraquinone Derivatives as Ectonucleoside Triphosphate Diphosphohydrolase (NTPDase) Inhibitors With Selectivity for NTPDase2 and NTPDase3. *Front. Pharmacol.* **2020**, *11* (August), 1–15. https://doi.org/10.3389/fphar.2020.01282.

(235) Baqi, Y.; Lee, S. Y.; Iqbal, J.; Ripphausen, P.; Lehr, A.; Scheiff, A. B.; Zimmennann, H.; Bajorath, J.; Müller, C. E. Development of Potent and Selective Inhibitors of Ecto-5′- Nucleotidase Based on an Anthraquinone Scaffold. *J. Med. Chem.* **2010**, *53* (5), 2076–2086. https://doi.org/10.1021/jm901851t.

(236) Ripphausen, P.; Freundlieb, M.; Brunschweiger, A.; Zimmermann, H.; Müller, C. E.; Bajorath, J. Virtual Screening Identifies Novel Sulfonamide Inhibitors of Ecto -

5'-Nucleotidase. *J. Med. Chem.* **2012**, *55* (14), 6576–6581. https://doi.org/10.1021/jm300658n.

(237) Iqbal, J.; Saeed, A.; Raza, R.; Matin, A.; Hameed, A.; Furtmann, N.; Lecka, J.; Sévigny, J.; Bajorath, J. Identification of Sulfonic Acids as Efficient Ecto-5′-Nucleotidase Inhibitors. *Eur. J. Med. Chem.* **2013**, *70*, 685–691. https://doi.org/10.1016/j.ejmech.2013.10.053.

(238) Rahimova, R.; Fontanel, S.; Lionne, C.; Jordheim, L. P.; Peyrottes, S.; Chaloin, L. Identification of Allosteric Inhibitors of the Dimer Interface. **2018**, 1–23.

(239) Ghoteimi, R.; Braka, A.; Rodriguez, C.; Cros-Perrial, E.; Duvauchelle, V.; Uttaro, J. P.; Mathé, C.; Ménétrier-Caux, C.; Jordheim, L. P.; Chaloin, L.; Peyrottes, S. Second-Generation CD73 Inhibitors Based on a 4,6-Biaryl-2-Thiopyridine Scaffold. *ChemMedChem* **2023**, *18* (7). https://doi.org/10.1002/cmdc.202200594.

(240) Adams, J. L.; Ator, L. E.; Duffy, K. J.; Graybill, T. L.; Kiesow, T. J.; Lian, Y.; Moore, M. L.; Ralph, J. M.; Ridgers, L. H. Benzothiadiazine Compounds. WO2017/098421.

(241) Dally, R. D.; Garcia Paredes, M. C.; Heinz, L. J. I.; HowelL, J. M.; Njoroge, F. G.; Wang, Y.; Zhao, G. CD73 Inhibitors. WO/2019/168744.

(242) Beatty, J.; Debien, L. P. P.; Drew, S. L.; Fournier, J.; Grange, R. L.; Jacob, S. D.; Jeffrey, J. L.; Lawson, K. V.; Leleti, M. R.; Lindsey, E. A.; Mandal, D.; Powers, J. P.; Tran, A. T.; THomas-Tran, R.; Yan, X. CD73 Inhibitors. WO/2020/046813.

(243) Beatty, J. W.; Lindsey, E. A.; Thomas-Tran, R.; Debien, L.; MANDAL, D.; Jeffrey, J. L.; Tran, A. T.; Fournier, J.; Jacob, S. D.; Yan, X.; Drew, S. L.; Ginn, E.; Chen, A.; Pham, A. T.; Zhao, S.; Jin, L.; Young, S. W.; Walker, N.; Leleti, M. R.; Moschütz, S.; Sträter, N.; Powers, J. P.; Lawson, K. V. Discovery of Potent and Selective Non-Nucleotide Small Molecule Inhibitors of CD73. *J. Med. Chem.* **2020**, *63*, 3935–3955. https://doi.org/10.1021/acs.jmedchem.9b01713.

(244) Mish, M. J. B. F. C. L. C. E. L. M. R. CD73 Compounds, 2024.

(245) Zou, M. Lyuh. X. Heterocycle Compounds for the Treatment of Cancer, 2024.

(246) Varano, F.; Catarzi, D.; Vincenzi, F.; Pasquini, S.; Pelletier, J.; Lopes Rangel Fietto,

J.; Espindola Gelsleichter, N.; Sarlandie, M.; Guilbaud, A.; Sévigny, J.; Varani, K.; Colotta, V. Structural Investigation on Thiazolo[5,4-d]Pyrimidines to Obtain Dual-Acting Blockers of CD73 and Adenosine A2A Receptor as Potential Antitumor Agents. *Bioorganic Med. Chem. Lett.* **2020**, *30* (9), 127067. https://doi.org/10.1016/j.bmcl.2020.127067.

(247) LopezLazaro, M. Flavonoids as Anticancer Agents: Structure-Activity Relationship Study. *Curr. Med. Chem. - Anti-Cancer Agents* **2002**, *2* (6), 691–714.

(248) Braganhol, E.; Tamajusuku, A. S. K.; Bernardi, A.; Wink, M. R.; Battastini, A. M. O. Ecto-5′-Nucleotidase/CD73 Inhibition by Quercetin in the Human U138MG Glioma Cell Line. *Biochim. Biophys. Acta - Gen. Subj.* **2007**, *1770* (9), 1352–1359. https://doi.org/10.1016/j.bbagen.2007.06.003.

(249) Lyu, S.; Zhao, Y.; Zeng, X.; Chen, X.; Meng, Q.; Ding, Z.; Zhao, W.; Qi, Y.; Gao, Y.; Du, J. Identification of Phelligridin-Based Compounds as Novel Human CD73 Inhibitors. *J. Chem. Inf. Model.* **2021**, *61* (3), 1275–1286. https://doi.org/10.1021/acs.jcim.0c00961.

(250) Ashraf, A.; Shafiq, Z.; Khan Jadoon, M. S.; Tahir, M. N.; Pelletier, J.; Sevigny, J.; Yaqub, M.; Iqbal, J. Synthesis, Characterization, and in Silico Studies of Novel Spirooxindole Derivatives as Ecto-5′-Nucleotidase Inhibitors. *ACS Med. Chem. Lett.* **2020**, *11* (12), 2397–2405. https://doi.org/10.1021/acsmedchemlett.0c00343.

(251) MEDI9447 Alone and in Combination With MEDI4736 in Adult Participants With Select Advanced Solid Tumors https://clinicaltrials.gov/study/NCT02503774?intr=MEDI9447&rank=10.

(252) A Phase 2 Study of Durvalumab (MEDI4736) and Oleclumab (MEDI9447) in Multi-Cancer Populations With Correlation to Clinical, Molecular and Immunologic Parameters With DNA MethylaTION (DOMINATION) https://clinicaltrials.gov/study/NCT04262375?intr=MEDI9447&rank=9.

(253) Paclitaxel + Carboplatin + Durvalumab With or Without Oleclumab for Previously Untreated Locally Recurrent Inoperable or Metastatic TNBC (SYNERGY) https://clinicaltrials.gov/study/NCT03616886?intr=MEDI9447&rank=4.

(254) AGEN1423 Plus Balstilimab With or Without Chemo in Pancreatic Cancer

https://clinicaltrials.gov/study/NCT05632328?intr=AGEN1423&rank=1.

(255) Nocentini, A.; Capasso, C.; Supuran, C. T. Small-Molecule CD73 Inhibitors for the Immunotherapy of Cancer: A Patent and Literature Review (2017–Present). *Expert Opin. Ther. Pat.* **2021**, *31* (10), 867–876. https://doi.org/10.1080/13543776.2021.1923694.

(256) A Study of the CD73 Inhibitor LY3475070 Alone or in Combination With Pembrolizumab in Participants With Advanced Cancer https://clinicaltrials.gov/study/NCT04148937?term=CD73&intr=LY3475070&rank=1.

(257) Schmies, C. C.; Rolshoven, G.; Idris, R. M.; Losenkova, K.; Renn, C.; Schäkel, L.; Al-Hroub, H.; Wang, Y.; Garofano, F.; Schmidt-Wolf, I. G. H.; Zimmermann, H.; Yegutkin, G. G.; Müller, C. E. Fluorescent Probes for Ecto-5′-Nucleotidase (CD73). *ACS Med. Chem. Lett.* **2020**. https://doi.org/10.1021/acsmedchemlett.0c00391.

(258) Spychala, J. Tumor-Promoting Functions of Adenosine. *Pharmacol. Ther.* **2000**, *87* (2–3), 161–173. https://doi.org/10.1016/S0163-7258(00)00053-X.

(259) Zhang, B. CD73 Promotes Tumor Growth and Metastasis. *Oncoimmunology* **2012**, *1* (1), 67–70. https://doi.org/10.4161/onci.1.1.18068.

(260) Freundlieb, M.; Zimmermann, H.; Müller, C. E. A New, Sensitive Ecto-5'-Nucleotidase Assay for Compound Screening. *Anal. Biochem.* **2014**, *446*, 53–58.

(261) Leone, R. D.; Emens, L. A. Targeting Adenosine for Cancer Immunotherapy. *J. Immunother. Cancer* **2018**, *6* (1), 57. https://doi.org/10.1186/s40425-018-0360-8.

(262) Allard, D.; Chrobak, P.; Allard, B.; Messaoudi, N.; Stagg, J. Targeting the CD73-Adenosine Axis in Immuno-Oncology. *Immunol. Lett.* **2019**, *205* (May), 31–39. https://doi.org/10.1016/j.imlet.2018.05.001.

(263) Augustin, R. C.; Leone, R. D.; Naing, A.; Fong, L.; Bao, R.; Luke, J. J. Next Steps for Clinical Translation of Adenosine Pathway Inhibition in Cancer Immunotherapy. *J. Immunother. Cancer* **2022**, *10* (2), 1–13. https://doi.org/10.1136/jitc-2021-004089.

(264) Junker, A.; Renn, C.; Dobelmann, C.; Namasivayam, V.; Jain, S.; Losenkova, K.;

Irjala, H.; Duca, S.; Balasubramanian, R.; Chakraborty, S.; Börgel, F.; Zimmermann, H.; Yegutkin, G. G.; Müller, C. E.; Jacobson, K. A. Structure-Activity Relationship of Purine and Pyrimidine Nucleotides as Ecto-5′-Nucleotidase (CD73) Inhibitors. *J. Med. Chem.* **2019**, *62* (7), 3677–3695. https://doi.org/10.1021/acs.jmedchem.9b00164.

(265) Hebanowska, A.; Mierzejewska, P.; Braczko, A. Effect of Estradiol on Enzymes of Vascular Extracellular Nucleotide Metabolism. *Hormones* **2020**. https://doi.org/10.1007/s42000-020-00242-6.

(266) Hatfield, S. M.; Sitkovsky, M. A2A Adenosine Receptor Antagonists to Weaken the Hypoxia-HIF-1α Driven Immunosuppression and Improve Immunotherapies of Cancer. *Curr. Opin. Pharmacol.* **2016**, *29* (Figure 1), 90–96. https://doi.org/10.1016/j.coph.2016.06.009.

(267) Sitkovsky, M. V.; Hatfield, S.; Abbott, R.; Belikoff, B.; Lukashev, D.; Ohta, A. Hostile, Hypoxia-A2-Adenosinergic Tumor Biology as the next Barrier to Overcome for Tumor Immunologists. *Cancer Immunol. Res.* **2014**, *2* (7), 598–605. https://doi.org/10.1158/2326-6066.CIR-14-0075.

(268) Gao, Z.-G.; Jacobson, K. A. Molecular Sciences A 2B Adenosine Receptor and Cancer. *Int. J. Mol. Sci.* **2019**, *1*, 1–18.

(269) Sepúlveda, C.; Palomo, I.; Fuentes, E. Role of Adenosine A2b Receptor Overexpression in Tumor Progression. *Life Sci.* **2016**, *166*, 92–99. https://doi.org/10.1016/j.lfs.2016.10.008.

(270) Ye, H.; Zhao, J.; Xu, X.; Zhang, D.; Shen, H.; Wang, S. Role of Adenosine A2a Receptor in Cancers and Autoimmune Diseases. *Immunity, Inflamm. Dis.* **2023**, *11* (4), e826. https://doi.org/10.1002/iid3.826.

(271) Mayssara A. Abo Hassanin Supervised, A.; Munawarah, S. H.; Misnaniarti, M.; Isnurhadi, I.; Komunitas, J. K.; Rumbai, P.; City, P.; Komitmen, P.; Kbpkp, P.; Commitment, S.; Kbpkp, F.; Dewi, N. M. .; Hardy, I. P. D. .; Sugianto, M. .; 19, T.; Ninla Elmawati Falabiba; Anton Kristijono; Sandra, C.; Herawati, Y. T.; Baroya, N.; Trirahayu, P.; Akbar, K. A.; Ramani, A.; Pencapaian, A.; Kapitasi, I.; Komitmen, B.; Victor, J.; Maramis, F.; Mandagi, C. K. F.; Wowor, R.; Kesehatan, F.;

Universitas, M.; Ratulangi, S.; Febriawati, H.; Yandrizal, Y.; Afriza, Y.; Pratiwi, B. A.; Yanuarti, R.; Suryani, D.; Hiv, K.; Aids, D. A. N.; Rumah, D. I.; Utara, U. S.; Badan Penyelenggara Jaminan Sosial (BPJS) Kesehatan; Mayssara A. Abo Hassanin Supervised, A.; Vii, B. A. B.; Husada, F. R. K.; Info BPJS Kesehatan; Anugrah, S. 2015; BPJS-Kesehatan; Trisnantoro, L.; LAILY, E. N.; Utami, D. siwi; Murti, B.; Suryani, N.; Kurnia, R.; Fadli; Kemkes RI; BPJS Kesehatan; Laksono, T.; dkk; Indonesia, U.; Maujudah, S. A.; Masyarakat, F. K.; Studi, P.; Kesehatan, I. CD73 Inhibitors DALLY; Robert Dean ; et Al. PCT/US2019/019074, 2019.

(272) Investigation of AB680 in clinical trials https://clinicaltrials.gov/search?intr=AB680.

(273) Phase 1 clinical study for LY-3475070 https://clinicaltrials.gov/search?intr=LY3475070.

(274) Antonioli, L.; Blandizzi, C.; Malavasi, F.; Ferrari, D.; Haskó, G. Anti-CD73 Immunotherapy: A Viable Way to Reprogram the Tumor Microenvironment. *Oncoimmunology* **2016**, *5* (9), 1–3. https://doi.org/10.1080/2162402X.2016.1216292.

(275) Doherty, G. A.; Bai, A.; Hanidziar, D.; Longhi, M. S.; Lawlor, G. O.; Putheti, P.; Csizmadia, E.; Nowak, M.; Cheifetz, A. S.; Moss, A. C.; Robson, S. C. CD73 Is a Phenotypic Marker of Effector Memory Th17 Cells in Inflammatory Bowel Disease. *Eur. J. Immunol.* **2012**, *42* (11), 3062–3072. https://doi.org/10.1002/eji.201242623.

(276) Caiazzo, E.; Maione, F.; Morello, S.; Lapucci, A.; Paccosi, S.; Steckel, B.; Lavecchia, A.; Parenti, A.; Iuvone, T.; Schrader, J.; Ialenti, A.; Cicala, C. Adenosine Signalling Mediates the Anti-Inflammatory Effects of the COX-2 Inhibitor Nimesulide. *Biochem. Pharmacol.* **2016**, *112*, 72–81. https://doi.org/10.1016/j.bcp.2016.05.006.

(277) Perry, H. M.; Görldt, N.; Sung, S. S. J.; Huang, L.; Rudnicka, K. P.; Encarnacion, I. M.; Bajwa, A.; Tanaka, S.; Poudel, N.; Yao, J.; Rosin, D. L.; Schrader, J.; Okusa, M. D. Perivascular CD73+ Cells Attenuate Inflammation and Interstitial Fibrosis in the Kidney Microenvironment. *Am. J. Physiol. - Ren. Physiol.* **2019**, *317* (3), F658–F669. https://doi.org/10.1152/ajprenal.00243.2019.

(278) Kabsch, W. (2010) XDS. Acta Crystallographica D, 66, 125-132. Kabsch W. Biological Crystallography. *Acta Crystallogr Sect D Biol Crystallogr* **2010**, No. D66, 125–132.

(279) Evans, P. R.; Murshudov, G. N. How Good Are My Data and What Is the Resolution? *Acta Crystallogr. Sect. D Biol. Crystallogr.* **2013**, *D69* (7), 1204–1214. https://doi.org/10.1107/S0907444913000061.

(280) Vonrhein, C. Tickle, I. J. Flensburg, C. Keller, P. Paciorek, W. Sharff , A. and Bricogne, G. Advances in Automated Data Analysis and Processing within AutoPROC, Combined with Improved Characterisation, Mitigation and Visualisation of the Anisotropy of Diffraction Limits Using STARANISO. *Acta Crystallogr. Sect. A* **2018**, *A74*, a360.

(281) Emsley, P.; Lohkamp, B.; Scott, W. G.; Cowtan, K. Features and Development of Coot. *Acta Crystallogr. Sect. D Biol. Crystallogr.* **2010**, *66* (4), 486–501. https://doi.org/10.1107/S0907444910007493.

(282) Liebschner, D.; Afonine, P. V.; Moriarty, N. W.; Poon, B. K.; Sobolev, O. V.; Terwilliger, T. C.; Adams, P. D. Polder Maps: Improving OMIT Maps by Excluding Bulk Solvent. *Acta Crystallogr. Sect. D Struct. Biol.* **2017**, *73* (2), 148–157. https://doi.org/10.1107/S2059798316018210.

(283) Servos, J. Catalytically Active Soluble Ecto-5'-Nucleotidase Purified after Heterologous Expression as a Tool for Drug Screening. *Drug Dev. Res.* **1998**, *45* (3–4), 269–276. https://doi.org/10.1002/(SICI)1098-2299(199811/12)45:3/4<269::AID-DDR25>3.0.CO;2-B.

(284) Reinhardt, J.; Landsberg, J.; Schmid-Burgk, J. L.; Ramis, B. B.; Bald, T.; Glodde, N.; Lopez-Ramos, D.; Young, A.; Ngiow, S. F.; Nettersheim, D.; Schorle, H.; Quast, T.; Kolanus, W.; Schadendorf, D.; Long, G. V.; Madore, J.; Scolyer, R. A.; Ribas, A.; Smyth, M. J.; Tumeh, P. C.; Tuting, T.; Holzel, M. MAPK Signaling and Inflammation Link Melanoma Phenotype Switching to Induction of CD73 during Immunotherapy. *Cancer Res.* **2017**, *77* (17), 4697–4709. https://doi.org/10.1158/0008-5472.CAN-17-0395.

(285) Kuschak, M.; Namasivayam, V.; Rafehi, M.; Voss, J. H.; Garg, J.; Schlegel, J. G.;

Abdelrahman, A.; Kehraus, S.; Reher, R.; Küppers, J.; Sylvester, K.; Hinz, S.; Matthey, M.; Wenzel, D.; Fleischmann, B. K.; Pfeifer, A.; Inoue, A.; Gütschow, M.; König, G. M.; Müller, C. E. Cell-Permeable High-Affinity Tracers for Gq Proteins Provide Structural Insights, Reveal Distinct Binding Kinetics and Identify Small Molecule Inhibitors. *Br. J. Pharmacol.* **2020**, *177* (8), 1898–1916. https://doi.org/10.1111/bph.14960.

(286) Lowry, O. H.; Rosebrough, N. J.; Farr, A. L.; Randall, R. J. Protein Measurement with the Folin Phenol Reagent. *J. Biol. Chem.* **1951**, *193* (1), 265–275. https://doi.org/10.1016/0922-338X(96)89160-4.

(287) Schaeffer, H. J. *Nucleosides and Nucleotides*; 1967; Vol. 2. https://doi.org/10.1016/S0065-7743(08)61527-4.

(288) Kalek, M.; Jemielity, J.; Stepinski, J.; Stolarski, R.; Darzynkiewicz, E. A Direct Method for the Synthesis of Nucleoside 5'-Methylenebis(Phosphonate)s from Nucleosides. *Tetrahedron Lett.* **2005**, *46* (14), 2417–2421. https://doi.org/10.1016/j.tetlet.2005.02.069.

(289) Abdelrahman, A. M. M. E. Development of Cell-Based Assays for Adenine Receptors and Selected Purine Receptor Subtypes: Receptor Characterization and Search for Novel Ligands, Bonn, Germany, 2010.

(290) Goswami, S.; Walle, T.; Cornish, A. E.; Basu, S.; Anandhan, S.; Fernandez, I.; Vence, L.; Blando, J.; Zhao, H.; Yadav, S. S.; Ott, M.; Kong, L. Y.; Heimberger, A. B.; de Groot, J.; Sepesi, B.; Overman, M.; Kopetz, S.; Allison, J. P.; Pe'er, D.; Sharma, P. Immune Profiling of Human Tumors Identifies CD73 as a Combinatorial Target in Glioblastoma. *Nat. Med.* **2020**, *26* (1), 39–46. https://doi.org/10.1038/s41591-019-0694-x.

(291) Demircan, T.; Yavuz, M.; Kaya, E.; Akgül, S.; Altuntaş, E. Cellular and Molecular Comparison of Glioblastoma Multiform Cell Lines. *Cureus* **2021**, *13* (6), 0–6. https://doi.org/10.7759/cureus.16043.

(292) Diao, W.; Tong, X.; Yang, C.; Zhang, F.; Bao, C.; Chen, H.; Liu, L.; Li, M.; Ye, F.; Fan, Q.; Wang, J.; Ou-Yang, Z. C. Behaviors of Glioblastoma Cells in in Vitro Microenvironments. *Sci. Rep.* **2019**, *9* (1), 1–9. https://doi.org/10.1038/s41598-018-

36347-7.

(293) Dong, K.; Lin, F.; Wang, H.; Long, M.; Zhang, H.; Wang, X.; Gao, Z. CD73 Promotes Proliferation and Migration of Human Cervical Cancer Cells Independent of Its Enzyme Activity. *BMC Cancer* **2017**, *17* (1), 1–8. https://doi.org/10.1186/s12885-017-3128-5.

(294) Eckle, T.; Fu, L.; Wehrmann, M.; Khoury, J.; Mittelbronn, M.; Ibla, J.; Rosenberger, P.; Eltzschig, H. K. Identication of Ectonucleotidases CD39 and CD73 in Innate Protection during Acute Lung Injury. *J. Immunol.* **2007**, *178* (12), 8127–8137.

(295) Jiang, T.; Xu, X.; Qiao, M.; Li, X.; Zhao, C.; Zhou, F.; Gao, G.; Wu, F.; Chen, X.; Su, C.; Ren, S.; Zhai, C.; Zhou, C. Comprehensive Evaluation of NT5E/CD73 Expression and Its Prognostic Significance in Distinct Types of Cancers. *BMC Cancer* **2018**, *18* (1), 1–10. https://doi.org/10.1186/s12885-018-4073-7.

(296) Wurm, M.; Schaaf, O.; Reutner, K.; Ganesan, R.; Mostbock, S.; Pelster, C.; Böttcher, J.; de Andrade Pereira, B.; Taubert, C.; Alt, I.; Serna, G.; Auguste, A.; Stadermann, K. B.; Delic, D.; Han, F.; Capdevila, J.; Nuciforo, P. G.; Kroe-Barrett, R.; Adam, P. J.; Vogt, A. B.; Hofmann, I. A Novel Antagonistic CD73 Antibody for Inhibition of the Immunosuppressive Adenosine Pathway. *Mol. Cancer Ther.* **2021**, *20* (11), 2250–2261. https://doi.org/10.1158/1535-7163.MCT-21-0107.

(297) Wettstein, M. S.; Buser, L.; Hermanns, T.; Roudnicky, F.; Eberli, D.; Baumeister, P.; Sulser, T.; Wild, P.; Poyet, C. CD73 Predicts Favorable Prognosis in Patients with Nonmuscle-Invasive Urothelial Bladder Cancer. *Dis. Markers* **2015**, *2015*. https://doi.org/10.1155/2015/785461.

(298) Strohmeier, G. R.; Lencer, W. I.; Patapoff, T. W.; Thompson, L. F.; Carlson, S. L.; Moe, S. J.; Carnes, D. K.; Mrsny, R. J.; Madara, J. L. Surface Expression, Polarization, and Functional Significance of CD73 in Human Intestinal Epithelia. *J. Clin. Invest.* **1997**, *99* (11), 2588–2601. https://doi.org/10.1172/JCI119447.

(299) Linda F. Thompson, Julie M. Ruedi, and M. G. L. Purification of 5'-Nucleotidase from Human Placenta after Release from Plasma Membranes by Phosphatidylingsitol-Rspecific Phospholipase. *Biochem. Biophys. Res. Commun.* **1987**, *145* (1), 118–125.

(300) Paulick, M. G.; Bertozzi, C. R. The Glycosylphosphatidylinositol Anchor: A Complex Membrane-Anchoring Structure for Proteins. *Biochemistry* **2008**, *47* (27), 6991–7000. https://doi.org/10.1021/bi8006324.

(301) BÜTIKOFER, P.; MALHERBE, T.; BOSCHUNG, M.; RODITI, I. GPI-anchored Proteins: Now You See 'em, Now You Don't. *FASEB J.* **2001**, *15* (2), 545–548. https://doi.org/10.1096/fj.00-0415hyp.

(302) Barboni, E.; Pliego Rivero, B.; George, A. J. T.; Martin, S. R.; Renouf, D. V.; Hounsell, E. F.; Barber, P. C.; Morris, R. J. The Glycophosphatidylinositol Anchor Affects the Conformation of Thy-1 Protein. *J. Cell Sci.* **1995**, *108* (2), 487–497. https://doi.org/10.1242/jcs.108.2.487.

(303) Wang, D.; Guo, W.; Hu, J.; Liu, F.; Chen, L.; Du, S.; Tang, Z. Estimating Atomic Sizes with Raman Spectroscopy. **2013**. https://doi.org/10.1038/srep01486.

(304) Giordani, R. B.; Weizenmann, M.; Rosemberg, D. B.; De Carli, G. A.; Bogo, M. R.; Zuanazzi, J. A. S.; Tasca, T. Trichomonas Vaginalis Nucleoside Triphosphate Diphosphohydrolase and Ecto-5′-Nucleotidase Activities Are Inhibited by Lycorine and Candimine. *Parasitol. Int.* **2010**, *59* (2), 226–231. https://doi.org/10.1016/j.parint.2010.02.004.

(305) Heyliger, C. E.; Panagia, V.; Dhalla, N. S. Effect of Cyclic AMP Phosphodiesterase Inhibitors on Cardiac Sarcolemmal 5'-Nucleotidase. *J. Pharmacol. Exp. Ther.* **1981**, *217* (2), 489–493.

(306) Renn, C. P. Assay Development, Identification, Optimization and Pharmacological Characterization of Inhibitors for Ecto-5′-Nucleotidase (CD73), University of Bonn, 2019.

(307) Nuhn, L.; De Koker, S.; Van Lint, S.; Zhong, Z.; Catani, J. P.; Combes, F.; Deswarte, K.; Li, Y.; Lambrecht, B. N.; Lienenklaus, S.; Sanders, N. N.; David, S. A.; Tavernier, J.; De Geest, B. G. Nanoparticle-Conjugate TLR7/8 Agonist Localized Immunotherapy Provokes Safe Antitumoral Responses. *Adv. Mater.* **2018**, *30* (45), 1–9. https://doi.org/10.1002/adma.201803397.

(308) Talelli, M.; Barz, M.; Rijcken, C. J. F.; Kiessling, F.; Hennink, W. E.; Lammers, T. *Core-Crosslinked Polymeric Micelles: Principles, Preparation, Biomedical*

Applications and Clinical Translation; 2015; Vol. 10. https://doi.org/10.1016/j.nantod.2015.01.005.

(309) Nuhn, L.; Vanparijs, N.; De Beuckelaer, A.; Lybaert, L.; Verstraete, G.; Deswarte, K.; Lienenklaus, S.; Shukla, N. M.; Salyer, A. C. D.; Lambrecht, B. N.; Grooten, J.; David, S. A.; De Koker, S.; De Geest, B. G. PH-Degradable Imidazoquinoline-Ligated Nanogels for Lymph Node-Focused Immune Activation. *Proc. Natl. Acad. Sci. U. S. A.* **2016**, *113* (29), 8098–8103. https://doi.org/10.1073/pnas.1600816113.

(310) Nuhn, L.; Van Hoecke, L.; Deswarte, K.; Schepens, B.; Li, Y.; Lambrecht, B. N.; De Koker, S.; David, S. A.; Saelens, X.; De Geest, B. G. Potent Anti-Viral Vaccine Adjuvant Based on PH-Degradable Nanogels with Covalently Linked Small Molecule Imidazoquinoline TLR7/8 Agonist. *Biomaterials* **2018**, *178*, 643–651. https://doi.org/10.1016/j.biomaterials.2018.03.026.

List of abbreviations

[2,8-3H]AMP	AMP tritiated at position 2 and 8
4T1.2	triple-negative breast cancer cells from mouse-derived clone 4T1.2
6xHis-Tag	6-fold histidine tag
10xHis-Tag	10-fold histidine tag
A_{280}	absorption at 280 nm
ADP	adenosine-5'-diphosphate
AMP	adenosine-5'-monophosphate
AMPCP	α,β-methylene-ADP
AP	alkaline phosphatase
APS	ammonium peroxydisulfate
ATP	adenosine-5'-triphosphate
BALB/c mice	albino, laboratory-bred strain of the house mouse
Bq	Becquerel
BSA	bovine serum albumin
b-TNAP	bovine tissue-non-specific alkaline phosphatase
CD39	NTPDase1
CD73	ecto-5'-nucleotidase
cADPR	cyclic ADP-ribose
cDNA	complementary DNA
CDP	cytidine-5'-diphosphate
c-IAP	tissue-specific calf intestinal alkaline phosphatase
CMP	cytidine-5'-monophosphate
CMPCP	α,β-methylene-CDP
DMEM	Dulbeccos's modified eagle medium
DMSO	dimethyl sulfoxide
DNA	deoxyribonucleic acid
EC_{50}	half maximal effective concentration for activators
ECL	enhanced chemiluminescence
EDTA	ethylenediaminetetraacetic acid
ER	estrogen receptor
f.c.	final concentration
FBS	fetal bovine serum
FDA	U.S. Food and Drug Administration
g	g-force
GMP	guanosine-5'-monophosphate
GPCR	G protein–coupled receptor
GPI	glycosylphosphatidylinositol
H118A mutation	histidine is replaced at position 118 to alanine
Hepes	4-(2-hydroxyethyl)piperazine-1-ethanesulfonic acid
HPLC	high-performance liquid chromatography
HTS	high-throughput screening
IBD	inflammatory bowel disease
IC_{50}	half maximal inhibitory concentration
IMP	inositol-5'-monophosphate
kDa	kilo-Dalton
K_i	inhibition constant

KM	Michaelis constant, substrate concentration at half V_{max}
LB media	lysogeny broth media
LOD	limit of detection
Ma.Mel65	melanoma cells from human clone Ma.Mel65
mAbs	monoclonal antibodies
MDA-MB-231	triple-negative breast cancer cells from human derived clone MDA-MB-231
Milli-Q	water purified water (grade 1 (ISO 3696))
MW	molecular weight
NaCl	sodium chloride
NADH	nicotinamide adenine dinucleotide
NanoBRET	Nanoluciferase bioluminesce resonance energy transfer
NAD^+	1,N^6-etheno-nicotinamide adenine dinucleotide$^+$
Ni^{2+} NTA	nickel ions chelated with nitrilotriacetic acid
NTPDase	ecto-nucleoside triphosphate diphosphohydrolase
NSB	Nonspecific binding
PBS	phosphate-buffered saline
rpm	rounds per minute
RPMI	medium Roswell Park Memorial Institute medium
RT	room temperature
sCD73	soluble CD73 (ecto-5'-nucleotidase)
SDS-PAGE	sodium dodecyl sulfate polyacrylamide gel electrophoresis
SEM	standard error of the mean
*Sf*9	insect cells derived from *Spodoptera frugiperda* 9
SB	specific binding
TB	total binding
TBS	tris-buffered saline
TBST	TBS with Tween® 20
TNBC	triple-negative breast cancer
Tris	tris(hydroxymethyl)aminomethane
UDP	uridine-5'-diphosphate
UMP	uridine-5'-monophosphate
UMPCP	α,β-methylene-UDP
V	velocity
V_{max}	maximal velocity
wt	wild-type

Acknowledgements

First and foremost, I express my gratitude to the Almighty Allah for granting us opportunities, guiding our paths, providing a supportive environment, and endowing us with the resilience to persevere through challenges.

I extend heartfelt thanks to Prof. Christa E. Müller for the opportunity to join her research group. I am profoundly grateful for this opportunity, which has not only enriched me academically but also on a personal level. Christa, your dedication in discussing results, offering insights, providing feedback, and refining drafts has been invaluable. Thank you for all the kind of support you have provided.

My gratitude extends to Prof. PD. Dr. Anke C. Schiedel my second supervisor, Prof. Martin Baunach and Prof. PD Dr. Marianne Engeser for agreeing to participate on my doctoral examination committee. Your time and efforts are deeply appreciated.

I would also like to acknowledge the Ministry of Higher Education and Scientific Research-Sudan, the German Academic Exchange Service (DAAD), and the international office of the University of Bonn for funding my studies.

Special thanks to Dorothee Müssemeier, the coordinator of the BIGSDrugS graduate school, for organizing enlightening lectures, kick-off meetings, and social gatherings.

I am indebted to my former colleague, Dr. Enas Malik, for acquainting me with life in Germany, navigating transportation in Bonn, and aiding in my settlement. Your assistance was invaluable during my initial phase.

Gratitude is also owed to all my colleagues who collaborated with me on the CD73 project, Dr. Thanigaimalai Pillaiyar, Dr. Constanze Schmies, Dr. Georg Wilhelm Rolshoven, Eugen Potaptschuk, Haneen Al-Hroub, and Patrick Riziki. I must also acknowledge Dr. Christian Renn, my predecessor on the project, for introducing me to colleagues, laboratories, and various experiments.

I extend my thanks to all colleagues who worked alongside me in the molecular biology lab, particularly Dr. Tobias Claff, Andhika Mahardika, and Victoria Vaaßen.

I'm also thankful to our international collaboration partners on the CD73 project: Prof. Kenneth A. Jacobson (NIH, USA), Prof. Edgar Haak (Institute of Chemistry, University of Magdeburg), Prof. Jens Carlsson (Uppsala University, Uppsala, Sweden), Prof. Anita R. Maguire (School of Chemistry, University College Cork, Ireland) and all their lab members.

Gratitude is also extended to my office colleagues Laura, Jan, Ahmed, Aliaa, Jessika and Sophie. My heartfelt thanks to my friends Haneen and Rasha for their kind support and joyful moments.

Special appreciation goes to my family in Egypt, USA and Sudan. To my parents for their continuous support and my siblings for their care and advice. Though distance limits our celebration, your presence is felt in spirit.

Lastly, I offer profound thanks to my husband, Mohamed, whose unwavering support enabled me to embark on and complete this journey. To my daughters, Leen, Yosr, and Talia, thank you for your understanding and support in daily life tasks.

Appendices

Appendix I: 2-Substituted AMPCP published article

Journal of Medicinal Chemistry

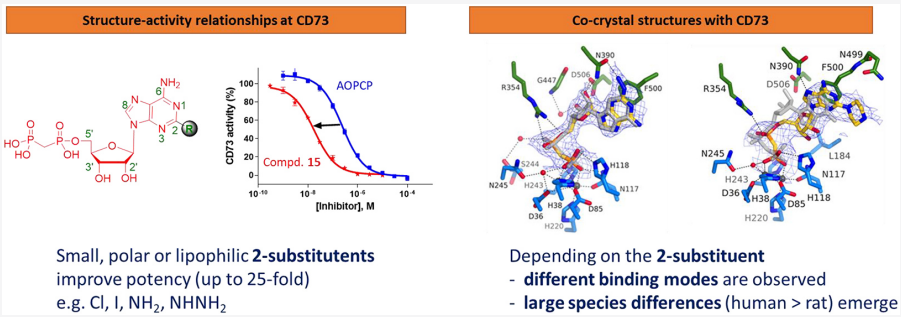
pubs.acs.org/jmc Article

2-Substituted α,β-Methylene-ADP Derivatives: Potent Competitive Ecto-5′-nucleotidase (CD73) Inhibitors with Variable Binding Modes

Sanjay Bhattarai, Jan Pippel, Emma Scaletti, Riham Idris, Marianne Freundlieb, Georg Rolshoven, Christian Renn, Sang-Yong Lee, Aliaa Abdelrahman, Herbert Zimmermann, Ali El-Tayeb, Christa E. Müller,* and Norbert Sträter*

Cite This: J. Med. Chem. 2020, 63, 2941−2957 Read Online

ACCESS | Metrics & More | Article Recommendations | Supporting Information



ABSTRACT: CD73 inhibitors are promising drugs for the (immuno)therapy of cancer. Here, we present the synthesis, structure−activity relationships, and cocrystal structures of novel derivatives of the competitive CD73 inhibitor α,β-methylene-ADP (AOPCP) substituted in the 2-position. Small polar or lipophilic residues increased potency, 2-iodo- and 2-chloro-adenosine-5′-*O*-[(phosphonomethyl)phosphonic acid] (**15**, **16**) being the most potent inhibitors with K_i values toward human CD73 of 3−6 nM. Subject to the size and nature of the 2-substituent, variable binding modes were observed by X-ray crystallography. Depending on the binding mode, large species differences were found, e.g., 2-piperazinyl-AOPCP (**21**) was >12-fold less potent against rat CD73 compared to human CD73. This study shows that high CD73 inhibitory potency can be achieved by simply introducing a small substituent into the 2-position of AOPCP without the necessity of additional bulky N^6-substituents. Moreover, it provides valuable insights into the binding modes of competitive CD73 inhibitors, representing an excellent basis for drug development.

■ INTRODUCTION

The main players in purinergic signaling are the nucleotides ATP and ADP and the nucleoside adenosine. Nucleotides can activate two subfamilies of membrane receptors: G protein-coupled P2Y receptors and ATP-gated P2X ion channels.[1] Adenosine acts as a potent anti-inflammatory and immunosuppressive agent by activating the G protein-coupled adenosine receptor subtypes A_{2A} and A_{2B} that are expressed on immune cells.[2] Moreover, many cancer cells upregulate the expression of adenosine A_{2B} receptors, whose activation leads to increased proliferation, angiogenesis, and metastasis.[3] The extracellular concentration of adenosine is controlled by ecto-5′-nucleotidase (CD73), which hydrolyzes AMP to adenosine (see Figure 1).[4,5] Human CD73 is a glycosylphosphatidylinositol (GPI)-anchored cell surface protein, which can also be cleaved off and act as a soluble enzyme in the extracellular fluid.[5−7] Mammalian CD73 functions as a homodimer. Each monomer contains a dimetal active center, and the natural enzyme probably contains Zn^{2+} but also other divalent metal ions activate the enzyme. The C- and N-terminal domains are connected by a hinge region, which allows the enzyme to undergo large domain reorientations and to switch between an open and a closed state.[6] In the closed conformation, the substrate is buried between the N-terminal and the C-terminal domains with the terminal phosphate group in close proximity to the catalytically active zinc ions.[8] It is likely that hydrolysis only occurs in the closed conformation.

Human CD73 is expressed on lymphocytes, endothelial, and epithelial cells, and its expression is elevated during stress responses, e.g., under hypoxic or inflammatory conditions.[9−11] Upregulation of human CD73 has been further reported for

Received: September 27, 2019
Published: February 11, 2020

ACS Publications © 2020 American Chemical Society

Journal of Medicinal Chemistry pubs.acs.org/jmc Article

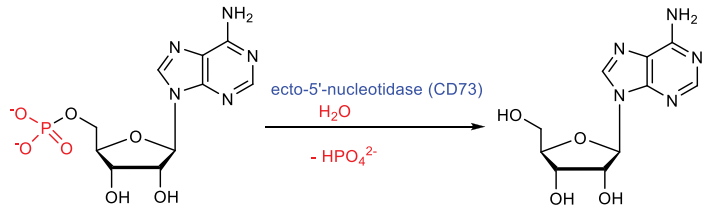


Figure 1. Catalysis of the natural substrate AMP by CD73.

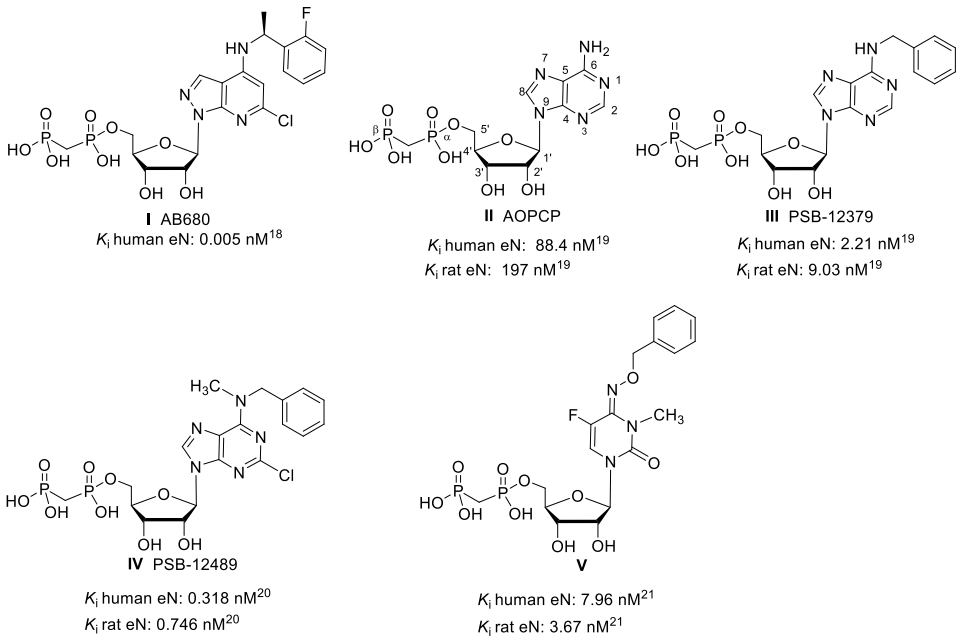


Figure 2. Structures of selected nucleotide-derived CD73 inhibitors.

various types of cancer, where it impairs antitumor responses and enhances tumor growth and metastasis by producing a microenvironment that contains high extracellular adenosine levels.[12,13] In agreement with these observations, a number of studies have demonstrated that targeted inhibition or disruption of human CD73, e.g., by knockout, siRNAs, small molecules, or antibodies, provides immune defense against cancers and inhibits tumor growth.[14−16]

Recently, monoclonal antibodies for CD73 have been moved forward into clinical trials, e.g., for treating pancreatic cancer,[17] and most recently, the development of the first small molecule clinical candidate (AB680, **I**) for blocking CD73 was announced and its characterization was described.[18]

Small molecule inhibitors may have significant advantages compared to antibodies, which typically show only partial enzyme inhibition and cannot be expected to penetrate well into solid tumors. Despite their great therapeutic potential, only a few CD73 inhibitors have been reported to date. Currently, the most promising class of CD73 inhibitors are analogues of nucleoside-5′-diphosphates, such as the ADP analogue α,β-methylene-ADP (AOPCP, **II**), its derivatives **III**[19] and **IV**,[20] and the uracil nucleotide analogue **V**[21] (see Figure 2), which act as competitive inhibitors blocking the substrate binding site.[19−22] All non-nucleotide-derived CD73 inhibitors published so far are only weakly potent, e.g., anthraquinone, sulfonamide, and polyphenol derivatives.[22−28]

Recently, we published the structure-guided development of a subnanomolar CD73 inhibitor displaying high selectivity and metabolic stability.[20] In our previously published crystal structures of human CD73 in complex with **II** (AOPCP, PDB 4H2I)[8] and **III** (PSB-12379, PDB 6S7F),[20] a pocket with polar as well as hydrophobic features close to the 2-position of the adenine moiety was observed. We found that a chloro substitution in this position led to a large increase in potency (see nucleotide analogue **IV**, PSB12489). In the present study, we synthesized a series of 2-substituted AOPCP derivatives to probe the size of the pocket and to explore the flexibility of the orthosteric CD73 binding site. The selection of 2-substituents was not only based on size but also on polarity/lipophilicity and structural diversity. For selected inhibitors, we determined cocrystal structures with human CD73 to support structure−activity relationship (SAR) analysis and to assess the quality of earlier molecular modeling and docking approaches.[19,21,23,24] Surprisingly, different binding modes were observed depending on the nature and size of the 2-substituent. These results provide an excellent basis for further drug design approaches aimed at the development of potent CD73 inhibitors.

https://dx.doi.org/10.1021/acs.jmedchem.9b01611
J. Med. Chem. 2020, 63, 2941−2957

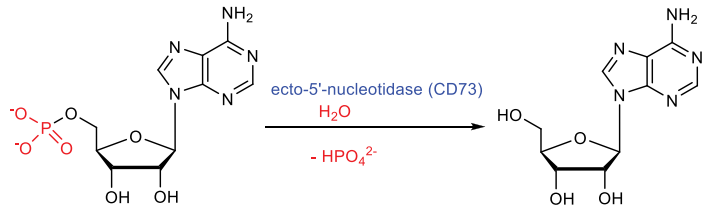


Figure 1. Catalysis of the natural substrate AMP by CD73.

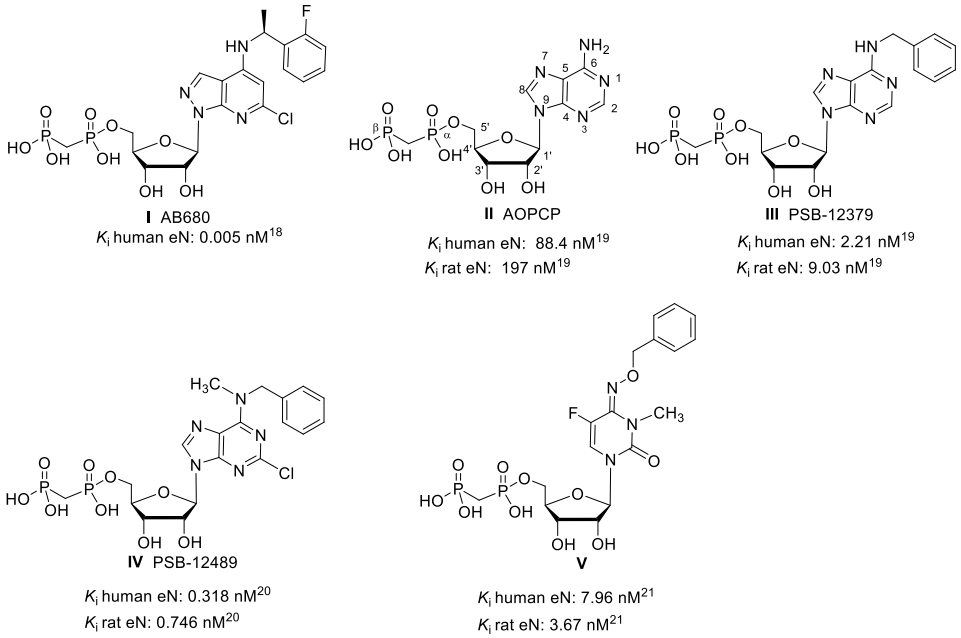


Figure 2. Structures of selected nucleotide-derived CD73 inhibitors.

various types of cancer, where it impairs antitumor responses and enhances tumor growth and metastasis by producing a microenvironment that contains high extracellular adenosine levels.[12,13] In agreement with these observations, a number of studies have demonstrated that targeted inhibition or disruption of human CD73, e.g., by knockout, siRNAs, small molecules, or antibodies, provides immune defense against cancers and inhibits tumor growth.[14−16]

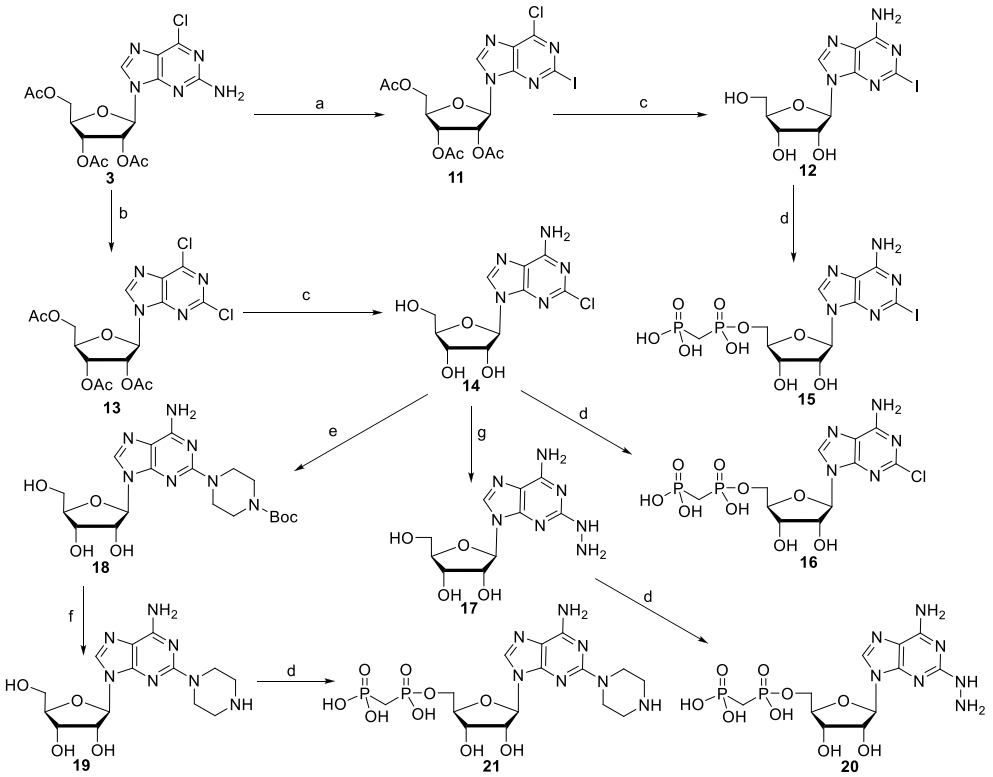
Recently, monoclonal antibodies for CD73 have been moved forward into clinical trials, e.g., for treating pancreatic cancer,[17] and most recently, the development of the first small molecule clinical candidate (AB680, **I**) for blocking CD73 was announced and its characterization was described.[18]

Small molecule inhibitors may have significant advantages compared to antibodies, which typically show only partial enzyme inhibition and cannot be expected to penetrate well into solid tumors. Despite their great therapeutic potential, only a few CD73 inhibitors have been reported to date. Currently, the most promising class of CD73 inhibitors are analogues of nucleoside-5′-diphosphates, such as the ADP analogue α,β-methylene-ADP (AOPCP, **II**), its derivatives **III**[19] and **IV**,[20] and the uracil nucleotide analogue **V**[21] (see Figure 2), which act as competitive inhibitors blocking the substrate binding site.[19−22] All non-nucleotide-derived CD73 inhibitors published so far are only weakly potent, e.g., anthraquinone, sulfonamide, and polyphenol derivatives.[22−28]

Recently, we published the structure-guided development of a subnanomolar CD73 inhibitor displaying high selectivity and metabolic stability.[20] In our previously published crystal structures of human CD73 in complex with **II** (AOPCP, PDB 4H2I)[8] and **III** (PSB-12379, PDB 6S7F),[20] a pocket with polar as well as hydrophobic features close to the 2-position of the adenine moiety was observed. We found that a chloro substitution in this position led to a large increase in potency (see nucleotide analogue **IV**, PSB12489). In the present study, we synthesized a series of 2-substituted AOPCP derivatives to probe the size of the pocket and to explore the flexibility of the orthosteric CD73 binding site. The selection of 2-substituents was not only based on size but also on polarity/lipophilicity and structural diversity. For selected inhibitors, we determined cocrystal structures with human CD73 to support structure−activity relationship (SAR) analysis and to assess the quality of earlier molecular modeling and docking approaches.[19,21,23,24] Surprisingly, different binding modes were observed depending on the nature and size of the 2-substituent. These results provide an excellent basis for further drug design approaches aimed at the development of potent CD73 inhibitors.

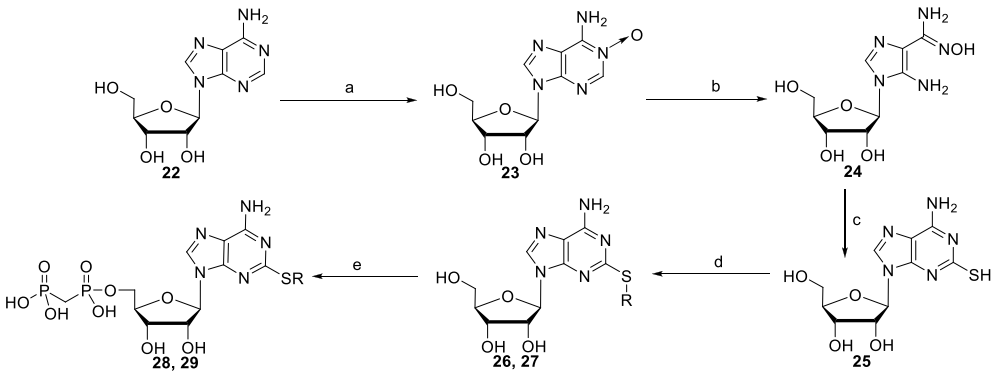
https://dx.doi.org/10.1021/acs.jmedchem.9b01611
J. Med. Chem. 2020, 63, 2941−2957

Scheme 2. Synthesis of 2-Chloro-, 2-Iodo-, 2-Hydrazinyl-, and 2-Piperazinyl-Substituted Adenosine-5′-*O*-[(phosphonomethyl)phosphonic acid] Derivatives[a]



[a]Reagents and conditions: (a) CuI, I_2, CH_2I_2, isoamyl nitrite in THF, 80 °C, 2 h, yield 75%; (b) benzyltriethylammonium nitrite, acetyl chloride, DCM, 2 h, yield 80%; (c) 2.0 M ammonia in ethanol, rt, 24 h, yield 75%; (d) two steps: (i) methylenebis(phosphonic dichloride), trimethyl phosphate, 4 °C, 30 min, (ii) TEAC buffer pH 7.6, rt, 15 min, yield 40−65%; (e) 1-Boc-piperazine, triethylamine, ethanol, 140 °C, 24 h, yield 85%; (f) 8% TFA, CH_2Cl_2, H_2O, 4 h, rt, yield 95%; (g) hydrazine hydrate, 4 h, rt, yield 97%. For details, see Supporting Information.

Scheme 3. Synthesis of 2-Allylthio- and 2-Cyclohexylethylthio-Substituted Adenosine-5′-*O*-[(phosphonomethyl)phosphonic acid] Derivatives[a]

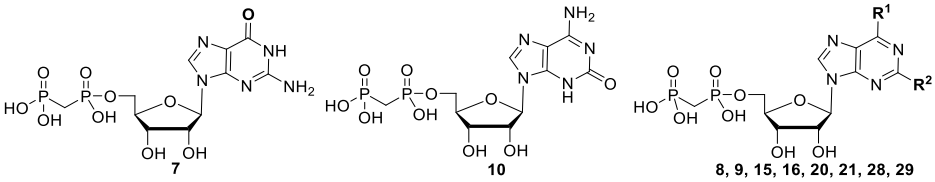


Compd	R
26, 28	allylthio
27, 29	cyclohexylethylthio

[a]Reagents and conditions: (a) acetic acid, H_2O_2, rt, 4 h, yield 86%; (b) NaOH, 2 h, rt; (c) carbon disulfide, MeOH, H_2O, autoclave, 980 kPa, 120 °C, 5 h, rt, yield 65%; (d) NaOH, alkyl bromide, 2 h, rt, yield 56−60%; (e) two steps: (i) methylenebis(phosphonic dichloride), trimethyl phosphate, 4 °C, 30 min, (ii) TEAC buffer pH 7.6, rt, 15 min, yield 35−45%. For details, see Supporting Information.

https://dx.doi.org/10.1021/acs.jmedchem.9b01611
J. Med. Chem. 2020, 63, 2941−2957

Table 1. Inhibitory Potencies of 2-Substituted Purine Riboside-5′-*O*-[(phosphonomethyl)phosphonic acid] Derivatives against Rat and Human CD73 in Comparison to Standard Inhibitor[a]



compd	R^1	R^2	rat soluble CD73 K_i ± SEM[a] (nM)	human soluble CD73 K_i ± SEM[a] (nM)	human CD73 in MDA-MB-231 cancer cells K_i ± SEM[a] (nM)
II AOPCP	amino	H	**197** ± 5	**88.4** ± 4.0[19]	**207** ± 6.0[20]
7 (guanosine derivative)	see structure above	see structure above	**1110** ± 350	**410** ± 90	**255** ± 83
8	chloro	amino	**268** ± 21	**23.6** ± 1.3	**32.2** ± 2.7
9 (PSB-12676)	amino	amino	**90.6** ± 7.3	**38.8** ± 4.5	**35.7** ± 9.4
10 (isoguanosine derivative) (PSB-12690)	see structure above	see structure above	**326** ± 42	nd[b]	nd[b]
15	amino	iodo	**15.1** ± 1.2	**3.59** ± 0.82	**3.33** ± 1.12
16	amino	chloro	**18.6** ± 3.8	**5.93** ± 1.64	**4.57** ± 1.20
20 (PSB-12646)	amino	hydrazinyl	**116** ± 18	**15.5** ± 1.2	**15.4** ± 0.9
21 (PSB-12604)	amino	*N*-piperazinyl	**2290** ± 240	**184** ± 27	**238** ± 26
28	amino	allylthio	**65.7** ± 5.6	**61.9** ± 13.4	**65.4** ± 9.1
29	amino	cyclohexyl-ethylthio	**56.6** ± 8.3	**46.9** ± 10.2	**49.1** ± 15.1

[a][^{3}H]AMP (5 μM) was used a substrate; K_m values 59, 17, and 14.8 μM, respectively, for purified recombinant soluble rat CD73, purified recombinant soluble human CD73, and native membrane-anchored human CD73 (in MDA-MB-231 cell membrane preparations). [b]nd, not determined

analogues (**20**, **21**) in overall yields of 33−40% (Scheme 2). The preparation of 2-thioadenosine (**25**) started from commercial adenosine (**22**), which was oxidized by hydrogen peroxide in the presence of acetic acid yielding adenosine-N^1-oxide (**13**). Subsequent ring opening with sodium hydroxide afforded carboximidamide intermediate **24**, which was thionated with carbon disulfide in an autoclave (pressure of 980 kPa) to give **25**. Subsequent alkylation with allyl bromide, or 2-cyclohexylethyl bromide, respectively, yielded the desired 2-alkylthio-substituted derivatives **26** and **27** in yields of 56−60%,[35] which were further phosphonylated to provide the final nucleotide analogues **28**, **29** in overall yields of 25−32% (Scheme 3).

The phosphonylation of nucleosides generally yielded mixtures of products and side products. Therefore, careful purification was required to obtain the target nucleotide analogues as pure products. All 2-substituted nucleotide analogues were purified by anion exchange chromatography, followed by reverse-phase high performance liquid chromatography (RP-HPLC).

Pharmacological Evaluation. The inhibitory potency of the nucleotide analogues was determined in a previously described sensitive enzyme inhibition assay using [^{3}H]AMP as a substrate.[36] Recombinant soluble rat CD73 was obtained by expression in *Spodoptera frugiperda* (Sf9) insect cells as previously described.[37] For all compounds, full concentration−response curves were determined and K_i values were calculated from the obtained IC_{50} using the Cheng−Prusoff equation.[38] The most potent compounds were also tested against recombinant soluble human CD73 expressed in the same system[21] in order to study potential species differences. In addition, we investigated the compounds with native membrane-bound CD73 from membrane preparations of a triple-negative human breast cancer cell line (MDA-MB-231 cells),[39] which shows a high expression level of CD73.[21] Results are summarized in Table 1 and selected concentration−inhibition curves are shown in Figure 3.

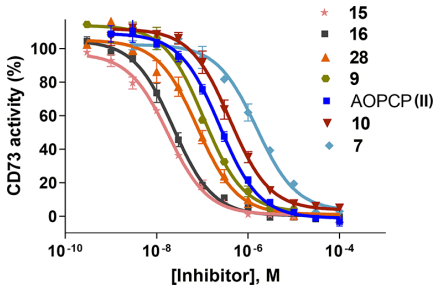


Figure 3. Concentration−inhibition curves of selected potent compounds in comparison to the lead structure AOPCP (**II**) at rat CD73. Rat enzyme K_m, 59 μM; AMP concentration, 5 μM. Data points represent means ± SEM from three separate experiments performed in triplicate.

Structure−Activity Relationships. The lead structure AOPCP (**II**), tested under the same conditions, showed a K_i value of 197 nM against rat CD73. Substitution in the 2-position with a small, polar amino group (2-amino-AOPCP, **9**) increased potency by 2-fold (K_i 90.6 nM). Replacing the 6-amino group in 2-amino-AOPCP by an oxo-function (guanosine analogue GOPCP, **7**) led to a strong reduction in potency (12-fold, K_i 1110 nM) compared to **9**. This indicated that a keto group at the purine C6-position was not tolerated, possibly due to the N^1-H,C6═O lactam structure of **7**, which abolishes the aromaticity of the pyrimidine ring. This result correlates with the previously observed low potency of

https://dx.doi.org/10.1021/acs.jmedchem.9b01611
J. Med. Chem. 2020, 63, 2941−2957

Journal of Medicinal Chemistry pubs.acs.org/jmc Article

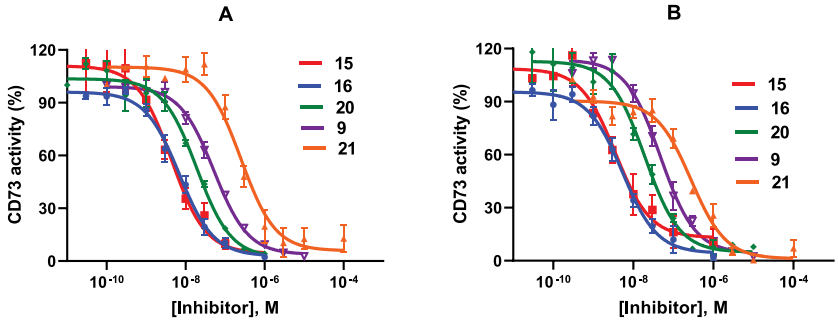


Figure 4. Concentration−inhibition curves of selected inhibitors against (A) recombinant human CD73 and (B) native CD73 expressed in triple-negative breast cancer cells (membrane preparations of MDA-MB-231 cells). AMP concentration, 5 μM. Results are plotted as the percentage of maximal activity measured in the absence of inhibitors. K_i values are shown in Table 1.

the inosine derivative IOPCP, an analogue of **7** lacking the 2-amino group (K_i 2830 nM),[19] which further confirms that the 2-amino group (in **7**) is beneficial. A 6-chloro substituent (**8**) preserving the aromatic ring structure, in contrast to the oxo substitution in **7**, was better tolerated (K_i 268 nM, only a 3-fold decrease compared to the analogous 2-amino-AOPCP, **9**).

For the following step, the 6-amino group in AOPCP was kept, whereas the 2-substituent was varied. Introduction of a 2-oxo function (in iso-GOPCP, **10**, K_i 326 nM) led to a slight reduction in potency compared to the lead structure AOPCP (**II**, 197 nM). The lactam tautomerism resulting in the loss of aromaticity could be the reason for the moderate potency of **10**, which contains a polar 2-substituent that was expected to increase the potency of the compound. In contrast, all further investigated 2-substituents (in **15**, **16**, **20**, **28**, **29**) led to increased potency of the AOPCP derivatives, with one exception (**21**). Small polar and small lipophilic residues in the 2-position of AOPCP were well tolerated and led to significant increases in potency. The order of potency by rank was as follows: 2-I (**15**, 15.1 nM) ≈ 2-Cl (**16**, 18.6 nM) > 2-(cyclohexylethylthio) (**29**, 56.6 nM) ≈ 2-(allylthio) (**28**, 65.6 nM) > 2-NH-NH_2 (**20**, 116 nM) > H (**I**, 197 nM) (Figure 3 and Table 1). Only the 2-(1-piperazinyl)-AOPCP (**21**) showed significantly reduced potency (>12-fold, K_i 2290 nM). It can therefore be concluded that small polar or lipophilic substituents in the 2-position of the adenine moiety of AOPCP can drastically improve potency. For larger substituents, the situation appears to depend on the flexibility and size of the substituent as well as on its hydrogen-bonding properties.

Rat and human CD73 are highly homologous sharing 89% protein sequence identity.[8] The substrate binding site is highly conserved, having only three amino acid differences near the active site (F500Y, N499S, and L389V, Supporting Information, Figure S5). F500 in human CD73 is involved in nucleobase stacking of AOPCP[8] and is replaced by tyrosine in rat CD73.

In previous studies, we observed that AOPCP and other nucleotide analogues were similarly potent against human and rat CD73; in some cases, they were somewhat more potent against the human enzyme, however the differences were always moderate.[19,20] To investigate whether this was also the case for various 2-substituted AOPCP derivatives, we further tested the inhibitors against recombinant soluble human CD73. In addition, we studied the same set of compounds using human membrane-bound CD73, which was natively expressed in a triple-negative breast cancer cell line (see Table 1). There were virtually no differences between the potencies of the inhibitors toward human soluble and human membrane-bound CD73 (Figure 4). However, several compounds were more potent against human compared to the rat enzyme (up to >12-fold). The most potent CD73 inhibitors of the present series were 2-iodo-AOPCP (**15**, human membrane-bound CD73, K_i 3.33 nM) and 2-chloro-AOPCP (**16**, K_i 4.57 nM). This indicates that a bulky N^6-substituent which is present in the previously developed inhibitors **III**[19] and **IV**[20] is not required for high potency. Low nanomolar inhibitors can be obtained by simple modification such as 2-halogen-substitution of N^6-unsubstituted AOPCP, resulting in CD73 inhibitors with molecular weights of less than 500 g/mol, while the previously published potent CD73 inhibitors (e.g., **III**−**V**) display significantly higher molecular weights of well above 500 g/mol. The largest species differences were observed for 2-amino-6-chloro-AOPCP (**8**, 6.3-fold), 2-hydrazinyl-AOPCP (**20**, 7.5-fold), and 2-(*N*-piperazinyl)-AOPCP (**21**, 12.5-fold) indicating that significant species differences may be found for orthosteric CD73 inhibitors depending on the substitution pattern. In contrast, 2-allylthio- and 2-cyclohexylthio-AOPCP were almost equally potent at rat and human CD73.

Crystal Structures of 2-Substituted Derivatives Bound to Human CD73. To explain the observed SARs for 2-substituted AOPCP derivatives and to investigate the flexibility of the binding pocket (in the following also designated as "C2-pocket") in regard to its diverse accommodation of polar, lipophilic, small, and large 2-substituents, we obtained cocrystal structures of human CD73 with the following selected inhibitors: **9** (PSB-12676), **10** (PSB-12690), **20** (PSB-12646), and **21** (PSB-12604). These compounds were cocrystallized in the closed state of the enzyme.

In addition, we analyzed X-ray structures of unliganded (PDB 6TVE) and AOPCP-bound (PDB 6TVG) CD73 in the open state of the enzyme at resolutions of 1.05 Å and 1.53 Å, respectively (Table 2). In contrast to the crystals of the closed form, which usually diffract to around 2.5 Å resolution, these high-resolution crystal structures allow for a detailed analysis of water structure within the active site. The rearrangement and displacement of water molecules upon ligand binding can play an important role in understanding ligand affinity.[40] A comparison of the binding modes of AOPCP in the open and closed enzyme forms shows that the ligands adopt very similar binding modes (Supporting Information, Figure S7D)

https://dx.doi.org/10.1021/acs.jmedchem.9b01611
J. Med. Chem. 2020, 63, 2941−2957

Journal of Medicinal Chemistry pubs.acs.org/jmc Article

Table 2. Details of the Crystal Structure Analysis

	PSB12676 (**9**)	PSB12690 (**10**)	PSB12646 (**20**)	PSB12604 (**21**)
PDB	**6TVX**	**6TW0**	**6TWA**	**6TWF**
Crystallization and Data Collection				
crystallization buffer	5−8% (w/v) polyethylene glycol 6000, 0.1 M NaMES pH 5.5−6.0	5−8% (w/v) polyethylene glycol 6000, 0.1 M NaMES pH 5.5−6.0	5−8% (w/v) polyethylene glycol 6000, 0.1 M NaMES pH 5.5−6.0	5−8% (w/v) polyethylene glycol 6000, 0.1 M NaMES pH 5.5−6.0
crystallization drop	1 μL of crystallization buffer + 1 μL of 3 mg/mL protein in 10 mM Tris pH 8.0, 100 μM $ZnCl_2$, and 1 mM of compound	1 μL of crystallization buffer + 1 μL of 3 mg/mL protein in 10 mM Tris pH 8.0, 100 μM $ZnCl_2$, and 1 mM of compound	1 μL of crystallization buffer + 1 μL of 3 mg/mL protein in 10 mM Tris pH 8.0, 100 μM $ZnCl_2$, and 1 mM of compound	1 μL of crystallization buffer + 1 μL of 3 mg/mL protein in 10 mM Tris pH 8.0, 100 μM $ZnCl_2$, and 1 mM of compound
cryobuffer	25% PEG200, 0.1 M Na-MES pH 5.5	25% PEG200, 0.1 M Na-MES pH 5.5	25% PEG200, 0.1 M Na-MES pH 5.5	25% PEG200, 0.1 M Na-MES pH 5.5
wavelength (Å)	0.91841	0.91841	0.91841	0.91841
resolution range (Å)[a]	47.70−2.6 (2.72−2.60)	48.12−2.50 (2.60−2.50)	47.82−2.00 (2.05−2.00)	47.60−2.50 (2.60−2.50)
space group	$C222_1$	$C222_1$	$C222_1$	$C222_1$
unit cell parameters *a*, *b*, *c* (Å)	54.5, 97.5, 233.7	54.5, 98.3, 233.8	53.9, 95.6, 233.6	54.5, 97.2, 234.4
total reflections[a]	129595 (15321)	161402 (17554)	181054 (12504)	119323 (12861)
unique reflections[a]	19655 (2370)	22226 (2464)	41158 (2987)	21964 (2435)
multiplicity[a]	6.6 (6.5)	7.3 (7.1)	4.4 (4.2)	5.4 (5.3)
completeness (%)[a]	99.8 (99.9)	99.7 (99.6)	99.6 (99.9)	99.6 (99.8)
mean $I/\sigma(I)$[a]	5.7 (0.5)	5.2 (0.4)	8.0 (0.4)	7.0 (0.7)
R meas[a]	0.385 (4.223)	0.375 (5.402)	0.161 (4.633)	0.223 (3.465)
R pim[a]	0.149 (1.653)	0.137 (2.007)	0.074 (2.211)	0.094 (1.461)
$CC^1/_2$[a]	0.989 (0.234)	0.992 (0.179)	0.998 (0.127)	0.997 (0.246)
Wilson *B* factor (Å^2)	142.12	124.64	40.45	45.21
Refinement				
Resolution range (Å)[a]	47.70−2.60 (2.74−2.60)	48.12−2.50 (2.62−2.50)	47.82−2.00 (2.05−2.00)	47.60−2.50 (2.62−2.50)
R work[a]	0.216 (0.299)	0.2361 (0.2928)	0.188 (0.240)	0.2199 (0.2349)
R free[a]	0.249 (0.313)	0.2656 (0.2892)	0.230 (0.166)	0.2618 (0.2749)
no. of non-hydrogen atoms				
protein	4022	4045	4062	4062
heterogen	30	28	29	33
water	19	15	123	4
rmsd				
bonds (Å)	0.008	0.008	0.010	0.010
angles (deg)	1.06	1.12	1.17	1.24
Ramachandran statistics				
favored (%)	96.30	96.10	95.75	95.95
allowed (%)	3.70	3.90	4.06	3.86
outliers (%)	0.00	0.00	0.19	0.19
B factor (Å^2)				
protein	96.0	96.9	70.7	108.4
ligands	88.4	92.4	67.3	115.7
solvent	69.1	63.1	56.9	79.5

https://dx.doi.org/10.1021/acs.jmedchem.9b01611
J. Med. Chem. 2020, 63, 2941−2957

Table 2. continued

	unliganded CD73	AMPCP open
PDB	6TVE	6TVG
Crystallization and Data Collection		
crystallization buffer	100 mM Tris pH 7.8 and 10% PEG6000	100 mM Tris pH 7.8 and 10% PEG6000
crystallization drop	1 μL of crystallization buffer + 1 μL of 7 mg/mL protein in 10 mM Tris pH 7.8, 100 μM $ZnCl_2$	1 μL of crystallization buffer + 1 μL of 7 mg/mL protein in 10 mM Tris pH 7.8, 100 μM $ZnCl_2$
soaking buffer	100 mM Tris pH 7.8, 10% PEG6000, 100 mM Gly-Pro[b], 10% DMSO	100 mM Tris pH 7.8, 10% PEG6000, 30 mM AMPCP, 10% DMSO
cryobuffer	100 mM Tris pH 7.8, 10% PEG6000 and 10% glycerol	100 mM Tris pH 7.8, 10% PEG6000 and 10% glycerol
wavelength (Å)	0.91841	0.89429
resolution range (Å)[a]	29.52−1.05 (1.09−1.05)	47.2−1.48 (1.53−1.48)
space group	$P2_12_12$	$P2_12_12$
unit cell parameters *a*, *b*, *c* (Å)	67.32, 131.38, 66.20	67.26, 131.27, 66.21
total reflections[a]	1754423 (74213)	486455 (22246)
unique reflections[a]	267271 (12510)	98145 (4759)
multiplicity[a]	6.6 (5.9)	5.0 (4.7)
completeness (%)[a]	98.5 (94.0)	99.4 (98.0)
mean $I/\sigma(I)$[a]	15.9 (1.9)	12.0 (1.7)
R meas[a]	5.5 (85.8)	11.6 (99.3)
$CC^1/_2$[a]	0.999 (0.636)	0.997 (0.554)
Wilson *B* factor (Å^2)	8.91	10.70
Refinement		
resolution range (Å)[a]	32.85−1.05 (1.09−1.05)	47.19−1.48 (1.49−1.48)
R work[a]	0.118 (0.239)	0.152 (0.268)
R free[a]	0.133 (0.249)	0.173 (0.279)
no. of non-hydrogen atoms		
protein	4255	4184
heterogen	56	31
water	685	549
rmsd		
bonds (Å)	0.006	0.008
angles (deg)	1.00	1.02
Ramachandran statistics		
favored (%)	95.1	95.5
allowed (%)	4.0	3.5
outliers (%)	0.9	1.0
B factor (Å^2)		
protein	11.3	12.4
ligands	39.4	19.0
solvent	29.0	24.0

[a]Values in parenthesis correspond to highest resolution shell. [b]This data set was collected as part of a fragment screening experiment. The dipeptide did not bind to the protein and this data set provides the highest resolution structure of unliganded CD73 so far.

https://dx.doi.org/10.1021/acs.jmedchem.9b01611
J. Med. Chem. 2020, 63, 2941−2957

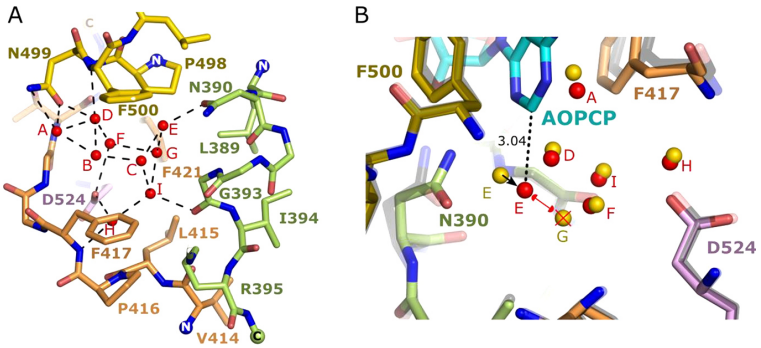


Figure 5. Water structure of the C2-pocket in unliganded CD73 and in the CD73 × AOPCP complex (both in the open state). (A) Water molecules in the pocket next to F500 and F417 as identified in the 1.05 Å structure of unliganded human CD73 in the open conformation. Only fully occupied water binding sites or predominantly occupied water molecules of alternative binding sites are shown. The view is from the nucleobase clamp into the pocket. Refer to Supporting Information, Figure S6 for further information. The carbon atoms of the protein residues are depicted in different colors for the four regions lining the C2-pocket. (B) Change in the water structure upon binding of AOPCP to the open state. Water molecules from the unliganded structure are shown in yellow, whereas waters from the ligand-bound complex are shown in red. The unliganded structure (PDB 6TVE, gray carbons, partial transparency) is superimposed onto AOPCP-bound CD73 (PDB 6TVG).

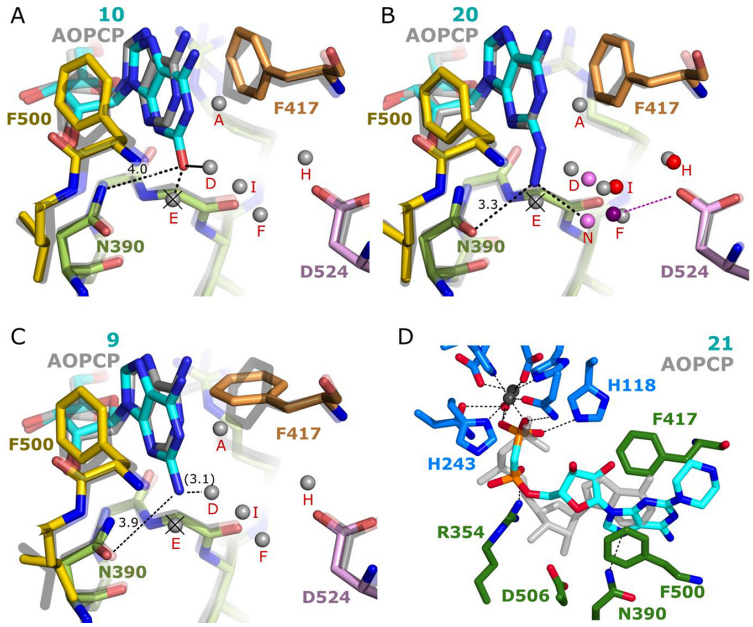


Figure 6. Crystal structures of human CD73 in the closed conformation in complex with different 2-substituted AOPCP derivatives **10** (A), **20** (B), **9** (C), and **21** (**D**). The color scheme for the protein residues of (A–C) is the same as in Figure 5. (D) Residues of the N-terminal and C-terminal domain are shown in blue and green, respectively. The inhibitors are colored cyan. For comparison, the binding mode of AOPCP (**I**, PDB 4H2I)[8] is depicted in gray together with the water structure. Water molecules in the C2-pocket are not visible for cocrystal structures of **9**, **10**, and **21** due to crystal quality. For the CD73 × **20** structure, fully occupied waters H and I are shown in red. Waters D and N (pink) are alternatively occupied with water F (purple) due to steric overlap.

and water structure in the C2-pocket. Therefore, high-resolution X-ray structures of CD73 in the open form are also suitable for the characterization of the C2-pocket structure in the inhibited closed-state structures bound with AOPCP derivatives.

The unliganded C2-pocket and the neighboring nucleobase clamp (F417 and F500) are filled by nine water molecules (designated A–I, Figure 5A, and Supporting Information, Figure S6). Upon binding of AOPCP, water binding sites B and C are not occupied due to steric overlap with the adenine ring (Figure 5B, and Supporting Information, Figure S7). Waters A, D, I, F, and H stay close to their positions in the unliganded structure and maintain their interactions with other water molecules and protein residues. Water molecule A forms a hydrogen bond to the N1 nitrogen of AOPCP. An interesting structural feature upon ligand binding is observed for water E, which moves ~1.1 Å closer to the center of the C2-pocket together with its coordinating protein residue N390. The

https://dx.doi.org/10.1021/acs.jmedchem.9b01611
J. Med. Chem. 2020, 63, 2941–2957

movement of this side chain is probably caused by the formation of hydrogen bonds between the side chain nitrogen and N3 of the adenine ring (3.3 Å) as well as O2′ of the ribose ring (3.0 Å). In the ligand-bound structures, water E is H-bonded to $O_{\delta 1}$ of N390 and water molecule D. A remarkable feature is its close distance to the C2-atom of the adenine base at 3.10 Å (PDB 4H2I, closed state) and 3.04 Å (PDB 6TVG, open state). The C−H···O angle in the two structures corresponds to 154°, in agreement with the existence of a C−H···X weak hydrogen bond. As a result of this movement, water binding site G is not occupied. Therefore, in the presence of the adenine base, binding of water E is more favorable than that of water G.

On the basis of the CD73 × AOPCP cocrystal structure (PDB 4H2I), we assumed that polar substituents at the C2-position of AOPCP might improve the inhibitory potency as they were expected to be accommodated in the water-filled C2-pocket formed by residues of the C-terminal domain of CD73.[8,20] The upper part of the pocket, in close proximity to the nucleobase, is predominantly hydrophilic but also contains some apolar patches formed by F417, F500, and G393. The base of the pocket has an apolar character (Figure 5A, and Supporting Information, Figure S6B). We now were interested in investigating, how various 2-substituents, 2-amino (**9**), 2-oxo (**10**), 2-hydrazinyl (**20**), and 2-(1-piperazinyl) (**21**), could be accommodated in the small binding pocketadjacent to C2 in the AOPCP-bound enzyme.

In the case of the 2-oxo-substituent in **10** (Figure 5B), the inhibitory potency is slightly lower compared to AOPCP. The cocrystal structure shows that the substituent is 4.0 Å away from the side chain nitrogen of N390 and also forms no hydrogen-bonding interactions with other protein residues (Figure 6A). The limited resolution obtained for the cocrystal structure with **10** in combination with overall high *B* factors does not allow for an analysis of the water structure of the C2-pocket. However, it is obvious that water binding site E cannot be occupied in the presence of any substituent at the C2 of AOPCP due to steric overlap. A superposition of the CD73 × **10** complex with the CD73 × AOPCP structure indicates that the 2-oxo substituent could interact with water D (Figure 6A). Thus, it is likely that the oxo-group can only form one favorable hydrogen-bonding interaction with water molecule D. The other lone electron pair of the oxygen either has no well-positioned donor partner, or a water molecule is positioned in a previously unobserved water binding site in order to interact with the oxo-group, however, this water molecule lacks a favorable low-energy hydrogen-bonding environment. Interestingly, a shift of the nucleobase is observed in the binding mode of **10** compared to AOPCP. This may be caused by the altered electrostatic potential due to the oxo-substituent in the C2-position, resulting in a loss of aromaticity[41] and a less favored π-stacking interaction with F417 and F500. Together with the suboptimal hydrogen-bonding interactions of the oxo group in the bound state, this in turn results in an increased K_i value.

In contrast to **10**, the 2-substituents in **9** (2-amino-substituted, Table 2, Figure 5A) and **20** (2-hydrazinyl, Table 2) resulted in increased affinity. For **20**, the binding mode closely matches that of AOPCP and an additional hydrogen bond is formed between the hydrazinyl substituent and the side chain oxygen atom of N390 (Figure 6B), which probably accounts for the improved K_i value (6-fold increase in potency toward human CD73). The electron density in the C2-pocket indicates that water binding sites H and I are fully occupied, whereas alternate occupancy is observed for waters F and D. Either water site F or water site D together with a new water position (labeled "N" in Figure 6B) are occupied. Both alternative water structures have unmatched H-bond donors or acceptors; when water F is not present, D504 lacks a hydrogen-bonding partner. When site N is not occupied, the terminal nitrogen of the hydrazinyl group has only one H-bond partner. As noted above, a relatively large difference is observed for the K_i values of **20** toward human vs rat CD73. We assume that the influence of the N499S substitution in rat CD73 on the water structure of the C2-pocket is responsible for the different inhibition parameters (Supporting Information, Figure S5B).

In contrast, for **9**, the situation for the amino-substituent at the C2-position is more similar to that of the oxo-substituent in **10**; the distance to the side chain of N390 is too long for a hydrogen-bonding interaction (Figure 6C). Formation of a H-bond with water D is likely (the water structure in the C2-pocket could not be characterized due to weak diffraction of the crystal). A remarkable characteristic of the nucleobase binding mode is that the base is shifted partly toward F500 and partly toward the C2-pocket. This shift is caused by F417, which interacts with the adenine ring of **9** in a side-on T-shaped orientation via two C−H···π interactions instead of the usual sandwich binding mode observed so far for all other AOPCP derivatives. We assume that the additional amino-substituent is responsible for this change of the $\pi-\pi$ interaction mode.

The piperazinyl-substituted derivative **21** features a bulky substituent with limited flexibility. The crystal structure analysis shows that the inhibitor adopts a new binding mode, in which the ribose group and the adenine ring are flipped by about 180°, while the terminal phosphate group only shifts slightly (Figure 6D). The N^6-amino group points into the C2-pocket and the 2-piperazinyl substituent is positioned in the interdomain cleft, where N^6-substituents bind in the canonical AOPCP binding mode. The 2-piperazinyl substituent of **21** most likely fails to adopt a low-energy conformation in the polar environment of N390 at the top rim of the C2-pocket. A consequence of the reorientation is the loss of the well-matched hydrogen bond network of the CD73 × AOPCP complex, which most likely is the major contributor to the loss in binding affinity. The AMP group of AOPCP forms eight hydrogen bonds with protein residues directly, whereas only four such interactions for this group are present in the CD73 × **21** complex.

We observed a remarkable species difference for binding of **21** to rat and human CD73. The 2-piperazinyl substitution of AOPCP results in an affinity loss by a factor of more than 10 in rat CD73, whereas the affinity is only reduced by a factor of 2 in human CD73. We attribute this difference in affinity change to the F500Y substitution in the rat enzyme (residue Y502 in rat CD73). F500 of the nucleobase clamp adopts a different side chain orientation in CD73 × **21** compared to CD73 × AOPCP, and it forms a favorable hydrophobic contact to L184 (Supporting Information, Figure S8A). The F → Y substitution in the rat enzyme leads to a close contact between the tyrosine OH group and the side chain of L184 (Supporting Information, Figure S8B), which is unfavorable compared to the unbound state, where the OH group is free to form a hydrogen bond to water.

It also appears likely that **29** binds via the same flipped binding mode of **21**, as modeling indicates that the bulky

https://dx.doi.org/10.1021/acs.jmedchem.9b01611
J. Med. Chem. 2020, 63, 2941−2957

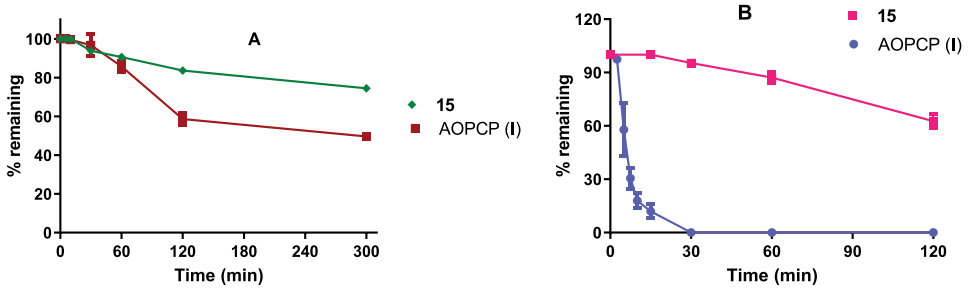


Figure 7. Metabolic stability of CD73 inhibitor **15** in comparison to AOPCP (A) in human blood plasma and B in rat liver microsomes. Results are presented as percentage of remaining compound measured by LC-MS at different time intervals. Data points are from three separate experiments performed in duplicates.

cyclohexylethylthio in the 2-position cannot be accommodated by the C2-pocket due to its size (data not shown). The flipped binding mode is an interesting starting point for further inhibitor development.

Selectivity. Selected potent compounds with diverse structural modifications were investigated in terms of their selectivity against different ecto-nucleotidases. The lead compound AOPCP (**II**) had been reported to block human ecto-nucleotide pyrophosphatase/phosphodiesterase1 (NPP1) with a K_i value of 16.5 μM.[19] We therefore investigated the AOPCP derivatives **8**, **15**, **16**, and **29** with NPP1 and its isoenzymes NPP2 and NPP3, however, none of the compounds showed a significant inhibition of these ecto-nucleotidases at a high concentration of 10 μM (see Supporting Information, Table S3). Because AOPCP is an analogue of ADP, we also studied whether selected derivatives (**8**, **16**, **29**) were able to activate the ADP-activated P2Y receptor subtypes $P2Y_1$ and $P2Y_{12}$. In contrast to ADP and 2-methylthio-ADP,[19] AOPCP and its 2-substituted derivatives did not significantly activate these receptors at a high concentration of 10 μM (see Supporting Information, Table S4). These results indicate that 2-substituted AOPCP derivatives show a high degree of selectivity for CD73, similar to what has previously been reforted for N^6-substituted AOPCP derivatives.[19,20]

Metabolic Stability. The presented AOPCP derivatives display high aqueous solubility due to deprotonation under physiological conditions and are therefore suitable for application by injection or infusion. Peroral bioavailability cannot be expected in their native form, but lipophilic ester prodrugs may allow peroral application as well. Compound **15**, which is the most potent CD73 inhibitor of the present series, was investigated for its metabolic stability in human blood plasma and rat liver microsomes compared to AOPCP.[19,20] Incubation was performed at 37 °C, after which the solutions were analyzed by LC-MS. Incubation in human blood plasma for 5 h showed that inhibitor **15** was more stable than AOPCP (**II**), with less than 25% degradation under the applied conditions, while AOPCP showed almost 50% degradation under the same conditions (Figure 7A). Incubation with rat liver microsomes showed that inhibitor **15** was quite stable and much more so relative to AOPCP (Figure 7B). While AOPCP was completely degraded within 30 min, inhibitor **15** was still almost completely intact even after 2 h of incubation, and less than 40% of the compound was metabolized under the same conditions. This shows that a simple substituent in the 2-position (2-iodo in **15**) is sufficient to prevent fast metabolism of AOPCP derivatives. This has also been observed for 2-substituted adenosine derivatives, e.g., 2-chloroadenosine, which are the poor substrates of adenosine deaminase.[42]

CONCLUSIONS

To probe the effects of diverse substituents in the 2-position of AOPCP on CD73 inhibiton, and to study their interactions with CD73 on a molecular level, we designed, synthesized, and analyzed a series of 2-substituted adenosine-5′-*O*-[(phosphonomethyl)phosphonic acid] derivatives. Substitution with small polar or lipophilic residues (e.g., $-NH_2$, Cl, I) already led to highly efficient CD73 inhibitors with low nanomolar potency, resulting in high ligand efficiency. Compared to the recently published clinical candidate **I**,[18] which is structurally based on the N^6-substituted AOPCP derivatives previously described by our groups,[19,20] the present compounds are easier to synthesize requiring less reaction steps, display significantly lower molecular weights, and are in a low nanomolar affinity range, which is ideal for their application as pharmacological tools or drugs. In contrast, compound **I** is a superpotent inhibitor with a very slow onset requiring careful kinetic studies.[18]

We obtained cocrystals structures for four different inhibitors of the present series with human CD73 and characterized the water structure of the C2-pocket at very high resolution. Surprisingly, we observed diverse binding modes for these competitive inhibitors, depending on the nature of the 2-substituent.

Size and flexibility of single substituents at the C2-position of AOPCP derivatives are of much greater importance for the inhibitory potency of CD73 inhibitors, as compared to those at the N^6-position, where small as well as bulky hydrophobic substituents are tolerated and enhance the inhibitory potency.[19] High-resolution structures together with SAR data demonstrate the importance of the water structure of the C2-pocket and of substitution effects on the $\pi-\pi$ interactions with the nucleobase clamp for understanding the affinity improvements caused by the substituents at the C2-position. While the relatively small single halogen substituents and single hydrophilic substituents currently result in the best potency, we assume that further structure-based exploration of the C2-pocket by designing substituents forming favorable contacts to the hydrophobic base might result in further affinity improvements. This may lead to potent competitive CD73 inhibitors, potentially without the charged bisphosphonate group. Overly large and inflexible hydrophobic moieties such as the piperazinyl substituent resulted in a flipped binding mode of

https://dx.doi.org/10.1021/acs.jmedchem.9b01611
J. Med. Chem. 2020, 63, 2941−2957

the AOPCP scaffold and loss in affinity. Surprisingly, this binding mode only resulted in a 2-fold loss in potency against human CD73 and it might therefore be a starting point for further inhibitor development.

In addition, while previous studies (mainly for N^6-substituted AOPCP derivatives) reported only minor species differences (typically >3-fold higher potency at human as compared to rat CD73), we observed very large species differences (of up 12.5-fold) between rat and human CD73-inhibitory potency for many of the 2-substituted AOPCP derivatives. This is likely related to the amino acid replacements N499S and F500Y in rat CD73, which influence the water structure of the C2-pocket, the $\pi-\pi$ interactions with the nucleobase, and also the conformational freedom of residue 500, as demonstrated for the CD73 × **21** complex. Compound **21** exhibited a very different binding mode compared to other AOPCP derivatives due to its large, unflexible 2-substituent and also displayed a particularly large species difference, being 12.5-fold more potent toward human CD73 compared to the rat enzyme. The present study provides valuable information for the further improvement of these inhibitors, which have great potential as future drugs.

EXPERIMENTAL SECTION

General. All reagents used for the synthesis and biological studies were commercially obtained from various producers (Acros, Aldrich, Fluka, Merck, and Sigma) and used without further purification and drying. The purity of all starting materials used was greater than 95%. Thin layer chromatography (TLC) using aluminum sheets with silica gel 60 F_{254} (Merck) were used to monitor the reactions. Silica gel 0.060−0.200 mm, pore diameter ca. 6 nm, was employed for column chromatography. LC/ESI-MS (HPLC analysis coupled to electrospray ionization mass spectrometry) was used to determine the final compounds' purity and was found to be greater than 95%. For LC/ESI-MS measurement, the samples were prepared by dissolving 1 mg/mL of compound in H_2O/MeOH (1:1) containing 2 mM ammonium acetate. Subsequently, a sample of 10 μL was injected into an HPLC instrument and elution was performed with a gradient of water/methanol (containing 2 mM ammonium acetate) from 90:10 to 0:100 for 15 min at a flow rate of 250 μL/min. The instrument was an API 2000 (Applied Biosystems, Darmstadt, Germany) mass spectrometer (turbo ion spray ion source) coupled with a Waters HPLC system (Agilent 1100) using a Phenomenex Luna 3 μ C18 column. ^{1}H, ^{31}P, and ^{13}C NMR spectra were performed on a Bruker Avance 500 and 600 MHz spectrometer and were recorded at room temperature using deuterated solvents (DMSO-d_6, MeOD-d_4, or D_2O). High-resolution mass spectroscopy (HRMS) analysis was performed using a Bruker Daltonik micrOTOF-Q. For lyophilization and for drying of the nucleosides before the final reactions, a freeze-dryer (Christ Alpha 1−4 LSC) was used. For purification of the final nucleotide analogues, a preparative HPLC purification system (Knauer Smartline 1050), and for anion exchange chromatography, an FPLC instrument (Amersham Biosciences) were used.

Triethylammoniumhydrogen carbonate buffer (TEAC, 1 M) was prepared as previously described[19] by adding dry ice slowly to 1 M triethylamine solution in water with stirring for 2−3 h until a pH value of approximately 7.4−7.6 was indicated (pH meter).

Altogether, 10 different 2-substituted AOPCP derivatives and analogues were synthesized and investigated, eight of which are new compounds not previously described in literature. Although the synthesis of guanosine-5′-*O*-[(phosphonomethyl)phosphonic acid] (**7**) and of 2-chloroadenosine-5′-*O*-[(phosphonomethyl)phosphonic acid](**16**) had previously been described,[43,44] their interaction with CD73 is reported for the first time in this publication. Some of the prepared intermediate nucleoside, which were not previously described, were also fully analyzed in the present study. ^{1}H NMR, ^{13}C NMR, DEPT-135 ^{31}P NMR spectroscopy, and HRMS were used to confirm the structures of the synthesized new compounds and all final products.

General Procedure for the Synthesis of Nucleotides. The nucleotides (**7**−**10**, **15**, **16**, **20**, **21**, **28**, and **29**) were synthesized by a previously reported method.[19] An ice-cooled solution of methylenebis(phosphonic dichloride) (3 mmol) in trimethyl phosphate (5 mL) was added to a suspension of the appropriate nucleoside (1 mmol) in trimethyl phosphate (2 mL) at 0 °C kept also on ice. After stirring for 15−25 min, upon disappearance of the nucleoside as indicated by TLC, 10 mL of cold 0.5 M aqueous TEAC solution (pH 7.4−7.6) was added. The mixture was further stirred at 0 °C for 30 min, followed by stirring at rt for 2 h. Next, trimethyl phosphate used for the synthesis was extracted using 2 × 100 mL of *tert*-butylmethyl ether, and the aqueous layer was subsequently collected and lyophilized for 3 days. The obtained mixture of the desired nucleotide analogue and side products were separated by ion-exchange chromatography on DEAE Sephadex (A-25, HCO^-_3 form), using a linear gradient of 0−800 mM of TEAC in distilled water. Fractions containing the product were pooled and evaporated to dryness in vacuo, while adding ethanol repeatedly to remove the TEAC buffer. Thus obtained liquid was lyophilized by adding 10 mL of water for 3 days to give glassy solids. The compound was then purified by RP-HPLC using a gradient of 50 mM ammonium hydrogencarbonate/acetonitrile from 100:0 to 40:60, and suitable fractions were pooled and lyophilized several times by adding 20 mL of water each time to finally obtain white coarse powder of the final products.

*Guanosine-5′-O-[(phosphonomethyl)phosphonic Acid] (**7**).* ^{1}H NMR (600 MHz, D_2O) δ 8.28 (s, 1H, C8-H), 5.95 (dd, J = 5.5 Hz, 1H, C1′-H), 4.57−4.51 (m, 1H, C2′-H), 4.40−4.37 (m, 1H, C3′-H), 4.37−4.33 (m, 1H, C4′-H), 4.25−4.08 (m, 2H, C5′-$\underline{H}_2$), 2.20 (t, J = 19.6 Hz, 2H, P-C$\underline{H}_2$-P). ^{13}C NMR (151 MHz, D_2O) δ 165.76 (1C, C6), 161.43 (1C, C2), 156.96 (1C, C4), 140.49 (1C, C8), 120.15 (1C, C5), 90.01 (1C, C1′), 86.76 (1C, C4′), 76.54 (1C, C2′), 73.06 (1C, C3′), 66.39 (1C, C5′), 49.52 (1C, P-$\underline{C}$H$_2$-P). ^{31}P NMR (243 MHz, D_2O) δ 18.69 (d, J = 9.5 Hz, $\mathbf{P}_\alpha$), 15.46 (d, J = 9.5 Hz, $\mathbf{P}_\beta$). LC-MS (m/z): negative mode 440 $[M - H]^-$, positive mode 442 $[M + H]^+$. Purity by HPLC-UV (254 nm)-ESI-MS: 100%. HRMS (ESI): m/z $[M - H]^-$ calcd for $C_{11}H_{17}N_5O_{10}P_2$ 440.0371, found 440.0381.

*2-Amino-6-chloropurine Riboside-5′-O-[(phosphonomethyl)-phosphonic Acid] (**8**).* ^{1}H NMR (500 MHz, D_2O) δ 8.28 (s, 1H, C8-H), 6.11 (dd, J = 5.7 Hz, 1H, C1′-H), 5.24−5.20 (m, 1H, C2′-H), 4.67−4.57 (m, 1H, C3′-H), 4.30−4.28 (m, 1H, C4′-H), 4.27−4.13 (m, 2H, C5′-$\underline{H}_2$), 2.16 (t, J = 19.9 Hz, 2H, P-C$\underline{H}_2$-P). ^{13}C NMR (126 MHz, D_2O) δ 155.11 (1C, C2), 153.87 (1C, C6), 151.33 (1C, C4), 142.82 (1C, C8), 132.05 (1C, C5), 91.59 (1C, C1′), 86.57 (1C, C4′), 74.05 (1C, C2′), 72.59 (1C, C3′), 66.39 (1C, C5′), 49.51 (1C, P-$\underline{C}$H$_2$-P). ^{31}P NMR (202 MHz, D_2O) δ 18.76 (d, J = 9.5 Hz, P_α), 15.37 (d, J = 9.5 Hz, P_β). LC-MS (m/z): negative mode 458 $[M - H]^-$, positive mode 460 $[M + H]^+$. Purity by HPLC-UV (254 nm)-ESI-MS: 100%. HRMS (ESI): m/z $[M - H]^-$ calcd for $C_{11}H_{16}ClN_5O_9P_2$ 458.0032, found 458.0038.

*2,6-Diaminopurine Riboside-5′-O-[(phosphonomethyl)-phosphonic Acid] (**9**).* ^{1}H NMR (500 MHz, D_2O) δ 8.22 (s, 1H, C8-H), 5.92−5.88 (m, 1H, C1′-H), 4.70−4.65 (m, 1H, C2′-H), 4.51−4.48 (m, 1H, C3′-H), 4.35−4.33 (m, 1H, C4′-H), 4.22−4.18 (m, 2H, C5′-$\underline{H}_2$), 2.21−2.15 (t, J = 19.8 Hz, 2H, P-C$\underline{H}_2$-P). ^{13}C NMR (126 MHz, D_2O) δ 165.69 (1C, C6), 156.87 (1C, C2), 150.67 (1C, C4), 142.30 (1C, C8), 120.33 (1C, C5), 90.19 (1C, C1′), 86.73 (1C, C4′), 76.74 (1C, C2′), 72.94 (1C, C3′), 66.47 (1C, C5′), 46.67 (1C, P-$\underline{C}$H$_2$-P). ^{31}P NMR (202 MHz, D_2O) δ 18.36 (d, J = 7.4 Hz, $\mathbf{P}_\alpha$), 16.90 (d, J = 9.8 Hz, $\mathbf{P}_\beta$). LC-MS (m/z): negative mode 439 $[M - H]^-$, positive mode 441 $[M + H]^+$. Purity by HPLC-UV (254 nm)-ESI-MS: 100%. HRMS (ESI): m/z $[M - H]^-$ calcd for $C_{11}H_{18}N_6O_9P_2$ 439.0530, found 439.0539.

*Isoguanosine-5′-O-[(phosphonomethyl)phosphonic Acid] (**10**).* ^{1}H NMR (500 MHz, D_2O) δ 8.27 (s, 1H, C8-H), 5.88 (dd, J = 5.2 Hz, 1H, C1′-H), 4.70−4.68 (m, 1H, C2′-H), 4.51−4.47 (m, 1H, C3′-H), 4.39−4.31 (m, 1H, C4′-H), 4.18−4.11 (m, 2H, C5′-$\underline{H}_2$), 2.24 (t, J = 19.9 Hz, 2H, P-C$\underline{H}_2$-P). ^{13}C NMR (151 MHz, D_2O) δ 165.97

https://dx.doi.org/10.1021/acs.jmedchem.9b01611
J. Med. Chem. 2020, 63, 2941−2957

(1C, C2), 154.91 (1C, C6), 152.66 (1C, C4), 141.36 (1C, C8), 120.33 (1C, C5), 90.86 (1C, C1′), 87.56 (1C, C4′), 77.10 (1C, C2′), 73.45 (1C, C3′), 66.48 (1C, C5′), 49.22 (1C, P-$\underline{C}H_2$-P). ^{31}P NMR (243 MHz, D_2O) δ 18.22 (d, J = 9.4 Hz, $\mathbf{P}_\alpha$), 17.35 (d, J = 9.5 Hz, $\mathbf{P}_\alpha$). LC-MS (m/z): negative mode 440 $[M - H]^-$, positive mode 442 $[M + H]^+$. Purity by HPLC-UV (254 nm)-ESI-MS: 100%. HRMS (ESI): m/z $[M - H]^-$ calcd for $C_{11}H_{17}N_5O_7P_2$ 440.0371, found 440.0378.

*2-Iodoadenosine-5′-O-[(phosphonomethyl)phosphonic Acid] (**15**).* ^{1}H NMR (600 MHz, D_2O) δ 8.43 (s, 1H, C8-H), 6.05 (dd, J = 5.4 Hz, 1H, C1′-H), 4.76−4.33 (m, 1H, C2′-H), 4.54−4.52 (m, 1H, C3′-H), 4.39−4. 36 (m, 1H, C4′), 4.22−4.09 (m, 2H, C5′-$\underline{H}_2$), 2.20 (t, J = 19.9 Hz, 2H, P-C$\underline{H}_2$-P). ^{13}C NMR (151 MHz, D_2O) δ 155.38 (1C, C6), 149.51 (1C, C4), 139.57 (1C, C8), 119.44 (1C, C2), 118.50 (1C, C5), 87.05 (1C, C1′), 83.90 (1C, C4′), 74.29 (1C, C2′), 70.13 (1C, C3′), 63.42 (1C, C5′), 46.62 (1C, P-$\underline{C}H_2$-P). ^{31}P NMR (243 MHz, D_2O) δ 18.67 (d, J = 9.7 Hz, $\mathbf{P}_\alpha$), 15.38 (d, J = 9.8 Hz, $\mathbf{P}_\beta$). LC-MS (m/z): negative mode 550 $[M - H]^-$, positive mode 552 $[M + H]^+$. Purity by HPLC-UV (254 nm)-ESI-MS: 100%. HRMS (ESI): m/z $[M - H]^-$ calcd for $C_{11}H_{16}IN_5O_9P_2$ 549.9388, found 549.9394.

*2-Chloroadenosine-5′-O-[(phosphonomethyl)phosphonic Acid] (**16**).* ^{1}H NMR (500 MHz, D_2O) δ 8.46 (s, 1H, C8-H), 6.01 (dd, J = 5.0 Hz, 1H, C1′-H), 4.71−4.69 (m, 1H, C2′-H), 4.53−4.50 (m, 1H, C3′-H), 4.31−4.26 (m, 1H, C4′-H), 4.16−4.12 (m, 2H, C5′-$\underline{H}_2$), 2.07 (t, J = 19.5 Hz, 2H, P-C$\underline{H}_2$-P). ^{13}C NMR (126 MHz, D_2O) δ 159.10 (1C, C6), 156.60 (1C, C2), 152.91 (1C, C4), 142.91 (1C, C8), 120.50 (1C, C5), 90.04 (1C, C1′), 86.63 (1C, C4′), 77.09 (1C, C2′), 72.84 (1C, C3′), 66.05 (1C, C5′), 49.48 (1C, P-$\underline{C}H_2$-P). ^{31}P NMR (202 MHz, D_2O) δ 21.25 (d, J = 9.6 Hz, $\mathbf{P}_\alpha$), 12.84 (d, J = 9.7 Hz, $\mathbf{P}_\beta$). LC-MS (m/z): negative mode 458 $[M - H]^-$, positive mode 460 $[M + H]^+$. Purity by HPLC-UV (254 nm)-ESI-MS: 100%. HRMS (ESI): m/z $[M - H]^-$ calcd for $C_{11}H_{16}ClN_5O_9P_2$ 458.0032, found 458.0040.

*2-Hydrazinyladenosine-5′-O-[(phosphonomethyl)phosphonic Acid] (**20**).* ^{1}H NMR (600 MHz, D_2O) δ 8.30 (s, 1H, C8-H), 5.98 (dd, J = 5.1 Hz, 1H, C1′-H), 5.04−4.94 (m, 1H, C2′-H), 4.62−4.48 (m, 1H, C3′-H), 4.38−4.30 (m, 1H, C4′-H), 4.27−4.14 (t, 2H, C5′-H_2), 2.28−2.13 (t, J = 19.5 Hz, 2H, P-C$\underline{H}_2$-P). ^{13}C NMR (151 MHz, D_2O) δ 159.06 (1C, C6), 157.10 (1C, C2), 152.80 (1C, C4), 142.75 (1C, C8), 120.14 (1C, C5), 90.89 (1C, C1′), 86.69 (1C, C4′), 75.81 (1C, C2′), 73.11 (1C, C3′), 66.45 (1C, C5′), 49.51 (1C, P-$\underline{C}H_2$-P). ^{31}P NMR (243 MHz, D_2O) δ 18.49 (d, J = 9.5 Hz, $\mathbf{P}_\alpha$), 16.14 (d, J = 9.4 Hz, $\mathbf{P}_\beta$). LC-MS (m/z): negative mode 454 $[M - H]^-$, positive mode 456 $[M + H]^+$. Purity by HPLC-UV (254 nm) ESI-MS: 100%. HRMS (ESI): m/z $[M - H]^-$ calcd for $C_{11}H_{19}N_7O_9P_2$ 454.0639, found 454.0651.

*2-(1-Piperazinyladenosine-5′-O-[(phosphonomethyl)-phosphonic Acid] (**21**).* ^{1}H NMR (600 MHz, D_2O) δ 8.15 (s, 1H, C8-H), 6.02 (dd, J = 5.3 Hz, 1H, C1′-H), 4.88−4.84 (m, C2′-H), 4.55−4.51 (m, 1H, C3′-H), 4.34−4.29 (m, 1H, C4′-H), 4.19−4.08 (m, 2H, C5′-$\underline{H}_2$), 3.83−3.76 (m, 4H, piperazinyl-H), 2.90−2.89 (m, 4H, piperazinyl-H), 2.13 (t, J = 19.3 Hz, 2H, P-C$\underline{H}_2$-P). ^{13}C NMR (151 MHz, D_2O) δ 161.50 (1C, C2), 158.82 (1C, C6), 154.30 (1C, C4), 141.32 (1C, C8), 120.14 (1C, C5), 90.00 (1C, C1′), 86.07 (1C, C4′), 76.05 (1C, C2′), 73.06 (1C, C3′), 66.58 (1C, C5′), 47.53 (1C, P-$\underline{C}H_2$-P), 45.89 (2C, piperazine), 44.46 (2C, piperazine). ^{31}P NMR (243 MHz, D_2O) δ 19.73 (d, J = 8.9 Hz, $\mathbf{P}_\alpha$), 14.49 (d, J = 9.0 Hz, $\mathbf{P}_\beta$). LC-MS (m/z): negative mode 508 $[M - H]^-$, positive mode 510 $[M + H]^+$. Purity by HPLC-UV (254 nm) ESI-MS: 100%. HRMS (ESI): m/z $[M - H]^-$ calcd for $C_{15}H_{25}N_7O_9P_2$ 508.1109, found 508.1100.

*2-Allylthioadenosine-5′-O-[(phosphonomethyl)phosphonic Acid] (**28**).* ^{1}H NMR (500 MHz, D_2O) δ 8.34 (s, 1H, C8-H), 6.09 (dd, J = 5.2, 1.8 Hz, 1H, C1′-H), 6.06−5.99 (m, 1H, S-CH_2-C$\underline{H}$=CH_2), 5.38−5.33 (dq, J = 17.0, 1.5 Hz, 1H, S-CH_2-CH=C$\underline{H}_2$), 5.17 (dt, J = 10.2, 1.3 Hz, 1H, S-CH_2-CH=C$\underline{H}_2$), 4.84−4.79 (m, 1H, C2′-H), 4.56−4.53 (m, C3′-H), 4.44−4.38 (m 1H, C4′-H), 4.22−4.01 (m, 2H, C5′-H_2), 3.82 (dt, J = 6.8, 1.4 Hz, 2H, S-$\underline{CH}_2$-CH=CH_2), 2.15 (t, J = 19.8 Hz, 2H, P-C$\underline{H}_2$-P). ^{13}C NMR (126 MHz, D_2O) δ 167.39 (1C, C2), 158.06 (1C, C6), 152.94 (1C, C4), 142.12 (1C, C8), 136.87 (1C, Allyl), 120.55 (1C, C5), 119.27 (1C, Allyl), 90.08 (1C, C1′), 86.38 (1C, C4′), 76.71 (1C, C2′), 73.02 (1C, C3′), 66.38 (1C, C5′), 49.50 (1C, P-$\underline{C}H_2$-P), 36.51 (1C, Allyl). ^{31}P NMR (202 MHz, D_2O) δ 19.33 (d, J = 8.5 Hz, $\mathbf{P}_\alpha$), 14.47 (d, J = 8.6 Hz, $\mathbf{P}_\beta$). LC-MS (m/z): negative mode 496 $[M - H]^-$, positive mode 498 $[M + H]^+$. Purity by HPLC-UV (254 nm) ESI-MS: 100%. HRMS (ESI): m/z $[M - H]^-$ calcd for $C_{14}H_{21}N_5O_9P_2S$ 496.0455, found 496.0463.

*2-Cyclohexylethylthioadenosine-5′-O-[(phosphonomethyl)-phosphonic Acid] (**29**).* A simplified purification procedure was developed for this compound after synthesis of a second batch. The obtained mixture of the crude nucleotide analogue was directly purified by RP-HPLC using a gradient of water/acetonitrile (containing 0.05% TFA) from 20:80 to 80:20, and suitable fractions were pooled and lyophilized to obtain the desired product as a white powder. Prior used ion-exchange chromatography is not required using this optimized procedure. ^{1}H NMR (500 MHz, D_2O) δ 8.37 (s, 1H, C8-H), 6.11 (dd, J = 4.7 Hz, 1H, C1′-H), 4.55−4.48 (m, 1H, C2′-H), 4.32−4.26 (m 1H, C3′-H), 4.28−4.21 (m, 1H, C4′-H), 4.19−4.08 (m, 2H, C5′-$\underline{H}_2$), 3.16−3.01 (m, 2H, −C$\underline{H}_2$-CH_2-), 2.19 (t, J = 19.8 Hz, 2H, P-C$\underline{H}_2$-P), 1.77−1.43 (m, 9H, -CH_2-C$\underline{H}_2$-cyclohexane-H), 1.34−1.02 (m, 4H, −CH_2-C$\underline{H}_2$-cyclohexane-H). ^{13}C NMR (126 MHz, D_2O) δ 167.64 (1C, C2), 157.32 (1C, C6), 152.90 (1C, C4), 142.11 (1C, C8), 118.83 (1C, C5), 89.77 (1C, C1′), 86.48 (1C, C4′), 76.82 (1C, C2′), 73.05 (1C, C3′), 66.43 (1C, C5′), 39.46 (1C, P-$\underline{C}H_2$-P), 35.46 (1C, $\underline{C}H_2$-CH_2−), 31.60 (1C, cyclohexane), 30.34 (1C, −CH_2-$\underline{C}H_2$-cyclohexane), 29.06 (2C, cyclohexane), 28.71 (3C, cyclohexane). ^{31}P NMR (202 MHz, D_2O) δ 18.68 (d, J = 9.8 Hz, $\mathbf{P}_\alpha$), 15.27 (d, J = 9.4 Hz, $\mathbf{P}_\beta$). LC-MS (m/z): negative mode 566 $[M - H]^-$, positive mode 568 $[M + H]^+$. Purity by HPLC-UV (254 nm)-ESI-MS: 100%. HRMS (ESI): m/z $[M - H]^-$ calcd for $C_{19}H_{31}N_5O_9P_2S$ 566.1238, found 566.1248.

CD73 Assay. Recombinant soluble rat CD73, recombinant soluble human CD73, or membrane preparations of MDA-MB-231 cells natively expressing human CD73 were prepared as previously described.[21,37] The enzyme inhibition assays were performed essentially as described.[21,36] Solutions of test compound of varying concentrations were prepared in demineralized water, and an aliquot (10 μL) was added to 70 μL of assay reaction buffer containing 25 mM Tris, 140 mM sodium chloride, and 25 mM sodium dihydrogen phosphate, pH 7.4. Then, 10 μL of CD73-containing solution or suspension (rat CD73, 1.63 ng; human CD73, 0.365 ng; membrane preparation of MDA-MB-231 cells expressing CD73, 7.4 ng of protein per vial) was added, followed by the addition of 10 μL of [2,8-^{3}H]AMP (specific activity: 20 mCi/ mmol, American Radiolabeled Chemicals, MO, USA, obtained via Hartmann Analytic, Braunschweig, Germany) for the initiation of the reaction (the final substrate concentration was 5 μM). The mixture was incubated for 25 min at 37 °C in a shaking water bath, then 500 μL of cold precipitation buffer (100 mM lanthanum chloride, 100 mM sodium acetate, pH 4.0) were added to stop the reaction and to facilitate the precipitation of unreacted substrate. The formed precipitate was separated by filtration through GF/B glass fiber filters using a cell harvester (M-48, Brandel, Gaithersburg, MD, USA) and washed three times with 400 μL of cold (4 °C) demineralized water per vial. The filtrate was collected, 5 mL of the scintillation cocktail (ULTIMA Gold XR, PerkinElmer, MA, USA) was added to each vial, and radioactivity was measured by scintillation counting (Tri-Carb 2900 TR, Packard/PerkinElmer; counting efficacy: 49−52%). The resulting data were plotted, and concentration−inhibition curves were fitted with GraphPad Prism 7 (GraphPad Software, La Jolla, USA). The mean IC_{50} ± standard error of the mean (SEM) from duplicate or triplicate determinations obtained from three independent experiments was used to calculate the K_i value using the Cheng−Prusoff equation.

Determination of Compound Stability in Human Blood Plasma. Blood plasma from healthy donors was obtained from the blood bank, University Clinic Bonn, and the study was performed as previously described.[19] Human plasma was added to an aqueous solution of inhibitor to obtain a final concentration of 200 μM

https://dx.doi.org/10.1021/acs.jmedchem.9b01611
J. Med. Chem. 2020, 63, 2941−2957

(volume: 2 mL) and incubated at rt. Then, 200 μL of reaction mixture were withdrawn at different time points (1, 5, 30, 60, 120, and 300 min intervals) and quenched with 400 μL of ice-cold acetonitrile to stop the reaction, followed by centrifugation at 8000*g* for 10 min. The supernatants were then transferred to clean LC-MS (liquid chromatography−mass spectroscopy) vials and analyzed by HPLC. Three separate experiments were performed in duplicate for each compound.

Determination of Compound Metabolism in Rat Liver Microsomes. Rat liver microsomes were prepared as previously described.[19] Compounds were incubated with rat liver microsomes (2 mg) at a concentration of 200 μM in a final volume of 2 mL with an NADPH regenerative system. The NADPH regenerative system consists of NADP (0.57 mM), NADH (0.57 mM), isocitrate (6.4 mM), isocitrate dehydrogenase (0.57 mM), and $MgCl_2$ (23.4 mM) (pH 7.2). The samples were incubated for different time intervals at 37 °C in a water bath. The reaction was stopped by adding ice-cold acetonitrile, followed by centrifugation at 8000*g*. The supernatant was analyzed by LC-MS.

Expression, Purification, and Crystallization of Refolded Human CD73. For cocrystallization experiments with AOPCP derivatives in the closed enzyme state, construct no. 3 of human CD73[8] was recombinantly expressed in *Escherichia coli* and refolded from inclusion bodies. This construct encodes for the mature human CD73 protein sequence (residues 27−549) and contains the T376A natural variation (database entry P21589/VAR_022091 of UniProtKB/Swiss-Prot) as well as four asparagine to aspartate mutations at the natural glycosylation sites and a C-terminal His_6 tag. For the crystal structures of the open form of CD73 construct no. 2 of human CD73 was used, which differs from construct no. 3 in the following additional surface mutations: K145S/K147S/K478S. The general procedure for the production of active human CD73 was performed according to Knapp et al.[45] Briefly, prepurified inclusion bodies were renatured by a fast dilution protocol in an arginine−glycerol buffer at 13 °C. Renatured, active protein was separated from misfolded species by an AMP-agarose affinity chromatography, followed by two steps of size exclusion chromatography. The protein was stored at −80 °C in aliquots until further use. For crystallization, vapor diffusion trials were set up at 19 °C. Then 1 μL of the protein solution containing 1 mM of the respective inhibitor and 100 μM of $ZnCl_2$ were mixed with an equal amount of reservoir buffer solution to give concentrations listed in Table 2. Crystals were stepwise transferred to a cryo buffer composed as reported in Table 2 and finally flash frozen in liquid nitrogen.

Crystallization, X-ray Data Collection and Structure Determination. X-ray data collection was carried out at 100 K on beamline 14.1 of the Berlin Synchrotron (BESSY, Berlin, Germany) equipped with a PILATUS 6 M detector (Dectris, Baden, Switzerland). The diffraction data were indexed, integrated, and scaled with XDS[46] or XDSAPP[47] as well as aimless[48] of the CCP4 suite (Collaborative Computational Project, no. 4, 1994). Coordinates of human CD73 in the closed conformation (PDB 4H2I)[8] or open state (PDB 4H2G)[8] were taken as starting models for rigid body refinement under REFMAC5.[49,50] The models were further improved by iterative cycles of TLS refinement using BUSTER[51] and manual rebuilding with COOT.[52] The two domains of residues 26−335 and 336−551 were used as TLS groups. Structures were validated by MOLPROBITY.[53] Coordinate files and restraint dictionaries for inhibitors were generated using the GRADE web server (http://grade.globalphasing.org/). Final structure building and interpretation were aided by feature enhanced maps calculated with PHENIX.[54,55] Relevant crystallographic parameters of the structures are listed in Table 2. Figures were prepared using PYMOL (http://pymol.org).

■ ASSOCIATED CONTENT

Supporting Information

The Supporting Information is available free of charge at https://pubs.acs.org/doi/10.1021/acs.jmedchem.9b01611.

Synthesis of 2-amino- and 2-oxo-substituted purineriboside-5′-*O*-[(phosphonomethyl)phosphonic acid] derivatives; synthesis of 2-chloro-, 2-iodo-, 2-hydrazinyl-, and 2-piperazinyl-substituted adenosine-5′-*O*-[(phosphonomethyl)phosphonic acid] derivatives; synthesis of 2-allylthio- and 2-cyclohexylethylthio-substituted adenosine-5′-*O*-[(phosphonomethyl)phosphonic acid] derivatives; yields and purities of nucleosides; yields and purities of nucleotides; procedure for the synthesis of 2′,3′,5′-tri-*O*-acetylguanosine (**2**); procedure for the synthesis of 2-amino-6-chloro-(2′,3′,5′-tri-*O*-acetyl-β-D-ribofuranosyl)-9*H*-purine (**3**); procedure for the synthesis of 2-amino-6-chloropurine riboside (**4**); procedure for the synthesis of 2,6-diaminopurine riboside (**5**); procedure for the synthesis of isoguanosine (**6**); procedure for the synthesis of 6-chloro-2-iodo-2′,3′,5′-triacetyl-purine riboside (**11**); procedure for the synthesis of 2-iodoadenosine (**12**); procedure for the synthesis of 2,6-dichloro-2′,3′,5′-triacetyl-purine riboside (**13**); procedure for the synthesis of 2-chloroadenosine (**14**); procedure for the synthesis of 2-hydrazinyladenosine (**17**); procedure for the synthesis of 2-*Boc*-(*N*-piperazinyl)adenosine (**18**); procedure for the synthesis of 2-(*N*-piperazinyl)adenosine (**19**); general procedure for the synthesis of 2-thioadenosine derivatives (**26**, **27**); LC/ESI-MS spectra of the synthesized nucleotide analogue **15**; LC/ESI-MS spectra of the synthesized nucleotide analogue **29**; sections of the ^{31}P NMR spectra for the purity control of compounds **15** and **20**; sections of the ^{31}P NMR spectra for the purity control of compounds **21** and **29**; activity of compounds at human NPPs and ADP-activated P2 receptor ($P2Y_1$ and $P2Y_{12}$) NPP1−3 assays; potency of selected derivatives at human NPP1−3; calcium mobilization assay for $P2Y_1$ receptor $P2Y_{12}$ receptor β-arrestin assay; potency of selected derivatives as agonists at ADP-activated P2Y receptors; comparison of human CD73 and rat CD73; water structure in the C2-pocket of unliganded CD73 in the open conformation; changes in the water structure of the C2-pocket upon binding of AOPCP and derivatives; superposition of the binding modes of AOPCP (gray, 4H2I) and of **21** (cyan) to CD73 (PDF)

Molecular formula strings of final compounds (CSV)

Accession Codes

Final coordinates and structure factors of cocrystals with inhibitors PSB-12676 (**9**), PSB-12690 (**10**), PSB-12646 (**20**), and PSB-12604 (**21**) and the cocrystal structures in the open form have been deposited in the Protein Data Bank (www.rcsb.org) with the corresponding accession codes listed in Table 2. Authors will release the atomic coordinates and experimental data upon article publication.

■ AUTHOR INFORMATION

Corresponding Authors

Norbert Sträter − *Institute of Bioanalytical Chemistry, Center for Biotechnology and Biomedicine, Leipzig University, D-04103 Leipzig, Germany;* orcid.org/0000-0002-2001-0500; Phone: +49 341 9731311; Email: strater@bbz.uni-leipzig.de; Fax: +49 341 9731319

Christa E. Müller − *PharmaCenter Bonn, Pharmaceutical Institute, Department of Pharmaceutical & Medicinal Chemistry, University of Bonn, D-53121 Bonn, Germany;*

https://dx.doi.org/10.1021/acs.jmedchem.9b01611
J. Med. Chem. 2020, 63, 2941−2957

orcid.org/0000-0002-0013-6624; Phone: +49-228-73-2301; Email: christa.mueller@uni-bonn.de.; Fax: +49-228-73-2567

Authors

Sanjay Bhattarai − *PharmaCenter Bonn, Pharmaceutical Institute, Department of Pharmaceutical & Medicinal Chemistry, University of Bonn, D-53121 Bonn, Germany*

Jan Pippel − *Institute of Bioanalytical Chemistry, Center for Biotechnology and Biomedicine, Leipzig University, D-04103 Leipzig, Germany*

Emma Scaletti − *Institute of Bioanalytical Chemistry, Center for Biotechnology and Biomedicine, Leipzig University, D-04103 Leipzig, Germany*

Riham Idris − *PharmaCenter Bonn, Pharmaceutical Institute, Department of Pharmaceutical & Medicinal Chemistry, University of Bonn, D-53121 Bonn, Germany*

Marianne Freundlieb − *PharmaCenter Bonn, Pharmaceutical Institute, Department of Pharmaceutical & Medicinal Chemistry, University of Bonn, D-53121 Bonn, Germany*

Georg Rolshoven − *PharmaCenter Bonn, Pharmaceutical Institute, Department of Pharmaceutical & Medicinal Chemistry, University of Bonn, D-53121 Bonn, Germany*

Christian Renn − *PharmaCenter Bonn, Pharmaceutical Institute, Department of Pharmaceutical & Medicinal Chemistry, University of Bonn, D-53121 Bonn, Germany*

Sang-Yong Lee − *PharmaCenter Bonn, Pharmaceutical Institute, Department of Pharmaceutical & Medicinal Chemistry, University of Bonn, D-53121 Bonn, Germany*

Aliaa Abdelrahman − *PharmaCenter Bonn, Pharmaceutical Institute, Department of Pharmaceutical & Medicinal Chemistry, University of Bonn, D-53121 Bonn, Germany*

Herbert Zimmermann − *Institute of Cell Biology and Neuroscience, Goethe-University, D-60438 Frankfurt am Main, Germany*

Ali El-Tayeb − *PharmaCenter Bonn, Pharmaceutical Institute, Department of Pharmaceutical & Medicinal Chemistry, University of Bonn, D-53121 Bonn, Germany*

Complete contact information is available at: https://pubs.acs.org/10.1021/acs.jmedchem.9b01611

Author Contributions

S.B., J.P., and E.S. contributed equally.

Notes

The authors declare the following competing financial interest(s): N.S. and C.E.M. have given scientific advice to Arcus Biosciences (Arcus Biosciences, Inc. is a publicly traded biotechnology company).

■ ACKNOWLEDGMENTS

S.B. and C.E.M. were supported by the Ministry for Innovation, Science, Research and Technology of the State of North-Rhine-Westfalia (NRW International Graduate Research School BIOTECH-PHARMA). C.E.M. was supported by the Deutsche Forschungsgemeinschaft (SFB1328). We thank Marion Schneider for LCMS analyses and Sabine Terhart-Krabbe and Annette Reiner for NMR spectra. Prof. Dr. Henrik Ditzel is acknowledged for the gift of MDA-MB-231 cells. N.S. thanks the SFB 1052 (Deutsche Forschungsgemeinschaft) for support. J.P., E.S., and N.S. are grateful to the Joint Berlin MX-Laboratory at BESSY II, Berlin, Germany, for beam time and assistance during synchrotron data collection and to the Helmholtz Zentrum Berlin for traveling support.

■ ABBREVIATIONS USED

AOPCP, α,β-methylene-ADP, [{5-(6-aminopurin-9-yl)-3,4-dihydroxyoxolan-2-yl}methoxy-hydroxyphosphoryl]-methylphosphonic acid; AP, alkaline phosphatase; Boc, 1-*tert*-butoxycarbonyl; CD73, cluster of differentiation 73; COPCP, α,β-methylene-CDP; DEAE, diethylaminoethyl; DMSO-d_6, deuterated dimethyl sulfoxide; D_2O, deuterated water; FPLC, fast protein liquid chromatography; LC-MS, liquid chromatography coupled to mass spectrometry; GPI, glycosylphosphatidylinositol; MeOD-d_4, deuterated methanol; eNPP, nucleotide pyrophosphatase; eNTPDase, ecto-nucleoside 5′-triphosphate diphosphohydrolase; PSB, Pharmaceutical Sciences Bonn; RP-HPLC, reverse phase-high performance liquid chromatography; SARs, structure−activity relationships; Sf9, *Spodoptera frugiperda* 9; TEAC, triethylammonium hydrogencarbonate; UOPCP, α,β-methylene-UDP

■ REFERENCES

(1) Burnstock, G. Physiology and pathophysiology of purinergic neurotransmission. *Physiol. Rev.* **2007**, *87*, 659−797.

(2) Müller, C. E.; Jacobson, K. A. Recent developments in adenosine receptor ligands and their potential as novel drugs. *Biochim. Biophys. Acta, Biomembr.* **2011**, *1808*, 1290−1308.

(3) Burnstock, G.; Verkhratsky, A. Long-term (trophic) purinergic signalling: purinoceptors control cell proliferation, differentiation and death. *Cell Death Dis.* **2010**, *1*, No. e9.

(4) Zimmermann, H. 5′-Nucleotidase: molecular structure and functional aspects. *Biochem. J.* **1992**, *285*, 345−365.

(5) Sträter, N. Ecto-5′-nucleotidase: structure-function relationships. *Purinergic Signalling* **2006**, *2*, 343−350.

(6) Zimmermann, H.; Zebisch, M.; Sträter, N. Cellular function and molecular structure of ecto-nucleotidases. *Purinergic Signalling* **2012**, *8*, 437−502.

(7) Heuts, D.P.H.M.; Weissenborn, M. J.; Olkhov, R. V.; Shaw, A. M.; Gummadova, J.; Levy, C.; Scrutton, N. S. Crystal structure of a soluble form of human CD73 withecto-5′-nucleotidase activity. *ChemBioChem* **2012**, *13*, 2384−2391.

(8) Knapp, K.; Zebisch, M.; Pippel, J.; El-Tayeb, A.; Müller, C. E.; Sträter, N. Crystal structure of the human ecto-5′-nucleotidase (CD73): Insights into the regulation of purinergic signaling. *Structure* **2012**, *20*, 2161−2173.

(9) Thompson, L. F.; Eltzschig, H. K.; Ibla, J. C.; Van De Wiele, C. J.; Resta, R.; Morote-Garcia, J. C.; Colgan, S. P. Crucial role for ecto-5′-nucleotidase (CD73) in vascular leakage during hypoxia. *J. Exp. Med.* **2004**, *200*, 1395−1405.

(10) Antonioli, L.; Pacher, P.; Vizi, E. S.; Haskó, G. CD39 and CD73 in immunity and inflammation. *Trends Mol. Med.* **2013**, *19*, 355−367.

(11) Bours, M. J. L.; Swennen, E. L. R.; Di Virgilio, F.; Cronstein, B. N.; Dagnelie, P. C. Adenosine 5′-triphosphate and adenosine as endogenous signaling molecules in immunity and inflammation. *Pharmacol. Ther.* **2006**, *112*, 358−404.

(12) Zhang, B. CD73: a novel target for cancer immunotherapy. *Cancer Res.* **2010**, *70*, 6407−6411.

(13) Stagg, J.; Divisekera, U.; McLaughlin, N.; Sharkey, J.; Pommey, S.; Denoyer, D.; Dwyer, K. M.; Smyth, M. J. Anti-CD73 antibody therapy inhibits breast tumor growth and metastasis. *Proc. Natl. Acad. Sci. U. S. A.* **2010**, *107*, 1547−1552.

(14) Antonioli, L.; Fornai, M.; Blandizzi, C.; Pacher, P; Haskó, G. Adenosine signaling and the immune system: When a lot could be too much. *Immunol. Lett.* **2019**, *205*, 9−15.

(15) Vijayan, D.; Young, A.; Teng, M. W. L.; Smyth, M. J. Targeting immunosuppressive adenosine in cancer. *Nat. Rev. Cancer* **2017**, *17*, 709−724.

(16) Allard, B.; Longhi, M. S.; Robson, S. C.; Stagg, J. The ectonucleotidases CD39 and CD73: Novel checkpoint inhibitor targets. *Immunol. Rev.* **2017**, *276*, 121−144.
(17) Hay, C. M.; Sult, E.; Huang, Q.; Mulgrew, K.; Fuhrmann, S. R.; McGlinchey, K. A.; Hammond, S. A.; Rothstein, R.; Rios-Doria, J.; Poon, E.; Holoweckyj, N.; Durham, N. M.; Leow, C. C.; Diedrich, G.; Damschroder, M.; Herbst, R.; Hollingsworth, R. E.; Sachsenmeier, K. F. Targeting CD73 in the tumor microenvironment with MEDI9447. *OncoImmunology* **2016**, *5*, No. e1208875.
(18) Bowman, C. E.; da Silva, R. G.; Pham, A.; Young, S. W. An exceptionally potent inhibitor of human CD73. *Biochemistry* **2019**, *58*, 3331−3334.
(19) Bhattarai, S.; Freundlieb, M.; Pippel, J.; Meyer, A.; Abdelrahman, A.; Fiene, A.; Lee, S-Y.; Zimmermann, H.; Yegutkin, G. G.; Sträter, N.; El-Tayeb, A.; Müller, C. E. α,β-Methylene-ADP derivatives and analogs: development of potent and selective ecto-5′-nucleotidase (CD73) inhibitors. *J. Med. Chem.* **2015**, *58*, 6248−6263.
(20) Bhattarai, S.; Pippel, J.; Meyer, A.; Freundlieb, M.; Schmies, C.; Abdelrahman, A.; Fiene, A.; Lee, S-Y.; Zimmermann, H.; El-Tayeb, A.; Yegutkin, G. G.; Sträter, N.; Müller, C. E. X-ray co-crystal structure guides the way to subnanomolar competitive ecto-5′-nucleotidase (CD73) inhibitors for cancer immunotherapy. *Adv. Therap.* **2019**, *2*, 1900075.
(21) Junker, A.; Renn, C.; Dobelmann, C.; Namasivayam, V.; Jain, S.; Losenkova, K.; Irjala, H.; Duca, S.; Balasubramanian, R.; Chakraborty, S.; Börgel, F.; Zimmermann, H.; Yegutkin, G. G.; Müller, C. E.; Jacobson, K. A. Structure-activity relationship of purine and pyrimidine nucleotides as ecto-5′-nucleotidase (CD73) inhibitors. *J. Med. Chem.* **2019**, *62*, 3677−3695.
(22) Dumontet, C.; Peyrottes, S.; Rabeson, C.; Cros-Perrial, E.; Géant, P. Y.; Chaloin, L.; Jordheim, L. P. CD73 inhibition by purine cytotoxic nucleoside analogue-based diphosphonates. *Eur. J. Med. Chem.* **2018**, *157*, 1051−1055.
(23) Baqi, Y.; Lee, S.-Y.; Iqbal, J.; Ripphausen, P.; Lehr, A.; Scheiff, A.; Zimmermann, H.; Bajorath, J.; Müller, C. E. Development of potent and selective inhibitors of ecto-5′-nucleotidase based on an anthraquinone scaffold. *J. Med. Chem.* **2010**, *53*, 2076−2086.
(24) Ripphausen, P.; Freundlieb, M.; Brunschweiger, A.; Zimmermann, H.; Müller, C. E.; Bajorath, J. Virtual screening identifies novel sulfonamide inhibitors of ecto-5′-nucleotidase. *J. Med. Chem.* **2012**, *55*, 6576−6581.
(25) Iqbal, J.; Saeed, A.; Raza, R.; Matin, A.; Hameed, A.; Furtmann, N.; Lecka, J.; Sévigny, J.; Bajorath, J. Identification of sulfonic acids as efficient ecto-5′-nucleotidase inhibitors. *Eur. J. Med. Chem.* **2013**, *70*, 685−691.
(26) Uchino, K.; Matsuo, T.; Iwamoto, M.; Tonosaki, Y.; Fukuchi, A. New 5′-nucleotidase inhibitors, NPF-86IA, NPF-86IB, NPF-86IIA, and NPF-86IIB from Areca catechu; Part I. Isolation and biological properties. *Planta Med.* **1988**, *54*, 419−422.
(27) Al-Rashida, M.; Batool, G.; Sattar, A.; Ejaz, S. A.; Khan, S.; Lecka, J.; Sévigny, J.; Hameed, A.; Iqbal, J. 2-Alkoxy-3-(sulfonylarylaminomethylene)-chroman-4-ones as potent and selective inhibitors of ectonucleotidases. *Eur. J. Med. Chem.* **2016**, *115*, 484−494.
(28) Corbelini, P. F.; Figueiró, F; das Neves, G. M.; Andrade, S.; Kawano, D. F.; Oliveira Battastini, A. M.; Eifler-Lima, V. L. Insights into ecto-5′-nucleotidase as a new target for cancer therapy: a medicinal chemistry study. *Curr. Med. Chem.* **2015**, *22*, 1776−1792.
(29) Wan, Z.-K.; Binnun, E.; Wilson, D. P.; Lee, J. A highly facile and efficient one-step synthesis of N^6-adenosine and N^6-2′-deoxyadenosine derivatives. *Org. Lett.* **2005**, *7*, 5877−5880.
(30) Middleton, R. J.; Briddon, S. J.; Cordeaux, Y.; Yates, A. S.; Dale, C. L.; George, M. W.; Baker, J. G.; Hill, S. J.; Kellam, B. New fluorescent adenosine A_1-receptor agonists that allow quantification of ligand-receptor interactions in microdomains of single living cells. *J. Med. Chem.* **2007**, *50*, 782−793.
(31) Nair, V.; Young, D. A. A new synthesis of isoguanosine. *J. Org. Chem.* **1985**, *50*, 406−408.
(32) Francom, P.; Robins, M. J. Nucleic acid related compounds. 118. Nonaqueous diazotization of aminopurine derivatives. Convenient access to 6-halo and 2,6-dihalopurine nucleosides and 2′-deoxynucleosides with acyl or silyl halides. *J. Org. Chem.* **2003**, *68*, 666−669.
(33) El-Tayeb, A.; Gollos, S. Synthesis and structure-activity relationships of 2-hydrazinyladenosine derivatives as A_{2A} adenosine receptor ligands. *Bioorg. Med. Chem.* **2013**, *21*, 436−447.
(34) Abiru, T.; Miyashita, T.; Watanabe, Y.; Yamaguchi, T.; Machida, H.; Matsuda, A. Nucleosides and nucleotides. 107. 2-(Cycloalkylalkynyl)adenosines: adenosine A2 receptor agonists with potent antihypertensive effects. *J. Med. Chem.* **1992**, *35*, 2253−2260.
(35) El-Tayeb, A.; Iqbal, J.; Behrenswerth, A.; Romio, M.; Schneider, M.; Zimmermann, H.; Schrader, J.; Müller, C. E. Nucleoside-5′-monophosphates as prodrugs of adenosine A_{2A} receptor agonists activated by ecto-5′-nucleotidase. *J. Med. Chem.* **2009**, *52*, 7669−7677.
(36) Freundlieb, M.; Zimmermann, H.; Müller, C. E. A new, sensitive ecto-5′-nucleotidase assay for compound screening. *Anal. Biochem.* **2014**, *446*, 53−58.
(37) Servos, J.; Reiländer, H.; Zimmermann, H. Catalytically active soluble ecto-5′-nucleotidase purified after heterologous expression as a tool for drug screening. *Drug Dev. Res.* **1998**, *45*, 269−276.
(38) Cheng, Y.-C.; Prusoff, W. H. Relationship between the inhibition constant (K_i) and the concentration of inhibitor which causes 50% inhibition (IC_{50}) of an enzymatic reaction. *Biochem. Pharmacol.* **1973**, *22*, 3099−3108.
(39) Qiao, Z.; Li, X.; Kang, N.; Yang, Y.; Chen, C.; Wu, T.; Zhao, M.; Liu, Y.; Ji, X. A novel specific anti-CD73 antibody inhibits triple-negative breast cancer cell motility by regulating autophagy. *Int. J. Mol. Sci.* **2019**, *20*, 1057.
(40) Schiebel, J.; Gaspari, R.; Wulsdorf, T.; Ngo, K.; Sohn, C.; Schrader, T. E.; Cavalli, A.; Ostermann, A.; Heine, A.; Klebe, G. Intriguing role of water in protein-ligand binding studied by neutron crystallography on trypsin complexes. *Nat. Commun.* **2018**, *9*, 3559.
(41) Salonen, L. M.; Ellermann, M.; Diederich, F. Aromatic rings in chemical and biological recognition: energetics and structures. *Angew. Chem., Int. Ed.* **2011**, *50*, 4808−4842.
(42) Maguire, M. H.; Sim, M. K. Studies on adenosine deaminase 2. Specificity and mechanism of action of bovine placental adenosine deaminase. *Eur. J. Biochem.* **1971**, *23*, 22−29.
(43) Engelsma, S. B.; Meeuwenoord, N. J.; Overkleeft, H. S.; van der Marel, G. A.; Filippov, D. V. Combined phosphoramidite-phosphodiester reagents for the synthesis of methylene bisphosphonates. *Angew. Chem., Int. Ed.* **2017**, *56*, 2955−2959.
(44) Gough, G.; Maguire, M. H.; Penglis, F. Analogues of adenosine 5′-diphosphate-new platelet aggregators. Influence of purine ring and and phosphate chain substitutions on the platelet-aggregating potency of adenosine 5′-diphosphate. *Mol. Pharmacol.* **1972**, *8*, 170−177.
(45) Knapp, K. Structural characterization of the human ecto-5′-nucleotidase: implications for purinergic signalling. Doctoral dissertation. Leipzig University, 2011; http://research.uni-leipzig.de/straeter/h5nt/
(46) Kabsch, W. XDS. *Acta Crystallogr., Sect. D: Biol. Crystallogr.* **2010**, *D66*, 125−132.
(47) Krug, M.; Weiss, M. S.; Heinemann, U.; Müller, U. XDSAPP. A graphical user interface for the convenient processing of diffraction data using XDS. *J. Appl. Crystallogr.* **2012**, *45*, 568−572.
(48) Evans, P. R.; Murshudov, G. N. How good are my data and what is the resolution? *Acta Crystallogr., Sect. D: Biol. Crystallogr.* **2013**, *69*, 1204−1214.
(49) Murshudov, G. N.; Vagin, A. A.; Dodson, E. J. Refinement of macromolecular structures by the maximum-likelihood method. *Acta Crystallogr., Sect. D: Biol. Crystallogr.* **1997**, *53*, 240−255.
(50) Murshudov, G. N.; Skubák, P.; Lebedev, A. A.; Pannu, N. S.; Steiner, R. A.; Nicholls, R. A.; Winn, M. D.; Long, F.; Vagin, A. A. REFMAC5 for the refinement of macromolecular crystal structures. *Acta Crystallogr., Sect. D: Biol. Crystallogr.* **2011**, *67*, 355−367.
(51) Blanc, E.; Roversi, P.; Vonrhein, C.; Flensburg, C.; Lea, S. M.; Bricogne, G. Refinement of severely incomplete structures with

https://dx.doi.org/10.1021/acs.jmedchem.9b01611
J. Med. Chem. 2020, 63, 2941−2957

maximum likelihood in BUSTER-TNT. *Acta Crystallogr., Sect. D: Biol. Crystallogr.* **2004**, *D60*, 2210−21.
(52) Emsley, P.; Lohkamp, B.; Scott, W. G.; Cowtan, K. Features and development of Coot. *Acta Crystallogr., Sect. D: Biol. Crystallogr.* **2010**, *66*, 486−501.
(53) Chen, V. B.; Arendall, W. B.; Headd, J. J.; Keedy, D. A.; Immormino, R. M.; Kapral, G. J.; Murray, L. W.; Richardson, J. S.; Richardson, D. C. MolProbity: all-atom structure validation for macromolecular crystallography. *Acta Crystallogr., Sect. D: Biol. Crystallogr.* **2010**, *66*, 12−21.
(54) Adams, P. D.; Afonine, P. V.; Bunkóczi, G.; Chen, V. B.; Davis, I. W.; Echols, N.; Headd, J. J.; Hung, L.-W.; Kapral, G. J.; Grosse-Kunstleve, R. W.; McCoy, A. J.; Moriarty, N. W.; Oeffner, R.; Read, R. J.; Richardson, D. C.; Richardson, J. S.; Terwilliger, T. C.; Zwart, P. H. PHENIX: a comprehensive Python-based system for macromolecular structure solution. *Acta Crystallogr., Sect. D: Biol. Crystallogr.* **2010**, *66*, 213−221.
(55) Afonine, P. V.; Moriarty, N. W.; Mustyakimov, M.; Sobolev, O. V.; Terwil-Liger, T. C.; Turk, D.; Urzhumtsev, A.; Adams, P. D. FEM: feature-enhanced map. *Acta Crystallogr., Sect. D: Biol. Crystallogr.* **2015**, *71*, 646−666.

https://dx.doi.org/10.1021/acs.jmedchem.9b01611
J. Med. Chem. 2020, 63, 2941−2957

Supporting Information

2-Substituted α,β-Methylene-ADP Derivatives: Potent Competitive Ecto-5′-nucleotidase (CD73) Inhibitors with Variable Binding Modes

Sanjay Bhattarai,[§x†] *Jan Pippel,*[‡†] *Emma Scaletti*,[†] *Riham Idris,*[§] *Marianne Freundlieb,*[§] Georg Rolshoven,[§] *Christian Renn*,[§] *Sang-Yong Lee,*[§] *Aliaa Abdelrahman,*[§] *Herbert Zimmermann,*[#] *Ali El-Tayeb,*[§] *Christa E. Müller,*[*,§] *and Norbert Sträter*[*,‡]

[§]PharmaCenter Bonn, Pharmaceutical Institute, Department of Pharmaceutical & Medicinal Chemistry, University of Bonn, An der Immenburg 4, D-53121 Bonn, Germany

[‡]Institute of Bioanalytical Chemistry, Center for Biotechnology and Biomedicine, Leipzig University, Deutscher Platz 5, D-04103 Leipzig, Germany

[#]Institute of Cell Biology and Neuroscience, Goethe-University, D-60438, Frankfurt am Main, Germany

*Address correspondence to:

Prof. Dr. Norbert Sträter
Institute of Bioanalytical Chemistry
Center for Biotechnology and Biomedicine
Leipzig University
Deutscher Platz 5
04103 Leipzig, Germany
phone: +49 341 9731311
Fax: +49 341 9731319
E-mail: strater@bbz.uni-leipzig.de

Prof. Dr. Christa E. Müller
Pharmaceutical Institute
Department of Pharmaceutical & Medicinal Chemistry
An der Immenburg 4
53121 Bonn, Germany
Phone: +49-228-73-2301
Fax: +49-228-73-2567
E-mail: christa.mueller@uni-bonn.de

Present Address

[x]Department of Medicinal Chemistry, University of Kansas, Lawrence, 66045, KS, USA (S.B.).

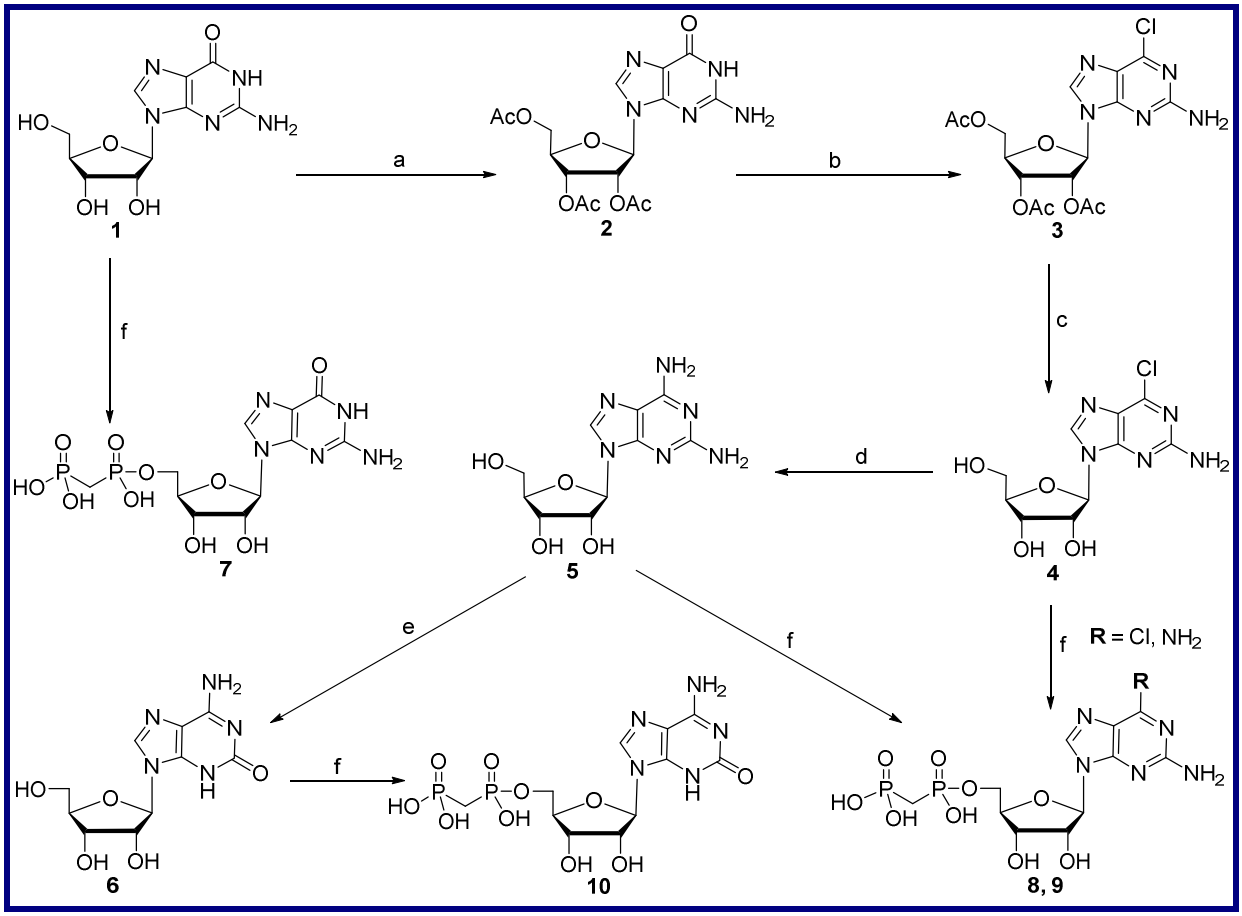
Table of Contents

Chemistry 3
Scheme S1. Synthesis of 2-amino- and 2-oxo-substituted purineriboside-5′-*O*-[(phosphonomethyl)phosphonic acid] derivatives 3
Scheme S2. Synthesis of 2-chloro-, 2-iodo-, 2-hydrazinyl- and 2-piperazinyl-substituted adenosine-5′-*O*-[(phosphonomethyl)phosphonic acid] derivatives 4
Scheme S3. Synthesis of 2-allylthio- and 2-cyclohexylethylthio-substituted adenosine-5′-*O*-[(phosphonomethyl)phosphonic acid] derivatives 5
Table S1. Yields and purities of nucleosides 6
Table S2. Yields and purities of nucleotides 7
Procedure for the synthesis of 2′,3′,5′-tri-*O*-acetylguanosine **(2)** 7
Procedure for the synthesis of 2-amino-6-chloro-(2′,3′,5′-tri-*O*-acetyl-*β*-**D**-ribofuranosyl)-9*H*-purine **(3)** 8
Procedure for the synthesis of 2-amino-6-chloropurine riboside (**4**) 8
Procedure for the synthesis of 2,6-diaminopurine riboside **(5)** 8
Procedure for the synthesis of isoguanosine (**6**) 9
Procedure for the synthesis of 6-chloro-2-iodo-2',3',5'-triacetyl-purine riboside **(11)** 9
Procedure for the synthesis of 2-iodoadenosine **(12)** 10
Procedure for the synthesis of 2,6-dichloro-2',3',5'-triacetyl-purine riboside (**13**) 10
Procedure for the synthesis of 2-chloroadenosine **(14)** 10
Procedure for the synthesis of 2-hydrazinyladenosine **(17)** 11
Procedure for the synthesis of 2-*Boc*-(*N*-piperazinyl)adenosine **(18)** 11
Procedure for the synthesis of 2-(*N*-piperazinyl)adenosine **(19)** 12
General procedure for the synthesis of 2-thioadenosine derivatives (26, 27) 13
Figure S1. LC/ESI-MS spectra of the synthesized nucleotide analog **15** 14
Figure S2. LC/ESI-MS spectra of the synthesized nucleotide analog **29** 15
Figure S3. Sections of the ^{31}P NMR spectra for the purity control of compounds **15** and **20** 16
Figure S4. Sections of the ^{31}P NMR spectra for the purity control of compounds **21** and **29** 17
Activity of compounds at human NPPs and ADP-activated P2 receptor ($P2Y_1$ and $P2Y_{12}$) 18
NPP1-3 assays 18
Table S3. Potency of selected derivatives at human NPP1-3 18
Calcium mobilization assay for $P2Y_1$ receptor 19
$P2Y_{12}$ receptor β-arrestin assay 19
Table S4. Potency of selected derivatives as agonists at ADP-activated P2Y receptors 19
Figure S5. Comparison of human CD73 and rat CD73 20
Figure S6. Water structure in the C2-pocket of unliganded CD73 in the open conformation 20
Figure S7. Changes in the water structure of the C2-pocket upon binding of AOPCP and derivatives . 21
Figure S8. Superposition of the binding modes of AOPCP (grey, 4H2I) and of **21** (cyan) to CD73. 22
References 22

Chemistry

The syntheses of nucleosides **2**, **3**, **4**, **5**, **6**, **11, 12, 13, 14, 17, 18, 19, 23, 24, 25, 26** and **27** were performed as described in the Schemes S1-S3. Yields and purities of the intermediate nucleosides are collected in Table S1. Yields and purities of the final nucleotides (**7**, **8**, **9**, **10**, **15**, **16**, **20**, **21**, **28** and **29**) are collected in Table S2. Procedures and spectral data of all new nucleosides are reported below.

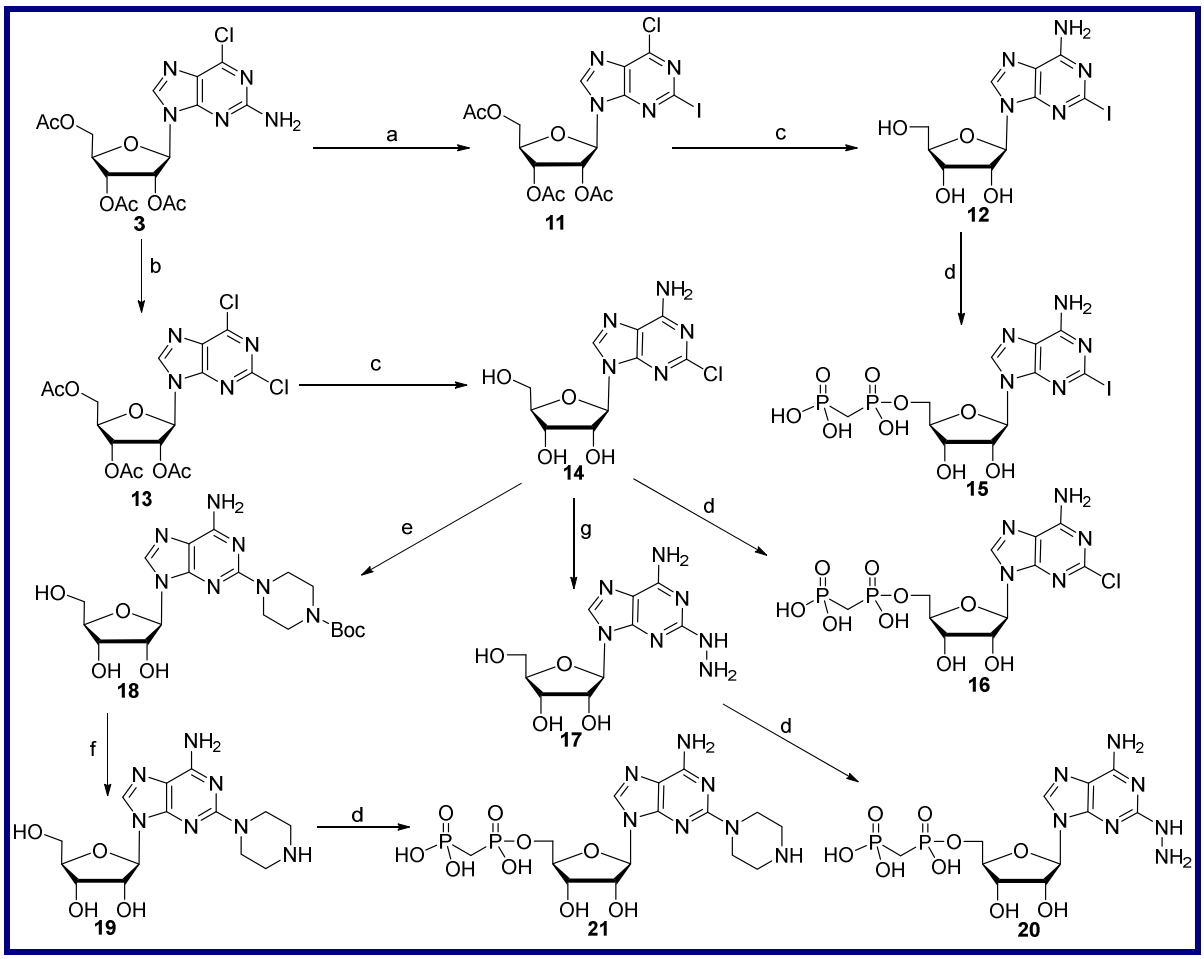
Scheme S1. Synthesis of 2-amino- and 2-oxo-substituted purine riboside-5′-*O*-[(phosphonomethyl)-phosphonic acid] derivatives[a]



[a]Reagents and conditions: (a) acetic anhydride, DMAP (4-dimethylaminopyridine), EDMA (ethyl dimethylamine), 40 °C, 1 h, yield 97%; (b) $POCl_3$, *N*,*N*-dimethylaniline, tetraethylammonium chloride, reflux, 110 °C, 15 min, yield 85%; (c) 2 % NaOMe in methanol, rt, 24 h, yield 80%; (d) ammonia in ethanol, rt, 24 h, yield 75%; (e) acetic acid, sodium nitrite, H_2O, 2 h, rt, yield 95%; (f) two steps: (i) methylenebis(phosphonic dichloride), trimethyl phosphate, 4 °C, 40 min; (ii) TEAC (triethylammonium hydrogencarbonate) buffer pH 7.4-7.6, rt, 15 min, yield 35-60%.

S4

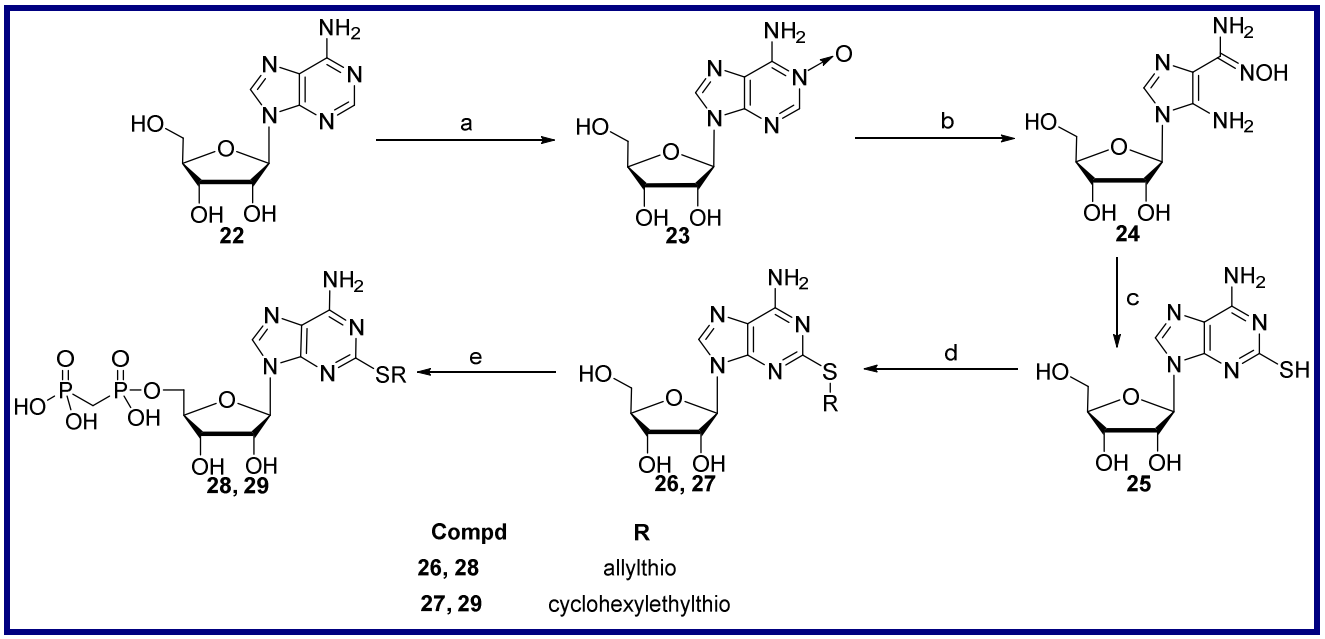
Scheme S2. Synthesis of 2-chloro-, 2-iodo-, 2-hydrazinyl-, and 2-piperazinyl-substituted adenosine-5′-*O*-[(phosphonomethyl)phosphonic acid] derivatives[a]



[a]Reagents and conditions: (a) CuI, I_2, CH_2I_2, isoamyl nitrite in THF, 80 °C, 2 h, yield 75%; (b) benzyltriethylammonium nitrite, acetyl chloride, DCM, 2 h, yield 80%; (c) 2.0 M ammonia in ethanol, rt, 24 h, yield 75%; (d) two steps: (i) methylenebis(phosphonic dichloride), trimethyl phosphate, 4 °C, 30 min; (ii) TEAC buffer pH 7.6, rt, 15 min, yield 40-65%; (e) 1-Boc-piperazine, triethylamine, ethanol, 140 °C, 24 h, yield 85%; (f) 8% TFA, CH_2Cl_2, H_2O, 4 h, rt, yield 95%; (g) hydrazine hydrate, 4 h, rt, yield 97%.

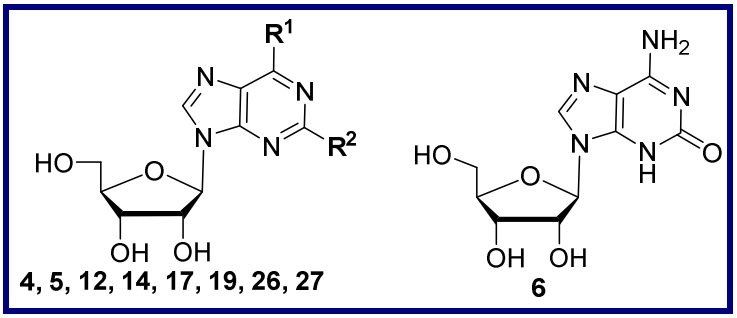
S5

Scheme S3. Synthesis of 2-allylthio- and 2-cyclohexylethylthio-substituted adenosine-5′-*O*-[(phosphonomethyl)phosphonic acid] derivatives[a]



[a]Reagents and conditions: (a) acetic acid, H_2O_2, rt, 4 h, yield 86%; (b) NaOH, 2 h, rt; (c) carbon disulfide, MeOH, H_2O, autoclave, 15 psi, 120 °C, 5 h, rt, yield 65%; (d) NaOH, alkyl bromide, 2 h, rt, yield 56-60%; (e) two steps: (i) methylenebis(phosphonic dichloride), trimethyl phosphate, 4 °C, 30 min, (ii) TEAC buffer pH 7.6, rt, 15 min, yield 35-45%.

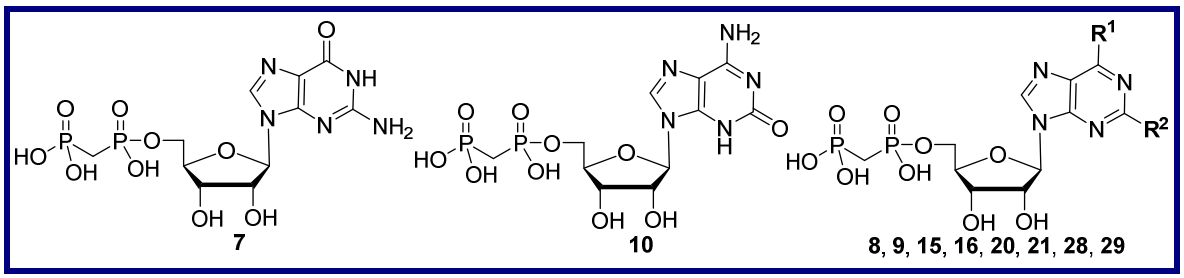
Table S1. Yields and purities of nucleosides



Compd.	R^1	R^2	Yield (%)[b]	LC-MS purity (%)
4	chloro	amino	80	99
5	amino	amino	75	100
6	*see the structure above*		95	100
12	amino	iodo	75	96
14	amino	chloro	75	95
17	amino	hydrazinyl	97	99
19	amino	*N*-piperazinyl	95	100
26	amino	allylthio	59	98
27	amino	cyclohexylethyl thio	56	100

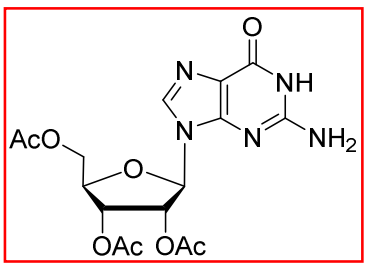
[b]Isolated yields.

Table S2. Yields and purities of synthesized nucleoside-5′-methylenebis(phosphonic acid) derivatives

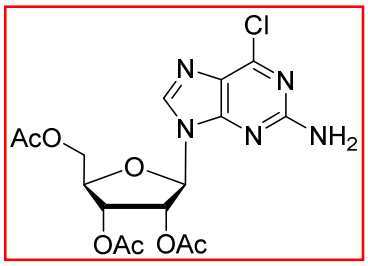


Compd.	R^1	R^2	yield (%)[b]	LC-MS purity (%)
7	**see the structure above**		55	100
8	chloro	amino	53	100
9	amino	amino	45	100
10	**see the structure above**		52	100
15	amino	iodo	57	100
16	amino	chloro	55	100
20	amino	hydrazinyl	41	100
21	amino	*N*-piperazinyl	40	100
28	amino	allythio	35	100
29	amino	cyclohexylethyl thio	65	100

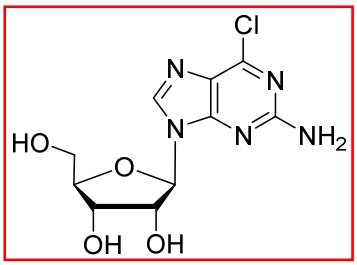
[b]Isolated yields.



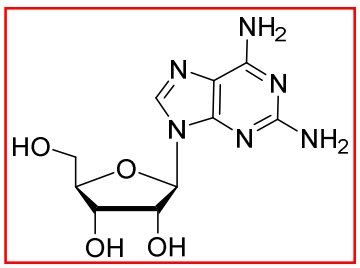
Procedure for the synthesis of 2′,3′,5′-tri-*O*-acetylguanosine (2). To 8.92 g (21.8 mmol) of commercial guanosine was added 0.2 g (1.64 mmol, 0.075 equiv) DMAP, 8.8 g (13 mL, 120 mmol, 5.5 equiv) of EDMA (*N*,*N*-dimethylethylamine) and 10.2 g (9.5 mL, 99.9 mmol) of acetic anhydride. The resulting mixture was suspended in 100 mL of acetonitrile and stirred for 15 min at rt until a clear solution was obtained. Excess acetic anhydride was subjected to methanolysis by adding 20 mL of methanol and stirring for additional 15 min. Finally, the reagents were removed in vacuo and the residue recrystallized from isopropanol, followed by crystallization from acetone and methanol gave titled product as white solid. **Yield:** 8.03 g (95%). **^{1}H NMR (500 MHz, DMSO-*d*$_6$):** δ 8.34 (s, 1H, C8-H), 6.49 (bs, 2H, N$\underline{H_2}$), 6.19 (dd, *J* = 5.7 Hz, 1H, C1′-H), 5.92 – 5.89 (m, 1H, C2′-H), 5.60 – 5.55 (m, 1H, C3′-H), 4.58 – 4.31 (m, 3H, H4′ and C5′-$\underline{H_2}$), 2.19 (s, 3H, OAc), 2.17 (s, 3H, OAc), 2.13 (s, 3H, OAc). **^{13}C NMR (125 MHz, DMSO-*d*$_6$):** δ 169.31, 169.84, 171.28 (3 xCO), 156.01 (1C, C6), 142.47 (1C, C2), 145.83 (1C, C4), 136.26 (1C, C8), 125.42 (1C, C5), 87.65 (1C, C1′), 82.44 (1C, C4′), 73.42 (1C, C2′), 70.81 (1C, C3′), 65.09 (1C, C5′), 22.61, 22.74, 22.85 (3C, 3xOAc). **LC/ESI-MS:** negative mode 408 ([M - H]$^-$), positive mode 410 ([M + H]$^+$). HRMS (ESI): *m/z* [M + H]$^+$ calcd for $C_{16}H_{19}N_5O_8$: 410.1314; found: 410.1323. **Melting Point (°C):** 227-229 [**literature**, 229-231].[1]



Procedure for the synthesis of 2-amino-6-chloro-(2′,3′,5′-tri-*O*-acetyl-β-D-ribofuranosyl)-9*H*-purine (3). A suspension of **2** (2.45 g, 6 mmol), *N*,*N*-dimethylaniline (0.8 g, 0.83 mL, 6.60 mmol, 1.1 equiv), tetraethylammonium chloride (1.88 g, 11.35 mmol, 1.90 equiv) and phosphorus oxychloride (20 g, 12.2 mL, 130 mmol) was stirred at rt for 7 min under an atmosphere of argon. The flask was heated in a preheated oil bath at 90 °C for 13 min. The solution was evaporated, and the resulting oil was stirred in DCM (20 mL) and ice (20 mL). The aqueous layer was extracted with DCM (2 x 25 mL). The combined organic layers were washed with 2M HCl (4 x 20 mL) and brine (2 x 20 mL), dried, and evaporated to green oil. Purification using silica chromatography (1:10 MeOH/DCM) yielded the title compound **3** as a pale orange oil, which was subsequently crystallized in hexane to yield a pale orange solid. **Yield:** 2.45 g (95%). **^{1}H NMR (500 MHz, DMSO-*d*$_6$):** δ 8.28 (s, 1H, C8-H), 6.20 (dd, *J* = 5.3 Hz, 1H, C1′-H), 5.75 – 5.55 (m, 1H, C2′-H), 5.55 – 5.52 (m, 1H, C3′-H), 4.48 – 4.43 (m, 1H, C4′-H), 4.43 – 4.37 (m, 2H, C5′-$\underline{H}_2$), 2.14 (s, 3H, OCOC$\underline{H}_3$), 2.12 (s, 3H, OCOC$\underline{H}_3$), 2.06 (s, 3H, OCOC$\underline{H}_3$). **^{13}C NMR (125 MHz, DMSO-*d*$_6$):** δ 170.17 (1C, O$\underline{C}$OCH$_3$), 169.65 (1C, O$\underline{C}$OCH$_3$), 169.35 (1C, O$\underline{C}$OCH$_3$), 160.03 (1C, C2), 153.45 (1C, C6), 143.91 (1C, C4), 142.28 (1C, C8), 130.90 (1C, C5), 86.52 (1C, C1′), 80.83 (1C, C4′), 73.21 (1C, C3′), 70.56 (1C, C2′), 62.61 (1C, C5′), 20.79 (1C, $\underline{C}$H$_3$-CO), 20.51 (1C, $\underline{C}$H$_3$-CO), 20.32 (1C, $\underline{C}$H$_3$-CO). **LC/ESI-MS:** negative mode 428 ([M - H]$^-$), positive mode 426 ([M + H]$^+$). HRMS (ESI): *m/z* [M + H]$^+$ calcd for $C_{16}H_{18}ClN_5O_7$: 428.0975; found: 428.0987. **Melting Point (°C):** 148-148 [**literature**, 152-153].[1]



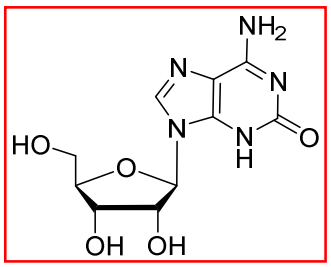
Procedure for the synthesis of 2-amino-6-chloropurine riboside (4). Compound **3** (2.0 g, 4.68 mmol) was dissolved in 5 mL of methanol. To it was added, 2% of 10 mL sodium methoxide in methanol. It was stirred for 24 h at rt. The resulting precipitate was filtered off. The solution was evaporated and purified by silica gel chromatography (1:10 MeOH/DCM) yielding the titled compound **4** as white solid. **Yield:** 1127 mg (80%). **^{1}H NMR (500 MHz, DMSO-*d*$_6$):** δ 8.36 (s, 1 H, C8-H), 6.92 (bs, 2H, N$\underline{H}_2$), 5.80 (dd, *J* = 5.1 Hz, 1 H, C1′-H), 5.42 (d, *J* = 5.8 Hz, 1 H, C2′-OH), 5.12 (d, 1 H, *J* = 4.9 Hz, C3′-OH), 4.99 (t, 1 H, *J* = 5.3 Hz, C5′-OH), 4.48 – 4.45 (m, 1 H, C2′-H), 4.12 – 4.08 (m, 1 H, C3′-H), 3.91 – 3.87 (m, 1 H, C4′-H), 3.65 – 3.61 (m, 1H, C5′-H), 3.56 – 3.51 (m, 1H, C5″-H). **^{13}C NMR (125 MHz, DMSO-*d*$_6$):** δ 152.98 (1C, C2), 151.41 (1C, C6), 143.27 (1C, C4), 142.82 (1C, C8), 133.54 (1C, C5), 87.32 (1C, C1′), 86.81 (1C, C4′), 73.55 (1C, C2′), 71.21 (1C, C3′), 62.01 (1C, C5′). **LC/ESI-MS:** negative mode 299 ([M - H]$^-$), positive mode 302 ([M + H]$^+$). HRMS (ESI): *m/z* [M + H]$^+$ calcd for $C_{10}H_{12}ClN_5O_4$: 302.0658; found: 302.0647. **Melting Point (°C):** 174-176 [**literature**, 171-172.[2]

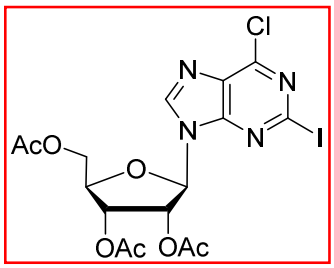


Procedure for the synthesis of 2,6-diaminopurine riboside (5). A suspension containing 0.5 g (1.65 mmol) of 2-amino-6-chloro-ribofuranosylpurine (**4**) dissolved in 25 mL of 2.0 M ethanolic ammonia solution was stirred at rt for three days. The solvent was removed under reduced pressure and the crude product was applied to a silica gel column with dichloromethane: methanol (9:1) elution. The collected fractions were freed from solvent, and a reversed-phase chromatography (HPLC) with an increasing gradient of methanol in water (10:90 to 90:10 over 70 min) was used. The solvent was removed by lyophilization to yield the desired compound as white solid. **Yield:** 351 mg (75%). **^{1}H NMR (500 MHz, DMSO-*d*$_6$):** δ 8.30 (s, 1H, C8-H), 6.75 (bs, 2H, 6-N$\underline{H}_2$), 5.82 – 5.65 (m, 3H, signal mixed between H2′-OH and 2-NH$_2$), 5.42 (dd, *J* = 5.1 Hz, 1H, C1′-H), 5.33 (dd, *J*

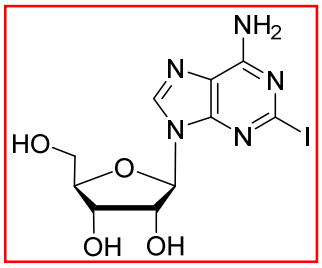
= 6.2 Hz, 1H, C3′-OH), 5.06 (t, *J* = 4.5 Hz, 1H, C5′-OH), 4.52 – 4.48 (m, 1H, C2′-H), 4.10 – 4.08 (m, 1H, C3′-H$_2$), 3.91 – 3.87 (m, 1H, C4′-H), 3.69 – 3.56 (m, 1H, C5′-H), 3.54 – 3.49 (m, 1H, C5″-H). **^{13}C NMR (126 MHz, DMSO-*d*$_6$):** δ 160.16 (1C, C6), 156.40 (1C, C2), 151.57 (1C, C4), 136.43 (1C, C8), 113.76 (1C, C5), 87.25 (1C, C1′), 85.68 (1C, C4′), 73.36 (1C, C2′), 70.87 (1C, C3′), 61.91 (1C, C5′). **LC-MS (*m/z*):** negative mode 281 $[M-H]^-$, positive mode 283 $[M+H]^+$. **Purity by HPLC-UV (254 nm)-ESI-MS:** 100%. HRMS (ESI): *m/z* $[M + H]^+$ calcd for $C_{10}H_{14}N_6O_4$: 283.1157; found: 283.1147. **Melting Point (°C):** 235-237 [**literature**, 240- 242].[3]

Procedure for the synthesis of isoguanosine (6).[2] 2,6-Diaminopurine riboside (**5**, 1.0 g, 3.55 mmol) was suspended in H_2O (2.5 mL) at 50 °C, then $NaNO_2$ (944 mg, 13.7 mmol) in H_2O (6 mL) was added. Subsequently AcOH (1.5 g, 1.41 mL, 24.5 mmol) was added at 50 °C over 5 min. The resulting clear solution was stirred for 5 min and then diluted with H_2O (15 mL). The excess of acetic acid was neutralized by adding 2 mL of aq. NH_3 solution (28% ammonia). The solution was evaporated and the remaining solid washed with H_2O to yield a light yellow powder. **Yield:** 953 mg (95%). **^{1}H NMR (500 MHz, DMSO-*d*$_6$):** δ 8.25 (s, 1H, C8-H), 7.93 (bs, 2H, NH), 5.86 (dd, *J* = 3.4 Hz, 1H, C1′-H), 5.44 (d, *J* = 6.2 Hz, 1H, C2′-OH), 5.33 (d, *J* = 6.3 Hz, 1H, C3′-OH), 5.31 (t, *J* = 4.2 Hz, 1H, C5′-OH), 4.90 – 4.87 (m, C2′-H), 4.18 – 4.14 (m, 1H, C3′-H), 3.97 – 3.93 (m, 1H, C4′-H), 3.60 – 3.47 (m, 2H, C5′-H and C5″-H). **^{13}C NMR (126 MHz, DMSO-*d*$_6$):** δ 155.10 (1C, C2), 151.32 (1C, C6), 138.01(1C, C4), 132.80 (1C, C8), 113.09 (1C, C5) , 89.35 (1C, C1′), 86.02 (1C, C4′), 82.86 (1C, C2′), 81.38 (1C, C3′), 61.90 (1C, C5′). **LC-MS (*m/z*):** negative mode 282 $[M-H]^-$, positive mode 284 $[M+H]^+$. HRMS (ESI): *m/z* $[M + H]^+$ calcd for $C_{10}H_{13}N_5O_5$: 284.0997; found: 284.0915. **Purity by HPLC-UV (254 nm)-ESI-MS:** 100%. **Melting Point (°C):** 238-240 [**literature**, 237-241].[4]

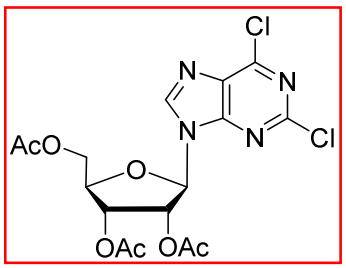




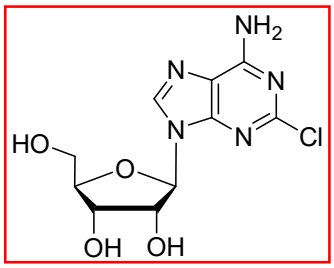
Procedure for the synthesis of 6-chloro-2-iodo-2',3',5'-triacetyl-purine riboside (11).[3] Isoamyl nitrate (4350 mg, 32.66 mmol, 27 equiv) was added to a mixture of **3** (500 mg, 1.2 mmol), I_2 (1000 mg, 3.94 mmol, 3.2 equiv), diiodomethane (30 mL) and CuI (2394 mg, 12.5 mmol, 10.4 equiv) in THF (50 mL). The mixture was heated at 80 °C for 2 h. Insoluble material was removed by filtration and the filtrate was evaporated in vacuo and subsequently subjected to column chromatography. The desired compound was eluted using 2% methanol in DCM as a brownish solid. **Yield:** 472 mg (75%). **^{1}H NMR (500 MHz, DMSO-*d*$_6$):** δ 8.26 (s, 1H, C8-H), 6.02 (dd, *J* = 5.7 Hz, 1H, C1′-H), 5.82 – 5.76 (m, 1H, C2′-H), 5.43 – 5.40 (m, 1H, C3′-H), 5.30 – 5.24 (m, 1H, C4′-H), 5.05 – 4.86 (m, 2H, C5′-H$_2$), 2.16 (s, 3H, COCH$_3$), 2.11 (s, 3H, COCH$_3$), 2.06 (s, 3H, COCH$_3$). **^{13}C NMR (125 MHz, DMSO-*d*$_6$):** δ 170.12 – 168.36 (3C, COCH$_3$), 154.23 (1C, C6), 151.30 (1C, C2), 150.45 (1C, C4), 138.20 (1C, C8), 131.35 (1C, C5), 87.65 (1C, C1′), 85.80 (1C, C4′), 73.28 (1C, C2′), 70.58 (1C, C3′), 61.66 (1C, C5′), 20.68 (1C, COCH$_3$), 20.34 (1C, COCH$_3$), 20.12 (1C, COCH$_3$). **LC/ESI-MS:** negative mode 537 ($[M - H]^-$), positive mode 539 ($[M + H]^+$). HRMS (ESI): *m/z* $[M + H]^+$ calcd for $C_{16}H_{16}ClIN_4O_7$: 538.9832; found: 538.9825. **Melting Point (°C):** 174-176. [**literature**, 181-183].[5]



Procedure for the synthesis of 2-iodoadenosine (12).[3] 6-Chloro-2-iodo-2',3',5'-triacetylribofuranosylpurine (**11**, 0.5 g) was dissolved in 25 mL of ethanolic ammonia solution (28% ammonia) and was stirred for three days at room temperature. The solvent was removed under reduced pressure and the crude product was applied to a silica gel column with dichloromethane: methanol (9:1) elution. The collected fractions were freed from solvent, and a reversed-phase chromatography (HPLC) with an increasing gradient of methanol in water (10:90 to 90:10 over 70 min) was used to remove acetamide. The solvent was removed by lyophilization to yield the desired compound as brownish-white solid. **Yield:** 273 mg (75%). **^{1}H NMR (500 MHz, DMSO-*d*$_6$):** δ 8.36 (s, 1H, C8-H), 7.80 (bs, 2H, N$\underline{H}_2$), 5.97 (dd, *J* = 5.9 Hz, 1H, C1′-H), 5.42 (d, *J* = 5.9 Hz, 1H, C2′-OH), 5.16 (d, *J* = 5.0 Hz, 1H, C3′-OH), 5.01 (t, *J* = 5.6 Hz, 1H, C5′-OH), 4.54 – 4.51 (m, 1H, C2′-H), 4.12 – 4.05 (m, 1H, C3′-H), 3.93 – 3.85 (m, 1H, C4′-H), 3.56 – 5.51 (m, 1H, C5′-H), 3.43 – 3.41 (m, 1H, C5″-H). **^{13}C NMR (125 MHz, DMSO-*d*$_6$):** δ 156.95 (1C, C6), 153.14 (1C, C2), 150.49 (1C, C4), 140.17 (1C, C8), 118.33 (1C, C5), 87.53 (1C, C1′), 85.86 (1C, C4′), 73.57 (1C, C2′), 70.53(1C, C3′), 61.53 (1C, C5′). **LC/ESI-MS:** negative mode 392 ([M - H]$^-$), positive mode 394 ([M + H]$^+$). HRMS (ESI): *m/z* [M + H]$^+$ calcd for $C_{18}H_{12}IN_5O_4$: 394.0014; found: 394.0018. **Melting Point (°C):** 185-186 [**literature**, 185-187].[6]

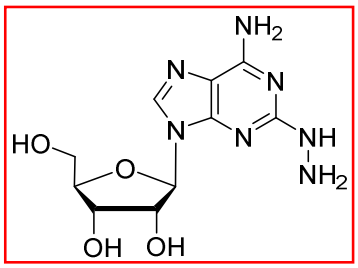


Procedure for the synthesis of 2,6-dichloro-2',3',5'-triacetyl-purine riboside (13). 2-Amino-6-chloro-2',3',5'-triacetylribofuranoslypurine (**3**, 0.6 g, 1.40 mmol) and acetyl chloride (0.92 g, 0.83 mL, 11.71 mmol) were added under argon atmosphere to 20 mL of anhydrous dichloromethane. Under ice cooling, 0.8 g (3.36 mmol) BTEA-nitrite (benzyltriethylammonium nitrite) dissolved in 10 mL of anhydrous dichloromethane was added dropwise within an hour. The mixture was stirred under ice-cooling and the progress of the reaction was monitored by TLC. After completion of the reaction after 5 h, the solution was extracted three times with 100 mL of water each. The organic phase was dried over magnesium sulfate, filtered and freed from solvent to yield the desired compound as white solid. **Yield:** 502 mg (80%). **^{1}H NMR (500 MHz, DMSO-*d*$_6$):** δ 8.28 (s, 1H, C8-H), 6.20 – 6.10 (m, 1H, C1′-H), 5.77 – 5.67 (m, 1H, C2′-H), 5.53 – 5.45 (m, 1H, C3′-H), 5.30 – 5.25 (m, 1H, C4′-H), 4.40 – 4.23 (m, 2H, C5′-$\underline{H}_2$), 2.15 (s, 3H, OCOC$\underline{H}_3$), 2.12 (s, 3H, OCOC$\underline{H}_3$), 2.07(s, 3H, OCOC$\underline{H}_3$). **^{13}C NMR (125 MHz, DMSO-*d*$_6$):** δ 170.17, 169.60, 169.35 (3C, 3xO$\underline{C}$OCH$_3$), 153.00 (1C, C2), 152.45 (1C, C6), 152.19 (1C, C4), 143.21 (1C, C8), 131.35 (1C, C5), 86.5 (1C, C1′), 80.8 (1C, C4′), 73.21 (1C, C2′), 70.5 (1C, C3′), 62.6 (1C, C5′), 20.7 (1C, 3xOCO$\underline{C}$H$_3$). **LC/ESI-MS:** negative mode 446 ([M - H]$^-$), positive mode 448 ([M + H]$^+$). HRMS (ESI): *m/z* [M + H]$^+$ calcd for $C_{16}H_{16}Cl_2IN_4O_7$: 447.0476; found: 447.0486. **Melting Point (°C):** 160-161 [**literature**, 158-159].[7]

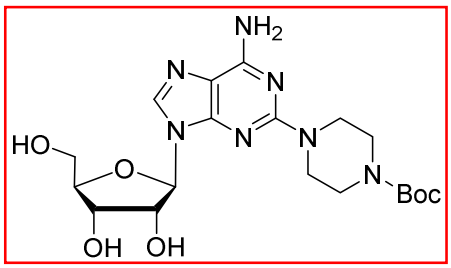


Procedure for the synthesis of 2-chloroadenosine (14). Ethanolic ammonia solution was prepared by introducing ammonia gas into 100 mL of dry ethanol under ice-cooling. The solution was used without further workup. 0.5 g (1.12 mmol) of 2,6-dichoro-2',3',5'-triacetylribofuranosylpurine (**13**) was dissolved in 25 mL of (~2.0 M) ethanolic ammonia solution and stirred for three days at rt. The solvent was removed under reduced pressure and the crude product was applied to a silica gel column eluting with dichloromethane: methanol elution (9:1). The collected fractions were freed from solvent, and a reversed-phase chromatography (HPLC) with an increasing gradient of methanol/water (10:90 to 90:10 over 70 min) was applied to remove acetamide. The solvent was removed by lyophilization to yield the title compound **14** as white solid. **Yield:** 252 mg (75%). **^{1}H NMR (500 MHz, DMSO-*d*$_6$):** δ 8.35 (s, 1H, C8-H), 7.80 (bs, 2H, N$\underline{H}_2$), 5.97 (dd, *J* = 5.9 Hz, 1H, C1′-H), 5.42 (d, *J*

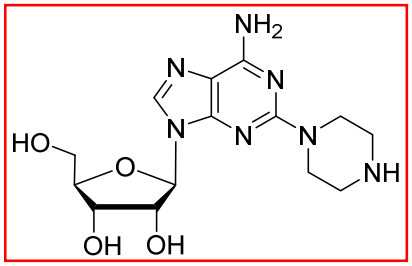
= 5.9 Hz, 1H, C2′-OH), 5.16 (d, *J* = 5.0 Hz, 1H, C3′-OH), 5.01 (t, *J* = 5.6 Hz, 1H, C5′-OH), 4.51 – 4.41 (m, 1H, C2′-H), 4.12 – 4.01 (m, 1H, C3′-H), 3.93 – 3.82 (m, 1H, C4′-H) , 3.56 – 3.54 (m, 1H, C5′-H), 3.51 – 3.41 (m, 1H, C5″-H). **^{13}C NMR (125 MHz, DMSO-*d*$_6$):** δ 156.95 (1C, C6), 153.14 (1C, C2), 150.49 (1C, C4), 140.17 (1C, C8), 118.33 (1C, C5), 87.53 (1C, C1′), 85.86 (1C, C4′), 73.57 (1C, C2′), 70.53 (1C, C3′), 61.53 (1C, C5′). **LC/ESI-MS:** negative mode 300 ([M - H]$^-$), positive mode 302 ([M + H]$^+$). HRMS (ESI): *m/z* [M + H]$^+$ calcd for $C_{10}H_{12}ClIN_5O_4$: 302.0685; found: 302.0681. **Melting Point (°C):** 146-147 [**literature**, 145-147].[8]



Procedure for the synthesis of 2-hydrazinyladenosine (17).[9] A solution of **14** (1.5 g, 5 mmol) in 5 mL of hydrazine hydrate was allowed to stir over night till the disappearance of **10** as determined by TLC (CH_2Cl_2: MeOH = 3:1). 2-Propanol (50 mL) was added to the reaction mixture and the formed gum was taken up in water (100 mL) and stirred for additional 5 h. The precipitated product was filtered, washed with water, and dried to give the pure product as white solid. **Yield:** 1435 mg (97%). **^{1}H NMR (500 MHz, DMSO-*d*$_6$):** δ 8.24 (s, 1H, C8-H), 7.45 (bs, 2H, 6-N$\underline{H}_2$), 7.41 (s, 1H, N$\underline{H}$-NH_2), 5.90 – 5.85 (m, 1H, C1′-H), 5.46 (d, *J* = 6.2 Hz, 1H, C2′-OH), 5.06 (d, *J* = 5.4 Hz, 1H, C2′-OH), 4.98 – 4.85 (m, 1H, C3′-OH), 4.45 – 4.40 (m, 3H, signal mixed C2′-H and –NH-N$\underline{H}_2$), 4.35 – 4.37 (m, 1H, C3′-H), 3.91 – 3.88 (m, 1H, C4′-OH) , 3.85 – 3.81 (m, 1H, C5′-H), 3.78 – 3.65 (m, 1H, C5″-H). **^{13}C NMR (125 MHz, DMSO-*d*$_6$):** δ 160.05 (1C, C2), 152.04 (1C, C6), 151.40 (1C, C4), 140.37 (1C, C8), 113.43 (1C, C5), 88.33 (1C, C1′), 87.46 (1C, C4′), 73.77 (1C, C2′), 70.50 (1C, C3′), 61.63 (1C, C5′). **LC/ESI-MS:** negative mode 296 ([M - H]$^-$), positive mode 298 ([M + H]$^+$). HRMS (ESI): *m/z* [M + H]$^+$ calcd for $C_{10}H_{15}N_7O_4$: 298.1266; found: 298.1258. **Melting Point (°C):** 157-159 [**literature**, 143 resolidifying and melting again at 155].[9]

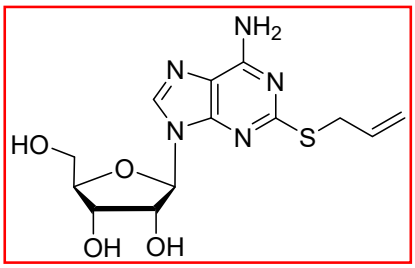


Procedure for the synthesis of 2-Boc-(*N*-piperazinyl)adenosine (18). A mixture of 2-chloropurine riboside (**14**, 500 mg, 1.66 mmol), and 1-Boc-piperazine (5.0 g, 5 mL, 26.84 mmol), 5 mL (3.65 g, 36 mmol) of Et_3N in a 1:1 mixture of 20 mL of ethanol and water was refluxed at 160 °C for 18 h. After completion of the reaction the mixture was evaporated under high vacuo. Purification using silica chromatography and precipitation using acetone (1:8 MeOH/DCM) yielded the title compound as a white solid. **Yield:** 636 mg (85%). **^{1}H NMR (500 MHz, DMSO-*d*$_6$):** δ 8.36 (s, 1H, C8-H), 6.84 (bs, 2H, N$\underline{H}_2$), 5.74 (dd, *J* = 5.9 Hz, 1H, C1′-H), 5.31 (d, *J* = 5.9 Hz, 1H, C2′-OH), 5.10 (d, *J* = 4.9 Hz, 1H, C3′-OH), 4.85 (t, *J* = 5.6 Hz, 1H, C5′-OH), 4.61 – 4.55 (m, 1H, C2′-H), 4.15 – 4.10 (m, 1H, C3′-H), 3.89 – 3.83 (m, 1H, C4′-H), 3.67 – 3.62 (m, 4H, piperazinyl), 3.61 – 3.58 (m, 1H, C5′-H), 3.52 – 3.48 (m, 1H, C5″-H), 3.38 – 3.34 (m, 4H, piperazinyl), 1.38 (s, 9H, 3xCH_3). **^{13}C NMR (125 MHz, DMSO-*d*$_6$):** δ 158.59 (1C, C2), 155.89 (1C, C6), 154.15 (1C, N$\underline{C}$OO), 151.60 (1C, C4), 137.24 (1C, C8), 113.69 (1C, C5), 87.00 (1C, C1′), 85.20 (1C, C4′), 79.07 (1C, C-3xCH_3), 73.09 (1C, C2′), 70.68 (1C, C3′), 61.80 (1C, C5′), 45.50 (2C, piperazinyl), 44.05 (2C, piperazinyl), 28.23 (3C, 3xCH_3). **LC/ESI-MS:** negative mode 450 ([M - H]$^-$), positive mode 452 ([M + H]$^+$). HRMS (ESI): *m/z* [M + H]$^+$ calcd for $C_{19}H_{29}N_7O_6$: 452.2259; found: 452.2268. **Melting Point (°C):** 178-179.



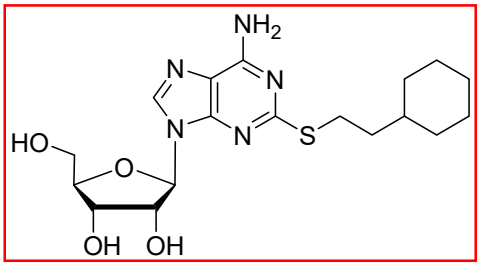
Procedure for the synthesis of 2-(*N*-piperazinyl)adenosine (19). Compound **18** (500 mg, 1.10 mmol) was dissolved in 4.5 mL dichloromethane then, 0.5 mL of water and 0.65 mL of triflouroacetic acid was added to it. It was stirred at room temperature for 3 h. After completion of the reaction, the mixture was evaporated and the solid was precipitated adding diethyl ether. Then the crude solid product was dissolved in 6 mL of water and 0.6 mL of methanol. It was then purified by RP-HPLC using a gradient of H_2O/MeOH from 100: 0 to 0: 100. The appropriate fractions were pooled and lyophilized to yield the final product as orange coloured solid. **Yield:** 377 mg (95%). **^{1}H NMR (500 MHz, DMSO-*d*$_6$):** δ 8.35 (s, 1H, C8-H), 5.72 (dd, *J* = 5.9 Hz, 1H, C1′-H), 5.30 (d, *J* = 5.2 Hz,1H, C2′-OH), 5.12 (d, *J* = 5.2 Hz,1H, C3′-OH), 4.95 – 4.78 (m, 1H, C5′-OH), 4.65 (m, C2′-H), 4.25 (m, 1H, C3′-H), 3.97 (m, 1H, C4′-H), 3.78 – 3.76 (m, 2H, C5′-H and C5″-H), 3.41 – 3.36 (m, 4H, piperazinyl), 2.75 – 2.58 (m, 4H, piperazinyl) . **^{13}C NMR (125 MHz, DMSO-*d*$_6$):** δ 160.69 (1C, C2), 157.88 (1C, C6), 151.64 (1C, C4), 140.23 (1C, C8), 113.64 (1C, C5), 97.03 (1C, C1′), 84.24 (1C, C4′), 73.79 (1C, C2′), 70.56 (1C, C3′), 61.86 (1C, C5′), 48.00 (2C, piperazinyl), 45.85 (2C, piperazinyl). **LC/ESI-MS:** negative mode 350 ([M - H]$^-$), positive mode 352 ([M + H]$^+$). HRMS (ESI): *m/z* [M + H]$^+$ calcd for $C_{14}H_{21}N_7O_4$: 352.1735; found: 352.1725. **Melting Point (°C):** 169-171[**literature**, 240].[10]

General procedure for the synthesis of 2-thioadenosine derivatives (26, 27).[11, 12] 2-Thioadenosine (**25**, 500 mg, 1 mmol) was dissolved in 20 mL of water: ethanol (1: 1) mixture, then 4 mL of sodium hydroxide (0.5 N) in water was added to the reaction mixture, followed by the addition of allyl bromide (243 mg, 1.2 mmol) or cyclohexylethyl bromide (385 mg, 1.2 mmol). The reaction mixture was stirred for 5 h at rt, and the completion of the reaction was determined by TLC (CH_2Cl_2: MeOH = 9:1). The crude product was extracted by ethyl acetate and evaporated to dryness under reduced pressure. The product was purified by silica gel column chromatography (CH_2Cl_2: MeOH = 9: 1) to afford the pure product as white solid.

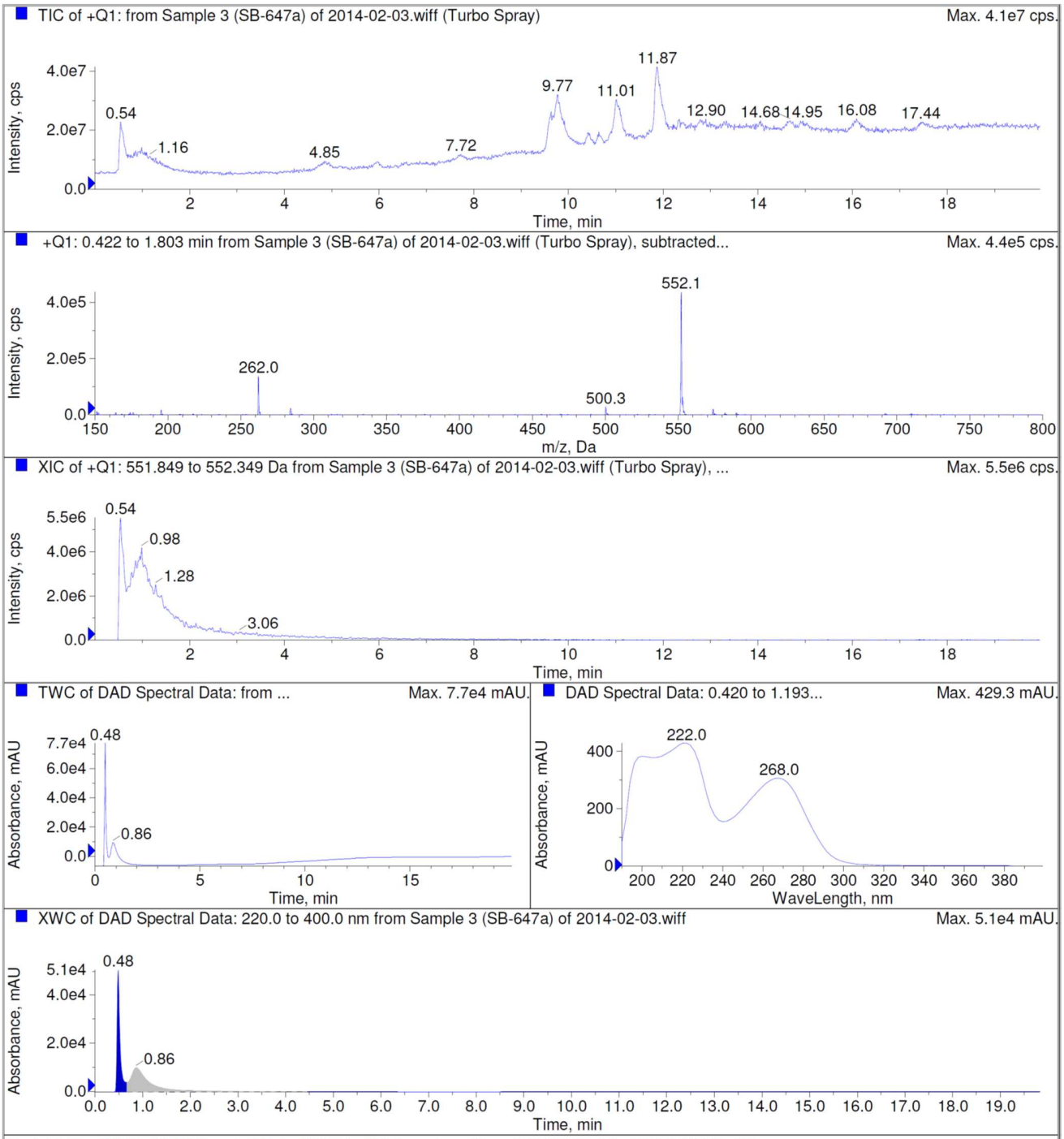


2-Allylthioadenosine (26). Yield: 393 mg (59%). **^{1}H NMR (500 MHz, DMSO-*d*$_6$):** δ 8.22 (s, 1H, C8-H), 7.35 (bs, 2H, 6-NH_2), 6.02 – 5.88 (m, 1H, S-CH_2-C<u>H</u>=CH_2), 5.82 (d, *J* = 5.8 Hz, 1H, C1′-H), 5.36 (d, *J* = 6.2 Hz, 1H, C2′-OH), 5.30 (dq, *J* = 17.0 Hz, 1.5 Hz, 1H, S-CH_2-C<u>H</u>=CH_2), 5.13 (d, *J* = 4.9 Hz, 1H, C3′-OH), 5.07 (dt, *J* = 10.0, 1.9 Hz, 2H, S-CH_2-CH=C<u>H$_2$</u>), 4.99 (t, *J* = 6.0 Hz, 1H, C5′-OH), 4.58 – 4.53 (m,1H, C2′-H), 4.13 – 4.09 (m, 1H, C3′-H), 3.92 – 3.88 (m, C4′), 3.77 (dt, *J* = 6.7, 1.2 Hz, 2H, S-C<u>H$_2$</u>-CH=CH_2), 3.65 – 3.60 (m, 1H, C5′), 3.54 – 3.49 (m,1H, C5″). **^{13}C NMR (125 MHz, DMSO-*d*$_6$):** δ 163.12 (1C, C2), 155.66 (1C, C6), 150.26 (1C, C4), 138.83 (1C, C8), 134.63 (1C, S-CH_2-<u>C</u>H=CH_2), 120.40 (1C,C5), 117.28 (1C, S-CH_2-CH=<u>C</u>H$_2$), 87.44 (1C, C1′), 85.57 (1C, C4′), 73.55 (1C, C2′), 70.58 (1C, C3′), 61.67 (1C, C5′), 33.22 (1C, S-<u>C</u>H$_2$-CH=CH_2). **LC/ESI-MS:** negative mode 338 ([M - H]$^-$), positive mode 340 ([M + H]$^+$). **Purity by HPLC-UV (254 nm)-ESI-MS:** 98.5%. HRMS (ESI): *m/z* [M + H]$^+$ calcd for $C_{14}H_{21}N_7O_4$: 340.1080; found: 340.1072. **Melting Point (°C):** 171-172 [**literature**, 161-163].[11]

S13



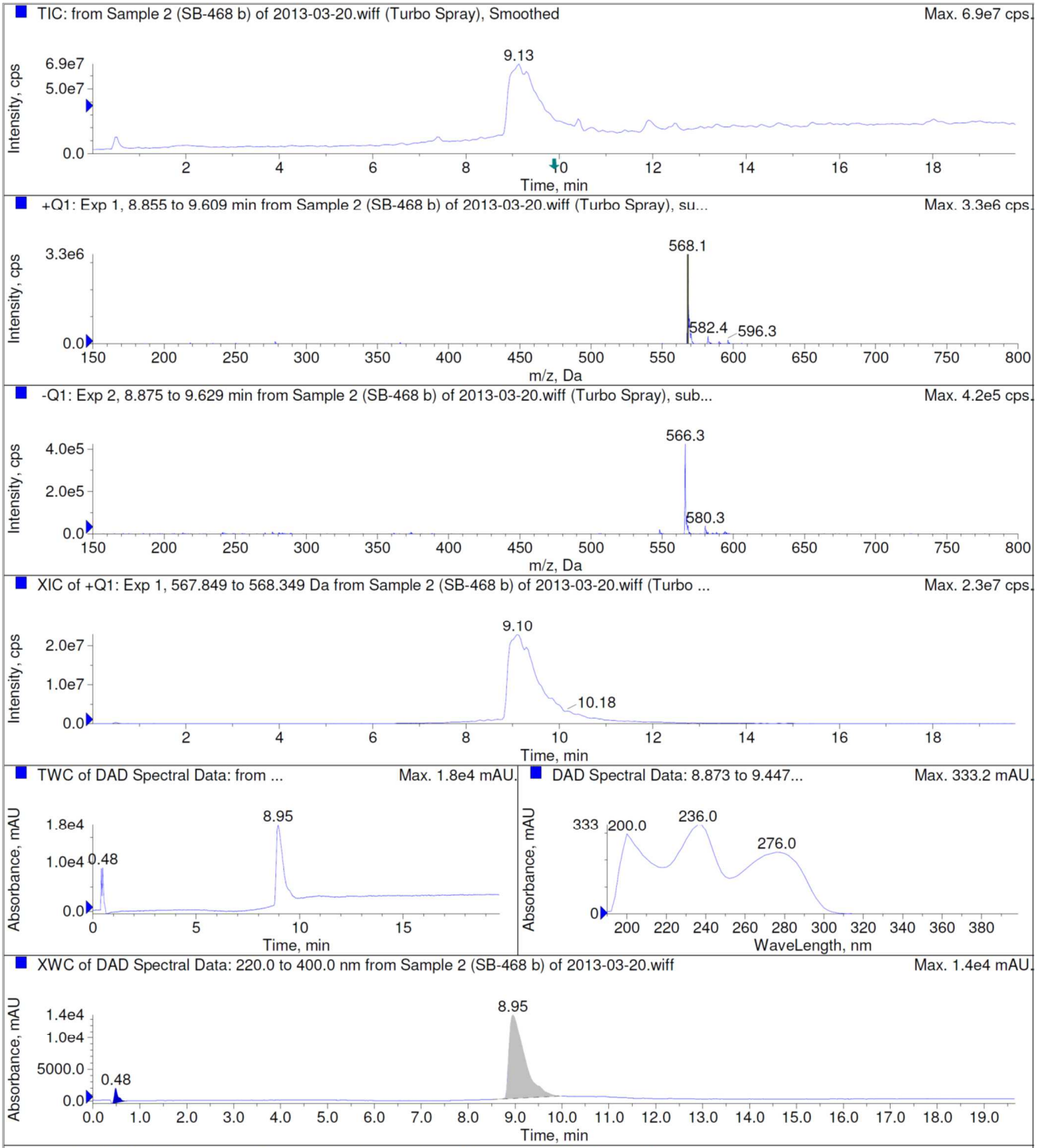
2-Cyclohexylethylthio-adenosine (27). Yield: 383 mg (56%). **^{1}H NMR (500 MHz, DMSO-*d*$_6$):** δ 8.19 (s, 1H, C8-H), 7.28 (bs, 2H, NH_2), 5.80 (dd, *J* = 5.9 Hz, 1H, C1′-H), 5.38 (d, 1H, *J* = 5.7 Hz, C2′-OH), 5.07 (d, *J* = 5.9 Hz, 1H, C3′-OH), 4.98 (t, *J* = 5.5 Hz, 1H, C5′-OH), 4.57 – 4.50 (m, 1H, C2′-H), 4.14 – 4.05 (m 1H, C3′-H), 3.90 – 3.85 (m, 1H, C4′), 3.64 – 3.50 (m, 2H, C5′-H and C5″-H), 3.14 – 3.00 (m, 2H, C$\underline{H_2}$), 1.74 – 1.61 (m, 2H, C$\underline{H_2}$), 1.60 – 0.87 (m, 11H, cyclohexane). **^{13}C NMR (125 MHz, DMSO-*d*$_6$):** δ 163.94 (1C, C2), 155.63 (1C, C6), 150.31 (1C, C4), 138.86 (1C, C8), 117.05 (1C, C5), 87.42 (1C, C1′), 85.57 (1C, C4′), 73.31 (1C, C2′), 70.60 (1C, C3′), 61.75 (1C, C5′), 36.82 (1C, $\underline{C}H_2$-CH_2- cyclohexane), 36.61 (1C, cyclohexane), 32.46 (1C, CH_2-$\underline{C}H_2$-cyclohexane), 27.94 (2C, cyclohexane), 26.26 (2C, cyclohexane), 25.89 (1C, cyclohexane). **LC/ESI-MS:** negative mode 408 ($[M - H]^-$), positive mode 410 ($[M + H]^+$). **Purity by HPLC-UV (254 nm)-ESI-MS:** 100%. HRMS (ESI): *m/z* $[M + H]^+$ calcd for $C_{18}H_{27}N_5O_4S$: 410.1864; found: 410.1861. **Melting Point (°C):** 181-183.[12]



Peak List for "XWC of DAD Spectral Data: 220.0 to 400.0 nm from Sample 3 (SB-647a) of 2014-02-03.wiff"

	Time (min)	Area (mAU x min)	% Area	Height (mAU)	% Height	Width (min)	Baseline Type
1	0.4848	2.2002e5	42.5269	5.1128e4	83.5642	0.3333	Valley
2	0.8620	2.9734e5	57.4731	1.0056e4	16.4358	3.7800	Valley

Figure S1. LC/ESI-MS spectra of the synthesized nucleotide analog **15** (mass spectra in the positive and negative mode)**,** HPLC chromatogram of **15** and its purity determined by HPLC-DAD from 220-300 nm (100 %). Both the peaks at 0.48 and 0.86 min (tailing peak) belongs to **15** (m/z = 551) as confirmed by Extracted Ion Chromatogram (**XIC**).



Peak List for "XWC of DAD Spectral Data: 220.0 to 400.0 nm from Sample 2 (SB-468 b) of 2013-03-20.wiff"

	Time (min)	Area (mAU x min)	% Area	Height (mAU)	% Height	Width (min)	Baseline Type
1	0.4839	1.2944e4	4.0909	2333.3881	14.9717	0.2733	Base to Base
2	8.9537	3.0346e5	95.9091	1.3252e4	85.0283	1.4800	Base to Base

Figure S2. LC/ESI-MS spectra of the synthesized nucleotide analog **29** (mass spectra in the positive and negative mode)**,** HPLC chromatogram of **29** and its purity determined by HPLC-DAD from 220-300 nm (100 %). The peak at 8.95 min belongs to **29** (m/z = 567).

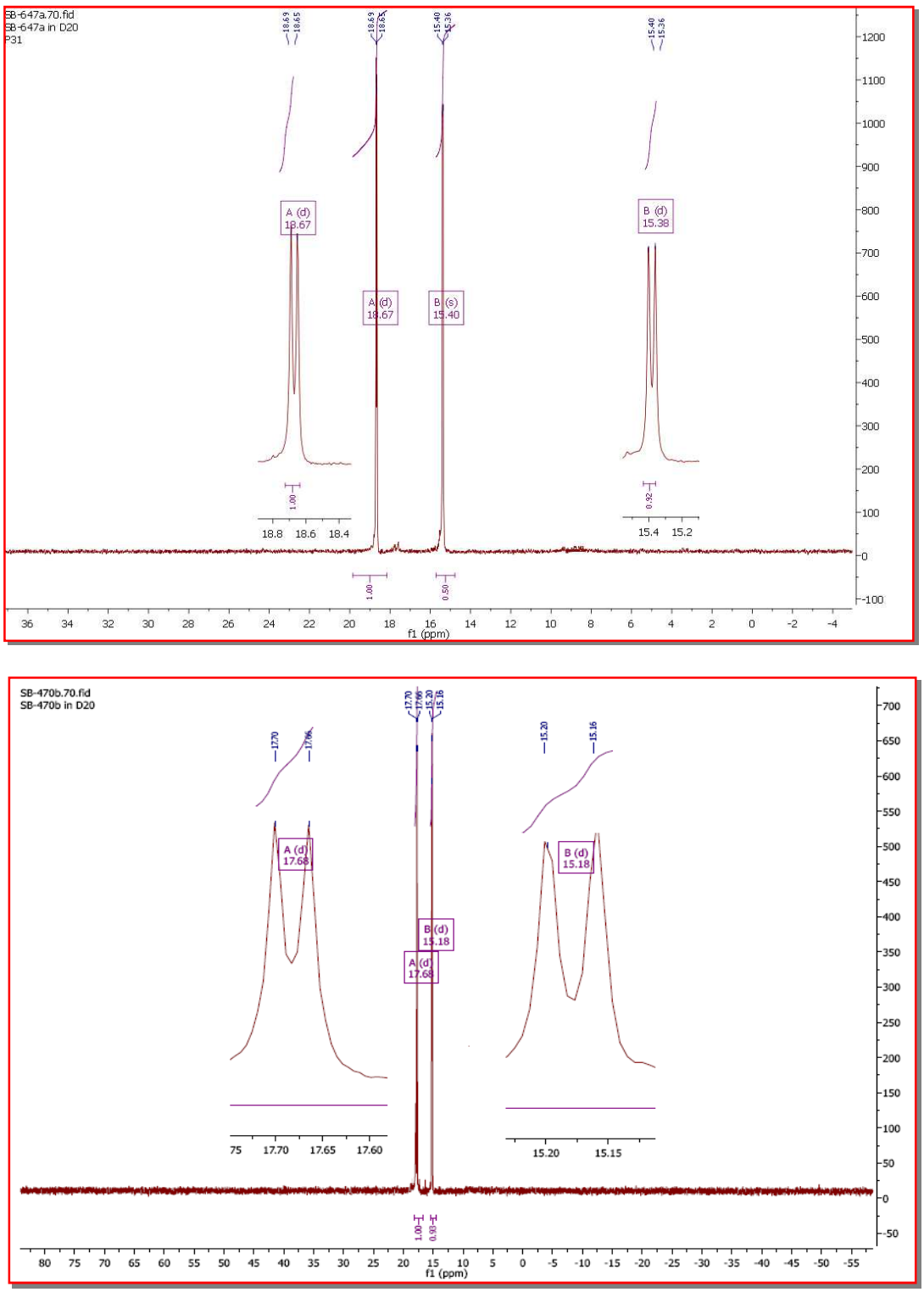


Figure S3. Sections of the ^{31}P NMR spectra (202 MHz, D_2O) for the purity control of compounds **15** (top) and **20** (bottom).

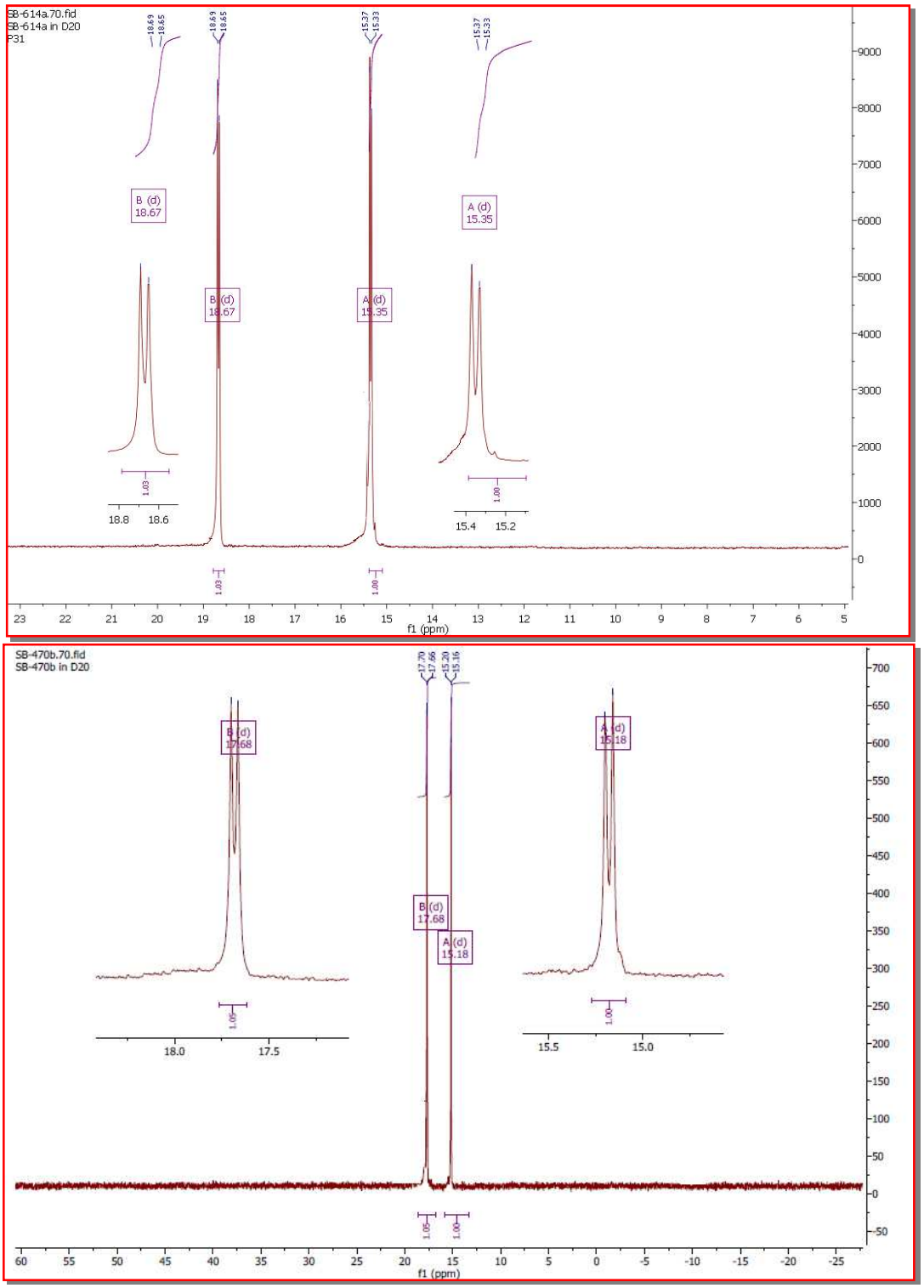


Figure S4. Sections of the ^{31}P NMR spectra (202 MHz, D_2O) for the purity control of compounds 1**6** (top) and **29** (bottom).

Activity of compounds at human NPPs and ADP-activated P2 receptor ($P2Y_1$ and $P2Y_{12}$)

NPP1-3 assays

Human recombinant NPP1-3[13] were prepared and assays were performed as previously described.[13-15] The test compounds were screened at a concentration of 10 µM in reaction buffer (1 mM $CaCl_2$, 200 µM $ZnCl_2$, 50 mM TRIS, pH 9.0) together with substrate: 400 µM *p*-nitrophenyl thymidine monophosphate (NPP1, NPP3) or 400 µM of lysophosphatidylcholine for NPP2. The reaction was initiated by adding 20 µL of human recombinant NPP1 (0.9 µg) or 10 µL of NPP2 (44 µg) or NPP3 (0.4 µg) and incubation was performed at 37 °C for 30 min. For NPP 1 and 3, the enzyme reaction was stopped by adding 1.0 N NaOH, and the liberated *p*-nitrophenolate was quantified at 400 nm. For NPP2 the released choline was quantified colorimetrically at 555 nm after incubation at 37 °C for 10 min with 50 µL of each, the peroxidase reagent (50 mM Tris at pH 9.0, 2 mM TOOS, 5 U/mL peroxidase) and the choline-oxidase reagent (50 mM Tris at pH 9.0, 2 mM aminoantipyrine, 5 U/mL choline-oxidase). All experiments were performed twice in triplicates. The percentage of inhibition was calculated and for the potent compounds, K_i values were determined by curve fitting of the data using Prism 5.0 (GraphPad, San Diego, USA).

Table S3. Potency of selected derivatives at human NPP1-3

Compd.	**human NPP 1** % inhibition at 10 µM, n=3 (% effect ± SEM)[a,b] or K_i ± SEM[a](nM)		
	NPP 1	**NPP 2**	**NPP 3**
AOPCP	**16500** ± 3.2[7] (21 ± 1)	>>10000 (4 ± 0)	>>10000 (1 ± 1)
ADP	>>10000 (28 ± 4)	>>10000 (4 ± 0)	>>10000 (2 ± 2)
8	>>10000 (22 ± 4)	>>10000 (2 ± 1)	>>10000 (0 ± 2)
15	>10000 (20 ± 3)	>>10000 (3 ± 1)	>>10000 (3 ± 2)
16	>>10000 (16 ± 2)	>>10000 (4 ± 1)	>>10000 (0 ± 1)
29	>>10000 (19 ± 1)	>>10000 (5 ± 2)	>>10000 (0 ± 2)

[a]Screening was performed at a concentration of 10 µM. [b]Effects were normalized to the effect induced by 400 µM of *p*-nitrophenyl thymidine monophosphate for NPP1 and NPP3, 400 µM of lysophosphatidylcholine for NPP2.

Calcium mobilization assay for $P2Y_1$ receptor

Calcium assays were performed according to published procedures.[13,16] 1321N1 astrocytoma cells recombinantly expressing the human $P2Y_1$ were harvested with 0.05 % trypsin / 0.02 % EDTA and rinsed with culture medium. Then the cells were incubated with under 5 % CO_2 at 37°C for 45 min, followed by centrifugation at 200 g at 4°C for 5 min. After that the cells were further incubated for 1 h at 25°C in Krebs-Ringer-HEPES buffer, pH 7.4 containing 3 µM Oregon Green BAPTA-1/AM and 1 % Pluronic® F127. Next, the cells were rinsed 3 times with KRH buffer, diluted and plated into 96-well plates with clear bottoms at a density of approximately 16,000 cells/well and left for 20 min. Finally, the fluorescence intensity was measured at 520 nm for 30 s at 0.4 s intervals using a Novostar® microplate reader after addition of test compound. Three independent experiments were performed each in duplicates.

$P2Y_{12}$ receptor β-arrestin assay

The assay was performed as previously described.[13, 17, 18] A permanent cell line was prepared by cloning the human $P2Y_{12}$ receptor sequence into a pCMV- ProLink1 vector followed by expression in a CHO-K1 cell line. The cells were kept growing in F12 medium (Gibco Life Technologies). One day prior to measurements, the cells were detached from the flask using dissociation buffer and seeded into 96-well plates at a density of 30000 cells/well followed by addition of 90 µL of Optimum medium. Compound dilutions were also prepared using Optimum medium without supplements, and 10 µL of diluted compounds were added to each well. After 90 min of incubation at 37 °C, 50 µL of detection reagent (DiscoverX, Fremont, CA) per well were added and then the plate was further incubated for 60 min at rt. Finally, luminescence was determined using a Topcount NXT plate reader (Perkin-Elmer, Meriden, CT). Three independent experiments were performed each in duplicates.

Table S4. Potency of selected derivatives at ADP-activated P2Y receptors

Compd.	Human $P2Y_1$ EC_{50} ± SEM (µM) (% Effect[a] ± SEM)	Human $P2Y_{12}$ EC_{50} ± SEM (µM) (% Effect[a] ± SEM)
ADP	**133** ± 2.6	**289 ±** 6.7
AOPCP	>>10000 (26± 7)	>10000 (5± 4)
8	>>10000 (7± 3)	>>10000 (3 ± 4)
16	>10000 (38 ± 6)	>>10000 (6 ± 5)
29	>>10000 (7± 9)	>10000 (34 ± 13)

[a]Screening was performed at a concentration of 10 µM.

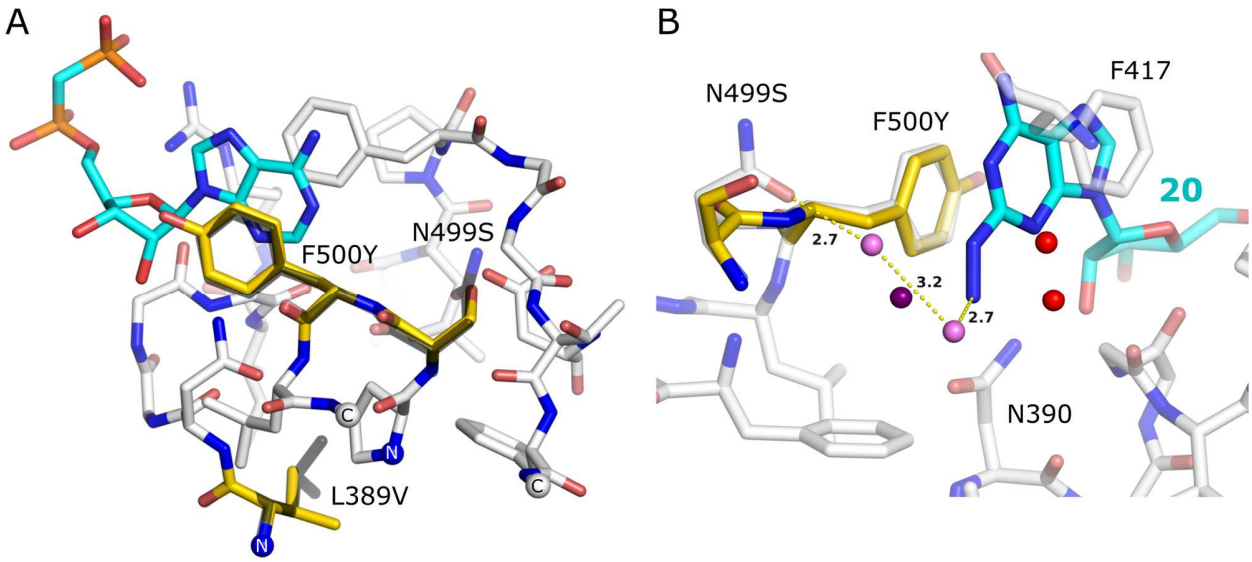


Figure S5. Comparison of human CD73 and rat CD73. (A) The two enzymes differ in three amino acids in the vicinity of the AOPCP binding site. These residues are shown in yellow for rat CD73 and in grey for human CD73. The residue labels denote the "mutations" from human to rat CD73 with the residue numbers of the human homolog. (B) Binding mode of **20** to human CD73 (white carbon atoms). The N499S substitution in rat CD73 (yellow) probably influences the water structure in the C2-pocket, which interacts with the hydrazinyl substituent of **20**. Fully occupied waters H and I are shown in red. Waters D and N (pink) are alternatively occupied with water F (purple) due to steric overlap (see also Figure 6B).

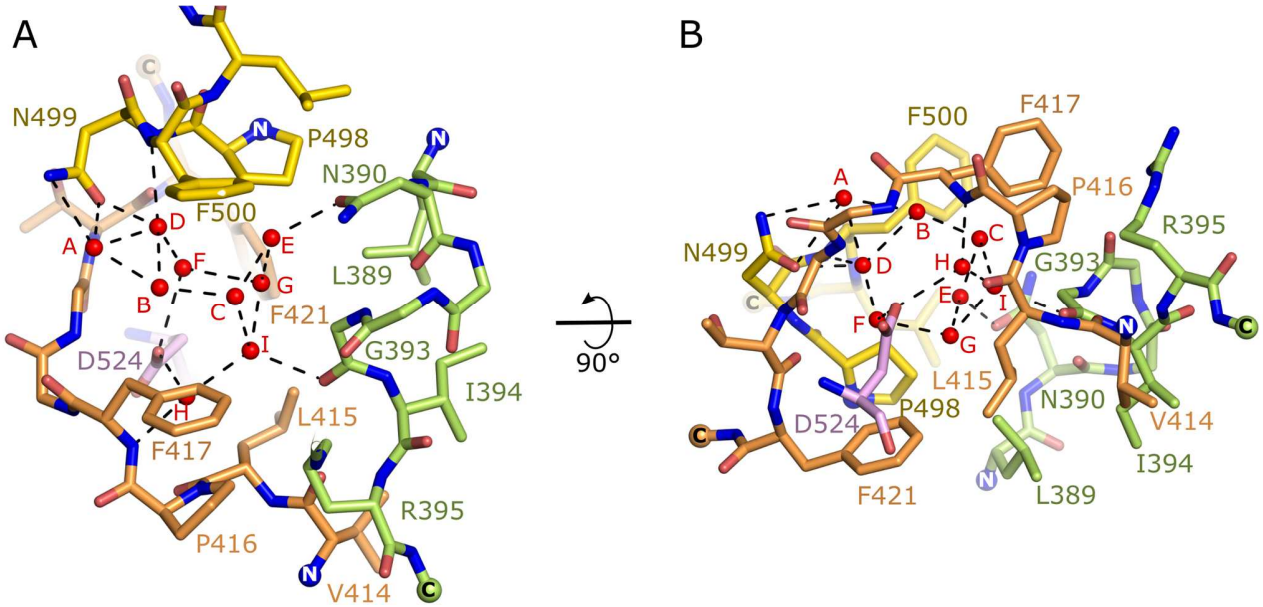


Figure S6. Water structure in the C2-pocket of unliganded CD73 in the open conformation. (A) Water molecules in the pocket next to F500 and F417 as identified in the 1.05 Å structure of unliganded human CD73 in the open conformation. Only fully occupied water binding sites or predominantly occupied water molecules of alternative binding sites are shown. The view is from the nucleobase tong into the pocket. The carbon atoms of the protein residues are depicted in different colors for the four regions lining the C2-pocket. This figure is identical to Figure 5A. (B) Side-view of the C2-pocket.

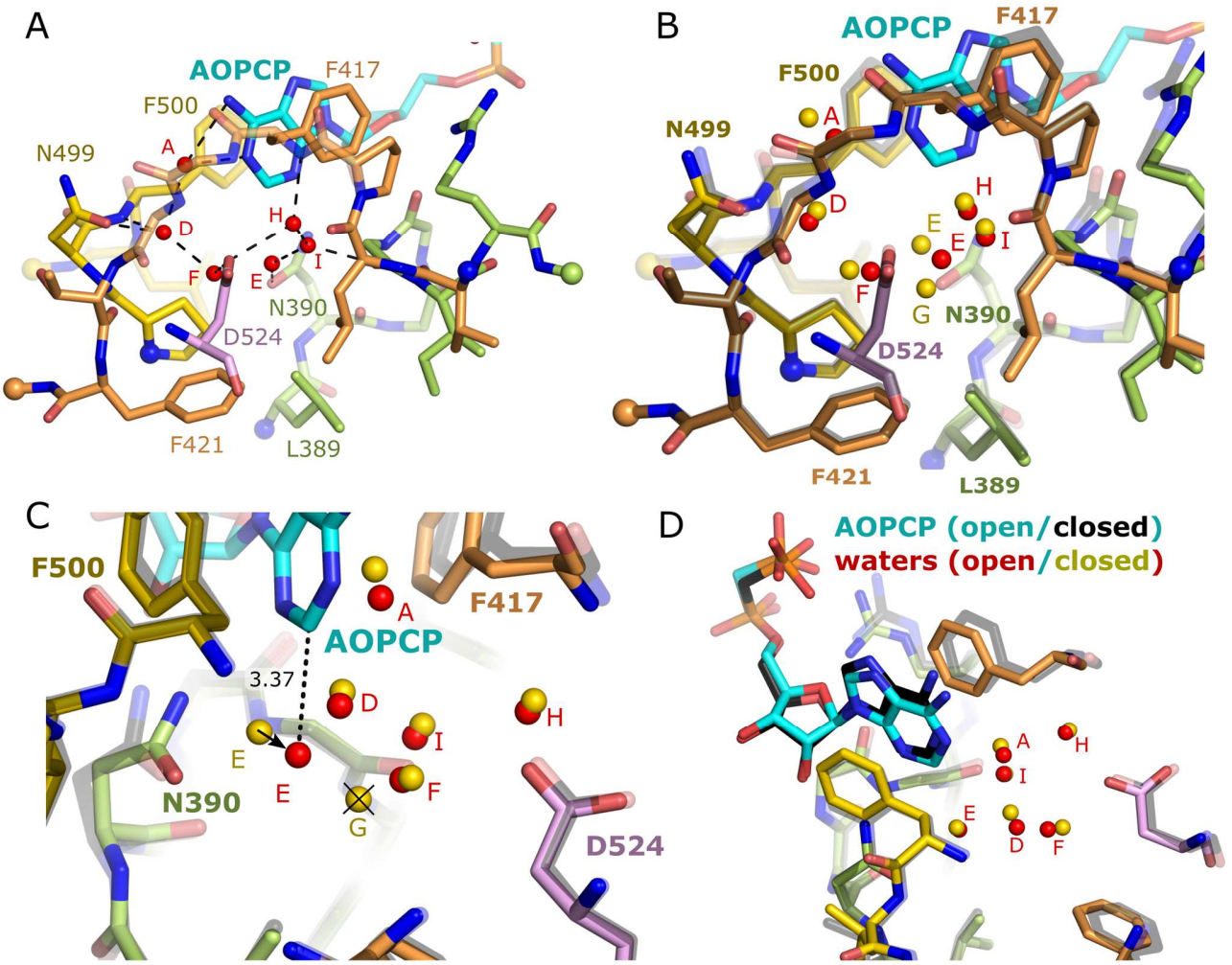


Figure S7. Changes in the water structure of the C2-pocket upon binding of AOPCP and derivatives. (A) CD73×AOPCP structure in the open form (pdb 6TVG). The coloring is as in Figure S6. (B) Zoom-in on the C2-pocket of a superposition of CD73×AOPCP (colored carbon atoms, red waters, pdb 6TVG) and unliganded CD73 (grey carbons, yellow waters, pdb 6TVE), both determined in the open form. (C) Movement of water E upon AOPCP binding and displacement of water G. The depicted structures and coloring are the same as in panel (B). (D) Comparison of the CD73×AOPCP complex structures in the open form (colored carbon atoms, red waters, AOPCP in cyan, pdb 6TVG) and in the closed form (grey carbons, yellow waters, pdb 4H2I). Despite the large difference in the orientations of the N-terminal domains (not shown) is the binding mode of AOPCP and the active site water structure conserved.

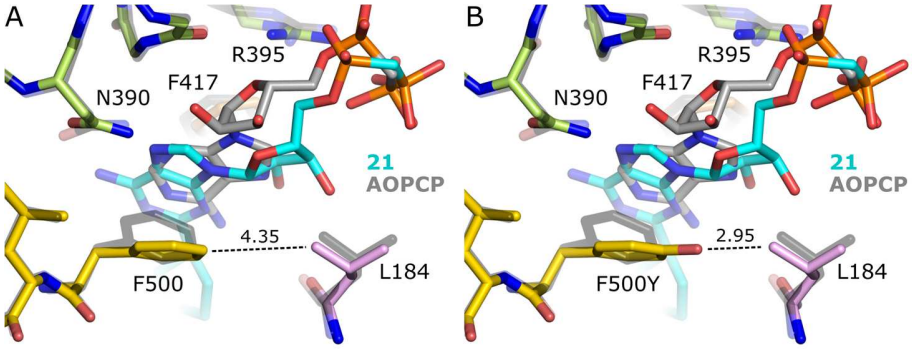


Figure S8. Superposition of the binding modes of AOPCP (grey, 4H2I) and of **21** (cyan, 6TWF) to CD73. In the CD73×**21** structure F500 adopts a different side chain conformation (of higher energy) to accomodate the flipped binding mode of **21**. (A) F500 forms a favorable hydrophobic contact to L184 (of the N-terminal domain). (B) A model for a F500Y substitution, which is present in rat CD73, shows that the phenolic OH-group is in close contact for a CH···O interaction with L184. While this is acceptable and no clash configuration, it is unfavorable compared to a stronger OH···OH_2 hydrogen bonding interaction that the tyrosine can form in the unbound state. The two different models are shown in a pseudo-stereo figure.

References

1. Liu, G.; Xu, J., Chen, N.; Zhang, S.; Ding, Z.; Du, H. Synthesis of N^6-alkyl(aryl)-2-alkyl(aryl)thioadenosines as antiplatelet agents. *Eur. J. Med. Chem.* **2012**, *53*, 114–123.
2. Robins, R. K. A New synthesis of chloropurine ribonucleosides. *J. Am. Chem. Soc.* **1960**, *82*, 2654–2655.
3. Ross, B. S.; Springer, R. H.; Ravikumar, V. T. An efficient and scalable synthesis of 2,6-diaminopurine riboside. *Nucleosides, Nucleotides & Nucleic Acids* **2008**, *27*, 67–69.
4. Cherbuliez, Emile.; Bernhard, Karl. Recherches sur la graine de croton. I. Sur le crotonoside (2-oxy-6-amino-purine-*D*-riboside). *Helvetica Chimica Acta* 1**932**, *15*, 464-471.
5. Nair, V.; Richardson, S. G. Modification of nucleic acid bases *via* radical intermediates: Synthesis of dihalogenated purine nucleosides. *Synthesis* **1982**, *8*, 670–672.
6. van Tilburg, E. W.; von Frijtag Drabbe Künzel, J.; de Groote, M.; Ijzerman, A. P. 2,5'-Disubstituted adenosine derivatives: evaluation of selectivity and efficacy for the adenosine A_1, A_{2A}, and A_3 receptor. *J. Med. Chem.* **2002**, *45*, 420–429.
7. Ishido, Y.; Tanaka, H.; Yoshino, T.; Sekiya, M.; Iwabuchi, K.; Sato, T. Acid-catalyzed and autocatalytic reactions of acetylated sugars with purine derivatives in organic solvents. *Tetrahedron Lett.* **1967**, *8*, 5245–5248.
8. Lioux, T.; Gosselin, G.; Mathe, C. Azido/tetrazole tautomerism in 2-azidoadenine-*β* –D pentofuranonucleoside derivatives. *Eur. J. Org. Chem*. **2003**, 3997-4002.

9. Schaeffer, H. J.; Thomas, H. J. Synthesis of potential anticancer agents. XIV. Ribosides of 2,6-disubstituted purines. *J. Am. Chem. Soc*. **1958**, *80*, 3738-3742.
10. Marumoto, R.; Yoshioka, Y.; Miyashita, O.; Shima, S.; Imai, K. I.; Kawazoe, K.; Honjo, M. Synthesis and coronary vasodilating activity of 2 substituted adenosines. *Chem. Pharm. Bull*. **1975**, *23*, 759–774.
11. German Patent 2331223, **1974**.
12. El-Tayeb, A.; Iqbal, J.; Behrenswerth, A.; Romio, M.; Schneider, M.; Zimmermann, H.; Schrader, J.; Müller, C. E. Nucleoside-5′-monophosphates as prodrugs of adenosine A_{2A} receptor agonists activated by ecto-5′-nucleotidase. *J. Med. Chem.* **2009**, *52*, 7669-7677.
13. Bhattarai, S.; Freundlieb, M.; Pippel, J.; Meyer, A.; Abdelrahman, A.; Fiene, A.; Lee, S-Y.; Zimmermann, H.; Yegutkin, G. G.; Sträter, N.; El-Tayeb, A.; Müller, C. E. *α,β*-Methylene-ADP derivatives and analogs: development of potent and selective ecto-5'-nucleotidase (CD73) inhibitors. *J. Med. Chem.* **2015**, *58*, 6248-6243.
14. Lee, S.-Y.; Levesque, S. A.; Sévigny, J.; Müller, C. E. A highly sensitive capillary electrophoresis method using *p*-nitrophenyl 5'-thymidine monophosphate as a substrate for the monitoring of nucleotide pyrophosphatase/phosphodiesterase activities. *J. Chromatogr. B* **2012**, *911*, 162-169.
15. Lee, S.-Y.; Fiene, A.; Li, W.; Hanck, T.; Brylev, K. A.; Fedorov, V. E.; Lecka, J.; Haider, A.; Pietzsch, H.-J.; Zimmermann, H.; Sévigny, J.; Kortz, U.; Stephan, H.; Müller, C. E. Polyoxometalates - potent and selective ecto-nucleotidase inhibitors. *Biochem. Pharmacol.* **2015**, *93*, 171-181.
16. Klein, C.; Grahnert, A.; Abdelrahman, A.; Müller, C. E.; Hauschildt, S. Extracellular NAD^+ induces a rise in Ca^{2+} in activated human monocytes via engagement of $P2Y_1$ and $P2Y_{11}$ receptors. *Cell Calcium* **2009**, *46*, 263-272.
17. Rempel, V.; Fuchs, A.; Hinz, S.; Karcz, T.; Lehr, M.; Koetter, U.; Müller, C. E. Magnolia extract, magnolol, and metabolites: Activation of cannabinoid CB_2 receptors and blockade of the related GPR55. *ACS Med. Chem. Lett.* **2012**, *4*, 41−45.
18. Funke, M, Thimm, D., Schiedel, A. C.; Müller, C. E. 8-Benzamidochromen-4-one-2-carboxylic acids: potent and selective agonists for the orphan G protein-coupled receptor GPR35. *J. Med. Chem.* **2013**, *56*, 5182-5197.

Appendix II: Cytidine-based CD73 inhibitor published article

Journal of Medicinal Chemistry

pubs.acs.org/jmc Article

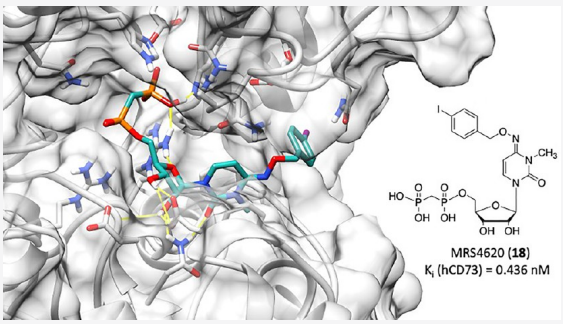
Structure–Activity Relationship of 3-Methylcytidine-5′-α,β-methylenediphosphates as CD73 Inhibitors

Mirko Scortichini,■ Riham Mohammed Idris, Susanne Moschütz, Antje Keim, Veronica Salmaso,■ Clemens Dobelmann, Paola Oliva, Karolina Losenkova, Heikki Irjala, Samuli Vaittinen, Jouko Sandholm, Gennady G. Yegutkin, Norbert Sträter, Anna Junker, Christa E. Müller, and Kenneth A. Jacobson*

Cite This: J. Med. Chem. 2022, 65, 2409–2433 Read Online

ACCESS | Metrics & More | Article Recommendations | Supporting Information

ABSTRACT: We recently reported N^4-substituted 3-methylcytidine-5′-α,β-methylenediphosphates as CD73 inhibitors, potentially useful in cancer immunotherapy. We now expand the structure–activity relationship of pyrimidine nucleotides as human CD73 inhibitors. 4-Chloro (MRS4598 **16**; K_i = 0.673 nM) and 4-iodo (MRS4620 **18**; K_i = 0.436 nM) substitution of the N^4-benzyloxy group decreased K_i by ∼20-fold. Primary alkylamine derivatives coupled through a *p*-amido group with a varying methylene chain length (**24** and **25**) were functionalized congeners, for subsequent conjugation to carrier or reporter moieties. X-ray structures of hCD73 with two inhibitors indicated a ribose ring conformational adaptation, and the benzyloxyimino group (*E* configuration) binds to the same region (between the C-terminal and N-terminal domains) as N^4-benzyl groups in adenine inhibitors. Molecular dynamics identified stabilizing interactions and predicted conformational diversity. Thus, by N^4-benzyloxy substitution, we have greatly enhanced the inhibitory potency and added functionality enabling molecular probes. Their potential as anticancer drugs was confirmed by blocking CD73 activity in tumor tissues in situ.



■ INTRODUCTION

In cancer immunotherapy, the body's immune system is mobilized to attack and eliminate a cancerous tumor. In this context, immunosuppresive adenosinergic signaling in the tumor microenvironment attenuates the therapeutic effect.[1−3] Cyclic AMP-dependent signaling through the A_{2A} and A_{2B} adenosine receptors (ARs) on immune cells (T cells, dendritic cells, NK cells, macrophages, and neutrophils) prevents their activation. Adenosine also enhances the immunosuppressive effects of myeloid-derived suppressor cells and regulatory T cells (T_{reg}) as well as angiogenesis and tumor cell invasion. Therefore, a means of weakening the extracellular adenosine effects would be beneficial in cancer immunotherapy either as a co-therapy or as a monotherapy. Two approaches are currently being explored to counteract adenosine effects in the tumor microenvironment, e.g., through preventing its production from AMP by *ecto*-5′-nucleotidase (also known as CD73) or by blocking its receptor interaction with specific antagonists. Various clinical trials in which a small molecule CD73 inhibitor or an anti-CD73 monoclonal antibody is combined with cancer immunotherapy, such as anti-PD-L1 therapy, are planned or in progress.[4−11] CD73 mouse knockout also inhibited tumor angiogenesis, which was dependent on multiple AR subtypes.[12]

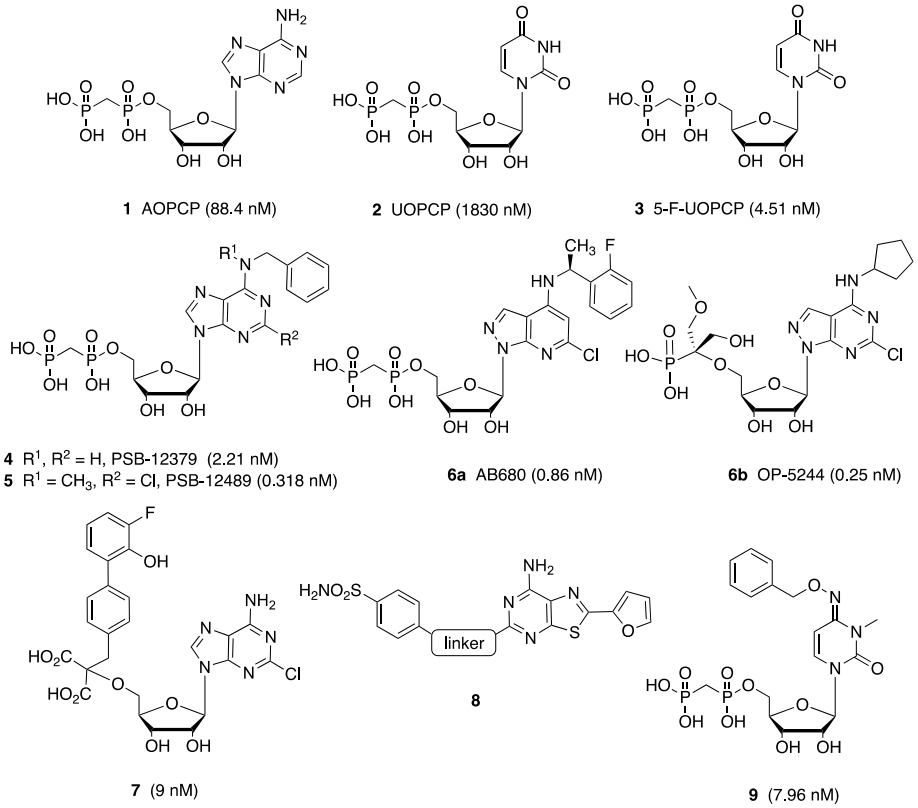
CD73 also mediates both adenosine-dependent and -independent effects in various organs, and CD73 blockade may produce beneficial or deleterious effects.[13] Rare genetic defects resulting in nonfunctional CD73 in humans cause widespread calcification in arteries and joints.[14] Also, pathological downregulation of CD73 is associated with postmenopausal bone loss.[15] CD73 inhibitors may eventually also prove to be useful in treating neurodegeneration and other central nervous system disorders, such as Parkinson's disease, early Alzheimer's disease and epilepsy, or fibrosis, or increasing the myocardial immune response to infections.[16−21] Nevertheless, the presence of CD73 was found to be important in neuronal development.[22,23] It should be noted that there are interspecies differences in the effects of a lack of CD73. Knockout of this enzyme in the mouse does not produce the same phenotype of calcification and arteriomegaly as seen in humans lacking CD73.[24]

Received: October 27, 2021
Published: January 26, 2022



ACS Publications © 2022 American Chemical Society

Chart 1. Structures of CD73 Inhibitors [showing the IC_{50} or K_i at membrane-bound human (h) CD73, except for 7, which was measured at soluble hCD73][26−29,31−33a]



[a]Compound **8** is a dual-acting A_{2A}AR inverse agonist and CD73 inhibitor. The linker moiety of **8** consists of various alkylamino and cycloalkylamino groups.

The affinity of the prototypical ADP-competitive CD73 inhibitor adenosine-5′-*α*,*β*-methylenediphosphonate [AOPCP, **1** (Chart 1)] has been enhanced in recently reported inhibitors.[11,25−28] Bhattarai and co-workers included N^6-benzyl and 2-chloro substitution of the adenine moiety to increase the inhibitory potency to subnanomolar levels.[25−27] Several other classes of nucleotides and nucleotide mimics as CD73 inhibitors have been reported. For example, a pyrazolo[3.4-*b*]pyridine nucleotide (**6a**, Quemliclustat) was recently reported by Arcus Biosciences and has entered a Phase 1 clinical trial for advanced pancreatic cancer in 2019 (ClinicalTrials.gov: NCT04104672, accessed November 30, 2021).[11,29,30] OP-5244 **6b** was recently reported by ORIC Pharmaceuticals.[9] Compounds **6a** and **6b** display oral bioavailability. Also, substitution of the phosphonate moiety with malonate groups (**7**) or introduction of novel chemotypes as CD73 inhibitors has produced significant inhibitory potency.[31−33]

We recently extended this approach by replacing the adenine-like nucleobase entirely, in pyrimidine 5′-nucleoside 3-methylcytidine-5′-*α*,*β*-methylenediphosphonate derivatives, such as compound **9**.[28] The cytidine 3-methyl group that is common to these potent inhibitors was shown previousy to completely block affinity at the UDP-selective $P2Y_6$ receptor.[34] These N^4-substituted 3-methylcytidine-5′-*α*,*β*-methylenediphosphonates do not produce adenosine derivatives as nucleoside metabolites, i.e., making AR activation less likely. We now further explore the structure−activity relationship (SAR) of these pyrimidine nucleotides as inhibitors of human (h) CD73.

RESULTS AND DISCUSSION

Chemical Synthesis. Compounds **1**−**3**, **9**, **75**, and **76** (Table 1) were prepared as previously reported.[26−28] As shown in Scheme 1, synthesis of compounds **10**−**21** required the preparation of various aryl-substituted benzyloxyamines (**32**−**43**). These benzyloxyamines were produced following the previously reported procedure,[34,35] starting from the corresponding substituted benzyl bromides. Similar methods were used to prepare phenylethyl and phenylpropyl homologues (structures not shown) of the benzyl derivatives.

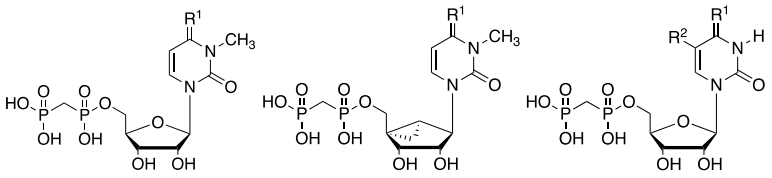
3-Methylcytidine (**44**) was prepared using iodomethane in dimethylacetamide (DMAc) without adding a base. Reaction of **44** with the desired substituted benzyloxyamine (**32**−**43**) in pyridine at 80 °C gave the desired intermediates **45**−**56**, respectively, in good yields. 5′-O-Phosphonylation of the latter was performed using methylenebis(phosphonic dichloride) in trimethyl phosphate to afford the desired final compounds **10**−**21**, respectively, in acceptable yields.

The envisaged synthetic route for the preparation of derivatives **22**−**25** is shown in Scheme 2. Hydrolysis of the methyl ester moiety of compound **56** using sodium hydroxide

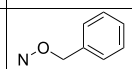
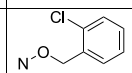
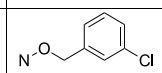
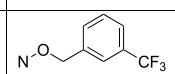
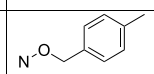
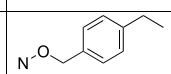
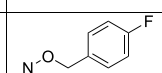
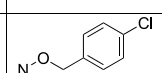
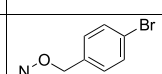
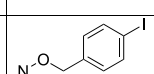
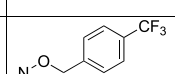
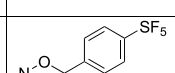
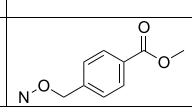
https://doi.org/10.1021/acs.jmedchem.1c01852
J. Med. Chem. 2022, 65, 2409−2433

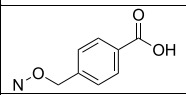
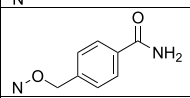
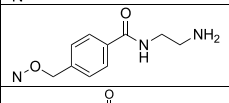
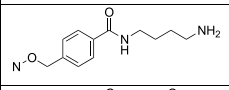
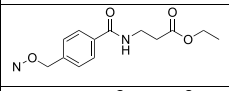
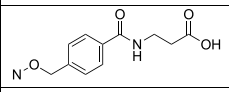
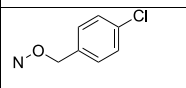
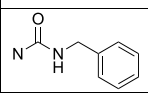
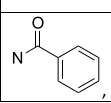
Journal of Medicinal Chemistry pubs.acs.org/jmc Article

Table 1. K_i Values of Compounds 10−31 and Archival Compounds 9, 75, and 76 in the Inhibition of Soluble hCD73 or as Otherwise Noted (triethylammonium salts were prepared and tested)[c]



9–27, 30 **28,29** **31, 75, 76**

No.	Structure R^1 = (other changes)	K_i ± SEM (nM, n=3)
9		10.6 ± 0.4[a], 3.67 ± 0.26[a,b]
10		1.63 ± 0.28
11		1.58 ± 0.06
12		1.27 ± 0.18
13		0.894 ± 0.175
14		3.50 ± 0.11
15		1.14 ± 0.06
16		0.673 ± 0.091
17		0.441 ± 0.157
18		0.436 ± 0.078
19		1.08 ± 0.34
20		0.511 ± 0.041
21		0.848 ± 0.229

No.	Structure R^1 = (other changes)	K_i ± SEM (nM, n=3)
22		14.1 ± 2.9
23		1.76 ± 0.43
24		0.626 ± 0.076
25		1.78 ± 0.33
26		2.51 ± 0.51
27		2.61 ± 0.94 (n=2)
28	O	> 50 μM (28% inhibition)
29		59.2 ± 5.58
30		71.5 ± 17.6
31	O, R^2 = F	2540 ±710
75	O, R^2 = CH_3	338 ± 56[a,b]
76	 , R^2 = H	4.58 ± 0.55[a], 13.9 ± 1.6[a,b]

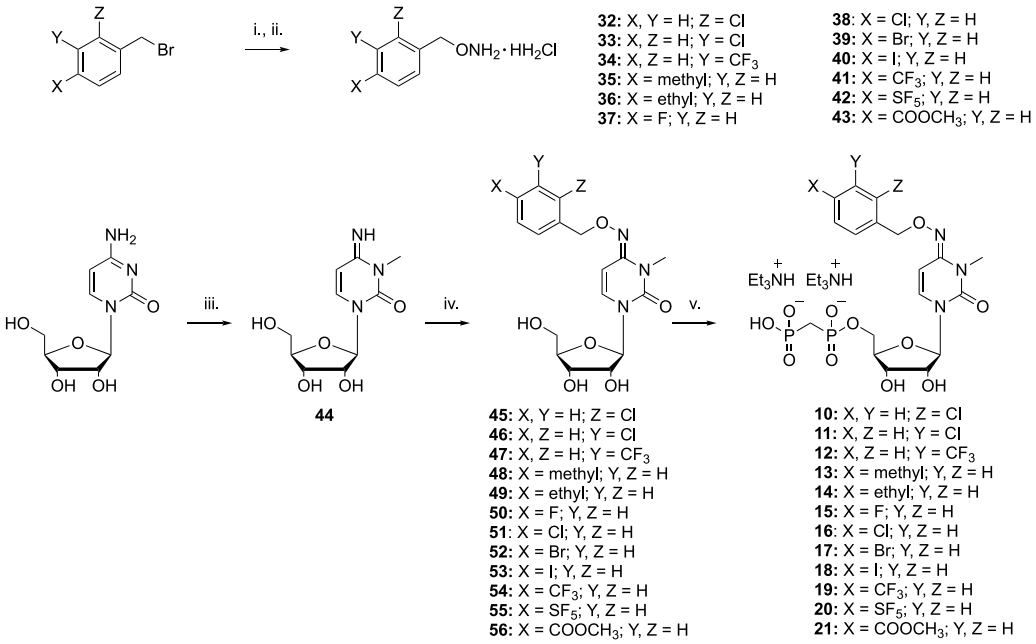
[a]Data from ref 28. [b]At rat soluble CD73.[28] [c]K_i is expressed as the mean of three independent determinations, each in duplicate, unless noted.

furnished the *p*-carboxybenzyl nucleoside intermediate **57**, which was 5′-phosphonylated as previously indicated to afford **22**.

Starting from compound **57**, we planned to prepare its methylamide derivative, using HATU and DIPEA as a coupling agent and base, respectively, to condense the carboxylic acid moiety with methylamine. LC-MS of the isolated product indicated that multiple acetylations had occurred, i.e., **58** (probably because of the presence of acetic acid traces used during the previous workup). **58** was directly reacted with ammonia to remove the acetyl groups and form an amide **59**. Nucleoside product **59** was used to prepare final phosphonate

https://doi.org/10.1021/acs.jmedchem.1c01852
J. Med. Chem. 2022, 65, 2409−2433

Scheme 1. Substitution of the Pyrimidine Scaffold with Diverse 4-Benzyloxyimino Substituents[a]



[a]Reagents and conditions: (i) $(Boc)_2NOH$,[33] DBU, DMF, 50 °C, 2 h; (ii) 4 N HCl in dioxane, rt, 12 h; (iii) MeI, DMAc, rt, 4 h, 95%; (iv) the desired benzylhydroxylamine (**32**−**43**), pyridine, 80 °C, 12 h, 35−97%; (v) methylenebis(phosphonic dichloride), $(CH_3O)_3PO$, 0 °C, 3 h, 5−40%.

derivative **23**. The two amine congeners **24** and **25** were synthesized by amination of **56** with ethylenediamine and 1,4-diaminobutane, respectively. The crude nucleoside amides thus obtained were directly subjected to 5′-O-phosphonylation without further purification, but using an increased amount of methylenebis(phosphonic dichloride) to ensure full conversion of the starting compounds to the desired products.

Molecular modeling analysis based on the X-ray co-crystal structure of **21** with soluble hCD73 (see below) suggested that the introduction of a carboxylic group with a two-carbon spacer from the benzamide moiety may improve the activity through formation of an H-bond with a lysine residue present in the pocket of the enzyme. On the basis of these predictions, we synthesized compounds **26** and **27** starting from **57** and *β*-alanine ethyl ester hydrochloride, as reported in Scheme 3.

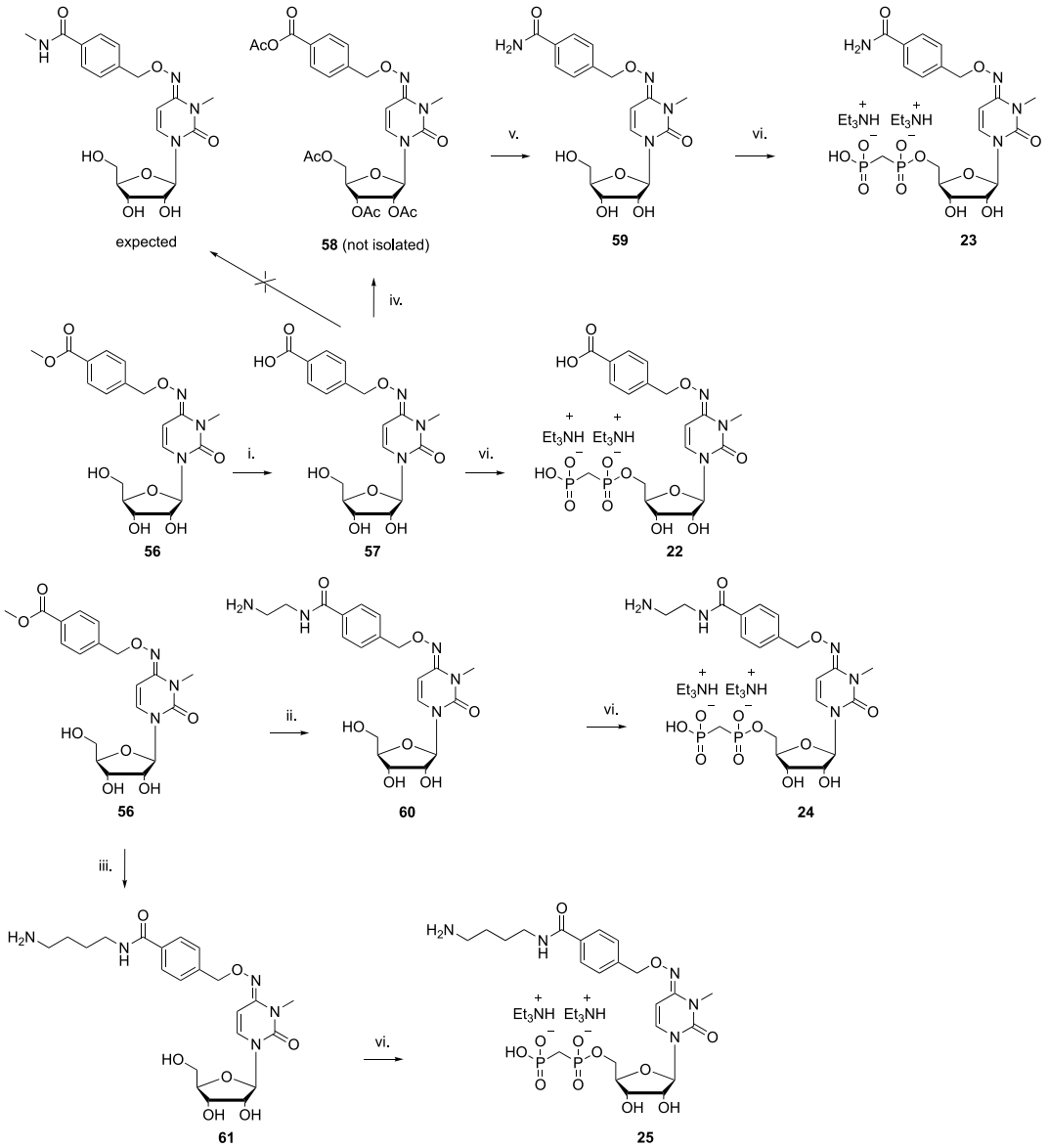
A methanocarba ([3.1.0]bicyclohexane) substitution of the ribose ring in nucleosides and nucleotides allows for the pre-establishment of either a north (N) or a south (S) pseudoribose conformation depending on the position of the cyclopropane ring fusion, tailored for the target protein interaction.[36] An (S)-methanocarba analogue in this chemical series was already shown to be a weak CD73 inhibitor.[28] Furthermore, inspection of the reported CD73 X-ray structures indicates that an (N)-ribose conformation is present.[37] Therefore, (N)-methanocarba analogues **28** and **29** were prepared (Scheme 4) by adapting reported procedures.[38,39] Sugar protection by acetylation was performed using the standard method with acetic anhydride to afford intermediate **65**. Next, the 4-ketone moiety was first activated through reaction with 2,4,6-triisopropylbenzenesulfonyl chloride (TPSCl), followed by nucleophilic displacement by 4-Cl-benzyloxyamine (**38**) to afford compound **66**. N-3 methylation of **66** was performed as described above to afford **67**, which was followed by acetyl group removal using a methanolic ammonia solution to afford intermediate **68** in good yield. The synthesis of methanocarba intermediate **67** required addition of K_2CO_3 as a base, as there was no free 4-amino group on the cytosine moiety that could stabilize the alkylation transition state. The two (N)-methanocarba-5′-*O*-*α*,*β*-methylenediphosphonates **28** and **29** were prepared starting from the corresponding precursors **64** and **68**, respectively, using a previously reported method.[38]

We also envisioned the preparation of a urea analogue (**30**); its synthesis is highlighted in Scheme 5. Benzylamine was activated through reaction with 1,1′-carbonyldiimidazole (CDI) following the reported procedure[40] to afford compound **69**. To avoid side reaction products, cytidine was protected as its 2′,3′,5′-tri-*O*-acetyl derivative (**70**) through the standard procedure with acetic anhydride. During this reaction, we also observed the formation of the 2′,3′,5′-tri-*O*-acetyl-N^4-acetyl derivative, which was isolated and converted into **70** in a microwave reactor in methanol at 100 °C. N-3 methylation was performed as already described, and reaction of **71** with **69** in the presence of triethylamine furnished intermediate **72**. Next, sugar deprotection using a methanolic ammonia solution, followed by phosphonylation, gave the desired product **30**. 5-F-UDP (**31**) was synthesized as reported previously[3] and was used for a comparison with its analogue 5-F-UOPCP (**3**).

In Vitro Biological Activity. We describe here the compounds' in vitro CD73 inhibitory activity before introducing the extensive structural probing of their protein interactions (below). The inhibitory potency of the various nucleotide analogues was determined with soluble hCD73 by previously reported methods (Table 1).[41−43] Many of the analogues were significantly more potent than reference compound N^4-benzyloxy-3-methylcytidine-5′-*α*,*β*-methylene-diphosphonate **9**, as we previously reported.[28]

https://doi.org/10.1021/acs.jmedchem.1c01852
J. Med. Chem. 2022, 65, 2409−2433

Scheme 2. Synthetic Strategies for Extension at the 4-Carboxyl Group on a 4-Benzyloxyimino Substituent[a]



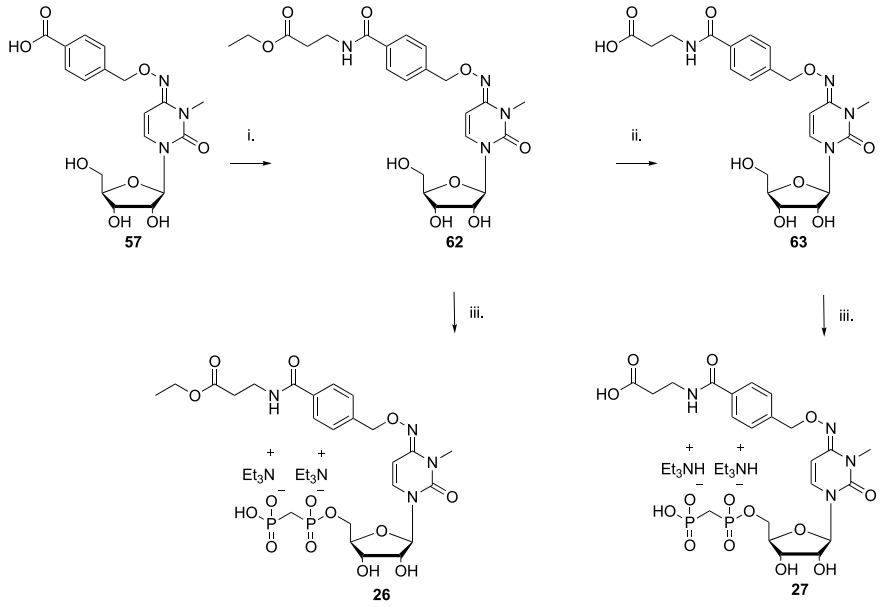
[a]Reagents and conditions: (i) 1 N NaOH, MeOH, rt, 20 min, 77%; (ii) ethylenediamine, rt, 2 h, 95%; (iii) 1,4-diaminobutane, rt, 2 h, 90%; (iv) $MeNH_2$, HATU, DIPEA, DMF, rt, 12 h; (v) NH_3/MeOH, rt, 12 h, 64% for steps iv and v; (vi) methylenebis(phosphonic dichloride), $(CH_3O)_3PO$, 0 °C, 3 h, 8−30%.

Halogen substitution of the benzyl ring of compound **9** produced a significant decrease in the K_i value at soluble hCD73. A chloro substitution at *o*-**10** or *m*-**11** positions produced a 6−7-fold increase in potency, while that of *p*-chloro analogue **16** was 16-fold enhanced (Figure 1A). Halogen substitution at the *para* position showed the following order of potency: I and Br > Cl > F. Thus, *p*-iodo analogue **18** displayed a K_i value of 0.436 nM (Figure 1B). Other neutral *para*-substituted analogues **13**, **14**, and **21** exhibited high potencies (0.5−3.5 nM). A *p*-pentafluorosulfenyl group, which is both highly electron-withdrawing and strongly lipophilic, provided a K_i of 0.511 nM (**20**). A comparison between methyl ester **21** and free carboxylate **22** indicated that a neutral group is preferred at the benzyl ring *para* position, although the carboxylate was still suitable as a linking group to form potent primary amino congeners **24** and **25**. The corresponding primary amide **23** was 2-fold weaker than methyl ester **21**. The K_i values of primary amine congeners **24** and **25** indicated that the two-methylene spacer of **24** (0.626 nM) was preferred. These amine congeners might be useful for conjugation to a variety of carrier or reporter moieties such as fluorophores for enzyme visualization or characterization, solid supports for affinity chromatography, and nanoparticles for altering pharmacokinetic and pharmacodynamic properties.

An (N)-methanocarba analogue **29** of *p*-chloro derivative **16** was an 88-fold weaker inhibitor. Also, simple uridine analogue

https://doi.org/10.1021/acs.jmedchem.1c01852
J. Med. Chem. 2022, 65, 2409−2433

Scheme 3. β-Alanine Derivatives for Introduction of Distal H-Bonding Groups to Reach Polar and Charged Amino Acid Residues Adjacent to the CD73 Binding Site[a]



[a]Reagents and conditions: (i) β-alanine ethyl ester hydrochloride, HATU, DIPEA, DMF, 12 h, rt, ~100%; (ii) 1 N NaOH, MeOH, rt, 12 h, 92%; (iii) methylenebis(phosphonic dichloride), $(CH_3O)_3PO$, 0 °C, 3 h, 10%.

28 displayed <50% inhibition between 0.03 nM and 50 μM, compared to the uridine analogue with a K_i value of 1830 ± 530 nM at rat CD73.[28] Thus, the enforcement of an N conformation by the [3.1.0]bicyclohexyl ring system is not potency-enhancing compared to ribose in this CD73 inhibitor series, but it does allow moderate inhibition (K_i = 59 nM in **29**) when favorable functionalization is present, e.g., 4-(*p*-chlorobenzyloxyimino). By comparison, the (S)-methanocarba analogue of **28** in the simple uridine series was inactive at 1 μM, but optimized analogues were not prepared.[28] The X-ray structures of bound nucleotides in CD73 display an N ribose conformation, consistent with the inhibition by **29**.[27,37]

An *N*-benzyl urea derivative **30** (71.5 nM) was only a moderately potent CD73 inhibitor compared to **9**, indicating the advantage of the 4-oxoimino linkage. One 5′-diphosphate analogue, 5-fluorouracil derivative **31**, was found to be a weak inhibitor with a K_i of 2.54 μM.

Later, on the basis of the obtained crystal structures, a molecular modeling investigation suggested that introduction of a β-alanine moiety connected to the carboxylic acid of compound **22** could improve the affinity of our derivatives. Consequently, derivatives **26** and **27**, which possess β-alanine-ethyl ester and β-alanine moieties, respectively, were 5-fold more potent than **22**.

The off-target activity of selected inhibitors (**9**, **16**, and **18**) was determined by the Psychoactive Drug Screening Program (PDSP, The University of North Carolina at Chapel Hill, Chapel Hill, NC).[44] The only hit among 46 receptors, channels, and transporters assayed was a weak binding inhibition by *p*-chloro analogue **16** at the σ_1 receptor (K_i = 2.61 ± 0.64 μM).

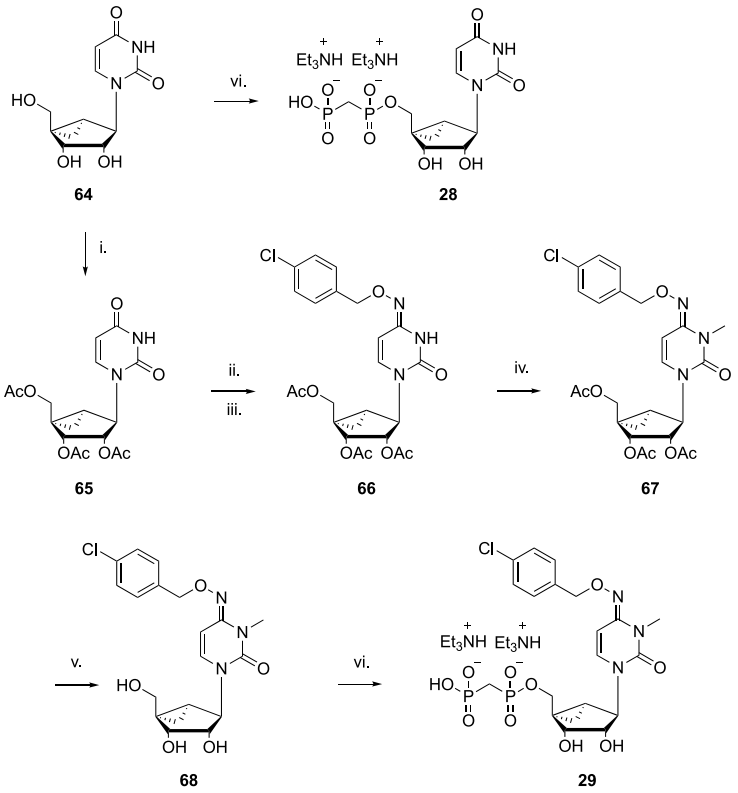
X-ray Crystallographic Structures. X-ray crystal structures of hCD73[45] (constructs in Figures S1 and S2) complexed with the two potent 5′-α,β-methylenediphosphonate inhibitors **16** (with a 4-Cl-*O*-benzyl substituent) and **21** (with an *O*-benzyl 4-methyl ester substituent) were determined in the open and closed states (Table 2 and Figure 2). The two compounds have very similar binding modes (Figure 2B). In both of these *N*-methyl analogues, the benzyloxyimino group adopts an *E* configuration, which is most clearly defined in the high-resolution structures of the open crystal forms (Figure S3). In the closed forms, the electron density is well-defined for the binding of **21**, indicating high occupancy and no significant conformational flexibility. In the complex with **16** in the closed state, the density of the 4-Cl-*O*-benzyl substituent is less well-defined. This may be a result of flexibility and/or of the generally poorer quality of this data set with a Wilson *B* factor of 93.6 Å^2 and a resolution of 2.9 Å.

Key features of the interaction of the two inhibitors with CD73 are the polar contacts of the bisphosphonate and ribose groups with both domains (Figure 2A). These interactions closely resemble those of the AOPCP derivatives. The NH_2 group of the Asn390 side chain forms hydrogen bonds to the ribose 2′-OH and the carbonyl oxygen of the 3-methylcytidine base (Figure 2B). The carbonyl oxygen thus takes the position of N-3 in the adenine base of AOPCP derivatives. A further important interaction is the hydrophobic stacking interaction of the nucleobase with Phe417 and Phe500. The N^4 substituents bind at the cleft between the two domains and interact with both domains, thus stabilizing the closed state (Figure 2C). The cleft has mixed polar and apolar character at this site, but the interactions of the N^4 substituents are mostly hydrophobic, which is quite similar to the situation for the N^6 substituents in AOPCP derivatives. An exception is the hydrogen bonding interaction of Gln88 with the ester carbonyl group of **21**.

A comparison to the complex structures of CD73 with AOPCP derivatives **4**–**6** shows an overall similar binding

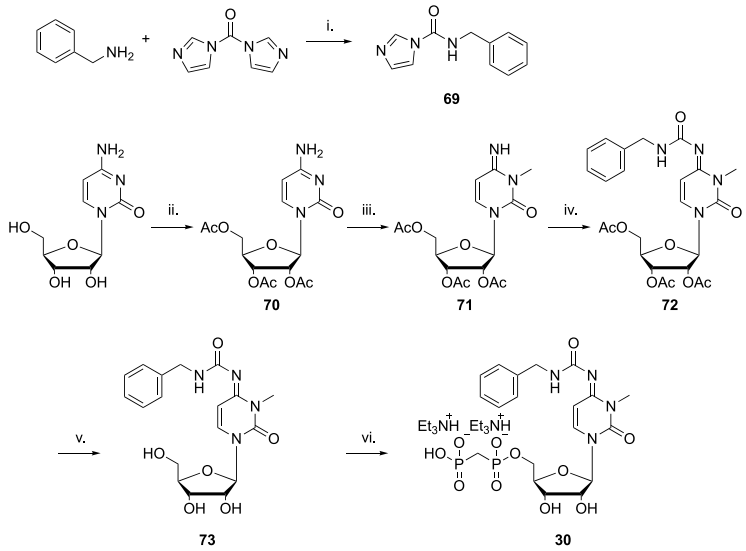
https://doi.org/10.1021/acs.jmedchem.1c01852
J. Med. Chem. 2022, 65, 2409−2433

Scheme 4. Substitution of the Flexible Ribose Moiety of 16 with the Conformationally Constrained (N)-Methanocarba Group[a]



[a]Reagents and conditions: (i) acetic anhydride, Et_3N, DMAP, CH_3CN, 2 h, rt, 67%; (ii) TPSCl, Et_3N, DMAP, CH_3CN, rt, 18 h; (iii) *p*-Cl-*O*-benzylhydroxylamine hydrochloride, Et_3N, CH_3CN, rt, 18 h, 26% for steps ii and iii; (iv) MeI, K_2CO_3, DMAc, 18 h, rt, 83%; (v) NH_3/MeOH, rt, 12 h, 91%; (vi) methylenebis(phosphonic dichloride), $(CH_3O)_3PO$, 0 °C, 3 h, 6−16%.

Scheme 5. Introduction of a Distal Urea-Type Substituent on the 4-Benzyloxyimino Group of the Pyrimidine Scaffold, to Potentially Enhance H-Bonding in That Region of the CD73 Binding Site[a]



[a]Reagents and conditions: (i) EtOH, reflux, 12 h, 72%; (ii) acetic anhydride, Et_3N, DMAP, CH_3CN, 10 min, rt, 95%; (iii) MeI, DMAc, rt, 4 h, 95%; (iv) **69**, Et_3N, THF, reflux, 12 h, 72%; (v) NH_3/MeOH, rt, 12 h, 87%; (vi) methylenebis(phosphonic dichloride), $(CH_3O)_3PO$, 0 °C, 3 h, 8.4%.

https://doi.org/10.1021/acs.jmedchem.1c01852
J. Med. Chem. 2022, 65, 2409−2433

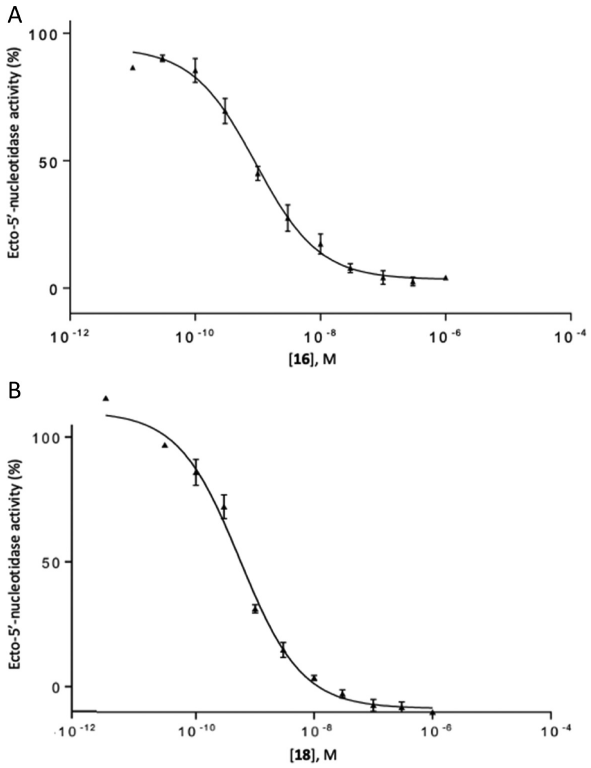


Figure 1. Concentration−response curve for inhibition of soluble hCD73 by **16** (A; K_i = 0.673 ± 0.091 nM) and **18** (B; K_i = 0.436 ± 0.078 nM) (mean of three independent determinations, each in duplicate).

mode (Figure 2D). The β-phosphonate groups superimpose well, but shifts of up to ∼1 Å are observed for the α-phosphonate, ribose, and base moieties. These differences are caused by a small change in the domain orientation and in addition by local conformational adaptations, in particular, of Phe417 and Gln88. The conformational differences avoid a close contact of Gln88 with the benzyl substituents of **16** and **21** and with Phe417. Indeed, a comparison of pyrimidine inhibitors **16** and **21** bound to the open and closed states shows that the nucleobase, Phe417, and Phe500 are positioned closer to the side of Gln88 in the closed states than in the open states, where Gln88 is not nearby due to the domain orientation (Figure S3C,F). The binding mode observed for pyrimidine-based compounds **16** and **21** matches most closely conformation A of **6a** with regard to the positions and binding modes of the nucleobases and the N^4 or N^6 substituents. The binding modes of **16** and **21** to the open state match that of the unsubstituted CMP substrate of Protein Data Bank (PDB) entry 7PA4[46] (Figure S3). Small differences are observed in the base position likely resulting from the N^4 substitution.

Molecular Modeling. The crystallographic complex of hCD73 in the closed form bound with compound **16** was subjected to molecular dynamics (MD) simulations (three replicates of 50 ns each) to assess the stability of the binding mode over time. During most of the simulation time, the ligand maintained a geometry compatible with a $\pi-\pi$ stacking interaction with Phe417 and Phe500 and the pattern of H-bonds observed in the X-ray state. Asp506 was engaged in H-bonding with the 2′- or 3′-hydroxyl groups during nearly all of the simulation time (99% on average over the three replicates). Asn390 interacted with the ribose 2′-hydroxyl group or with the carbonyl at position 2 of the cytosine for 80% of the simulation time. An H-bond between His118 and the β-phosphonate was found on average in 69% of the trajectory time, and an H-bond between Arg354 and the α-phosphonate occurred during 89% of the trajectory time. Arg395 was engaged in an H-bond with the α-phosphonate or β-phosphonate in 81% of the simulation time on average (Table S2 and Figure 3B). Compound **16**, and especially its nucleotide-like scaffold, remained close to its original position during the simulation: the ligand's heavy atom root-mean-square deviation (RMSD) relative to the X-ray pose showed an average value of 2.12 ± 0.60 Å (±standard deviation) over the three replicates (Table S2), with lower values in the case of replicate 2 (average of 1.70 Å) but reaching maximum values of 3.70 and 3.17 Å in replicates 1 and 3, respectively. Notably, the RMSD reached higher values in the second half of the simulation in replicates 1 and 3, as shown in Figure 3C, and the last frames of these two trajectories showed a deviation of the *p*-Cl-benzyl substituent compared to replicate 2, which resembled the initial state (Figure 3A). The per-atom root-mean-square fluctuation (RMSF) highlights that the atoms deviating more from the average position belong to the *p*-Cl-benzyl substituent (Figure 3D). The RMSD of the nucleotide scaffold alone (all heavy atoms except the *p*-Cl-benzyl substituent) fluctuated with a small deviation around the lower average value of 1.71 ± 0.27 Å (Figure 3E).

To investigate the conformational exploration of the *p*-Cl-benzyl substituent of **16** within the surrounding protein environment, we clustered the trajectories on the basis of the RMSD of this moiety (Figure 4A). In particular, the trajectories were combined, then aligned superposing the ligand nucleotide-like scaffold to its initial conformation, and sampled every 200 ps. The RMSD of the *p*-Cl-benzyl

Table 2. Summary of Key Crystallographic Parameters

	16 open	**16** closed	**21** open	**21** closed
PDB entry	7QGA	7QGM	7QGL	7QGO
crystallization buffer	10 mM **16**, 100 μM $ZnCl_2$, 8% PEG 6000, and 0.1 M MES (pH 6.2)	10 mM **16**, 10 μM $ZnCl_2$, 10% PEG 3350, and 0.1 M BisTris (pH 5.6)	10 mM **21**, 100 μM $ZnCl_2$, 8% PEG 6000, and 0.1 M MES (pH 6.2)	10 mM **21**, 10 μM $ZnCl_2$, 10% PEG 4000, and 0.1 M BisTris (pH 5.7)
final buffer	10 mM **16** and 20% PEG200	10 mM **16** and 20% PEG200	10 mM **21** and 20% PEG200	10 mM **21** and 20% PEG200
d_{min} (Å)	1.5	2.9	1.5	2.21
$CC_{1/2}$[a]	0.603	0.649	0.743	0.250
R_{work}/R_{free} (%)	0.165/0.184	0.261/0.294	0.158/0.175	0.227/0.269
$B_{protein}$ (Å^2)	12.4	99.1	12.0	83.9

[a]$CC_{1/2}$ in the highest-resolution shell. See Table S1 for further details.

https://doi.org/10.1021/acs.jmedchem.1c01852
J. Med. Chem. 2022, 65, 2409−2433

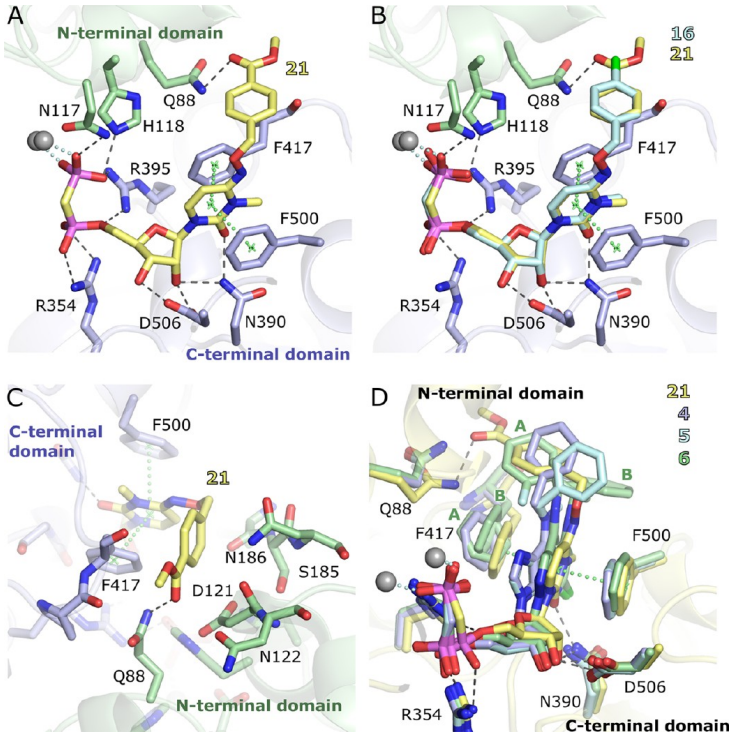


Figure 2. X-ray structures of the complex of **16** and **21** with the closed form of hCD73. (A) Binding mode of **21**. (B) Superposition of the binding modes of **16** and **21** based on the Cα atoms of the C-terminal protein domains. (C) Interactions of the N^4 substituent of **21** at the cleft between the two domains. (D) Superposition of the crystal structures of **21**, **4** (PDB entry 6S7F),[27] **5** (PDB entry 6S7H),[27] and **6** (AB680, PDB entry 6Z9D)[11] based on the C-terminal domains. For **6**, the N^6 substituent and the Phe417 side chain have been modeled in alternative conformations, labeled A and B.

substituent heavy atoms was used as a parameter to cluster the trajectories using Wordom's QT-like method.[47] The most populated clusters (including at least 5% of total frames) were considered, resulting in three examples. Cluster 1 presented the ligand in a conformation comparable to the X-ray structure (Figure 4C), and it collected the initial frames of replicates 1 and 3 and approximately the entire replicate 2 (cluster population equal to 47% of the whole combined simulations). In this conformation, the *p*-Cl-benzyl substituent was surrounded (distance of ≤4 Å) by Gln88, Asp121, Asn186, Pro416, and Phe417 in at least 40% of the cluster frames (Figure 4B). Cluster 2 (cluster population of ∼24%) collected an ensemble of intermediate conformations from replicate 1 and those explored in the second half of replicate 3: the ligand *p*-Cl-benzyl substituent pointed toward the N-terminal domain of hCD73 (Figure 4E) and was in contact with Asp121 and Asn186 in almost all of the cluster frames (Figure 4D). Cluster 3 was represented during only the second half of replicate 1 (cluster population of ∼19%), and in this conformation, the *p*-Cl-benzyl substituent faced a cleft between the N-terminal and C-terminal domains opposite the cleft occupied by the the *p*-Cl-benzyl substituent in the X-ray structure (Figure 4G). The substituent was mainly (>40% of the cluster frames) in contact with Asn186, Pro187, Phe500, and Asn503 (Figure 4F). It is interesting to note that in the described clusters, the *p*-Cl-benzyl substituent was often in the proximity of an Asn or Gln residue, which could potentially stabilize the moiety through polar interactions. Moreover, the flexibility of the *p*-Cl-benzyl moiety was not surprising, considering that two alternative positions comparable to those identified in clusters 1 and 3 have already been shown in the X-ray structure of inhibitor **6a** bound to hCD73 (PDB entry 6Z9D[11]), whose 1-(2-fluorophenyl)ethyl substituent is reported in two alternate states (Figure S7). Also, in a comparison of the binding modes of different AOPCP derivatives, the N^6 substituent was positioned at different sites of the cleft between the two domains and often had poorer density and higher *B*-factors indicating flexibility.[26,27,44] The ligand conformation represented in cluster 2 seemed to be an intermediate state between these two opposite conformations, and the transition from cluster 1 to cluster 3 conformations going through cluster 2 can be seen in Video S1 (trajectory of replicate 1). The three conformations appear to mainly originate from the three rotational preferences around the N−O−C−C torsion angle (Figure S8).

Following the results of the compound **16** simulations, we applied the same simulation and analysis protocol to compound **18**, the most active of the series. In this case, the complex between the enzyme and the compound was obtained by building the ligand in place of compound **16**, i.e., substituting the Cl atom with I. The same pattern of H-bonds observed for compound **16** was also maintained in this case, with persisting H-bonds with His118, Arg354, Asn390, Arg395, and Asp506 (Table S2 and Figure 5B). Compound **18** showed an increased geometrical stability, with an average heavy atom RMSD of 1.62 ± 0.41 Å over the three replicates. In this case, the average RMSD of the whole ligand was closer to the RMSD of the nucleotide scaffold ($RMSD_{ave}$ = 1.57 ±

https://doi.org/10.1021/acs.jmedchem.1c01852
J. Med. Chem. 2022, 65, 2409−2433

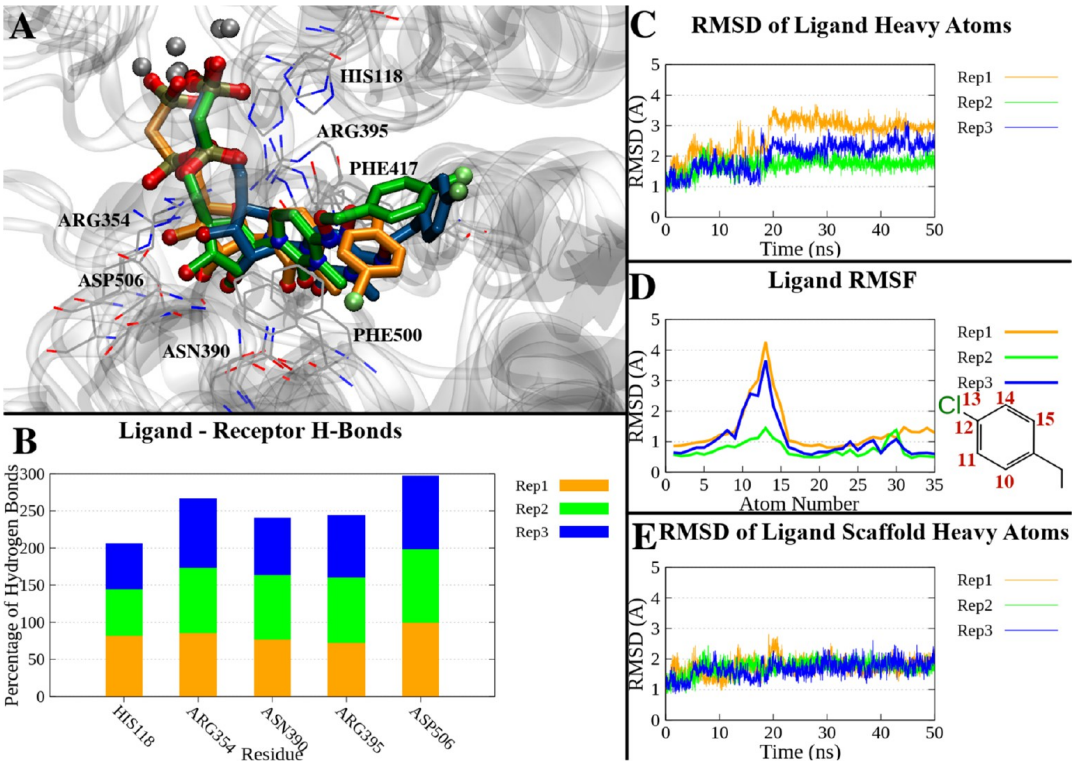


Figure 3. (A) Superposition of the last frames of three 50 ns trajectories of the compound **16**-hCD73 complex in the closed form. The trajectories have been aligned by superposing the Cα atoms on the initial state. Proteins are represented by a gray ribbon, interacting residues as gray lines, and ligands of replicates 1−3 as orange, green, and blue sticks, respectively. (B) Percentage of H-bonds between compound **16** and hCD73 residues during the three replicates. Only residues interacting on average >10% of the simulations are shown. (C) RMSDs of compound **16** heavy atoms over time in the three replicates. (D) RMSF of compound **16** heavy atoms in the three replicates. The atom numbers of atoms with higher RMSFs are reported in the two-dimensional depiction of the *p*-Cl-benzyl moiety. (E) RMSDs of the heavy atoms of the nucleotide scaffold (all heavy atoms except the *p*-Cl-benzyl) in the three replicates.

0.28 Å): the *p*-I-benzyl moiety deviated less from its initial conformation, just in the last frames of replicates 2 and 3 (Figure 5A,C−E). The cluster analysis identified a main cluster collecting ∼90% of the frames, with the ligand oriented as in the starting pose (Figure S5B,C). In a second cluster (population of ∼7%), the *p*-I-benzyl moiety pointed toward the N-terminal domain of the enzyme, surrounded principally by Asp121, Asn186, and Pro187 (Figure S5D,E), similar to the previous observation of cluster 2 of compound **16**. Interestingly, the presence of Gln or Asn surrounding the *p*-I-benzyl substituent was confirmed in both clusters, with these residues potentially able to interact with and stabilize the I substituent of the highly potent compound **18**.

Analogously, we analyzed the X-ray structure of the complex between hCD73 and compound **21**, and we observed the presence of two main clusters (Figure S6A): cluster 1 (population of ∼49%), collecting the first part of replicates 1 and 3 and almost all of replicate 2, where the *p*-methoxycarbonyl-benzyl maintained the original position (Figure S6B,C), and cluster 2 (population of ∼40%). Cluster 2 appeared in the second part of replicates 1 and 3 and showed a conformation of the substituent pointing toward the enzyme's N-terminal domain (Figure S6D,E), which is similar to the intermediate state described in clusters 2 of compounds **16** and **18**. The evolution of replicate 2 in its final frames (Figure 6A and Figure S6A) can be described by a further small cluster (population of ∼3%), where the *p*-methoxycarbonyl-benzyl was rotated ∼180° around the benzyloxy bond to interact with Asn503 (Figure S6F,G). Regardless of the flexibility and conformational variability of the *p*-methoxycarbonyl-benzyl substituent, the nucleotide-like scaffold was stable, as assessed by an average RMSD of 1.20 ± 0.28 Å (Table S2 and Figure 6C−E), which correlated with H-bonds to His118, Arg354, Asn390, Arg395, and Asp506 being maintained during most of the simulation time (Figure 6B). The methyl ester of compound **21** is an H-bond acceptor, and in fact, it engaged in additional transient H-bonds during the simulations, i.e., with Gln88 and Asn186 (average persistence over the three replicates of >10%).

In addition to analyzing the benzylic substituent behavior and the persistence of interactions typical of the bound state, we also exploited the collected MD trajectories to monitor the puckering of the ribose ring in a dynamic environment. In fact, the X-ray structures of the complexes between hCD73 and compound **16** and **21** showed that the ligands assumed an N conformation in the bound state, as shown by their phase angle of pseudorotation (P) and degree of deformation from the plane (ν_{max}) reported in the pseudorotational cycle in Figure 7B). This agrees with the general trend of nucleotide-like compounds in the hCD73 active site already deposited in the PDB (Figure 7D). The N puckering was maintained by all of the compounds during the MD simulations, where the ring

https://doi.org/10.1021/acs.jmedchem.1c01852
J. Med. Chem. 2022, 65, 2409−2433

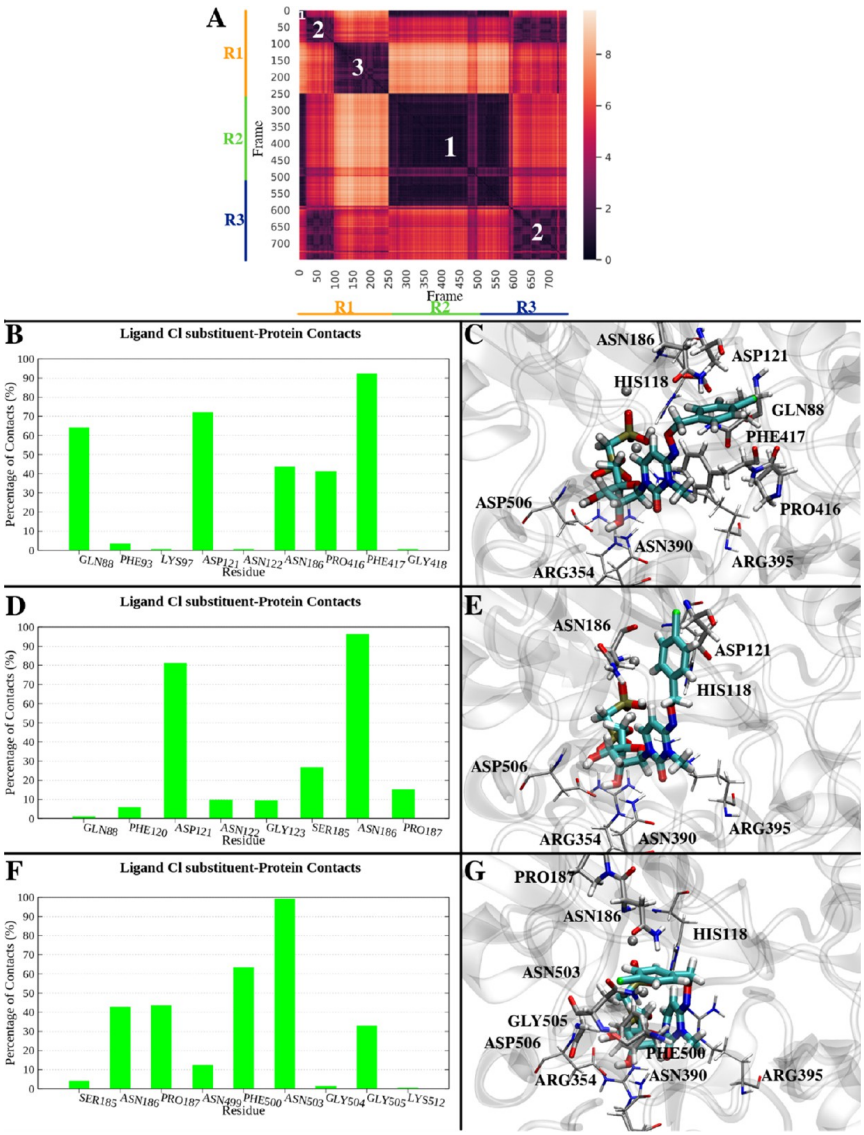


Figure 4. MD simulation of compound **16** bound to the closed form of hCD73. (A) Conformational distance (RMSD) matrix, reporting the frame number on the *x*- and *y*-axes, and RMSDs of *p*-Cl-benzyl heavy atoms on a colorimetric scale going from dark to bright colors [low to high RMSD values (Å)]. The frames of three 50 ns replicates have been merged for the sake of the analysis and sampled every 200 ps (750 frames total) after superposition of the nucleotide-like scaffold of compound **16** to the starting conformation. The frames of each replicate are identified by bars parallel to the *x*- and *y*-axes (replicates 1−3 in orange, green, and blue, respectively). White numbers on the matrix highlight the most represented clusters (population of >5%): cluster 1 (349 frames, ∼47%), cluster 2 (183 frames, ∼24%), and cluster 3 (145 frames, ∼19%). (B) Residues in contact (distance of ≤4 Å) with compound **16** in cluster 1. The persistence of each contact is indicated by the percentage of frames of the cluster where that contact is present. (C) Center of cluster 1 (replicate 1, frame 1, 0.02 ns). The ligand is depicted as cyan sticks, and the protein is colored gray. Residues in contact with the ligand in >40% frames of the cluster are shown. (D) Residues in contact (distance of ≤4 Å) with compound **16** in cluster 2. (E) Center of cluster 2 (replicate 3, frame 1611, 32.22 ns). The ligand is depicted as cyan sticks, and the protein is colored gray. Residues in contact with the ligand in >40% frames of the cluster are shown. (F) Residues in contact (distance of ≤4 Å) with compound **16** in cluster 3. (G) Center of cluster 3 (replicate 1, frame 991, 19.82 ns). The ligand is depicted as cyan sticks, and the protein is colored gray. Residues in contact with the ligand in >40% frames of the cluster are shown.

only transiently assumed the S conformation (Figure S9A,C,E). This suggested application of a chemical constraint of the ribose ring to maintain the enzyme-preferred N conformation. Therefore, the ribose furan ring was substituted with a bicyclo[3.1.0]hexane (N)-methanocarba moiety, driven by the previous successful experience provided by this bicyclic structure to freeze the puckering of A_3 adenosine receptor agonists in their receptor-preferred N conformation,[36,48] thereby increasing the affinity. However, compound **29**, the (N)-methanocarba analogue of compound **16**, did not show an expected increase in binding affinity (K_i ∼ 59 nM) but instead was ∼90-fold less potent than ribose analogue **16** (K_i ∼ 0.67 nM). This could be explained by the protein environment hosting the O4′ position of the ligand: the X-ray structure of

https://doi.org/10.1021/acs.jmedchem.1c01852
J. Med. Chem. 2022, 65, 2409−2433

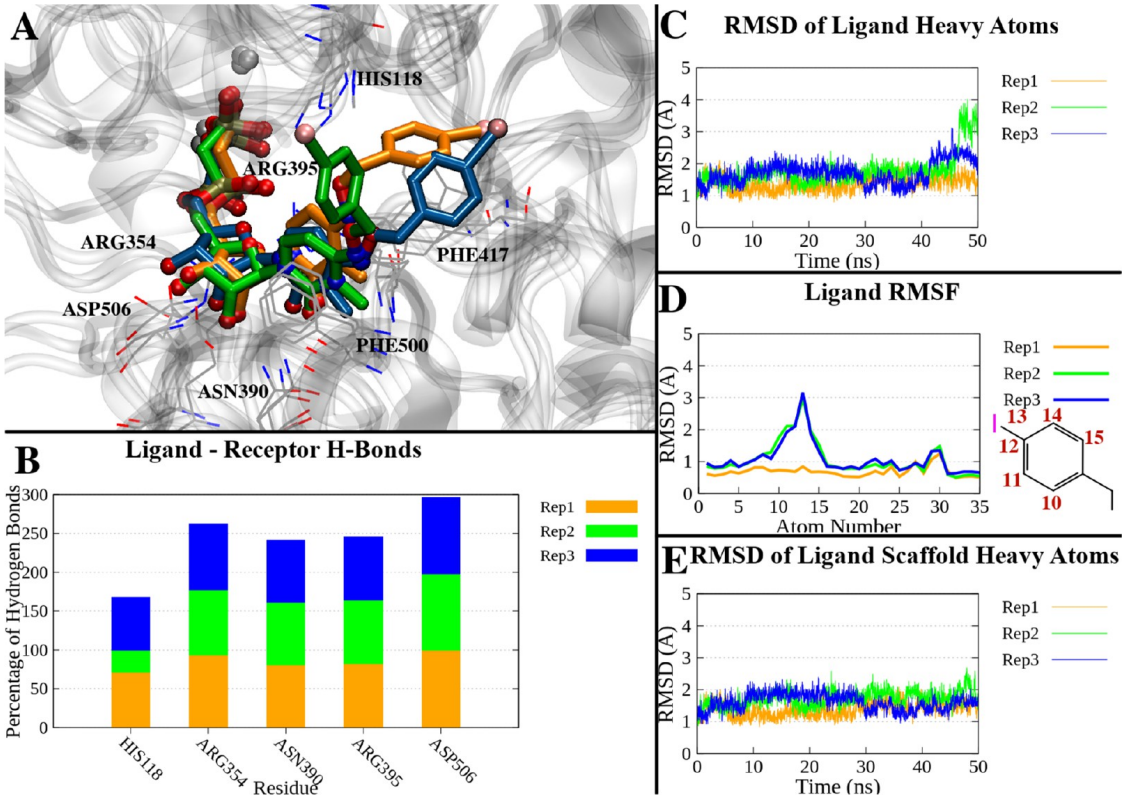


Figure 5. (A) Superposition of the last frames of three 50 ns trajectories of the compound **18**-hCD73 complex in the closed form. The trajectories have been aligned by superposing the Cα atoms to the initial state. Proteins are represented as a gray ribbon, interacting residues as gray lines, and ligands of replicates 1−3 as orange, green, and blue sticks, respectively. (B) Percentage of H-bonds between compound **18** and hCD73 residues during the three replicates. Only residues interacting with on average >10% of the simulations are shown. (C) RMSDs of compound **18** heavy atoms over time in the three replicates. (D) RMSFs of compound **18** heavy atoms in the three replicates. The atom numbers of atoms with higher RMSFs are reported in the two-dimensional depiction of the *p*-I-benzyl moiety. (E) RMSDs of the heavy atoms of the nucleotide scaffold (all heavy atoms except the *p*-I-benzyl) in the three replicates.

the compound **16**-hCD73 complex showed an H-bond between this atom and Arg395, which was not directly present in the case of compound **21** and did not persist during MD simulations. However, an examination of residues in contact with atom O4′ in the MD trajectories (Figure 7F) showed that Arg395 was in the proximity of the atom in nearly all of the simulations (all compounds, all replicates), suggesting that the local polar binding site environment was more favorable with O4′ present than for the (N)-methanocarba bicyclic ring.

In addition to these modeling studies, the availability of the X-ray structures reported here was the starting point of prospective molecular docking studies, aimed to suggest the synthesis of new compounds.[26,27,44] Docking of compound **24** (K_i ∼ 0.63 nM), among the most active in the series, confirmed a binding mode comparable to the crystallographic pose of compounds **16** and **21** but placed the primary charged amino group in the proximity of Lys97 (Figure 8A). This suggested a substitution of the primary amine with a carboxylate moiety, giving compound **27**, to exploit an ionic interaction with the protein Lys, as shown by the docking pose of the compound (Figure 8B). However, this did not result in an increase in the binding affinity (K_i ∼ 2.61 nM), and this could be explained by the solvent exposure of this possible ionic interaction.

In Situ *ecto*-5′-Nucleotidase Activity Assay. The effect of potent CD73 inhibitors on *ecto*-5′-nucleotidase activity in human tissues was evaluated in situ by using surgically removed human head and neck squamous cell carcinoma (HNSCC) and palatine tonsils[28] as appropriate enzyme sources. Staining of the HNSCC cryosections with hematoxylin and eosin (H&E) enabled the visualization of the main histological structures (Figure 9A). The tissue-specific distribution of AMPase activity and the expression level of CD73 in the tumor microenvironment (TME) were determined by using lead nitrate-based enzyme histochemistry (Figure 9B) and immunofluorescence staining (Figure 9C), respectively. Histological analysis of the HNSCC sample identified two different areas of differentiation, with significant AMPase activity and CD73 immunoreactivity being detected on nonkeratinized poorly differentiated squamous carcinoma cells (Figure 9, top insets), but not on well-differentiated squamous carcinoma cells and neoplastic cells (Figure 9, bottom insets). High CD73 activity was also detected on other benign components of the TME, including the basal epithelial layer, blood vessels, tumor-infiltrating leukocytes, and muscle cells. We have shown earlier that CD73 is also expressed in human tonsils, with high AMPase activity detected in the germinal centers, in connective tissues, and, to a lesser extent, in the interfollicular area (see also Figure 10B).[28,49]

https://doi.org/10.1021/acs.jmedchem.1c01852
J. Med. Chem. 2022, 65, 2409−2433

Journal of Medicinal Chemistry pubs.acs.org/jmc Article

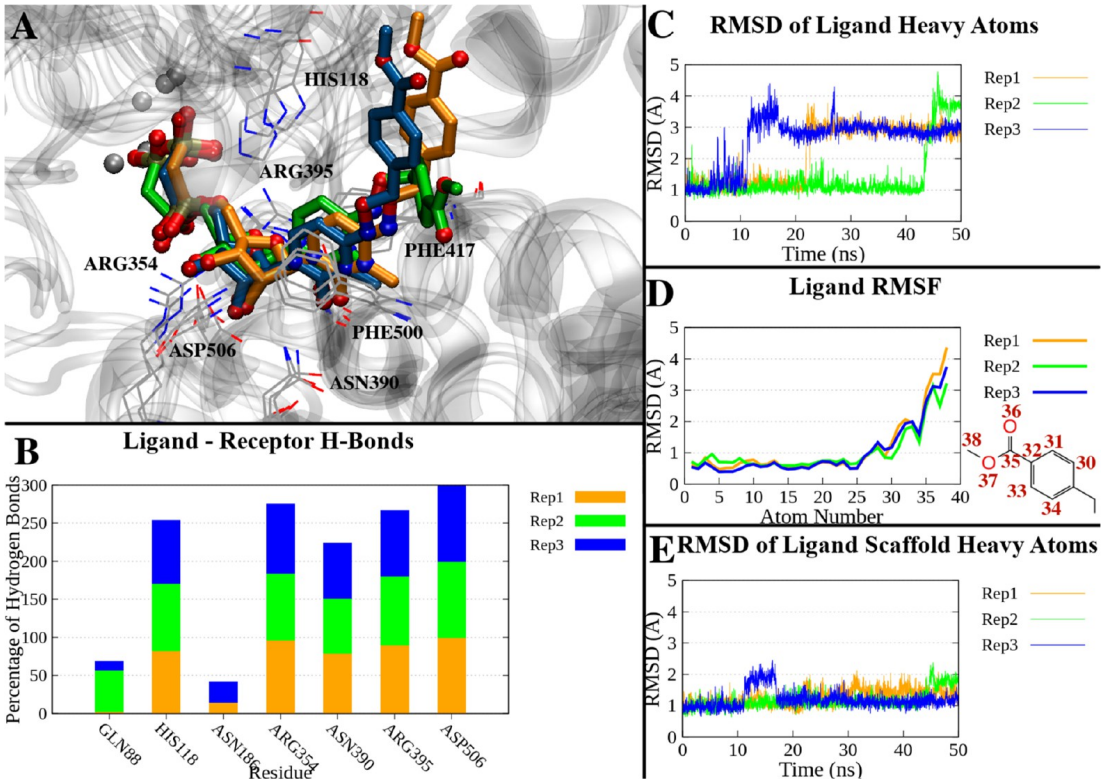


Figure 6. (A) Superposition of the last frames of three 50 ns trajectories of the compound **21**-hCD73 complex in the closed form. The trajectories have been aligned by superposing the Cα atoms with the initial state. Proteins are represented as a gray ribbon, interacting residues as gray lines, and ligands of replicates 1−3 as orange, green, and blue sticks, respectively. (B) Percentage of H-bonds between compound **21** and hCD73 residues during the three replicates. Only residues interacting with on average >10% of the simulations are shown. (C) RMSDs of compound **21** heavy atoms over time in the three replicates. (D) RMSFs of compound **21** heavy atoms in the three replicates. The atom numbers of atoms with higher RMSFs are reported in the two-dimensional depiction of the *p*-methoxycarbonyl-benzyl moiety. (E) RMSDs of the heavy atoms of the nucleotide scaffold (all heavy atoms except the *p*-methoxycarbonyl-benzyl) in the three replicates.

Subsequent competitive analysis of CD73-mediated AMPase activities was performed by incubating human tissue cryosections with AMP in the presence of $Pb(NO_3)_2$ and different concentrations of CD73 inhibitors. The lead orthophosphate precipitated during the course of *ecto*-5′-nucleotidase activity was visualized as a brown deposit. Figure 10 depicts representative images of tumor (panel A) and tonsillar (panel B) AMP-specific staining determined in the absence (control) and presence of the indicated compounds. Given the uneven distribution of CD73 in the tissues, we selected the same matched areas of poorly differentiated squamous carcinoma cells (Figure 10A) and tonsillar germinal centers (B) in the control and treated samples and further compared their mean pixel intensities using QuPath version 0.2.3 (Table S3). Treatment of tissue cryosections with the increasing concentrations of compounds **18** and **20** (50−250 nM), but not with equimolar concentrations of classical CD73 inhibitor AOPCP (compound **1**), decreased the catalytic activities of both tumor and tonsillar CD73 in a concentration-dependent manner (Figure 10C).

CONCLUSIONS

We have explored the SAR of nucleotide inhibitors of CD73 in the pyrimidine series, building on our recent publication and focusing mainly on cytidine functionalization at the N^4 position.[28] We have substantially improved the potency compared to those of our previous inhibitors and demonstrated efficacy in actual cancer tissue. Although this study is restricted to various substituted N^4-benzyloxy groups, future work will evaluate the N^4 position more broadly. This work also contains extensive structural characterization, including four new X-ray structures with our inhibitors bound. Molecular dynamics identified stabilizing interactions and predicted conformational diversity. The most potent analogue **18** contained 4-iodo substitution of the N^4-benzyloxy group with a K_i value of 0.436 nM, which represents a 24-fold enhancement over **9**. Many of the substituted benzyl derivatives presented here are 10−20-fold more potent than the previously most potent inhibitors in this series. Inclusion of a ribose substitution that enforces an N conformation, similar to that present in crystallographic CD73 structures,[33] greatly decreased the inhibitory potency. Thus, the rigid methanocarba ring system is not a means of enhancing the pyrimidine nucleotide potency at CD73. Furthermore, we have introduced additional functionality that can be useful in bivalent molecular probes.[50,51] The utility of novel compounds as potential anticancer drugs was further ascertained by their ability to efficiently block CD73 activity in the human HNSCC tissue in situ. The ability to potently inhibit CD73 using pyrimidine-

https://doi.org/10.1021/acs.jmedchem.1c01852
J. Med. Chem. 2022, 65, 2409−2433

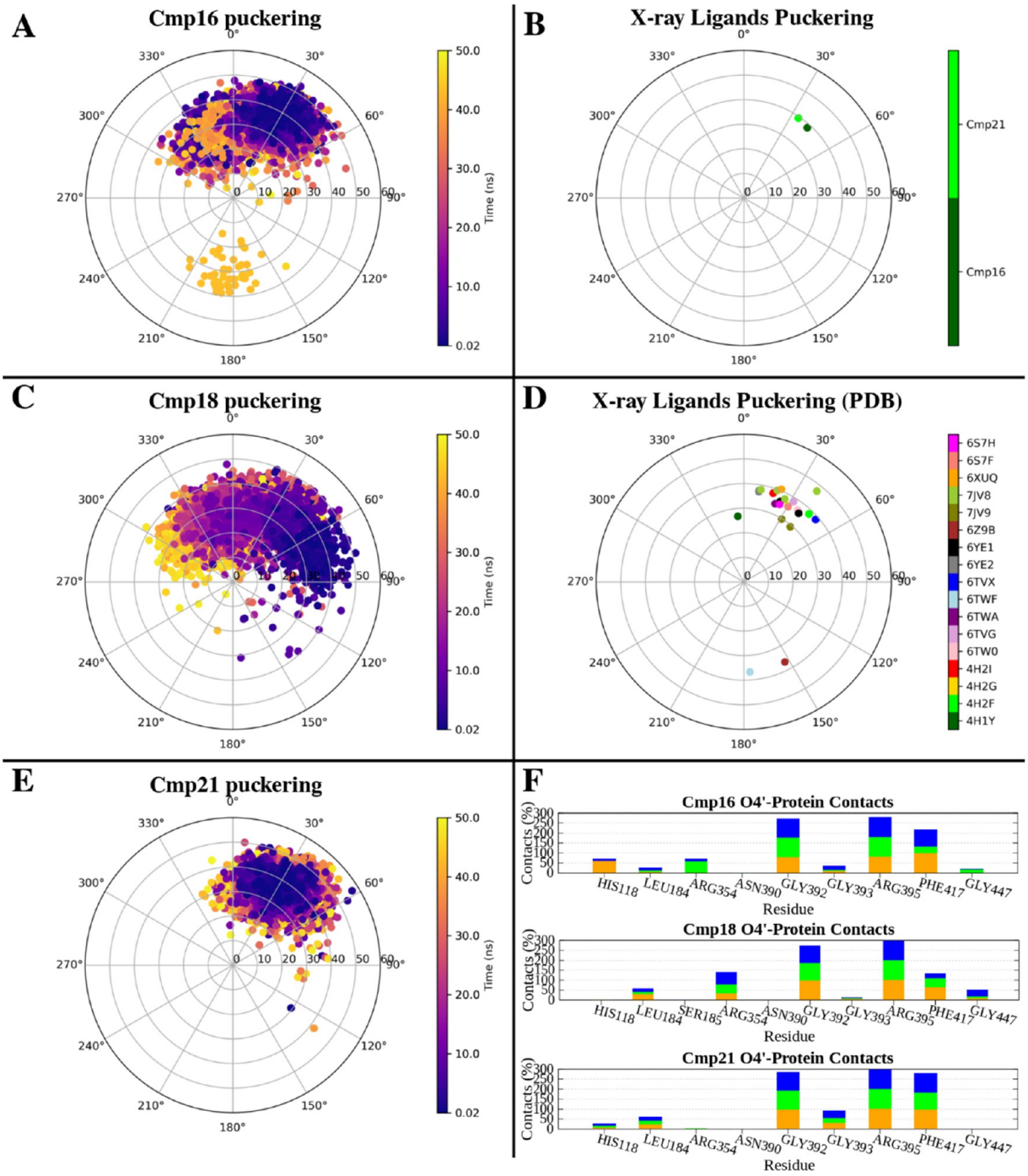


Figure 7. (A, C, and E) Puckering of the ribose ring of compounds **16**, **18**, and **21**, respectively, during MD simulations (combination of three 50 ns replicates). The phase angle of pseudorotation (P) and degree of deformation of the plane (ν_{max}) are reported on the angular and radial coordinates, respectively. (B) Puckering of the ribose ring of compounds **16** (dark green) and **21** (light green), in the X-ray structures. (D) Puckering of all of the nucleoside/nucleotide-like ligands bound to hCD73 deposited so far in the PDB. (F) Number of contacts (percentage of frames) between the O4′ atom of compounds **16**, **18**, and **21** and hCD73 residues during the three MD replicates.

based nucleotide analogues provides new opportunities for translational studies for cancer treatment.

EXPERIMENTAL PROCEDURES

Chemical Synthesis. *Reagents and Instrumentation.* All reagents were of analytical grade and purchased from Sigma-Aldrich (St. Louis, MO). Anhydrous solvents were obtained directly from

https://doi.org/10.1021/acs.jmedchem.1c01852
J. Med. Chem. 2022, 65, 2409−2433

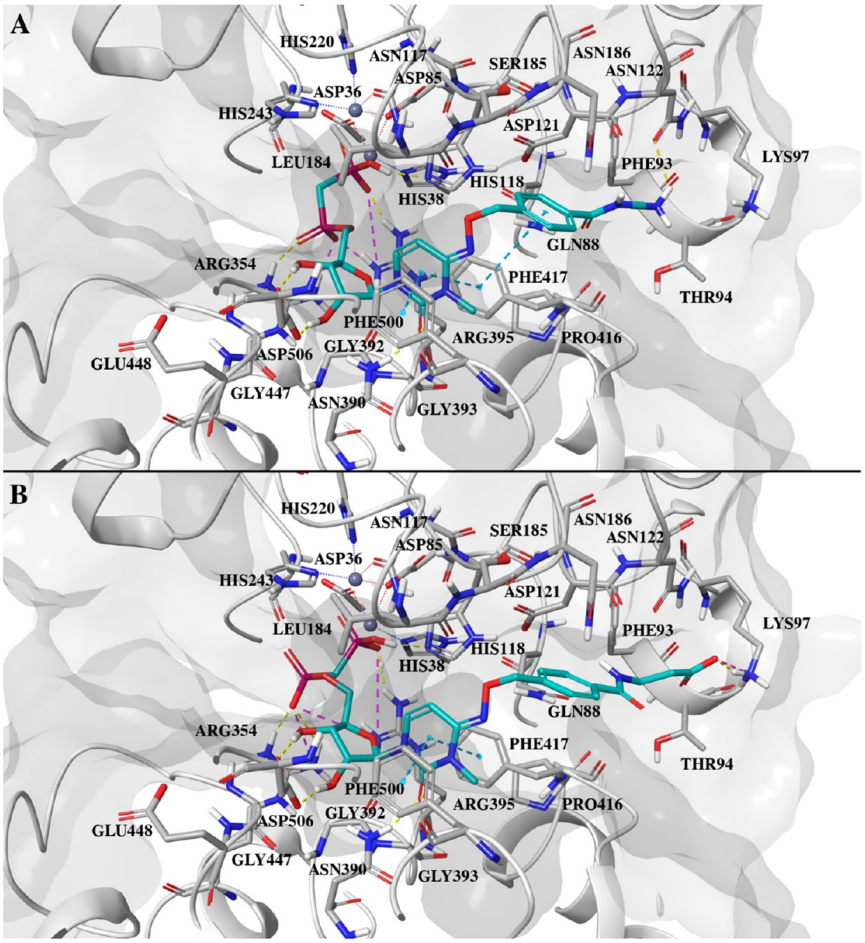


Figure 8. (A) Docking pose of compound **24** at the closed form hCD73 active site. (B) Docking pose of compound **27** at the hCD73 active site. In both cases, the ligand is shown as cyan sticks, with the protein colored gray. Protein residues within 4 Å of the ligand are shown as sticks. Hydrogen bonds are shown as yellow dashed lines, ionic interactions as magenta dashed lines, and $\pi-\pi$ interactions as cyan dashed lines.

commercial sources. All reactions were carried out under a nitrogen atmosphere using anhydrous solvents. Room temperature (rt) refers to 25 ± 2 °C. NMR spectra were recorded on a Bruker 400 MHz spectrometer. Chemical shifts are given in parts per million (δ), calibrated to the residual solvent signals or TMS and frequency calibrated internally (Xi) for ^{31}P NMR. High-resolution mass measurements were performed on a Micromass/Waters LCT Premier Electrospray Time of Flight (TOF) mass spectrometer coupled with a Waters HPLC system, unless noted. Ion-exchange chromatography (IE-LPLC) was performed using 10 mm × 100 mm Pharmacia column packed with GE Bioscience SOURCE 15Q resins, which was connected to an Agilent 1100 HPLC system. The IE-LPLC mobile phase condition is as follows: 100% H_2O from 0 to 5 min, 0% to 100% linear gradient of 1 M TEAB/H_2O from 5 to 40 min, eluent flow rate of 2 mL/min. RP-HPLC was performed using a Phenomenex Luna 5 μm C18(2)100A, AXIA, 21.2 mm × 250 mm column. Purity was determined using an Agilent Eclipse XDB-C18, 5 μm, 4.6 mm × 250 mm column and a linear gradient from 0% to 100% acetonitrile/5 mM tetrabutylammonium dihydrogen phosphate (TBAP) as the mobile phase at a flow rate of 1 mL/min. All of the derivatives tested for the biological activity showed >95% purity by HPLC analysis (detection at 254 nm).

*General Procedure for the Synthesis of Nucleotides (**10**–**30**).* To a solution of methylenebis(phosphonic dichloride) (3 equiv) in trimethylphosphate (3 mL) at 0 °C was added a solution of the desired compound (1 equiv) in trimethylphosphate (2 mL) at 0 °C. The so obtained mixture was stirred at 0 °C for 3 h, and then a sample was withdrawn for LC-MS to check the disappearance of the nucleoside. Then, the reaction was quenched with 7 mL of a cold 1 M aqueous triethylammonium hydrogen carbonate buffer solution (pH 8.4–8.6), and the mixture stirred at rt for 1 h. The solvent was removed by lyophilization, and the residue dissolved in water and purified first by ion-exchange chromatography and then by RP-HPLC to afford the pure product.

*N^4-(2-Chlorobenzyloxy)-3-methylcytidine-5′-α,β-methylenediphosphonate Triethylammonium Salt (**10**).* The product was obtained as a white solid after lyophilization (9.8 mg, 20%; RP-HPLC acetonitrile/10 mM triethylammonium acetate, 15/85 to 35/65 in 40 min at a rate of 5 mL/min): ^{1}H NMR (D_2O, 400 Hz) δ 7.45–7.55 (m, 2H), 7.29–7.40 (m, 3H), 6.44 (d, J = 8.3 Hz, 1H), 5.93 (d, J = 4.5 Hz, 1H), 5.12 (s, 2H), 4.35 (s, 2H), 4.21 (s, 1H), 4.10 (s, 2H), 3.11–3.22 (m, 15H), 2.18 (t, J = 19.7 Hz, 2H), 1.26 (t, J = 7.1 Hz, 18H); ^{31}P NMR (D_2O) δ 18.20, 14.21; HRMS calcd for $C_{18}H_{23}ClN_3O_{11}P_2$ $(M-H)^-$ 554.0496, found 554.0490.

*N^4-(3-Chlorobenzyloxy)-3-methylcytidine-5′-α,β-methylenediphosphonate Triethylammonium Salt (**11**).* The product was obtained as a white solid after lyophilization (3.7 mg, 2.0%; RP-HPLC acetonitrile/10 mM triethylammonium acetate, 15/85 to 35/65 in 40 min at a rate of 5 mL/min): ^{1}H NMR (D_2O, 400 Hz) δ 7.49 (s, 1H), 7.32–7.42 (m, 3H), 6.45 (d, J = 8.4 Hz, 1H), 5.93 (d, J = 4.9 Hz, 1H), 5.03 (s, 2H), 4.30–4.39 (m, 2H), 4.21 (s, 1H), 4.12 (s, 2H), 3.11–3.29 (m, 9H), 2.18 (t, J = 19.7 Hz, 2H), 1.26 (t, J = 6.7 Hz,

https://doi.org/10.1021/acs.jmedchem.1c01852
J. Med. Chem. 2022, 65, 2409–2433

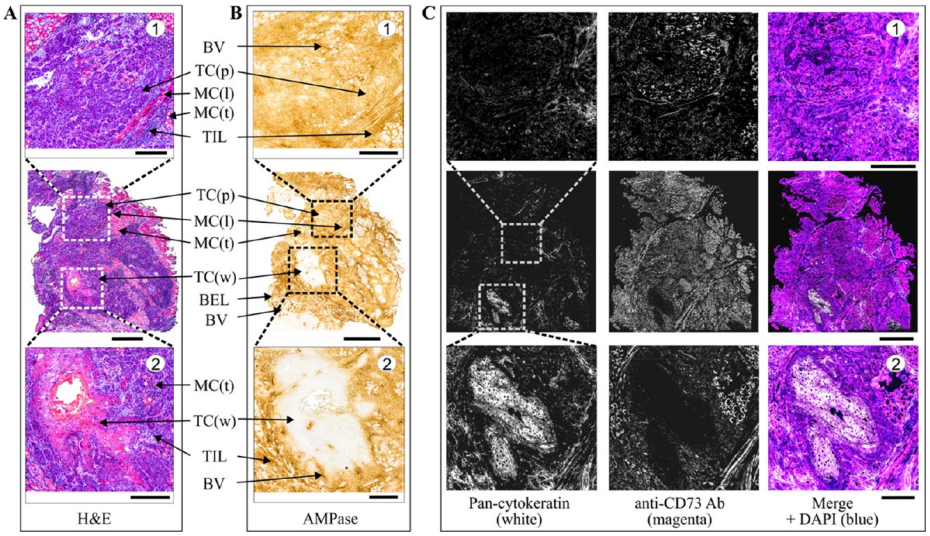


Figure 9. Distribution of AMPase activity and the expression level of CD73 in the TME. A tumor was obtained from the patient with squamous cell carcinoma of mobile tongue. (A) Staining of tissue cryosections with H&E enabled the visualization of the malignant and benign cells in the TME. (B) Tissue-specific distribution of AMPase activity determined by incubating the slides with 100 μM AMP in the presence of $Pb(NO_3)_2$ followed by microscopic detection of the nucleotide-derived inorganic phosphate (P_i) as a brown precipitate. (C) For immunofluorescence staining, tumor sections were stained with the anti-CD73 antibody, together with Alexa Fluor-488-conjugated pan-cytokeratin mAb serving as a marker of well-differentiated epithelial tumor cells. Single channels are shown in grayscale, and the right-hand panels display merged images with nuclei counterstained with DAPI. Abbreviations: BEL, basal epithelial layer; BV, blood vessels; MC(l), muscular cells (longitudinally oriented); MC(t), muscular cells (transverse orientation); TC(p), tumor cells (poorly differentiated); TC(w), tumor cells (well differentiated); TIL, tumor-infiltrating leukocytes. Scale bars are 1 mm (A–C) and 300 μm (top and bottom insets).

9H); ^{31}P NMR (D_2O) δ 20.50, 12.50; HRMS calcd for $C_{18}H_{23}ClN_3O_{11}P_2$ $(M - H)^-$ 554.0496, found 554.0503.

*N^4-[(3-Trifluoromethyl)benzyloxy]-3-methylcytidine-5′-α,β-methylenediphosphate Triethylammonium Salt (**12**).* The product was obtained as a white solid after lyophilization (4.2 mg, 9.5%; RP-HPLC acetonitrile/10 mM triethylammonium acetate, 15/85 to 35/65 in 40 min at a rate of 5 mL/min): ^{1}H NMR (D_2O, 400 Hz) δ 7.64 (s, 1H), 7.56 (d, J = 7.6 Hz, 2H), 7.45 (t, J = 7.6 Hz, 1H), 7.22 (d, J = 8.3 Hz, 1H), 6.32 (d, J = 8.3 Hz, 1H), 5.80 (d, J = 4.7 Hz, 1H), 4.95 (s, 2H), 4.20 (d, J = 4.8 Hz, 2H), 4.08 (s, 1H), 3.97 (s, 2H), 3.00–3.11 (m, 15H), 2.02 (t, J = 19.7 Hz, 2H), 1.13 (t, J = 7.1 Hz, 18H); ^{31}P NMR (D_2O) δ 29.00, 24.00; ^{19}F NMR (D_2O) δ −62.40; HRMS calcd for $C_{19}H_{23}F_3N_3O_{11}P_2$ $(M - H)^-$ 588.0760, found 588.0756.

*N^4-[(3-Methyl)benzyloxy]-3-methylcytidine-5′-α,β-methylenediphosphonate Triethylammonium Salt (**13**).* The product was obtained as a white solid after lyophilization (21.1 mg, 40%; RP-HPLC acetonitrile/10 mM triethylammonium acetate, 10/90 to 25/75 in 40 min at a rate of 5 mL/min): ^{1}H NMR (D_2O, 400 Hz) δ 7.21–7.25 (m, 3H), 7.16 (d, 2H, J = 7.8 Hz), 6.32 (d, 1H, J = 8.4 Hz), 5.84 (d, 1H, J = 5.0 Hz), 4.87 (s, 2H), 4.22–4.24 (m, 2H), 4.11 (s, 1H), 4.01–4.02 (m, 2H), 3.06–3.12 (m, 15H), 2.23 (s, 3H), 2.07 (t, 2H, J = 19.8 Hz), 1.17 (t, 18H, J = 7.3 Hz); ^{31}P NMR (D_2O) δ 18.23, 14.66; HRMS calcd for $C_{19}H_{26}N_3O_{11}P_2$ $(M - H)^-$ 534.1043, found 534.1053.

*N^4-[(3-Ethyl)benzyloxy]-3-methylcytidine-5′-α,β-methylenediphosphonate Triethylammonium Salt (**14**).* The product was obtained as a white solid after lyophilization (24.6 mg, 37%; RP-HPLC acetonitrile/10 mM triethylammonium acetate, 10/90 to 25/75 in 40 min at a rate of 5 mL/min): ^{1}H NMR (D_2O, 400 Hz) δ 7.29 (d, 2H, J = 7.9 Hz), 7.18–7.23 (m, 3H), 6.32 (d, 1H, J = 8.3 Hz), 5.84 (d, 1H, J = 5.0 Hz), 4.87 (s, 2H), 4.20–4.24 (m, 2H), 4.10 (s, 1H), 4.00–4.02 (m, 2H), 3.06–3.11 (m, 15H), 2.54 (dd, 2H, J = 7.6, 15.2 Hz), 2.07 (t, 2H, J = 19.8 Hz), 1.17 (t, 18H, J = 7.3 Hz), 1.08 (t, 3H, J = 7.6 Hz); ^{31}P NMR (D_2O) δ 18.21, 14.67; HRMS calcd for $C_{20}H_{28}N_3O_{11}P_2$ $(M - H)^-$ 548.1199, found 548.1209.

*N^4-(4-Fluorobenzyloxy)-3-methylcytidine-5′-α,β-methylenediphosphonate Triethylammonium Salt (**15**).* The product was obtained as a white solid after lyophilization (12.9 mg, 27.0%; RP-HPLC acetonitrile/10 mM triethylammonium acetate, 15/85 to 35/65 in 40 min at a rate of 5 mL/min): ^{1}H NMR (D_2O, 400 Hz) δ 7.36 (t, J = 6.8 Hz, 2H), 7.22 (d, J = 7.7 Hz, 1H), 7.02 (t, J = 8.7 Hz, 2H), 6.30 (d, J = 8.1 Hz, 1H), 5.81 (s, 1H), 4.84 (s, 2H), 4.16–4.27 (m, 2H), 3.91–4.09 (m, 3H), 3.00–3.12 (m, 15H), 2.00 (t, J = 19.7 Hz, 2H), 1.13 (t, J = 7.2 Hz, 18H); ^{31}P NMR (D_2O) δ 21.00, 13.00; ^{19}F NMR (D_2O) δ −75.50; HRMS calcd for $C_{18}H_{23}FN_3O_{11}P_2$ $(M - H)^-$ 538.0792, found 538.0789.

*N^4-(4-Chlorobenzyloxy)-3-methylcytidine-5′-α,β-methylenediphosphonate Triethylammonium Salt (**16**).* The product was obtained as a white solid after lyophilization (35.4 mg, 33.0%; RP-HPLC acetonitrile/10 mM triethylammonium acetate, 15/85 to 35/65 in 40 min at a rate of 5 mL/min): ^{1}H NMR (D_2O, 400 Hz) δ 7.23 (s, 4H), 7.19 (d, J = 8.4 Hz, 1H), 6.23 (d, J = 8.3 Hz, 1H), 5.79 (d, J = 5.0 Hz, 1H), 4.82 (s, 2H), 4.18–4.22 (m, 2H), 4.08 (d, J = 1.8 Hz, 1H), 4.12 (s, 2H), 3.98–4.00 (m, 2H), 3.08 (dd, J = 7.3, 14.6 Hz, 12H), 2.99 (s, 3H), 2.06 (t, J = 19.7 Hz, 2H), 1.12 (t, J = 7.3 Hz, 18H); ^{31}P NMR (D_2O) δ 22.00, 15.00; HRMS calcd for $C_{18}H_{23}ClN_3O_{11}P_2$ $(M - H)^-$ 554.0496, found 554.0501.

*N^4-(4-Bromobenzyloxy)-3-methylcytidine-5′-α,β-methylenediphosphonate Triethylammonium Salt (**17**).* The product was obtained as a white solid after lyophilization (3.5 mg, 20.0%; RP-HPLC acetonitrile/10 mM triethylammonium acetate, 15/85 to 35/65 in 40 min at a rate of 5 mL/min): ^{1}H NMR (D_2O, 400 Hz) δ 7.50 (d, J = 8.0 Hz, 2H), 7.28 (d, J = 8.16 Hz, 3H), 6.36 (d, J = 8.2 Hz, 1H), 5.82 (d, J = 4.5 Hz, 1H), 4.91 (s, 2H), 4.31 (s, 1H), 4.22 (s, 1H), 4.00–4.12 (m, 3H), 3.10 (d, J = 7.2 Hz, 21H), 1.95 (t, J = 19.1 Hz, 2H), 1.20 (s, 27H); ^{31}P NMR (D_2O) δ 21.00, 12.00; HRMS calcd for $C_{18}H_{23}BrN_3O_{11}P_2$ $(M - H)^-$ 597.9991, found 597.9988.

*N^4-(4-Iodobenzyloxy)-3-methylcytidine-5′-α,β-methylenediphosphonate Triethylammonium Salt (**18**).* The product was obtained as a white solid after lyophilization (8.2 mg, 22.1%; RP-HPLC acetonitrile/10 mM triethylammonium acetate, 15/85 to 35/65 in 40 min at a rate of 5 mL/min): ^{1}H NMR (D_2O, 400 Hz) δ 7.69 (d, J = 8.0 Hz, 2H), 7.24 (d, J = 8.2 Hz, 1H), 7.12 (d, J = 8.0 Hz, 2H), 6.32 (d, J = 8.2 Hz, 1H), 5.82 (d, J = 5.0 Hz, 1H), 4.88 (s, 2H), 4.25

https://doi.org/10.1021/acs.jmedchem.1c01852
J. Med. Chem. 2022, 65, 2409–2433

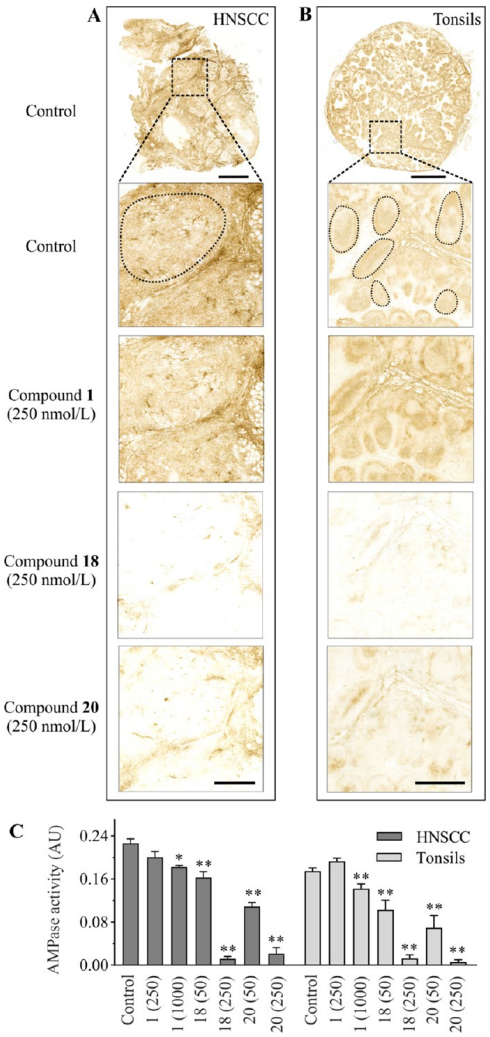


Figure 10. Effect of CD73 inhibitors on AMPase activity in human tumors and tonsils. The effect of CD73 inhibitors on AMPase activity was determined in situ by incubating human (A) HNSCC and (B) tonsillar cryosections with 100 μM AMP and 1.5 mM $Pb(NO_3)_2$ in the absence (Control) and presence of the indicated concentrations of tested compounds. AMPase activity was determined in the selected regions, corresponding to pan-cytokeratin$^-$/CD73$^+$ poorly differentiated tumor cells (A) and CD73$^+$ tonsillar germinal centers (B). (C) Mean pixel intensities of AMP-specific brown staining were quantified in the selected regions using QuPath version 0.2.3 and expressed as arbitrary units (AU) (mean ± standard error of the mean). Compared with the control, *P < 0.05 and **P < 0.01, determined by one-way analysis of variance with Dunnett's multiple-comparison test. Scale bars are 1 mm (A, top image; B, inset), 4 mm (B, top image), and 300 μm (A, insets).

(t, J = 5.5 Hz, 2H), 4.12 (s, 1H), 4.01 (s, 2H), 3.10 (t, J = 6.7 Hz, 6H), 3.03 (s, 3H), 2.05 (t, J = 19.5 Hz, 2H), 1.18 (t, J = 6.6 Hz, 9H); ^{31}P NMR (D_2O) δ 23.00, 12.00; HRMS calcd for $C_{18}H_{23}IN_3O_{11}P_2$ (M − H)$^-$ 645.9852, found 645.9861.

*N^4-[4-(Trifluoromethyl)benzyloxy]-3-methylcytidine-5′-α,β-methylenediphosphonate Triethylammonium Salt (**19**).* The product was obtained as a white solid after lyophilization (1.4 mg, 10.0%; RP-HPLC acetonitrile/10 mM triethylammonium acetate, 15/85 to 35/65 in 40 min at a rate of 5 mL/min): ^{1}H NMR (D_2O, 400 Hz) δ 7.58 (d, J = 6.3 Hz, 2H), 7.43 (d, J = 6.3 Hz, 2H), 7.22 (d, J = 6.5 Hz, 1H), 6.32 (d, J = 6.6 Hz, 1H), 5.79 (d, J = 3.9 Hz, 1H), 4.94 (s, 2H), 4.23 (s, 1H), 4.17 (d, J = 4.1 Hz, 1H), 4.00−4.05 (m, 2H), 3.92 (s, 1H), 3.02 (dd, J = 5.8, 11.6 Hz, 6H), 2.98 (s, 3H), 1.91 (t, J = 15.2 Hz, 2H), 1.10 (t, J = 5.8 Hz, 9H); ^{31}P NMR (D_2O) δ 22.00, 12.50; ^{19}F NMR (D_2O) δ −62.00; HRMS calcd for $C_{19}H_{23}F_3N_3O_{11}P_2$ (M − H)$^-$ 588.0760, found 588.0755.

*N^4-[4-(Pentafluorosulfanyl)benzyloxy]-3-methylcytidine-5′-α,β-methylenediphosphonate Triethylammonium Salt (**20**).* The product was obtained as a white solid after lyophilization (8.0 mg, 23.0%; RP-HPLC acetonitrile/10 mM triethylammonium acetate, 15/85 to 35/65 in 40 min at a rate of 5 mL/min): ^{1}H NMR (D_2O, 400 Hz) δ 7.75 (d, J = 8.6 Hz, 2H), 7.46 (d, J = 8.1 Hz, 2H), 7.23 (d, J = 8.3 Hz, 1H), 6.37 (d, J = 8.3 Hz, 1H), 5.82 (d, J = 5.0 Hz, 1H), 4.99 (s, 2H), 4.22 (dd, J = 4.4, 11.8 Hz, 2H), 4.11 (s, 1H), 4.00 (s, 2H), 3.09 (dd, J = 7.3, 14.6 Hz, 6H), 3.02 (s, 3H), 2.05 (t, J = 19.7 Hz, 2H), 1.14 (t, J = 14.6 Hz, 9H); ^{31}P NMR (D_2O) δ 22.00, 12.00; ^{19}F NMR (D_2O) δ −75.55; HRMS calcd for $C_{18}H_{23}F_5N_3O_{11}P_2S$ (M − H)$^-$ 646.0449, found 646.0452.

*N^4-[4-(Methoxycarbonyl)benzyloxy]-3-methylcytidine-5′-α,β-methylenediphosphonate Triethylammonium Salt (**21**).* The product was obtained as a white solid after lyophilization (38.7 mg, 32.0%; RP-HPLC acetonitrile/10 mM triethylammonium acetate, 15/85 to 30/70 in 40 min at a rate of 5 mL/min): ^{1}H NMR (D_2O, 400 Hz) δ 7.80 (d, J = 8.0 Hz, 2H), 7.33 (d, J = 8.0 Hz, 2H), 7.20 (d, J = 8.3 Hz, 1H), 6.30 (d, J = 8.3 Hz, 1H), 5.77 (d, J = 5.0 Hz, 1H), 4.91 (s, 2H), 4.21 (t, J = 5.2 Hz, 2H), 4.07 (s, 1H), 3.98 (s, 2H), 3.74 (s, 3H), 3.09 (dd, J = 7.1, 14.4 Hz, 12H), 2.92 (s, 3H), 2.04 (t, J = 19.7 Hz, 2H), 1.13 (t, J = 7.2 Hz, 18H); ^{31}P NMR (D_2O) δ 17.50, 14.00; HRMS calcd for $C_{20}H_{26}N_3O_{13}P_2$ (M − H)$^-$ 578.0941, found 578.0943.

*N^4-[4-(Carbonyl)benzyloxy]-3-methylcytidine-5′-α,β-methylenediphosphonate Triethylammonium Salt (**22**).* The product was obtained as a white solid after lyophilization (11.9 mg, 29.0%; RP-HPLC acetonitrile/10 mM triethylammonium acetate, 5/95 to 15/85 in 40 min at a rate of 5 mL/min): ^{1}H NMR (D_2O, 400 Hz) δ 7.75 (d, J = 7.8 Hz, 2H), 7.39 (d, J = 7.7 Hz, 2H), 7.22 (d, J = 8.2 Hz, 1H), 6.37 (d, J = 8.2 Hz, 1H), 5.83 (s, 1H), 4.96 (s, 2H), 4.23 (s, 2H), 4.09 (s, 1H), 4.00 (s, 2H), 3.74 (s, 3H), 3.06 (dd, J = 7.2, 14.3 Hz, 21H), 2.05 (t, J = 19.6 Hz, 2H), 1.14 (t, J = 7.2 Hz, 27H); ^{31}P NMR (D_2O) δ 21.00, 15.40; HRMS calcd for $C_{19}H_{24}N_3O_{13}P_2$ (M − H)$^-$ 564.0784, found 564.0781.

*N^4-[4-(Carbamoyl)benzyloxy]-3-methylcytidine-5′-α,β-methylenediphosphate Triethylammonium Salt (**23**).* The product was obtained as a white solid after lyophilization (1.6 mg, 9.6%; RP-HPLC acetonitrile/10 mM triethylammonium acetate, 5/95 to 15/85 in 40 min at a rate of 5 mL/min): ^{1}H NMR (D_2O, 400 Hz) δ 7.71 (d, J = 8.1 Hz, 2H), 7.45 (d, J = 8.1 Hz, 2H), 7.25 (d, J = 8.3 Hz, 1H), 6.37 (d, J = 8.4 Hz, 1H), 5.83 (d, J = 5.3 Hz, 1H), 4.98 (s, 2H), 4.21−4.26 (m, 2H), 4.09 (s, 1H), 4.01 (s, 2H), 3.08 (d, J = 7.0 Hz, 6H), 3.05 (s, 3H), 2.02 (t, J = 19.9 Hz, 2H), 1.16 (t, J = 6.9 Hz, 9H); ^{31}P NMR (D_2O) δ 19.90, 13.50; HRMS calcd for $C_{19}H_{25}N_4O_{12}P_2$ (M − H)$^-$ 563.0944, found 563.0950.

*N^4-[4-[(2-Aminoethyl)carbamoyl]benzyloxy}-3-methylcytidine-5′-α,β-methylenediphosphonate Triethylammonium Salt (**24**).* The product was obtained as a white solid after lyophilization (4.1 mg, 10.5%, two-step yield; RP-HPLC acetonitrile/10 mM triethylammonium acetate, 5/95 to 15/85 in 40 min at a rate of 5 mL/min): ^{1}H NMR (D_2O, 400 Hz) δ 7.69 (d, J = 8.2 Hz, 2H), 7.45 (d, J = 8.1 Hz, 2H), 7.21 (d, J = 8.4 Hz, 1H), 6.28 (d, J = 8.3 Hz, 1H), 5.80 (d, J = 4.8 Hz, 1H), 4.96 (s, 2H), 4.22 (d, J = 4.7 Hz, 1H), 4.18 (t, J = 4.9 Hz, 1H), 4.01 (s, 2H), 3.60 (t, J = 5.7 Hz, 2H), 3.16−3.04 (m, 17H), 2.00 (t, J = 18.7 Hz, 2H), 1.17 (t, J = 7.3 Hz, 18H); ^{31}P NMR (D_2O) δ 20.00, 13.00; HRMS calcd for $C_{21}H_{30}N_5O_{12}P_2$ (M − H)$^-$ 606.1366, found 606.1362.

*N^4-[4-[(2-Aminobutyl)carbamoyl]benzyloxy}-3-methylcytidine-5′-α,β-methylenediphosphonate Triethylammonium Salt (**25**).* The product was obtained as a white solid after lyophilization (1.8 mg, 8.0%, two-step yield; RP-HPLC acetonitrile/10 mM triethylammonium acetate, 5/95 to 15/85 in 40 min at a rate of 5 mL/min): ^{1}H NMR (D_2O, 400 Hz) δ 7.66 (d, J = 8.3 Hz, 2H), 7.46 (d, J = 8.3 Hz,

https://doi.org/10.1021/acs.jmedchem.1c01852
J. Med. Chem. 2022, 65, 2409−2433

2H), 7.27 (d, J = 8.3 Hz, 1H), 6.36 (d, J = 8.3 Hz, 1H), 5.85 (d, J = 5.2 Hz, 1H), 4.99 (s, 2H), 4.20−4.28 (m, 2H), 4.12 (s, 1H), 4.03 (d, J = 5.0 Hz, 2H), 3.35 (t, J = 6.1 Hz, 2H), 3.07−3.15 (m, 4H), 2.95 (t, J = 7.1 Hz, 2H), 2.04 (t, J = 19.2 Hz, 2H), 1.63 (d, J = 3.04 Hz, 4H), 1.19 (t, J = 7.2 Hz, 5H); ^{31}P NMR (D_2O) δ 19.92, 13.29; HRMS calcd for $C_{23}H_{34}N_5O_{12}P_2$ $(M - H)^-$ 634.1679, found 634.1685.

*N^4-{4-[(3-Ethoxy-3-oxopropyl)carbamoyl]benzyloxy}-3-methylcytidine-5′-α,β-methylenediphosphonate Triethylammonium Salt (**26**).* The product was obtained as a white solid after lyophilization (4.2 mg, 10.4%; RP-HPLC acetonitrile/10 mM triethylammonium acetate, 15/85 to 35/65 in 40 min at a rate of 5 mL/min): ^{1}H NMR (D_2O, 400 Hz) δ 7.60 (d, J = 8.2 Hz, 2H), 7.41 (d, J = 8.1 Hz, 2H), 7.24 (d, J = 8.5 Hz, 1H), 6.35 (d, J = 8.4 Hz, 1H), 5.81 (d, J = 5.2 Hz, 1H), 4.95 (s, 2H), 4.18−4.24 (m, 2H), 3.99−4.08 (m, 4H), 3.54 (t, J = 6.4 Hz, 2H), 3.02−3.09 (m, 15 H), 2.07 (t, J = 6.4 Hz, 2H), 2.01 (t, J = 19.6 Hz, 2H), 1.14 (t, J = 7.3 Hz, 18H), 1.06 (t, J = 7.1 Hz, 3H); ^{31}P NMR (D_2O) δ 19.15, 13.79; HRMS calcd for $C_{24}H_{35}N_4O_{14}P_2$ $(M - H)^-$ 665.1625, found 665.1625.

*N^4-{4-[(2-Carboxyethyl)carbamoyl]benzyloxy}-3-methylcytidine-5′-α,β-methylenediphosphonate Triethylammonium Salt (**27**).* The product was obtained as a white solid after lyophilization (3.3 mg, 9.1%; RP-HPLC acetonitrile/10 mM triethylammonium acetate, 10/90 to 35/65 in 40 min at a rate of 5 mL/min): ^{1}H NMR (D_2O, 400 Hz) δ 7.61 (d, J = 8.2 Hz, 2H), 7.40 (d, J = 8.1 Hz, 2H), 7.23 (d, J = 8.5 Hz, 1H), 6.35 (d, J = 8.4 Hz, 1H), 5.78 (d, J = 5.2 Hz, 1H), 4.94 (s, 2H), 4.26 (t, J = 4.6 Hz, 1H), 4.19 (t, J = 5.1 Hz, 1H), 3.96−4.05 (m, 3H), 3.45 (t, J = 7.0 Hz, 2H), 3.01−3.05 (m, 21H), 2.36 (t, J = 7.1 Hz, 2H), 1.92 (t, J = 19.5 Hz, 2H), 1.13 (t, J = 6.6 Hz, 27H); ^{31}P NMR (D_2O) δ 21.66, 11.49; HRMS calcd for $C_{22}H_{29}N_4O_{14}P_2$ $(M - H)^-$ 635.1155, found 635.1162.

*{[({(2R,3S,4R,5S)-4-[2,4-Dioxo-3,4-dihydropyrimidin-1(2H)-yl]-2,3-dihydroxy-1λ^5-bicyclo[3.1.0]hexan-1-yl}methoxy)(hydroxy)-phosphoryl]methyl}phosphonic Acid Triethylammonium Salt (**28**).* The product was obtained as a white solid after lyophilization (1.6 mg, 6.1%; RP-HPLC acetonitrile/10 mM triethylammonium acetate, 0/100 to 10/90 in 40 min at a rate of 5 mL/min): ^{1}H NMR (D_2O, 400 Hz) δ 7.91 (d, J = 7.8 Hz, 1H), 5.82 (d, J = 7.8 Hz, 1H), 4.28 (dd, J = 5.1, 11.0 Hz, 1H), 3.86 (d, J = 6.6 Hz, 1H), 3.70 (d, J = 11.0 Hz, 1H), 3.60 (dd, J = 5.2, 10.5 Hz, 1H), 2.55−3.30 (sbr, 6H), 2.04 (t, J = 19.8 Hz, 2H), 1.48 (d, J = 7.8 Hz, 1H), 1.14−1.25 (m, 11H), 0.81 (d, J = 7.3 Hz, 1H); ^{31}P NMR (D_2O) δ 21.00, 13.03; HRMS calcd for $C_{12}H_{18}N_2O_{10}P_2$ $(M - H)^-$ 411.0358, found 411.0355.

*[({[(2R,3S,4R,5S)-4-(4-{[(4-Chlorobenzyl)oxy]imino}-3-methyl-2-oxo-3,4-dihydropyrimidin-1(2H)-yl)-2,3-dihydroxy-1λ^5-bicyclo-[3.1.0]hexan-1-yl]methoxy}(hydroxy)phosphoryl)methyl]-phosphonic Acid Triethylammonium Salt (**29**).* The product was obtained as a white solid after lyophilization (6.9 mg, 16.0%; RP-HPLC acetonitrile/10 mM triethylammonium acetate, 15/85 to 35/65 in 40 min at a rate of 5 mL/min): ^{1}H NMR (D_2O, 400 Hz) δ 7.32 (s, 4H), 7.26 (d, J = 8.3 Hz, 1H), 6.28 (d, J = 8.2 Hz, 1H), 4.87 (s, 2H), 4.53−4.58 (m, 2H), 4.23 (dd, J = 5.4, 10.9 Hz, 1H), 3.79 (d, J = 6.8 Hz, 1H), 3.64 (dd, J = 4.9, 10.9 Hz, 1H), 3.05 (s, 21H), 1.95 (t, J = 19.6 Hz, 2H), 1.38 (t, J = 4.4 Hz, 2H), 1.15 (s, 27H), 0.75 (t, J = 6.6 Hz, 1H); ^{31}P NMR (D_2O) δ 22.00, 12.00; HRMS calcd for $C_{20}H_{26}ClN_3O_{10}P_2$ $(M - H)^-$ 564.0704, found 564.0702.

*4-[(Benzylcarbamoyl)imino]-3-methylcytidine-5′-α,β-methylenediphosphonate Triethylammonium Salt (**30**).* The product was obtained as a white solid after lyophilization (7.6 mg, 8.4%; RP-HPLC acetonitrile/10 mM triethylammonium acetate, 15/85 to 35/75 in 40 min at a rate of 5 mL/min): ^{1}H NMR (D_2O, 400 Hz) δ 7.64 (d, J = 8.2 Hz, 1H), 7.25−7.7.46 (m, 5H), 6.13 (d, J = 8.2 Hz, 1H), 5.97 (d, J = 3.1 Hz, 1H), 4.42 (s, 2H), 4.35 (s, 2H), 4.24 (s, 1H), 4.14 (s, 2H), 3.31 (s, 3H), 3.19 (dd, J = 7.3, 14.6 Hz, 12H), 2.16 (t, J = 19.7 Hz, 2H), 1.26 (t, J = 7.0 Hz, 18H); ^{31}P NMR (D_2O) δ 20.00, 13.00; HRMS calcd for $C_{19}H_{25}N_4O_{11}P_2$ $(M - H)^-$ 547.0995, found 547.0995.

*General Procedure for the Synthesis of Substituted O-Benzylhydroxylamine Hydrochloride (**32**−**43**).* Compounds **32**−**43** were synthesized following the reported procedure[33] starting from the corresponding benzyl bromide.

*O-2-Chlorobenzylhydroxylamine Hydrochloride (**32**).* The product was obtained as a white solid (120 mg) in 63% yield: ^{1}H NMR (MeOD, 400 Hz) δ 7.35−7.55 (m, 4H), 5.20 (s, 2H).

*O-3-Chlorobenzylhydroxylamine Hydrochloride (**33**).* The product was obtained as a white solid (105 mg) in 74% yield: ^{1}H NMR (MeOD, 400 Hz) δ 7.36−7.47 (m, 4H), 5.02 (s, 2H).

*O-3-(Trifluoromethyl)benzylhydroxylamine Hydrochloride (**34**).* The product was obtained as a white solid (130 mg) in 68% yield: ^{1}H NMR (MeOD, 400 Hz) δ 7.61−7.78 (m, 4H), 5.12 (s, 2H).

*O-3-Methylbenzylhydroxylamine Hydrochloride (**35**).* The product was obtained as a white solid (272 mg) in 97% yield: ^{1}H NMR (MeOD, 400 Hz) δ 7.33 (d, 2H, J = 7.9 Hz), 7.26 (d, 2H, J = 7.9 Hz), 4.98 (s, 2H), 2.37 (s, 3H).

*O-3-Ethylbenzylhydroxylamine Hydrochloride (**36**).* The product was obtained as a white solid (198 mg) in 84% yield: ^{1}H NMR (MeOD, 400 Hz) δ 7.37 (d, 2H, J = 7.8 Hz), 7.29 (d, 2H, J = 8.0 Hz), 4.99 (s, 2H), 2.68 (dd, 2H, J = 7.5, 15.1 Hz), 1.24 (t, 3H, J = 7.6 Hz).

*O-4-Fluorobenzylhydroxylamine Hydrochloride (**37**).* The product was obtained as a white solid (150 mg) in 75% yield: ^{1}H NMR (MeOD, 400 Hz) δ 7.48 (dd, J = 5.4, 8.4 Hz, 2H), 7.16 (t, J = 8.7 Hz, 2H), 5.03 (s, 2H).

*O-4-Chlorobenzylhydroxylamine Hydrochloride (**38**).* The product was obtained as a white solid (100 mg) in 70% yield: ^{1}H NMR (MeOD, 400 Hz) δ 7.45−7.59 (m, 4H), 5.04 (s, 2H).

*O-4-Bromobenzylhydroxylamine Hydrochloride (**39**).* The product was obtained as a white solid (120 mg) in 74% yield: ^{1}H NMR (MeOD, 400 Hz) δ 7.60 (d, J = 8.3 Hz, 2H), 7.38 (d, J = 8.2 Hz, 2H), 5.02 (s, 2H).

*O-4-Iodobenzylhydroxylamine Hydrochloride (**40**).* The product was obtained as a white solid (124 mg) in 64% yield: ^{1}H NMR (MeOD, 400 Hz) δ 7.82 (d, J = 8.3 Hz, 2H), 7.22 (d, J = 8.2 Hz, 2H), 4.98 (s, 2H).

*O-4-(Trifluoromethyl)benzylhydroxylamine Hydrochloride (**41**).* The product was obtained as a white solid (145 mg) in 76% yield: ^{1}H NMR (MeOD, 400 Hz) δ 7.95 (d, J = 8.0 Hz, 2H), 7.65 (d, J = 8.0 Hz, 2H), 5.12 (s, 2H).

*O-4-(Pentafluorosulfanyl)benzylhydroxylamine Hydrochloride (**42**).* The product was obtained as a white solid (114 mg) in 59% yield: ^{1}H NMR (MeOD, 400 Hz) δ 7.90 (d, J = 8.7 Hz, 2H), 7.60 (d, J = 8.3 Hz, 2H), 5.10 (s, 2H).

*O-4-(Methylbenzoate)benzylhydroxylamine Hydrochloride (**43**).* The product was obtained as a white solid (123 mg) in 64% yield: ^{1}H NMR (MeOD, 400 Hz) δ 8.09 (d, J = 8.2 Hz, 2H), 7.56 (d, J = 8.1 Hz, 2H), 5.11 (s, 2H), 3.92 (s, 3H).

*3-Methylcytidine (**44**).* To a solution of cytidine (1.0 g, 4.1 mmol) in *N*,*N*-dimethylacetamide (DMAc, 25 mL) was added methyl iodide (0.77 mL, 12.3 mmol), and the mixture was stirred at rt for 4 h. The solvent was removed under reduced pressure, and the resulting crude mixture resuspended in dichloromethane with the formation of a white precipitate that was filtered, affording 1.0 g of the pure compound (95% yield): ^{1}H NMR (MeOD, 400 Hz) δ 8.5 (d, J = 7.8 Hz, 1H), 6.15 (d, J = 7.9 Hz, 1H), 5.87 (d, J = 2.6 Hz, 1H), 4.14−4.21 (m, 2H), 4.08 (t, J = 3.1 Hz, 1H), 3.95 (dd, J = 2.12, 12.4 Hz, 1H), 3.79 (dd, J = 2.12, 12.4 Hz, 1H), 3.49 (s, 3H); HRMS calcd for $C_{10}H_{17}N_3O_5$ $(M + H)^+$ 258.1087, found 258.1090.

*General Procedure for the Synthesis of Compounds **45**−**56**.* A solution of compound **44** (N^3-methylcytidine, 0.8 mmol) and the desired *O*-benzylhydroxylamine (**32**−**43**, 1.6 mmol) in dry pyridine was stirred at 80 °C for 12 h. Then the reaction mixture was concentrated under reduced pressure and purified with a silica gel column.

*N^4-(2-Chlorobenzyloxy)-3-methylcytidine (**45**).* Compound **45** was synthesized following the procedure described above starting from *O*-(2-chlorobenzyl)hydroxylamine hydrochloride. The crude was purified by silica gel column (8/92 methanol/dichloromethane) to afford 96 mg of a white solid (97% yield): ^{1}H NMR (MeOD, 400 Hz) δ 7.45−7.50 (m, 1H), 7.40−7.43 (m, 1H), 7.25−7.35 (m, 3H), 6.30 (d, J = 8.3 Hz, 1H), 5.89 (d, J = 4.8 Hz, 1H), 5.11 (s, 2H), 4.10−4.17 (m, 2H), 3.95 (t, J = 3.3 Hz, 1H), 3.80 (dd, J = 2.7, 12.1 Hz,

https://doi.org/10.1021/acs.jmedchem.1c01852
J. Med. Chem. 2022, 65, 2409−2433

1H), 3.70 (dd, J = 2.7, 12.1 Hz, 1H), 3.18 (s, 3H); HRMS calcd for $C_{17}H_{21}ClN_3O_6$ $(M + H)^+$ 398.1119, found 398.1121.

*N^4-(3-Chlorobenzyloxy)-3-methylcytidine (**46**).* Compound **46** was synthesized following the procedure described above starting from *O*-(3-chlorobenzyl)hydroxylamine hydrochloride. The crude was purified by silica gel column (5/95 methanol/dichloromethane) to afford 66 mg of a white solid (74% yield): ^{1}H NMR (MeOD, 400 Hz) δ 7.38 (s, 1H), 7.25−7.35 (m, 4H), 6.26 (d, J = 8.3 Hz, 1H), 5.89 (d, J = 4.8 Hz, 1H), 5.00 (s, 2H), 4.10−4.16 (m, 2H), 3.95 (t, J = 3.3 Hz, 1H), 3.80 (dd, J = 2.7, 12.1 Hz, 1H), 3.70 (dd, J = 2.7, 12.1 Hz, 1H), 3.18 (s, 3H); HRMS calcd for $C_{17}H_{21}ClN_3O_6$ $(M + H)^+$ 398.1178, found 398.1121.

*N^4-(3-Trifluoromethylbenzyloxy)-3-methylcytidine (**47**).* Compound **47** was synthesized following the procedure described above starting from *O*-(3-trifluoromethylbenzyl)hydroxylamine hydrochloride. The crude was purified by a silica gel column (5/95 methanol/dichloromethane) to afford 29 mg of a white solid (59% yield): ^{1}H NMR (MeOD, 400 Hz) δ 7.50−7.65 (m, 5H), 7.31 (d, J = 8.4 Hz, 1H), 6.23 (d, J = 8.3 Hz, 1H), 5.05 (s, 2H), 4.10−4.16 (m, 2H), 3.95 (t, J = 3.2 Hz, 1H), 3.80 (dd, J = 2.7, 12.1 Hz, 1H), 3.68 (dd, J = 2.7, 12.1 Hz, 1H), 3.15 (s, 3H); HRMS calcd for $C_{18}H_{21}F_3N_3O_6$ $(M + H)^+$ 431.1298, found 431.1304.

*N^4-(3-Methylbenzyloxy)-3-methylcytidine (**48**).* Compound **48** was synthesized following the procedure described above starting from *O*-(3-methylbenzyl)hydroxylamine hydrochloride. The crude was purified by a silica gel column (5/95 methanol/dichloromethane) to afford 181 mg of a white solid (62% yield): ^{1}H NMR (MeOD, 400 Hz) δ 7.23−7.29 (m, 3H), 7.14 (d, 2H, J = 7.8 Hz), 6.22 (d, 1H, J = 8.3 Hz), 5.87 (d, 1H, J = 4.7 Hz), 4.93 (s, 2H), 4.09−4.14 (m, 2H), 3.94 (dd, 1H, J = 3.2, 6.4 Hz), 3.79 (dd, 1H, J = 2.6, 12.1 Hz), 3.69 (dd, 1H, J = 3.3, 12.1 Hz), 3.19 (s, 3H), 2.33 (s, 3H); HRMS calcd for $C_{18}H_{24}N_3O_6$ $(M + H)^+$ 378.1665, found 378.1659.

*N^4-(3-Ethylbenzyloxy)-3-methylcytidine (**49**).* Compound **49** was synthesized following the procedure described above starting from *O*-(3-ethylbenzyl)hydroxylamine hydrochloride. The crude was purified by a silica gel column (5/95 methanol/dichloromethane) to afford 150 mg of a white solid (72% yield): ^{1}H NMR (MeOD, 400 Hz) δ 7.27 (d, 3H, J = 8.4 Hz), 7.17 (d, 2H, J = 7.9 Hz), 6.23 (d, 1H, J = 8.3 Hz), 5.87 (d, 1H, J = 4.7 Hz), 4.94 (s, 2H), 4.09−4.14 (m, 2H), 3.94 (dd, 1H, J = 3.2, 6.4 Hz), 3.79 (dd, 1H, J = 2.7, 12.1 Hz), 3.69 (dd, 1H, J = 3.3, 12.2 Hz), 3.20 (s, 3H), 2.63 (dd, 2H, J = 7.6, 15.2 Hz), 1.22 (t, 3H, J = 7.6 Hz); HRMS calcd for $C_{19}H_{26}N_3O_6$ $(M + H)^+$ 392.1822, found 392.1827.

*N^4-(4-Fluorobenzyloxy)-3-methylcytidine (**50**).* Compound **50** was synthesized following the procedure described above starting from *O*-(4-fluorobenzyl)hydroxylamine hydrochloride. The crude was purified by silica gel column (5/95 methanol/dichloromethane) to afford 56 mg of a white solid (35% yield): ^{1}H NMR (MeOD, 400 Hz) δ 7.32−7.41 (m, 2H), 7.29 (d, J = 8.4 Hz, 1H), 7.00−7.10 (m, 2H), 6.21 (d, J = 8.2 Hz, 1H), 5.85 (d, J = 4.6 Hz), 4.95 (s, 2H), 4.05−4.15 (m, 2H), 3.95 (t, J = 3.2 Hz, 1H), 3.75 (dd, J = 2.7, 12.1 Hz, 1H), 3.68 (dd, J = 2.7, 12.1 Hz, 1H), 3.16 (s, 3H); HRMS calcd for $C_{17}H_{21}FN_3O_6$ $(M + H)^+$ 382.1409, found 382.1414.

*N^4-(4-Chlorobenzyloxy)-3-methylcytidine (**51**).* Compound **51** was synthesized following the procedure described above starting from *O*-(4-chlorobenzyl)hydroxylamine hydrochloride. The crude was purified by a silica gel column (5/95 methanol/dichloromethane) to afford 96 mg of a white solid (97% yield): ^{1}H NMR (MeOD, 400 Hz) δ 7.33−7.36 (m, 4H), 7.30 (d, J = 8.4 Hz, 1H), 6.21 (d, J = 8.2 Hz, 1H), 5.88 (d, J = 4.6 Hz, 1H), 4.98 (s, 2H), 4.08−4.15 (m, 2H), 3.95 (t, J = 3.2 Hz, 1H), 3.78 (dd, J = 2.7, 12.1 Hz, 1H), 3.69 (dd, J = 2.7, 12.1 Hz, 1H), 3.19 (s, 3H); HRMS calcd for $C_{17}H_{21}ClN_3O_6$ $(M + H)^+$ 397.1041, found 397.1050.

*N^4-(4-Bromobenzyloxy)-3-methylcytidine (**52**).* Compound **52** was synthesized following the procedure described above starting from *O*-(4-bromobenzyl)hydroxylamine hydrochloride. The crude was purified by a silica gel column (6/94 methanol/dichloromethane) to afford 40 mg of a white solid (39% yield): ^{1}H NMR (MeOD, 400 Hz) δ 7.49 (d, J = 8.3 Hz, 2H), 7.26−7.32 (m, 3H), 6.22 (d, J = 8.2 Hz, 1H), 5.88 (d, J = 4.6 Hz, 1H), 4.98 (s, 2H), 4.08−4.15 (m, 2H), 3.95 (t, J = 3.2 Hz, 1H), 3.80 (dd, J = 2.7, 12.1 Hz, 1H), 3.70 (dd, J = 2.7, 12.1 Hz, 1H), 3.17 (s, 3H); HRMS calcd for $C_{17}H_{21}BrN_3O_6$ $(M + H)^+$ 442.0614, found 442.0614.

*N^4-(4-Iodobenzyloxy)-3-methylcytidine (**53**).* Compound **53** was synthesized following the procedure described above starting from *O*-(4-iodobenzyl)hydroxylamine hydrochloride. The crude was purified by a silica gel column (5/95 methanol/dichloromethane) to afford 108 mg of a white solid (92% yield): ^{1}H NMR (MeOD, 400 Hz) δ 7.30 (d, J = 8.3 Hz, 2H), 7.26−7.32 (m, 3H), 6.22 (d, J = 8.2 Hz, 1H), 5.87 (d, J = 4.6 Hz, 1H), 4.98 (s, 2H), 4.08−4.15 (m, 2H), 3.94 (t, J = 3.2 Hz, 1H), 3.78 (dd, J = 2.7, 12.1 Hz, 1H), 3.69 (dd, J = 2.7, 12.1 Hz, 1H), 3.17 (s, 3H); HRMS calcd for $C_{17}H_{21}IN_3O_6$ $(M + H)^+$ 490.0471, found 490.0475.

*N^4-(4-Trifluorobenzyloxy)-3-methylcytidine (**54**).* Compound **54** was synthesized following the procedure described above starting from *O*-(4-trifluoromethylbenzyl)hydroxylamine hydrochloride. The crude was purified by a silica gel column (5/95 methanol/dichloromethane) to afford 111 mg of a white solid (83% yield): ^{1}H NMR (MeOD, 400 Hz) δ 7.64 (d, J = 8.0 Hz, 2H), 7.53 (d, J = 8.0 Hz, 2H), 7.32 (d, J = 8.3 Hz, 1H), 6.27 (d, J = 8.2 Hz, 1H), 5.88 (d, J = 4.6 Hz, 1H), 5.07 (s, 2H), 4.08−4.14 (m, 2H), 3.95 (t, J = 3.2 Hz, 1H), 3.79 (dd, J = 2.7, 12.1 Hz, 1H), 3.70 (dd, J = 2.7, 12.1 Hz, 1H), 3.16 (s, 3H); HRMS calcd for $C_{18}H_{21}F_3N_3O_6$ $(M + H)^+$ 432.1375, found 432.1382.

*N^4-[4-(Pentafluorosulfanyl)benzyloxy]-3-methylcytidine (**55**).* Compound **55** was synthesized following the procedure described above starting from *O*-(4-pentafluorosulfanylbenzyl)hydroxylamine hydrochloride. The crude was purified by a silica gel column (2/98 methanol/dichloromethane) to afford 68 mg of a white solid (69% yield): ^{1}H NMR (MeOD, 400 Hz) δ 7.78 (d, J = 8.6 Hz, 2H), 7.51 (d, J = 8.2 Hz, 2H), 7.32 (d, J = 8.3 Hz, 1H), 6.26 (d, J = 8.3 Hz, 1H), 5.86 (d, J = 4.6 Hz, 1H), 5.07 (s, 2H), 4.11−4.16 (m, 2H), 3.95 (t, J = 3.2 Hz, 1H), 3.79 (dd, J = 2.7, 12.1 Hz, 1H), 3.71 (dd, J = 2.7, 12.1 Hz, 1H), 3.16 (s, 3H); HRMS calcd for $C_{17}H_{21}F_5N_3O_6S$ $(M + H)^+$ 490.1071, found 490.1071.

*Methyl 4-{[({-1-[(2R,3R,4S,5R)-3,4-Dihydroxy-5-(hydroxymethyl)-tetrahydrofuran-2-yl]-3-methyl-2-oxo-2,3-dihydropyrimidin-4(1H)-ylidene}amino)oxy]methyl}benzoate (**56**).* Compound **56** was synthesized following the procedure described above starting from methyl 4-[(aminooxy)methyl]benzoate hydrochloride. The crude was purified by a silica gel column (5/95 methanol/dichloromethane) to afford 26 mg of a white solid (48% yield): ^{1}H NMR (MeOD, 400 Hz) δ 7.79 (d, J = 8.2 Hz, 2H), 7.46 (d, J = 8.1 Hz, 2H), 7.31 (d, J = 8.3 Hz, 1H), 6.26 (d, J = 8.3 Hz, 1H), 5.86 (d, J = 4.7 Hz, 1H), 5.05 (s, 2H), 4.10−4.16 (m, 2H), 3.94 (t, J = 3.2 Hz, 1H), 3.89 (s, 3H), 3.79 (dd, J = 2.7, 12.1 Hz, 1H), 3.69 (dd, J = 2.7, 12.1 Hz, 1H), 3.16 (s, 3H); HRMS calcd for $C_{19}H_{24}N_3O_8$ $(M + H)^+$ 422.1558, found 422.1547.

*Synthesis of Compound **57** through Hydrolysis of the Methyl Ester Moiety.* To a solution of compound **56** (84 mg, 0.2 mmol) in MeOH (2 mL) was added a 1 N solution of NaOH (2 mL), and the reaction mixture was stirred at rt for 40 min. Glacial acetic acid was added until neutrality. Then, the mixture was diluted with water and extracted with ethyl acetate (3 × 15 mL). The combined organic layer was dried over sodium sulfate, filtered, and evaporated to afford 62 mg (77%) of the pure compound as a white solid: ^{1}H NMR (MeOD, 400 Hz) δ 8.05 (d, J = 8.1 Hz, 2H), 7.50 (d, J = 8.0 Hz, 2H), 7.41 (d, J = 8.3 Hz, 1H), 6.37 (d, J = 8.3 Hz, 1H), 5.99 (d, J = 4.7 Hz, 1H), 5.14 (s, 2H), 4.20−4.27 (m, 2H), 4.05 (d, J = 3.2 Hz, 1H), 3.87−3.93 (m, 1H), 3.78−3.84 (m, 1H), 3.28 (s, 3H); HRMS calcd for $C_{18}H_{22}N_3O_8$ $(M + H)^+$ 408.1407, found 408.1408.

*Synthesis of Compound **59** through Hydrolysis of the Acetylated Intermediate Formed by Serendipity.* To a solution of compound **57** (30 mg, 0.07 mmol, with traces of acetic acid), HATU (42 mg, 0.11 mmol), and DIPEA (19 μL, 0.11 mmol) in anhydrous DMF was added methylamine hydrochloride (6.5 mg, 0.09 mmol), and the reaction mixture was stirred at rt for 12 h. Next, the solvent was removed, and the crude purified by a silica gel column (5% MeOH/DCM) to afford an acetylated intermediate as a white solid (**58**). The latter was treated with methanolic ammonia for 2 h at rt to deblock

https://doi.org/10.1021/acs.jmedchem.1c01852
J. Med. Chem. 2022, 65, 2409−2433

the acetylated group and eventually recover the starting material. TLC analysis showed formation of a new compound that was obtained pure directly after removal of the solvent. NMR and LC-MS confirmed the formation of compound **59** (19 mg, 64%, two-step yield): ^{1}H NMR (MeOD, 400 Hz) δ 7.85 (d, J = 8.2 Hz, 2H), 7.46 (d, J = 8.1 Hz, 2H), 7.30 (d, J = 8.3 Hz, 1H), 6.27 (d, J = 8.2 Hz, 1H), 5.88 (d, J = 4.6 Hz, 1H), 5.06 (s, 2H), 4.10−4.16 (m, 2H), 3.95 (d, J = 3.1 Hz, 1H), 3.77−3.82 (m, 1H), 3.67−3.73 (m, 1H), 3.18 (s, 3H); HRMS calcd for $C_{18}H_{22}N_4O_7$ $(M + H)^+$ 407.1567, found 407.1567.

*General Procedure for the Synthesis of Derivatives **60** and **61** by Amination of Methyl Ester **56**.* A solution of compound **56** (20 mg, 0.047 mmol; 50 mg, 0.119 mmol) in the required amine (ethylene diamine for compound **60** or 1,4-diaminobutine for compound **61**, 2 mL) was stirred at rt for 2 h. LC-MS analysis showed full conversion to the amide product. The solvent was removed under reduced pressure, and the so obtained crude mixture directly used for the next step.

*Synthesis of the β-Alanine-ethyl Ester Derivative **62**.* A mixture of compound **57** (50 mg, 0.2 mmol), β-alanine-ethyl ester hydrochloride (18 mg, 0.2 mmol), HATU (68 mg, 0.2 mmol), and DIPEA (32 μL, 0.2 mmol) in DMF (4 mL) was stirred at rt for 12 h. Next, the solvent was removed, and the crude product purified by a silica gel column (2% methanol in dichloromethane) to afford the pure compound as a white powder (60 mg, quantitative): ^{1}H NMR (MeOD, 400 Hz) δ 7.77 (d, J = 8.1 Hz, 2H), 7.44 (d, J = 8.0 Hz, 2H), 7.31 (d, J = 8.3 Hz, 1H), 6.25 (d, J = 8.3 Hz, 1H), 5.88 (d, J = 4.7 Hz, 1H), 5.04 (s, 2H), 4.10−4.17 (m, 4H), 3.96 (d, J = 3.2 Hz, 1H), 3.81−3.82 (m, 1H), 3.78−3.79 (m, 1H), 3.62−3.69 (m, 2H), 3.15 (s, 3H), 2.65 (t, J = 7.4 Hz, 2H), 1.24 (t, J = 7.1 Hz, 3H); HRMS calcd for $C_{23}H_{31}N_4O_9$ $(M + H)^+$ 507.2091, found 507.2093.

*Synthesis of the β-Alanine Derivatives **63**.* Compound **62** (40 mg, 0.1 mmol) was dissolved in a mixture of methanol (1 mL) and a 1 N NaOH water solution (1 mL), and the mixture was stirred at rt for 12 h. Next, phosphate buffer (pH 7.4) was added to neutralize the mixture. The solvent was removed, and the crude product dissolved in MeOH with formation of a precipitate that was removed by filtration. The collected filtrate was dried under reduced pressure to afford the desired compound as a white solid (38 mg, 92%): ^{1}H NMR (MeOD, 400 Hz) δ 7.78 (d, J = 8.1 Hz, 2H), 7.44 (d, J = 8.0 Hz, 2H), 7.32 (d, J = 8.3 Hz, 1H), 6.26 (d, J = 8.3 Hz, 1H), 5.88 (d, J = 4.7 Hz, 1H), 5.04 (s, 2H), 4.13 (s, 2H), 3.96 (d, J = 3.2 Hz, 1H), 3.78−3.81 (m, 1H), 3.72−3.73 (m, 1H), 3.61−3.64 (m, 2H), 3.16 (s, 3H), 2.62 (t, J = 6.7 Hz, 2H): HRMS calcd for $C_{21}H_{27}N_4O_9$ $(M + H)^+$ 479.1778, found 479.1777.

*(2R,3S,4R,5S)-1-(Acetoxymethyl)-4-[2,4-dioxo-3,4-dihydropyrimidin-1(2H)-yl]-1λ^5-bicyclo[3.1.0]hexane-2,3-diyl Diacetate (**65**).* Compound **64** was prepared following the reported procedure.[3,4] A mixture of compound **64** (100 mg, 0.4 mmol), acetic anhydride (148 μL, 1.6 mmol), triethylamine (219 μL, 1.6 mmol), and DMAP (24 mg, 0.2 mmol) in acetonitrile (3 mL) was stirred at rt for 2 h. The solvent was removed under reduced pressure, and the residue purified by a silica gel column (50% ethyl acetate in hexane) to afford 100.0 mg of the pure compound as a white solid (67%): ^{1}H NMR ($CDCl_3$, 400 Hz) δ 9.95 (s, 1H), 7.36 (d, J = 7.9 Hz, 1H), 5.67 (dd, J = 7.7, 12.9 Hz, 2H), 5.15 (d, J = 7.2 Hz, 1H), 4.58 (s, 1H), 4.34 (d, J = 12.0 Hz, 1H), 3.96 (d, J = 12.0 Hz, 1H), 2.04 (s, 3H), 1.99 (s, 6H), 1.47 (dd, J = 3.8, 8.4 Hz, 1H), 1.21 (dd, J = 5.3, 9.6 Hz, 2H), 0.95 (t, J = 7.0 Hz, 1H); HRMS calcd for $C_{17}H_{22}N_2O_8$ $(M + H)^+$ 382.1381, found 382.1384.

*(2R,3S,4R,5S)-1-(Acetoxymethyl)-4-(4-{[(4-chlorobenzyl)oxy]-imino}-2-oxo-3,4-dihydropyrimidin-1(2H)-yl)-1λ^5-bicyclo[3.1.0]-hexane-2,3-diyl Diacetate (**66**).* Compound **66** was synthesized following the reported procedure[33] starting from compound **65** and *O*-4-chlorobenzylhydroxylamine hydrochloride (**38**). Purification was performed by a silica gel column (50% ethyl acetate in hexane) to afford 36 mg of the pure product as a white powder (26% yield for two steps): ^{1}H NMR ($CDCl_3$, 400 Hz) δ 8.13 (s, 1H), 7.30 (dd, J = 8.3, 19.6 Hz, 4H), 6.77 (d, J = 8.1 Hz, 1H), 5.65 (d, J = 6.3 Hz, 1H), 5.56 (dd, J = 2.0, 8.1 Hz, 1H), 5.14 (d, J = 7.1 Hz, 1H), 4.97 (s, 2H), 4.62 (s, 1H), 4.42 (d, J = 12.0 Hz, 1H), 3.90 (d, J = 12.0 Hz, 1H), 2.07 (s, 3H), 2.04 (s, 6H), 1.42 (dd, J = 4.0, 8.7 Hz, 1H), 1.22−1.29 (m, 2H), 0.94 (t, J = 6.8 Hz, 1H); HRMS calcd for $C_{24}H_{28}ClN_3O_8$ $(M + H)^+$ 520.1487, found 520.1481.

*1-(Acetoxymethyl)-4-(4-{[(4-chlorobenzyl)oxy]imino}-3-methyl-2-oxo-3,4-dihydropyrimidin-1(2H)-yl)-1λ^5-bicyclo[3.1.0]hexane-2,3-diyl Diacetate (**67**).* To a mixture of compound **66** (36.0 mg, 0.07 mmol) and K_2CO_3 (15 mg, 0.10 mmol) in *N*,*N*-dimethylacetamide (DMAc, 2.0 mL) was added methyl iodide (13 μL, 0.20 mmol), and the mixture was stirred at rt for 18 h. The solvent was removed under reduced pressure, and the resulting crude mixture purified by a silica gel column (50% ethyl acetate in hexane) to afford 31 mg of the pure product (83%): ^{1}H NMR ($CDCl_3$, 400 Hz) δ 7.30 (s, 4H), 6.80 (d, J = 8.2 Hz, 1H), 6.16 (d, J = 8.2 Hz, 1H), 5.69 (d, J = 7.2 Hz, 1H), 5.14 (d, J = 7.2 Hz, 1H), 4.96 (s, 2H), 4.58 (s, 1H), 4.41 (d, J = 12.0 Hz, 1H), 3.92 (d, J = 12.0 Hz, 1H), 3.19 (s, 3H), 2.10 (s, 3H), 2.04 (s, 6H), 1.42 (dd, J = 4.0, 8.7 Hz, 1H), 1.25 (t, J = 4.9 Hz, 2H), 0.94 (t, J = 7.3 Hz, 1H); HRMS calcd for $C_{25}H_{30}ClN_3O_8$ $(M + H)^+$ 534.1643, found 534.1647.

*4-{[(4-Chlorobenzyl)oxy]imino}-1-[(1S,2R,3S,4R)-3,4-dihydroxy-5-(hydroxymethyl)-5λ^5-bicyclo[3.1.0]hexan-2-yl]-3-methyl-3,4-dihydropyrimidin-2(1H)-one (**68**).* A solution of compound **67** (30.7 mg, 0.06 mmol) in a NH_3 methanol solution (2.0 mL) was stirred at rt for 18 h. The solvent was removed, and the crude purified by a silica gel column (5% methanol in dichloromethane) to afford 21 mg of the pure product (91%): ^{1}H NMR (MeOD, 400 Hz) δ 7.38 (d, J = 8.2 Hz, 1H), 7.32 (d, J = 1.0 Hz, 4H), 6.17 (d, J = 8.2 Hz, 1H), 4.95 (s, 2H), 4.65 (s, 1H), 4.55 (d, J = 6.7 Hz, 1H), 4.16 (d, J = 11.7 Hz, 1H), 3.75 (d, J = 6.7 Hz, 1H), 3.23 (d, J = 11.7 Hz, 1H), 3.17 (s, 3H), 1.26−1.33 (m, 2H), 0.64 (t, J = 3.3 Hz, 1H); HRMS calcd for $C_{19}H_{24}ClN_3O_5$ $(M + H)^+$ 408.1326, found 408.1330.

*Synthesis of Compound **70** by Acylation of Cytidine.* A mixture of cytidine (200 mg, 0.8 mmol), acetic anhydride (310 μL, 3.3 mmol), triethylamine (458 μL, 3.3 mmol), and DMAP (50 mg, 0.4 mmol) in acetonitrile (4 mL) was stirred at rt for 10 min with formation of both tri-*O*-acetyl-cytidine and tetra-*O*,*N*^{4}-acetyl-cytidine. The solvent was removed under reduced pressure, and the two derivatives were separated by a silica gel column (10% methanol in dichlomethane). Next, the tetra-*O*,*N*^{4}-acetyl-cytidine was dissolved in MeOH (3 mL) and heated at 105 °C for 3 h in a microwave reactor with full conversion of the latter to tri-*O*-acetyl-cytidine (purified by the same method used previously).[5] The total yield for two steps was 95% (289 mg).

*tri-O-Acetyl-3-methylcytidine (**71**).* Compound **71** was synthesized as reported above for the 3-methylcytidine, starting from compound **70**: ^{1}H NMR ($CDCl_3$, 400 Hz) δ 7.4 (s, 1H), 7.05 (d, J = 8.0 Hz, 1H), 6.00 (d, J = 8.0 Hz, 1H), 5.95 (d, J = 4.7 Hz, 1H), 5.27−5.36 (m, 2H), 4.29−4.33 (m, 3H), 3.44 (s, 3H), 2.12 (s, 3H), 2.08 (t, J = 4.9 Hz, 6H); HRMS calcd for $C_{16}H_{23}N_3O_8$ $(M + H)^+$ 384.1407, found 384.1410.

*tri-O-Acetyl-4-[(benzylcarbamoyl)imino]-3-methylcytidine (**72**).* *N*-Benzyl-1*H*-imidazole-1-carboxamide (**69**) was synthesized as reported previously.[38] A solution of compound **71** (73 mg, 0.2 mmol), compound **69** (77 mg, 0.4 mmol), and triethylamine (27 μL, 0.2 mmol) in THF (3 mL) was stirred at reflux for 12 h. The solvent was removed under reduced pressure, and the crude mixture purified by a silica gel column (2% methanol in dichloromethane) to afford the pure product as a white solid (72 mg, 72%): ^{1}H NMR ($CDCl_3$, 400 Hz) δ 7.26−7.33 (m, 5H), 7.13 (d, J = 8.2 Hz, 1H), 6.78 (d, J = 8.2 Hz, 1H), 6.00 (d, J = 4.4 Hz, 1H), 5.27−5.36 (m, 2H), 4.45 (d, J = 5.9 Hz, 2H), 4.32 (s, 3H), 3.33 (s, 3H), 2.12 (s, 3H), 2.09 (s, 3H), 2.08 (s, 3H); HRMS calcd for $C_{24}H_{29}N_4O_9$ $(M + H)^+$ 517.1935, found 517.1940.

*4-[(Benzylcarbamoyl)imino]-3-methylcytidine (**73**).* A suspension of compound **72** (72 mg, 0.1 mmol) in a methanolic ammonia solution (2 mL) was stirred at rt for 12 h. The solvent was removed, and the crude mixture purified by a silica gel column (7% methanol in dichloromethane) to afford the pure product as a white solid (47 mg, 87%): ^{1}H NMR (MeOD, 400 Hz) δ 7.72 (d, J = 8.2 Hz, 1H),7.22−7.33 (m, 5H), 6.18 (d, J = 8.2 Hz, 1H), 5.90 (d, J = 3.7 Hz, 1H), 4.38 (s, 2H), 4.12 (dd, J = 4.4, 8.2 Hz, 2H), 3.98 (d, J = 3.0 Hz, 1H), 3.83

https://doi.org/10.1021/acs.jmedchem.1c01852
J. Med. Chem. 2022, 65, 2409−2433

(dd, J = 2.8, 12.2 Hz, 1H), 3.71 (dd, J = 2.8, 12.2 Hz, 1H), 3.35 (s, 3H); HRMS calcd for $C_{18}H_{23}N_4O_6$ $(M + H)^+$ 391.1618, found 391.1616.

Tissue Collection. A human tumor was obtained from a 44-year-old male patient with squamous cell carcinoma of mobile tongue (oral cavity, T3N2cM0, grade II) undergoing surgery at the Department of Otorhinolaryngology-Head and Neck Surgery of Turku University Hospital. The collection of the tissues is part of an ongoing sample collection performed under the license ETMK 166/2015 with written informed consent from the patients. Palatine tonsils were obtained from an adult patient with chronic tonsillitis undergoing routine tonsillectomy at Turku University Hospital (permission TO6/033/18 from the Hospital Research Council). The excised tumor and tonsil samples were embedded in the cryo-mold with Tissue-Tek O.C.T. compound (Sakura Finetek Europe B.V., Alphen aan den Rijn, The Netherlands), cut at 10 μm onto superfrost glass slides using a cryostat, and stored at −80 °C.

Immunofluorescence Staining. Tumor cryosections were processed for the immunofluorescence analysis of CD73 expression, as described elsewhere.[48] Briefly, the slides were incubated overnight at 4 °C in a Shandon Sequenza Staining System (Thermo Scientific) with the rabbit anti-human CD73 antibody (h5NT-1_L, http://ectonucleotidases-ab.com/) diluted at 1/400 in 200 μL of PBS containing 2% bovine serum albumin (BSA) and 0.1% (v/v) Triton X-100 (blocking buffer). The samples were washed and subsequently incubated for 2 h at rt with the Alexa Fluor-546-conjugated goat anti-rabbit antibody (ThermoFisher Life Technologies), diluted 1/800 in blocking buffer. The Alexa Fluor 488-conjugated pan-cytokeratin monoclonal antibody (catalogue no. MA5-18156, ThermoFisher) was added during the incubation with the secondary antibody for labeling the well-differentiated epithelial tumor cells. The slides were mounted with a ProLong Gold Antifade reagent with DAPI (ThermoFisher) and imaged using a Pannoramic Midi FL Slide Scanner (3DHistech Ltd., Budapest, Hungary) with a 20× objective.

In Situ ecto-5′-Nucleotidase Activity Assay. For localization of AMPase activities in human tumors and tonsils, the lead nitrate-based enzyme histochemistry was employed.[28,49] In brief, tissue cryosections were preincubated for 60 min at rt in 40 mmol/L Trizma-maleate buffer (TMB, pH 7.3) supplemented with 250 mmol/L sucrose, the alkaline phosphatase inhibitor levamisole (2 mmol/L), and different concentrations of CD73 inhibitors. The enzymatic reaction was then performed for 45 min at 37 °C in a final volume of 20 mL of TMB containing 250 mmol/L sucrose, 2 mmol/L levamisole, 1.5 mmol/L $Pb(NO_3)_2$, 1 mmol/L $CaCl_2$, 100 μmol/L AMP, and tested CD73 inhibitors at the same concentrations as during the preincubation step. The lead orthophosphate precipitated over the course of nucleotidase activity was visualized as a brown deposit by incubating sections in 0.5% $(NH_4)_2S$ for 10 s, followed by three washes in TMB for 5 min each. Slides were mounted with Aquatex medium (Merck). Tissue sections were also stained with H&E. Whole slide imaging was performed using a Pannoramic-250 Flash slide scanner (3DHistech Ltd.) with a 20× objective. AMPase activity was determined by measuring AMP-specific brown staining intensities from the images using QuPath version 0.2.3.[52] Shortly, a project including all images was created. Tissue areas were detected using the threshold classifier. The classifier was run with full resolution (240 nm/pixel) for the whole project. The DAB channel and Gaussian prefiltering were selected. The threshold was set to 1.15 without smoothing, and areas above the threshold were classified as "positive". Representative areas were manually selected, and the average DAB intensity level was used for AMPase intensity quantification. The script for intensity analysis is shown in Table S3.

X-ray Crystallographic Studies. For the crystallographic experiments, two constructs of human CD73 were used. These constructs were generated by gene synthesis of the natural signal peptide and the coding region of human CD73 with several variations as indicated in Figures S1 and S2. The synthesized gene included the residues up to the linkers highlighted in green. The remaining C-terminal residues were coded by the expression vectors, pHLsec for the 8.01His construct and pHLsec_StrepII for the 8.1Strep construct, using the *Eco*RI and *Kpn*I restriction sites.[53] For small-scale expression tests, HEK293S GntI$^-$ cells were grown in an adherent culture in 24-well TPP plates at 310 K in a humidified atmosphere containing 5% CO_2. The cell viability was supported by Dulbecco's modified Eagle's medium (Gibco) supplemented with 10% (v/v) fetal bovine serum (Gibco), 1% Glutmax (Gibco), and 1% non-essential amino acids (Gibco). The cells were transfected with the expression plasmid after growth to 90% confluency using polyethylenimine (Sigma-Aldrich) as a transfection reagent in a 1.5-fold excess (w/w) with respect to plasmid DNA. For preparative expression, cells from one confluent T175 bottle (Greiner) were seeded into roller bottles (Greiner) with a surface of 2125 cm^2 per bottle for 5 days before transfection. The roller bottles were incubated at 310 K with a rotation speed of 0.9 rpm and filled with 250 mL of medium per bottle.

Both constructs were purified using similar procedures as follows. The culture supernatant (1−2 L) was collected 5 days after transfection and separated from detached cells by centrifugation and filtration using a 0.22 μm bottle-top filter (TPP). To prepare the supernatant for purification by immobilized metal affinity chromatography (construct 8.01His), the buffer was exchanged via an ultrafiltration unit (10 kDa molecular weight cutoff, GE Healthcare) using 5 L of buffer A [50 mM Tris and 400 mM NaCl (pH 8.0)]. The resulting protein solution (volume of ∼100 mL) was adjusted to 20 mM imidazole by adding elution buffer B [50 mM Tris, 400 mM NaCl, and 500 mM imidazole (pH 8.0)]. After this, the protein solution was loaded onto a HisTrap HP column (1 mL volume, GE Healthcare), washed with 30 mL of 50 mM imidazole in buffer A, and eluted with a linear gradient from buffer A to buffer B over 5 mL. For purification of the 8.1Strep construct, the supernatant of the roller bottle expression was also concentrated to a volume of ∼100 mL by ultrafiltration. Then 0.6 mL of a DMEM/biotin blocking solution was added, and the solution was centrifuged at 20000g or filtered through a 0.45 μm filter. The protein was applied in a buffer of 50 mM Tris (pH 8.0) and 150 mM NaCl to a 5 mL StrepTrap HP column (GE Healthcare) and eluted with the same buffer containing 2.5 mM desthiobiotin. After affinity chromatography, fractions containing CD73 were pooled and concentrated to 2 mL using Amicon Ultra centrifugal filter units (10 kDa molecular weight cutoff, Merck Millipore) and further purified on a Superdex 200 16/60 gel-filtration column (120 mL volume, GE Healthcare) using a buffer consisting of 50 mM Tris (pH 8.0) and 100 mM NaCl. Pure protein fractions were pooled, concentrated to 5−10 mg mL^{-1}, and stored at −80 °C in aliquots for further use.

For crystallization, vapor diffusion trials were set up at 19 °C. One microliter of the protein solution containing the respective inhibitor (1 mM) and $ZnCl_2$ (100 μM) was mixed with an equal amount of a reservoir buffer solution to give the concentrations listed in Table S1. Crystals were transferred in a stepwise manner to a cryo buffer composed as reported in Table 2 and Table S1 and finally flash-frozen in liquid nitrogen.

X-ray data collection was carried out at 100 K as specified in Table S1. Data were collected at a Rigaku Synergy R home source and at the BESSY beamlines BL14.1 and BL14.2. The diffraction data were indexed, integrated, and scaled with XDS.[54] Coordinates of human CD73 in the closed conformation (PDB entry 4H2I) or in the open conformation (PDB entry 4H2G) were taken as starting models for rigid body refinement. In addition, the pipedream software was used for automatic refinement and ligand placement.[55] The models were further improved by iterative cycles of TLS refinement using BUSTER-TNT[55] and manual rebuilding with COOT.[56] Restraint dictionaries for inhibitors were generated using the GRADE web server (http://grade.globalphasing.org). Relevant crystallographic parameters of the structures are listed in Table S1. Figures were prepared using PYMOL (http://pymol.org).

Molecular Modeling. *Protein Preparation.* The X-ray structures of the complexes between hCD73 and compounds **16** and **21** were prepared using the Protein Preparation Wizard tool of the Schrödinger suite (Maestro 2020-1).[57,58] Missing residues (residues 376−382 and 374−382) were built using Prime (knowledge-based method),[59,60] used also to revert the Asn residues at positions 53, 311,

https://doi.org/10.1021/acs.jmedchem.1c01852
J. Med. Chem. 2022, 65, 2409−2433

333, and 403 into wild-type Asp. The following protomeric and tautomeric states were predicted for His residues: hydrogen at Nδ for His38, His118, His220, His304, His383, and His440; hydrogen at Nε for His33, His103, His243, His437, His456, and His518; and hydrogens at Nδ and Nε for His375. The protein was capped at the N-terminal position with an acetyl group (ACE) and at the C-terminal position with an *N*-methyl amide (NME). The two catalytic zinc ions and the calcium ion present in the X-ray structures were maintained during the simulations. The ligands were monoprotonated at the β-phosphonate.

Docking. Compounds **24** and **27** were drawn using the Schrödinger suite (Maestro 2020-1)[57] starting from compound **21** and then minimized using the OPLS3 force field and implicit solvent (water).[61] The compounds were docked to the hCD73 structure prepared starting from the X-ray complex with compound **21**. Glide XP[62] was used for docking, employing a grid centered on compound **21**, with an inner box of 10 Å and an outer box of 30 Å. Maximum 20 poses were generated for each compound, and a postdocking minimization of the ligand was included in the docking protocol. The poses with the highest score were selected.

Molecular Dynamics Simulations. The systems for molecular dynamics (MD) simulations were prepared using AmberTools20.[63] Antechamber[64] was used to assign AM1-BCC[65] charges and atom types to the ligands. Few modifications were manually introduced to the atom types: cd, cd, and cc were assigned to carbon atoms at positions 4, 5 and 6 of the pyrimidine ring, respectively, and op, oq, and or atom types were adopted for deprotonated and protonated phosphonate oxygens and the bridging 5′-oxygens.[66]

The complexes were inserted in a cubic water box (TIP3P[67] explicit solvent) with a distance of at least 30 Å between any atom and the edge of the box, and the systems were neutralized with NaCl (concentration of 0.15 M), by using tleap (AmberTools20). The Amber ff14SB[68] and GAFF[69] force fields were used for the simulations, and the MD simulations were carried out with Acemd3.[70]

After 500 steps of minimization, each system was subjected to an equilibration stage of 4 ns in the *NPT* ensemble, with atomic restraints on protein and ligand atoms in the first 3 ns of the simulation. Specifically, restraints of 1 kcal mol^{-1} $Å^{-2}$ were applied and gradually decreased (in the case of protein Cα atoms, the restraints were kept fixed to 1 kcal mol^{-1} $Å^{-2}$ in the first nanosecond and subsequently gradually decreased from 1 to 3 ns). Starting from each equilibrated system, three 50 ns simulations were collected in the *NVT* ensemble. A Langevin thermostat was used to keep the temperature at 310 K during the simulations (damping constants of 1 and 0.1 ps^{-1} for equilibration and production, respectively), and a Monte Carlo barostat was employed to keep the pressure at 1 atm during the equilibration phase. In all of the simulations, a 9 Å cutoff was used for nonbonded interactions, with a switching distance of 7.5 Å for van der Waals interactions, and the particle-mesh Ewald (PME)[71] summation was enabled for long-range electrostatic interactions. A time step of 2 fs was adopted, and simulations were saved with a stride of 20 ps (or of 50 ps, in the case of equilibration simulations).

The simulations were carried out on the NIH HPC Biowulf cluster (http://hpc.nih.gov, accessed May/June 15, 2021) using Tesla P100 GPUs.

Trajectory Analysis. Before the RMSD of the ligand (or ligand nucleotide-like scaffold) heavy atoms was measured, each trajectory was aligned superposing the protein Cα atoms on the starting conformation. Calculation of the RMSFs of the ligand heavy atoms was performed using the average trajectory structure as reference. RMSD and RMSF analysis was conducted with Wordom.[47]

For the cluster analysis, the three replicates of each system were sampled every 200 ps, aligned superposing the ligand nucleotide-like scaffold heavy atoms, and the RMSD of the *para*-substituted benzyl moiety was used to build the distance matrix. Wordom's QT-like method with a 2 Å cutoff was employed for clustering analysis.

Contacts and H-bonds were computed with an in-house script written in Tcl, employing VMD 1.9.3.[72] Contacts were calculated as the presence of any residue atom within 4 Å of any ligand atom. H-Bonds were computed using the Hbonds plugin, applying a donor−acceptor distance of 3.5 Å and a donor−H−acceptor angle of 30°.

Puckering analysis was accomplished with an in-house python script, with minor modification of what was reported previously.[37,48]

Averages and standard deviations were computed through a python script employing Pandas functions.[73] Plots were generated using matplotlib[74] and gnuplot.[75]

■ ASSOCIATED CONTENT

Supporting Information

The Supporting Information is available free of charge at https://pubs.acs.org/doi/10.1021/acs.jmedchem.1c01852.

^{1}H NMR spectra of all final compounds, details of the X-ray crystallographic studies, molecular modeling procedures and figures, and key to video and PDB files (PDF)

Video S1 (AVI)

Molecular strings file (CSV)

Protein Data Bank file with atomic coordinates of the model of **18** bound to hCD73 (PDB)

■ AUTHOR INFORMATION

Corresponding Author

Kenneth A. Jacobson − *Molecular Recognition Section, Laboratory of Bioorganic Chemistry, National Institute of Diabetes and Digestive and Kidney Diseases, National Institutes of Health, Bethesda, Maryland 20892, United States;* orcid.org/0000-0001-8104-1493; Phone: 301-496-9024; Email: kennethj@niddk.nih.gov; Fax: 301-480-8422

Authors

Mirko Scortichini − *Molecular Recognition Section, Laboratory of Bioorganic Chemistry, National Institute of Diabetes and Digestive and Kidney Diseases, National Institutes of Health, Bethesda, Maryland 20892, United States*

Riham Mohammed Idris − *PharmaCenter Bonn, Pharmaceutical Institute, Pharmaceutical Chemistry I, University of Bonn, D-53121 Bonn, Germany*

Susanne Moschütz − *Center for Biotechnology and Biomedicine, Leipzig University, 04103 Leipzig, Germany*

Antje Keim − *Center for Biotechnology and Biomedicine, Leipzig University, 04103 Leipzig, Germany*

Veronica Salmaso − *Molecular Recognition Section, Laboratory of Bioorganic Chemistry, National Institute of Diabetes and Digestive and Kidney Diseases, National Institutes of Health, Bethesda, Maryland 20892, United States*

Clemens Dobelmann − *European Institute for Molecular Imaging (EIMI), University of Münster, D-48149 Münster, Germany*

Paola Oliva − *Molecular Recognition Section, Laboratory of Bioorganic Chemistry, National Institute of Diabetes and Digestive and Kidney Diseases, National Institutes of Health, Bethesda, Maryland 20892, United States*

Karolina Losenkova − *Medicity Research Laboratory, University of Turku, 20520 Turku, Finland*

Heikki Irjala − *Department of Otorhinolaryngology-Head and Neck Surgery, Turku University Hospital and Turku University, 20520 Turku, Finland*

Samuli Vaittinen − *Department of Pathology, Turku University Hospital and Turku University, 20520 Turku, Finland*

https://doi.org/10.1021/acs.jmedchem.1c01852
J. Med. Chem. 2022, 65, 2409−2433

Jouko Sandholm − *Turku Bioscience Centre, University of Turku and Åbo Akademi University, 20520 Turku, Finland*
Gennady G. Yegutkin − *Medicity Research Laboratory, University of Turku, 20520 Turku, Finland;* orcid.org/0000-0001-6684-7982
Norbert Sträter − *Center for Biotechnology and Biomedicine, Leipzig University, 04103 Leipzig, Germany;* orcid.org/0000-0002-2001-0500
Anna Junker − *European Institute for Molecular Imaging (EIMI), University of Münster, D-48149 Münster, Germany*
Christa E. Müller − *PharmaCenter Bonn, Pharmaceutical Institute, Pharmaceutical Chemistry I, University of Bonn, D-53121 Bonn, Germany;* orcid.org/0000-0002-0013-6624

Complete contact information is available at: https://pubs.acs.org/10.1021/acs.jmedchem.1c01852

Author Contributions

■M.S. and V.S. contributed equally to this work.

Notes

The authors declare no competing financial interest.

■ ACKNOWLEDGMENTS

The authors thank Dr. John Lloyd [National Institute of Diabetes and Digestive and Kidney Diseases (NIDDK)] for mass spectral determinations, Prof. Jean Sevigny for the antibody against human CD73, Prof. Dr. Henrik Ditzel for MDA-MB-231, and Prof. Dr. Michael Hölzel for MaMel.65-CD73^{ko} cells. The authors acknowledge support from the NIDDK Intramural Research Program (ZIADK031116). The authors thank Bryan L. Roth, National Institute of Mental Health's Psychoactive Drug Screening Program (The University of North Carolina at Chapel Hill, Contract HHSN-271-2008-00025-C), for screening data. The authors also thank the Biocenter Finland and Cell Imaging and Cytometry Core of Turku Bioscience Centre for imaging instrumentation. Financial support of A.J. by the Deutsche Forschungsgemeinschaft (German Research Foundation, JU 2966/2-1) and the Cells-in-Motion (CiM) cluster of excellence (Münster, Germany) is gratefully acknowledged. We thank the MX Laboratory at the Helmholtz Zentrum Berlin (BESSY II) for beam time as well as for travel support. We also acknowledge the EMBL beamlines of the DESY synchrotron in Hamburg for beamtime.

■ ABBREVIATIONS USED

AR, adenosine receptor; ACN, acetonitrile; AOPCP, *α,β*-methylene-ADP, adenosine-5′-*O*-[(phosphonomethyl)-phosphonic acid], {[5-(6-aminopurin-9-yl)-3,4-dihydroxyoxolan-2-yl]methoxyhydroxyphosphoryl}methylphosphonic acid; BisTris, 2-[bis(2-hydroxyethyl)amino]-2-(hydroxymethyl)-propane-1,3-diol; CD73, cluster of differentiation 73; CE, capillary electrophoresis; CMP, cytidine 5′-monophosphate; DAB, 3,3′-diaminobenzidine; DAPI, 4,6-diamidino-2-phenylindole; DIPEA, diisopropylethylamine; DMAc, *N,N*-dimethylacetamide; DMEM, Dulbecco's modified Eagle's medium; EC, enzyme commission; *e*N, *ecto*-5′-nucleotidase; *e*NPP, *ecto*-nucleoside pyrophosphatases/phosphodiesterase; *e*NTPDase, *ecto*-nucleoside triphosphate diphosphohydrolase; FBS, fetal bovine serum; GPI, glycophosphatidylinositol; HATU, 1-[bis(dimethylamino)methylene]-1*H*-1,2,3-triazolo[4,5-*b*]-pyridinium 3-oxide hexafluorophosphate; H&E, hematoxylin and eosin; HNSCC, head and neck squamous cell carcinoma; MES, 2-(*N*-morpholino)ethanesulfonic acid; MOE, Molecular Operating Environment; NK cells, natural killer cells; PD-L1, programmed death ligand 1; PDSP, Psychoactive Drug Screening Program; POM, polyoxometalate; PSB, Pharmaceutical Sciences Bonn; RMSF, root-mean-square fluctuation; SF9, *Spodoptera frugiperda* 9; TEA, triethylamine; TEAC, triethylammonium hydrogen carbonate; TMB, Trizma-maleate buffer; TME, tumor microenvironment; TPSCl, 2,4,6-triisopropylbenzenesulfonyl chloride

■ REFERENCES

(1) Vigano, S.; Alatzoglou, D.; Irving, M.; Ménétrier-Caux, C.; Caux, C.; Romero, P.; Coukos, G. Targeting adenosine in cancer immunotherapy to enhance T-cell function. *Front. Immunol.* **2019**, *10*, 925.
(2) Boison, D.; Yegutkin, G. G. Adenosine metabolism: Emerging concepts for cancer therapy. *Cancer Cell* **2019**, *36*, 582−596.
(3) Allard, B.; Allard, D.; Buisseret, L.; Stagg, J. The adenosine pathway in immuno-oncology. *Nat. Rev. Clin. Oncol.* **2020**, *17*, 611−629.
(4) Chen, L.; Diao, L.; Yang, Y.; Yi, Y.; Rodriguez, B. L.; Li, Y.; Villalobos, P. A.; Cascone, T.; Liu, X.; Tan, L.; Lorenzi, P. L.; Huang, A.; Zhao, Q.; Peng, D.; Fradette, J. J.; Peng, D. H.; Ungewiss, C.; Roybal, J.; Tong, P.; Oba, J.; Skoulidis, F.; Peng, W.; Carter, B. W.; Gay, C. M.; Fan, Y.; Class, C. A.; Zhu, J.; Rodriguez-Canales, J.; Kawakami, M.; Byers, L. A.; Woodman, S. E.; Papadimitrakopoulou, V. A.; Dmitrovsky, E.; Wang, J.; Ullrich, S. E.; Wistuba, I. I.; Heymach, J. V.; Qin, X.-F.; Gibbons, D. L. CD38-mediated immunosuppression as a mechanism of tumor cell escape from PD-1/PD-L1 blockade. *Cancer Discovery* **2018**, *8*, 1156−1175.
(5) Hay, C. M.; Sult, E.; Huang, Q.; Mulgrew, K.; Fuhrmann, S. R.; McGlinchey, K. A.; Hammond, S. A.; Rothstein, R.; Rios-Doria, J.; Poon, E.; Holoweckyj, N.; Durham, N. M.; Leow, C. C.; Diedrich, G.; Damschroder, M.; Herbst, R.; Hollingsworth, R. E.; Sachsenmeier, K. F. Targeting CD73 in the tumor microenvironment with MEDI9447. *Oncoimmunology* **2016**, *5*, e1208875.
(6) Jadidi-Niaragh, F. Potential of CD73 as a target for cancer immunotherapy. *Immunotherapy* **2019**, *11* (16), 1353−1355.
(7) Luke, J. J.; Powderly, J. D.; Merchan, J. R.; Barve, M. A.; Hotson, A. N.; Mobasher, M.; Kwei, L.; Luciano, G.; Buggy, J. J.; Piccione, E.; Miller, R. A. Immunobiology, preliminary safety, and efficacy of CPI-006, an anti-CD73 antibody with immune modulating activity, in a phase 1 trial in advanced cancers. *J. Clin. Oncol.* **2019**, *37*, 2505.
(8) Harvey, J. B.; Phan, L. H.; Villarreal, O. E.; Bowser, J. L. CD73's potential as an immunotherapy target in gastrointestinal cancers. *Front. Immunol.* **2020**, *11*, 508.
(9) (a) Du, X.; Moore, J.; Blank, B. R.; Eksterowicz, J.; Sutimantanapi, D.; Yuen, N.; Metzger, T.; Chan, B.; Huang, T.; Chen, X.; Chen, Y.; Duong, F.; Kong, W.; Chang, J. H.; Sun, J.; Zavorotinskaya, T.; Ye, Q.; Junttila, M. R.; Ndubaku, C.; Friedman, L. S.; Fantin, V. R.; Sun, D. Orally bioavailable small-molecule CD73 inhibitor (OP-5244) reverses immunosuppression through blockade of adenosine production. *J. Med. Chem.* **2020**, *63* (18), 10433−10459. (b) Bowman, C. E.; da Silva, R. G.; Pham, A.; Young, S. W. An exceptionally potent inhibitor of human CD73. *Biochemistry* **2019**, *58*, 3331−3334. (c) Chen, L.; Li, J.; Sjogren, E. B.; Billedeau, R. J. Ectonucleotidase inhibitors and methods of use thereof. U.S. Patent US10,472,364 B2, 2019.
(10) Jeffrey, J. L.; Lawson, K. V.; Powers, J. P. Targeting metabolism of extracellular nucleotides via inhibition of ecto-nucleotidases CD73 and CD39. *J. Med. Chem.* **2020**, *63*, 13444−13465.
(11) Lawson, K. V.; Kalisiak, J.; Lindsey, E. A.; Newcomb, E. T.; Leleti, M. R.; Debien, L.; Rosen, B. R.; Miles, D. H.; Sharif, E. U.; Jeffrey, J. L.; Tan, J. B. L.; Chen, A.; Zhao, S.; Xu, G.; Fu, L.; Jin, L.; Park, T. W.; Berry, W.; Moschütz, S.; Scaletti, E.; Sträter, N.; Walker, N. P.; Young, S. W.; Walters, M. J.; Schindler, U.; Powers, J. P. Discovery of AB680: A potent and selective inhibitor of CD73. *J. Med. Chem.* **2020**, *63*, 11448−11468.

https://doi.org/10.1021/acs.jmedchem.1c01852
J. Med. Chem. 2022, 65, 2409−2433

(12) Koszałka, P.; Gołuńska, M.; Urban, A.; Stasiłojć, G.; Stanisławowski, M.; Majewski, M.; Składanowski, A. C.; Bigda, J. Specific activation of A_3, A_{2A} and A_1 adenosine receptors in CD73-Knockout mice affects B16F10 melanoma growth, neovascularization, angiogenesis and macrophage infiltration. *PLoS One* **2016**, *11* (3), e0151420.
(13) Minor, M.; Alcedo, K. P.; Battaglia, R. A.; Snider, N. T. Cell type- and tissue-specific functions of ecto-5′-nucleotidase (CD73). *Am. J. Physiol. Cell. Physiol.* **2019**, *317*, C1079−C1092.
(14) St. Hilaire, C.; Ziegler, S. G.; Markello, T. C.; Brusco, A.; Groden, C.; Gill, F.; Carlson-Donohoe, H.; Lederman, R. J.; Chen, M. Y.; Yang, D.; Siegenthaler, M. P.; Arduino, C.; Mancini, C.; Freudenthal, B.; Stanescu, H. C.; Zdebik, A. A.; Chaganti, R. K.; Nussbaum, R. L.; Kleta, R.; Gahl, W. A.; Boehm, M. NT5E mutations and arterial calcifications. *N. Engl. J. Med.* **2011**, *364*, 432−442.
(15) Shih, Y.-R. V.; Liu, M.; Kwon, S. K.; Iida, M.; Gong, Y.; Sangaj, N.; Varghese, S. Dysregulation of ectonucleotidase-mediated extracellular adenosine during postmenopausal bone loss. *Science Advances* **2019**, *5* (8), eaax1387.
(16) Nedeljkovic, N. Complex regulation of ecto-5′-nucleotidase/CD73 and A2AR-mediated adenosine signaling at neurovascular unit: a link between acute and chronic neuroinflammation. *Pharmacol. Res.* **2019**, *144*, 99−115.
(17) Carmo, M.; Gonçalves, F. Q.; Canas, P. M.; Oses, J.-P.; Fernandes, F. D.; Duarte, F. V.; Palmeira, C. M.; Tomé, A. R.; Agostinho, P.; Andrade, G. M.; Cunha, R. A. Enhanced ATP release and CD73-mediated adenosine formation sustain adenosine A_{2A} receptor over-activation in a rat model of Parkinson's disease. *Br. J. Pharmacol.* **2019**, *176* (18), 3666−3680.
(18) Barros-Barbosa, A. R.; Ferreirinha, F.; Oliveira, A.; Mendes, M.; Lobo, M. G.; Santos, A.; Rangel, R.; Pelletier, J.; Sévigny, J.; Cordeiro, J. M.; Correia-de-Sá, P. Adenosine A_{2A} receptor and ecto-5′-nucleotidase/CD73 are upregulated in hippocampal astrocytes of human patients with mesial temporal lobe epilepsy (MTLE). *Purinergic Signal.* **2016**, *12*, 719−734.
(19) Meng, F.; Guo, Z.; Hu, Y.; Mai, W.; Zhang, Z.; Zhang, B.; Ge, Q.; Lou, H.; Guo, F.; Chen, J.; Duan, S.; Gao, Z. CD73-derived adenosine controls inflammation and neurodegeneration by modulating dopamine signalling. *Brain.* **2019**, *142* (3), 700−718.
(20) Ponce, N. E.; Sanmarco, L. M.; Eberhardt, N.; García, M. C.; Rivarola, H. W.; Cano, R. C.; Aoki, M. P. CD73 inhibition shifts cardiac macrophage polarization toward a microbicidal phenotype and ameliorates the outcome of experimental Chagas cardiomyopathy. *J. Immunol.* **2016**, *197*, 814−823.
(21) De Leve, S.; Wirsdörfer, F.; Jendrossek, V. The CD73/Ado System—A new player in RT induced adverse late effects. *Cancers* **2019**, *11*, 1578.
(22) Heilbronn, A.; Maienschein, V.; Carstensen, K.; Gann, W.; Zimmermann, H. Crucial role of ecto-5′-nucleotidase in differentiation and survival of developing neural cells. *NeuroReport* **1995**, *7*, 257−261.
(23) Badimon, A.; Strasburger, H. J.; Ayata, P.; Chen, X.; Nair, A.; Ikegami, A.; Hwang, P.; Chan, A. T.; Graves, S. M.; Uweru, J. O.; Ledderose, C.; Kutlu, M. G.; Wheeler, M. A.; Kahan, A.; Ishikawa, M.; Wang, Y. C.; Loh, Y. E.; Jiang, J. X.; Surmeier, D. J.; Robson, S. C.; Junger, W. G.; Sebra, R.; Calipari, E. S.; Kenny, P. J.; Eyo, U. B.; Colonna, M.; Quintana, F. J.; Wake, H.; Gradinaru, V.; Schaefer, A. Negative feedback control of neuronal activity by microglia. *Nature* **2020**, *586* (7829), 417−423.
(24) Joolharzadeh, P.; St. Hilaire, C. CD73 (Cluster of Differentiation 73) and the differences between mice and humans. *Arterioscler., Thromb., Vasc. Biol.* **2019**, *39* (3), 339−348.
(25) Bhattarai, S.; Pippel, J.; Scaletti, E.; Idris, R.; Freundlieb, M.; Rolshoven, G.; Renn, C.; Lee, S. Y.; Abdelrahman, A.; Zimmermann, H.; El-Tayeb, A.; Müller, C. E.; Sträter, N. 2-Substituted α,β-methylene-ADP derivatives: Potent competitive ecto-5′-nucleotidase (CD73) inhibitors with variable binding modes. *J. Med. Chem.* **2020**, *63* (6), 2941−2957.
(26) Bhattarai, S.; Freundlieb, M.; Pippel, J.; Meyer, A.; Abdelrahman, A.; Fiene, A.; Lee, S.-Y.; Zimmermann, H.; Yegutkin, G. G.; Sträter, N.; El-Tayeb, A.; Müller, C. E. α,β-Methylene-ADP (AOPCP) derivatives and analogues: development of potent and selective ecto-5′-nucleotidase (CD73) inhibitors. *J. Med. Chem.* **2015**, *58*, 6248−6263.
(27) Bhattarai, S.; Pippel, J.; Meyer, A.; Freundlieb, M.; Schmies, C.; Abdelrahman, A.; Fiene, A.; Lee, S. Y.; Zimmermann, H.; El-Tayeb, A.; Yegutkin, G. G.; Sträter, N.; Müller, C. E. X-Ray co-crystal structure guides the way to subnanomolar competitive ecto-5′-nucleotidase (CD73) inhibitors for cancer immunotherapy. *Adv. Therap.* **2019**, *2* (0), 1900075.
(28) Junker, A.; Renn, C.; Dobelmann, C.; Namasivayam, V.; Jain, S.; Losenkova, K.; Irjala, H.; Duca, S.; Balasubramanian, R.; Chakraborty, S.; Börgel, F.; Zimmermann, H.; Yegutkin, G. G.; Müller, C. E.; Jacobson, K. A. Structure-activity relationship of purine and pyrimidine nucleotides as ecto-5′-nucleotidase (CD73) inhibitors. *J. Med. Chem.* **2019**, *62*, 3677−3695.
(29) Schindler, U.; Becker, A.; Lawson, K.; Jin, L.; Jeffrey, J.; Kalisiak, j.; Yin, F.; Zhang, K.; Chen, A.; Swinarski, D.; Walters, M. J.; Young, S.; Powers, J. P.; Tan, J. AB680, a potent and selective CD73 small molecule inhibitor, reverses the AMP/adenosine-mediated impairment of immune effector cell activation by immune checkpoint inhibitors. Abstract P04.03. *Eur. J. Cancer.* **2018**, *92*, S14.
(30) Ghoteimi, R.; Nguyen, V. T.; Rahimova, R.; Grosjean, F.; Cros-Perrial, E.; Uttaro, J. P.; Mathé, C.; Chaloin, L.; Jordheim, L. P.; Peyrottes, S. Synthesis of substituted 5′-aminoadenosine derivatives and evaluation of their inhibitory potential toward CD73. *ChemMedChem.* **2019**, *14* (15), 1431−1443.
(31) Nocentini, A.; Capasso, C.; Supuran, C. T. Small-molecule CD73 inhibitors for the immunotherapy of cancer: a patent and literature review (2017−present). *Exp. Opin. Therap. Patents* **2021**, *31* (10), 867−876.
(32) Varano, F.; Catarzi, D.; Vincenzi, F.; Pasquini, S.; Pelletier, J.; Lopes Rangel Fietto, J.; Espindola Gelsleichter, N.; Sarlandie, M.; Guilbaud, A.; Sévigny, J.; Varani, K.; Colotta, V. Structural investigation on thiazolo[5,4-d]pyrimidines to obtain dual-acting blockers of CD73 and adenosine A_{2A} receptor as potential antitumor agents. *Bioorg. Med. Chem. Lett.* **2020**, *30* (9), 127067.
(33) Beatty, J. W.; Lindsey, E. A.; Thomas-Tran, R.; Debien, L.; Mandal, D.; Jeffrey, J. L.; Tran, A. T.; Fournier, J.; Jacob, S. D.; Yan, X.; Drew, S. L.; Ginn, E.; Chen, A.; Pham, A. T.; Zhao, S.; Jin, L.; Young, S. W.; Walker, N. P.; Leleti, M. R.; Moschütz, S.; Sträter, N.; Powers, J. P.; Lawson, K. V. Discovery of potent and selective non-nucleotide small molecule inhibitors of CD73. *J. Med. Chem.* **2020**, *63* (8), 3935−3955.
(34) Oliva, P.; Scortichini, M.; Dobelmann, C.; Jain, S.; Gopinatth, V.; Toti, K. S.; Phung, N. B.; Junker, A.; Jacobson, K. A. Structure activity relationship of pyrimidine nucleotides containing a 5′-α,β-methylene diphosphonate as $P2Y_6$ receptor agonists. *Bioorg. Med. Chem. Lett.* **2021**, *45*, 128137.
(35) Jayasekara, P. S.; Jacobson, K. A. Rapid Synthesis of alkoxyamine hydrochloride derivatives from alkyl bromide and N,N'-di-tert-butoxycarbonylhydroxylamine [$(Boc)_2NOH$]. *Synth. Commun.* **2014**, *44*, 2344−2347.
(36) Jacobson, K. A.; Salmaso, V.; Suresh, R. R.; Tosh, D. K. Expanding the repertoire of methanocarba nucleosides from purine receptors to diverse targets. *RSC Med. Chem.* **2021**, *12*, 1808−1825.
(37) Salmaso, V.; Jacobson, K. A. Survey of ribose ring pucker of signaling nucleosides and nucleotides. *Nucleos. Nucleotid. Nucl. Acids* **2020**, *39*, 322−341.
(38) Toti, K. S.; Jain, S.; Ciancetta, A.; Balasubramanian, R.; Chakraborty, S.; Surujdin, R.; Shi, Z. D.; Jacobson, K. A. Pyrimidine nucleotides containing a (S)-methanocarba ring as $P2Y_6$ receptor agonists. *Med. Chem. Commun.* **2017**, *8* (10), 1897−1908.
(39) Kim, H. S.; Ravi, R. G.; Marquez, V. E.; Maddileti, S.; Wihlborg, A. K.; Erlinge, D.; Malmsjö, M.; Boyer, J. L.; Harden, T. K.; Jacobson, K. A. Methanocarba modification of uracil and adenine nucleotides: high potency of northern ring conformation at $P2Y_1$,

https://doi.org/10.1021/acs.jmedchem.1c01852
J. Med. Chem. 2022, 65, 2409−2433

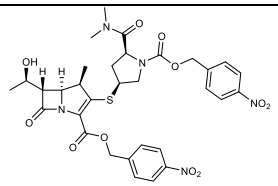
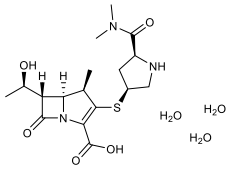
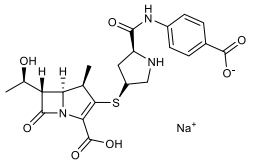
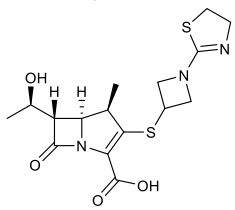
$P2Y_2$, $P2Y_4$, and $P2Y_{11}$ but not $P2Y_6$ receptors. *J. Med. Chem.* **2002**, *45* (1), 208−218.
(40) Rawling, T.; McDonagh, A. M.; Tattam, B.; Murray, M. Synthesis of unsymmetrical biaryl ureas from N-carbamoylimidazoles: kinetics and application. *Tetrahedron* **2012**, *68*, 6065−6070.
(41) Freundlieb, M.; Zimmermann, H.; Müller, C. E. A new, sensitive ecto-5′-nucleotidase assay for compound screening. *Anal. Biochem.* **2014**, *446*, 53−58.
(42) Servos, J.; Reiländer, H.; Zimmermann, H. Catalytically active soluble ecto-5′-nucleotidase purified after heterologous expression as a tool for drug screening. *Drug Dev. Res.* **1998**, *45*, 269−276.
(43) Cheng, Y.-C.; Prusoff, W. H. Relationship between the inhibition constant (Ki) and the concentration of inhibitor which causes 50% inhibition (IC_{50}) of an enzymatic reaction. *Biochem. Pharmacol.* **1973**, *22*, 3099−3108.
(44) Besnard, J.; Ruda, G. F.; Setola, V.; Abecassis, K.; Rodriguiz, R. M.; Huang, X. P.; Norval, S.; Sassano, M. F.; Shin, A. I.; Webster, L. A.; Simeons, F. R.; Stojanovski, L.; Prat, A.; Seidah, N. G.; Constam, D. B.; Bickerton, G. R.; Read, K. D.; Wetsel, W. C.; Gilbert, I. H.; Roth, B. L.; Hopkins, A. L. Automated design of ligands to polypharmacological profiles. *Nature* **2012**, *492*, 215−220.
(45) Knapp, K.; Zebisch, M.; Pippel, J.; El-Tayeb, A.; Müller, C. E.; Sträter, N. Crystal structure of the human ecto-5′-nucleotidase (CD73): Insights into the regulation of purinergic signaling. *Structure* **2012**, *20*, 2161−2173.
(46) Scaletti, E.; Huschmann, F. U.; Müller, U.; Weiss, M. S.; Sträter, N. Substrate binding modes of purine and pyrimidine nucleotides to human ecto-5′-nucleotidase (CD73) and inhibition by their bisphosphonic acid derivatives. *Purinergic Signalling* **2021**, *17*, 693−704.
(47) Seeber, M.; Felline, A.; Raimondi, F.; Muff, S.; Friedman, R.; Rao, F.; Caflisch, A.; Fanelli, F. Wordom: a user-friendly program for the analysis of molecular structures, trajectories, and free energy surfaces. *J. Comput. Chem.* **2011**, *32*, 1183−1194.
(48) Tosh, D. K.; Salmaso, V.; Rao, H.; Campbell, R.; Bitant, A.; Gao, Z.-G.; Auchampach, J. A.; Jacobson, K. A. Direct comparison of (N)-methanocarba and ribose-containing 2-arylalkynyladenosine derivatives as A_3 receptor agonists. *ACS Med. Chem. Lett.* **2020**, *11*, 1935−1941.
(49) Losenkova, K.; Paul, M.; Irjala, H.; Jalkanen, S.; Yegutkin, G. G. Histochemical approach for simultaneous detection of ectonucleotidase and alkaline phosphatase activities in tissues. *Methods Mol. Biol.* **2020**, *2041*, 107−116.
(50) Jacobson, K. A. Functionalized congener approach to the design of ligands for G protein−coupled receptors (GPCRs). *Bioconjugate Chem.* **2009**, *20*, 1816−1835.
(51) Schmies, C.; Rolshoven, G.; Idris, R. M.; Losenkova, K.; Renn, C.; Schäkel, L.; Al-Hroub, H.; Wang, Y.; Garofano, F.; Schmidt-Wolf, I. G. H.; Zimmermann, H.; Yegutkin, G. G.; Müller, C. E. Fluorescent Probes for Ecto-5′-nucleotidase (CD73). *ACS Med. Chem. Lett.* **2020**, *11* (11), 2253−2260.
(52) Bankhead, P.; Loughrey, M. B.; Fernández, J. A.; Dombrowski, Y.; McArt, D. G.; Dunne, P. D.; McQuaid, S.; Gray, R. T.; Murray, L. J.; Coleman, H. G.; James, J. A.; Salto-Tellez, M.; Hamilton, P. W. QuPath: Open source software for digital pathology image analysis. *Sci. Rep.* **2017**, *7*, 16878.
(53) Aricescu, A. R.; Lu, W.; Jones, E. Y. *Acta Crystallogr. D Biol. Crystallogr.* **2006**, *62* (10), 1243−1250.
(54) Kabsch, W. XDS. *Acta Crystallogr.* **2010**, *D66*, 125−132.
(55) Blanc, E.; Roversi, P.; Vonrhein, C.; Flensburg, C.; Lea, S. M.; Bricogne, G. Refinement of severely incomplete structures with maximum likelihood in BUSTER-TNT. *Acta Crystallogr.* **2004**, *D60*, 2210−2221.
(56) Emsley, P.; Lohkamp, B.; Scott, W. G.; Cowtan, K. Features and development of Coot. *Acta Crystallogr., Sect. D: Biol. Crystallogr.* **2010**, *66*, 486−501.
(57) *Maestro*, release 2020-1; Schrödinger, LLC: New York, 2019.
(58) Madhavi Sastry, G.; Adzhigirey, M.; Day, T.; Annabhimoju, R.; Sherman, W. Protein and ligand preparation: Parameters, protocols, and influence on virtual screening enrichments. *J. Comput.-Aided Mol. Des.* **2013**, *27*, 221−234.
(59) Jacobson, M. P.; Pincus, D. L.; Rapp, C. S.; Day, T. J. F.; Honig, B.; Shaw, D. E.; Friesner, R. A. A hierarchical approach to all-atom protein loop prediction. *Proteins: Struct., Funct., Genet.* **2004**, *55*, 351−367.
(60) Jacobson, M. P.; Friesner, R. A.; Xiang, Z.; Honig, B. On the role of the crystal environment in determining protein side-chain conformations. *J. Mol. Biol.* **2002**, *320* (3), 597−608.
(61) Harder, E.; Damm, W.; Maple, J.; Wu, C.; Reboul, M.; Xiang, J. Y.; Wang, L.; Lupyan, D.; Dahlgren, M. K.; Knight, J. L.; Kaus, J. W.; Cerutti, D. S.; Krilov, G.; Jorgensen, W. L.; Abel, R.; Friesner, R. A. OPLS3: A force field providing broad coverage of drug-like small molecules and proteins. *J. Chem. Theory Comput.* **2016**, *12*, 281−296.
(62) Friesner, R. A.; Murphy, R. B.; Repasky, M. P.; Frye, L. L.; Greenwood, J. R.; Halgren, T. A.; Sanschagrin, P. C.; Mainz, D. T. Extra Precision Glide: Docking and scoring incorporating a model of hydrophobic enclosure for protein-ligand complexes. *J. Med. Chem.* **2006**, *49* (21), 6177−6196.
(63) Case, D. A.; Aktulga, H. M.; Belfon, K.; Ben-Shalom, I. Y.; Brozell, S. R.; Cerutti, D. S.; Cheatham, T. E., III; Cruzeiro, V. W. D.; Darden, T. A.; Duke, R. E.; Giambasu, G.; Gilson, M. K.; Gohlke, H.; Goetz, A. W.; Harris, R.; Izadi, S.; Izmailov, S. A.; Jin, C.; Kasavajhala, K.; Kaymak, M. C.; King, E.; Kovalenko, A.; Kurtzman, T.; Lee, T. S.; LeGrand, S.; Li, P.; Lin, C.; Liu, J.; Luchko, T.; Luo, R.; Machado, M.; Man, V.; Manathunga, M.; Merz, K. M.; Miao, Y.; Mikhailovskii, O.; Monard, G.; Nguyen, H.; O'Hearn, K. A.; Onufriev, A.; Pan, F.; Pantano, S.; Qi, R.; Rahnamoun, A.; Roe, D. R.; Roitberg, A.; Sagui, C.; Schott-Verdugo, S.; Shen, J.; Simmerling, C. L.; Skrynnikov, N. R.; Smith, J.; Swails, J.; Walker, R. C.; Wang, J.; Wei, H.; Wolf, R. M.; Wu, X.; Xue, Y.; York, D. M.; Zhao, S.; Kollman, P. A. *Amber 2021*; University of California, San Francisco: San Francisco, 2021.
(64) Wang, J.; Wang, W.; Kollman, P. A.; Case, D. A. Automatic atom type and bond type perception in molecular mechanical calculations. *J. Mol. Graph. Model.* **2006**, *25*, 247−260.
(65) Jakalian, A.; Jack, D. B.; Bayly, C. I. Fast, efficient generation of high-quality atomic charges. AM1-BCC model: II. Parameterization and validation. *J. Comput. Chem.* **2002**, *23*, 1623−1641.
(66) Steinbrecher, T.; Latzer, J.; Case, D. A. Revised AMBER parameters for bioorganic phosphates. *J. Chem. Theory Comput.* **2012**, *8*, 4405−4412.
(67) Jorgensen, W. L.; Chandrasekhar, J.; Madura, J. D.; Impey, R. W.; Klein, M. L. Comparison of simple potential functions for simulating liquid water. *J. Chem. Phys.* **1983**, *79* (2), 926.
(68) Maier, J. A.; Martinez, C.; Kasavajhala, K.; Wickstrom, L.; Hauser, K. E.; Simmerling, C. ff14SB: Improving the accuracy of protein side chain and backbone parameters from ff99SB. *J. Chem. Theory Comput.* **2015**, *11*, 3696−3713.
(69) Wang, J.; Wolf, R. M.; Caldwell, J. W.; Kollman, P. A.; Case, D. A. Development and testing of a general amber force field. *J. Comput. Chem.* **2004**, *25*, 1157−1174.
(70) Harvey, M. J.; Giupponi, G.; Fabritiis, G. D. ACEMD: Accelerating biomolecular dynamics in the microsecond time scale. *J. Chem. Theory Comput.* **2009**, *5*, 1632−1639.
(71) Essmann, U.; Perera, L.; Berkowitz, M. L.; Darden, T.; Lee, H.; Pedersen, L. G. A smooth particle mesh Ewald method. *J. Chem. Phys.* **1995**, *103*, 8577−8593.
(72) Humphrey, W.; Dalke, A.; Schulten, K. VMD: visual molecular dynamics. *J. Mol. Graph.* **1996**, *14*, 33−38.
(73) McKinney, W. Data structures for statistical computing in python. In *Proceedings of the 9th Python in Science Conference*; SciPy, 2010; pp 56−61.
(74) Hunter, J. D. Matplotlib: A 2D graphics environment. *Comput. Sci. Eng.* **2007**, *9*, 90−95.
(75) Williams, T.; Kelley, C. *Gnuplot 5.0.[Sl]*; http://www.gnuplot.info.

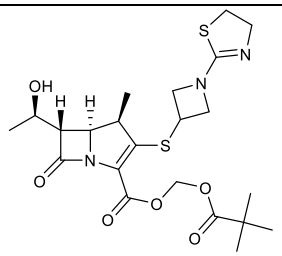
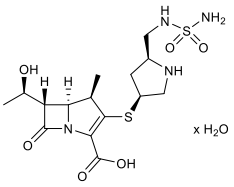
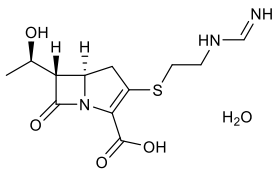
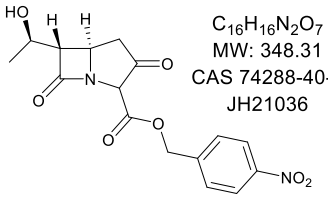
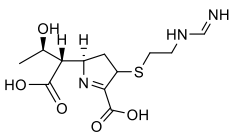
https://doi.org/10.1021/acs.jmedchem.1c01852
J. Med. Chem. 2022, 65, 2409−2433

Appendix III: Screening of imipenem and related compounds at human CD73

Imipenem and related compounds were screened at soluble human CD73 at 20 µM concentration. An enzyme inhibition assay based on measurement of radiolabeled adenosine generated by the catalytic hydrolysis of radiolabeled AMP at a concentration of 5 µM was applied to evaluate the biological activity of test the compounds.[170] Results are presented in **Table 31** and **Figure 100**. None of the test compounds showed activity against soluble human CD73 recombinantly expressed in *Sf*9 insect cell.

Table 29. Screening result for selected imipenem molecules at soluble human CD73

No.	Test compound	Structure	Inhibition (% ± SEM) of soluble human CD73 at 20 µM (n=2)
1	PZB00421007A	 Chemical Formula: $C_{32}H_{36}N_5O_{11}S$ Molecular Weight: 697,72	**5** ± 2
2	PZB00421008A	Trihydrate: Chemical Formula: $C_{17}H_{31}N_3O_8S$ Molecular Weight: 437,51  Chemical Formula: $C_{17}H_{25}N_3O_5S$ Molecular Weight: 383,46	**2** ± 7
3	PZB00421009A	Chemical Formula: $C_{22}H_{24}N_3NaO_7S$ Molecular Weight: 497,50  Chemical Formula: $C_{22}H_{24}N_3O_7S^-$ Molecular Weight: 474,51	**1** ± 1
4	PZB00421010A	 Chemical Formula: $C_{16}H_{21}N_3O_4S_2$ Molecular Weight: 383,48	**-1** ± 5

5	PZB00421011A	 Chemical Formula: $C_{22}H_{31}N_3O_6S_2$ Molecular Weight: 497,63	**0** ± 6
6	PZB00421012A	Hydrate: Chemical Formula: $C_{15}H_{24}N_4O_6S_2$ Molecular Weight: 420,50  Chemical Formula: $C_{15}H_{24}N_4O_6S_2$ Molecular Weight: 420,50	**7** ± 7
7	PZB00421013A	**Imipenem monohydrat:** Chemical Formula: $C_{12}H_{19}N_3O_5S$ Molecular Weight: 317,36  Chemical Formula: $C_{12}H_{17}N_3O_4S$ Molecular Weight: 299,35	**5** ± 4
8	PZB00421005A	 $C_{16}H_{16}N_2O_7$ MW: 348.31 CAS 74288-40-7 JH21036	**4** ± 6
9	PZB00421006B	 Chemical Formula: $C_{12}H_{19}N_3O_5S$ Molecular Weight: 317,36 JH21030	**6** ± 2

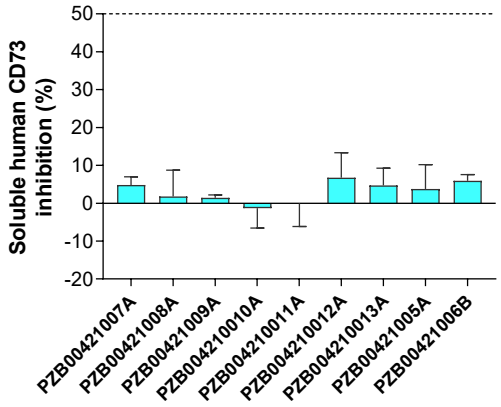


Figure 100. Screening results for imipenem derivatives at soluble human CD73 at 20 µM concentration. Data points are means ± SEM of two independent experiments, performed in duplicates.

These results show that adenosine formation is likely not involved in the effects of the antibiotic imipenem on the immune system during sepsis therapy.

Appendix IV: DNA sequences of various CD73 constructs

10xHis-tag-protease cleavage site-soluble human CD73

ATGGTAAGCGCTATTGTTTTATATGTGCTTTTGGCGGCGGCGGCGCATTCTGCCTTTGCG
GCGGATCTTGGATCCCACCATCATCACCATCATCACCACCACCACCTGGAGGTGCTCTTC
CAGGGTCCCTGGGAGCTTACGATTTTGCACACCAACGACGTGCACAGCCGGCTGGAGCAG
ACCAGCGAGGACTCCAGCAAGTGCGTCAACGCCAGCCGCTGCATGGGTGGCGTGGCTCGG
CTCTTCACCAAGGTTCAGCAGATCCGCCGCGCCGAACCCAACGTGCTGCTGCTGGACGCC
GGCGACCAGTACCAGGGCACTATCTGGTTCACCGTGTACAAGGGCGCCGAGGTGGCGCAC
TTCATGAACGCCCTGCGCTACGATGCCATGGCACTGGGAAATCATGAATTTGATAATGGT
GTGGAAGGACTGATCGAGCCACTCCTCAAAGAGGCCAAATTTCCAATTCTGAGTGCAAAC
ATTAAAGCAAAGGGGCCACTAGCATCTCAAATATCAGGACTTTATTTGCCATATAAAGTT
CTTCCTGTTGGTGATGAAGTTGTGGGAATCGTTGGATACACTTCCAAAGAAACCCCTTTT
CTCTCAAATCCAGGGACAAATTTAGTGTTTGAAGATGAAATCACTGCATTACAACCTGAA
GTAGATAAGTTAAAAACTCTAAATGTGAACAAAATTATTGCACTGGGACATTCGGGTTTT
GAAATGGATAAACTCATCGCTCAGAAAGTGAGGGGTGTGGACGTCGTGGTGGGAGGACAC
TCCAACACATTTCTTTACACAGGCAATCCACCTTCCAAAGAGGTGCCTGCTGGGAAGTAC
CCATTCATAGTCACTTCTGATGATGGGCGGAAGGTTCCTGTAGTCCAGGCCTATGCTTTT
GGCAAATACCTAGGCTATCTGAAGATCGAGTTTGATGAAAGAGGAAACGTCATCTCTTCC
CATGGAAATCCCATTCTTCTAAACAGCAGCATTCCTGAAGATCCAAGCATAAAAGCAGAC
ATTAACAAATGGAGGATAAAATTGGATAATTATTCTACCCAGGAATTAGGGAAAACAATT
GTCTATCTGGATGGCTCCTCTCAATCATGCCGCTTTAGAGAATGCAACATGGGCAACCTG
ATTTGTGATGCAATGATTAACAACAACCTGAGACACACCGATGAAATGTTCTGGAACCAC
GTATCCATGTGCATTTTAAATGGAGGTGGTATCCGGTCGCCCATTGATGAACGCAACAAT
GGCACAATTACCTGGGAGAACCTGGCTGCTGTATTGCCCTTTGGAGGCACATTTGACCTA
GTCCAGTTAAAAGGTTCCACCCTGAAGAAGGCCTTTGAGCATAGCGTGCACCGCTACGGC
CAGTCCACTGGAGAGTTCCTGCAGGTGGGCGGAATCCATGTGGTGTATGATCTTTCCCGA
AAACCTGGAGACAGAGTAGTCAAATTAGATGTTCTTTGCACCAAGTGTCGAGTGCCCAGT
TATGACCCTCTCAAAATGGACGAGGTATATAAGGTGATCCTCCCAAACTTCCTGGCCAAT
GGTGGAGATGGGTTCCAGATGATAAAAGATGAATTATTAAGACATGACTCTGGTGACCAA
GATATCAACGTGGTTTCTACATATATCTCCAAAATGAAAGTAATTTATCCAGCAGTTGAA
GGTCGGATCAAGTTTAGCTAA

10xHis-tag-protease cleavage site-linker-soluble human CD73

ATGGTGAGTGCCATAGTATTATATGTATTGTTAGCGGCTGCCGCACACTCGGCGTTCGCG
GCGGGGTCTCATCACCACCACCACCACCACCATCATCATCTCGAAGTCCTATTTCAAGGC
CCCGGAGGCGGGGGTAGCTGGGAGCTAACTATCCTGCATACGAACGACGTGCACAGCCGG
CTGGAGCAGACCAGCGAGGACTCCAGCAAGTGCGTCAACGCCAGCCGCTGCATGGGTGGC
GTGGCTCGGCTCTTCACCAAGGTTCAGCAGATCCGCCGCGCCGAACCCAACGTGCTGCTG
CTGGACGCCGGCGACCAGTACCAGGGCACTATCTGGTTCACCGTGTACAAGGGCGCCGAG
GTGGCGCACTTCATGAACGCCCTGCGCTACGATGCCATGGCACTGGGAAATCATGAATTT
GATAATGGTGTGGAAGGACTGATCGAGCCACTCCTCAAAGAGGCCAAATTTCCAATTCTG
AGTGCAAACATTAAAGCAAAGGGGCCACTAGCATCTCAAATATCAGGACTTTATTTGCCA

TATAAAGTTCTTCCTGTTGGTGATGAAGTTGTGGGAATCGTTGGATACACTTCCAAAGAA
ACCCCTTTTCTCTCAAATCCAGGGACAAATTTAGTGTTTGAAGATGAAATCACTGCATTA
CAACCTGAAGTAGATAAGTTAAAAACTCTAAATGTGAACAAAATTATTGCACTGGGACAT
TCGGGTTTTGAAATGGATAAACTCATCGCTCAGAAAGTGAGGGGTGTGGACGTCGTGGTG
GGAGGACACTCCAACACATTTCTTTACACAGGCAATCCACCTTCCAAAGAGGTGCCTGCT
GGGAAGTACCCATTCATAGTCACTTCTGATGATGGGCGGAAGGTTCCTGTAGTCCAGGCC
TATGCTTTTGGCAAATACCTAGGCTATCTGAAGATCGAGTTTGATGAAAGAGGAAACGTC
ATCTCTTCCCATGGAAATCCCATTCTTCTAAACAGCAGCATTCCTGAAGATCCAAGCATA
AAAGCAGACATTAACAAATGGAGGATAAAATTGGATAATTATTCTACCCAGGAATTAGGG
AAAACAATTGTCTATCTGGATGGCTCCTCTCAATCATGCCGCTTTAGAGAATGCAACATG
GGCAACCTGATTTGTGATGCAATGATTAACAACAACCTGAGACACACCGATGAAATGTTC
TGGAACCACGTATCCATGTGCATTTTAAATGGAGGTGGTATCCGGTCGCCCATTGATGAA
CGCAACAATGGCACAATTACCTGGGAGAACCTGGCTGCTGTATTGCCCTTTGGAGGCACA
TTTGACCTAGTCCAGTTAAAAGGTTCCACCCTGAAGAAGGCCTTTGAGCATAGCGTGCAC
CGCTACGGCCAGTCCACTGGAGAGTTCCTGCAGGTGGGCGGAATCCATGTGGTGTATGAT
CTTTCCCGAAAACCTGGAGACAGAGTAGTCAAATTAGATGTTCTTTGCACCAAGTGTCGA
GTGCCCAGTTATGACCCTCTCAAAATGGACGAGGTATATAAGGTGATCCTCCCAAACTTC
CTGGCCAATGGTGGAGATGGGTTCCAGATGATAAAAGATGAATTATTAAGACATGACTCT
GGTGACCAAGATATCAACGTGGTTTCTACATATATCTCCAAAATGAAAGTAATTTATCCA
GCAGTTGAAGGTCGGATCAAGTTTAGCTAA

Soluble human CD73-linker-protease cleavage site-6xHis-tag

ATGGTAAGCGCTATTGTTTTATATGTGCTTTTGGCGGCGGCGGCGCATTCTGCCTTTGCG
GCGGATCTTGGATCCTGGGAGCTTACGATTTTGCACACCAACGACGTGCACAGCCGGCTG
GAGCAGACCAGCGAGGACTCCAGCAAGTGCGTCAACGCCAGCCGCTGCATGGGTGGCGTG
GCTCGGCTCTTCACCAAGGTTCAGCAGATCCGCCGCGCCGAACCCAACGTGCTGCTGCTG
GACGCCGGCGACCAGTACCAGGGCACTATCTGGTTCACCGTGTACAAGGGCGCCGAGGTG
GCGCACTTCATGAACGCCCTGCGCTACGATGCCATGGCACTGGGAAATCATGAATTTGAT
AATGGTGTGGAAGGACTGATCGAGCCACTCCTCAAAGAGGCCAAATTTCCAATTCTGAGT
GCAAACATTAAAGCAAAGGGGCCACTAGCATCTCAAATATCAGGACTTTATTTGCCATAT
AAAGTTCTTCCTGTTGGTGATGAAGTTGTGGGAATCGTTGGATACACTTCCAAAGAAACC
CCTTTTCTCTCAAATCCAGGGACAAATTTAGTGTTTGAAGATGAAATCACTGCATTACAA
CCTGAAGTAGATAAGTTAAAAACTCTAAATGTGAACAAAATTATTGCACTGGGACATTCG
GGTTTTGAAATGGATAAACTCATCGCTCAGAAAGTGAGGGGTGTGGACGTCGTGGTGGGA
GGACACTCCAACACATTTCTTTACACAGGCAATCCACCTTCCAAAGAGGTGCCTGCTGGG
AAGTACCCATTCATAGTCACTTCTGATGATGGGCGGAAGGTTCCTGTAGTCCAGGCCTAT
GCTTTTGGCAAATACCTAGGCTATCTGAAGATCGAGTTTGATGAAAGAGGAAACGTCATC
TCTTCCCATGGAAATCCCATTCTTCTAAACAGCAGCATTCCTGAAGATCCAAGCATAAAA
GCAGACATTAACAAATGGAGGATAAAATTGGATAATTATTCTACCCAGGAATTAGGGAAA
ACAATTGTCTATCTGGATGGCTCCTCTCAATCATGCCGCTTTAGAGAATGCAACATGGGC
AACCTGATTTGTGATGCAATGATTAACAACAACCTGAGACACACCGATGAAATGTTCTGG
AACCACGTATCCATGTGCATTTTAAATGGAGGTGGTATCCGGTCGCCCATTGATGAACGC
AACAATGGCACAATTACCTGGGAGAACCTGGCTGCTGTATTGCCCTTTGGAGGCACATTT
GACCTAGTCCAGTTAAAAGGTTCCACCCTGAAGAAGGCCTTTGAGCATAGCGTGCACCGC

TACGGCCAGTCCACTGGAGAGTTCCTGCAGGTGGGCGGAATCCATGTGGTGTATGATCTT
TCCCGAAAACCTGGAGACAGAGTAGTCAAATTAGATGTTCTTTGCACCAAGTGTCGAGTG
CCCAGTTATGACCCTCTCAAAATGGACGAGGTATATAAGGTGATCCTCCCAAACTTCCTG
GCCAATGGTGGAGATGGGTTCCAGATGATAAAAGATGAATTATTAAGACATGACTCTGGT
GACCAAGATATCAACGTGGTTTCTACATATATCTCCAAAATGAAAGTAATTTATCCAGCA
GTTGAAGGTCGGATCAAGTTTAGCGGTGGAGGAAGCCTGGAAGTTCTGTTCCAGGGGCCC
CATCATCACCATCACCACTAA

Soluble human CD73-Nluc

ATGGTAAGCGCTATTGTTTTATATGTGCTTTTGGCGGCGGCGGCGCATTCTGCCTTTGCG
GCGGATCTTGGATCCCACCATCATCACCATCATCACCACCACCACCTGGAGGTGCTCTTC
CAGGGTCCCTGGGAGCTTACGATTTTGCACACCAACGACGTGCACAGCCGGCTGGAGCAG
ACCAGCGAGGACTCCAGCAAGTGCGTCAACGCCAGCCGCTGCATGGGTGGCGTGGCTCGG
CTCTTCACCAAGGTTCAGCAGATCCGCCGCGCCGAACCCAACGTGCTGCTGCTGGACGCC
GGCGACCAGTACCAGGGCACTATCTGGTTCACCGTGTACAAGGGCGCCGAGGTGGCGCAC
TTCATGAACGCCCTGCGCTACGATGCCATGGCACTGGGAAATCATGAATTTGATAATGGT
GTGGAAGGACTGATCGAGCCACTCCTCAAAGAGGCCAAATTTCCAATTCTGAGTGCAAAC
ATTAAAGCAAAGGGGCCACTAGCATCTCAAATATCAGGACTTTATTTGCCATATAAAGTT
CTTCCTGTTGGTGATGAAGTTGTGGGAATCGTTGGATACACTTCCAAAGAAACCCCTTTT
CTCTCAAATCCAGGGACAAATTTAGTGTTTGAAGATGAAATCACTGCATTACAACCTGAA
GTAGATAAGTTAAAAACTCTAAATGTGAACAAAATTATTGCACTGGGACATTCGGGTTTT
GAAATGGATAAACTCATCGCTCAGAAAGTGAGGGGTGTGGACGTCGTGGTGGGAGGACAC
TCCAACACATTTCTTTACACAGGCAATCCACCTTCCAAAGAGGTGCCTGCTGGGAAGTAC
CCATTCATAGTCACTTCTGATGATGGGCGGAAGGTTCCTGTAGTCCAGGCCTATGCTTTT
GGCAAATACCTAGGCTATCTGAAGATCGAGTTTGATGAAAGAGGAAACGTCATCTCTTCC
CATGGAAATCCCATTCTTCTAAACAGCAGCATTCCTGAAGATCCAAGCATAAAAGCAGAC
ATTAACAAATGGAGGATAAAATTGGATAATTATTCTACCCAGGAATTAGGGAAAACAATT
GTCTATCTGGATGGCTCCTCTCAATCATGCCGCTTTAGAGAATGCAACATGGGCAACCTG
ATTTGTGATGCAATGATTAACAACAACCTGAGACACACCGATGAAATGTTCTGGAACCAC
GTATCCATGTGCATTTTAAATGGAGGTGGTATCCGGTCGCCCATTGATGAACGCAACAAT
GGCACAATTACCTGGGAGAACCTGGCTGCTGTATTGCCCTTTGGAGGCACATTTGACCTA
GTCCAGTTAAAAGGTTCCACCCTGAAGAAGGCCTTTGAGCATAGCGTGCACCGCTACGGC
CAGTCCACTGGAGAGTTCCTGCAGGTGGGCGGAATCCATGTGGTGTATGATCTTTCCCGA
AAACCTGGAGACAGAGTAGTCAAATTAGATGTTCTTTGCACCAAGTGTCGAGTGCCCAGT
TATGACCCTCTCAAAATGGACGAGGTATATAAGGTGATCCTCCCAAACTTCCTGGCCAAT
GGTGGAGATGGGTTCCAGATGATAAAAGATGAATTATTAAGACATGACTCTGGTGACCAA
GATATCAACGTGGTTTCTACATATATCTCCAAAATGAAAGTAATTTATCCAGCAGTTGAA
ggtcggatcaagtttagccTCGAGGGAGGTGGTAGCGTCTTCACACTCGAAGATTTCGTT
GGGGACTGGCGACAGACAGCCGGCTACAACCTGGACCAAGTCCTTGAACAGGGAGGTGTG
TCCAGTTTGTTTCAGAATCTCGGGGTGTCCGTAACTCCGATCCAAAGGATTGTCCTGAGC
GGTGAAAATGGGCTGAAGATCGACATCCATGTCATCATCCCGTATGAAGGTCTGAGCGGC
GACCAAATGGGCCAGATCGAAAAAATTTTTAAGGTGGTGTACCCTGTGGATGATCATCAC
TTTAAGGTGATCCTGCACTATGGCACACTGGTAATCGACGGGGTTACGCCGAACATGATC
GACTATTTCGGACGGCCGTATGAAGGCATCGCCGTGTTCGACGGCAAAAAGATCACTGTA

ACAGGGACCCTGTGGAACGGCAACAAAATTATCGACGAGCGCCTGATCAACCCCGACGGC
TCCCTGCTGTTCCGAGTAACCATCAACGGAGTGACCGGCTGGCGGCTGTGCGAACGCATT
CTGGCGTAA

Nluc-Soluble human CD73

ATGAACTCCTTCTCCACAAGCGCCTTCGGTCCAGTTGCCTTCTCCCTGGGCCTGCTCCTG
GTGTTGCCTGCTGCCTTCCCTGCCCCAGTCTTCACACTCGAAGATTTCGTTGGGGACTGG
CGACAGACAGCCGGCTACAACCTGGACCAAGTCCTTGAACAGGGAGGTGTGTCCAGTTTG
TTTCAGAATCTCGGGGTGTCCGTAACTCCGATCCAAAGGATTGTCCTGAGCGGTGAAAAT
GGGCTGAAGATCGACATCCATGTCATCATCCCGTATGAAGGTCTGAGCGGCGACCAAATG
GGCCAGATCGAAAAAATTTTTAAGGTGGTGTACCCTGTGGATGATCATCACTTTAAGGTG
ATCCTGCACTATGGCACACTGGTAATCGACGGGGTTACGCCGAACATGATCGACTATTTC
GGACGGCCGTATGAAGGCATCGCCGTGTTCGACGGCAAAAAGATCACTGTAACAGGGACC
CTGTGGAACGGCAACAAAATTATCGACGAGCGCCTGATCAACCCCGACGGCTCCCTGCTG
TTCCGAGTAACCATCAACGGAGTGACCGGCTGGCGGCTGTGCGAACGCATTCTGGCGGGT
GGAGGAAGCGGATCCTGGGAGCTTACGATTTTGCACACCAACGACGTGCACAGCCGGCTG
GAGCAGACCAGCGAGGACTCCAGCAAGTGCGTCAACGCCAGCCGCTGCATGGGTGGCGTG
GCTCGGCTCTTCACCAAGGTTCAGCAGATCCGCCGCGCCGAACCCAACGTGCTGCTGCTG
GACGCCGGCGACCAGTACCAGGGCACTATCTGGTTCACCGTGTACAAGGGCGCCGAGGTG
GCGCACTTCATGAACGCCCTGCGCTACGATGCCATGGCACTGGGAAATCATGAATTTGAT
AATGGTGTGGAAGGACTGATCGAGCCACTCCTCAAAGAGGCCAAATTTCCAATTCTGAGT
GCAAACATTAAAGCAAAGGGGCCACTAGCATCTCAAATATCAGGACTTTATTTGCCATAT
AAAGTTCTTCCTGTTGGTGATGAAGTTGTGGGAATCGTTGGATACACTTCCAAAGAAACC
CCTTTTCTCTCAAATCCAGGGACAAATTTAGTGTTTGAAGATGAAATCACTGCATTACAA
CCTGAAGTAGATAAGTTAAAAACTCTAAATGTGAACAAAATTATTGCACTGGGACATTCG
GGTTTTGAAATGGATAAACTCATCGCTCAGAAAGTGAGGGGTGTGGACGTCGTGGTGGGA
GGACACTCCAACACATTTCTTTACACAGGCAATCCACCTTCCAAAGAGGTGCCTGCTGGG
AAGTACCCATTCATAGTCACTTCTGATGATGGGCGGAAGGTTCCTGTAGTCCAGGCCTAT
GCTTTTGGCAAATACCTAGGCTATCTGAAGATCGAGTTTGATGAAAGAGGAAACGTCATC
TCTTCCCATGGAAATCCCATTCTTCTAAACAGCAGCATTCCTGAAGATCCAAGCATAAAA
GCAGACATTAACAAATGGAGGATAAAATTGGATAATTATTCTACCCAGGAATTAGGGAAA
ACAATTGTCTATCTGGATGGCTCCTCTCAATCATGCCGCTTTAGAGAATGCAACATGGGC
AACCTGATTTGTGATGCAATGATTAACAACAACCTGAGACACACCGATGAAATGTTCTGG
AACCACGTATCCATGTGCATTTTAAATGGAGGTGGTATCCGGTCGCCCATTGATGAACGC
AACAATGGCACAATTACCTGGGAGAACCTGGCTGCTGTATTGCCCTTTGGAGGCACATTT
GACCTAGTCCAGTTAAAAGGTTCCACCCTGAAGAAGGCCTTTGAGCATAGCGTGCACCGC
TACGGCCAGTCCACTGGAGAGTTCCTGCAGGTGGGCGGAATCCATGTGGTGTATGATCTT
TCCCGAAAACCTGGAGACAGAGTAGTCAAATTAGATGTTCTTTGCACCAAGTGTCGAGTG
CCCAGTTATGACCCTCTCAAAATGGACGAGGTATATAAGGTGATCCTCCCAAACTTCCTG
GCCAATGGTGGAGATGGGTTCCAGATGATAAAAGATGAATTATTAAGACATGACTCTGGT
GACCAAGATATCAACGTGGTTTCTACATATATCTCCAAAATGAAAGTAATTTATCCAGCA
GTTGAAGGTCGGATCAAGTTTAGCGGTGGAGGAAGCCTGGAAGTTCTGTTCCAGGGGCCC
CATCATCACCATCACCACTAA

Nluc-membrane-bound CD73

ATGAACTCCTTCTCCACAAGCGCCTTCGGTCCAGTTGCCTTCTCCCTGGGCCTGCTCCTG
GTGTTGCCTGCTGCCTTCCCTGCCCCAGTCTTCACACTCGAAGATTTCGTTGGGGACTGG
CGACAGACAGCCGGCTACAACCTGGACCAAGTCCTTGAACAGGGAGGTGTGTCCAGTTTG
TTTCAGAATCTCGGGGTGTCCGTAACTCCGATCCAAAGGATTGTCCTGAGCGGTGAAAAT
GGGCTGAAGATCGACATCCATGTCATCATCCCGTATGAAGGTCTGAGCGGCGACCAAATG
GGCCAGATCGAAAAAATTTTTAAGGTGGTGTACCCTGTGGATGATCATCACTTTAAGGTG
ATCCTGCACTATGGCACACTGGTAATCGACGGGGTTACGCCGAACATGATCGACTATTTC
GGACGGCCGTATGAAGGCATCGCCGTGTTCGACGGCAAAAAGATCACTGTAACAGGGACC
CTGTGGAACGGCAACAAAATTATCGACGAGCGCCTGATCAACCCCGACGGCTCCCTGCTG
TTCCGAGTAACCATCAACGGAGTGACCGGCTGGCGGCTGTGCGAACGCATTCTGGCGGGC
TCGAGCGGAtgggagcttacgattttgcacaccaacgacgtgcacagccggctggagcag
accagcgaggactccagcaagtgcgtcaacgccagccgctgcatgggtggcgtggctcgg
ctcttcaccaaggttcagcagatccgccgcgccgaacccaacgtgctgctgctggacgcc
ggcgaccagtaccagggcactatctggttcaccgtgtacaagggcgccgaggtggcgcac
ttcatgaacgccctgcgctacgatgccatggcactgggaaatcatgaatttgataatggt
gtggaaggactgatcgagccactcctcaaagaggccaaatttccaattctgagtgcaaac
attaaagcaaaggggccactagcatctcaaatatcaggactttatttgccatataaagtt
cttcctgttggtgatgaagttgtgggaatcgttggatacacttccaaagaaacccctttt
ctctcaaatccagggacaaatttagtgtttgaagatgaaatcactgcattacaacctgaa
gtagataagttaaaaactctaaatgtgaacaaaattattgcactgggacattcgggtttt
gaaatggataaactcatcgctcagaaagtgaggggtgtggacgtcgtggtgggaggacac
tccaacacatttctttacacaggcaatccaccttccaaagaggtgcctgctgggaagtac
ccattcatagtcacttctgatgatgggcggaaggttcctgtagtccaggcctatgctttt
ggcaaatacctaggctatctgaagatcgagtttgatgaaagaggaaacgtcatctcttcc
catggaaatcccattcttctaaacagcagcattcctgaagatccaagcataaaagcagac
attaacaaatggaggataaaattggataattattctacccaggaattagggaaaacaatt
gtctatctggatggctcctctcaatcatgccgctttagagaatgcaacatgggcaacctg
atttgtgatgcaatgattaacaacaacctgagacacaccgatgaaatgttctggaaccac
gtatccatgtgcattttaaatggaggtggtatccggtcgcccattgatgaacgcaacaat
ggcacaattacctgggagaacctggctgctgtattgccctttggaggcacatttgaccta
gtccagttaaaaggttccaccctgaagaaggcctttgagcatagcgtgcaccgctacggc
cagtccactggagagttcctgcaggtgggcggaatccatgtggtgtatgatctttcccga
aaacctggagacagagtagtcaaattagatgttctttgcaccaagtgtcgagtgcccagt
tatgaccctctcaaaatggacgaggtatataaggtgatcctcccaaacttcctggccaat
ggtggagatgggttccagatgataaaagatgaattattaagacatgactctggtgaccaa
gatatcaacgtggtttctacatatatctccaaaatgaaagtaatttatccagcagttgaa
ggtcggatcaagttttccacaggaagtcactgccatggaagcttttctttaatatttctt
tcactttgggcagtgatctttgttttataccaatag

Nluc between serine^{520}-isoleusine^{525} of membrane-bound CD73

atgtgtccccgagccgcgcgggcgcccgcgacgctactcctcgccctgggcgcggtgctg
tggcctgcggctggcgcctgggagcttacgattttgcacaccaacgacgtgcacagccgg

ctggagcagaccagcgaggactccagcaagtgcgtcaacgccagccgctgcatgggtggc
gtggctcggctcttcaccaaggttcagcagatccgccgcgccgaacccaacgtgctgctg
ctggacgccggcgaccagtaccagggcactatctggttcaccgtgtacaagggcgccgag
gtggcgcacttcatgaacgccctgcgctacgatgccatggcactgggaaatcatgaattt
gataatggtgtggaaggactgatcgagccactcctcaaagaggccaaatttccaattctg
agtgcaaacattaaagcaaaggggccactagcatctcaaatatcaggactttatttgcca
tataaagttcttcctgttggtgatgaagttgtgggaatcgttggatacacttccaaagaa
acccctttctctcaaatccagggacaaatttagtgtttgaagatgaaatcactgcatta
caacctgaagtagataagttaaaaactctaaatgtgaacaaaattattgcactgggacat
tcgggttttgaaatggataaactcatcgctcagaaagtgaggggtgtggacgtcgtggtg
ggaggacactccaacacatttctttacacaggcaatccaccttccaaagaggtgcctgct
gggaagtacccattcatagtcacttctgatgatgggcggaaggttcctgtagtccaggcc
tatgcttttggcaaatacctaggctatctgaagatcgagtttgatgaaagaggaaacgtc
atctcttcccatggaaatcccattcttctaaacagcagcattcctgaagatccaagcata
aaagcagacattaacaaatggaggataaaattggataattattctacccaggaattaggg
aaaacaattgtctatctggatggctcctctcaatcatgccgctttagagaatgcaacatg
ggcaacctgatttgtgatgcaatgattaacaacaacctgagacacaccgatgaaatgttc
tggaaccacgtatccatgtgcatttaaatggaggtggtatccggtcgcccattgatgaa
cgcaacaatggcacaattacctgggagaacctggctgctgtattgccctttggaggcaca
tttgacctagtccagttaaaaggttccaccctgaagaaggcctttgagcatagcgtgcac
cgctacggccagtccactggagagttcctgcaggtgggcggaatccatgtggtgtatgat
ctttcccgaaaacctggagacagagtagtcaaattagatgttctttgcaccaagtgtcga
gtgcccagttatgaccctctcaaaatggacgaggtatataaggtgatcctcccaaacttc
ctggccaatggtggagatgggttccagatgataaaagatgaattattaagacatgactct
gGTGACCGTGTCTTCACACTCGAAGATTTCGTTGGGGACTGGCGACAGACAGCCGGCTAC
AACCTGGACCAAGTCCTTGAACAGGGAGGTGTGTCCAGTTTGTTTCAGAATCTCGGGGTG
TCCGTAACTCCGATCCAAAGGATTGTCCTGAGCGGTGAAAATGGGCTGAAGATCGACATC
CATGTCATCATCCCGTATGAAGGTCTGAGCGGCGACCAAATGGGCCAGATCGAAAAAATT
TTTAAGGTGGTGTACCCTGTGGATGATCATCACTTTAAGGTGATCCTGCACTATGGCACA
CTGGTAATCGACGGGGTTACGCCGAACATGATCGACTATTTCGGACGGCCGTATGAAGGC
ATCGCCGTGTTCGACGGCAAAAAGATCACTGTAACAGGGACCCTGTGGAACGGCAACAAA
ATTATCGACGAGCGCCTGATCAACCCCGACGGCTCCCTGCTGTTCCGAGTAACCATCAAC
GGAGTGACCGGCTGGCGGCTGTGCGAACGCATTCTGGCGGATatcaacgtggtttctaca
tatatctccaaaatgaaagtaatttatccagcagttgaaggtcggatcaagttttccaca
ggaagtcactgccatggaagcttttctttaatatttctttcactttgggcagtgatcttt
gttttataccaatag

Soluble mouse CD73

ATGGTGAGTGCCATAGTATTATATGTATTGTTAGCGGCTGCCGCACACTCGGCGTTCGCG
GCGGGGTCTCATCACCACCACCACCACCACCATCATCATCTCGAAGTCCTATTTCAAGGC
CCCGGAGGCGGGGGTAGCTGGGAGCTAACTATCCTGCATACGAACGACGTGCATTCCCGC
TTAGAGCAGACATCTGATGATTCCACTAAGTGTCTCAACGCCAGCCTGTGCGTCGGAGGA
GTTGCACGATTGTTCACAAAAGTCCAACAGATTAGGAAGGAGGAGCCGAATGTGCTTTTT
CTAGACGCAGGAGACCAGTATCAAGGAACCATATGGTTCACCGTGTATAAAGGACTTGAA

GTGGCCCATTTTATGAACATCCTGGGGTACGACGCAATGGCGTTAGGTAATCATGAGTTT
GATAACGGTGTCGAAGGACTAATAGACCCGCTCCTAAGAAATGTTAAATTCCCAATCCTG
TCAGCTAACATCAAAGCTCGTGGTCCTTTGGCGCACCAGATAAGTGGGTTGTTCCTGCCA
TCTAAAGTTCTATCGGTCGGGGGTGAAGTTGTTGGCATTGTTGGTTATACATCTAAGGAG
ACTCCATTTCTATCAAACCCGGGCACGAATTTGGTTTTCGAAGATGAAATATCTGCCCTG
CAGCCCGAGGTGGACAAGCTAAAAACCTTAAACGTCAACAAGATAATCGCACTTGGTCAC
TCGGGATTTGAAATGGACAAACTCATTGCCCAAAAGGTAAGGGGGGTGGATATCGTAGTT
GGGGGTCACAGTAATACATTCTTGTACACCGGGAACCCTCCCAGCAAAGAGGTGCCTGCG
GGCAAGTACCCATTTATCGTGACTGCTGATGATGGGCGGCAAGTGCCTGTGGTGCAGGCG
TATGCATTCGGTAAATATCTTGGTTACCTTAAAGTCGAATTTGACGATAAGGGAAACGTA
ATCACTAGCTACGGCAATCCGATCCTCCTCAATAGCTCCATACCCGAGGATGCTACGATA
AAGGCCGACATTAATCAGTGGCGAATAAAATTAGACAATTATAGTACTCAGGAGCTGGGT
CGTACCATTGTGTACCTGGATGGTTCTACTCAAACCTGTAGATTTCGCGAGTGCAATATG
GGGAACTTGATATGCGACGCCATGATAAATAATAACCTGCGTCATCCCGATGAAATGTTC
TGGAACCATGTGTCGATGTGTATCGTCAACGGAGGCGGGATTCGGTCTCCCATTGACGAA
AAAAATAACGGTACTATTACATGGGAAAATCTGGCTGCTGTTTTACCGTTTGGGGGCACG
TTCGACCTCGTCCAGTTGAAAGGGTCGACCTTAAAGAAGGCTTTTGAACATTCCGTCCAT
AGGTACGGTCAGTCAACAGGCGAGTTCTTGCAAGTAGGAGGCATACACGTAGTCTACGAT
ATTAACCGTAAGCCTTGGAATAGAGTCGTACAACTTGAGGTTCTTTGCACAAAGTGTCGC
GTCCCGATTTATGAACCACTTGAAATGGACAAAGTATACAAGGTTACGTTACCTTCATAC
CTCGCAAATGGAGGTGATGGATTTCAAATGATTAAGGACGAGCTTCTCAAGCACGATAGC
GGCGATCAAGATATCTCGGTGGTTTCAGAGTATATTAGTAAAATGAAGGTAGTATATCCT
GCAGTTGAAGGCCGAATCAAATTCTCCTGA

CD73, Nluc, Linkers, His-tags